# The timing of prograde metamorphism in the Garhwal Himalaya, India

## Thesis

# The timing of prograde metamorphism in the Garhwal Himalaya, India

by

Christophe Iain Prince B.A (Hons) (Cantab)

A thesis accepted for the degree of Doctor of Philosophy

at the

Department of Earth Sciences, Open University

**June 1999**

# The timing of prograde metamorphism in the Garhwal Himalaya, India

by

Christophe Iain Prince B.A (Hons) (Cantab)

A thesis accepted for the degree of Doctor of Philosophy

at the

Department of Earth Sciences, Open University

**June 1999**

# Acknowledgements

First of all I would like to thank my parents who made it possible for me to do this thesis and my brother who stopped me walking off into the darkness way before then. To Derek and Nigel sorry about the first draughts and thankyou for all your time and patience. By the way Derek "I'll get this round and the next and the ....". Randy and Simon thanks for wading through it all and the doorstops are on the way. A big high to the Himalayan crowd; Mike, Elric, Gavin, Helen, and Tom. Especial thanks to Gavin, Helen and Tom for enjoyable and occasionally fruitful discussions. Remember that the view is just once but stomach flora are forever. Cheers to Wheeler-ji, it's been a long wait but here it is. Special thanks to Judy for all her help - may the law be with you. Jan see you over a beer sometime. Talat and all at the Wadia institute thanks for the help and sorry about the lost pots. Everyone in the Ghastoli "no not Ghastoli" Military camp - thanks for the welcome.

Big thanks to Chris Vincze my erstwhile companion high in the hills "Ek chai chini nahi". Rhiannon for putting up with the roads. Also to all fellow PhDers in the department especially Sarah. Louise, one day I will return all those pens and no I didn't take the mug. Thanks to Alison for the luxury Indian breaks and company.

Felix Oberli and all at ETHZ specially Robert, Wolfgang and Giulio for the welcome they showed me during my brief stay in the bowels of Zurich's hillside and Ayse for sustaining me when I popped out into the light.

The Badgers in their various guises – it's time for the parade hurry up. Phil are you still there? Mabs, Peter and all in the labs - run away be free. Andy "probe man" Tindle and John "XRF" Watson thanks. All in the thin section room - really they were *all* necessary. Finally and not least thanks to Flo for being there throughout and the London crowd for keeping me sane in the last few months.

# Abstract

The Himalaya provide the most significant example of present-day orogenesis and consequently have been extensively studied to gain an understanding of the principle controls on the response of the crust to continental collision. However, our understanding of the prograde metamorphic evolution of the orogen remains poor. This thesis builds on recent advances in the study of PTt paths, using garnet chronometry, to better constrain the thermobarometric evolution of the Garhwal section of the Indian Himalaya. Results show that the metamorphic core of the Garhwal Himalaya – the High Himalayan Crystalline Series (HHCS) - records a complex, continuous prograde thermal history from initial burial ~10 Ma after continental collision at ~50 Ma, up to cooling and exhumation at 20-16 Ma BP. PT paths obtained from garnets indicate that prograde metamorphism occurred during crustal thickening and "peak" thermobarometric estimates show that the presently exposed HHCS records temperatures of ~700 °C throughout the section accompanied by a decrease in pressures from ~13 kbar at the base to ~6 kbar at the top. However, chronometric information shows that reorganisation of the orogenic wedge resulted in the juxtaposition of rocks which attained different PT conditions at different times and places during orogenesis. Additionally, temperatures were sufficient in the early stages of orogenesis for the development of small leucogranitic bodies to form by fluid-present melting. The HHCS in Garhwal, therefore, cannot be considered as a single coherent crustal slice. Furthermore, the continued reorganisation of the orogen since collision also means the heat generation within the overthickened orogenic wedge is sufficient for anatexis of the crust to form the well-studied melts intruding the upper levels of the HHCS.

However, interpretation of the results is complicated by the isotopic systematics involved in garnet chronometry and by the role of small inclusions with high concentrations of the critical elements of– Nd, Pb, Sr. The systematics of the Sm-Nd

system in garnet has been investigated by a comparison of concentrations obtained *in-situ* by LA-ICP-MS with those obtained by isotope dilution. Results show that while such inclusions can pose a problem to chronometry, their effects can be identified and constrained.

In the course of such work data was obtained on the trace-element zonation in garnet, which acts as a monitor of the chemical evolution of the rock. While the controls on such zonation are still poorly understood the data presented here emphasise the importance of fractionation of the chemical system from which the garnet grows by both accessory minerals and by garnet itself. Furthermore, different minerals fractionate distinctly different elements this can be recognised in the trace-element zonation preserved in garnet.

# Table of contents

# Table of figures

## Chapter 1



## Chapter 2



## Chapter 3



## Chapter 4

## Chapter 5



## Chapter 6



## Chapter 7



## Chapter 8



## Appendix A

# Table of tables

## Chapter 1



## Chapter 3



## Chapter 4



## Chapter 5



## Chapter 6



## Appendix B



## Appendix H

# Chapter 1 - Introduction

## *1.1 Introduction*

The redistribution of heat within the Earth is the main driving force behind plate tectonic processes (Turcotte and Schubert, 1982). As such knowledge of the pressure and temperature distribution within the Earth's crust, particularly during orogenesis, is essential to quantifying plate tectonics. While the broad processes involved in the thermal evolution of the oceanic lithosphere are rather simple and increasingly well understood (Parsons and McKenzie, 1978) the processes controlling the thermal evolution of the continents are less well-defined. In the continents the exposure of metamorphic rocks which have undergone high pressures and temperatures testifies to the movement of heat and mass within the continental crust. The petrological study of such rocks has led to an understanding of the processes involved and, in particular, the importance of continental collision. However, numerical modelling of simple collision emphasises the need to obtain not only pressure and temperature estimates but also time information (e.g. England and Thompson, 1984). This is of particular importance within the Himalaya, an ongoing example of a continent-continent collision which can be used to understand ancient collisional belts. Constraining different models of the evolution of the Himalayan belt has depended critically upon such time information (e.g. Hubbard and Harrison, 1989; Sorkhabi and Stump, 1993; Harrison et al., 1997b). However, due to the nature of the chronometers used much of the time information obtained is difficult to relate to the thermal history or has been restricted to the cooling of the belt and magmatic processes. Therefore our understanding of the early thermal structure of the belt is still poor.

This thesis aims to build upon recent advances in garnet chronometry, an approach which allows us to obtain time information on prograde processes and, critically, relate

timing to pressure and temperature information obtained from the garnet and other major minerals (Vance and O'Nions, 1990; Vance, 1995). Through such techniques, combined with structural and traditional metamorphic studies of the belt, a better understanding of the thermotectonic evolution of the Himalayan orogeny can be obtained.

## *1.2 Chapter format*

This chapter outlines the general geological setting of the Himalaya and then focuses upon the metamorphic belt with a review of the current state of knowledge concerning the different aspects of Himalayan tectonics. Key questions that remain open will be identified and briefly discussed. This chapter concludes with an outline of the structure of the thesis.

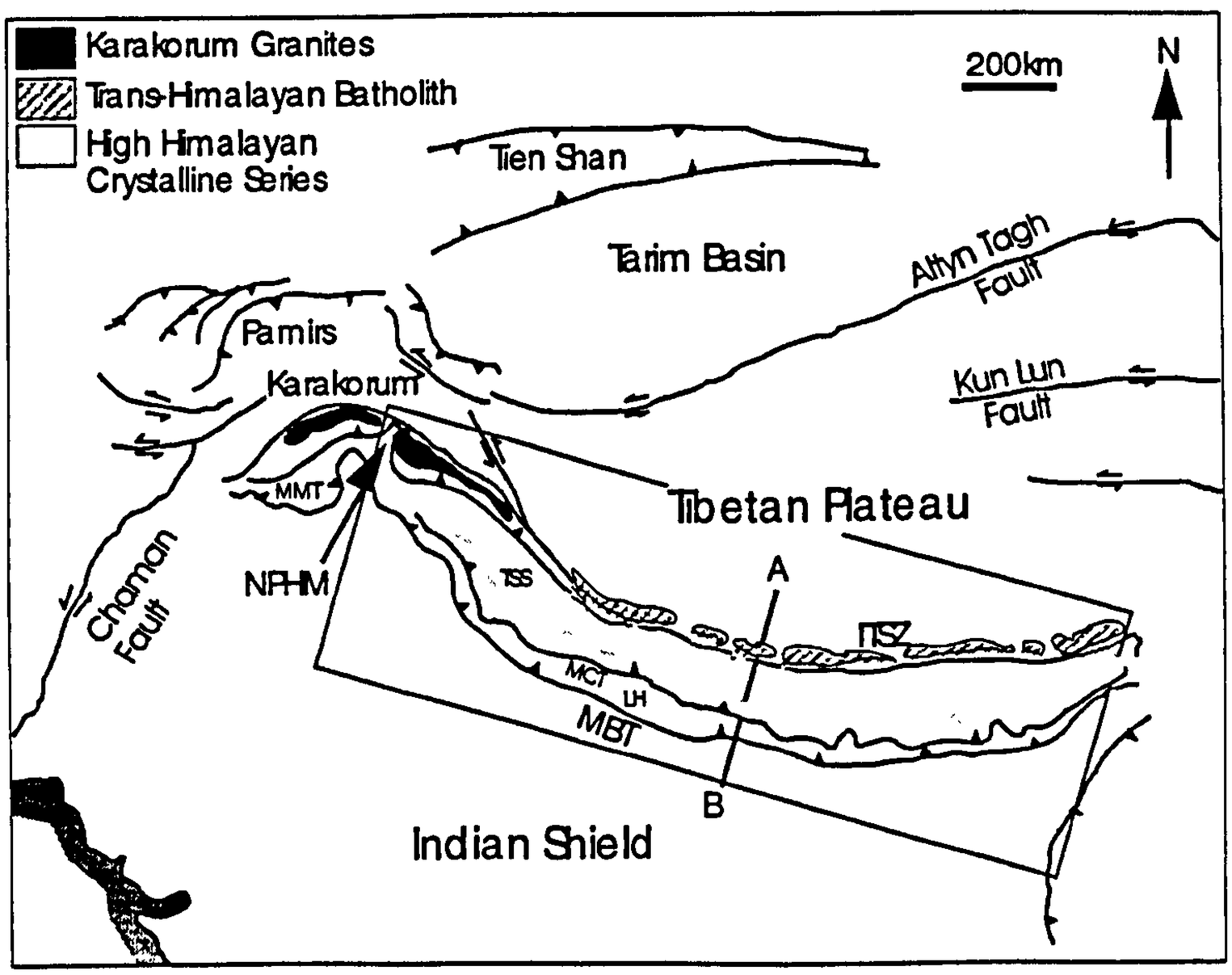


*Figure 1.1 Map illustrating the large-scale tectonic features of the Himalayan orogen and Tibetan plateau, after Massey (1994). NPHM= Nanga Parbat Haramosh Massif; MMT= Main Mantle Thrust; LH= Lesser Himalayas; TSS=Tibetan Sedimentary Series; MCT=Main Central Thrust; MBT=Main Boundary Thrust; ITSZ=Indus Tsangpo Suture Zone; A-B indicates the line of section in Figure 1.3*

## 1.3 Geological setting

The following section gives an overview of the geodynamic framework of the Indian-Asian collision prior to the onset of continental collision, discusses our knowledge of the timing of collision and looks at the extent of, and constraints on, deformation since collision.

### 1.3.1 The Himalayan Belt

The Himalaya are considered a classic example of continent-continent collision. Orogenesis is ongoing and this mountain belt represents an ideal area for the study of thermotectonic processes. The 2500km chain extends from south-eastern China in the east to northern Pakistan in the west and is part of the Alpine-Himalayan chain which stretches all the way to Europe (Le Fort, 1975). The chain delineates the boundary between various fragments of Gondwana and the southern margin of Laurasia.

To the north of the Himalaya lies the Tibetan plateau, comprised of at least three microplates which had already accreted to Eurasia by the time the closure of the Neo-Tethys resulted in the collision of the Indian plate. The remnants of the Neo-Tethys are preserved in the form of flysch, mollase and fragmented ophiolites in the Indus Tsangpo Suture Zone (ITSZ) (Figure 1.3) (Gansser, 1964). The Tethyan Sediments on the southern side of the ITSZ are recognised as the passive margin shelf deposits of the Indian Plate (Gaetani and Garzanti, 1991) which have been folded and faulted during the collision. The Trans Himalayan batholith found to the North of the ITSZ (Figure 1.1) form a 2000km long belt of Andean-type magmatism, the geochemistry and timing of which suggest association with the northward subduction of the Tethyan oceanic lithosphere (Debon et al., 1986). The continent-continent collision that resulted in the Himalaya followed the closure of the Tethys.

### 1.3.2 Timing of collision

The timing of collision and closure of the Tethys is still poorly constrained, in part, due to difficulty in defining the meaning of "closure". Closure is, in the strictest sense, the first contact between continental lithosphere from either side. It is therefore useful to separate the collision into several stages; initiation of collision (indicated by plate bending and changes in sedimentation), ocean-continent transition (indicated by sediment type) and final suturing (locking of the collision zone). Some of the literature has been summarised in Table 1.1 and published timings have been assigned to one of the three possible stages of collision. Where the interpretation is not explicitly stated in the literature it has been assigned to one of the above options.

One of the principal ways of identifying the collision is ophiolite emplacement and changes in sedimentation history. In Ladakh, Searle et al. (1997a) showed that the initiation of collision, as demonstrated by ophiolite emplacement, occurred as early as the Late Cretaceous and that the transition from oceanic to continental sedimentation occurred at 54-50 Ma. However, Gaetani and Garzanti (1991) concluded that collision-related sedimentation started in Zanskar at 50.7 Ma and terminated at 49-45.7 Ma: later than the timing proposed by Searle et al. (1997a). Further to the North in Waziristan, Pakistan, Beck et al. (1995) showed that sediments from the trench and accretionary prism were first thrust onto the passive continental shelf between 65-55 Ma with suturing complete by 49 Ma. However, Rowley (1996) suggests that the early initiation age obtained by Beck et al. (1995) relates to an intra-oceanic collision predating final closure of the Neo-Tethys proper.

At Malla Johar in Nepal the initiation of collision is poorly dated to between 49 Ma and 41.3 Ma (Rowley, 1996). In the Everest area the youngest unequivocal oceanic sediments suggest that the ocean was still extant sometime in the Lutetian (49-41.4 Ma) and perhaps later (Rowley, 1996). More recent work based on the subsidence history in

*Table 1 Summary of closure timings from different areas and techniques. Areas are ordered from the West to the East with estimates based on non-Himalayan samples last. Where possible the timing has been placed in one of four categories; initiation, ocean-continent transition, continent collision and suturing. Where no timing for suturing has been suggested the implied minimum age is indicated in brackets. APWP = apparent polar wander paths. Mag. Anomaly = magnetic anomaly methods. Sediment = all sedimentological methods.*

| *Author* | *Method* | *Area* | *Initiation* | *Ocean-Continent Transition* | *Continent collision* | *Suturing* |
|---|---|---|---|---|---|---|
| (Beck et al., 1995) | Sediment | Pakistan West of NP | 66-55.5 | | | 49 |
| (Searle et al., 1997a) | Structural sediment | Ladakh | Cretaceous | <54 | | (<54) |
| (Rowley, 1996) | Sediment | Zanskar | 50.7 | | | 49-45.7 |
| (Rowley, 1996) | Sediment | Mala Johar | 49-41.3 (36.9) | | | (<49) |
| (Rowley, 1996) | Sediment | Everest | | <49-41.4 | | (<49) |
| (Rowley, 1998) | Sediment | Everest (Zephure) | <45.8 | | | (<45.8) |
| (Besse et al., 1984) | APWP Mag. Anomaly | E. Himalaya- S. Tibet | 53-47 | | | (<47) |
| (Rowley, 1996) | Sediment | Nagaland | | <41.4-36.9 | | (<41.4) |
| (Patriat and Achache, 1984) | Mag. Anomaly | N. A. | | | 50 | 44 |
| (Klootwijk et al., 1992) | | N. A. | | | 55* | |
| (Patzelt et al., 1996) | APWP | N. A. | 65-60 | | | 55-50 |

** Klootwijk et al. (1992) use the change in northward movement to infer the suturing at this stage. In the opinion of the author such rate changes do not constrain the termination of deformation in the ITSZ*

the Zhepure mountain of the Everest section shows that there is no accelerated subsidence up to the youngest rocks of 45.8 Ma and that, therefore, collision must post-date that age (Rowley, 1998). Much further to the east, beyond the eastern syntaxis in Nagaland, Cretaceous to early Eocene limestones are overlain by poorly dated coarse clastics with an age at least as old as middle Eocene i.e. 41.4-36.9 Ma. (Rowley, 1996) concludes therefore that collision was diachronous across the range commencing in the Northeast (<52 Ma) and occurring later in the East (41 Ma).

A more indirect approach which was the first used to date the collision has been paleomagnetic studies of oceanic magnetic anomalies and sediments from either side of the suture zone. Using ocean floor magnetic anomalies, Patriat and Achache (1984) placed the collision between anomalies 22 and 21, ~48-50 Ma based on the irregularity of India's motion at that time. Alternatively, Besse et al. (1984) combined apparent polar wander paths (APWP) obtained from southern Tibetan continental sediments with the data of Patriat and Achache (1984), suggesting the final suturing and locking of the ITSZ between 53 and 47 Ma. More recent APWP determined from paleomagnetic studies of Indian ocean sediments and basement rocks (Klootwijk et al., 1992) suggest that the northward drift of the Indian oceanic lithosphere slowed at ~55 Ma. Combined with paleomagnetic studies from the continents, these data led these authors to conclude that initial collision in the Northwest occurred before the K/T boundary. Patzelt et al. (1996) also used paleomagnetics on southern Tibetan sediments and, by comparison with the Lhasa block to the North, calculated that contact was established by 65-60 Ma and suturing was complete by 55-50 Ma.

Interestingly the ages obtained in the far west of the Himalaya (Beck et al., 1995) span the entire range obtained by all other collision ages including those obtained in the far East by Besse et al. (1984). Paleomagnetic studies, relying in part on magnetic stripes in the ocean floor (Besse et al., 1984; Patriat and Achache, 1984), suggest ages for

suturing around 50 Ma, whereas paleomagnetic studies carried out on sediments from the seafloor and continents (Klootwijk et al., 1992; Patzelt et al., 1996) suggest slightly older ages for suturing of 55-50 Ma and much older ages for the initiation of collision ~65 Ma. The difference between initiation of collision, ocean closure and suturing may account for some of the timing variation. Sedimentological methods will depend upon the local geometry at the time of collision and may respond first to initiation of collision whilst APWP and determinations based on overlying sediments will take into account some shortening in the form of crustal deformation. In addition, calculations based on plate-tectonic scale processes will measure the response to plate stresses such as slab pull which may include significant time periods of absorbed deformation on the scale of the study. Taking into account these factors the data strongly suggest the accretion of some material as early as the K/T boundary, with the transition from oceanic to continental sedimentation around 55-50 Ma and the lock up of the ITSZ by 49 Ma.

While Rowley (1996; 1998) suggests that the sediments of the Everest section record later initiation of collision and that there is some diachroneity along the orogen, the extent of such studies is still not large enough to draw strong conclusions especially given the poor quality data to the east of the orogen.

### 1.3.3 Post-collision

Whilst the northward movement of the Indian plate slowed at 50 Ma it did not stop and continues today at a rate of 58±4 mm/yr (Bilham et al., 1997). Assuming collision occurred at 50 Ma Patriat and Achache (1984) estimated that some 2500km of shortening between the Asian and Indian cratons is required. The distribution of this shortening since collision has been hotly debated and various mechanisms for achieving it have been proposed. These include: underthrusting of the Indian crust beneath Asia (e.g. Powell, 1986); homogenous thickening of the Asian lithosphere (e.g. England and Houseman, 1988); eastwards extrusion of the Asian lithosphere along major strike-slip

faults in Tibet (Figure 1.1) (e.g. Molnar and Tapponnier, 1975); or movement on thrust faults within the Himalaya (e.g. Coward and Butler, 1985; Searle, 1986).

Seismic anisotropy measurements (Hirn et al., 1995) and seismic reflection profiles (Zhao et al., 1993) suggest that there has been some underthrusting of the Indian continental lithosphere to the South of the ITSZ. Since paleomagnetic studies by Lin and Watts (1988) suggest that some 2000±800 km of movement has occurred between the Lhasa block and Asia (a terrane that was accreted before the collision of India), significant shortening over the Tibetan Plateau can be inferred. Alternatively, Tapponier and Molnar (1976) suggested that lateral extrusion of Tibet along strike-slip faults could absorb some of the northward movement. Finally, estimates of the northward movement absorbed across the Himalaya vary from 1500 km (Patzelt et al., 1996), to 400±400 km (Besse et al., 1984), accommodated by underthrusting along major faults within the Himalaya (Coward and Butler, 1985; Searle, 1986) and crustal thickening to the South of the suture zone.

## *1.4 Metamorphism and deformation in the Himalaya*

The accommodation of this deformation resulted in the burial, metamorphism and southward thrusting of the High Himalayan Crystalline Series (HHCS), the metamorphic core of the Himalaya. A simple, schematic, picture of faulting and the units within the Himalaya is shown in Figure 1.2 and Figure 1.3. A significant proportion of the deformation accommodated by southward thrusting is attributed to the Main Central Thrust (MCT) which juxtaposes the HHCS over Lesser Himalayan rocks (Ahmad et al., In press). The HHCS is bound to the North by a normal fault system known as the Southern Tibetan Detachment System (STDS) which places the weakly or unmetamorphosed Tethyan Sedimentary Series (TSS) on top of high-grade metasediments (Burchfiel and Royden, 1985; Herren, 1987; Burchfiel et al., 1992; Dransfield, 1995).

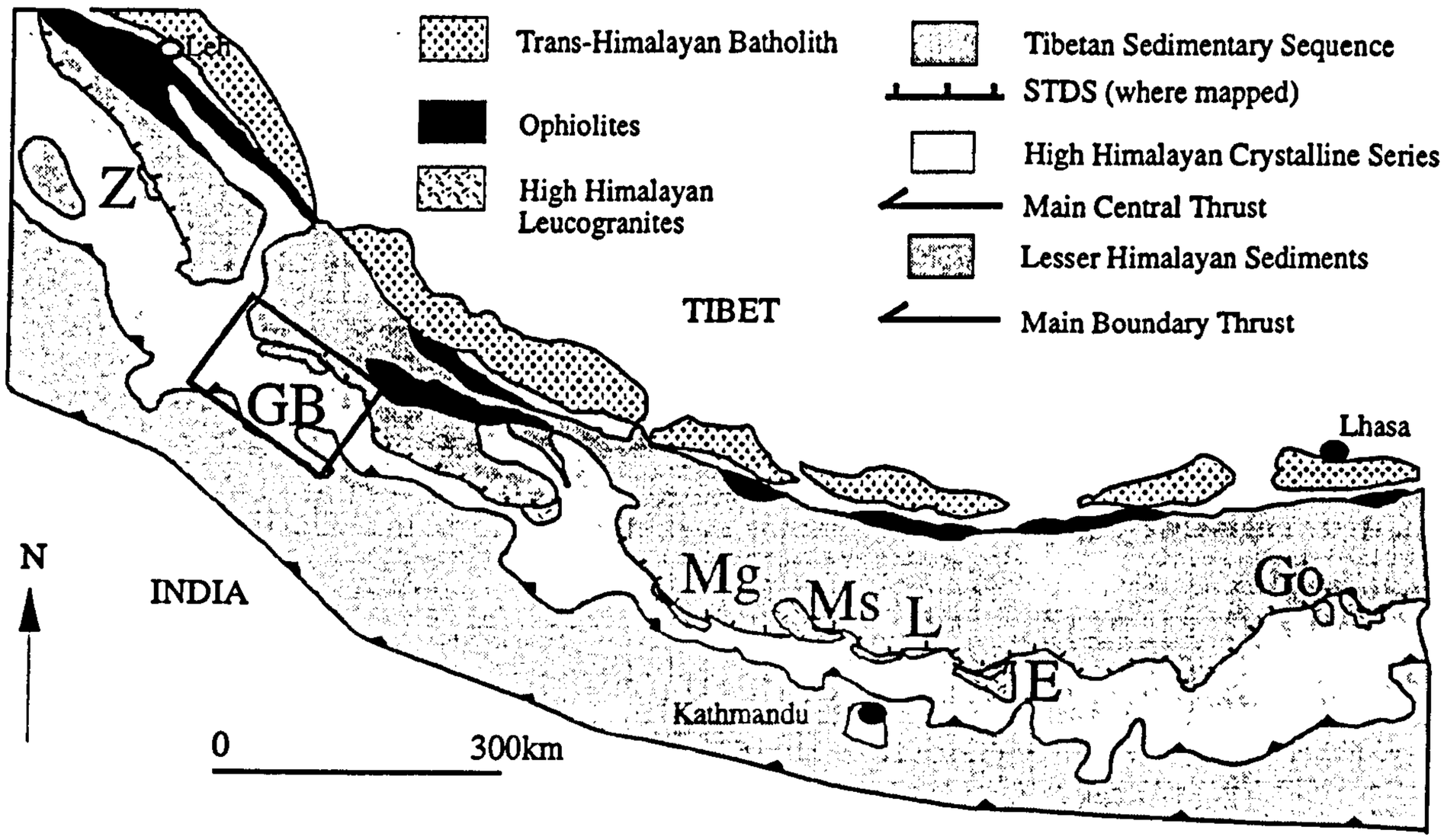


*Figure 1.2 Map of the Himalayan belt showing the principal lithotectonic units and the positions of studied areas. Z= Zanskar; GB= Garhwal-Badrinath; Mg=Mustang; MS= Manaslu; L= Langtang; E= Everest; Go=Gophu La*

Below the HHCS and Lesser Himalaya, and south of the MCT, lies the Main Boundary Thrust which places the Lesser Himalaya over the clastic rocks of the Himalayan foredeep molasse (Meigs et al., 1995) which are in turn thrust to the South along the Main Frontal Thrust.

These fault systems (ITSZ, STDS, MCT, Main Boundary Thrust and Main Frontal Thrust) and tectonic units (Tethyan Sedimentary Series, HHCS, Lesser Himalaya) can be traced almost the entire length of the Himalaya and form a simple framework for study of the orogen (Figure 1.2 and Figure 1.3).

### 1.4.1 Petrological and structural observations

*High Himalayan Crystalline series*

The HHCS is composed of gneisses, schists, calc-silicates, amphibolites, migmatites and leucogranites. The protolith is thought to be of Late Palaeoproterozoic to Mesoproterozoic age (Ahmad et al., In press) and was either deposited or underwent metamorphism around 550 Ma as shown by $^{87}Sr/^{86}Sr$ errorchrons (Pognante et al., 1990;

Ahmad et al., In press) as well as inherited zircon ages (Pognante et al., 1990; Parrish, 1993).

One of the most intriguing features of the HHCS is an inverted metamorphism whereby the preserved metamorphic field gradients increase up section to the sillimanite + K-feldspar zone. The latter isograd is often accompanied by intruded leucogranite dykes and sills culminating in leucogranitic plutons discontinuously distributed along the chain (Brunel and Kienast, 1986; Pecher, 1989; Inger and Harris, 1992; Metcalfe, 1993; Macfarlane, 1995; Neogi et al., 1998; Vannay and Grasemann, 1998). Exceptions to this occur at either end of the orogen, in Zanskar and Bhutan, where the highest grade rocks occur in the core of the HHCS and are surrounded by lower grade rocks (Pognante and Lombardo, 1989; Searle and Rex, 1989; Davidson et al., 1997). In upper levels of the HHCS, decompression textures are observed along the whole chain (Brunel and Kienast, 1986; Hodges et al., 1992; Inger and Harris, 1992; Hodges et al., 1993; Davidson et al., 1997; Neogi et al., 1998; Vannay and Grasemann, 1998).

The HHCS has a well developed shear fabric generally dipping to the north as well as evidence of syn-kinematic metamorphism such as rotated garnets and staurolite, pressure shadows and mica fish (Brunel and Kienast, 1986; Stäubli, 1989; Inger and Harris, 1992; Davidson et al., 1997; Vannay and Grasemann, 1998). Both the fabrics parallel to the strike of the orogen and the evidence of syn-kinematic metamorphism suggest that mineral assemblages in the HHCS are predominantly a result of the Himalayan orogeny, although relict pre-Himalayan assemblages and fabrics have been suggested Pognante et al. (1990).

*Main Central Thrust Zone*

Below the HHCS proper lies a sequence of crystalline rocks which are generally more deformed and variable in lithology than the HHCS proper. The fault separating the two units is the MCT (Valdiya, 1980). Unfortunately, however, definitions of the MCT

vary from one area to another and structural, metamorphic and lithologic criteria have all been used. Also many authors prefer to describe the MCT as a wide zone of deformation (Hubbard and Harrison, 1989; Searle and Rex, 1989; Metcalfe, 1990; Jain and Manickavasagam, 1993; Macfarlane, 1995; Harrison et al., 1997b) and place the "MCT" proper either at the base or top of the zone.

Taking descriptions of the MCT and MCT zone at face value the metamorphic grade within the zone varies along the length of the Himalaya: e.g. the top of the MCTZ in Nepal is in the sillimanite zone (Hubbard, 1989) and in Garhwal in the staurolite zone (Metcalfe, 1990). Some of the variation may result from post-metamorphic imbrication of portions of the HHCS with the Lesser Himalaya and a cutting of metamorphic isograds across the orogen by late reactivation of the MCT.

However, it appears that there are two consistent features across the whole orogen: (a) that the base of the MCTZ is generally in unmetamorphosed to chlorite zone sediments (Jain and Anand, 1988; Srivastava and Mitra, 1995) and; (b) the MCTZ shows syn-kinematic metamorphism and an inverted metamorphic field gradient (see 1.4.1 Brunel and Kienast, 1986; Jain and Anand, 1988; Pecher, 1989; Stäubli, 1989; Metcalfe, 1993; Macfarlane, 1995; Vannay and Grasemann, 1998).

A recent study by Ahmad et al. (In press) has shown that the MCT in the Garhwal Himalaya corresponds to changes in $\varepsilon_{Nd}$ across the section. Other studies have found a similarly marked variation in both $\varepsilon_{Nd}$ and detrital zircon ages across the MCTZ (France-Lanord et al., 1993; Massey, 1994; Parrish and Hodges, 1996). Ahmad et al. (In press) suggest that the MCT in the Garhwal Himalaya is thus best described as a terrane boundary. Whether this definition is applicable across the whole orogen is not yet clear, but a geochemical definition of the MCT is extremely useful due to the considerable difficulties in comparing field definitions of the MCT.

### 1.4.2 Present day geometry - major structures

Perhaps the most important constraints on the present day geometry of the Himalaya come from the INDEPTH project (e.g. Zhao et al., 1993) in which major crustal reflections are attributed to the basal decollement (Main Himalayan Thrust – MHT) and the STDS. The MCT presently soles onto the MHT and is interpreted to have been the active basal decollement during its movement (Hauck et al., 1998). Such large scale geometric constraints are supplemented by detailed structural studies in the lesser Himalaya (e.g. Srivastava and Mitra, 1994) and in the Tethyan Himalaya (e.g. Ratschbacher et al., 1994).

Also visible on the INDEPTH profiles (Hauck et al., 1998), and bounding the top of the HHCS, the STDS outcrops along the length of the Himalayan orogen and, at its base, places the low-grade sediments of the Tethyan Himalaya against the high-grade metasediments, gneisses and granites of the HHCS (Burg et al., 1984; Burchfiel and Royden, 1985; Herren, 1987; Burchfiel et al., 1992; Coleman, 1996; Edwards et al., 1996; Inger, 1998). Detailed structural studies have shown that it is characterised by top-to-the-north shear indicating normal movement (Burg et al., 1984; Burchfiel and Royden, 1985; Herren, 1987; Burchfiel et al., 1992) although Pecher (1991) emphasised the dextral component of shear associated with it. The STDS may take the form of a series of sharp faults or as a zone of truncated isograds (Herren, 1987). It is certainly not a simple single fault (Searle, 1999) and may be highly variable in character across the orogen. Furthermore, many authors suggest that, prior to normal fault movement, the STDS was an active thrust (Burg and Chen, 1984; Gapais et al., 1992; Patel et al., 1993; Vannay and Hodges, 1996; Dezes et al., 1999).

Such complicated history for the STDS and unclear definition for the MCT often make chronometric constraints on fault movements in the Himalaya difficult to assess. Nevertheless, from the INDEPTH studies it is clear that the two main structures in the

Himalaya are, at present, the MHT (of which the MCT was once a part) and the STDS.

### 1.4.3 Kinematic constraints on deformation

*Main Central Thrust*

Displacement distances on the MCT thrust are poorly constrained but, based on the INDEPTH profile (Hauck et al., 1998) suggested a minimum of ~200 km shortening along the MCT, comparable with the estimates of Schelling (1992) for the Nepal Himalaya but smaller than the 354-421 km estimate of Srivastava and Mitra (1994) for the Garhwal Himalaya. These estimates are all thought of as minima by the various authors and do not include any deformation within the HHCS. Thus displacements during MCT movement may be larger than those proposed and are likely to be in excess of 200 km.

U-Pb data from Nepal place ductile movement on the MCT at 22 Ma (Parrish, 1993), in agreement with ~20 Ma $^{39}Ar/^{40}Ar$ dates on hornblende considered to date peak metamorphism in Garhwal and Nepal (Hubbard and Harrison, 1989; Metcalfe, 1993). In the Marsyandi valley of Nepal, Coleman (1998) obtained monazite ages from a migmatised garnet, staurolite, kyanite bearing pelitic schist in the range 18-21 Ma and inferred this to be the time of metamorphism, pushing the timing of high-temperature metamorphism within the MCTZ to younger ages.

Catlos et al. (1997) suggest that the MCT was reactivated at ~8 Ma indicated by the preservation of 6.5 Ma monazite ages in garnet. Additionally they obtained monazite ages in garnets from the MCTZ between Nepal and Garhwal at 38 Ma and 17.5 Ma which are probably related to early tectonic burial and the main phase of MCT movement - as are the data for the lower part of the HHCS presented in Chapter 4.

MacFarlane (1993) used $^{39}Ar/^{40}Ar$ to date the latest brittle movement on the MCT in Langtang to 2.3 Ma, with ductile movement terminating by 5.8 Ma. Thus the MCT and

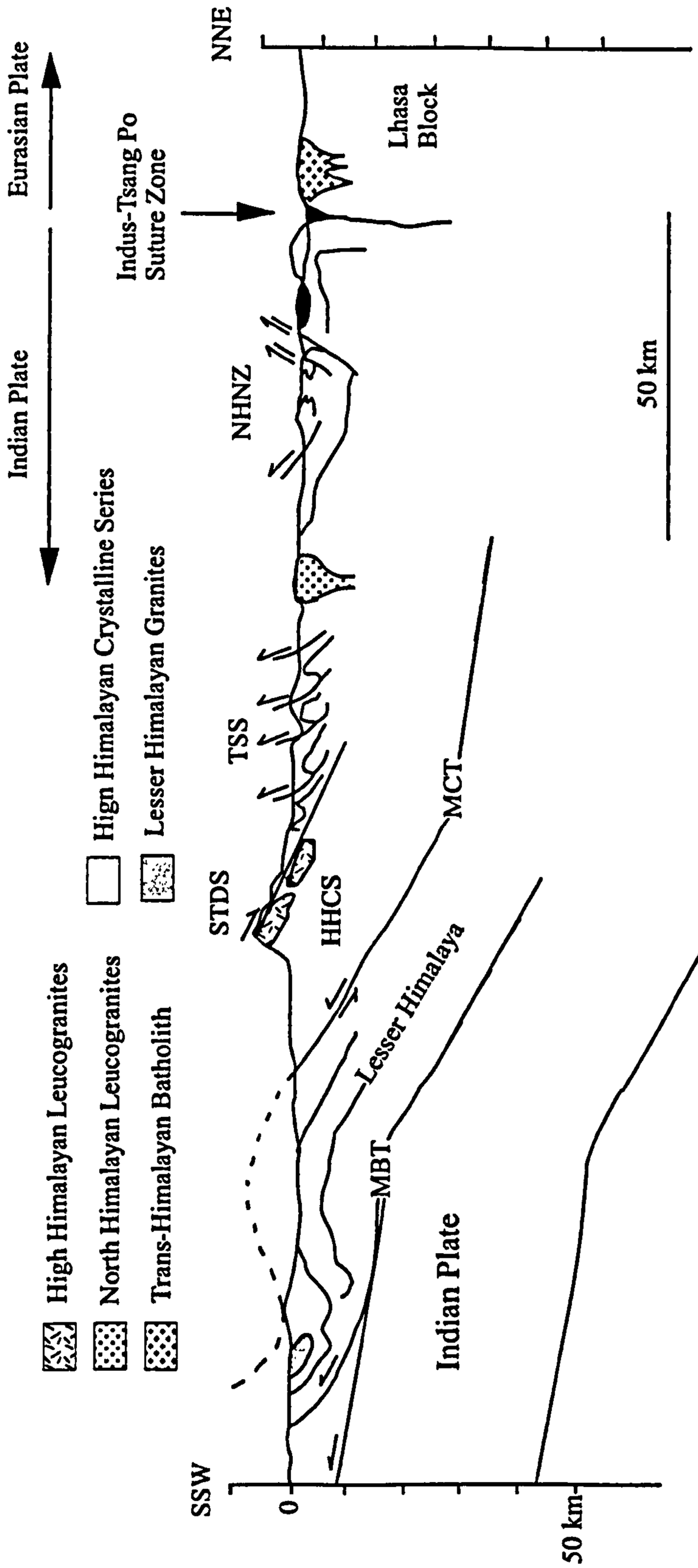


*Figure 1.3 Schematic cross-section across the Central Himalayas (A-B on Figure 1.1), illustrating the major lithotectonic units and fault systems in the Himalaya. Modified after Le Fort et al. (1983) and Molnar et al. (1983). Abbreviations not in text; NHNZ=North Himalayan Nappe Zone*

MCTZ appear to have been active by 22 Ma and intermittently since.

Unfortunately these data do not allow a precise estimate of the slip rate on the MCT. However, displacements on the MCT of >200 km principally between 22 Ma and 8 Ma implies slip rates of ~14 mm/yr. This is, however, likely to be a minimum slip rate for the main period of movement because of the minimum displacement estimates and the probable periods of quiesence. Our detailed knowledge of thrust movements is still poor and while the error on such slip estimates is unknown, it is likely to be large.

*Southern Tibetan Detachment System*

The timing of movement and fault displacements are perhaps better constrained for the STDS than the MCT. In Zanskar Inger (1998) placed the initiation of movement on the STDS prior to 25 Ma. Vance et al. (1998a) confirmed that extensional movement in Zanskar started at ~26 Ma. Other constraints on the movement of the STDS come from crosscutting leucogranites which suggest that STDS movement must have occurred in; Manaslu prior to 19-23 Ma (Harrison et al., 1999); Shisa Pangma predominantly after 17 Ma (Searle et al., 1997b); Khulu Kangri until at least ~13 Ma (Edwards and Harrison, 1997). It must be borne in mind, however, that the STDS is not a simple single fault plane (Searle, 1999) and different strands may have been active at different times and indeed, like the MCT, it may have been reactivated several times.

Whilst movement of the fault may have occurred over a long period of time the work of Hodges et al. (1998), using a combination of U-Pb dating of titanite in a gneiss, xenotime in a sheared sillimanite gneiss and biotite $^{39}Ar/^{40}Ar$ cooling ages for a crosscutting leucogranite, constrained movement on the Qomolangma detachment on the north side of Everest to between 16.7 Ma and 16.4 Ma. This suggests that individual detachments within the system may have been associated with extremely rapid denudation rates of $\geq 8.2\ mma^{-1}$. In Zanskar vertical displacement based on shortening of metamorphic isograds by the fault has been estimated at ~19 km (Herren, 1987).

More recently Dezes et al. (1999) suggest vertical displacements of ~12 km - calculated from relative thermobarometry estimates in the footwall and hangingwall. In Zanskar a minimum constraint on the rate of tectonic denudation can be obtained from the earliest movement at ~25 Ma (Inger, 1998) and termination at ~20 Ma (Dezes et al., 1999), resulting in tectonic denudation at rates of >2.4 $mma^{-1}$.

Summarising the available data it appears that the STDS was active as early as 25 Ma and continues to be active today, with the main phase between 23-17 Ma. The rates of displacement appear to be extremely rapid for individual segments of the fault and studies of the thermal response of the HHCS to exhumation suggest that cooling in the crust was delayed relative to the tectonic denudation (see 1.4.7 and (Vance et al., 1998a). While there may be considerable along-strike variation in its activity (see Edwards and Harrison, 1997) it appears that in individual segments of the Himalaya the main phase of activity was restricted to periods ~5-6 Myr long.

### 1.4.4 Quantitative PT estimates in the HHCS

To elucidate the inverted metamorphic field gradients, PT estimates across the HHCS have been determined for several sections. There remains, however, confusion over the robustness of many of the techniques as they often result in very different absolute PT estimates for different sections and, in some cases, different PT trends for the same sections (e.g. Inger and Harris, 1992; Macfarlane, 1995).

One consistent feature, however, is that the HHCS as a whole displays an isothermal to inverted temperature profile (Hodges and Silverberg, 1988; Hubbard, 1989; Mohan et al., 1989; Inger and Harris, 1992; Macfarlane, 1995; Neogi et al., 1998; Vannay and Grasemann, 1998; Vannay, 1999). In most of these sections (except Sikkim) this feature, along with a normal pressure gradient (i.e. decreasing pressure up section), could explain the presence of sillimanite and migmatites at the top. Recent work in Sikkim and the Sutlej valley (Davidson et al., 1997; Vannay and Grasemann, 1998),

however, suggests that the isothermal profile may be due, in part, to retrograde re-equilibration of the geothermometers. Such retrograde re-equilibration suggests that the true profile was originally even more pronounced with the highest temperatures at the top of the section as in Sikkim (Neogi et al., 1998).

### 1.4.5 Timing of melt generation and intrusion

There are two principal belts of leucogranites found in the Himalaya, the High Himalayan Leucogranites and the North Himalayan Leucogranites (see Harrison et al., 1997a). The High Himalayan leucogranites form a discontinuous series of intrusive sheet complexes which form some of the highest peaks across the range, from Bhutan in the east to Zanskar in the west. They are small-volume melts produced at fairly constant PT while trace elements and isotopic compositions are consistent with derivation from the HHCS (Vidal et al., 1982; Vidal et al., 1984; Deniel et al., 1987; Le Fort et al., 1987; Inger and Harris, 1993). Importantly for discussions of their formation, the largest leucogranite bodies are often found at the top of belt between the HHCS and the Tethyan sediments and may locally cross cut the STDS (Pecher, 1989; Searle et al., 1993; Guillot et al., 1995).

The North Himalayan leucogranites outcrop ~80 km to the north of the main mountain belt, are generally younger, and possibly formed at higher temperatures than the HHL (Harrison et al., 1997a). However, their formation ages are 17-10 Ma and younger than the metamorphism in the HHCS which is the principal subject of study for this thesis and they will not be discussed further.

The HHL formed from 24-17 Ma with the main phase of melt generation at 24-19 Ma (Harrison et al., 1998). Recently, Harrison et al. (1999) obtained detailed age data by *in-situ* dating of the Manaslu leucogranite in Nepal and suggested that magma generation occurred over a period of ~4 Ma. The generality of this result remains to be tested elsewhere in the range.

### 1.4.6 Melt production conditions, chemistry and volume

The chemistry of the melts, melt production mechanisms and their source regions are intricately linked (Harris et al., 1993). However, there is growing agreement that much of the present HHL formed by muscovite-dehydration melting from a source within the HHCS (Harris and Massey, 1994). Additionally, many lines of evidence suggest that the presently exposed migmatites at the top of the HHCS *are not* the source for the High Himalayan Leucogranites (Swapp and Hollister, 1991; Hodges et al., 1993; Inger and Harris, 1993; Harris and Massey, 1994; Barbey et al., 1996). Rather, the sources appear to lie in the lower section of the HHCS (see Chapter 5). While the bulk of the leucogranites are sourced from the lower structural levels of the orogen the contribution of various source regions in the HHCS is still not resolved.

Geochemical constraints obtained by Harrison et al. (1999) for Manaslu suggest that a second phase of melting was produced at higher temperatures and with a lower $^{87}Sr/^{86}Sr_i$ than the first. This is contrary to findings of Ayres (1997), for Zanskar, which suggest that the later intruded tourmaline leucogranites formed at lower temperatures than the earlier biotite leucogranites.

### 1.4.7 Cooling (and exhumation) of the HHCS

Subsequent to intrusion of the leucogranites the HHCS underwent a period of rapid cooling at 17-20 Ma which is well constrained from the large numbers of $^{39}Ar/^{40}Ar$ studies across the orogen. This is often attributed to movement on both the STDS and MCT which resulted in rapid tectonic denudation and exhumation (Hubbard and Harrison, 1989; Metcalfe, 1990; MacFarlane, 1993; see review in Sorkhabi and Stump, 1993; Vance et al., 1998a).

Studies in several sections across the range show that cooling occurred progressively later towards the base (Metcalfe, 1990; MacFarlane, 1993; Vance et al., 1998a). In a study of mica cooling ages across the Zanskar area Vance et al. (1998a) suggested that

the thermal response of the belt to extensional fault movement varies with structural depth in the belt – the earliest response being felt closest to the normal fault. In fact the response of the core of the orogen in Zanskar to thermal perturbations caused by extensional faulting is delayed by some 3-5 Ma relative to earliest fault movement. Cooling rates for the centre of the orogen were nevertheless $\geq 50°CMa^{-1}$. The rapid cooling rates in the rocks affected last may be a result of rapid exhumation compressing the isotherms in the exhuming rock pile (e.g. Whittington, 1995). The thermal response to tectonic exhumation and denudation is readily explainable in terms of simple thermal diffusivity constraints for the crust whereby a thermal perturbation – in this case the placement of cool rocks against hot rocks by the STDS – diffuses through the crust.

### 1.4.8 Thermal and heat-producing properties of the crust

The thermal-conductivity and heat-producing properties of the crust are extremely important for the thermal evolution of the orogen (e.g. England and Thompson, 1984) and are inextricably linked to geometry and tectonic displacements. Constraints for heat production within the lithosphere are usually obtained from standard models in which the heat producing elements are concentrated in the upper crust. However, tectonic processes will redistribute material in an orogenic wedge with important consequences for Jamieson et al. (1998). Additionally, tectonic processes will also result in a redistribution of rocks with different thermal properties and their geometries can dramatically effect the thermal regime within the crust (Jaupart and Provost, 1985; Grasemann, 1993). However, this aspect of Himalayan geology remains poorly studied.

## *1.5 Outstanding debates*

### 1.5.1 Models for crustal anatexis

The High Himalayan Leucogranites have posed a problem for Himalayan geologists because simple modelling suggested that, with collision at 50-55 Ma, there would not

have been sufficient heat for prograde crustal anatexis at 20 Ma (England et al., 1992). Alternatively, to explain their formation Le Fort (1975) suggested that the leucogranites could have formed during movement of the HHCS over the Lesser Himalaya along the MCT, resulting in the infiltration of fluids from the latter inducing melting in the former. However, geochemical modelling (Harris and Inger, 1992; Harris et al., 1993; Harris et al., 1995) suggests that the high Himalayan leucogranites formed by muscovite breakdown under vapour-absent conditions. While fluids could trigger melting under such conditions the slope of the muscovite-dehydration reaction in PT space allows melting to occur during the well-documented decompression of the HHCS (Swapp and Hollister, 1991; Harris and Inger, 1992; Harris et al., 1993; Hodges et al., 1993; Harris and Massey, 1994).

Decompression melting requires extremely fast, adiabatic exhumation of the peak P-T assemblages (Harris and Massey, 1994) – something that might be expected beneath a large extensional fault. Such rapid exhumation rates have, in fact, been suggested by dating on the STDS (Hodges et al., 1993). However, high temperatures in the source region prior to decompression are still required at 25-20 Ma – a requirement that is at odds with simple thermal models previously mentioned (England et al., 1992).

An alternative mechanism for the production of the leucogranites is the supply of extra heat, such as shear heating along the MCT. Despite the theoretical difficulty of producing high shear stresses in the crust in the presence of a melt, this idea still has proponents (England et al., 1992; Harrison et al., 1998).

An assessment of the different potential heat sources requires a detailed knowledge of the thermal history of the source rocks prior to anatexis, something which is lacking at present.

### 1.5.2 Inverted metamorphism

In light of the recent findings that the MCT was reactivated in the late-Miocene (Catlos

et al., 1999) and the geographic relationships for the MCT and the HHCS in Kumaon and Garhwal, the MCTZ and the HHCS are best treated as separate entities and related only when firm evidence suggests this should be the case. Thus in the authors opinion there are two inverted metamorphic field gradients in the Himalaya: one in the MCTZ from greenschist facies at the base to lower- or upper-amphibolite at the top, the other in the HHCS from kyanite-zone at the base to sillimanite- or sillimanite+K-feldspar zone at the top.

*High Himalayan Crystalline Series*

The models used to explain the exposed profiles can be described in terms of two possible endmembers: i) the profile represents a frozen static geotherm or ii) the profile is purely the product of deformation.

Falling into the first category, Hodges et al. (1988) suggested that the isothermal profile could result from the buffering of temperatures by anatexis and advection of heat by leucogranites from lower to higher levels. While such a model may explain the isothermal profile in the sections in which migmatites are found, it does not explain other areas, including Garhwal, in which the migmatites and leucogranites are restricted to upper levels of the HHCS.

In the same category of model Jaupart and Provost (1985) suggested that elevated temperatures throughout the HHCS and principally at the top could have been produced by thermal blanketing caused by low thermal conductivity sediments on top of high heat production gneisses.

Alternatively, the exposed profile could be the result of deformation - syn- or post-metamorphism - (e.g. Jain and Manickavasagam, 1993; Grujic et al., 1996). Syn-metamorphic models lie somewhere between the two endmembers and may result in an abnormal steady-state geotherm or a transient geotherm. In such models the timing relationship between deformation and metamorphism is critical - but is a feature often

poorly constrained.

The two end members are not mutually exclusive such that processes producing elevated profiles may have acted alongside deformation. To assess the extent to which each may have contributed to the exposed field gradients and PT profiles requires both detailed structural studies and a detailed knowledge of the PT *history* of the HHCS. Unfortunately, while much is known about the timing of cooling in the Himalaya, little is known about the timing of prograde metamorphism. Furthermore, there is only a small amount of quantitative data on deformation in the HHCS (Jain and Anand, 1988; Grujic et al., 1996).

Whether the Himalaya had an inverted to isothermal profile prior to exhumation is still poorly known and while few authors would deny that deformation has played a role in the exposed field and PT profiles the extent to which this controlled the field thermal profile is poorly constrained. However, it is clear that inverted metamorphic field gradients are a ubiquitous feature of the Himalayan orogeny suggesting a similar process along the whole chain.

*Main Central Thrust Zone*

Based on the end member of a frozen geotherm, Le Fort (1975) suggested that the inverted profile below the MCT was produced by the emplacement of the hot HHCS over the cold Lesser Himalayan formations, producing a sawtooth geotherm. However, 2-D numerical modelling of overthrusting of a hot crustal slice (Grasemann, 1993) shows that the isotherms below the thrust can't be inverted with geologically feasible slip rates.

Such constraints led some authors to suggest that shear heating along the MCT (e.g. England and Molnar, 1993b) may have contributed to the inversion of the metamorphic field gradients. This is not consistent with the PT data which suggests that the thermal high is not at the fault but, rather, slightly above it (e.g. Hubbard, 1989).

At the other end of the scale Stäubli (1989), Hubbard (1996) and Harrison et al. (1997b) all suggested that post-metamorphic deformation is the principal cause for the observed field gradients. The diachroneity of ages across the top of the MCT (Harrison et al., 1997b) and the clear cross cutting relationships shown by the MCT in Garhwal (Jutogh thrust of Jain and Anand, 1988) support this view.

In reality the process is likely to lie somewhere between the two endmembers and, in fact, an analytical solution of a syn-metamorphic deformation model in which the footwall is progressively accreted to an eroding hangingwall (Royden, 1993) produces PT profiles similar to traverses of the MCTZ in Nepal (Hubbard, 1989).

## *1.6 Summary*

The present day exposure of the Himalaya can be represented by a simplified sequence from south to the north as follows; the unmetamorphosed Lesser Himalaya sediments are overlain by the metamorphic core of the Himalaya, the High Himalayan Crystallines Series (HHCS), along a broad zone of deformation often referred to as the Main Central Thrust Zone (MCTZ). Small leucogranitic intrusions are emplaced into the upper lithologies of the HHCS, the result of crustal anatexis during the Himalayan orogeny. Further to the north, the HHCS is bounded by a low angle normal fault which places the low-grade Tethyan sediments of the continental shelf against the high-grade HHCS.

Whilst some of the differences in thermal models used to explain the various features preserved in the HHCS and MCTZ along the Himalayan belt may be the result of true along-strike variations, the consistency of the lithotectonic units, inverted metamorphism and leucogranite production point to broadly similar processes operating along the strike of the orogen. The current knowledge of the timing of these events permits us to describe an approximate outline for the evolution of the belt. After continental collision of India and Asia at ~50 Ma metamorphism occurred in the HHCS at 35-25 Ma by post-collision thermal relaxation associated with crustal thickening

(Vance and Harris, 1999). Movement on the MCT, the STDS and the formation of High Himalayan Leucogranites overlap along much of the orogen between 25-16 Ma (Schärer et al., 1986; Hodges et al., 1992) and was closely followed by a period of rapid cooling at the top of the HHCS (Sorkhabi and Stump, 1993). Movement in the MCTZ occurred either intermittently or continuously from ~22 Ma until ~2 Ma (Harrison et al., 1997b). However, the exact relationship between the movement on both the MCT and the STDS and the formation of an inverted field gradient in both the MCTZ and the HHCS is still not well defined.

## *1.7 Thesis structure*

Chapter 2 presents the results of structural and petrological studies of the Garhwal Himalaya and as such forms a reference point for later chapters in the thesis as well as constraining tectonic models applicable to the area.

Chapter 3 presents thermometry and barometry carried out on samples in the transects presented in Chapter 2.

Chapter 4 presents the garnet chronometry carried out by the author combined with *in-situ* monazite analyses. These elucidate the prograde thermal history of the Garhwal Himalaya, with special reference to the formation of inverted metamorphism in the HHCS and anatexis.

Chapter 5 looks at the geochemistry of a small group of deformed leucogranites which indicate melting of the HHCS at 40 Ma by vapour-present melting.

Chapter 6 explores the Sm-Nd systematics of garnet using new *in-situ* trace element analyses of garnet with LA-ICP-MS. Further analysis of the petrological information contained in trace-element zoning within garnet crystals is presented in Chapter 7.

Finally the conclusions and tectonic model are contained in Chapter 8.

# Chapter 2 - Field Relations and petrology

## 2.1 Introduction

This chapter summarises field observations and presents general petrological descriptions for rocks of the Garhwal Himalaya based on fieldwork by the author and previous studies. These are followed by descriptions of the lithology, structure and petrology of the Bhagirathi and the Saraswati and Dhauli valleys (see Figure 2.1 for positions of the valleys). The Bhagirathi is treated separately from the other two given the lithological and structural differences. The ambiguities and some of the specific questions raised in this chapter are discussed in more detail at the end.

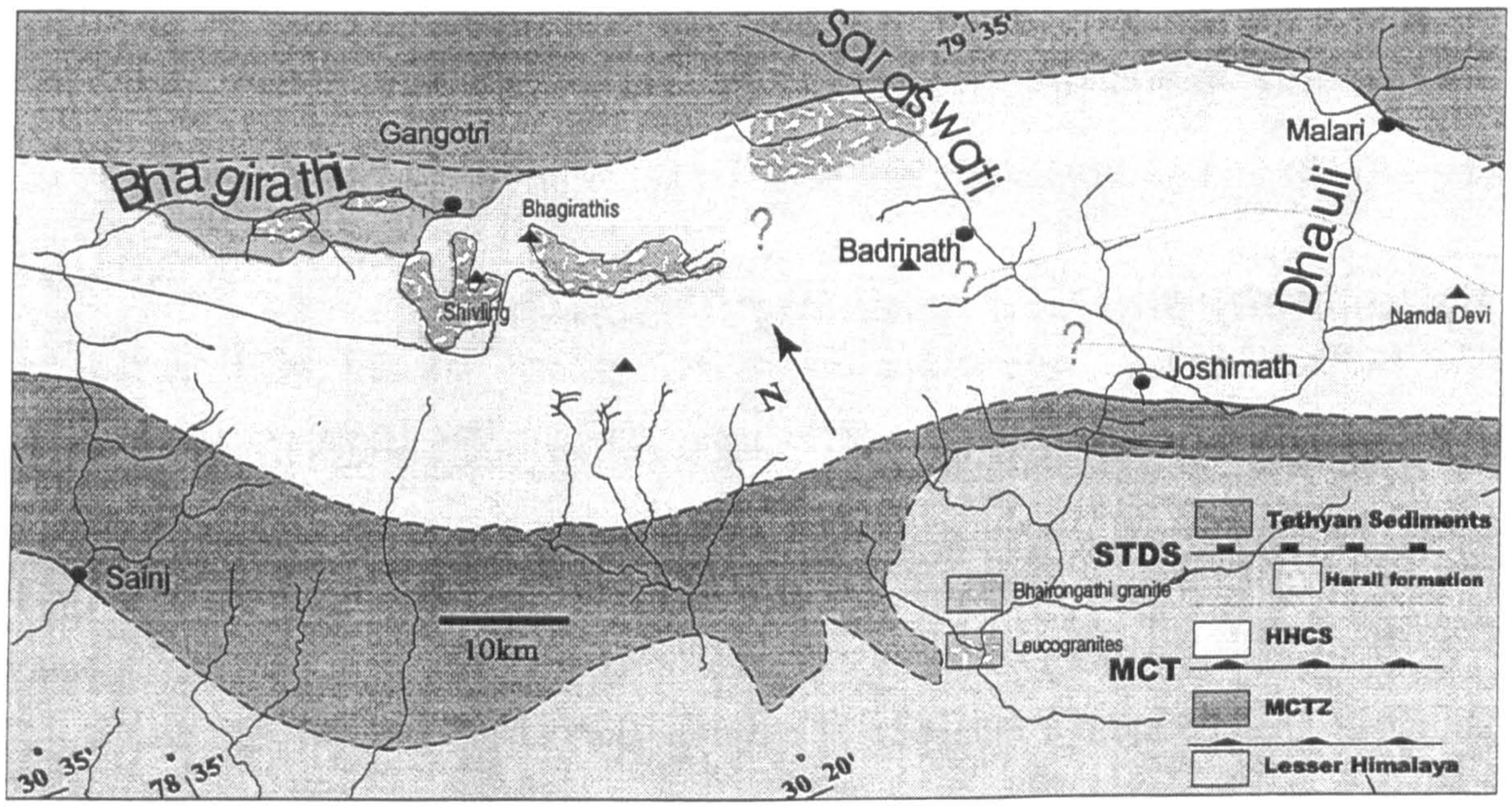


*Figure 2.1 Sketch map of the Garhwal Himalaya showing the Bhagirathi, Alaknanda (Saraswati) and Dhauli valleys. Also shown are the tectonostratigraphic units used in this thesis.*

## 2.2 Previous work

Auden (1937) first carried out reconnaissance work in the Garhwal Himalaya and, with the later work of Heim and Gansser (1939), identified the principal lithotectonic units. They suggested that the sequence from the Lesser Himalayan (LH) up through the High

Himalayan Crystalline Series (HHCS) resulted from the overthrusting of successive units from the north to the south. This work already highlighted the problem of inverted metamorphism. Later work, discussed in greater detail below, reflects the range of problems the area presents and has concentrated on specific aspects of the region, namely: the definition and nomenclature of the MCT fault systems and metamorphism in the Lesser Himalaya (Valdiya, 1980; Bahuguna and Saklani, 1988; Johnson and Oliver, 1990; Srivastava and Mitra, 1994; Oliver et al., 1995); structure and metamorphism of the High Himalayan Crystallines (Virdi, 1986; Hodges and Silverberg, 1988; Pecher and Scaillet, 1989; Metcalfe, 1990; Metcalfe, 1993); geochemistry, formation and emplacement of the leucogranites (Seitz et al., 1976; Stern et al., 1989; Scaillet et al., 1990; Searle et al., 1993; Scaillet et al., 1995; Searle et al., Subm.); the stratigraphy of the Tethys Himalaya (Shah and Sinha, 1974); and uplift and exhumation (Sorkhabi et al., 1996; Searle et al., Subm.).

## *2.3 Petrography and field relations; Bhagirathi*

Though it is certainly true that, compared to many orogens, the Himalaya show a remarkable degree of lateral continuity in terms of the overall nature of the geological units exposed, there is still considerable complexity in detail. To some extent the large-scale simplicity may be more a reflection of a rudimentary state of knowledge than a real situation. Certainly, in detail, sections are highly variable throughout the Himalaya and the Bhagirathi, Alaknanda and Dhauli valleys are no exceptions. Nevertheless some generalisations can be made for the units. Here the deformation and metamorphism in each unit are assigned to different events on the basis of relative timing and kinematic or grade similarities. This may artificially separate different structural features which are in fact the result of a continuous process. Conversely, where the relationship between some of the features in any one unit remains ambiguous, this approach may mask a greater diversity in events.

### 2.3.1 The Main Central Thrust Zone

Considerable confusion exists in the literature about the position of the MCT in the Kumaon and Garhwal Himalaya. The MCT was defined by Heim and Gansser (1939) as the first appearance of metamorphic rocks in the Alaknanda, Dhauli and, to the east, in the Kumaon Himalaya. Later workers, mostly from India, continued this tradition but showed that the metamorphic rocks in the area of Kumaon and Garhwal were in fact imbricated. A host of local names and terminology was developed with as many as three MCTs.

This situation became increasingly complicated with the adoption of the apparently simple classification in Nepal. Studies by Valdiya (1980; 1988) attempted to correlate the known thrusts along the entire chain in line with the work in Nepal. This process was complicated by along strike variations in lithologies and structural style which are extremely pronounced even within the ~200km section of the Kumaon and Garhwal Himalaya (Valdiya, 1980; Pati and Rao, 1983; Saklani and Bahuguna, 1983; Bahuguna and Saklani, 1988; Jain and Anand, 1988; Pecher and Scaillet, 1989; Metcalfe, 1993). However, one feature appears consistent in the Garhwal Himalaya: the position of the upper boundary separating gneisses on top from the imbricate zone below. It is this boundary, locally known as the Vaikrita thrust, that Valdiya (1980) termed the MCT.

Metcalfe (1993) attempted to simplify the terminology by referring to the metamorphosed rocks below the Vaikrita thrust as the Main Central Thrust Zone (MCTZ). Unfortunately the lower Munsiari thrust does not coincide with more detailed studies in the same valley (e.g. Bahuguna and Saklani, 1988). However in view of the more widespread availability of the Metcalfe (1993) study his terminology is adopted here for the upper and lower thrusts bounding the MCTZ; the Vaikrita and Munsiari thrust respectively. Furthermore, Valdiya (1980) suggestion that the Vaikrita is equivalent to the MCT elsewhere is also accepted here. Thus the MCTZ is bound to the

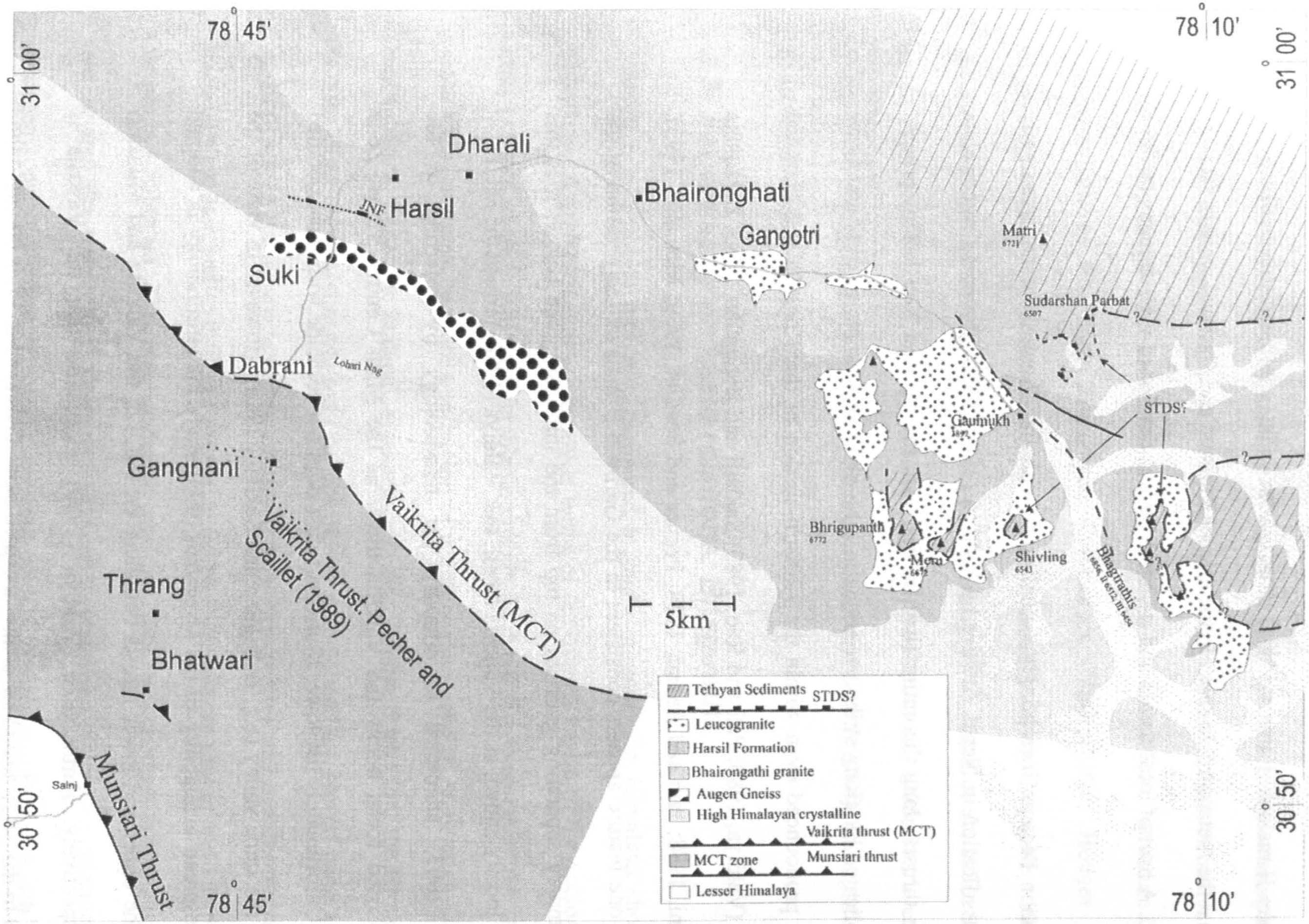


*Figure 2.2 Schematic geological map of the Bhagirathi valley compiled from field work by the author and from Pecher and Scaillet (1989), Jain et al. (1995) and Scaillet et al. (1995).*

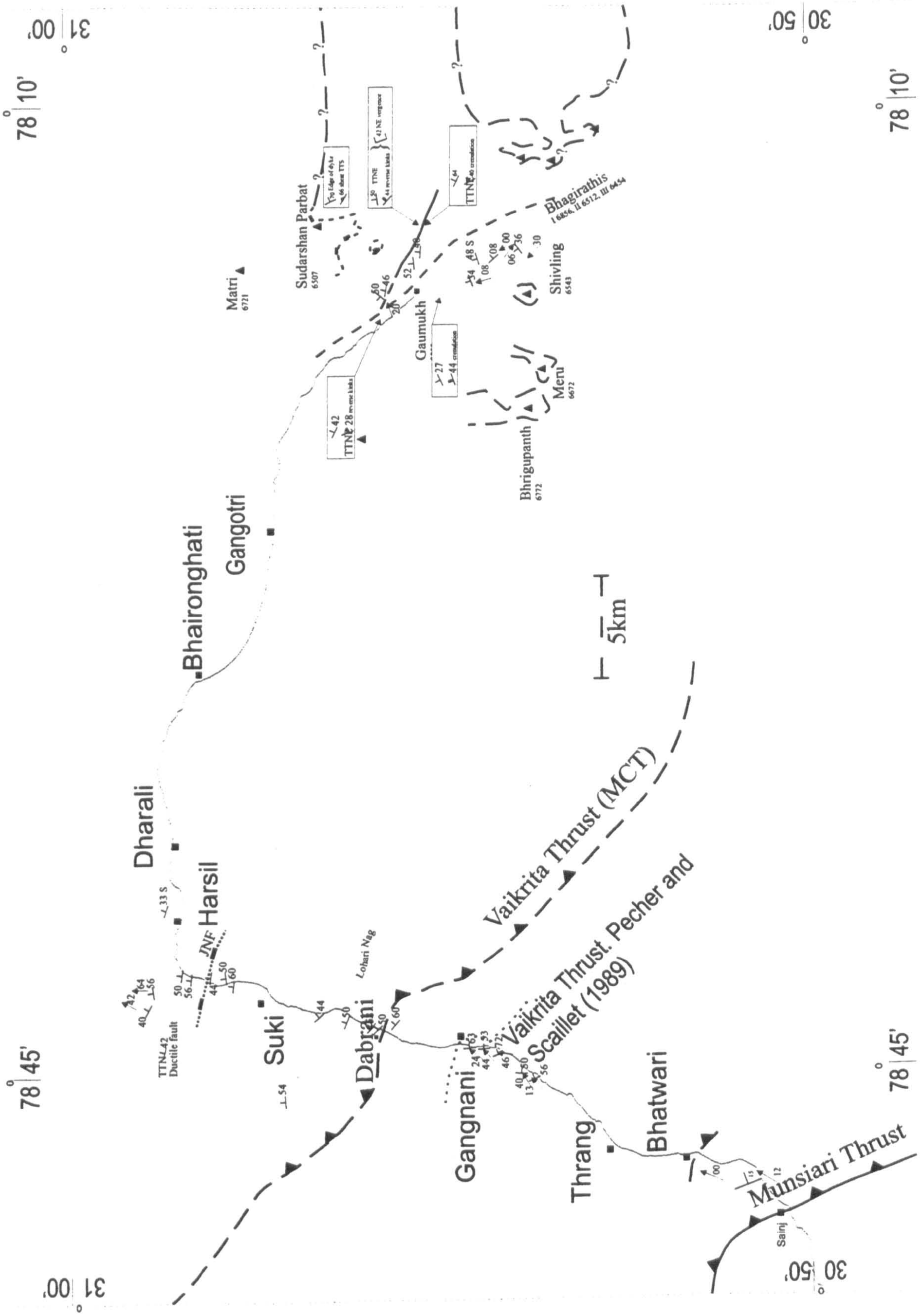


*Figure 2.3 Structural map of the Bhagirathi valley showing dip and strike of the beds and mineral lineations.*

south by the Munsiari thrust and to the north by the Vaikrita/MCT as shown on Figure 2.2. The Munsiari thrust (Metcalfe, 1990; 1993) occurs just to the north of Sainj in the Bhagirathi valley and separates the quartzites of the lesser Himalaya from the MCTZ. The MCT at the top is based on a change in lithology and structural style from the highly sheared gneisses and schists of the MCTZ to the less deformed gneisses at Dabrani (Metcalfe, 1990; 1993).

Structurally the MCTZ shows variable strike from E-W to N-S with a dip of 50-70° and often with the development of a low angle C plane dipping to the north. There is a well-developed NNE mineral lineation which lies almost parallel to the strike of the beds in some parts of the MCTZ (Figure 2.3).

Although the dominant lithology varies within the MCTZ, rather than attempt to separate the MCTZ into distinct formations, it will be treated as one unit and the lithologies described separately. The base of the MCTZ in the Bhagirathi valley contains amphibolites, quartzites, augen gneiss and granodiorite, the last of which dominates for approximately 6km from the base of the section (Metcalfe, 1990). The MCTZ is highly tectonised but in places intrusive relationships are preserved (Figure 2.4a) in which amphibolites are intruded by augen gneiss which is in turn intruded by a leucocratic granite-gneiss. The granodiorite and augen gneiss contain K-feldspar + plagioclase + biotite + quartz ± muscovite ± clinozoisite. It has inhomogeneously distributed high strain shear zones which have well developed quartz ribbon textures (Figure 2.4b). K-feldspar is rounded and shows breakdown to muscovite and quartz.

Amphibolites occur throughout the MCTZ and consist of biotite + quartz + plagioclase ± hornblende ± actinolite ± zoisite. The amphibolites retain igneous textures in the core but near the strained margins hornblende is replaced by actinolite (Metcalfe, 1990). The more high-strain samples develop S-C fabrics defined by biotite with small broken crystals of sphene. Biotite occasionally shows rutile exsolution fabrics.

1km south of Bhatwari boudinaged aplite dykes intrude foliated biotite-schist and in the vicinity of Bhatwari small calc-silicate bands outcrop (Metcalfe, 1990).

High-strain augen gneisses also occur throughout the section and become common from just north of Bhatwari until Gangnani. They contain K-feldspar + biotite + quartz + plagioclase ± muscovite. K-feldspar and plagioclase form sericitised augen in a fine-grained groundmass with quartz ribbon textures and muscovite fabrics wrapping the augen.

Pelites occur throughout the section and garnet first appears south of Thrang (Metcalfe, 1993). Pelites are intercalated, increasing in proportion upstream, with augen gneiss and amphibolites. Around Gangnani pelites become the dominant lithology and consist variously of garnet + biotite + quartz + muscovite ± plagioclase ± chlorite. Chlorite and muscovite form the fabric south of Gangnani with a few platy biotite at an angle to the fabric. At Gangnani the fabric is formed by biotite and muscovite with some retrogressive chlorite. Chlorite usually forms unoriented retrogressive rims to garnet but occasionally replaces a resistant mineral and forms in kinks (Figure 2.4d). Early deformation ($S_1$) represented by small scale folds is preserved in the core of garnets from near Gangnani and is continuous with the matrix. Elsewhere garnet inclusion trails are at an angle to the main foliation. Staurolite + garnet assemblages are found north of Ghuttu in the Bhilangana valley to the east (Metcalfe, 1990).

To the north of Gangnani chlorite-schists outcrop which contain quartz lenses characterised by isoclinal folds and a well developed S-C fabric. Pecher and Scaillet (1989) consider these the retrogressive parts of the HHCS and place the MCT to the south of Gangnani. Jain et al. (1995) place the MCT on the high point of the road to the north of Gangnani in the vicinity of a landslide. However, outcrops of amphibolites, calc-silicates and slivers of augen gneiss within, and to the north of this point, indicate that the lithological boundary lies further to the north and just south of Dabrani as

mapped by Bahuguna and Saklani (1988) and Metcalfe (1993) and shown in Figure 2.3. The gneisses and calc-silicates north of Gangnani are mylonitised (Figure 2.4e). $D_2$, the main deformational phase, forms the axial planar cleavage, $S_2$, to isoclinal folds in the pelites to the north of Gangnani. $D_2$ is a top-to-the-south-west directed shear as indicated by C fabric relationships, rotated garnet inclusion trails and asymmetric augen (Metcalfe, 1990). The close association between high-strain mylonitic augen gneiss and schists displaying top-to-the-southwest S-C fabrics a few kilometres south of Gangnani suggests that the deformation of the augen gneiss and the production of the S-C fabrics in the schists occurred simultaneously. The similarity between these augen gneisses and the deformation in the augen gneisses and granodiorites lower in the sequence suggests that the same stress regime occurred throughout the MCTZ. The final deformation ($D_3$) is represented by localised top-to-the-southwest brittle-ductile shears (Figure 2.4f).

Around Gangnani early folds and fabric ($S_1$) are preserved in garnet cores which grew under at least greenschist-facies conditions ($M_1$). Rotated inclusion trails (Metcalfe, 1990) indicate syn-kinematic growth for some garnet and the fabric wrapping garnets indicate continued deformation after their growth. The metamorphic assemblages lower down in the MCTZ do not constrain the grade although chloritoid has been reported just to the south of Bhatwari (Jain et al., 1995). $M_1$ was followed by $M_2$, a static retrogression to lower-greenschist facies conditions shown by chlorite overprints on garnet. Despite the scarcity of appropriate lithologies lower in the MCTZ a complicated field gradient is apparent from actinolite-bearing schists near the Munsiari thrust at Sainj up to lower-amphibolite facies, garnet-mica schists around Gangnani and back to greenschist facies chlorite-schists just north of Gangnani.

The age of metamorphism within the MCTZ is constrained by a hornblende $^{40}Ar/^{39}Ar$ age that suggests that temperatures of ~550°C where maintained until 19.8±2.6 Ma (Metcalfe, 1993). Additionally Metcalfe (1993) obtained K-Ar ages on muscovite

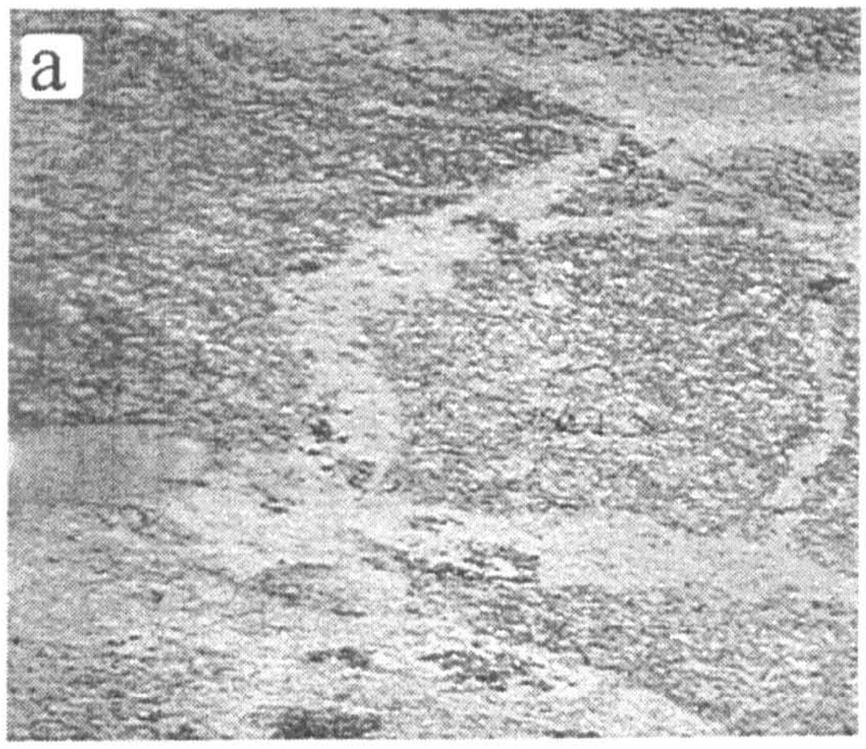


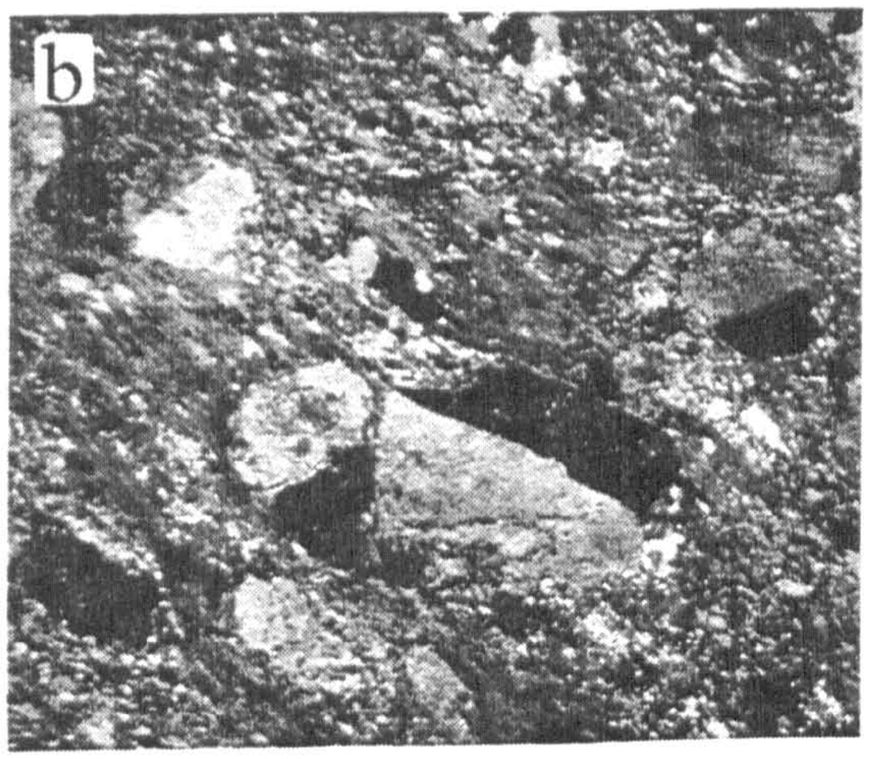


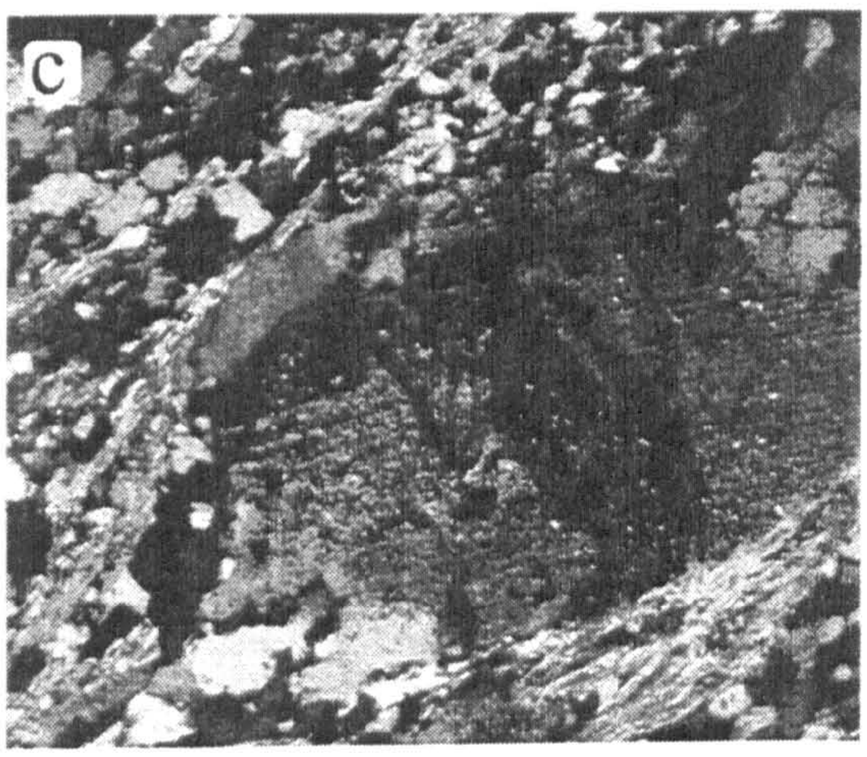


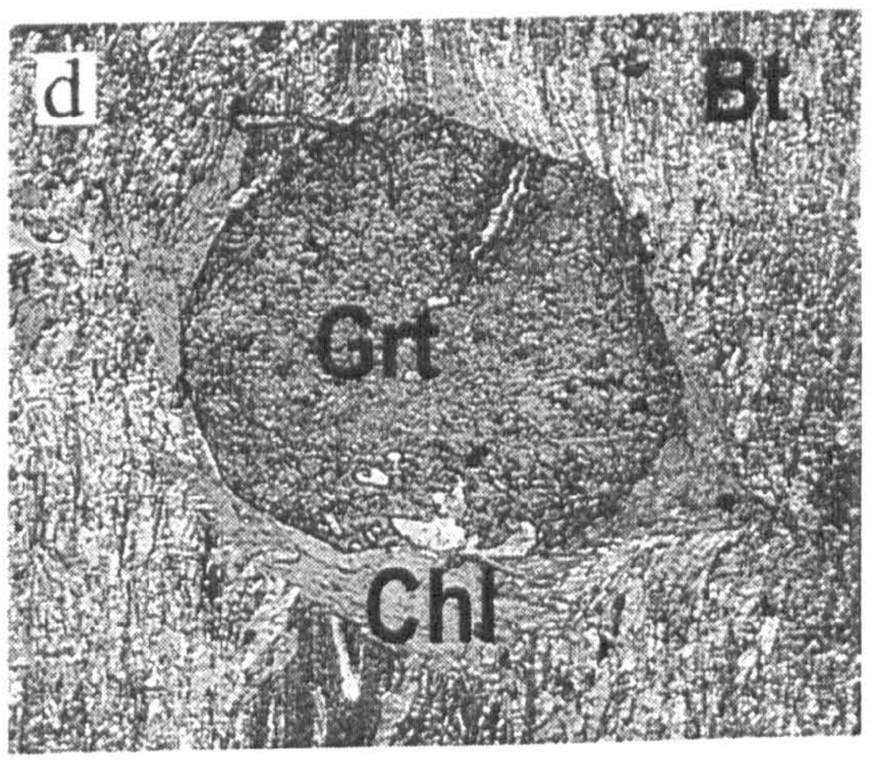


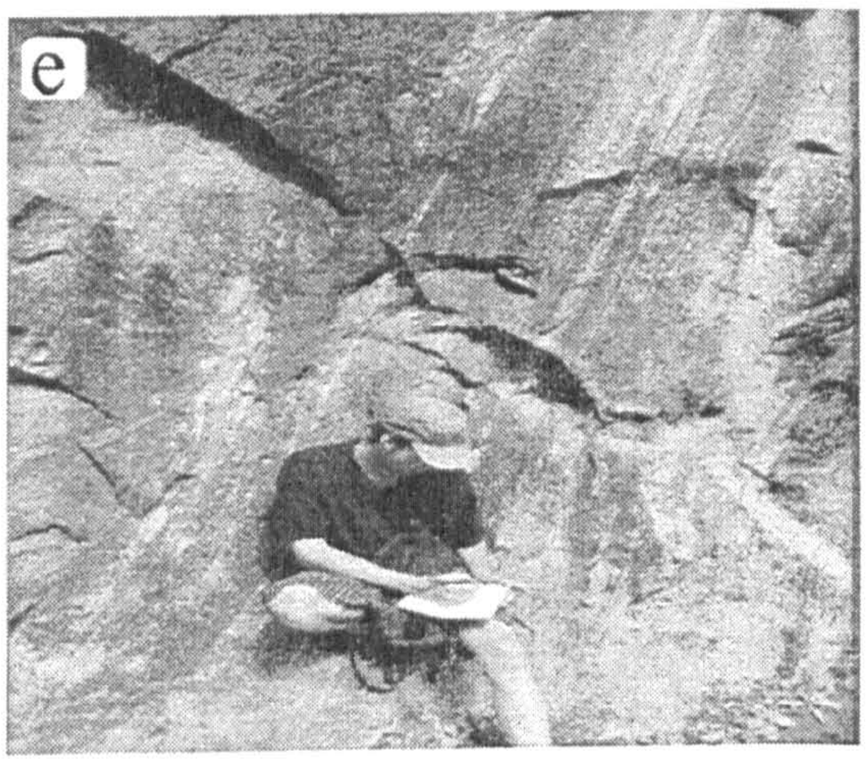


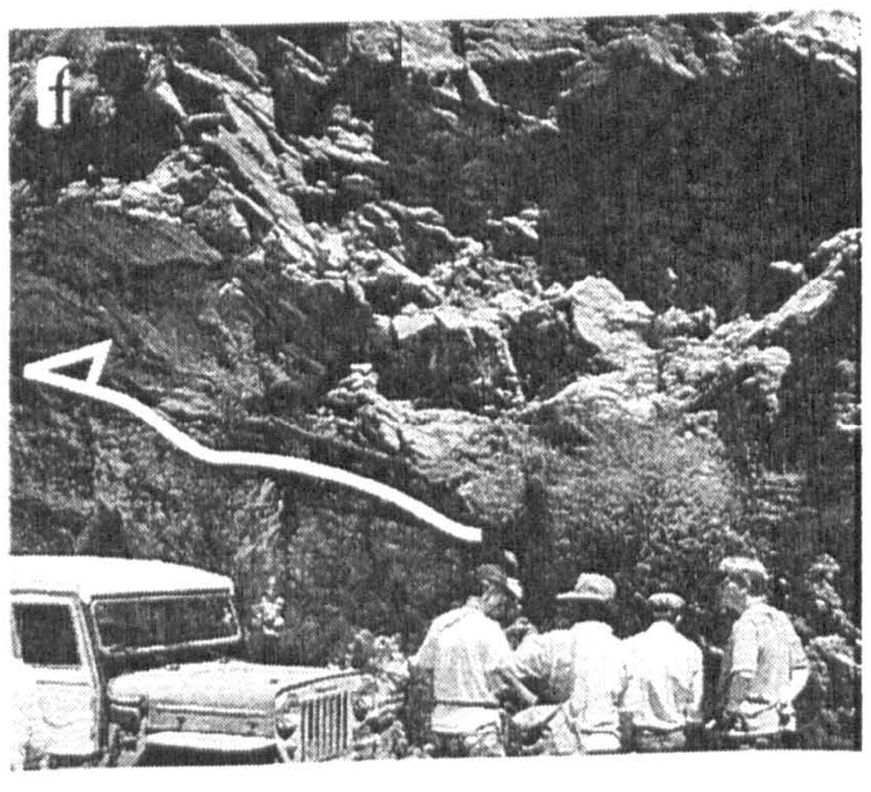


*Figure 2.4 Field relations and petrological observations for the MCTZ in the Bhagirathi valley. Numbers in parentheses relate to sample numbers or localites for all figures in Chapter 2. (a) Intrusive relationships in the MCTZ of the Bhagirathi valley. Granite gneiss (foliated) intruded by leucocratic gneiss (white with black flecks); (b) Photomicrograph of biotite and quartz fabrics wrapping broken feldspar crystals (field of view (FOV) = 5mm) (60); (c) Photomicrograph of an augen of plagioclase wrapped by muscovite. Well developed quartz ribbon textures in the matrix (FOV = 2mm) (47); (d) Photomicrograph of static overgrowth of chlorite on edges of garnet. (FOV = 2mm) (45); (e) Mylonites below the Vaikrita thrust (12Y); (f) Example of a brittle thrust in the MCTZ indicated with a white line (1J).*

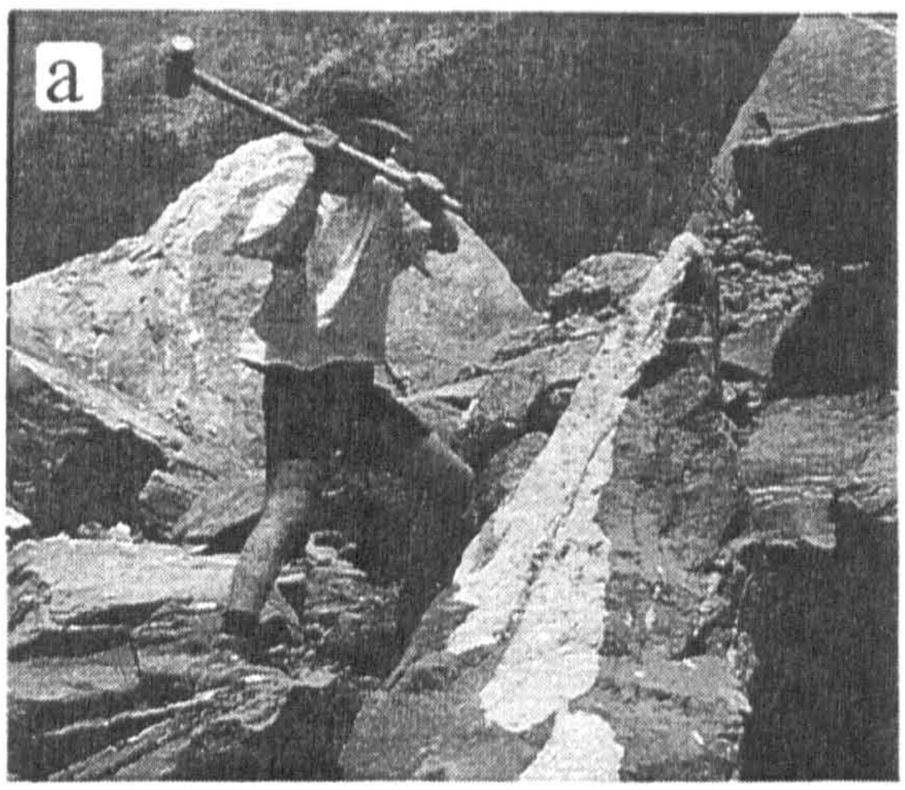


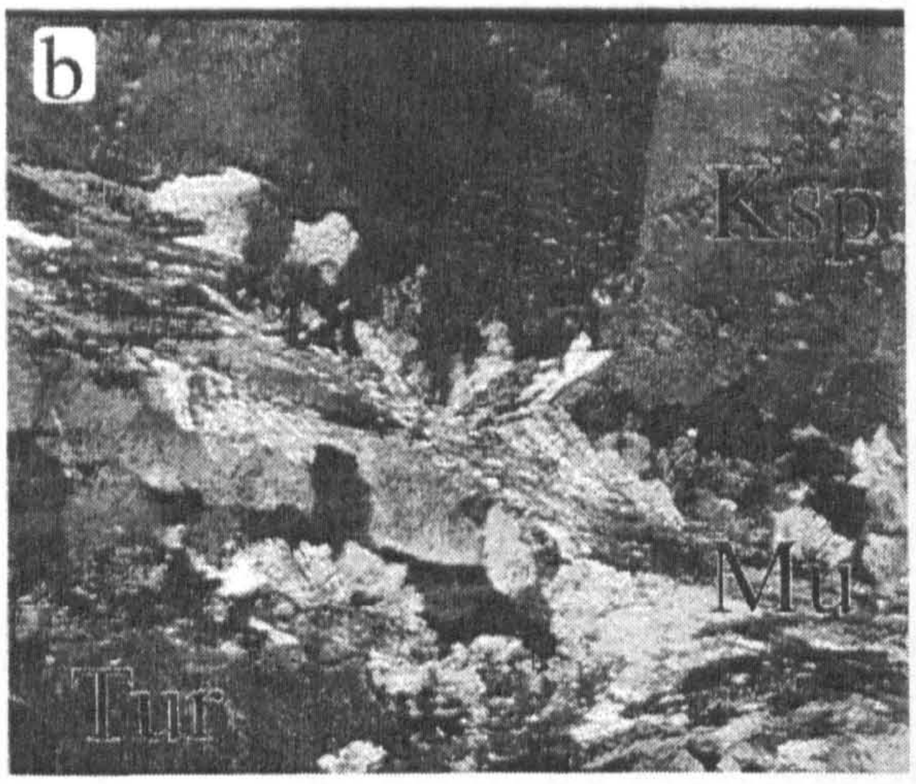


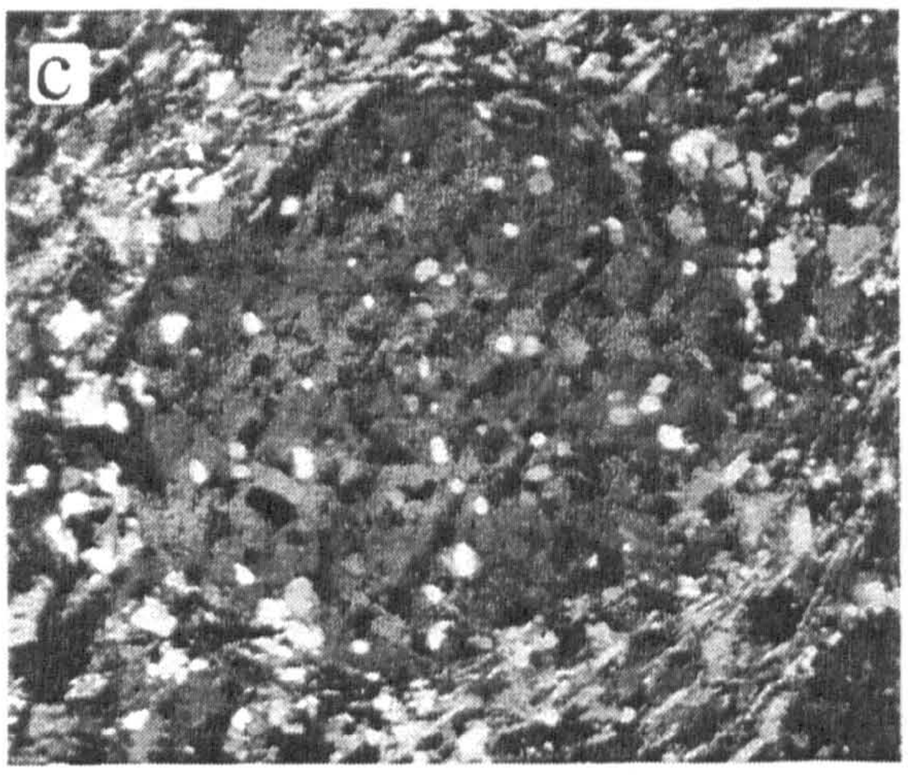


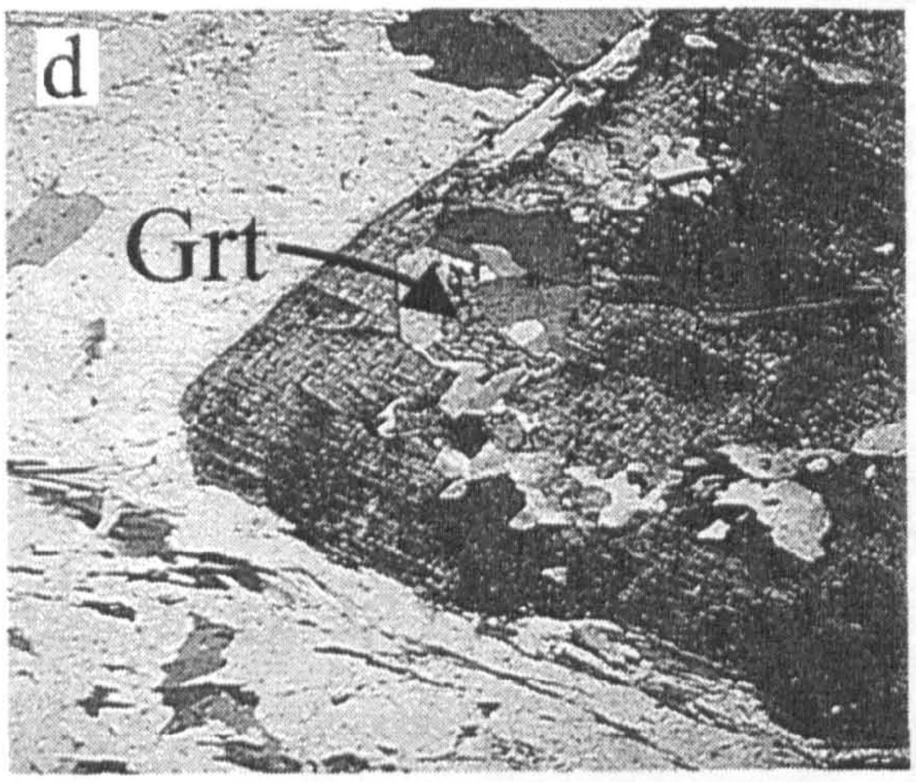


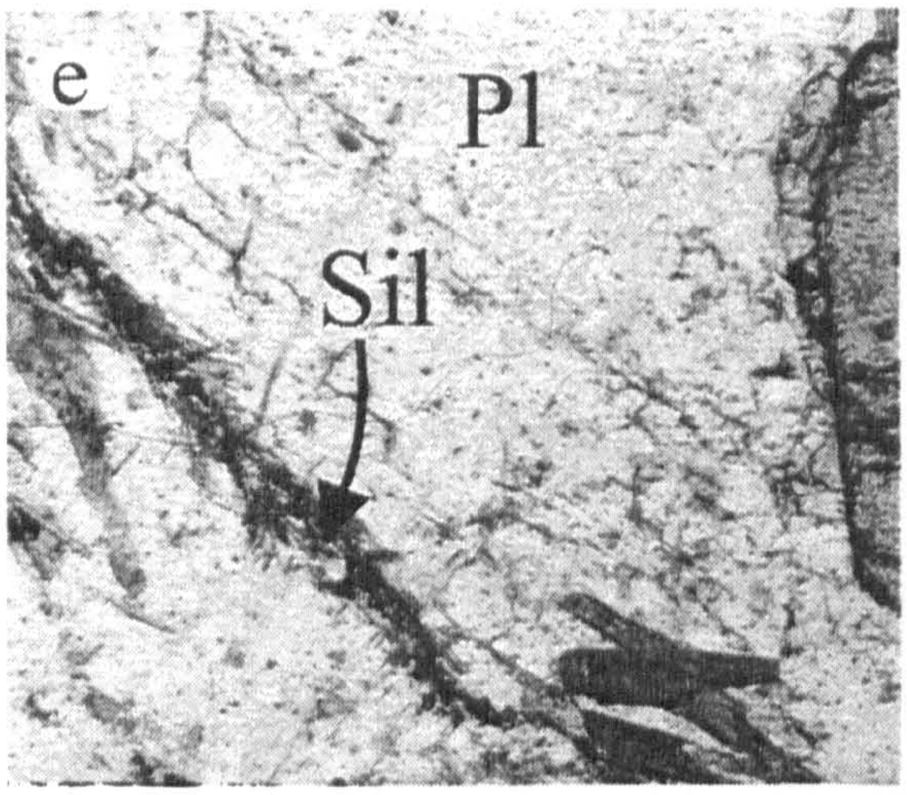


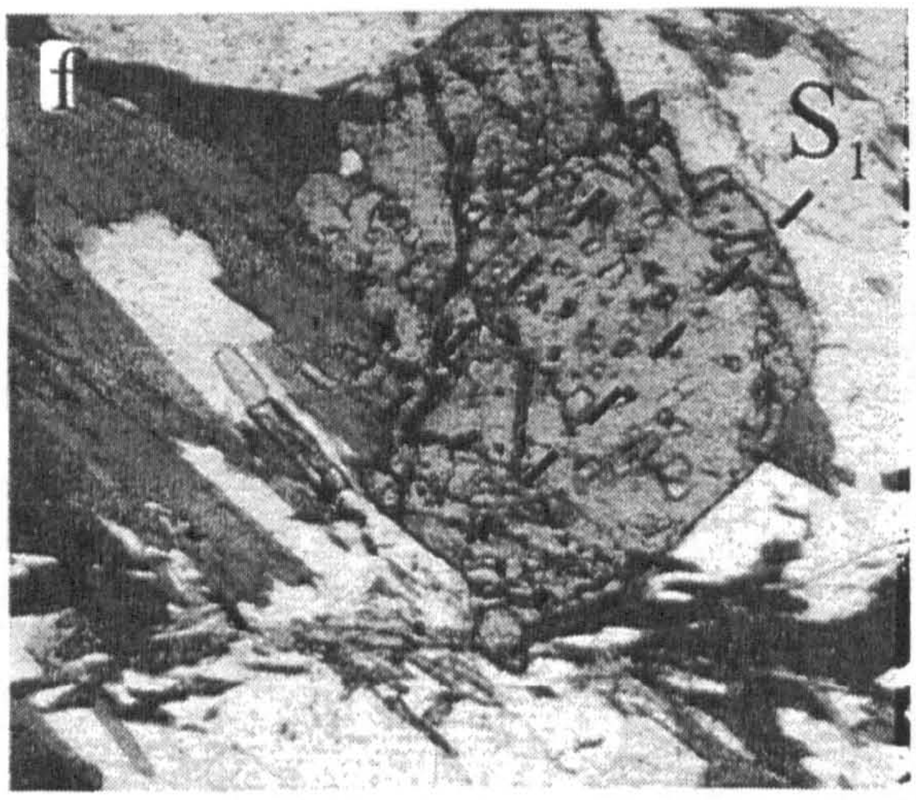


*Figure 2.5 Field relations and petrological observations for the HHCS and Harsil formation in the Bhagirathi valley. (a) Landslide at Lohari Nag exposing migmatitic gneiss; (b) Photomicrograph of muscovite and myrmekite veins cutting through K-feldspar crystals indicating fluid infiltration (FOV = 2mm) (51.4); (c) Photomicrograph of K-feldspar porphyroblasts overgrowing biotite, muscovite and quartz assemblage. Only biotite and quartz are found within the K-feldspar (FOV = 3.5mm) (157); (d) Photomicrograph of garnet, retrogressed to biotite, in large kyanite porphyroblast (FOV=5mm) (55); (e) Photomicrograph of fine needles of unidentified mineral growing in basal HHCS (FOV = 1.5mm) (56); (f) Photomicrograph of $S_1$ fabric preserved as inclusion trails in garnet. Orientation is perpendicular to the main fabric defined by biotite (FOV = 2mm) (56).*

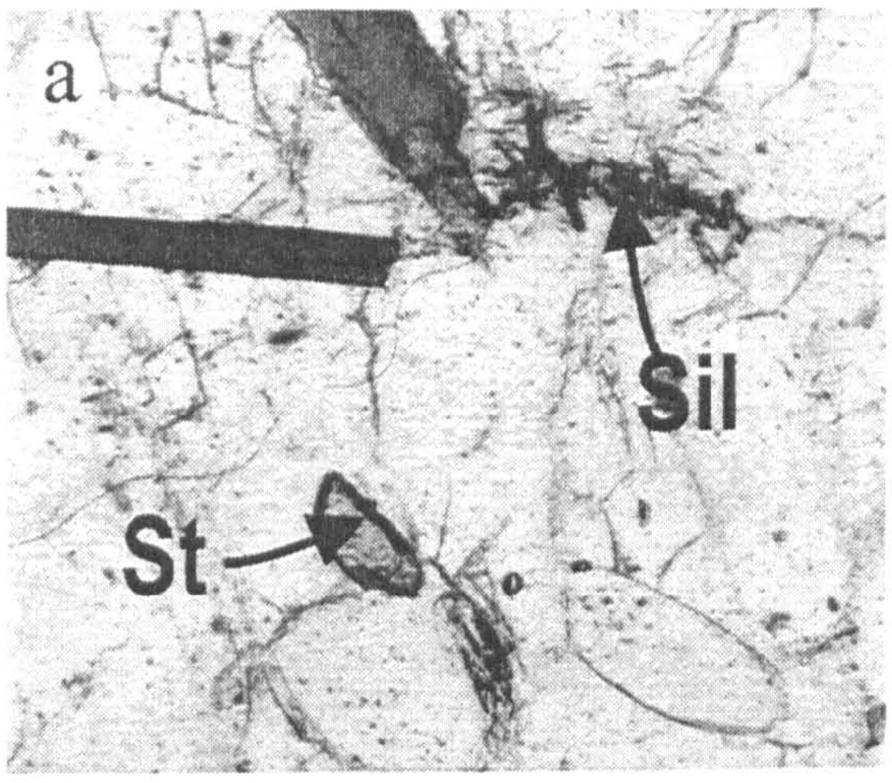


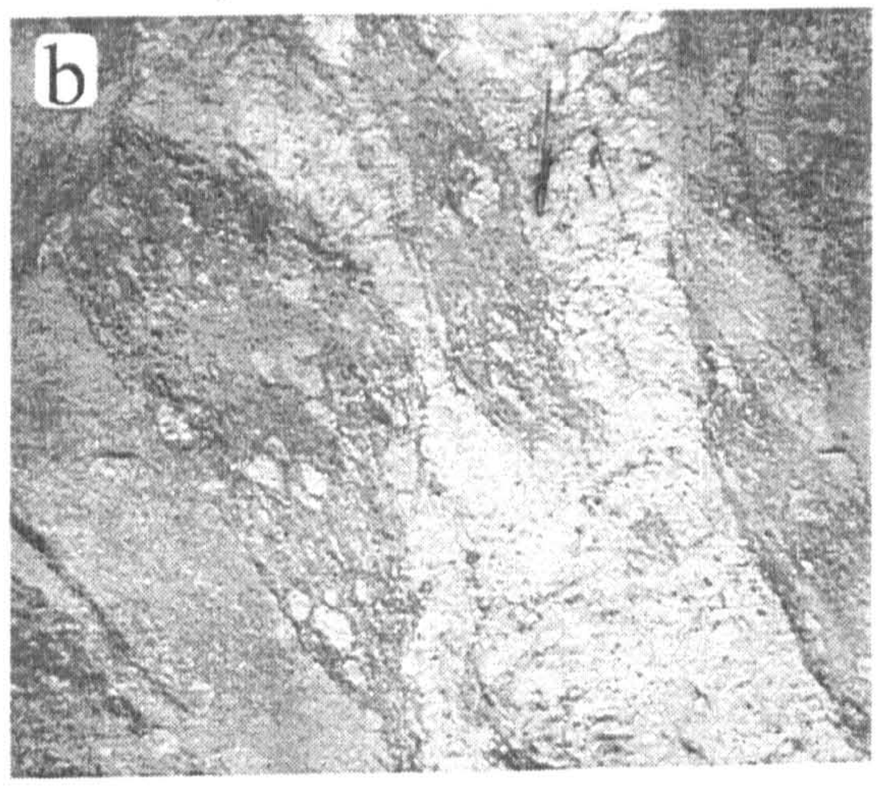


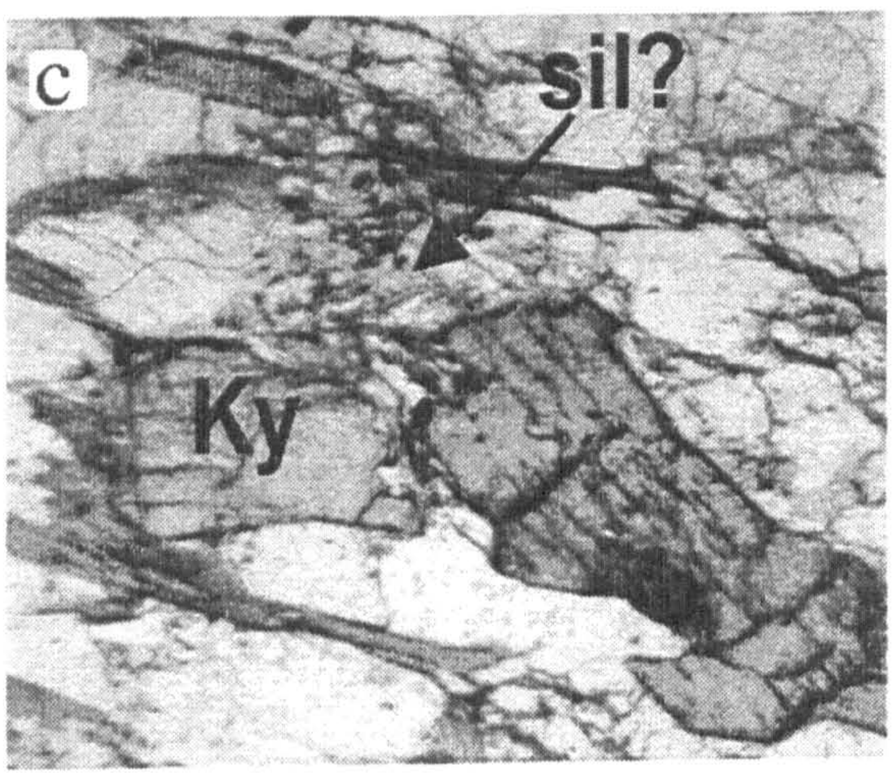


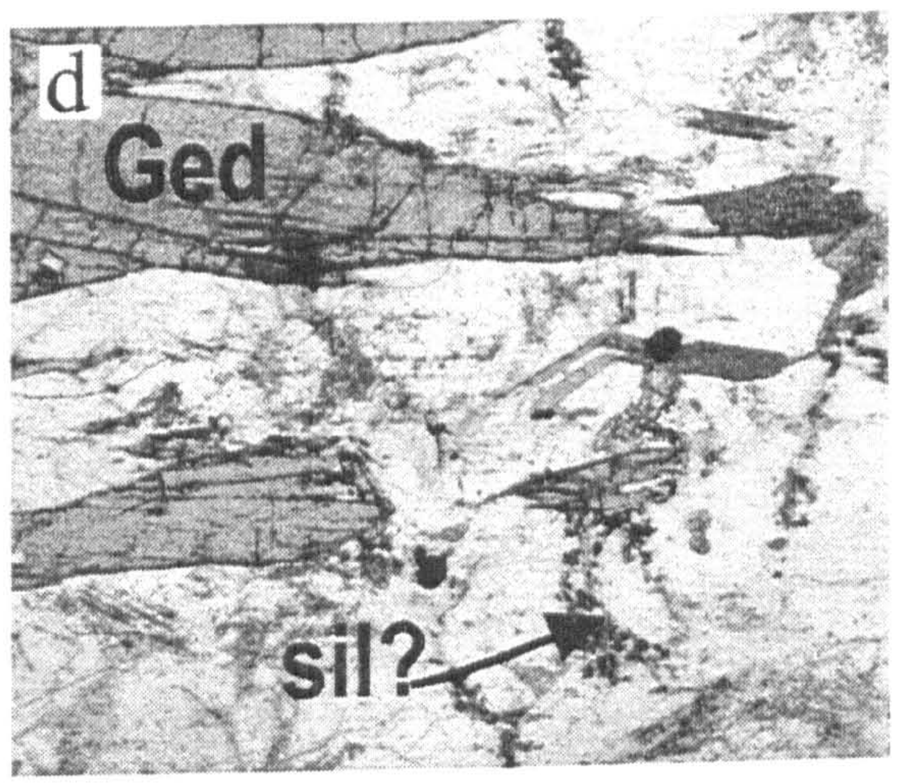


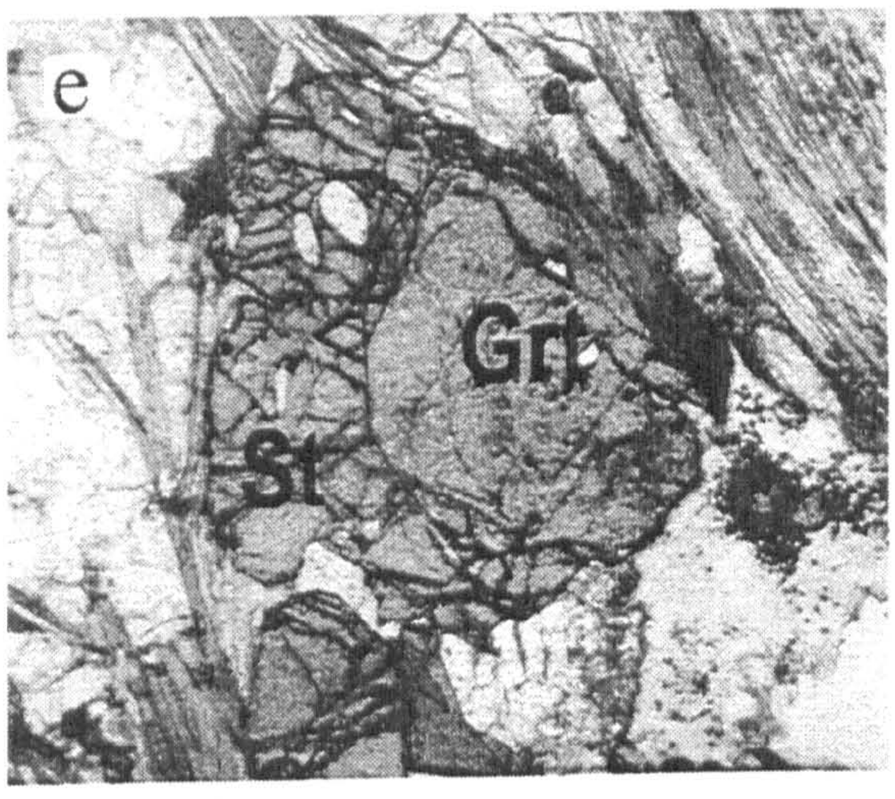


*Figure 2.6 Field relations and petrological observations for the Harsil formation in the Bhagirathi valley. (a) Photomicrograph of retrogressed staurolite in the Bhagirathi HHCS. Note also the development of fine needles as for Figure 2.4e (FOV = 0.5mm) (62); (b) Pegmatite (white) cross-cutting the augen gneiss (foliated) at the top of the Bhagirathi HHCS (4K); (c) Photomicrograph of broken kyanite with the possible development of sillimanite. Harsil formation (FOV = 1.5mm) (100); (d) Photomicrograph of gedrite (large porphyroblasts) with the formation of small needles in the groundmass along grain boundaries. Harsil formation (FOV = 2mm) (88); (e) Photomicrograph staurolite overgrowth on garnet with rotated inclusion trails (FOV = 2mm) (79).*

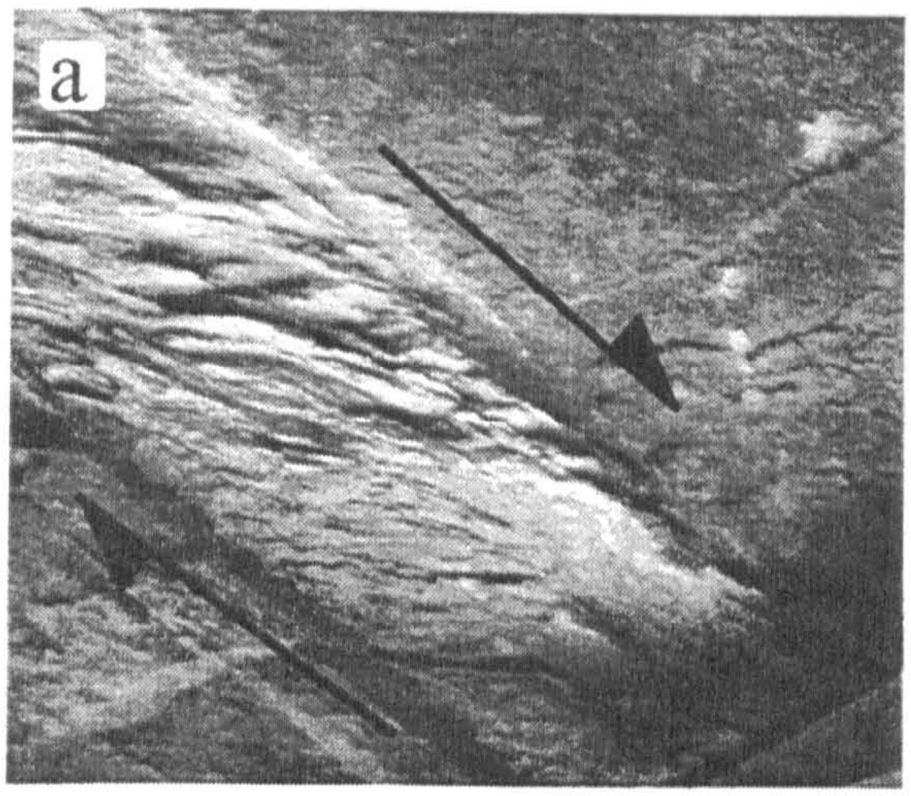


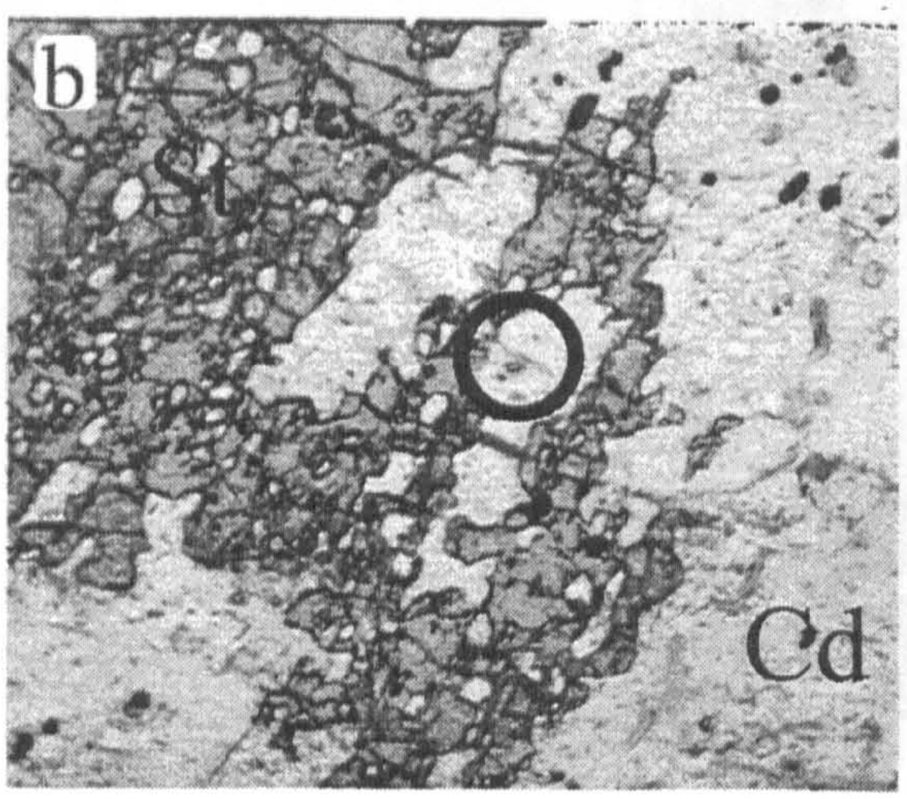


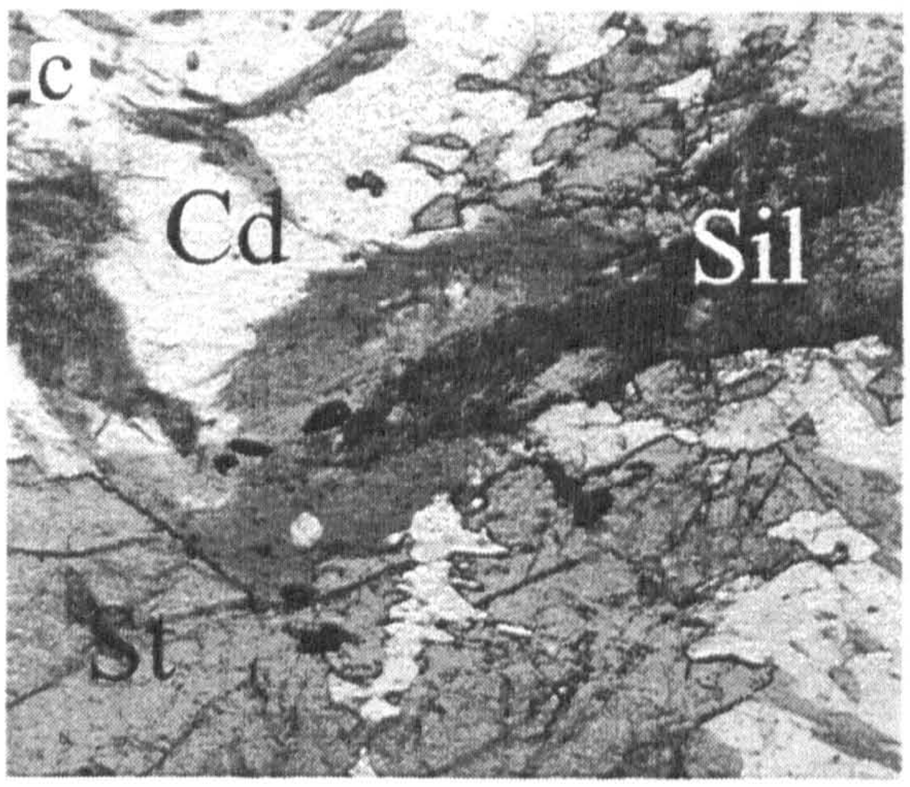


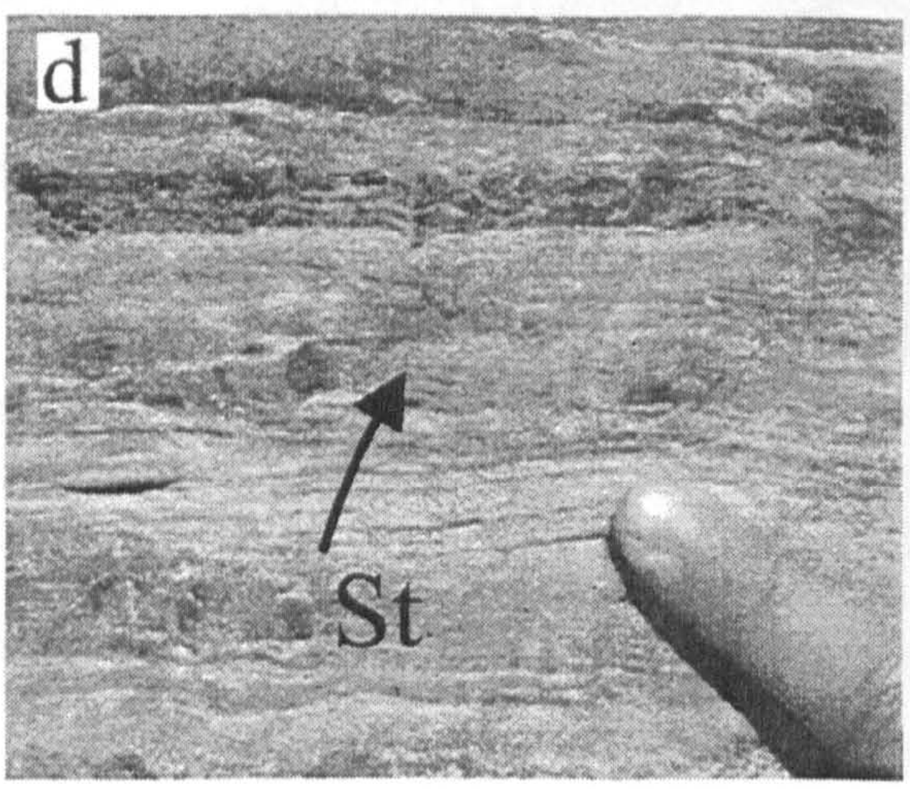


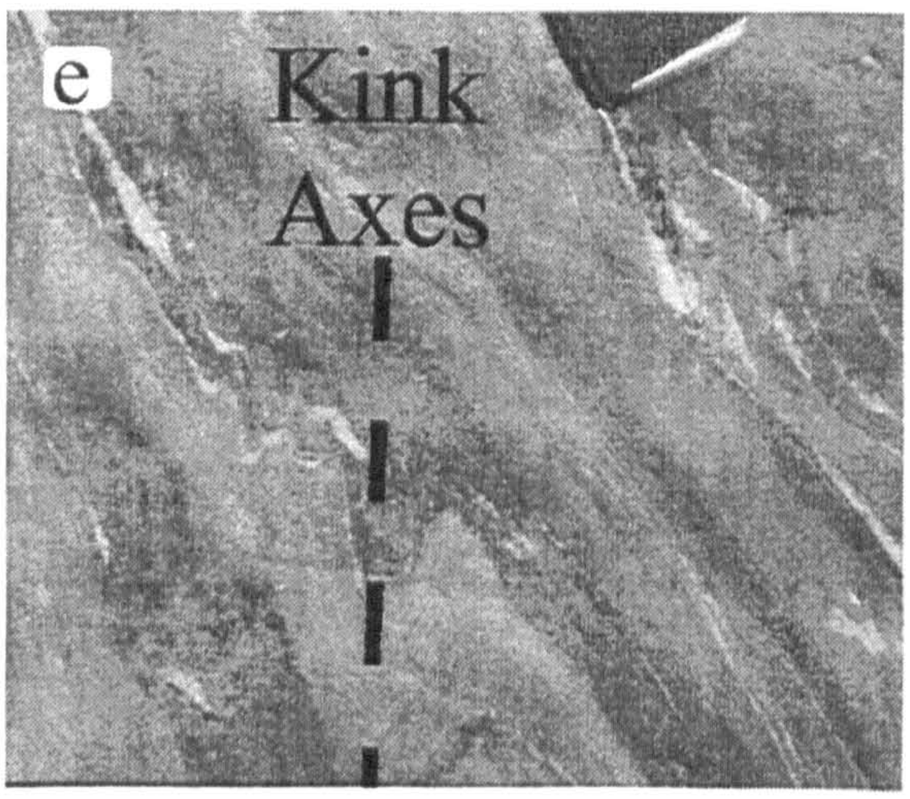


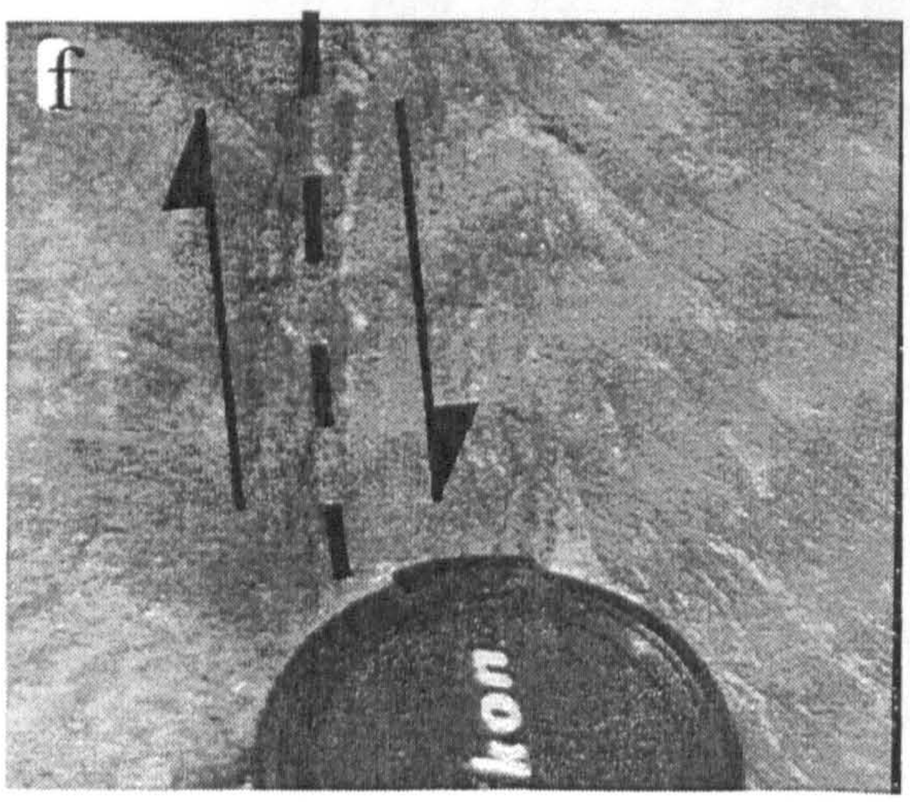


*Figure 2.7 Field relations and petrological observations for the Harsil formation in the Bhagirathi valley. (a) A top-to-the-north brittle-ductile fault identified in the vicinity of Jhala bridge; (b) Photomicrograph of overgrowth of cordierite on staurolite. Pleochroic halo in circle (FOV = 1.5mm) (135); (c) Photomicrograph of sillimanite and biotite in cordierite overgrowths on staurolite (FOV = 2mm) (10/97); (d) Staurolite porphyroblasts overgrowing a crenulation cleavage which is almost parallel to the lithological layering (1N); (e) north verging fold in the Harsil formation which has developed reverse kinks (axial plane marked) (1N); (f) top-to-the-north shears on leucogranite dyke margins (1N).*

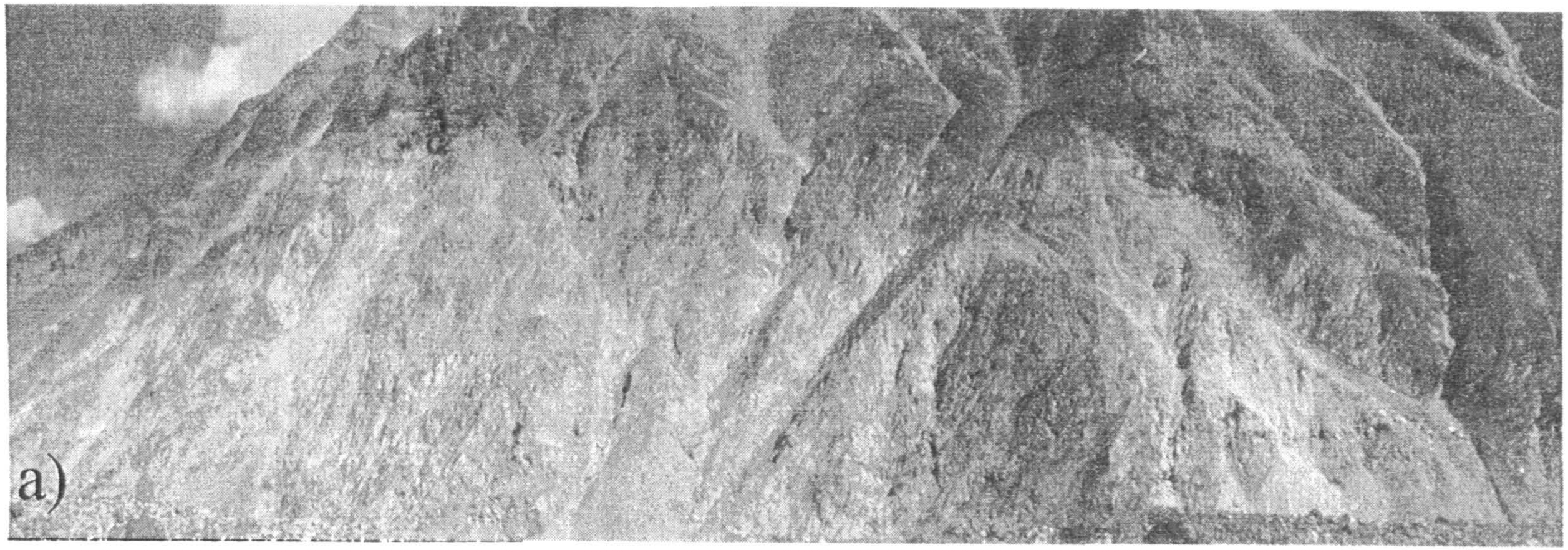


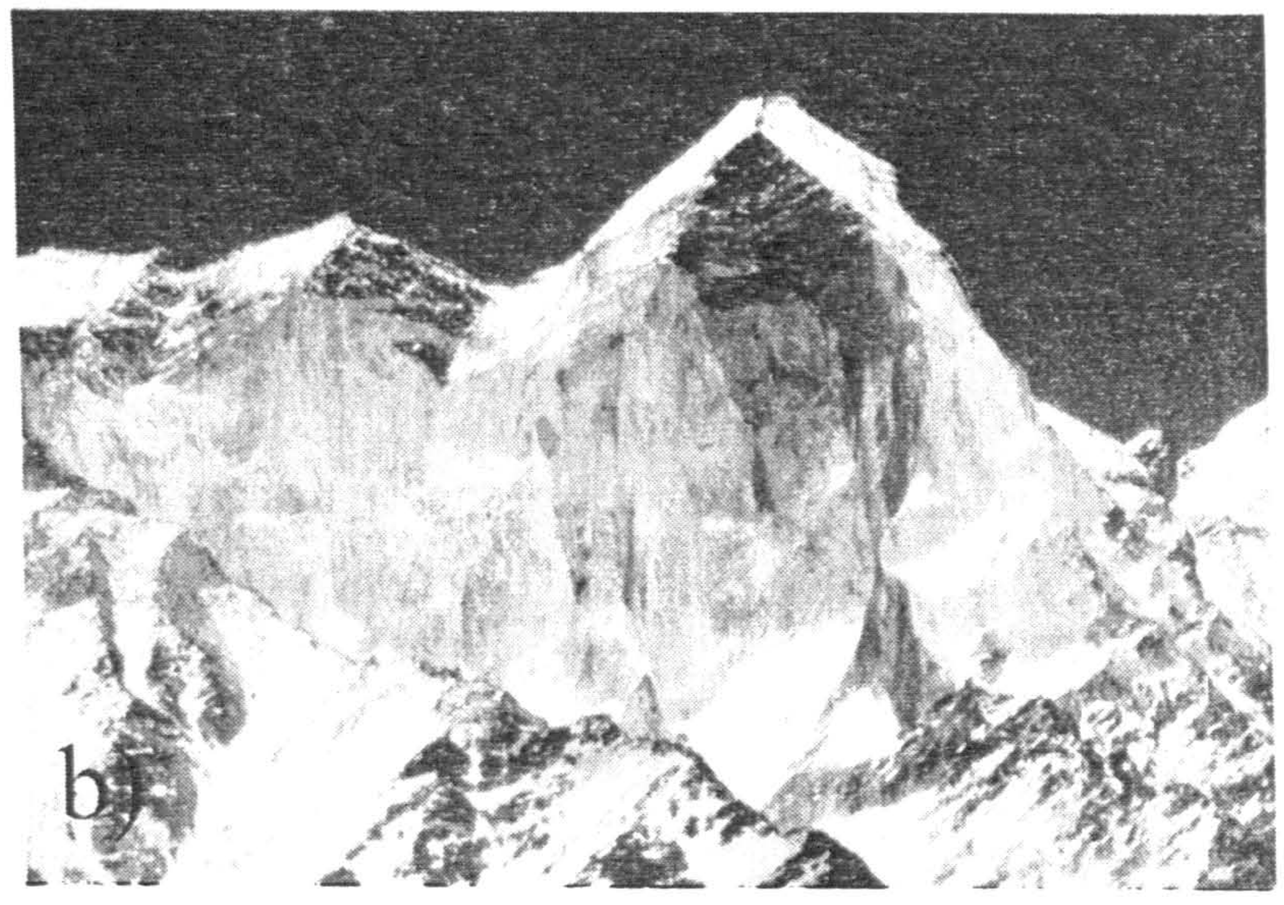


*Figure 2.8 Granites in the Bhagirathi valley, Gaumukh. (a) Bhairongathi granite (pinkish rock) intruding the Harsil formation (dark rock) in the Ratkvarn glacier. (b) south face of Bhagirathi mountains showing the emplacement of the leucogranite (white rock) into the Harsil formation (dark rock). The boundary between the two is indistinct due to the rafting of small slivers of Harsil formation into the leucogranite.*

within the garnet-mica schists as young as 5.7 Ma suggesting that temperatures of ~350°C were maintained until that time. However the K-Ar and $^{40}Ar/^{39}Ar$ ages showed significant scatter, probably as a result of both later displacement along faults leading to recrystallisation and excess argon. Recently, monazite ages in the MCTZ of ~6.5 Ma, as well as 17.5 Ma and 38 Ma, have been interpreted as indicating reactivation of the MCT at ~8 Ma as for other parts of the MCT (Harrison et al., 1997; Catlos et al., 1999). The interpretation of these data is somewhat difficult as the temperature of monazite growth is unclear and the position of the samples in the MCTZ is critical but poorly constrained. However, the monazite data suggest that the MCTZ was affected by some early metamorphism as early as 38 Ma and underwent a sustained period of heating and metamorphism up to ~20 Ma rapidly cooling afterwards. Later reactivation resulted in minor burial and subsequent cooling.

### 2.3.2 The High Himalayan Crystalline

The MCT is identified in this section by the change to a monotonous foliated gneiss. The major mineral assemblage of the gneiss consists of quartz + K-feldspar + plagioclase + biotite ± muscovite ± garnet ± kyanite. The gneisses are well-foliated and strike NW-SE at between 40-60°N with a lower angle C fabric occasionally developed indicating top-to-the-south shear (Figure 2.3). Garnet shows slight retrogression to biotite. Approximately 1km to the north of Dabrani kyanite first appears.

The gneisses give way to a thin band of calc-silicates before the large landslide south of Lohari Nag. The fresh landslide (Figure 2.5a) is comprised of migmatitic gneisses with layering on a 10-50cm scale. Leucosomes may locally form up to 70% of the rock and contain biotite + muscovite + quartz + plagioclase ± tourmaline ± apatite ± K-feldspar ± garnet. The mesosomes contain garnet + biotite + muscovite + tourmaline + epidote + apatite. The non-minimum melt composition of the leucosomes, the presence of epidote and the lack of any aluminosilicate phases suggest that the migmatites did not form by

anatexis. There is evidence for late fluid infiltration within the leucocratic layers, which contain veins of muscovite cross-cutting and altering the K-feldspar and plagioclase (Figure 2.5b). Outcrops just to the south of the landslide contain K-feldspar porphyroblasts, possibly metasomatic in origin, which have overgrown a biotite-muscovite assemblage and contain inclusions of biotite and quartz (Figure 2.5c).

This lithology gives way after 2km to coarse-grained gneiss containing large kyanite laths which coincides with the beginning of leucogranitic aplite and pegmatite dykes and sills. Kyanite has overgrown garnet which is severely retrogressed to biotite (Figure 2.5d).

Within the lower unit kyanite and garnet form the primary assemblage ($M_1$) which grew over an earlier fabric ($S_1$) that is sub-parallel to the later S-C fabric (Figure 2.5f). Kyanite has inclusions of rutile and occasionally includes garnet. Later metamorphism ($M_2$) severely retrogressed garnet to biotite and deformed and fractured kyanite. Small needles of kyanite or sillimanite occur along grain boundaries away from the garnet and kyanite (Figure 2.5e).

750m south of Suki small outcrops of psammites and semi-pelites occur. Staurolite appears in these rocks but is severely broken down and may be forming sillimanite (Figure 2.6a). Garnet and kyanite are also breaking down to biotite and muscovite respectively. As seen in the assemblages further south, fine needles form along grain boundaries.

To the north of Suki an augen gneiss outcrops with large porphyroclasts of plagioclase in a foliated groundmass of K-feldspar + biotite + quartz and accessories of sphene, allanite and muscovite (Metcalfe, 1990). This is cross-cut by pegmatites (Figure 2.6b).

Further to the east, around the base of Shivling, gneisses of the HHCS contain kyanite which are broken and corroded by muscovite. Additionally fibrolitic sillimanite forms the fabric in biotite and other samples show that chlorite also forms parallel to the

schistosity.

### 2.3.3 Harsil formation

The augen gneiss is taken as the boundary between the HHCS and the Harsil formation in which pelites and psammites become dominant. The assemblages consist of biotite + quartz + plagioclase + muscovite ± kyanite ± garnet ± tourmaline ± sillimanite. Kyanite is broken (Figure 2.6c) and garnet is often severely corroded by biotite as in the gneisses in the HHCS. Just north of Jhala bridge fibrolitic sillimanite becomes visible in hand specimen and occurs along the foliation until mid-way between Jhala bridge and the bend in the river to the north. In thin section sillimanite forms along grain boundaries. Up to the bend in the river small layers of semi-pelite occur containing the ortho-amphibole gedrite (Figure 2.6d). The mineral assemblage was verified by electronmicroprobe and is thought to have been mistakenly identified as sillimanite by Metcalfe (1990). To the east along the Bhagirathi the dominant lithologies are pelites, semi-pelites and psammites which occasionally contain staurolite and kyanite. Some garnet is corroded by biotite. Garnet and staurolite are wrapped by the fabric and inclusion trails indicate syn-kinematic growth (Figure 2.6e).

Within the Harsil formation around Harsil several generations of folds can be found indicating two phases of intrafolial folding, the second of which develops an axial planar foliation parallel to the main foliation elsewhere. The main foliation trends E-W at an angle of 33-60°N with a lower angle C fabrics indicating top-to-the-south shearing (Figure 2.3). The final deformation ($D_3$) is a top-to-the-north phase represented by only a few brittle-ductile features (Figure 2.7a).

The psammites and pelites found in the vicinity of Jhala to Harsil appear to be the same as those found to the east of Gaumukh, which also have kyanite + staurolite bearing assemblages but which additionally show overprints of cordierite (Figure 2.7b). Only rarely can fibrolitic sillimanite be found which cross-cuts cordierite (Figure 2.7c).

However, the Harsil formation in the area of Gaumukh shows a different structural history to the Jhala bridge area. Lithological layering, $S_0$, forms the main foliation and is broadly parallel to the main foliation in the Harsil area. However, the first recognisable deformation phase is the localised development of a crenulation cleavage ($S_1$) bounded by $S_0$ and overgrown by the $M_1$ staurolite and kyanite porphyroblasts (Figure 2.7d). The rocks were subsequently folded by NE-E-verging asymmetric folds with axial planes striking ~340°N (Figure 2.7e). The orientation of the folds and the reverse kinks indicate a top-to-the-north shear and have a similar orientation to the folds north-east of the Bhagirathis (Searle et al., 1993). The final stage of deformation is found on the margins of leucogranitic dykes with the development of top-to-the-northeast shear fabrics (Figure 2.7f).

The relationship between the top-to-the-south shearing experienced by the Harsil formation in the west of the Bhagirathi valley and the top-to-the-northeast deformation in the Gaumukh area around Shivling is not determined but both post-date the growth of the primary metamorphic assemblage. In both areas leucogranitic dykes cross cut the main foliation and are only weakly deformed, thus bracketing the main deformation event between metamorphic mineral growth and leucogranite formation. The two deformation phases are designated $D_{2a}$ and $D_{2b}$ in the west and east respectively.

*HHCS and Harsil formation. Tethyan sediments?*

Given the lack of agreement on the boundaries in the Himalaya the choice of boundary between the Harsil formation and the HHCS deserves some discussion.

Metcalfe (1990) placed a tectonic boundary between the HHCS and the Harsil formation – the Jhala Normal Fault - just to the north of Jhala bridge which was based on the metamorphic grade change northward from apparently upper-amphibolite facies, indicated by sillimanite, to a maximum of lower-amphibolite facies indicated by hornblende-bearing calc-silicates. This author has two major disagreements with this

interpretation and classification of the units. Firstly the grade change is not as significant as suggested by Metcalfe (1990) as garnet + staurolite + kyanite bearing assemblages have been found, in the Harsil formation, to the north of the Jhala Normal Fault. Secondly, although minor brittle-ductile faults have been found (Figure 2.7a) they are unlikely to be responsible for major displacement and there is little, if any, structural data to suggest the existence of a major normal fault in the vicinity of Jhala. It is, therefore, not possible to confirm Metcalfe's proposition that the boundary between the HHCS and the Tethyan sediments lies at this point.

Pecher and Scaillet (1989) appear to have used lithological criteria for the separation of the Bhagirathi section into Harsil formation and HHCS. However, their boundary lies significantly to the south of Suki resulting in the mylonitic augen gneiss north of Suki belonging to the Harsil formation. These authors also appear to incorporate the coarse gneisses to the south of Suki in the Harsil formation, although the latter is unclear due to the scale of mapping.

Given the lithological definition for the MCT to the south, the sequence of rocks in the section have been separated into two formations: 1) the HHCS proper and; 2) the Harsil formation representing the more pelitic assemblages found to the north of Suki. This results in a few staurolite-bearing assemblages being included into the HHCS but the Harsil formation is exclusively psammites-pelites. This proposed lithological boundary can be correlated with the change in rock type found on the southern side of Shivling much further to the east. However, it must be borne in mind that this boundary may, in detail, be both gradational and imbricated.

Metcalfe (1990) also suggested that the Harsil formation is the equivalent of the Tethyan sediments found elsewhere in the Himalayan orogen. These are generally low- to unmetamorphosed sediments as in the Dhauli valley at Malari (see "Malari Fault"). Indeed unmetamorphosed turbidites are known to outcrop to the north of Gaumukh. The

relationship between the Harsil formation and the unmetamorphosed Tethyan sediments cannot be easily investigated given the limited access to areas further north but the pelitic nature and probable sedimentary protolith of the Harsil formation suggest that the Harsil formation represents the basal section of the Tethyan sediments metamorphosed in the Himalayan orogeny (see Chapter 4 for further discussion of timing).

### 2.3.4 Bhairongathi Granite

A biotite-granite, intruded into the Harsil formation, has been correlated with other Palaeozoic granites in the Himalaya by Stern et al. (1989) based on its geochemistry. The biotite-granite is intrusive into the metasediments in the Ratkvarn valley (Figure 2.8a) but the contacts are poorly exposed elsewhere. The granite is foliated and folded along its basal contact though it is not penetratively foliated throughout (Stern et al., 1989). It is cross-cut by leucogranite dykes, sills, and small plutons.

### 2.3.5 Leucogranites

North of Lohari Nag leucogranitic dykes intrude the Harsil formation and become increasingly prevalent towards the leucogranite laccoliths in the Gangotri area. Some leucogranitic dykes were intruded near the end of the deformation history of the rocks, and into an extensional regime, as shown by top-to-the-north C fabrics on dyke margins (Figure 2.7f).

Leucogranite laccoliths and plutons stretch from Gangotri on the Bhagirathi river, where they form isolated small plutons intruded into the Harsil formation between the HHCS and the TSS, to east of the Alaknanda where they outcrop extensively in militarily sensitive areas. In the Gangotri region it is known as the Gangotri granite and in the east as the Badrinath granite. The Gangotri granite is spectacularly exposed in the faces of the Bhagirathi and Shivling mountains (Figure 2.8b).

The leucogranite is chemically similar to other HHL bodies, is fine-grained, contains

quartz + K-feldspar + plagioclase + tourmaline + muscovite ± biotite ± garnet ± beryl with apatite as the most abundant accessory mineral (Scaillet et al., 1990). The high $^{87}Sr/^{86}Sr$ ratios (0.746-0.780) and low initial $^{143}Nd/^{144}Nd$ ratios (0.5119) (Stern et al., 1989; Scaillet et al., 1990) indicate the granites generation from continental crust without a mantle contribution. The inhomogeneous distribution of $^{87}Sr/^{86}Sr$ in the granite suggests that little mixing occurred between the different batches of magma (Scaillet et al., 1990).

Based on the shape of the laccoliths, deformation of feeder dykes below the intrusions and structures in the underlying gneisses, the granite is thought to have been emplaced syn- to post- extensional movement (Searle et al., 1993; Scaillet et al., 1995). Details of the internal structure, determined using magnetic studies Pecher (1989), however, fail to point to any clear role for top-to-the-north deformation but showed a component of dextral shear within the main body.

Early K-Ar age determination by Seitz et al. (1976) from the Arwa Valley to the north of Badrinath gave cooling ages of 18.4±0.7 Ma. A later Rb-Sr isochron by Stern et al. (1989) gave an age of 64±11 Ma. This latter age probably reflects incomplete isotope mixing on the scale of sampling. Additional K-Ar and $^{40}Ar/^{39}Ar$ muscovite cooling ages from the bodies in Gangotri cluster around ~18 Ma (Stern et al., 1989; Sorkhabi et al., 1996). A recent study by Searle et al. (Subm.) obtained U-Pb monazite ages of 23±0.2 Ma from the Shivling leucogranite.

## *2.4 Petrography and field relationships: Alaknanda and Dhauli*

### 2.4.1 Main Central Thrust Zone

Despite lithological differences in the MCTZ between the Bhagirathi and Alaknanda valleys the upper boundary to the MCTZ is termed the MCT/Vaikrita thrust and the base is termed the Munsiari thrust in line with the studies in the Bhagirathi valley

(Figure 2.9).

Recent geochemical work by Ahmad et al. (In press) has shed more light on the nature of the lithological changes in the Alaknanda. They showed that the hanging wall of the Vaikrita thrust in the Alaknanda is characterised by $\varepsilon_{Nd}$ of -14 to -19 whereas the rocks of the MCTZ and the LH have a significantly lower $\varepsilon_{Nd}$ of -23 to -28. This would place the major thrust, in this case defined as the boundary between two formations of different provenance, some 2 ½ km south of the MCT as defined by previous authors. The isotopic MCT does not coincide with either the lithological change from schist to gneiss or the structural change from rotated minerals to unoriented garnet and kyanite. The more southerly, isotopic, MCT lies south of the garnet isograd, and, if accepted, garnet-mica schists containing rotated garnet would be included in the HHCS.

The apparent dichotomy between the isotopic and field MCT may be the result of the imbrication of tectonic slices within the MCTZ, combined with sampling bias towards rock types predominantly sourced from one or other of the units. This may be the case in Ahmad et al. (In press) as all the measured samples to the north of the isotopic MCT are gneisses and, if imbrication within the MCTZ does occur, are likely to have been sourced from the HHCS. Despite these concerns the work shows that some of the rocks within the field-defined MCTZ have a distinct source from the HHCS.

The present work, however, will be based on the field-determined position for the MCT as shown on Figure 2.9.

The Munsiari thrust south of Helang is marked by the change from phyllonitic and highly-sheared dirty limestones to chloritic-schists. The chloritic schists do not show a tectonic break with the underlying quartzites and calc-silicates. The lithologies north of the chloritic schists are: (i) an amphibolitic schist, (ii) interleaved augen gneiss, quartzites and micaschists and, (iii) foliated gneisses of the HHCS at the MCT/Vaikrita thrust. In the Dhauli valley similar outcrops occur with more abundant amphibolite

layers.

The pelites in the Alaknanda and in the Dhauli contain biotite + muscovite + quartz + plagioclase + graphite ± garnet ± staurolite ± tourmaline ± chlorite with accessory allanite, zircon and ilmenite. Garnets often contain rotated inclusion trails (Figure 2.10a) and isoclinal folds are occasionally preserved in the groundmass. Chlorite forms in the fabric in some samples but generally forms unoriented overgrowths to garnet. Thin bands of gneiss occur in the MCTZ with similar mineralogy to the pelites.

Augen gneisses are similar to those found in the Bhagirathi valley with rounded K-feldspar overgrown by muscovite (Figure 2.10b,c). Amphibolites containing small south-verging folds outcrop throughout the MCTZ and, around Tapoban, contain hornblende + quartz + biotite + rutile + clinozoisite with a strong fabric defined by hornblende. Rare calc-silicates occur and contain calcite + clinopyroxene + garnet + biotite + quartz + muscovite. Quartzites occur throughout but occasionally form thicker bands as shown on Figure 2.9.

The MCTZ has a well developed schistosity dipping at around 30-50°N and a well developed cross-cutting C fabric at 0-45°N (Figure 2.11). The numerous S-C fabrics attest to a top-to-the-south non-coaxial shear strain and occasional isoclinal folds can be found with a strongly developed axial-planar cleavage in both outcrop and hand specimen. The whole of the MCTZ is highly sheared but deformation is inhomogenously distributed (Figure 2.10d).

The deformation throughout the sequence is similar to the Bhagirathi valley with $M_1$ garnets preserving an early $S_1$ fabric. The $M_1$ assemblage is wrapped and deformed by biotite-muscovite S-C fabrics during $D_2$. The isoclinal intrafolial folds and an attendant axial planar cleavage are cut by the pervasive low angle $D_2$ C fabric but their relationship to $M_1$ is not clear. The metamorphic assemblages suggest that $M_1$ reached lower amphibolite facies and was subsequently overprinted by a syn-kinematic

greenschist facies metamorphism (M2).

### 2.4.2 High Himalayan Crystallines

The boundary between the HHCS and the MCTZ is marked by the MCT (Vaikrita thrust) (Valdiya, 1980; Virdi, 1986). The actual fault has not been identified by the author and Virdi (1986) suggests that there is, in fact, no tectonic break - as did Pati and Rao (1983) in the Bhagirathi valley. However, there is a marked change in lithology from the foliated intercalated quartzites and mica schists of the MCTZ to a less foliated biotite gneiss. The HHCS in the Dhauli and the Alaknanda valleys can be separated into three principal units, though the boundaries between each unit are gradational. These are the basal, middle and upper units.

The biotite-gneiss of the basal-HHCS, just above the MCT, contains plagioclase + quartz + biotite ± muscovite ± garnet ± K-feldspar ± kyanite ± rutile and is segregated on a 2-20cm scale (Figure 2.12a). This unit gradually becomes more quartz-rich and grades into the massive dirty quartzite of the middle unit of the HHCS (Figure 2.9). Small calc-silicates can be found near the top of the basal-HHCS and throughout the rest of the HHCS.

Garnet in the Dhauli valley just below the quartzites overgrew an early fabric ($S_1$) (Figure 2.12b) but in less deformed rocks tends to be randomly oriented in the foliation. The biotite-gneiss contains isoclinal folds with a well developed axial-planar schistosity which is cut by a weak C fabric. This deformation event ($D_2$) post-dates the $M_1$ assemblage and rotates and deforms kyanite. A second generation of small acicular to stubby crystals form along grain boundaries (Figure 2.12c). The secondary crystals have been identified as kyanite by Hodges and Silverberg (1988) but the author has not been able to confirm their composition due to the extremely small size. The $M_1$ assemblage shows retrogression by a second metamorphism ($M_2$) in which biotite and platy muscovite cross-cut the fabric of the gneiss in many places.

The basal-HHCS also has open folds, found below Joshimath, but the relationship to the isoclinal folds is not clear. As for elsewhere in the Garhwal Himalaya, shear is inhomogeneously distributed throughout, and the Dhauli river garnetiferous mica-schists outcrop along with mylonitised gneiss (Figure 2.12d).

The quartzites of the middle unit in both the Alaknanda and Dhauli valleys contain minor biotite and muscovite and are interlayered with calc-silicate and pelite layers up to 50cm thick. The quartzites then grade back into gneisses and near the top in the Dhauli valley, contain intrusions of granitic gneiss. The outcrops become gradually more biotite rich and some leucogranite intrusions can be found cross-cutting the foliation. The quartzites are openly folded on a 300m scale and are pervasively isoclinally folded (Figure 2.12e), with the axes of the folds rotated into the direction of the shear. Most fabrics within the quartzites indicate top-to-the-southwest shear sense but rare top-to-the-east ductile faults with biotite-muscovite fabrics can be found (Figure 2.12f). Thin calc-silicate layers are common in the quartzites and contain garnet + clinopyroxene + hornblende + epidote + quartz + calcite + sphene.

The upper units differ in the Alaknanda and Dhauli valleys. In the Alaknanda the quartzites grade into biotite gneisses and schists. Just to the south of Badrinath small intrusions of leucogranite occur which have been subsequently deformed (Figure 2.13a; Chapter 5). The sequence then changes orientation from northerly dipping gneisses to almost flat-lying calcsilicates near Badrinath. Just south of Mana the quartz-rich gneisses dip to the north, with increasing amounts of relatively undeformed leucogranitic dykes and sills.

The area north of Mana is a highly sensitive military area where access is difficult to obtain and limited to the area south of Ghastoli. The Arwa valley, which is cut from east to west by a leucogranite pluton, contains no outcrop except at the base of the cliffs which are constantly bombarded by rock fall from the hanging glaciers along its length.

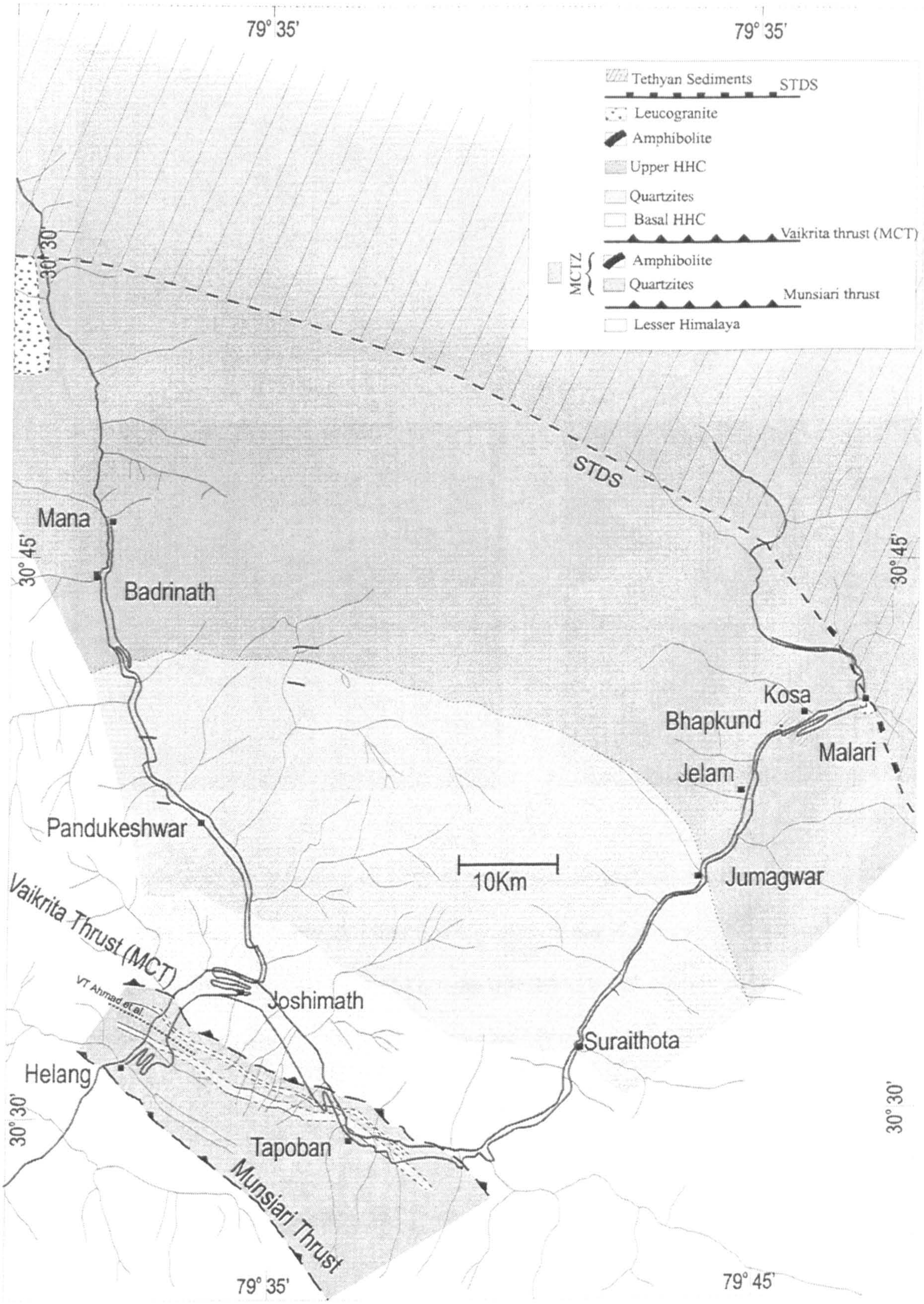


*Figure 2.9 Schematic geological map of the Alaknanda valley compiled from field work by the author and from Virdi (1986).*

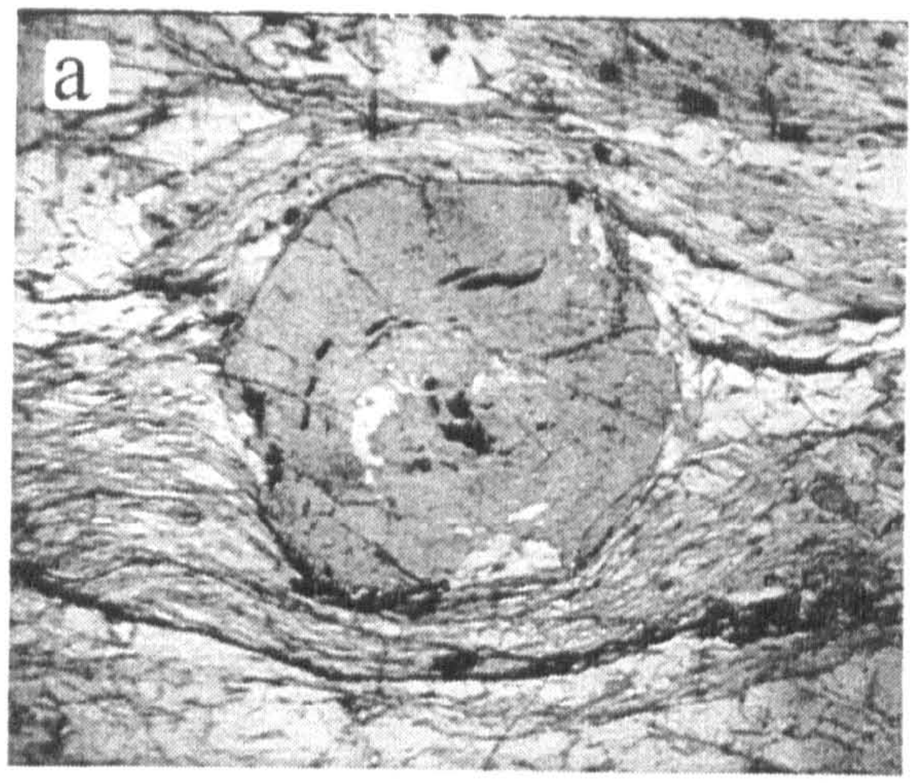


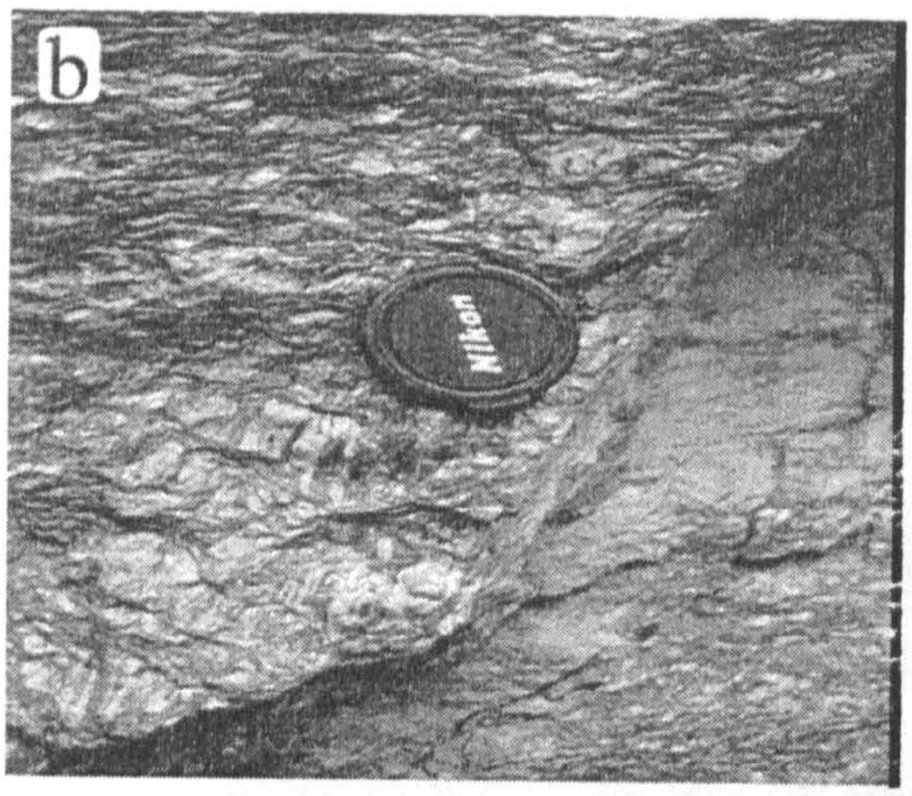


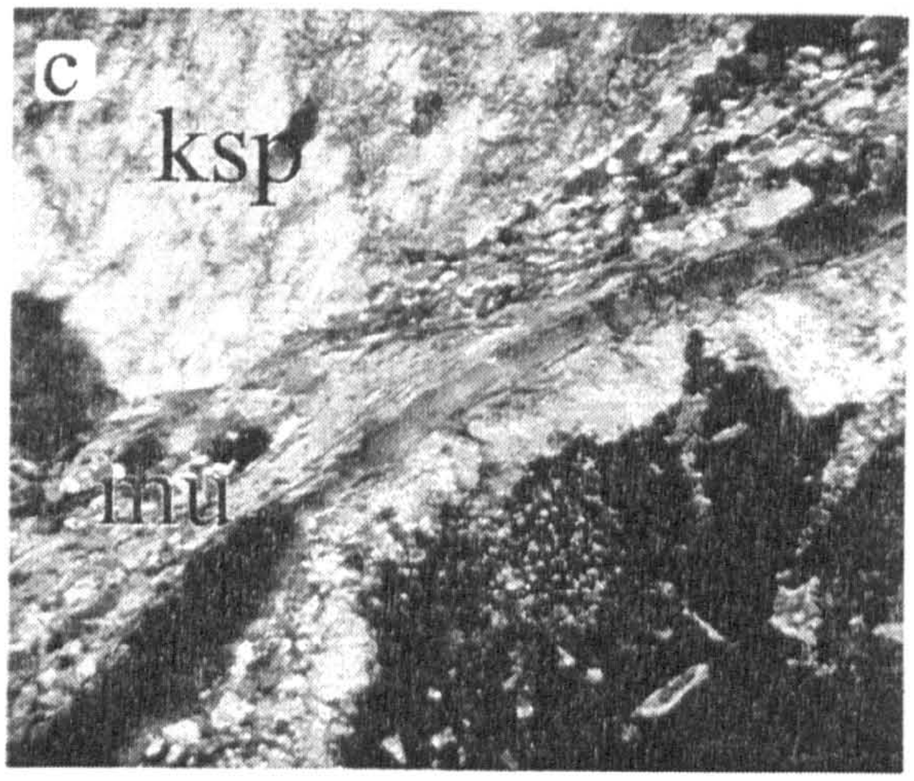


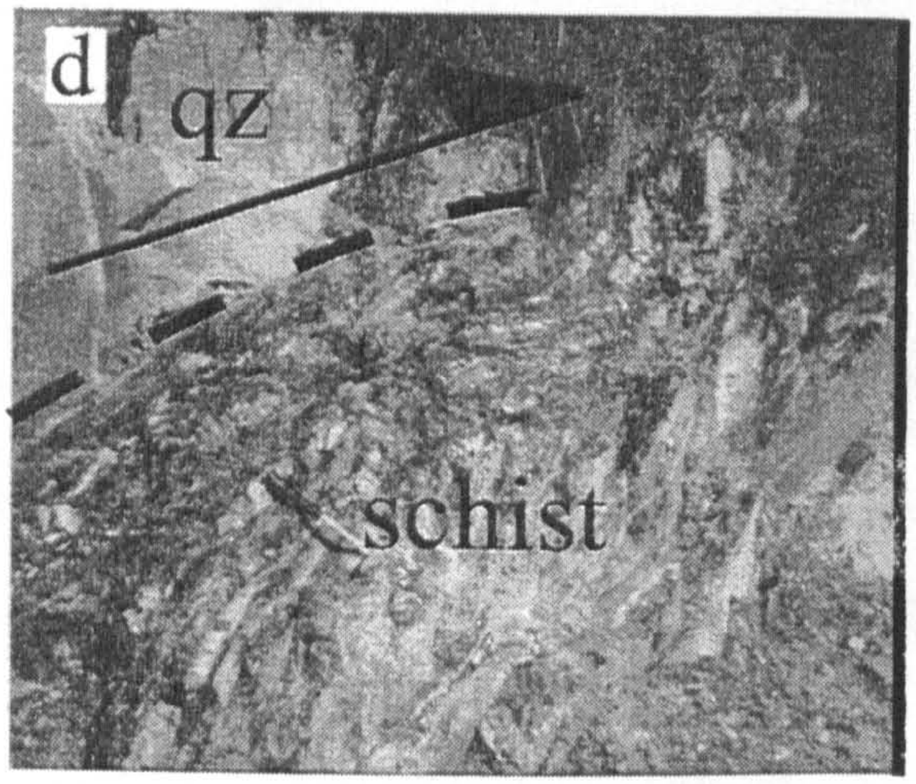


*Figure 2.10 Field relations and petrological observations for the MCTZ in the Alaknanda and Dhauli valleys. (a) Photomicrograph of rotated inclusion trails in garnet (FOV = 5 mm) (4a3); (b) Streaky augen gneiss with the development of a strong stretching lineation defined by deformed augen of feldspar; (c) Photomicrograph of edge of an augen of K-feldspar. The augen is wrapped by a muscovite and quartz fabric (FOV = 10mm) (43/97); (d) Deformed schists and quartzites in the MCTZ indicating high shear.*

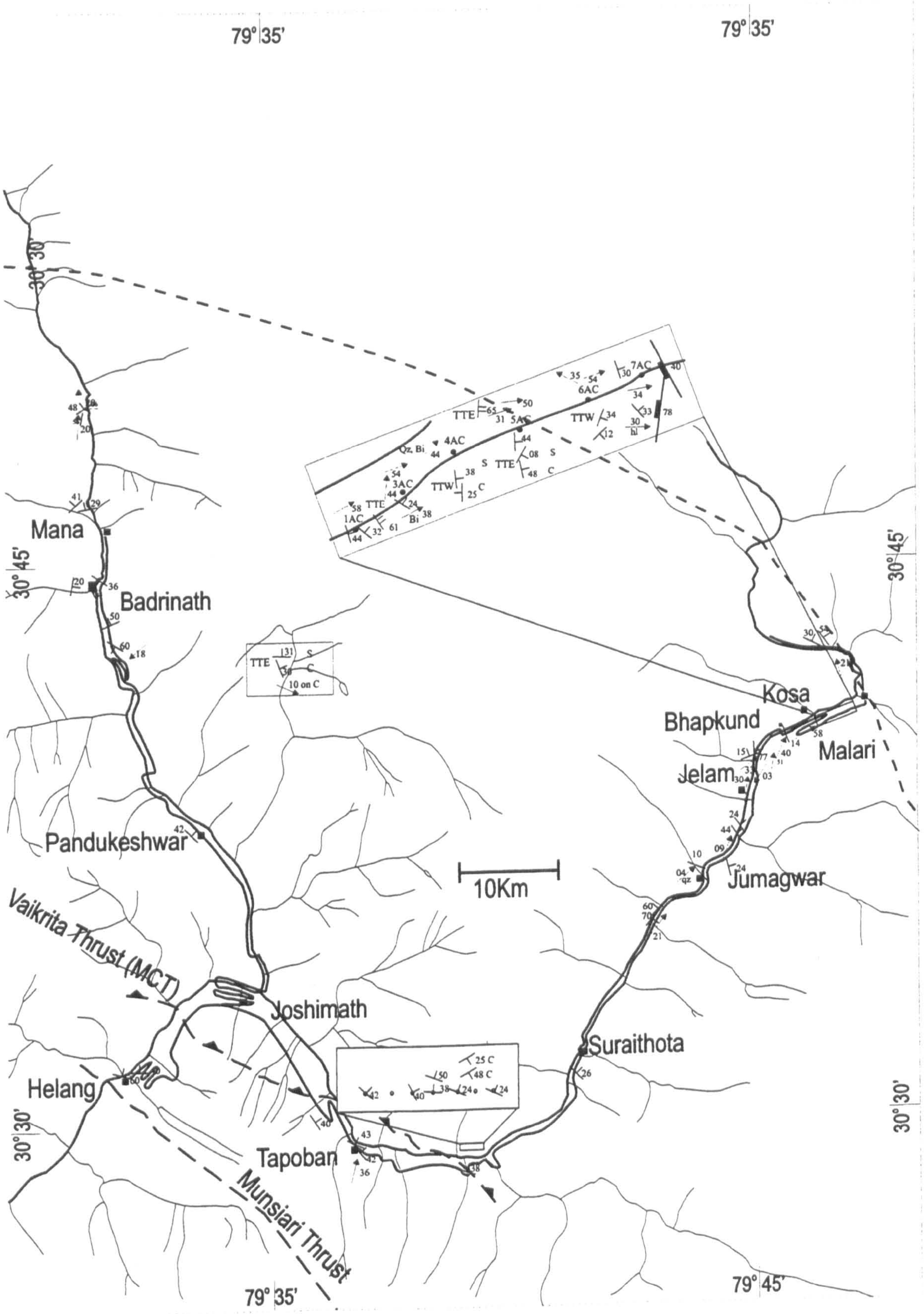


*Figure 2.11 Structural map of the Alaknanda valley showing dip and strike of the beds and mineral lineations.*

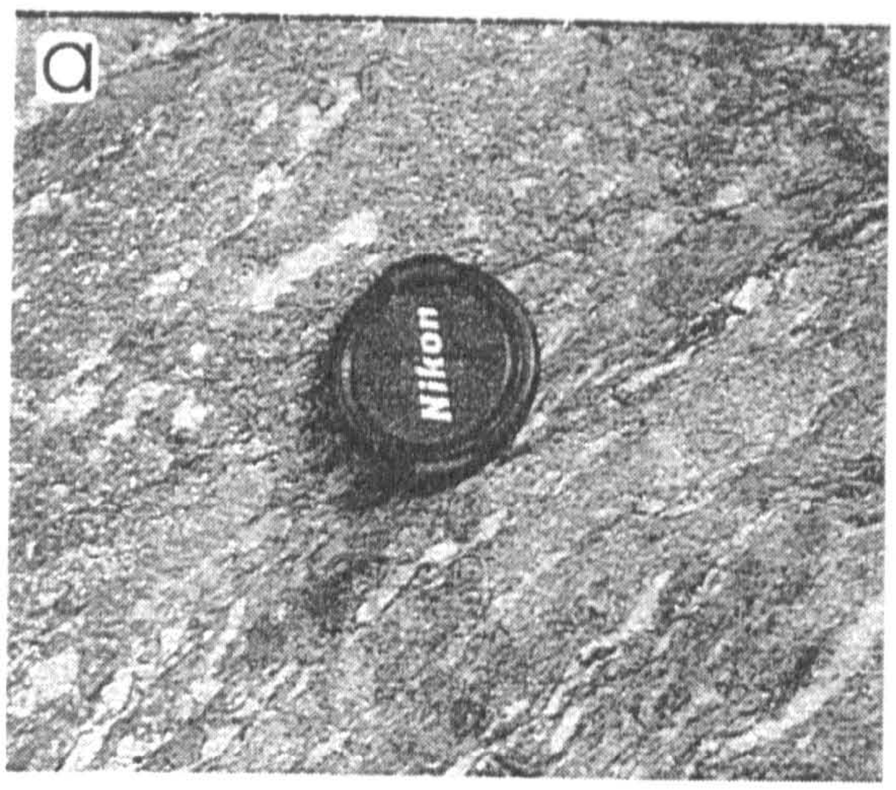


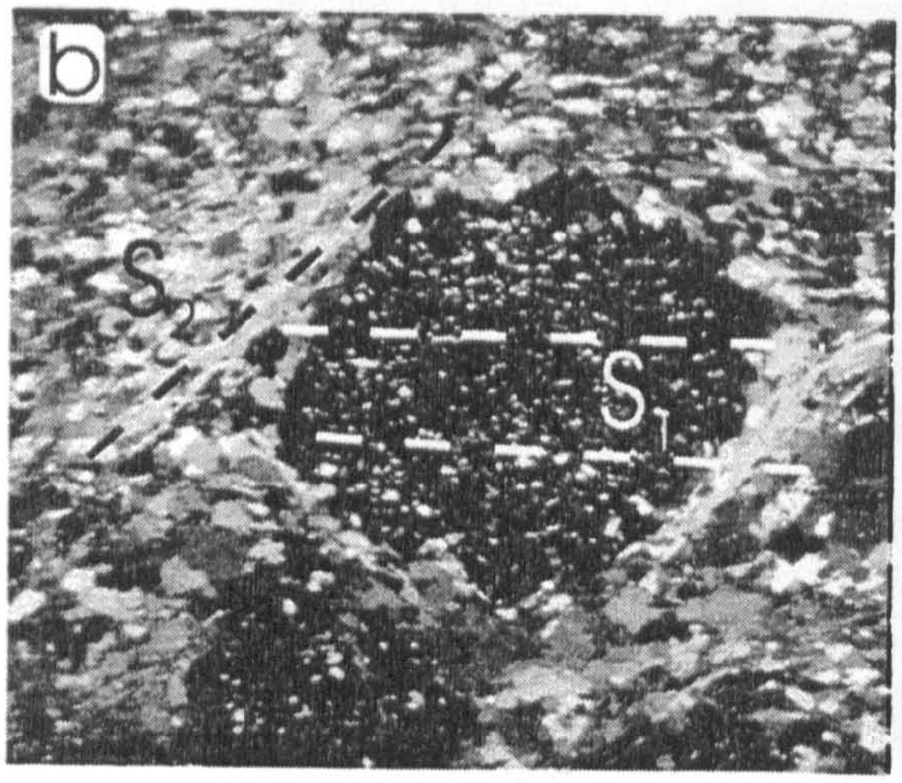


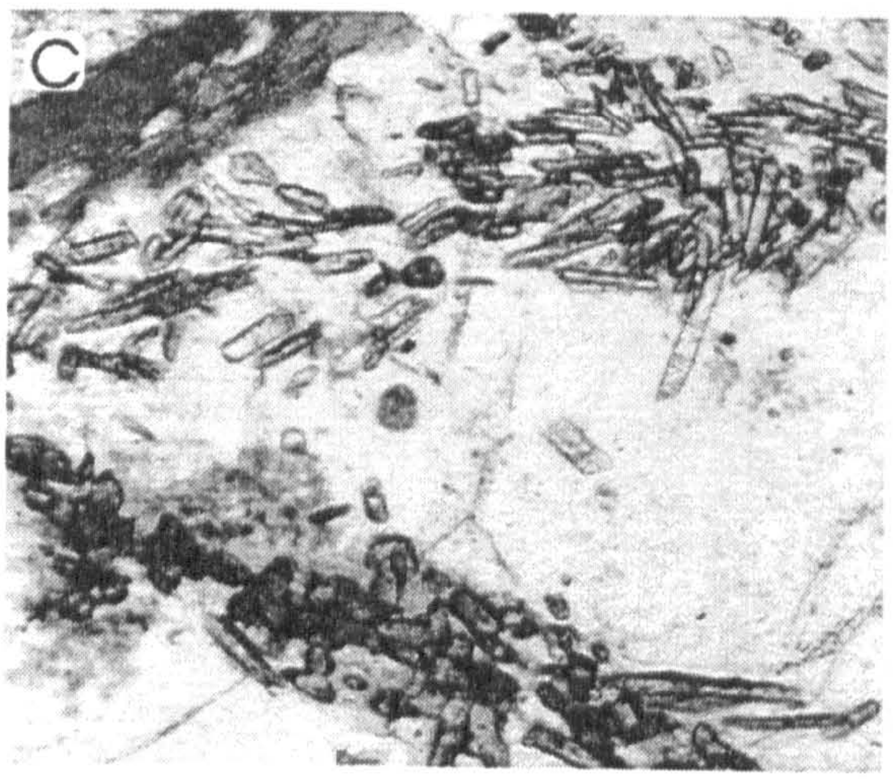


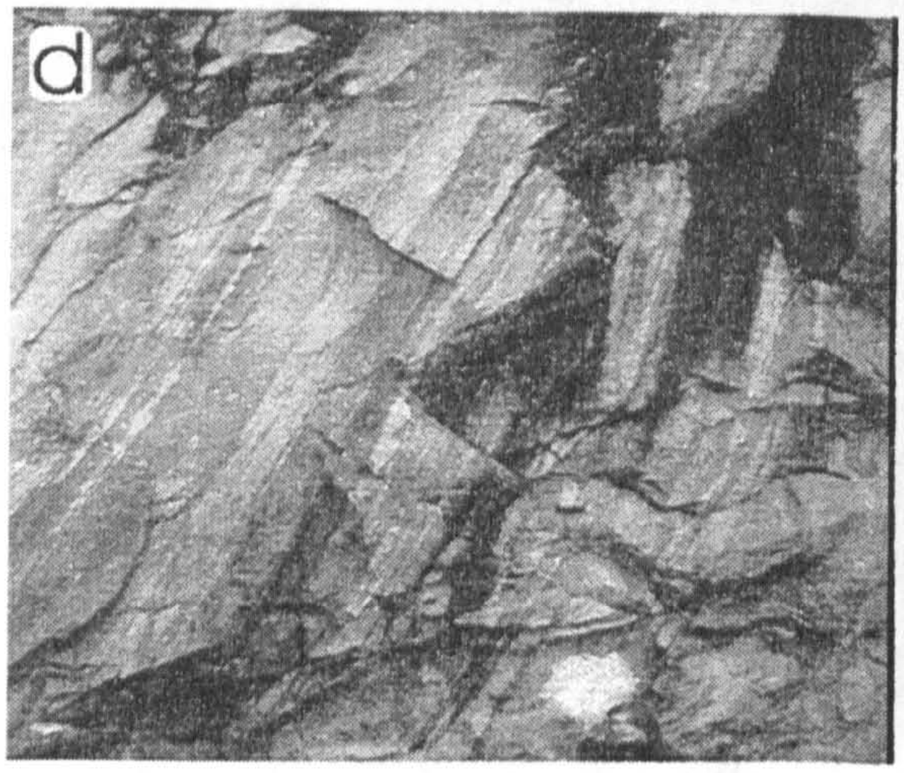


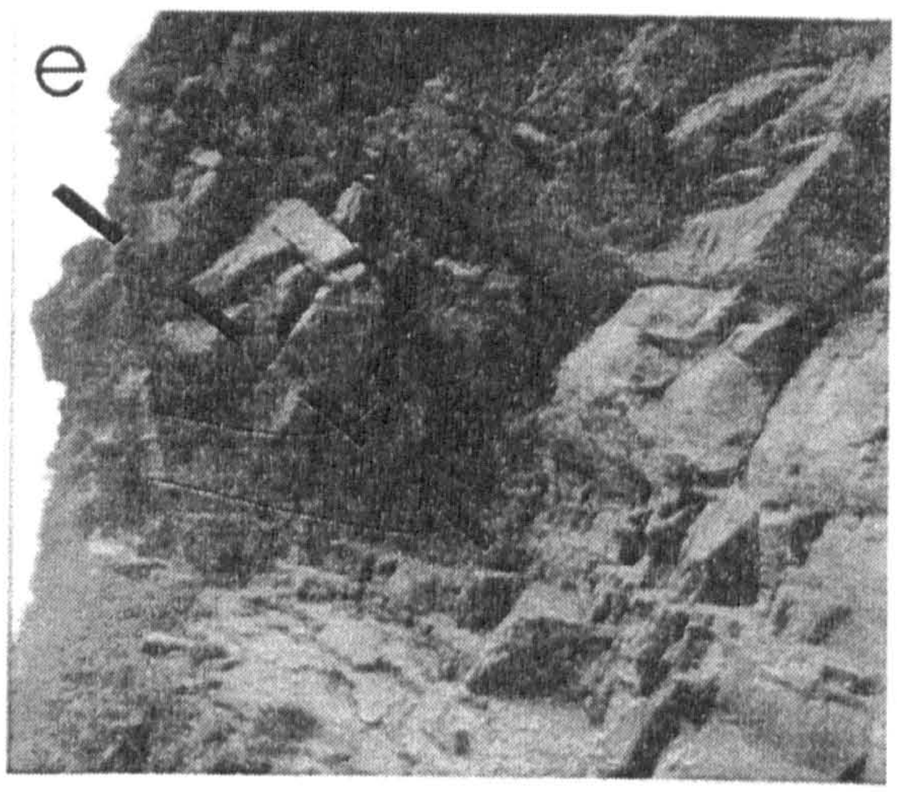


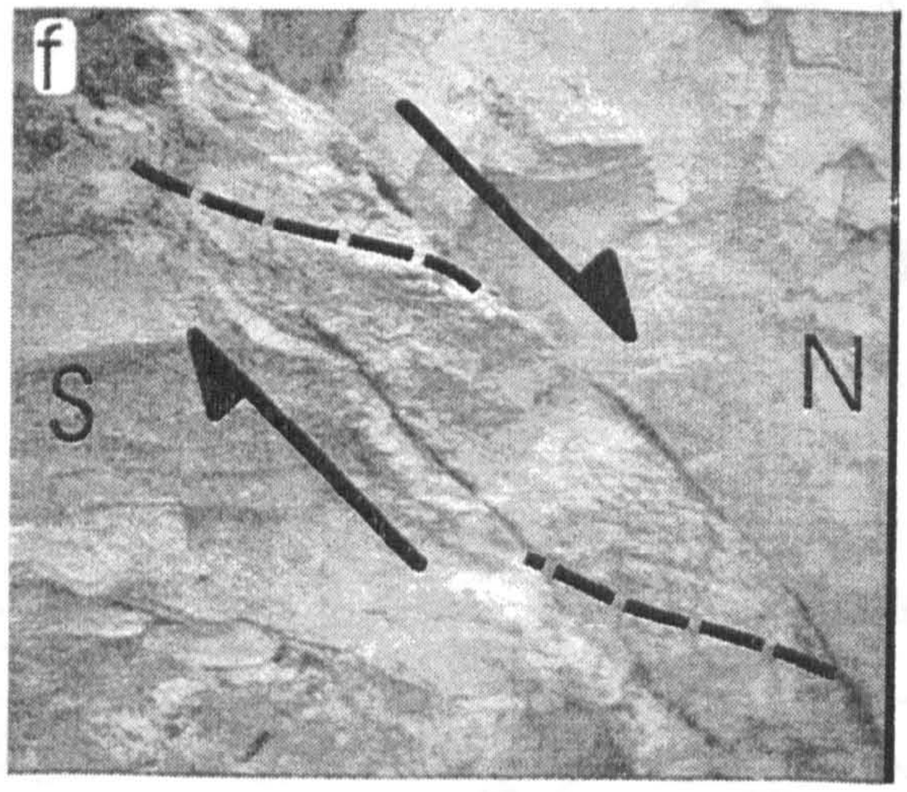


*Figure 2.12 Field relations and petrological observations for the HHCS in the Alaknanda and Dhauli valleys. (a) Gneiss of the basal HHCS (6A); (b) Photomicrograph of $S_1$ preserved in garnet cores at an angle to the main foliation (FOV = 5mm) (8); (c) Photomicrograph of acicular needle growth in the basal-HHCS (FOV = 1mm) (2B2); (d) Mylonitised gneiss, schists and granite from near the MCT in the Dhauli valley indicating high shear; (e) Isoclinal folds in the quartzites. The hinge axis has been rotated parallel to the stretching lineation (FOV = 2m); (f) TTE ductile fault in quartzites indicating influence of extensional tectonics ~40Êkm south of the STDS.. Shear zone ~10cm wide.*

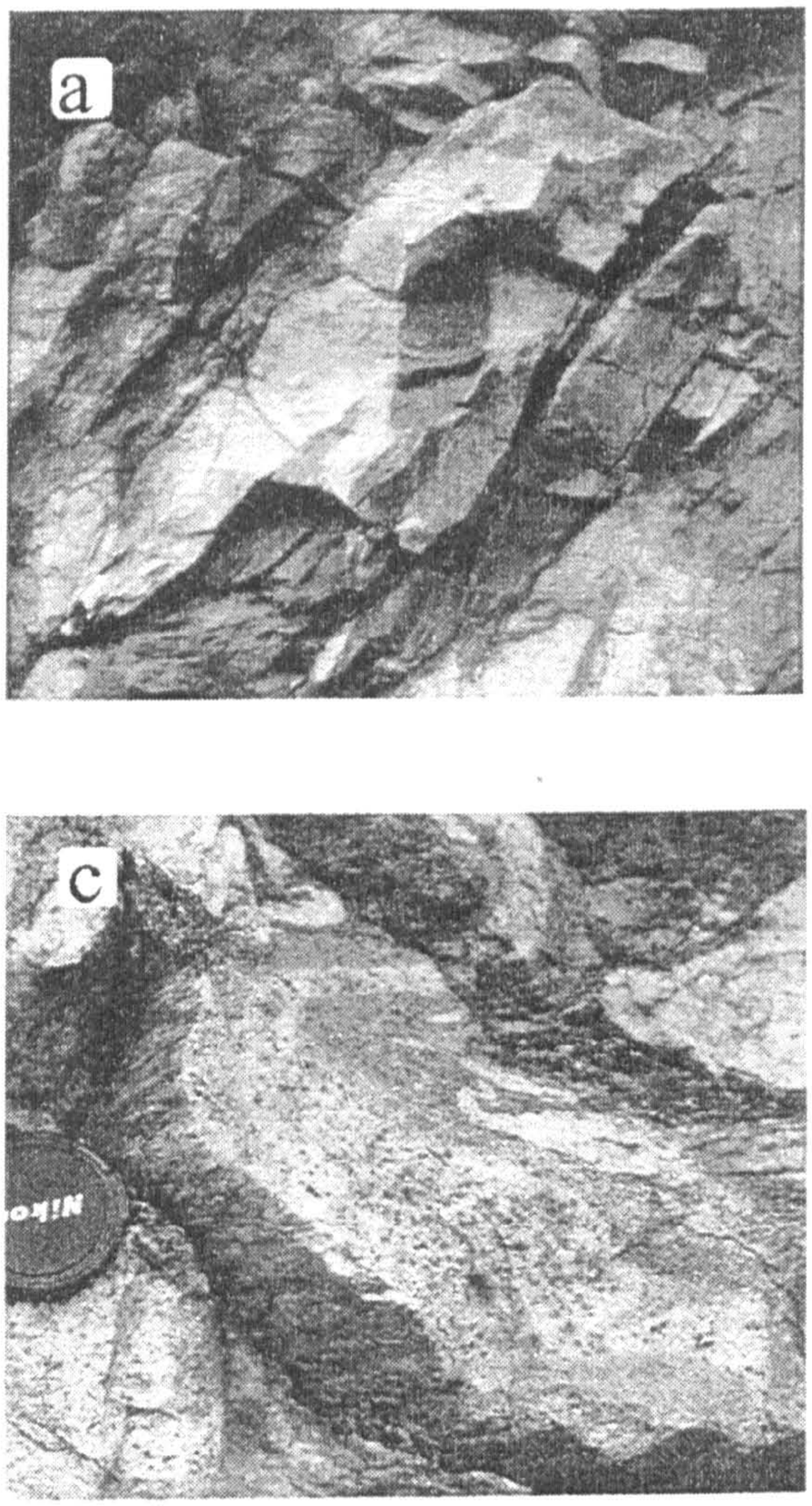


*Figure 2.13 Field relations and petrological observations for the upper-HHCS of the Alaknanda and Dhauli valleys. (a) Deformed leucogranite dykes (white) in the upper-HHCS of the Alaknanda valley Intrusion ~1m wide (G31(1)); (b) disharmonically folded gneiss in the Dhauli valley (FOV~1m); (c) Folded anatectic migmatites in the Dhauli valley. Pale bands are tourmaline bearing leucogranites in a gray foliated gneiss. Main foliation forms axial plane to folds; (d) Photomicrograph of fibrolitic sillimanite overgrown by muscovite. The muscovite forms at an angle to the main foliation defined by biotite on the bottom edge of the photograph (FOV = 0.5mm) (18).*

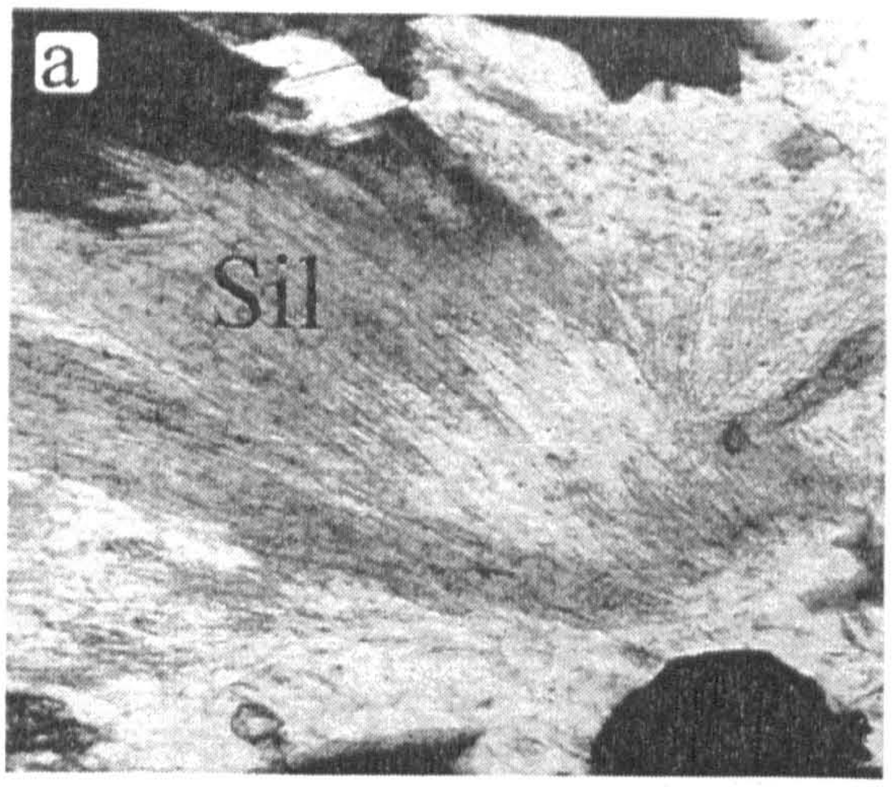


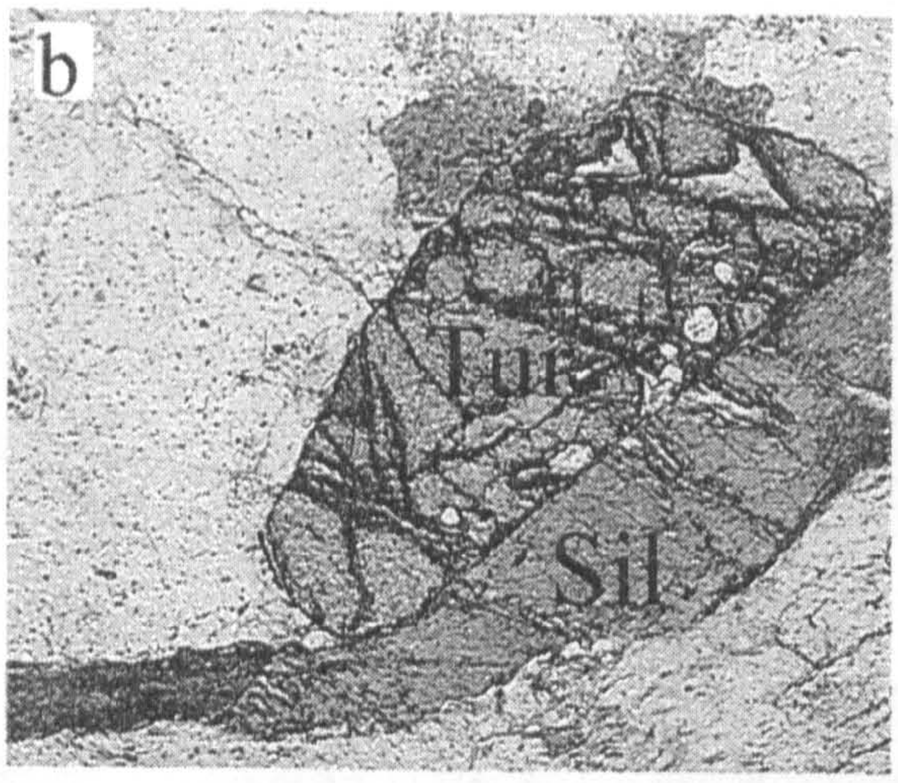


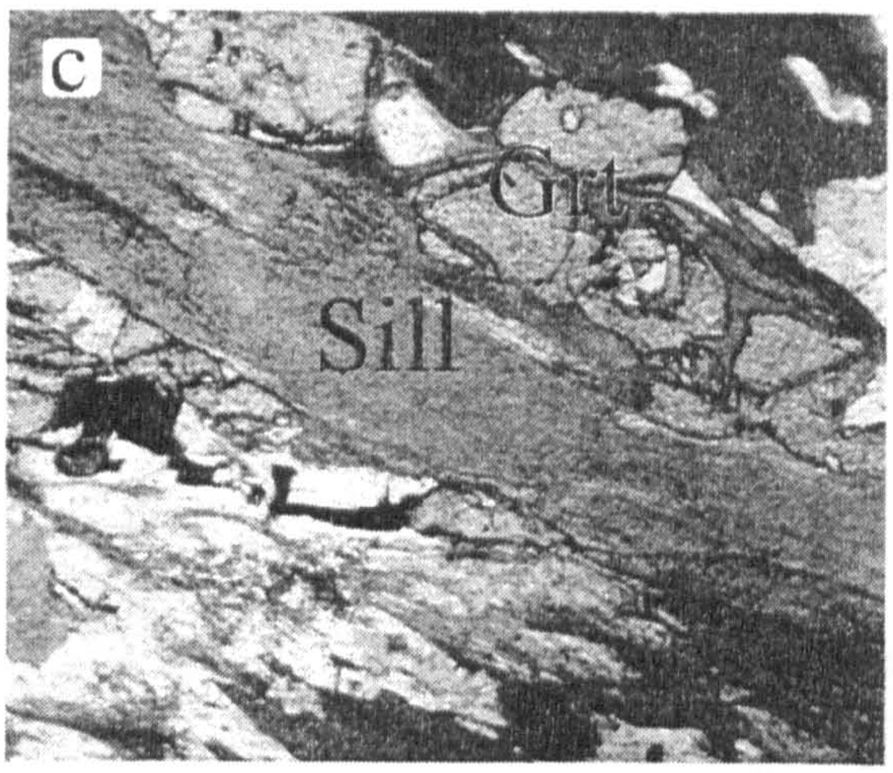


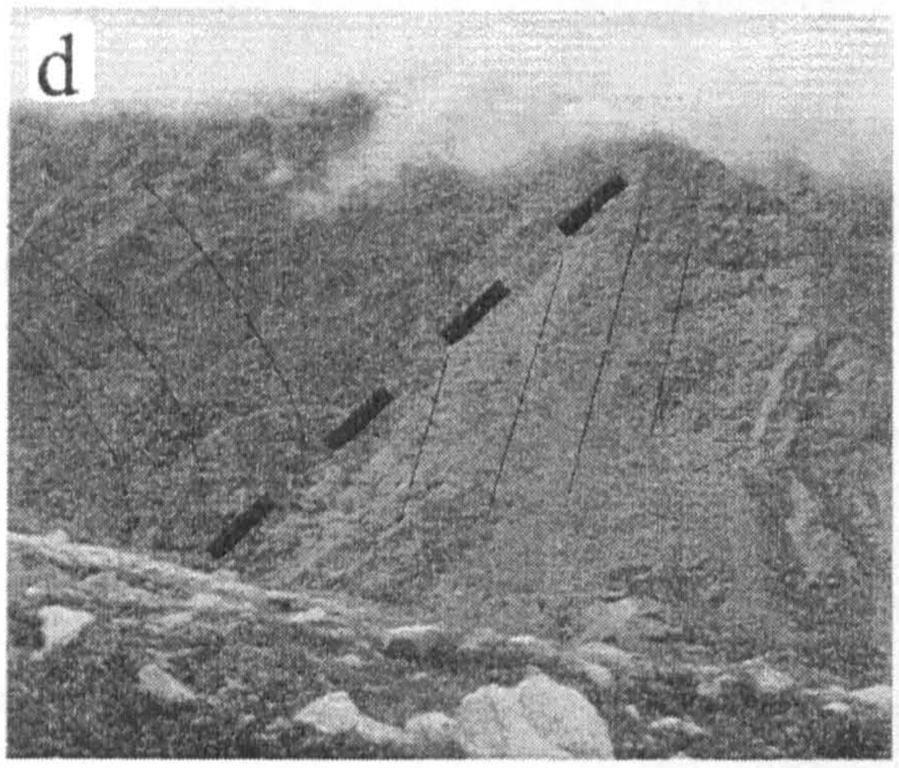



*Figure 2.14 Field relations and petrological observations for the upper-HHCS of the Alaknanda, Dhauli and Bhagirathi valleys. (a) Photomicrograph of fibrolite in biotite (top left hand corner) with slight retrogression to muscovite (center) (FOV = 1.5mm) (211); (b) Photomicrograph of fibrolite cross-cutting tourmaline crystal in the deformed leucogranite shown in Figure 2.12a (FOV = 2 mm) (G31(1)); (c) Photomicrograph of fibrolite-biotite fabrics cross-cutting garnet porphyroblasts (FOV = 1.5mm) (27/97); (d) Fault in Raktvarn valley potentially responsible for extensional fabrics (see text); (e) Peak 5167, east side of Gangotri valley. Possible fault boundary between Bhairongathi granite and the Tethyan sediments, tentatively correlated with the upper boundary of the leucogranites as shown in Figure 2.7b.*

However, the characteristic erosion style of rounded valleys and smooth hillsides in contrast to the sharp valleys of the HHCS suggests that Tethyan sediments lie to the north of Ghastoli. Heim and Gansser (1939) report leucogranite, capped by garnet-bearing schists, at the end of the Satopanth valley to the west of Mana and also suggest that the meta-sediments of the TSS outcrop to the north of Ghasotli. Float from the Arwa valley, which has a very restricted drainage, also contains kyanite overgrown by cordierite.

In the upper unit in the Dhauli river the dominant lithologies are a dis-harmonically folded gneiss (Figure 2.13b) and biotite-gneiss, both with minor calc-silicate. Many cross-cutting leucogranites and pegmatites occur from 3km above the quartzites until the fault at Malari. In the vicinity of Bhapkund anatectic migmatites can be found with leucogranitic segregations and abundant sillimanite and K-feldspar (Figure 2.13c). Just behind Malari a small, highly deformed, leucogranitic intrusion can be found.

The gneisses of the upper unit in both the Alaknanda and Dhauli valleys contain garnet + plagioclase + quartz + biotite ± tourmaline ± muscovite ± fibrolitic sillimanite ± K-feldspar with only one sample containing staurolite inclusions in garnet and another with kyanite inclusions in plagioclase. The sillimanite either forms parallel to the main foliation or as aggregates and is often retrogressed to unoriented muscovite (Figure 2.13d). Further up section, around Jelam, sillimanite and biotite form the fabric (Figure 2.14a) but there is still some retrogressive muscovite. In the Alaknanda valley some of the small leucogranite intrusions (Figure 2.13a) containing tourmaline and garnet, are cross-cut by sillimanite fabrics (Figure 2.14b).

Sillimanite throughout the upper HHCS shows an extreme variation in style. It is predominantly fibrolitic but in some samples the fibrolite aggregates appear to be forming prismatic sillimanite. Sillimanite is often preserved in the cores of muscovite which form at an angle to the main foliation defined by biotite (Figure 2.13d). In other

samples fibrolite is intergrown with biotite (Figure 2.14a). Sillimanite is more abundant in the Dhauli valley than elsewhere in Garhwal. Furthermore there appears to be a pattern to the sillimanite fabrics in the upper unit of the HHCS in the Dhauli, whereby sillimanite intergrown with biotite increases in abundance towards the fault at Malari but is retrogressed to varying degrees throughout. Sillimanite is almost always fabric-forming and cross-cuts garnets (Figure 2.14c).

The upper unit of the HHCS in the Dhauli valley shows a complicated metamorphic and deformation history and the relationship between the various events is poorly constrained. $S_1$ is occasionally preserved in garnet cores as an inclusion fabric. $M_{1a}$ resulted in the primary assemblage which may have reached kyanite zone. The formation of small melts may have resulted from the first metamorphic event ($M_{1b}$). The whole of the upper HHCS is pervasively deformed, producing isoclinal folds with an axial planar schistosity. Deformation certainly continued post-porphyroblast growth with the development of a strong fabric. In both the Dhauli and Alaknanda valleys late C fabrics, cutting the main foliation, indicate top-to-the-south shear.

In thin section and hand specimen the primary assemblage of garnet and plagioclase is cross-cut by sillimanite-forming fabrics in both the Dhauli and the Alaknanda valleys. Sillimanite more pervasive in the Dhauli valley. $M_2$ sillimanite stretching lineations in the Dhauli valley rotate from NNE to almost ENE, perpendicular to the fault at Malari (Figure 2.11), and shear fabrics containing sillimanite often demonstrate a top-to-the-northeast/east sense of movement. Whether sillimanite formed during top-to-the-north/northeast shear, or formed during top-to-the-south/southwest directed shear and was subsequently rotated is not clear.

The isoclinal folds are cut by and thus predate the post-M1 top-to-the-south and top-to-the-northeast shearing, but the relative timing of the top-to-the-south and top-to-the-northeast deformation as well as the relative timing of $M_1$ and isoclinal folds is

unresolved. However, the presence of extensional shears on the margins of undeformed pegmatites (Figure 2.14d) suggests that the extensional top-to-the-northeast fabrics formed late in the history of the upper-HHCS but as yet no clear cross cutting relationship has been found between the two fabrics either in hand specimen or thin section. The source for the pegmatites and leucogranites that occur north of Malari as well as the much larger plutons in the Bhagirathi and Alaknanda valleys is not clear. Folded anatectic migmatites, restricted to the Dhauli valley, contain sillimanite + K-feldspar overgrown by muscovite which is itself deformed; yet the dykes and plutons show very little deformation. Given both the deformation history and the small size of the anatectic migmatite outcrop it is likely that the source for the large leucogranite bodies near Malari is still unexposed.

*Malari fault*

The fault passing through Malari and Kailash Pur juxtaposes the very low-grade TSS against the high-grade gneisses and leucogranites of the HHCS. It is represented by a zone of brittle deformation from ~200m to <20m wide comprising slivers of both footwall and hanging wall. The change in lithology either side of the fault can be clearly distinguished in the mountains around Malari, from the jagged peaks and sharp valleys of the HHCS to the more rounded valleys of the Tethyan sediments. Shah and Sinha (1974) consider the granites found just north of Malari to be intruded into a small sliver of the Martoli formation (Tethyan sediments) which has been considerably truncated by the fault. No intrusive contacts for the granite were found and, given the poor nature of the outcrop in the proximity of the village, it is not possible to confirm or deny this hypothesis.

In the vicinity of Malari the fault is near vertical and trends at ~330°N. It has been related to the Dar-Martoli fault or the Malari thrust (Valdiya, 1988). Evidence of normal movement to the ENE is principally derived from the presence of S-C fabrics in the

gneisses of the HHCS. Additionally the sillimanite lineations rotate to perpendicular with the fault (Figure 2.11).

### 2.4.3 Tethyan sediments

The Tethyan sediments to the northeast of Malari along the Girthi Ganga range from Precambrian to Cretaceous in age (Shah and Sinha, 1974) and comprise shales, green quartzites, fossilliferous limestones and conglomerates. The entire sequence is affected by numerous small faults and folds. Cross bedding and grading indicate that many of the beds have been overturned while numerous shear indicators attest to the pervasive low-grade deformation. Shah and Sinha (1974) suggest that the Martoli formation, comprised of phyllites and greenish sandy slates, is unconformably overlain in the vicinity of Malari by the Ralam formation, a sequence of conglomerates with a quartzite matrix. Given the deformed nature of the outcrops behind Malari and the limited access allowed to the author, it was not possible to confirm this suggestion and large-scale variations in dip seen in the area north of Malari may equally be the result of faulting.

## *2.5 Summary for the Garhwal Himalaya*

The deformation and metamorphic history of the Garhwal Himalaya are summarised in Figure 2.15. The area has been split into four tectonostratigraphic units which show distinct structural, metamorphic and lithologic characteristics.

The MCTZ in all three valleys consists of augen gneiss, amphibolites, quartzites and mica schists with intrusive and tectonic boundaries and may contain slivers of HHCS gneisses. Early fabrics are overgrown by syn-kinematic assemblages of up to lower amphibolite facies which have been subsequently sheared and weakly retrogressed to greenschist facies. The MCTZ is highly sheared throughout and the dominant transport direction is consistently S-SW. Given the relatively simple history it is plausible to suggest that the deformation and metamorphism is the result of a single S to SW-

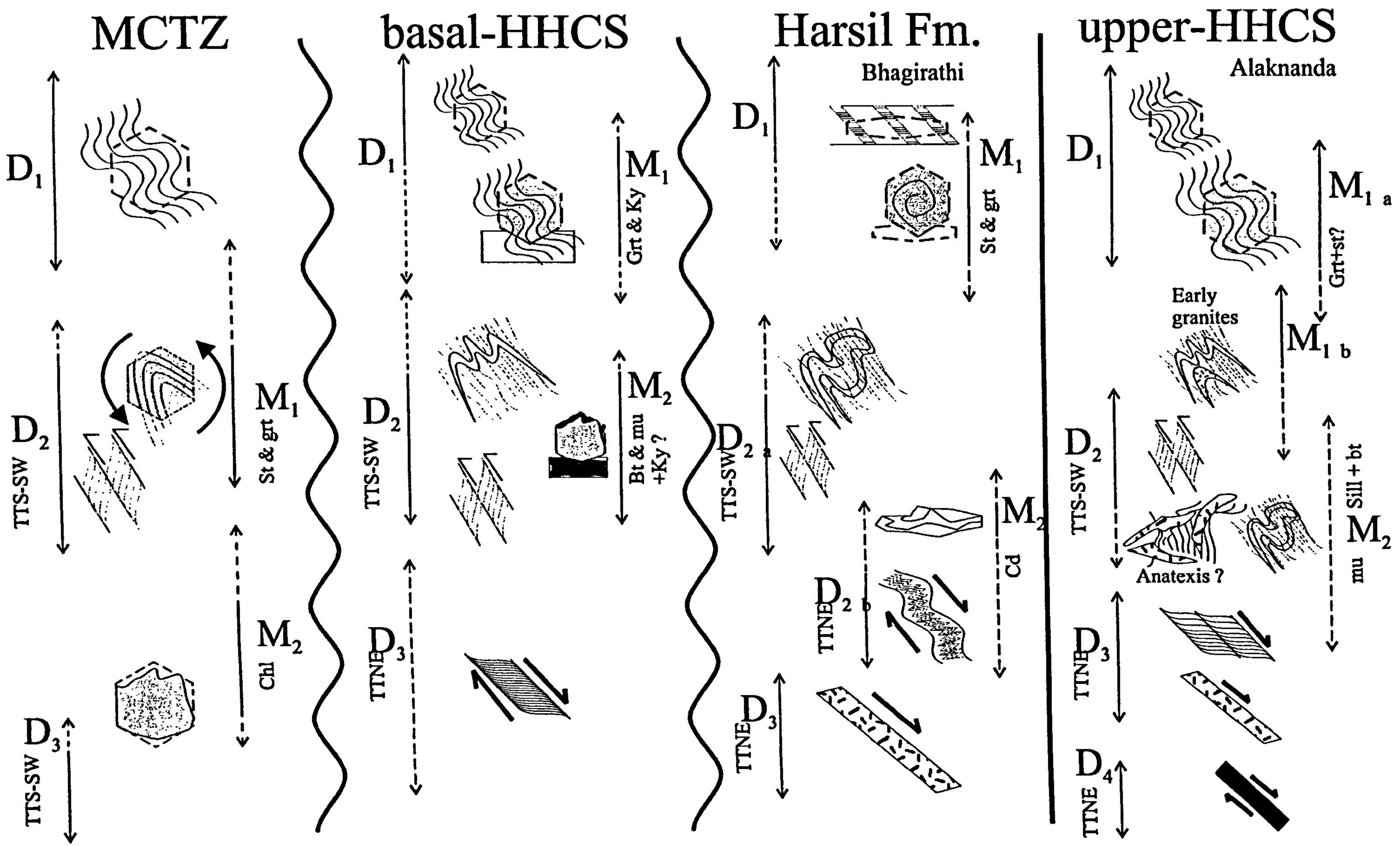


*Figure 2.15 Summary of the deformation and metamorphism in the Garhwal Himalaya. Sequences of events are described in the text. The Garhwal Himalaya are separated into the MCTZ (Bhagirathi, Alaknanda and Dhauli), basal-HHCS (Bhagirathi, Alaknanda and Dhauli), Harsil formation (Bhagirathi) and upper-HHCS (Alaknanda and Dhauli). Relative age increases from top to bottom. Solid line represents definite period of event dashed line is postulated period. Temporal relationships between D2a and D2b in the Harsil formation are unknown.*

directed thrusting event during the Himalayan orogeny.

The upper boundary to this zone of deformation in both the Bhagirathi, Alaknanda and Dhauli valleys is the MCT, an enigmatic thrust locally called the Vaikrita Thrust which separates the MCTZ from the gneisses of the HHCS. An early randomly oriented metamorphic assemblage of garnet and kyanite has been deformed, with the possible development of secondary kyanite or sillimanite, and partially retrogressed with overgrowths of muscovite and biotite. Structurally, the basal HHCS contains isoclinal folds with a well-developed axial planar schistosity which has been deformed in top-to-the-south shears ($D_2$). The relationship of these folds to the metamorphism is not clear and they may predate garnet and kyanite growth. The basal-HHCS in the Dhauli also contains zones of mylonitic deformation. Despite the differences between the basal-HHCS and the MCTZ, it is probable that south-directed shearing occurred simultaneously with that in the MCTZ; i.e. $D_2$ in the MCTZ is simultaneous with D2 in the basal-HHCS.

Above the basal HHCS the valleys differ greatly with a large thickness of quartzite separating the basal-HHCS from the upper gneisses in the Alaknanda and Dhauli valleys, whereas the HHCS is superseded by the Harsil formation in the Bhagirathi valley. However, in all three valleys the transition is from coarse gneisses to metamorphic rocks with sedimentary protoliths. While it is possible that the middle and upper HHCS in the Dhauli and Alaknanda valleys are equivalent to the Harsil formation they have distinct differences in crystallinity, deformational history and extent of metamorphism – implying a more pronounced reworking of the upper HHCS in the Dhauli and Alaknanda.

The Harsil formation and the upper HHCS in the Alaknanda-Dhauli section may both have been characterised by the assemblage garnet + staurolite + kyanite but in the Alaknanda and Dhauli staurolite and kyanite have been replaced by biotite and

muscovite. The $M_1$ assemblage in both areas overgrew a pre-existing fabric and grew syn-kinematically. In the Alaknanda early metamorphism may have resulted in crustal anatexis, as shown by deformed leucogranites. In both valleys post $M_1$ deformation wrapped the early porphyroblasts.

Sillimanite growth in the upper-HHCS is complicated but clearly postdates the main metamorphic assemblage in both the Alaknanda and Dhauli and was subsequently retrogressed to muscovite late in the deformation history of the rocks. Anatexis of the crust and intrusion of leucogranites occurred late in the history of the units and in the Dhauli valley some may have occurred during top-to-the-north-east extension.

As for the upper-HHCS, deformation continued after $M_1$ in the area of Harsil. However, there is no sign that anatexis occurred. In the eastern exposures of the Harsil formation $M_1$ assemblages were overprinted by cordierite, indicating a high-T and low-P event as seen in calc-silicates in the Alaknanda valley. The high-T and low-P event is unlikely to have been caused by the intrusion of the leucogranites due to their small size. It is more likely to be the result of rapid decompression of an already hot sequence of rocks. However, the relationship between this metamorphism and the extensional top-to-the-northeast deformation – which would result in decompression - is, as yet, unclear.

## 2.6 Discussion

### 2.6.1 The Main Central Thrust: how is it defined and where is it?

Across the whole orogen lithological, structural and metamorphic criteria have all been used by different authors to define the MCT in the field. However, difficulty arises when the boundaries chosen do not coincide and attempts are made to correlate from one "MCT" defined by certain criteria to another "MCT" defined by others. Indeed the lithological boundaries may control the metamorphic and structural styles. These problems become acute when discussing models for inverted metamorphism.

Resolving this difference is key to some models of the evolution of the orogen. Implicitly the term "Main Central Thrust" has been used to distinguish one fault in the whole of the geographic Himalaya as the principal plane of transport bringing the high-grade rocks into contact with lower grade rocks. However, even a cursory study of the HHCS, MCTZ and the LH indicates that the entire sequence underwent significant shear and that transport of material occurred throughout: it is unlikely that it was restricted to any single definable fault. A detailed structural study within the MCTZ in the Garhwal Himalaya to the west of the Bhagirathi indicates that shear was concentrated towards but not restricted to individual thrusts (Jain and Anand, 1988). As long as no thorough structural analysis of the shear distribution in the valleys of interest has been undertaken, it is probably impossible to pin-point the zone of greatest transport and thus name it the ***main*** central thrust.

In the Alaknanda and Bhagirathi valleys, field definitions of the MCT are relatively simple as there is a distinct lithological and structural boundary between the foliated biotite gneisses of the basal HHCS and the highly sheared schist, augen gneiss and quartzites of the MCTZ. The metamorphic criteria are less unequivocal but the MCT coincides loosely with the kyanite-in isograd in the Bhagirathi, Alaknanda and Dhauli valleys. Given the lithological difference across the field-mapped MCT, it is likely that deformation would be concentrated in the schists below. Furthermore, ignoring the fine detail of the Nd isotope systematics of the rocks in the MCTZ, it is clear that the bulk of the HHCS in Garhwal had a distinct protolith source region from some MCTZ rocks and the Lesser Himalaya. Therefore the MCTZ, as presently defined, is likely to be the upper boundary for the zone responsible for the transport of the crustal rocks of the HHCS over the Lesser Himalaya - and as such responsible for a significant proportion of the shortening since collision.

### 2.6.2 High Himalayan Crystallines and Tethyan sediments

In a structural and P-T analysis of the Bhagirathi valley Metcalfe (1990) did not study the Harsil formation in detail as the Jhala Normal Fault (JNF) was thought to bring low-grade metasediments in contact with the sillimanite zone rocks of the HHCS. Therefore, the rocks above the "JNF" were part of the TSS and not related to, or containing information about, the metamorphic portion of the Himalayan orogeny. The JNF was thus correlated with the Southern Tibetan Detachment System found elsewhere in the Himalaya (e.g. Burchfiel and Royden, 1985; Herren, 1987). This causes geometric difficulties when one attempts to link the fault bounding the High Himalayan Leucogranites in the Gangotri area with the JNF. In contrast this work, carried out in two field seasons and guided by other workers (Jain et al., 1995), found examples of high-grade metamorphic assemblages in the Harsil formation. Field work carried out by the author and others failed to find any convincing structural evidence for a large normal fault in the vicinity of Jhala, although some minor faulting was found. Given the field evidence, the Harsil formation cannot be considered as low-grade to unmetamorphosed Tethyan sediments. If the Harsil formation is considered continuous across the Gangotri region as a formation in its own right, the mapping of the area is simplified in that outcrops of schists around Gaumukh, can be correlated along strike with the rocks around Harsil (as proposed by Pecher and Scaillet (1989)).

The Harsil formation contains high-grade assemblages and is thus, based on the arguments presented above, part of the HHCS. Yet the Harsil formation is clearly sedimentary in origin and retains pre-Himalayan intrusive relationships. The same is true for the middle and upper units of the HHCS in the Alaknanda and Dhuali valleys which are quartzites and high-grade metasediments respectively. The author, therefore, tentatively correlates the base of the Harsil formation in the Bhagirathi section with the base of the quartzites in the Alaknanda-Dhuali section.

Moving up through the sequence, the Harsil formation in the Bhagriathi valley is intruded by leucogranites emplaced during extensional top-to-the-north shear movement (Searle et al., 1993; Scaillet et al., 1995). Any extensional shear is likely to have been concentrated on the boundaries of the leucogranites and specifically lie on the upper boundary of the leucogranites with the schists above as shown on Figure 2.2. The STDS would thus mark the boundary between the Harsil formation and the "Tethyan sediments", represented by the "black shales" on the peaks of the mountains (Figure 2.8b).

However, several other lines of evidence suggest, in fact that the Harsil formation is continuous with the "Tethyan" sediments above the leucogranites. Firstly the metamorphic grade of the rocks does not change dramatically upwards through the leucogranites as garnet schists have been reported from above the leucogranites in the Satopanth valley (Heim and Gansser, 1939) and staurolite has been reported in the schists above the leucogranites at Gaumukh (Stern et al., 1989). Below the leucogranites the pelites are also staurolite-kyanite grade schists. Secondly, the outcrop pattern of the intrusion in the Kedar Valley (Scaillet et al., 1995) shows that little disruption of the rocks occurred and that, therefore, there is a continuous sequence from the Harsil formation below the leucogranites to the TSS above the leucogranites.

If the STDS does form the roof of the leucogranites then it does not juxtapose unmetamorphosed sediments against high-grade gneisses as elsewhere in the Himalaya. Also the distinction between Harsil formation (part of the HHCS) and TSS is arbitrary and it is only the fortuitous juxtaposition of low-grade material against high-grade material by normal faults that allows the distinction to work in most situations. Therefore, it is possible that the Harsil formation and Tethyan sediments in the Gangotri region represent a complete, right way up metamorphic sequence which has been disturbed by limited north-directed shearing and leucogranite intrusion. Mapping the

STDS as a single fault is a simplification and in greater detail it is likely that the extensional faulting is distributed through either broad shear zones or on multiple faults. Nevertheless the above arguments still stand as to the relationship between the Harsil formation and the Tethyan sediments.

This hypothesis, of a continuous sequence from HHCS (Harsil formation) to the TSS, is supported by mapping of the area to the east of the Dhauli and to the north of Nanda Devi, in which the Malari fault is shown to cut E-W through the Tethyan sediments which have a non-tectonic boundary with the HHCS (Valdiya, 1988).

Thus the normal faulting which is part of the orogen wide Southern Tibetan Detachment System is not *necessarily* the boundary between high-grade and unmetamorphosed sediments. This may account for the gradational change in the Lhozhag-La Kang area of southern Tibet, where the upper-amphibolite injection complex rocks of the HHCS appear to have no structural or metamorphic discontinuity with the Tethyan Mesozoic sediments above (Burchfiel et al., 1992), although the isograds are foreshortened. This hypothesis could be tested using geochemical comparisons between metasediments of the HHCS and unmetamorphosed sediments of undisputed Tethyan sediments and by structural analyses in areas where the STDS is postulated to lie in the Tethyan sediments. One place where this appears to occur is to the north of Nanda Devi (extremely inaccessible) or possibly in the Kumaon Himalaya along the Goriganga valley, where mapping suggests that the HHCS grade into the Tethyan sediments and that there is no tectonic break between them (Heim and Gansser, 1939; Thakur and Choudhuri, 1983).

### 2.6.3 Normal Faulting, where is it, and does the "Jhala Normal Fault" exist?

In the Garhwal region normal faulting has two contrasting styles - the Malari fault and the fault bounding the leucogranites in the Gaumukh area - both of which share features of the STDS as seen elsewhere along the orogen.

In the Gaumukh area, other workers have considered normal faulting to occur above the leucogranites of the Gangotri area (Searle et al., 1993; Scaillet et al., 1995). Unfortunately the normal movement is mostly constrained by the geometry of the leucogranites and some sheared leucogranite dykes (Searle et al., 1993; Scaillet et al., 1995). Searle et al. (1993) reports top-to-the-N/NE S-C fabrics concentrated around the leucogranite intrusions as well as open folds with vertical axes striking at 133°N behind the Bhagirathi peaks in the Chaturangi glacier, interpreted as the result of gravitational collapse.

Work presented here suggests that the main foliation to the east of Gaumukh was deformed as a result of north-directed shearing. The relationship of this north-directed shearing to any single structure is not well constrained but two possible faults exist: i) a fault identified in the eastern side of the Raktvarn valley (Figure 2.14e) which is orientated similar to the kink axes and the N-verging fold axes and has garnet-schists in its footwall; ii) the postulated fault above the leucogranites. Additionally, field evidence suggests that on the north side of the Raktvarn valley a flat-lying fault juxtaposes the biotite-granite and metasediments (Figure 2.14f), although this has not been properly identified because of the altitude of the exposure. This fault may be the continuation of the fault bounding the leucogranites (Figure 2.8b and Figure 2.2) and would be similar, in orientation, to the shallow dipping STDS in Nepal, although the grade change across it is not as significant as described in section 2.6.2.

In contrast, the position of the fault in the Dhauli valley is not in doubt and the structural style and metamorphic grade change is very different from the faulting in the Gaumukh area. Here the fault is a steeply dipping brittle feature which produced ductile deformation in its footwall. Hot springs can be found along its length and rocks on either side demonstrate a large metamorphic grade change from sillimanite zone to sub-greenschist facies with brittle deformation in a wide zone between. The grade change is

similar to that found in most of the Nepalese STDS sections (Burchfiel et al., 1992) and to the Zanskar shear zone (Herren, 1987). However, the fault at Malari is much steeper than elsewhere and the movement on the fault (NE-E) is different from that inferred in the Gaumukh area (N). It is intriguing that the orientation of the Malari fault is similar to the Gangotri fault postulated to lie between the Bhagirathis and Shivling (Figure 2.2) and may represent a different tectonic regime from the normal fault above the leucogranites.

### 2.6.4 ..and finally.

The rocks of the HHCS, the Harsil formation and the MCTZ show a complicated history of igneous activity, metamorphism and deformation. This is clearly demonstrated by the intrusion of granites, thought to be ~550 Ma, into the Harsil formation as well as by the igneous relationships in the HHCS and MCTZ. It is, therefore, probable that the development of some of the structural and metamorphic features relates to events that predate the collision of the Indian and Asian plates. This may account for some of the fabric relationships described above.

Even for events that are clearly Himalayan in age many features remain ambiguous, such as the relationship between the decompression events in the Gaumukh area (cordierite coronas) and the compressional events in the Harsil area or the relative timing of the sillimanite fabrics and anatexis in the Dhauli valley. To constrain these requires not only chronometric information but also detailed structural and petrographic studies of the area.

One of the more intractable problems remains the nomenclature of the tectonstratigraphic units and fault systems which prevents effective communication between geologists working on the same areas and/or processes. For example, of the three principle studies of the Bhagirathi valley (this study, Pecher and Scaillet, 1989; Metcalfe, 1990) there are three different boundaries for the Harsil formation and two

different boundaries for the MCT. Given the complicated nature of the outcrops, the logistical problems and the difficulty in field mapping at 1:150000, this may take some time to resolve. With this taken into account the author freely admits to oversimplification and in his desire to see order may have created it where there was none.

# Chapter 3 - Thermobarometry

In the previous chapter several tectonostratigraphic units were identified within the Garhwal Himalaya, each with different metamorphic and structural histories. Specifically these are the Main Central Thrust Zone (MCTZ), the high Himalayan Crystalline Series (HHCS) and the Harsil formation. In the Alaknanda the HHCS was further subdivided into the basal-, mid- and upper-HHCS. One aspect of particular interest is the inverted metamorphic field gradient, based on index minerals: (i) within the MCTZ, from chlorite zone to staurolite zone, and (ii) from the basal-HHCS to the upper-HHCS in the Alaknanda and Dhauli and the less distinct inversion in the Bhagirathi between the HHCS and the base of the Harsil formation. In the Bhagirathi this takes the form of a transition from kyanite zone to sillimanite (fibrolite) zone at the base of the Harsil formation with only limited fibrolite development elsewhere. In the Dhauli and Alaknanda there is major development of fibrolite in the upper-HHCS and, in contrast to other areas of the Himalaya, only a few outcrops of K-feldspar + sillimanite bearing migmatites (restricted to the Dhuali valley). Throughout this chapter "metamorphic field gradient" will refer to the exposed sequence of index minerals and "temperature or pressure field gradient" will refer to PT estimates obtained from exposed assemblages.

While it is possible to identify different metamorphic assemblages and structural styles it is important to quantify the depths and temperatures the rocks were subjected to in order to constrain the movement of heat and material during orogenesis. The various approaches to this problem depend upon correlating the mineral assemblages in the field to known mineral relationships determined experimentally. At present there are many different methods for relating experimental and theoretical data to the natural system although in all cases there are necessary simplifications.

The aim of this chapter is to constrain the pressures and temperatures in the Garhwal Himalaya and, perhaps more importantly, the pressure and temperature differences within and between different lithotectonic units. To this end PT estimates obtained along the Alaknanda and Dhauli valleys will be presented followed by pseudosections determined for rocks from the MCTZ, HHCS and Harsil formation. First, however, a brief description of the different methods used for PT determinations, along with their advantages and inconveniences, is presented below.

## 3.1 PT Methods

Many different methods have been used to extract P and T information from metamorphic rocks in the Himalaya and it is worth briefly describing the methods, their advantages and drawbacks here. In the case of all the methods described below, the same basic thermodynamic dataset for mineral phases can be used. In the last 10 years a number of internally-consistent databases have become available (e.g. Berman, 1988; Holland and Powell, 1998) and all the work described here uses that of Holland and Powell (1998).

- **Petrogenetic grids** represent the earliest method of determining P and T and are the familiar basis for the interpretation of metamorphic assemblages. With a combination of experimental equilibria, petrological observations and simple rules the phase relationships for different minerals in a model compositional system can be obtained. Such methods usually model a limited chemical system, such as KFMASH (K, Fe, Mg, Al, Si, H2O), and predict the phase relationships between minerals in that system. Such grids can be used to: (i) relate mineral assemblages to specific PT conditions and; (ii) interpret reaction textures from poorly equilibrated systems.
- **Specific calibrated equilibria** or so-called "conventional" barometers and

thermometers are based on experimental calibrations of individual equilibria among phases that are common in metamorphic rocks. Examples include the Fe-Mg exchange thermometer between garnet and biotite (e.g. Ferry and Spear, 1978) and a number of mass transfer\Ca exchange equilibria involving garnet and plagioclase commonly used as barometers (e.g. Newton and Haselton, 1981). Equilibria which are steep in PT space make good thermometers and those which are shallow make good barometers. One potential pitfall of this method is that the effective blocking temperatures for different equilibria may vary, such that the Fe-Mg exchange between garnet and biotite may only cease below 550°C whereas Ca exchange would be expected to close at a higher temperature as it depends on the net transfer of material rather than diffusional exchange. Indeed it has been suggested that this may explain the isothermal profiles obtained elsewhere in the Himalaya (Vannay and Grasemann, 1998). Additional difficulties arise from the great difference in temperatures obtained using different calibrations, differences that appear to be largely due to uncertainties and imperfections in the activity models for complex mineral phases.

- **Thermocalc** is a program with the facility to examine all the independent equilibria recorded by the assemblage of a given rock (Powell and Holland, 1994; Powell et al., 1998) and uses the internally-consistent database of Holland and Powell (1998). It then calculates a best-fit pressure and temperature defined by the overlap in P-T space of all these reactions. The additional advantage of Thermocalc is that it weights the importance of each reaction according to both uncertainty in the thermodynamic dataset and uncertainty in endmember activities. The intersection of the independent reactions is calculated using average PT (avPT) and the statistical fit of the point in PT space to all the reactions allows the estimation of realistic errors. Additionally disequilibrium

mineral phases can be identified by dramatic improvements in the fit resulting from their omission. The method is discussed in more detail below and in Appendix B.

- **Pseudosections**. Petrogenetic grids correspond to all compositions in a specific model compositional space (e.g. KFMASH) so that all reactions for all sub-bulk compositions are calculated. In many cases, a specific bulk composition will not encounter some of the reactions and stability fields (e.g. low Al pelites may not develop aluminosilicates even though the rock reaches PT conditions where they are stable). However, given a sufficiently large compositional system and internally consistent datasets (e.g. Powell et al., 1998), the mineral assemblage and their compositions can be accurately predicted for a specific bulk composition. Pseudosections produced in this manner can be used in a similar way to petrogenetic grids for interpreting reaction textures or inclusion assemblages and have the added advantage of predicting mineral compositions which can be used, for example, to interpret garnet compositional zoning. This is a potentially powerful method for interpreting metamorphic rocks, especially for high variance assemblages in which the compositional contours can be used to better constrain PT. Such an approach has been used successfully in the Zanskar Himalaya (Vance and Mahar, 1998). Pseudosections have the additional advantage, shared with any phase diagram based approach, of portraying the phase relationships in a wide area of PT space so that inter-relationships between different stability fields can be visualised.

All the above approaches assume that the mineral assemblages are in equilibrium, although petrogenetic grids and pseudosections can be used to interpret disequilibrium textures. It is clear, however, in almost all samples in the Garhwal Himalaya that equilibrium is rare - especially when taking into account that garnet zoning is a

disequilibrium feature. This may result in the use, in exchange reactions, of mineral pairs which have never been in equilibrium or, for pseudosections, the calculation of mineral assemblages based on incorrect determinations of the effective bulk composition. While calibrated mineral equilibria cannot be readily assessed for equilibrium, multiple mineral equilibria methods using internally consistent data sets often highlight suspect data.

A second problem is that the different methods do not always give consistent results for the same mineral data and it is impossible to be sure which is more accurate. Furthermore many exchange reactions quote errors significantly less than the variation between the different calibrations. To circumvent this problem many authors use a single set of calibrated reactions so that the relative PT can be better estimated.

Lastly it is usually assumed that the extant assemblage and mineral compositions represent the peak conditions obtained by the rock. However, as previously mentioned many of the exchange reactions in a rock may not stop at the peak if sufficiently high temperatures are maintained. While this problem is not resolvable with any of the present methods, it may limit the accuracy and precision of many of the methods described above.

Two of the advantages of Thermocalc are that it determines realistic errors for PT estimates and can highlight suspect data. For these reasons it will be used consistently throughout this chapter and while the errors may be large, the relative errors will be significantly smaller and can be calculated (Worley and Powell, 1999). This chapter is separated into two sections: section 3.2 which will use rim thermobarometry to look at the PT variation along a transect across the HHCS and; 0 which will look more closely at the PT evolution of selected samples using pseudosections.

## 3.2 Rim thermobarometry along the Alaknanda-Dhauli traverse

PT determinations on a suite of samples (Figure 3.1) from the Dhauli and Alaknanda

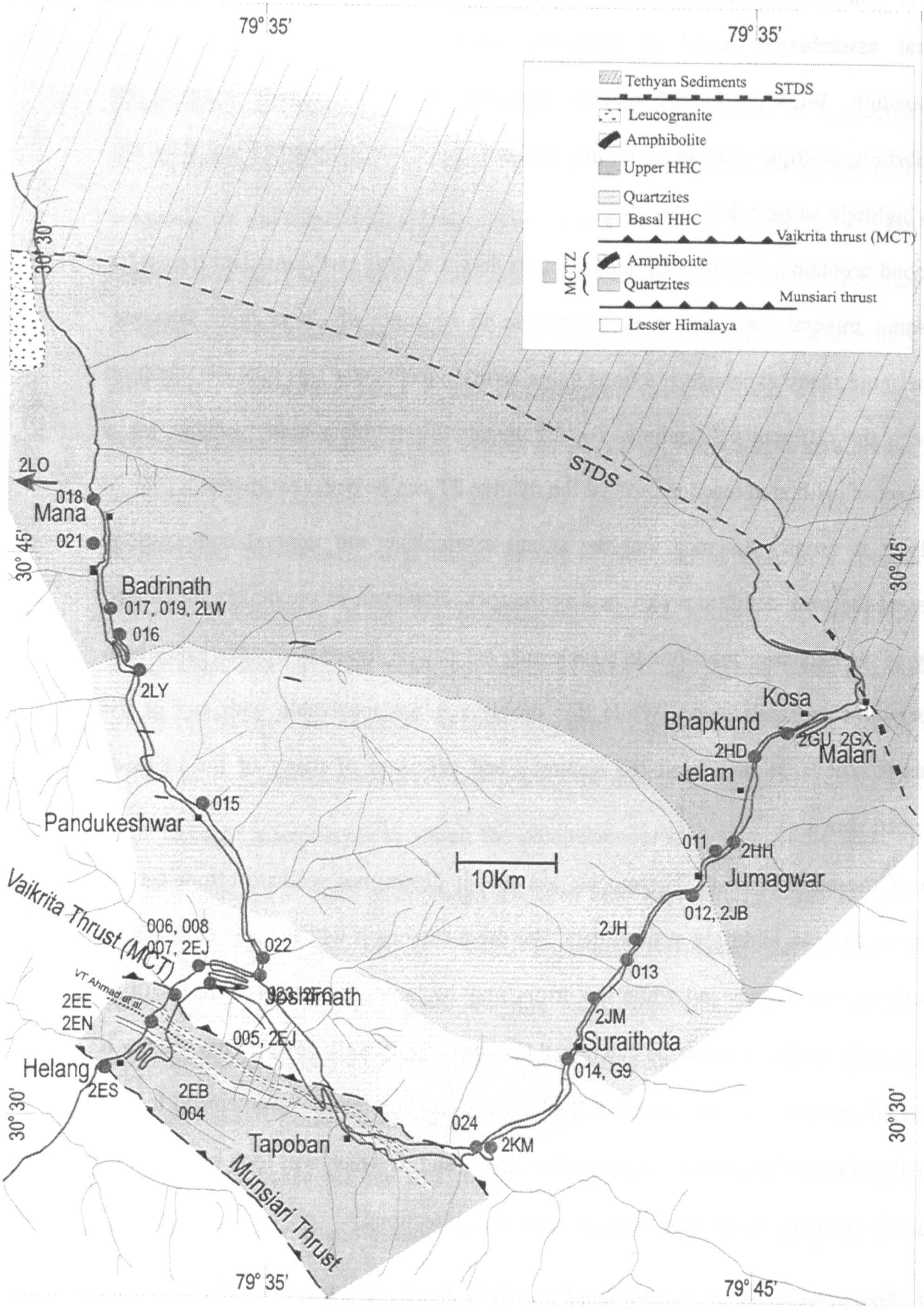


*Figure 3.1 Sample localities used for PT estimates in the Alaknanda and Dhauli valley.*

valleys have been obtained using Thermocalc. The advantage of this transect is that the MCT has the smallest degree of imbrication and the transect extends to the Malari fault (equivalent to the STDS) at the head of the Dhauli river.

### 3.2.1 Analytical methods and data selection

Mineral analyses were made using the electron microprobe at the Open University and the Jeol at the University of Cambridge. Analyses obtained at the University of Cambridge were made by Dr Judy Baker and indicated in the Appendix E. Traverses of garnet established the extent of intracrystalline diffusion and the development of Mn-rich rims - thought to represent the resorption of garnet and back diffusion of Mn (Vance and Mahar, 1998). Matrix minerals were analysed and, where appropriate, traverses taken. Biotite in contact with garnet was avoided due to the well known retrogressive diffusion of Fe and Mg between biotite and garnet. Selected mineral analyses are presented in Appendix E and a full data set is available on CD-rom by request.

To ensure mineral compositions used for PT estimates approached equilibrium, garnet rim and matrix minerals were used. In zoned garnets for which a selection of rim compositions were available, the garnet rim with the lowest Mn concentration and, where possible the highest Fe/Fe+Mg ratio, was used. For garnets with an increase in Mn at the rim, the composition just within the increase was chosen, except for the garnets in the upper-HHCS which displayed no clear zoning pattern, in which case the rim values were selected. In theory this should result in the calculated P-T most closely approaching the thermal maximum. Muscovite analyses were compared and, where possible, separated into different chemical groups. Commonly there was no significant variation between petrologically defined groups (e.g. c-fabric muscovite, muscovite with sillimanite, etc.) and in such cases the most representative analysis was chosen.

Where large variations occurred, low-Si and high-Na muscovite were chosen. Again this should lead to the P-T conditions most closely approaching peak conditions (Waters, 1999). Although biotite showed a consistently lower X(Fe) for c-fabric biotite compared to s-fabric biotite, the difference did not significantly effect the calculated PT. Feldspar rim values were used. Where present aluminosilicates were included.

Activity values for use in Thermocalc were calculated using non-ideal solutions with the mineral recalculation program Ax98. The calculated activities are, however, sensitive to the temperature at which they are calculated. To constrain the appropriate temperature to use for activity calculation an initial estimate was entered into Thermocalc. The resulting calculated temperature was then reused in the calculation of the end-member activities in an iterative fashion until the temperature obtained from Thermocalc and used in the calculation of activities were within 50°C. Solid-solution models are given in Appendix B. Thermocalc was used in average PT (avPT) mode and a sample Thermocalc output and a description of how Thermocalc determines PT and errors is provided in Appendix B.

Pressure and temperature estimates using Thermocalc are often highly sensitive to water activity as many of the independent reactions involve dehydration. However, there is no readily accessible way of determining water activity in the rocks of interest. *A priori* the rocks in the Garhwal Himalaya are likely to have been fluid saturated and have had a water activity of unity. This is because the rock protoliths are pelitic and quartzitic sediments and other fluid sources, such as carbonates ($CO_2$), are limited. Therefore the PT traverse presented below is calculated assuming water saturation in all the samples unless otherwise stated. The problem of water activity is, however, discussed further in section 3.2.3.

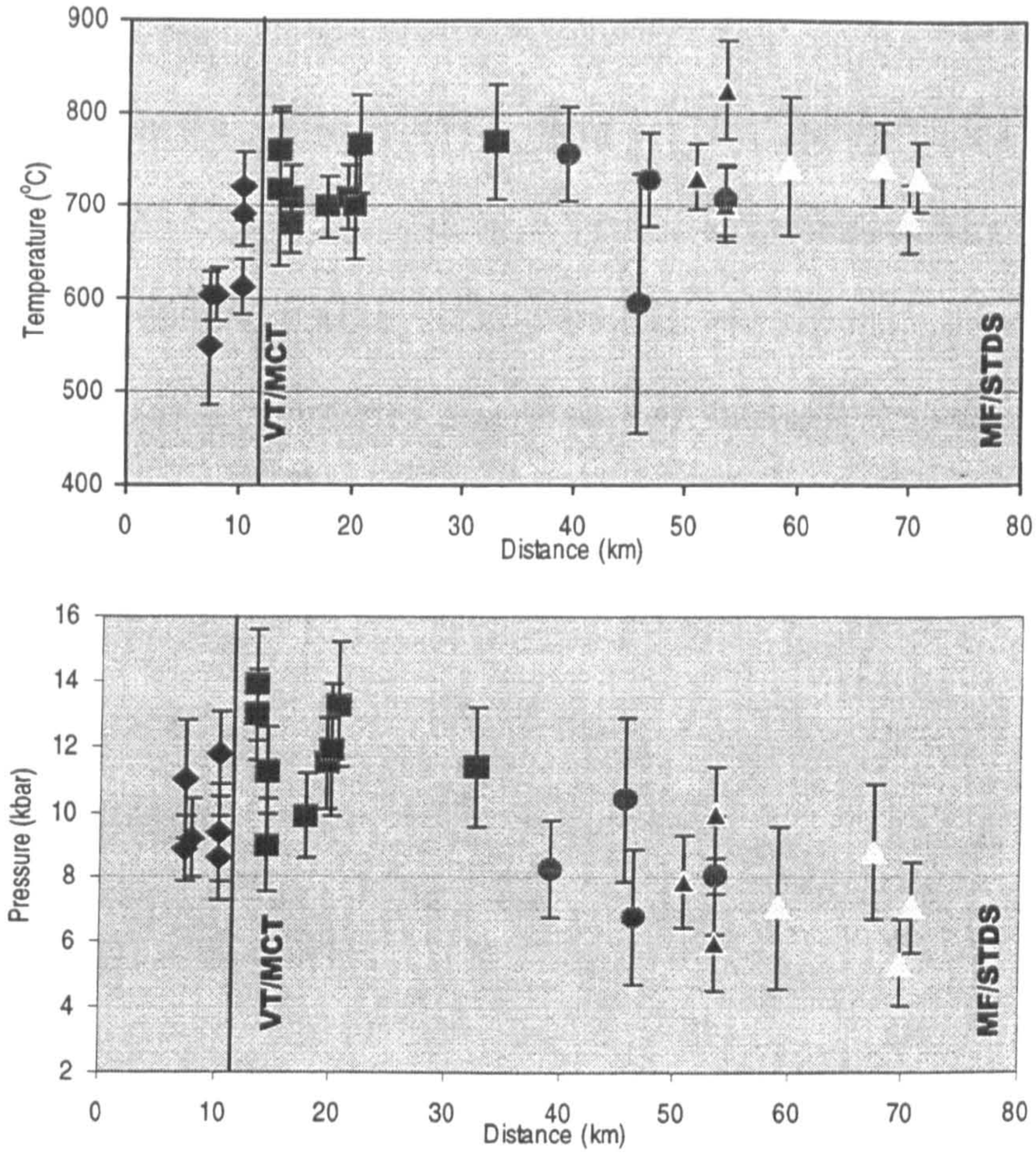


*Figure 3.2 Pressure and temperature profiles along the Dhauli and Alaknanda calculated from mineral equilibria using Thermocalc. Data are separated into lithotectonic units described in Chapter 2; MCTZ (blue diamonds), basal-HHCS (pink squares), mid-HHCS (brown circles) and upper-HHCS (yellow diamonds). Samples from the Alaknanda have black fills. Horizontal distances are measured from the base of the MCTZ (Munsiari thrust). The Vaikrita thrust/MCT is marked and the position of the Malari fault/STDS (80 km) is taken from the Dhauli valley.*

### 3.2.2 Results

The results of average PT calculations are presented in Figure 3.2, plotted against the horizontal distance from the Munsiari thrust (base of the MCTZ), and in Figure 3.3, plotted against the principal solidii for crustal rocks and aluminosilicate stability fields. There is a maximum uncertainty of ± 1km on horizontal distances but relative positions are correct. Samples are grouped into lithotectonic units as shown on Figure 3.1. All PT estimates satisfy the "fit" i.e. the errors represent 95% confidence levels. There are four principle observations from the traverse data: (i) there is an increase in P and T towards and over the MCT with the maximum recorded above the MCT; (ii) there is a constant

T up section from the MCT to the fault at Malari; (iii) there is a decrease in P up section from the maximum above the MCT to the fault at Malari; (iv) there is often a large variation in recorded PT between samples at the same locality.

The first observation is that the calculated profile is consistent with the observed "inverted" metamorphic field gradient: the occurrence of sillimanite at the top of the slab is the result of high temperatures and low pressures. Secondly the temperatures are consistently higher, by almost 150°C, than those obtained by Hodges and Silverberg (1988) using pelitic thermobarometers along the same sections. As discussed previously this is likely to be a result of the different mineral-activity models used in different calibrated equilibria aswell as different analytical techniques. Indeed Hodges and Silverberg (1988) use analyses obtained from garnet rims, these are likely to have been affected by retrogression and hence will record a lower temperature than the inner rims used here. However, the important feature is that the relative thermobarometry is similar: both record an almost isothermal profile with a decrease in pressure of ~600MPa (6 kbar) from just above the MCT to the Malari fault. PT estimates by Metcalfe (1993) in the Bhagirathi also show a similar, although less well-defined, pattern with a peak in P and T just above the MCT and a near isothermal profile of ~600°C and an isobaric profile of ~7.5 kbar in the HHCS. Thus although absolute temperatures and pressures differ the relative profiles obtained by different authors and different methods are reassuringly similar.

In addition the thermal profile obtained across the MCT and in the HHCS is similar to that obtained by Hubbard (1989) along the Dudh Kosi and Hinku-Hongu transects in the Everest section of Nepal (see Figure 3.4 below). The pressures, however, differ as the peak in Nepal lies at the base of the MCTZ and drops consistently up sequence. The almost isothermal profiles in the HHCS found in Garhwal and Nepal are also similar to transects in the Sutlej Valley to the west (Vannay and Grasemann, 1998), the Manaslu

section, Nepal (Hodges et al., 1988) and the Langtang section, Nepal (Macfarlane, 1995). These profiles have had a variety of explanations which are discussed below. In interpreting and comparing these results it is important to bear in mind that, in the authors opinion, there are two distinct "inverted" metamorphic field gradients - the first in the HHCS up to the STDS and the second within the MCTZ and into the basal-HHCS.

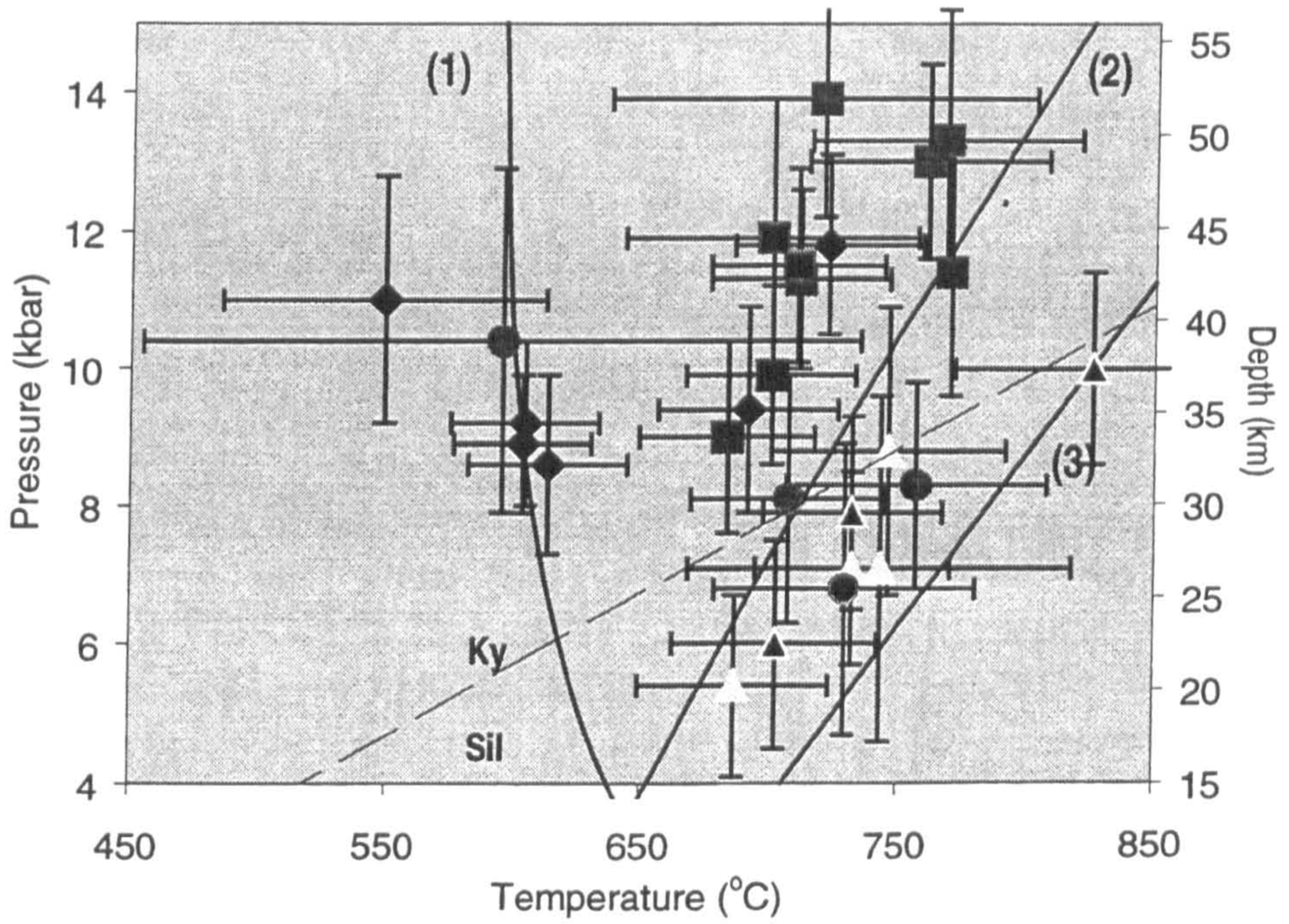


*Figure 3.3 PT estimates from Figure 3.2 plotted in PT space. Line (1) represents the wet-melting solidus of Le Breton and Thompson (1988). Line (2) represents muscovite-melting solidus of Petö (1976). Line (3) represents the high-temperature dehydration-melting solidus for a kyanite-zone metapelite from the HHCS of Langtang, Nepal (Patino Douce and Harris, 1998) .Other symbols as for Figure 3.2.*

Figure 3.3 shows the data plotted in PT space with the wet-melting solidus of Le Breton and Thompson (1988), the muscovite-melting solidus of Petö (1976) and the high-temperature dehydration-melting solidus of Patino Douce and Harris (1998). Samples from the near the MCTZ show the greatest variation in temperature, lying on both the lower and higher T sides of the wet-melting solidus. The data from the basal-HHCS lie predominantly at higher temperatures than the wet-melting solidus but beneath the dehydration-melting solidus.

The last two groupings, the middle- and upper-HHCS, also lie above the wet-melting solidus of Le Breton and Thompson (1988), at similar temperatures to the basal-HHCS samples but below the experimental curve for dehydration-melting of a metapelite from the HHCS of Langtang, Nepal (Patino Douce and Harris, 1998).

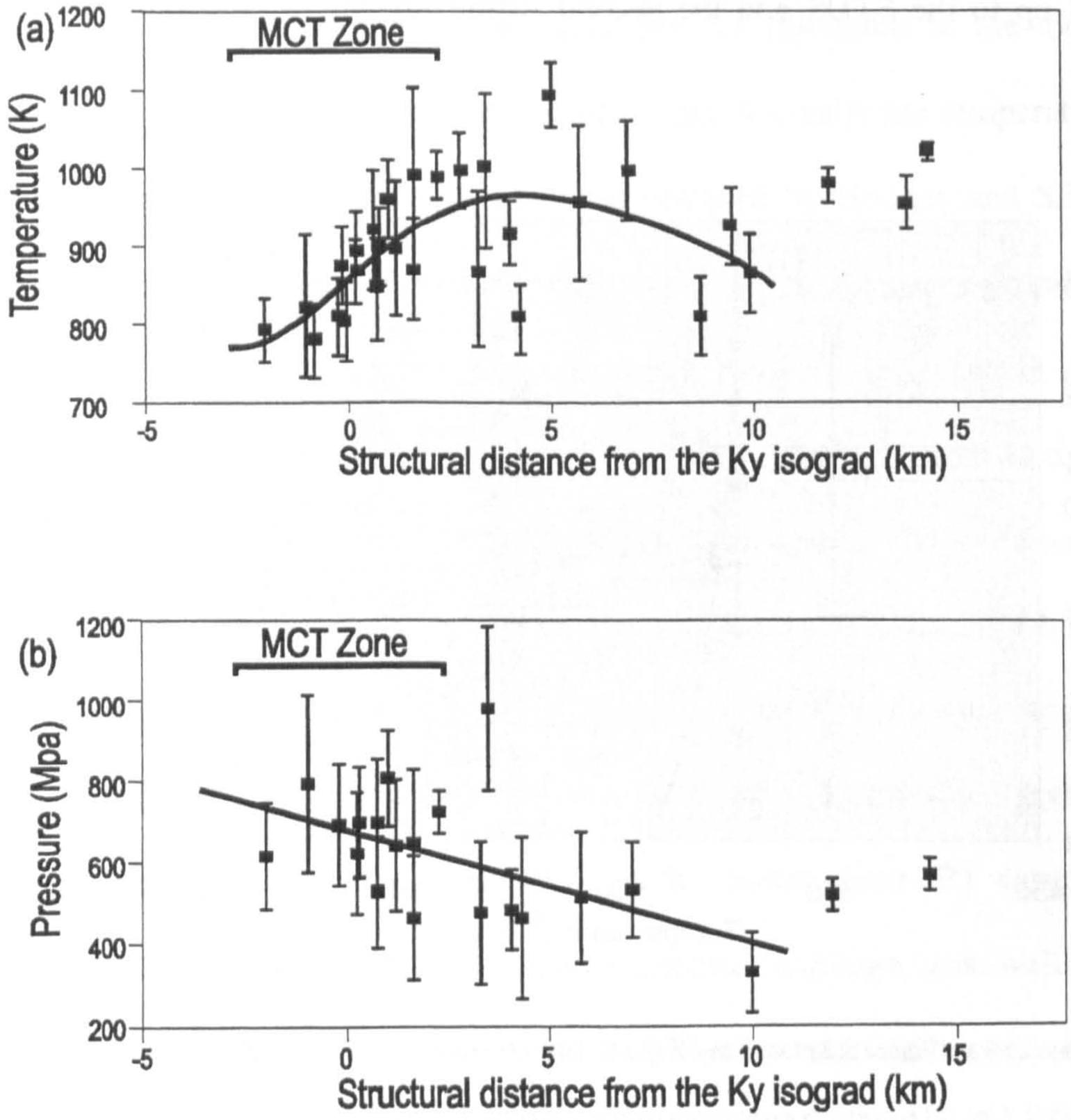


*Figure 3.4 Data and diagrams from Hubbard (1989).Thermobarometric results from the Dudhh Kosi and Hinku-Hongu transects plotted versus structural distance above the kyanite isograd. Error bars indicate two standard deviation precision. (a) Temperature data with fifth order polynomial fit to data from the MCT zone and lower Tibetan Slab (HHCS). (b) Pressure data with straight line fit to data from the MCT zone and lower Tibetan slab (slope ~28MPa/km).*

Figure 3.3 further emphasises the consistency of these PT estimates with the "inverted" metamorphic field gradients: all the samples with sillimanite (fibrolite) lie within the sillimanite stability field and as such are simply the result of high-temperature equilibration at low pressures. Thus there is no thermal inversion but merely an

isothermal field gradient accompanied by lower pressures at higher levels. This, nevertheless, still poses some difficulties since temperature estimates for a crustal slice should record both decreasing pressure and temperature towards structurally higher levels.

### 3.2.3 Effect of water activity

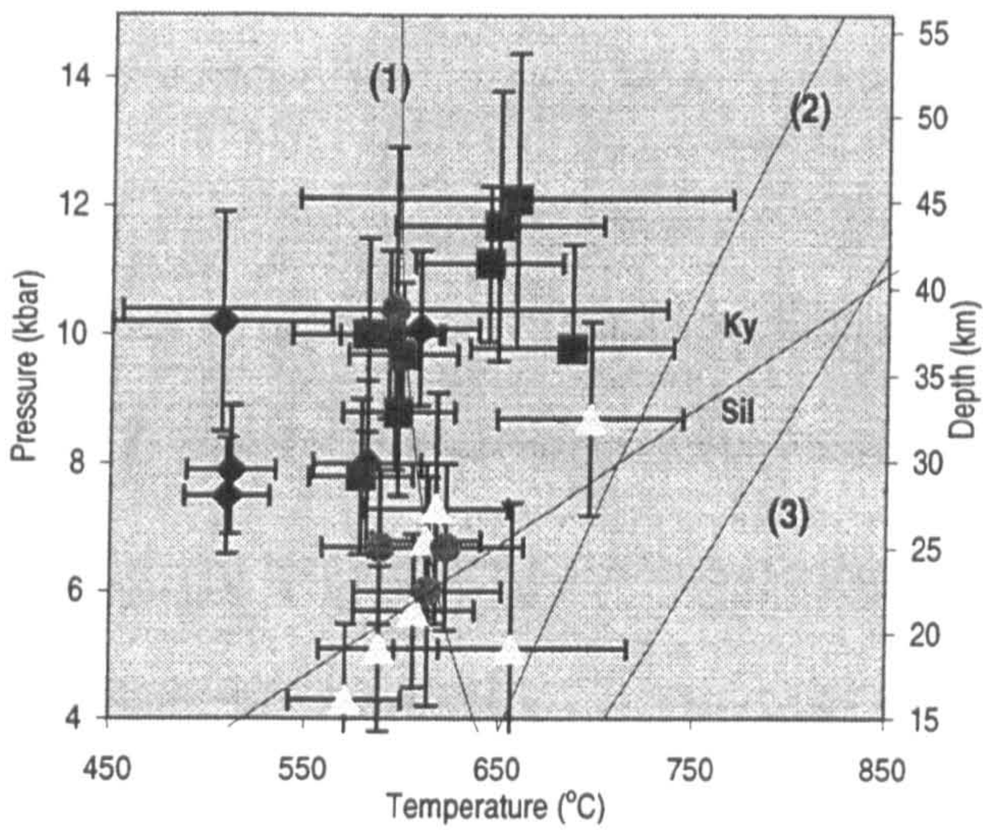


*Figure 3.5 PT estimates as for Figure 3.3 recalculated with an $a_{H2O}$ of 0.4.*

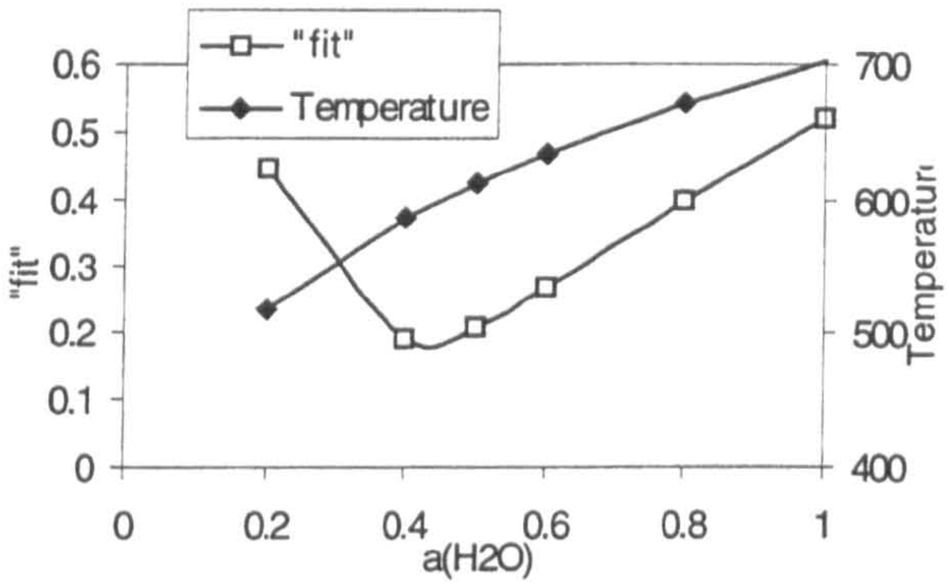


*Figure 3.6 Change in the "fit" parameter and temperature from Thermocalc with changing $a_{H2O}$. The minimum in fit occurs at $X(H_2O)$=0.4 yielding a temperature of ~600 °C.*

Many of the samples presented here lie above the wet-melting solidus and it seems that the use of an $a_{H2O}$ of 1 is incompatible with the lack of melt. This may be the result of metastability (Rubie and Brearley, 1990) or, possibly, that the small melt fractions produced by wet-melting (Thompson and Connoly, 1995) are not observed. Alternatively, the $a_{H2O}$ was not 1 in these rocks.

Without fortuitous sampling of rocks containing $a_{H2O}$ sensitive reactions (e.g. Vance and O'Nions, 1992) the $a_{H2O}$ in the rocks is difficult to constrain. However, the potential effect water activity has on the PT estimates can be evaluated by using an arbitrary range of values $a_{H2O}$. In Figure 3.5 the same mineral assemblages as for Figure 3.3 have been recalculated with an $a_{H2O}$ of 0.4. This results in a marked decrease in the temperature estimates of ~100°C bringing many of

the samples out of the wet-melting field. The temperature decrease also results in a decrease in the pressure estimates (~ 1.3 kbar) due to the correlation between the two. However, the relative changes in PT across the section are not affected.

An alternative method can be employed to constrain water activity and involves using Thermocalc in much the same way as suspect data are highlighted (Vance and O'Nions, 1992). This is done by minimising the "fit" by changing either; (i) water activity in fluid-undersaturated rocks or (ii) changing the proportion of $H_2O$ in a fluid saturated rock. The "fit" is a statistical measure of the intersection of the independent reactions calculated by Thermocalc. It is essentially a chi-squared type statistic that quantifies the degree to which the independent reactions that Thermocalc uses to obtain a P and T overlap at a single point. Specifically, it ratios the deviations of each equilibrium line in P-T space to the error on that line and takes a weighted average. In this sense it is similar to the MSWD used in geochronology. A large "fit" indicates that the reactions cross at widely dispersed points and a low "fit" that they all intersect in a small range of PT. The specific value of the "fit" that represents the cut-off for 95% significance varies with the number of equilibria involved but is generally 1.4 to 1.7. By varying the water activity or fluid proportions and monitoring the "fit", the activity which minimises the "fit" can be selected.

An example is sample 017a from the upper-HHCS in the Alaknanda valley. The mineral phases present are garnet, biotite, muscovite, quartz, plagioclase and sillimanite. By varying the $a_{H20}$ during calculations of average PT, the "fit" varies as do the PT estimates (Figure 3.6). A minimum in "fit" occurs at $a_{H20} = 0.4$ indicating that the calculated equilibria at that $a_{H20}$ gives the closest intersection. The lower $a_{H20}$ results in a large change in the T estimate from an $a_{H20}$ of unity; for an $a_{H20}$ of 1 the PT is 702 ± 40°C and 6 ± 1.5 kbar while for an $a_{H20}$ of 0.4 the PT is 588 ± 31°C and 5.1 ± 1.3 kbar.

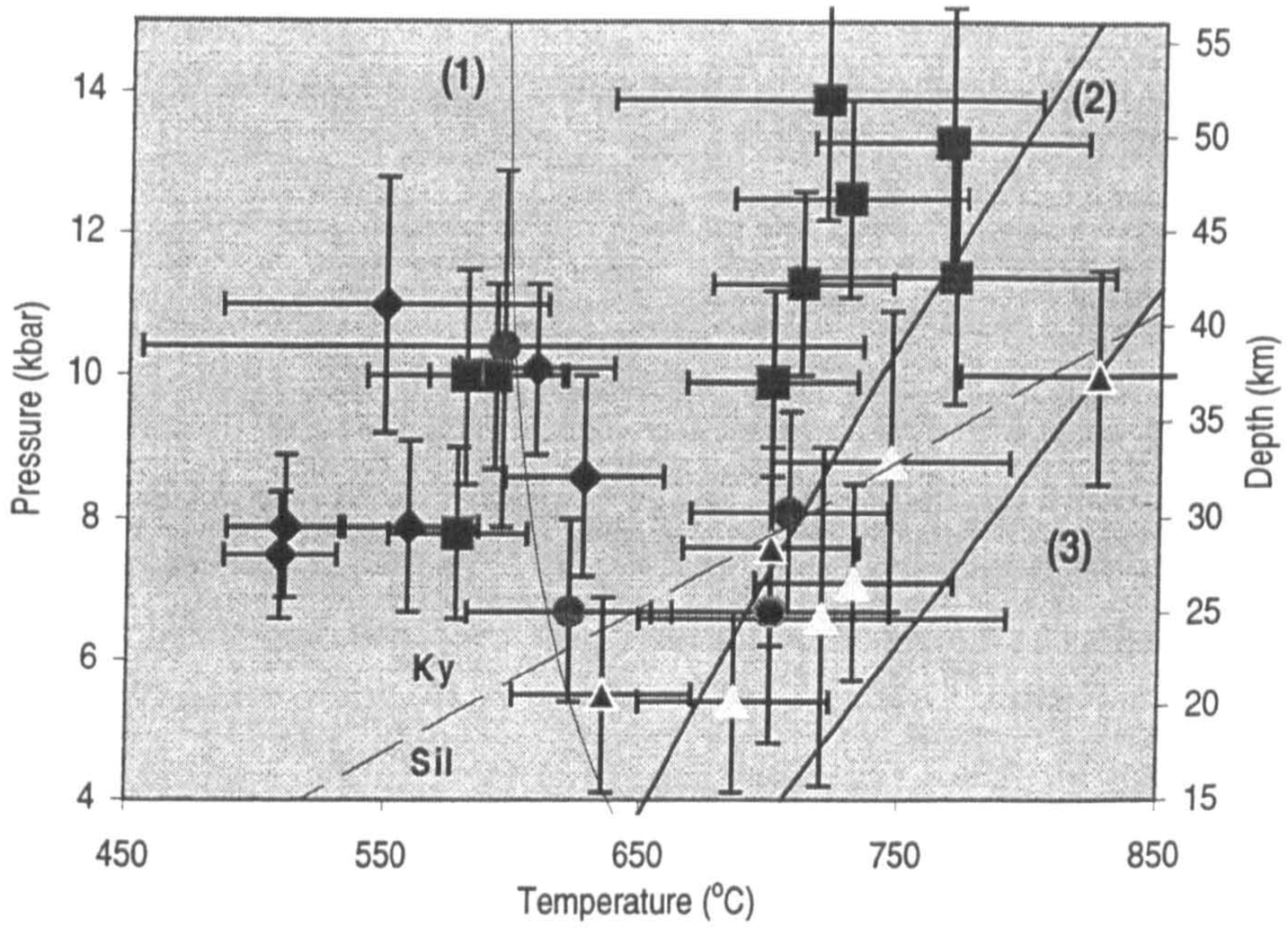


*Figure 3.7 As for Figure 3.3, PT estimates are recalculated by varying $a_{H20}$ so as to minimise the statistical error.*

The results of such a process applied to all the samples in Figure 3.3 are shown in Figure 3.7. The samples with minimised PT at low $a_{H20}$ are those most effected whereas those with $a_{H20}$ of 1 are unchanged from Figure 3.3 This results in a closer grouping of the MCTZ zone samples towards lower temperatures – between 475-650°C. Three samples from the basal-HHCS minimise fit at low $a_{H20}$ and are thus displaced to lower temperatures and pressures. However, the majority of samples in the basal-HHCS and the upper-HHCS are unchanged.

Figure 3.8 shows the recalculated data against horizontal distance (as for Figure 3.2). In the traverse the changes to the MCTZ samples and the basal-HHCS result in less scatter in the MCTZ and, taking the upper temperature limits, a more pronounced variation from the MCTZ into the basal-HHCS. However, minimising the "fit" in this way also produces three outliers in the basal-HHCS – accentuating the variability when compared to Figure 3.2. The pressure profile is, however, largely unchanged.

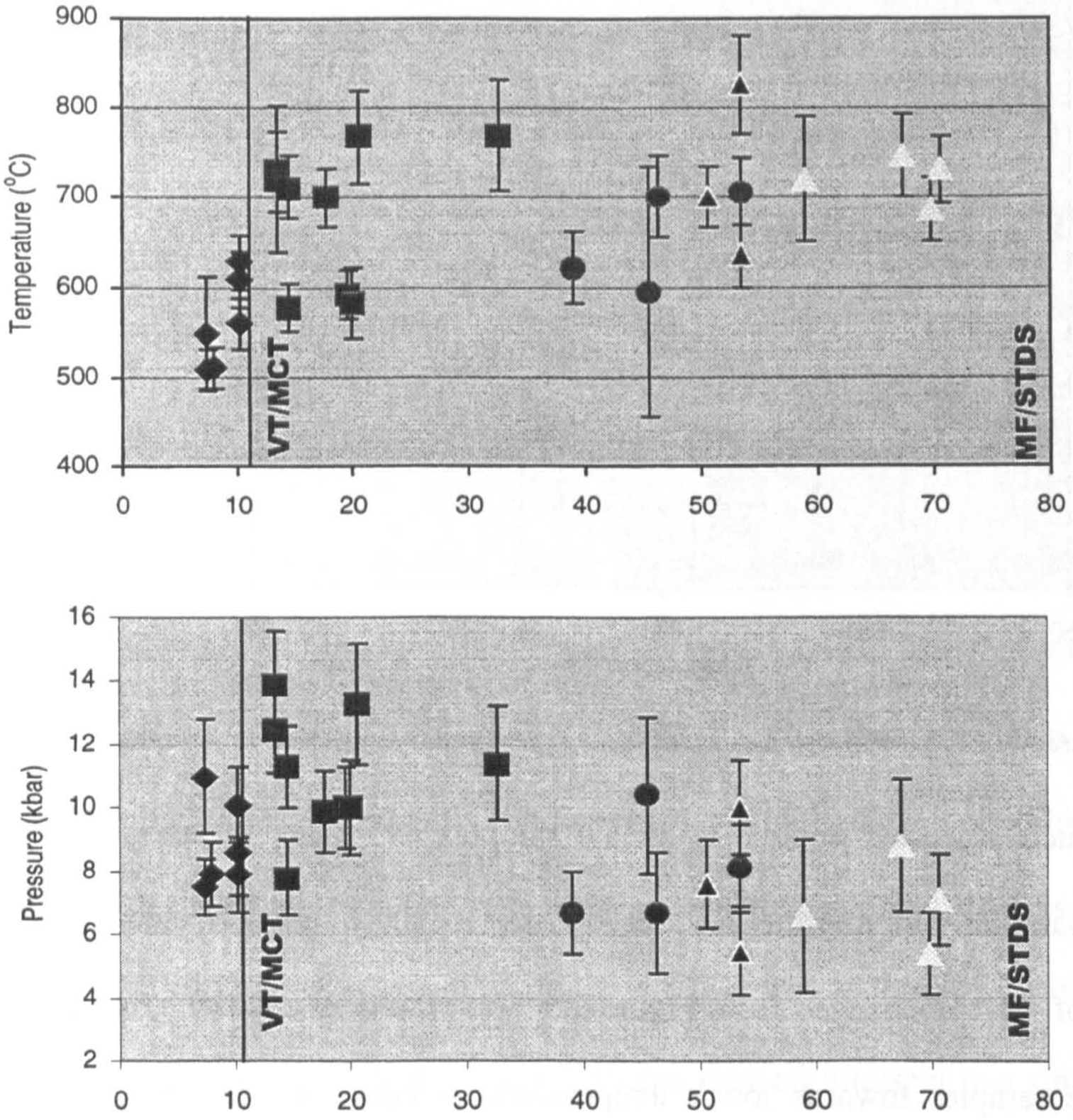


*Figure 3.8 As for Figure 3.2 except that the PT estimates are recalculated by varying $a_{H2O}$ so as to minimise the statistical error.*

## 3.3 PT paths from pseudosections

### 3.3.1 Introduction

While average PT estimates give important information on the peak or near peak metamorphic conditions across the orogen, in order to constrain the interaction between structures, metamorphism and magmatism we need to understand the thermal *evolution* of the orogen.

However, it is only in relatively few metamorphic rocks that the pressure-temperature history during garnet growth can be obtained by inclusion thermobarometry (e.g. St. Ongé, 1987) or by comparison of the inclusion assemblage in the garnet with

petrogenetic grids (Vance and Holland, 1993). In the vast majority of cases, the preservation of inclusions is so incomplete and the variance of the inclusion assemblage so high that this is not possible. The approach developed by Vance and Mahar (1998) and used here exploits the fact that, in a given, specified, bulk composition, both the mineral assemblage and the compositions of individual minerals are completely determined for given pressure-temperature conditions. In that case, by comparing modelled garnet compositions across PT space to the real garnet compositions measured in the sample, the pressure and temperature evolution during garnet growth can, in principle, be obtained. Vance and Mahar (1998) have used the approach to successfully model, and to obtain the pressure and temperature of formation of, garnet cores. However, in practice, garnet growth itself alters the effective bulk composition of the rock so that, in general, the garnet composition outside of the core is generally not successfully modelled (for further discussion see Vance and Mahar, 1998). To obtain such pseudosections requires a thermodynamic dataset for the minerals involved, such as provided by Berman (1988) and Holland and Powell (1990; 1998). The latter has been successfully used by Mahar et al. (1997) to study the effect of Mn on the stability of garnet in metapelitic assemblages and by Vance and Mahar (1998) to constrain the PT paths for garnets from the Zanskar Himalaya.

The following section of this chapter employs this method on three samples from different lithotectonic units in the Garhwal Himalaya; the MCTZ (4a3), basal-HHCS (G9) and Harsil formation (G135).

### 3.3.2 Whole rock and major-element chemistry

The whole rock major-element compositions for the studied rocks are summarised and compared to an "average" pelite (Symmes and Ferry, 1991) in Table 3.1. These were obtained from XRF analyses made at the Open University on 0.7g of sample (see Appendix C). All the samples are richer in Si and Al than the average pelite of Symmes

and Ferry (1991). It is worth noting the very high Mg concentration in G135 compared to both the average pelite and the other samples. The important data for the pseudosection calculations, however, is summarised in A', X(Fe) and X(Mn) at the base of the Table 3.1. These values take into account the more complicated 9 component system used here and, therefore, have been calculated differently from conventional AFM diagrams. A' can be thought of as the amount of Al left after its incorporation into micas, plagioclase and ferromagnesian minerals and as such a large positive value would be reflected by the greater stability of Al-rich minerals such as staurolite and the Al-silicates. High values of X(Mn) promote garnet stability and lead to its growth at lower pressures and temperatures.

### 3.3.3 Mineral chemistry

Selected mineral data used for rim PT analyses for the three samples are summarised in Table 3.3 and are discussed below.

*Table 3.1 Major-element compositions of Garhwal Himalaya rocks.*

| Sample | G135 | G9 | 4A3 | Average Pelite[1] |
|---|---|---|---|---|
| $SiO_2$ | 61.60 | 68.80 | 64.63 | 59.77 |
| $Al_2O_3$ | 19.33 | 17.21 | 18.33 | 16.57 |
| FeO | 5.97 | 4.54 | 6.10 | 5.88 |
| MgO | 5.83 | 0.87 | 1.39 | 2.62 |
| MnO | 0.09 | 0.13 | 0.08 | 0.07 |
| $K_2O$ | 1.19 | 3.62 | 3.91 | 3.53 |
| $Na_2O$ | 1.38 | 1.90 | 0.83 | 1.73 |
| CaO | 0.17 | 0.60 | 0.58 | 2.17 |
| A[2] | 0.356 | 0.125 | 0.208 | -0.120 |
| X(Fe) | 0.362 | 0.744 | 0.709 | 0.550 |
| X(Mn) | 0.005 | 0.021 | 0.010 | 0.007 |

*1 Average pelite composition from Symmes and Ferry (1991)*

*2 Calculated from mole percent oxides as follows: A' = (Al2O3-3K2O-CaO-Na2O)/(Al2O3-3K2O-CaO-Na2O+FeO+MgO), X(Fe) = FeO/(FeO+MgO), X(Mn) = MnO/(MnO+FeO+MgO) (Mahar et al., 1997).*

Sample G135 is from the Harsil formation in the Bhagirathi valley at Gaumukh and contains the assemblage staurolite, kyanite, biotite, cordierite, quartz, chlorite, apatite, rutile, opaques, sillimanite and muscovite. The fabric is defined by biotite and chlorite. Quartz and plagioclase form inclusion trails in kyanite and staurolite parallel to the main foliation. Cordierite appears to be in equilibrium with biotite and chlorite and overgrows large euhedral kyanite and

corroded staurolite. The cordierite is well-preserved and shows only slight retrogression. Muscovite is a minor component and occurs as small laths associated with cordierite. Sillimanite forms very small needle aggregates which have only been identified from their crystal habit. No garnet has been found. Plagioclase is Na rich. Ti oxides are present as abundant rutile inclusions in cordierite, staurolite and kyanite.

Petrological observations indicate that a probable stable equilibrium assemblage of staurolite, kyanite, biotite, quartz, plagioclase ± chlorite was overprinted by cordierite with the possible intermediate growth of sillimanite.

G9 is a mica schist from near the top of the basal-HHCS in the kyanite zone of the Dhauli valley. It contains a high variance assemblage of garnet, muscovite, biotite, plagioclase and quartz. Garnets are ≤ 4 mm and have a bell-shaped Mn profile (Figure 3.9), an increasing Fe content from core to rim and a step in Ca and Mg near the rim ($Alm_{80\text{-}57}$, $Py_{10\text{-}20}$, $Grs_{19\text{-}6}$ and $Sps_{25\text{-}10}$). The change in the Ca and Mg cation ratios is marked by a ring of quartz and feldspar inclusions. The increase in Mn at the rim is attributed to resorption of garnet.

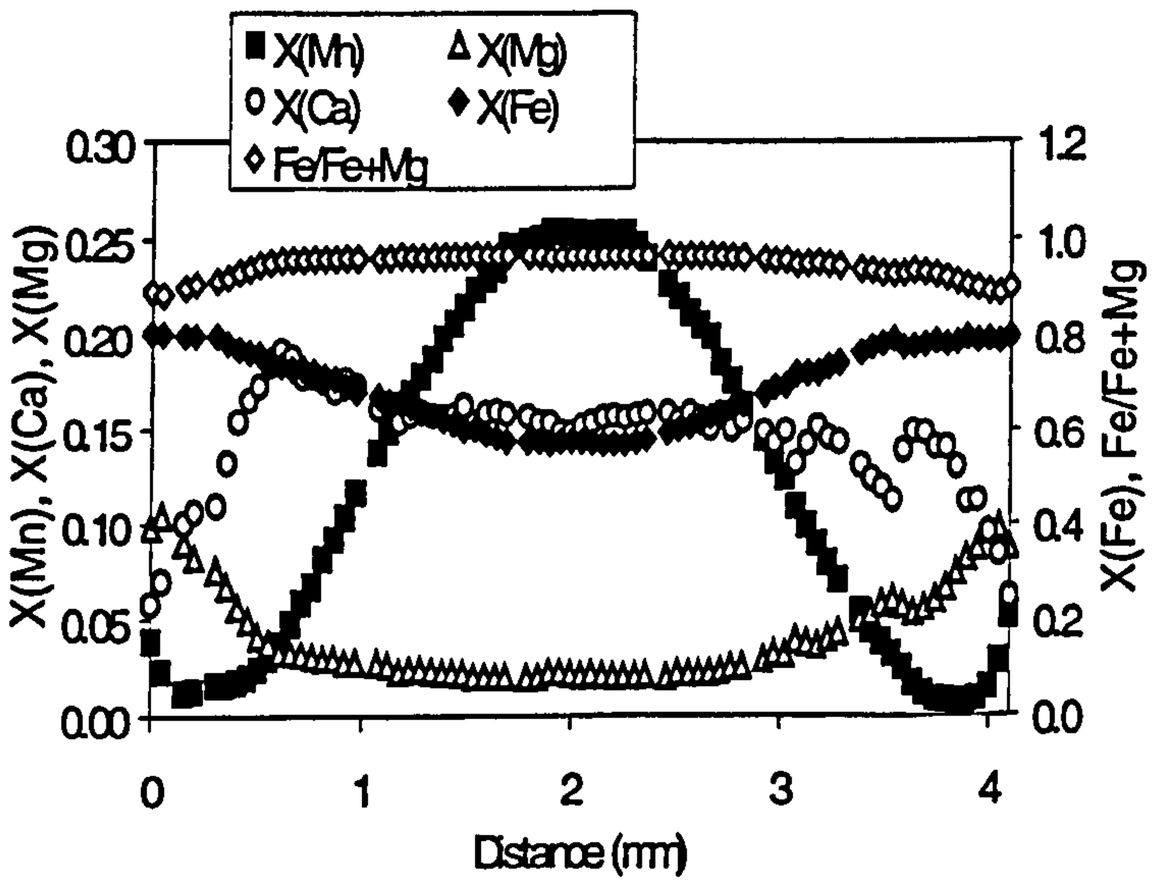


*Figure 3.9 Major-element composition of garnet in sample G9 measured by electron-microprobe. Recalculated as mole fractions. Also shown is the Fe/Fe+Mg ratio. Note the asymmetric Ca profile, smooth bell-shaped Mn profile and retrogressive rims.*

Muscovite forms most of the rock and wraps the garnet porphyroblasts. Minor biotite occurs and is in greatest concentration in the quartz segregations. Feldspars show no zoning patterns.

Sample 4A3 is a mica schist from the MCTZ in the Alaknanda valley to the south

of Joshimath. Garnets are euhedral, ≤ 4 mm and often appear fractured. They contain minor quartz, tourmaline, graphite and opaque inclusions. These form rotated inclusion trails indicating synkinematic growth. The garnet displays a bell-shaped Mn profile with increasing Fe and Mg content towards the rim (Figure 3.10). Ca decreases towards the rim with a slight increase halfway from the core to rim. Feldspar has not been optically identified although a single analysis of K-feldspar was obtained on the electron microprobe.

Minor staurolite occurs as small porphyroblasts ≤ 500 microns which overgrow the main fabric. The staurolite contains high concentrations of Zn (up to 4wt%; Table 3.3). Muscovite forms asymmetric fish and the muscovite layers contain isoclinal folds producing banding between quartz-rich and muscovite-rich layers.

### 3.3.4 Methodology

Pseudosection calculations were made using Thermocalc (Powell et al., 1998) and the internally consistent database of Holland and Powell (1998) for the model system Mn, Ca, Na, K, $Fe^{2+}$, Mg, Al, Si, and $H_2O$, which represents the major components in minerals of petrological interest. However, this system excludes Ti, $Fe^{3+}$ and Zn which may be of importance to some equilibria. For example Mn concentrations may be high in early-formed Ti oxides so that excluding Ti may effect the

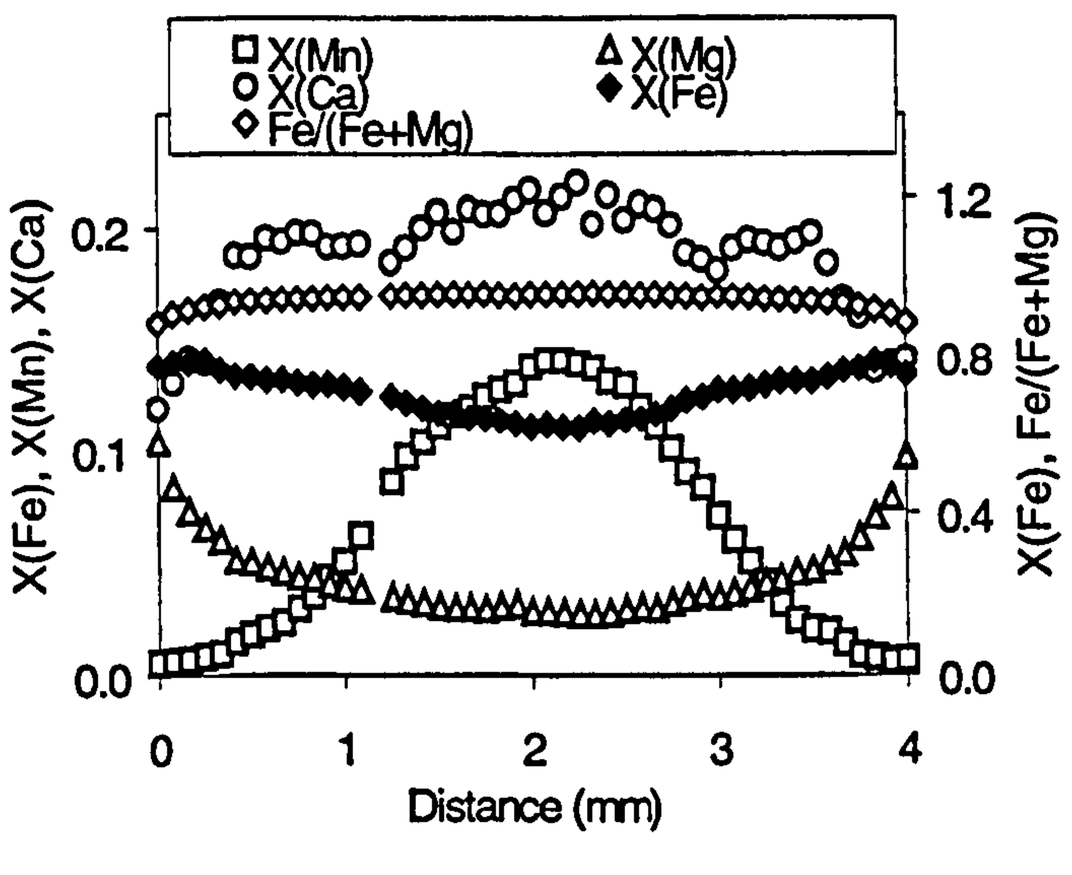


*Figure 3.10 Major-element composition of garnet in sample 4A3 measured by electron-microprobe and recalculated as mole fraction. Also shown is the Fe/Fe+Mg ratio. Note the well developed bell-shaped Mn profile indicating prograde zoning without significant intra-crystalline diffusion..*

modelling of early garnet in which Mn concentrations are also high (e.g. Vance and Mahar, 1998). Similarly Zn may play an important role in stabilising staurolite (Grambling, 1981; Tuisku et al., 1987; Droop and Harte, 1995) although Zn does not partition significantly into any coexisting minerals (Grambling, 1981; Dymoke and Sandiford, 1992) and so its only effect is to increase size of the stability field for staurolite. $Fe^{3+}$ is likely to exist as a component in many of the phases (e.g. garnet, staurolite, biotite) but no minerals are observed in which it is a major component (e.g. epidote). It is thus unlikely to play a significant role in the pseudosections derived below.

All calculations are made assuming the presence of an $H_2O$ fluid phase. This assumption is potentially violated at high temperature or in rocks which have undergone several metamorphic events leading to dehydration. However, for the assemblages modelled here there is little evidence that such high temperatures were reached. Furthermore, the breakdown of biotite to form garnet produces significant amounts of $H_2O$, enough to maintain water-saturated conditions up to 700°C (Vance and Mahar, 1998).

Perhaps the most important potential source of error is the assumption that the measured bulk rock chemistry represents the effective bulk composition (EBC) from which the minerals grew. This is undermined if: (i) the system is open to the modelled components such that elements are either supplied or removed during or after metamorphism; (ii) the sample used in determination of the bulk composition is not representative of the EBC (this would be true for a banded rock in which small scale bulk composition variations result in varying mineral stabilities) and; (iii) if mineral growth results in the preferential removal of elements from the EBC (e.g. garnet cores removing Mn from the EBC).

It is generally assumed that major elements are not mobile over significant distances in

metamorphic rocks. The volatiles and silica may be mobile (e.g. Ague, 1991) but they will not significantly affect the modelling of pseudosections since $SiO_2$ and $H_2O$ are modelled as being in excess. Porphyroblast growth is more problematic and, in the case of the samples studied here, it is clear that porphyroblasts do sequester elements such as Mn and Al. While this can potentially be taken account of, the present version of Thermocalc is not capable of determining this effect and it is therefore dealt with qualitatively.

Apart from the geological errors mentioned above, Thermocalc propagates errors from the thermodynamic data and endmember activities. These result in typical errors on univariant lines of ±10°C and invariant points of ±10-20°C, the larger errors being typical of the cordierite-bearing assemblages. Thermocalc also calculates errors on the modal proportion of minerals in the stability fields which, in the case of the divariant fields, are often larger than the modal proportions themselves. Although the interpretation of such errors is as yet uncertain, such fields are often so small as to be insignificant in the interpretation of the rock in many cases. Despite the importance of understanding the size of likely errors, the main feature of interest in these diagrams is the *relative* position of the fields - which are unaffected by the principal sources of error in these calculations.

### 3.3.5 Phase relationships

In all cases quartz and $H_2O$ were in excess and chloritoid was omitted. In samples G9 and 4A3, muscovite was also in excess and cordierite was omitted.

The phase relationships for a rock of the composition of G135, plotted in Figure 3.11, are somewhat complicated and include two divariant fields - one lying on the sillimanite-kyanite transition (inset (a) Figure 3.11) and the other in the sillimanite field (inset (b) Figure 3.11). The pseudosection predicts that chlorite remains stable up to high temperatures (>660°C) which is supported by the observation that chlorite is fabric

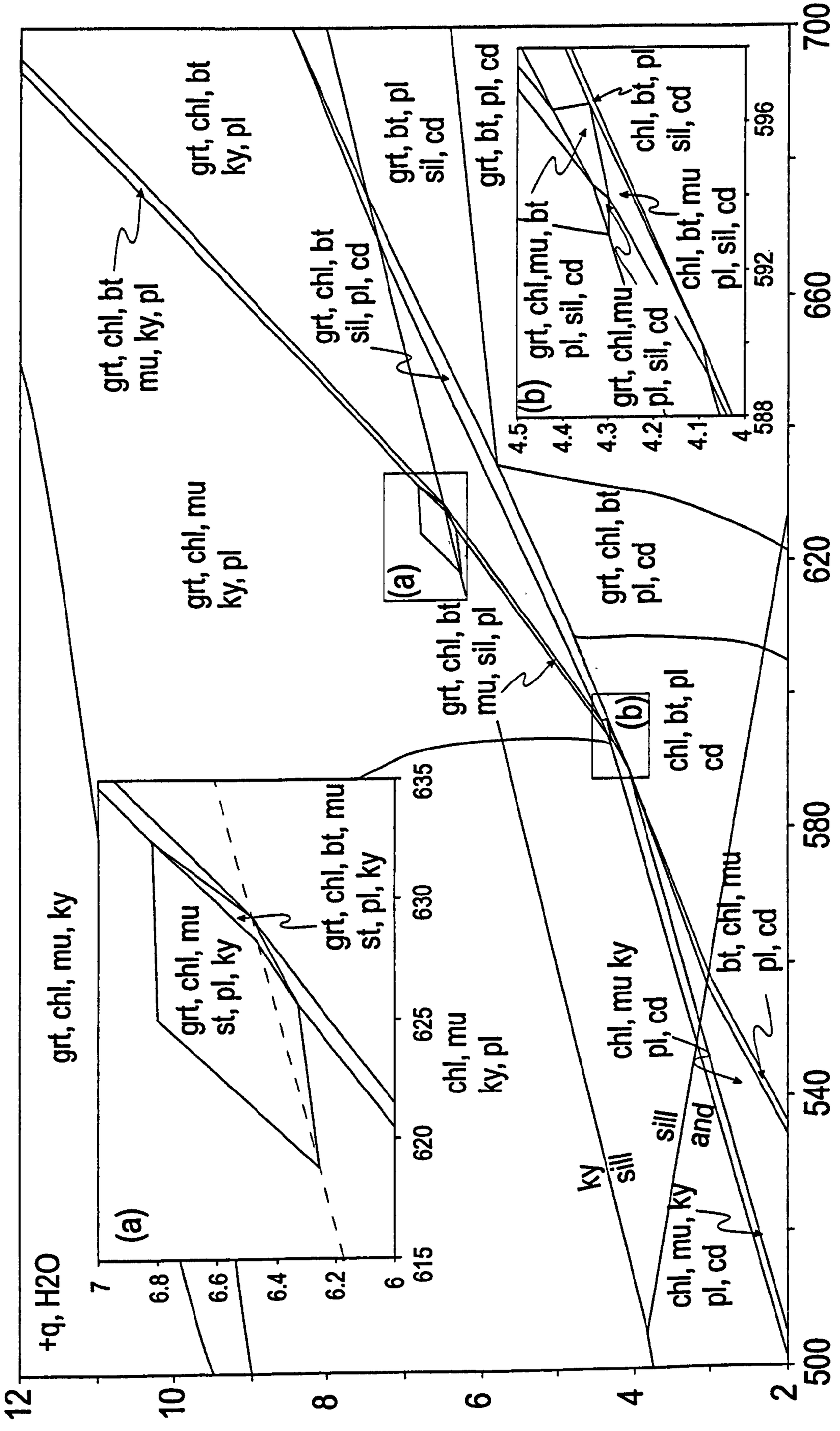


*Figure 3.11 Modelled PT pseudosection for sample G135. With inset detail of staurolite-sillimanite bearing divariant field (a) and cordierite bearing divariant field (b).*

forming. The persistence of chlorite to high temperatures is essentially the result of chlorite's preference for Mg and the high Mg content of the rock. Additionally, muscovite and biotite only coexist in a very narrow field. Kyanite is stable over a large range of P and T and garnet is restricted to high temperatures relative to other pseudosections for pelitic rocks (Mahar et al., 1997; Vance and Mahar, 1998).

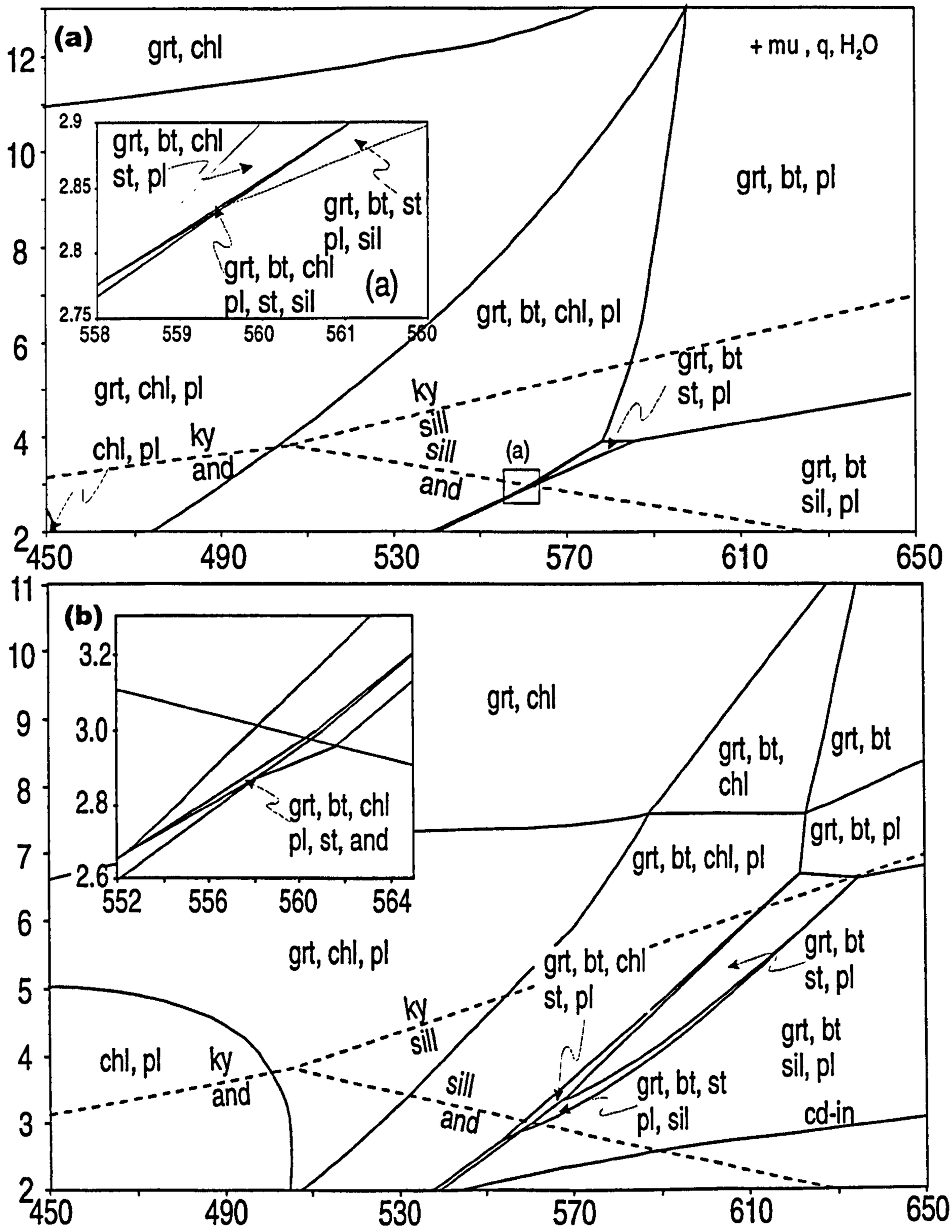


*Figure 3.12 (a) Modelled PT pseudosections for sample G9, with inset detail of divariant field. (b) Modelled PT pseudosection for sample 4A3, with inset detail of divariant field*

The phase diagram for G9, shown in Figure 3.12a, predicts that staurolite is stable over a small range of P and T and that kyanite is not stable. This explains the absence of kyanite in this rock despite falling in the kyanite zone of the HHCS. Overall, the modelling results in a very simple phase diagram in the PT areas of interest with only a small staurolite stable field below 4 kbar. Garnet becomes stable at ~450°C at 2 kbar – i.e. lower P and T than in other grids calculated for pelitic samples (Mahar et al., 1997; Vance and Mahar, 1998) - which is a function of the higher Mn content of the rock. Plagioclase is predicted to disappear from the rock at pressures above 11 kbar at 450°C and is stable to higher pressures at higher temperatures.

The phase diagram for 4A3, presented in Figure 3.12b, predicts a larger staurolite stability field than for G9 and kyanite is not stable below 630°C. Interestingly plagioclase disappears from the rock at pressures above 6.5-8 kbar, in agreement with the observed lack of plagioclase in the sample. It is important however, to remark that the predicted staurolite stability field may be enlarged in the real rock due to the stabilising effect of Zn on staurolite.

### 3.3.6 Quantitative results

The lack of garnet in sample G135 weakens the constraints on the PT field of this sample since garnet often preserves the PT history in its zoning and is an integral phase for virtually all pelitic thermometers and barometers. Fortunately, however, the PT field in which the original assemblage of staurolite and kyanite coexist, prior to the growth of cordierite, is extremely small (615-635 °C and 6.2-6.8 kbar; upper left inset in Figure 3.11). While this does not allow us to constrain the prograde path the overgrowth of cordierite allows us to place constraints on the minimum decompression suffered by this rock. The present stable assemblage of chlorite, biotite, plagioclase and cordierite is only stable at a minimum of 1.5 kbar and ~20°C lower than the stability field for coexisting staurolite and kyanite, indicating the minimum decompression if the

assemblages grew as a part of a continuous process.

One possible problem with this result is that fractionation of material into kyanite and staurolite may have altered the EBC from which the cordierite grew, thus changing the pseudosection calculation. The extent to which the absolute position of the phase equilibria are affected by such changes to the EBC can be qualitatively investigated by changing the bulk composition and recalculating the equilibria: relict kyanite and staurolite are likely to reduce the Al and Fe content of the EBC (the bulk of Mg is stored in chlorite and biotite). In fact changing the Al content by up to 10% makes no difference to the position of the chlorite, biotite, plagioclase and cordierite field and decreasing the Fe content moves it up temperature and up pressure by only a small amount. It is thus likely that the minimum values estimated for decompression and cooling are robust.

*Garnet compositional contours*

An alternative method for obtaining quantitative results from the pseudosections, when the mineral variance is high, is by comparing the analysed composition of minerals with the predicted composition from the pseudosection calculations (for garnet composition see Figure 3.14). In the case of rocks bearing zoned garnet the PT path should be constrained by the compositional isopleths. Figure 3.13 shows the compositional contours for garnet calculated by Thermocalc and corresponding to the core composition of G9 (summarised in Table 3.3). The three contours intersect at high angles resulting in a very precise estimate for the PT conditions of core growth: 521 ± 9 °C and 6.0 ± 0.4 kbar. The same approach can be applied for points

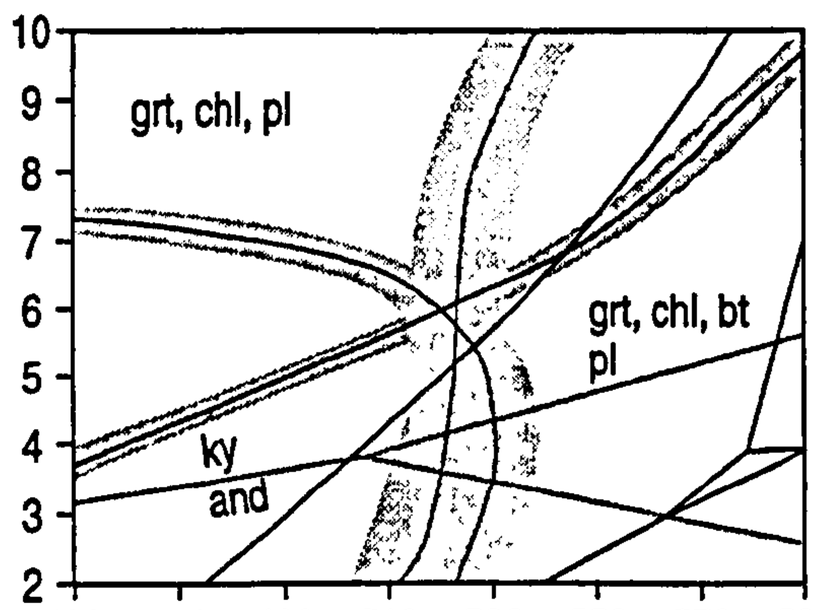


*Figure 3.13 Calculated compositional contours, with uncertainties, corresponding to the real composition of garnet core in G9. Fe contour shown in red, Ca contour in blue and Mn in green.*

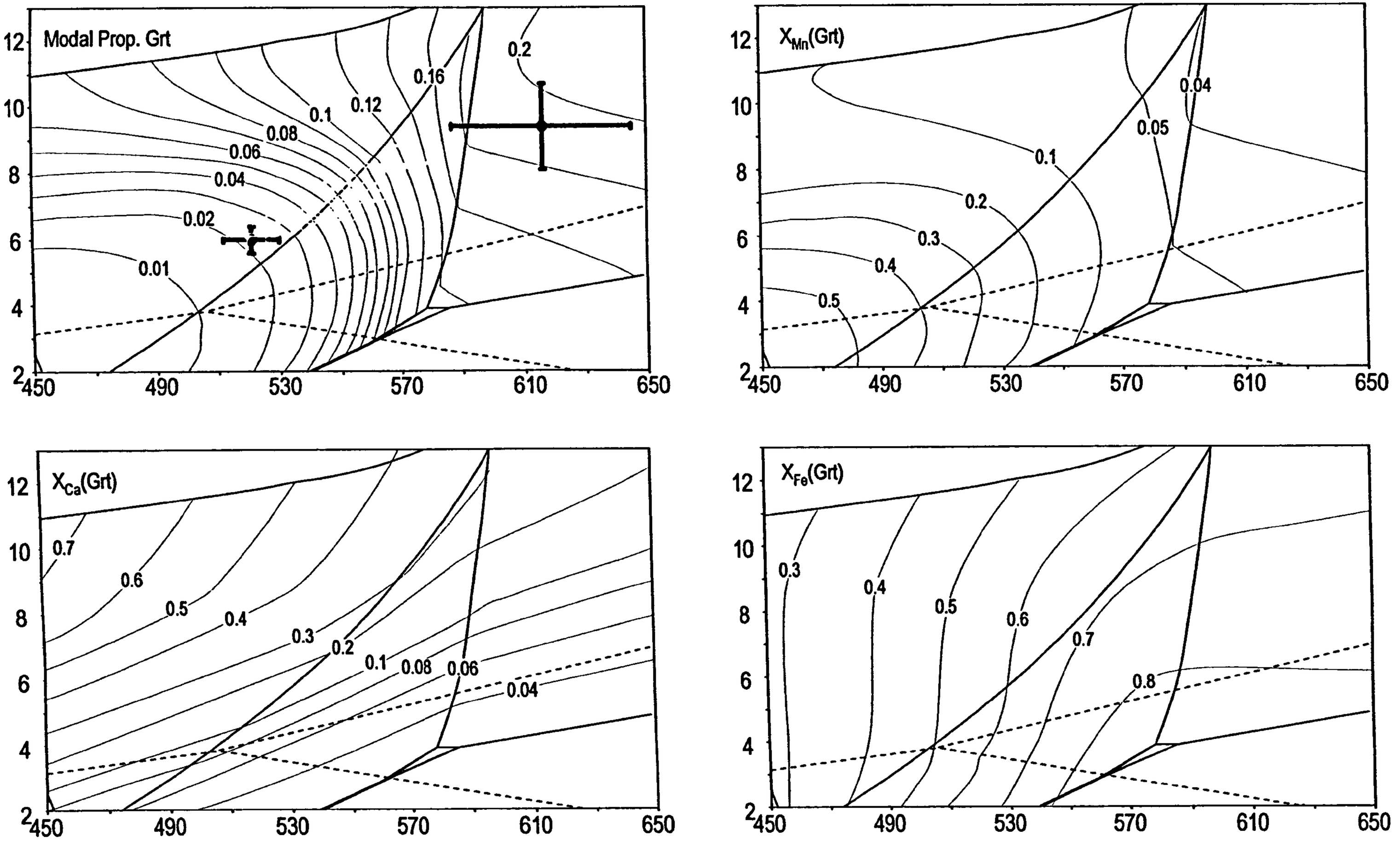


*Figure 3.14 Garnet modal proportions and compositional contours for garnet in G9. Composition expressed as molar proportions of Fe, Ca and Mn in the octahedral site. The bold lines are from the pseudosection boundaries in Figure 3.12. Core and rim PT calculations shown in red. Intermediate PT estimates shown in grey.*

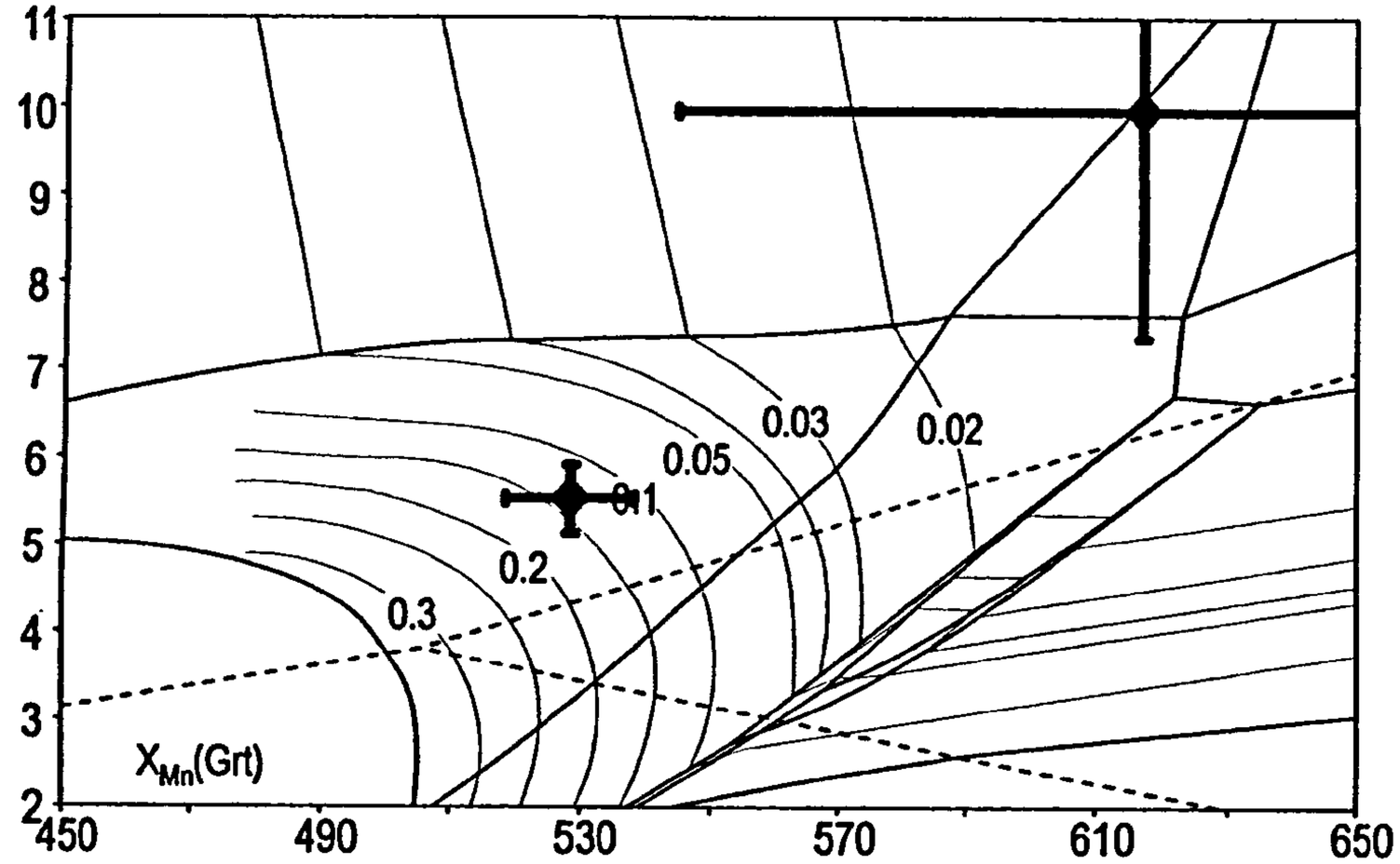


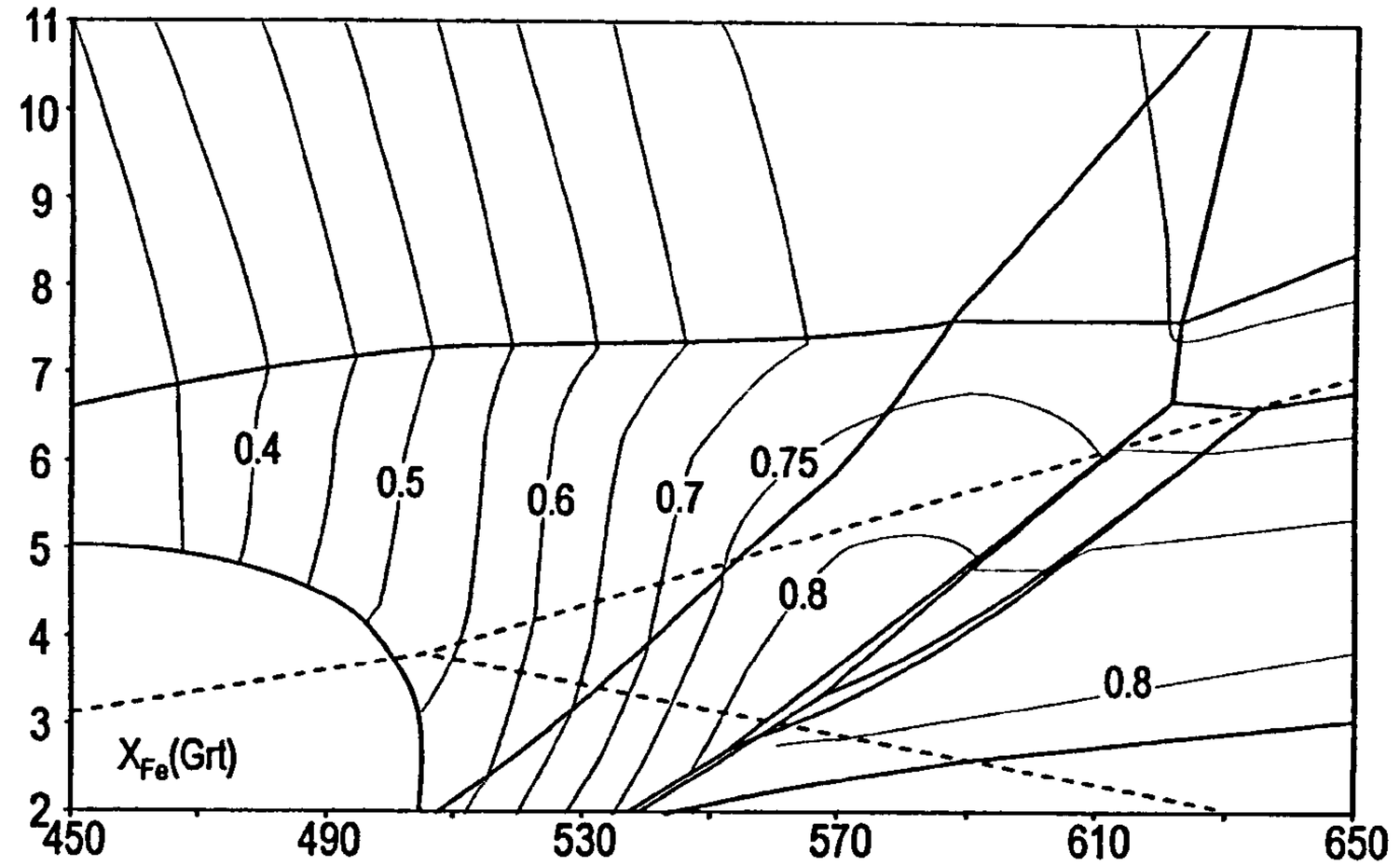


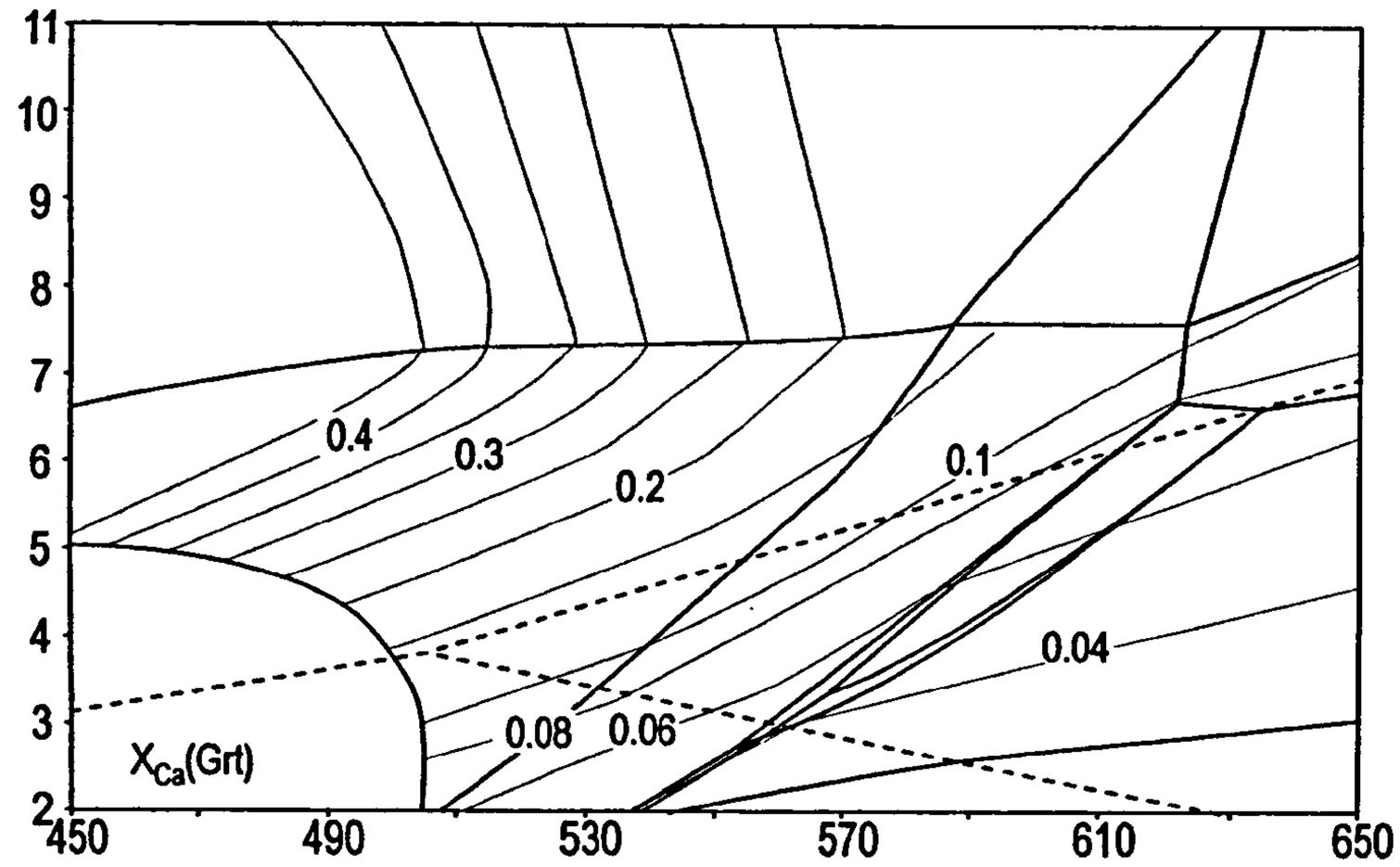


*Figure 3.15 Compositional contours for garnet in 4A3. Composition of garnet expressed as molar proportions for Fe, Ca and Mn in the octahedral site. The bold lines are from the pseudosections boundaries shown in Figure 3.12. Core and rim PT calculations shown on Mn diagram.*

outside of the core (analyses detailed in Appendix E) in order to obtain the PT evolution of the garnet, the results of which are shown in Figure 3.14. The PT path for garnet in G9 can be obtained as far as about half of the distance to the rim - where Mn ≈ 7 mole percent – resulting in a shallow PT path up to ~570°C and 8.5 kbar. Beyond this point the Fe and Ca contours diverge markedly and while they overlap within error it is difficult to obtain a sensible estimate on the calculated pressure and temperature. This is probably due to increased divergence of the bulk rock composition from the effective reservoir from which the garnet grew, as discussed by Vance and Mahar (1998). This unfortunate result occurs because the garnet sequesters elements during growth, thus modifying the effective bulk composition.

It is worth noting that the PT estimate for initial growth lies off the predicted garnet-in reaction at a modal proportion of 0.02. This may be an artefact of the method due to real processes. For example, it may be the result of slow kinetics at low temperatures and the requirement to overstep the activation energy for garnet nucleation. Alternatively diffusional modification of the garnet core at high temperatures, may lead to a present composition that is slightly different from that at core growth..

In the same way garnet core PT conditions for 4A3 can be extracted by comparing the measured composition (Table 3.3 and Figure 3.10) with the calculated compositional contours (Figure 3.15). This gives an exceptional intersection at 528 ± 10 °C and 5.5 ± 0.4 kbar although this modelling is unsatisfactory outside of the garnet core.

Finally the orientation of the modal proportion contours for garnet in G9 Figure 3.15 indicate that decompression of this sample would result in consumption of garnet (unless associated with a temperature increase). Consumption of garnet shows up in the zonation pattern as an increase in X(Mn) near the rim. This is a result of the effect of the extreme compatibility of Mn in garnet so that Mn released by garnet breakdown diffuses back into the remaining crystal. Thus the Mn-rich rim in G9 (Figure 3.9)

suggests that sample G9 underwent decompression sufficiently slowly for some garnet resorption to occur.

*Additional constraints from conventional rim thermobarometry*

The peak P and T can be constrained using conventional thermobarometry on the present assemblage, calculated using Thermocalc in "avPT" mode as for assemblages from the transect along the Dhauli and Alaknanda.

*Table 3.2 Summary of mineral endmember activity data and output from Thermocalc avPT calculations.*

| Sample | 4A3 | G9 | G135 |
|---|---|---|---|
| py[1] | 0.002 | 0.002 | - |
| gr | 0.002 | 0.000 | - |
| alm | 0.440 | 0.490 | - |
| spss | - | 0.000 | - |
| an | - | 0.160 | 0.09 |
| ab | - | 0.880 | 0.94 |
| phl | 0.069 | 0.028 | 0.11 |
| ann | 0.037 | 0.081 | 0.02 |
| east | 0.051 | 0.027 | 0.08 |
| mu | 0.680 | 0.670 | - |
| pa | 0.980 | 0.960 | - |
| cel | 0.019 | 0.022 | - |
| mst | 0.002 | - | - |
| fst | 0.410 | - | - |
| crd | - | - | 0.62 |
| fcrd | - | - | 0.06 |
| mncrd | - | - | 0.00 |
| clin | - | - | 0.08 |
| daph | - | - | 0.01 |
| ames | - | - | 0.07 |
| q | 1 | 1 | 1 |
| $H_2O$ | 1 | 1 | 1 |
| T (°c) | 616 | 616 | 513 |
| s.d. | 77 | 29 | 47 |
| P (kbar) | 10 | 9.4 | 1.2 |
| s.d. | 2.8 | 1.3 | 1.2 |
| cor | -0.231 | 0.730 | 0.995 |
| Fit | 1.27 | 0.61 | 0.81 |

[1] mineral endmember abbreviations in Appendix B

Using the mineral data from Table 3.3, endmember activities have been calculated by Ax98 (Table 3.2). For G9, the mineral assemblage used for PT calculations is consistent with the pseudosection field in which it falls (Figure 3.14). For 4A3 the observed equilibrium assemblage includes staurolite which is not consistent with the calculated final PT conditions and pseudosection (Figure 3.15). This may be due to the effect of Zn on staurolite stability. Zn, however, has no effect on the PT calculation which only uses the relative Fe and Mg composition of the staurolite.

It is also possible to calculate the PT for sample G135 despite the high variance and disequilibrium in the sample. By combining all the minerals potentially in equilibrium (i.e. excluding only kyanite and staurolite) an estimate of 513 ± 47 °C and 1.2 ± 1.2 kbar is obtained. While petrography suggests late growth of muscovite the mineral endmember information supplied by Thermocalc does not highlight any of the muscovite

endmembers as suspect as would be expected for a disequilibrium assemblage. Nevertheless it is worth treating this estimate with caution.

These PT estimates can be combined with the core PT estimates obtained from pseudosection calculations to constrain the PT path of the sample and are plotted for G9 and 4A3 on Figure 3.15 and Figure 3.14 respectively. These garnets in both samples grew under very similar conditions, involving heating and burial from 530°C-620°C and 6-10 kbar, even though they lie some ~9 km (250 MPa) structurally apart.

## 3.4 Discussion

The following section will discuss the implications for reconstructing the thermo-tectonic history of the Himalayan metamorphic belt in Garhwal and compare it with that recorded by previous authors and elsewhere along the chain.

### 3.4.1 Prograde metamorphism

Unfortunately G135 does not provide prograde path information but "peak" paleopressures recorded by G135 of $6.5 \pm 0.5$ kbar imply that there was at least 22 km of cover which, based on field observations, is likely to correspond to the overburden of Tethys Himalaya sediments with which the Harsil Formation has been tentatively correlated (Metcalfe, 1990; Metcalfe, 1993). This compares with estimates of ~10 km for the thickness of restored Tethys Himalaya sediments (Searle, 1986) and implies that some thickening of the Tethys Himalaya must have occurred prior to the formation of these assemblages. This must be the result of reverse movement on faults structurally above and to the north of the present level of G135.

Pseudosection modelling of sample G9 indicates that garnet growth occurred during heating and burial, with a shallower PT path than for garnets in Zanskar (Vance and Mahar, 1998). The increase in pressure indicates that the sample was being buried by active thrusting at structurally higher levels and the fact that the PT path is shallow

*Table 3.3 Summary of mineral data used for PT estimates of samples for which pseudosections are presented*

| **Sample** | **4A3** | | | | | **9** | | | | | **135** | | | | | |
|---|---|---|---|---|---|---|---|---|---|---|---|---|---|---|---|---|
| Mineral | Grt core | grt rim | st | mu | bt | Grt core | grt rim | Pl | mu | bt | Fsp | chl | mu | bt | crd | St |
| $SiO_2$ | 37.81 | 37.11 | 28.01 | 47.43 | 36.49 | 36.89 | 37.59 | 66.35 | 46.41 | 35.91 | 68.54 | 26.09 | 48.23 | 38.50 | 49.23 | 28.20 |
| $TiO_2$ | 0.04 | 0.07 | 0.53 | 0.37 | 1.38 | 0.11 | 0.00 | 0.00 | 0.79 | 2.04 | 0.00 | 0.11 | 0.22 | 1.36 | 0.00 | 0.66 |
| $Al_2O_3$ | 21.33 | 20.98 | 54.24 | 36.21 | 18.39 | 20.40 | 20.22 | 21.83 | 33.74 | 18.19 | 20.74 | 23.76 | 37.24 | 19.95 | 33.13 | 53.54 |
| $Fe_2O_3$ | 0.42 | 1.06 | 0.00 | 0.00 | 0.00 | 0.95 | 0.07 | 0.00 | 0.00 | 0.00 | 0.06 | 0.00 | 0.81 | 0.00 | 1.31 | 0.00 |
| FeO | 34.99 | 27.76 | 12.40 | 0.80 | 17.11 | 24.85 | 35.71 | 0.00 | 1.70 | 21.80 | 0.00 | 19.47 | 0.31 | 13.89 | 4.71 | 12.49 |
| MnO | 0.24 | 6.18 | 0.04 | 0.00 | 0.01 | 11.50 | 0.48 | 0.00 | 0.00 | 0.12 | 0.00 | 0.08 | 0.02 | 0.00 | 0.08 | 0.27 |
| MgO | 2.61 | 0.69 | 1.72 | 0.65 | 11.12 | 0.47 | 2.09 | 0.00 | 0.84 | 8.13 | 0.00 | 18.66 | 0.68 | 13.61 | 9.36 | 2.15 |
| CaO | 4.19 | 7.18 | 0.00 | 0.00 | 0.10 | 5.37 | 3.92 | 2.38 | 0.00 | 0.02 | 1.15 | 0.04 | 0.00 | 0.01 | 0.00 | 0.00 |
| $Na_2O$ | 0.00 | 0.00 | 0.07 | 2.02 | 0.24 | 0.00 | 0.00 | 10.33 | 1.15 | 0.16 | 9.72 | 0.04 | 1.01 | 0.20 | 0.55 | 0.00 |
| $K_2O$ | 0.00 | 0.00 | 0.00 | 8.22 | 7.96 | 0.00 | 0.00 | 0.08 | 9.61 | 9.26 | 0.05 | 0.01 | 8.00 | 8.64 | 0.00 | 0.00 |
| ZnO[1] | | | 4.18 | | | | | | | | | | | | | |
| Totals | 101.64 | 101.04 | 101.18 | 95.70 | 92.80 | 100.55 | 100.08 | 100.97 | 94.25 | 95.64 | 100.26 | 88.27 | 96.54 | 96.17 | 98.36 | 97.30 |
| | | | | | | | | | | | | | | | | |
| Si | 2.99 | 2.97 | 7.77 | 3.10 | 2.79 | 2.99 | 3.04 | 2.89 | 3.12 | 2.75 | 2.97 | 2.64 | 3.10 | 2.79 | 5.01 | 7.82 |
| Ti | 0.00 | 0.01 | 0.11 | 0.02 | 0.08 | 0.01 | 0.00 | 0.00 | 0.04 | 0.12 | 0.00 | 0.01 | 0.01 | 0.07 | 0.00 | 0.14 |
| Al | 1.99 | 1.98 | 17.75 | 2.79 | 1.66 | 1.95 | 1.93 | 1.12 | 2.68 | 1.64 | 1.06 | 2.83 | 2.83 | 1.70 | 3.97 | 17.50 |
| $Fe^{3+}$ | 0.03 | 0.06 | 0.00 | 0.00 | 0.00 | 0.06 | 0.00 | 0.00 | 0.00 | 0.00 | 0.00 | 0.00 | 0.04 | 0.00 | 0.10 | 0.00 |
| $Fe^{2+}$ | 2.31 | 1.86 | 2.88 | 0.04 | 1.09 | 1.68 | 2.41 | 0.00 | 0.10 | 1.40 | 0.00 | 1.65 | 0.02 | 0.84 | 0.40 | 2.90 |
| Mn | 0.02 | 0.42 | 0.01 | 0.00 | 0.00 | 0.79 | 0.03 | 0.00 | 0.00 | 0.01 | 0.00 | 0.01 | 0.00 | 0.00 | 0.01 | 0.06 |
| Mg | 0.31 | 0.08 | 0.71 | 0.06 | 1.27 | 0.06 | 0.25 | 0.00 | 0.09 | 0.93 | 0.00 | 2.81 | 0.07 | 1.47 | 1.42 | 0.89 |
| Ca | 0.36 | 0.62 | 0.00 | 0.00 | 0.01 | 0.47 | 0.34 | 0.11 | 0.00 | 0.00 | 0.05 | 0.01 | 0.00 | 0.00 | 0.00 | 0.00 |
| Na | 0.00 | 0.00 | 0.04 | 0.26 | 0.04 | 0.00 | 0.00 | 0.87 | 0.15 | 0.02 | 0.82 | 0.01 | 0.13 | 0.03 | 0.11 | 0.00 |
| K | 0.00 | 0.00 | 0.00 | 0.69 | 0.78 | 0.00 | 0.00 | 0.00 | 0.83 | 0.91 | 0.00 | 0.00 | 0.66 | 0.80 | 0.00 | 0.00 |
| Sum[2] | 8.00 | 8.00 | 29.26 | 6.96 | 7.71 | 8.00 | 8.00 | 4.99 | 6.99 | 7.78 | 4.91 | 9.95 | 6.85 | 7.70 | 11.01 | 29.30 |
| X(Fe) | 0.773 | 0.625 | | | | 0.562 | 0.795 | | | | | | | | | |
| X(Mn) | 0.005 | 0.141 | | | | 0.263 | 0.011 | | | | | | | | | |
| X(Mg) | 0.103 | 0.028 | | | | 0.019 | 0.083 | | | | | | | | | |
| X(Ca) | 0.119 | 0.207 | | | | 0.156 | 0.112 | | | | | | | | | |

[1]ZnO included for reference but not used in recalculation of cations by "Ax98"

[2]Formulae recalculated on the basis of 12 (garnet), 46 (staurolite), 11 (biotite and muscovite), 8 (plagioclase), 14 (chlorite), 3 (rutile) and 18 (cordierite) oxygens

suggests that the sample responded rapidly to the thermal effect of burial. This would imply that the sample was relatively close to the active thrust – samples at greater structural distance from the thrust will respond first to the pressure increase and only later to heating from thermal re-equilibration. However, in isolation the sample cannot be used to constrain the position of such thrusts and more PT paths are needed to see if there is a systematic variation with structural position.

The PT path obtained from garnet zonation in sample 4A3 also indicates burial and heating during growth of the garnet. Rim estimates indicate that such burial attained depths of ~25 km and temperatures of ~620°C. The similarity of the rim estimates and PT paths for G9 and 4A3 indicates the importance of the MCT as a structural discontinuity juxtaposing samples from different sedimentary units (Ahmad et al., In press) and from different metamorphic units.

The many kinematic indicators in the MCTZ and petrology of the samples suggests that much of the metamorphism within the unit occurred during a single syn-kinematic metamorphic event (see Chapter 2), attributed to the MCT. Attempting to constrain the movement of this fault is more difficult but if the burial of 4A3 was uniquely the result of thrust movement on a plane dipping at 30° this would imply a horizontal displacement of ~40 km – significantly short of other estimates for MCT movement (see Chapter 1).

Together these three samples indicate that the metamorphic assemblages in different levels of the Garhwal Himalaya all developed as a result of burial and thickening of the crust. The Harsil formation must have been buried by faults to its north, as was the basal-HHCS in the Alaknanda. The MCTZ also grew during burial and metamorphism in response to thrust movement on the MCT.

### 3.4.2 "Peak" metamorphism

Assemblages in the MCT and HHCS attained the peak temperatures and pressures

presented in Figure 3.2 and Figure 3.3. Before going on to discuss these data a brief discussion of the potential errors and the limits they place on interpretation are required.

The interpretation of PT profiles, such as that presented in the first section of this chapter, is usually based on the assumption that they record peak metamorphic pressures and temperatures. There are, however, several problems with the methodology used here in the measurement of P and T. Firstly water activity, which has a profound effect on P-T estimates, is difficult to constrain in these pelitic assemblages. Changes in $a_{H20}$ from 1 to 0.4 result in changes of ~100°C and 1.3 kbar – on the order of the differences between different garnet-biotite exchange calibrations. However, the relative PT estimates do not change significantly. The minimisation of the statistical error on PT estimates results in significant changes in PT estimates but for only a limited number of samples and, as for selecting an arbitrary $a_{H20}$, does not significantly change the relative PT estimates (Figure 3.8). As long as the water activity is not independently constrained the PT estimates will remain flawed, but interpretations based on the relative PT estimates are still useful.

A second problem is that the thermometers and barometers may be recording diachronous attainment of P and T and may record conditions during the retrograde path rather than the "peak". While Thermocalc takes into account all possible equilibria, the average PT is still strongly dependent upon data used to produce the the garnet-biotite Fe-Mg exchange reaction (e.g. Ferry and Spear, 1978) and the Ca net-transfer reaction between garnet and plagioclase (GAQP Newton and Haselton, 1981; GMPB Hodges and Crowley, 1985). It has been shown that biotite and garnet will continue to exchange Fe and Mg after the peak of metamorphism, during the retrograde path, and that this will result in an underestimation of the peak temperature (Spear, 1991; Florence and Spear, 1993; Spear et al., 1995). How this effects the measured temperatures is a

function of the cooling rate and much attention has been paid to this aspect of intercrystalline diffusion for geospeedometry (Lasaga, 1983; Spear and Parrish, 1996). Recent studies using oxygen isotope thermometry in the Sutlej valley to the west show an inverted thermal profile in agreement with P-T estimates based on petrogenetic grids (Vannay, 1999). In the Sutlej section the traditional cation-exchange equilibria produce an isothermal profile across the HHCS, as is seen in Garhwal. The disparity between the isothermal profile obtained using cation-exchange equilibria and oxygen-isotope thermometry is attributed to the closure temperature of the garnet-biotite thermometer (Vannay and Grasemann, 1998), a problem which may also apply to Garhwal.

An additional consideration is that the PT estimates may be combining inappropriate mineral assemblages. From petrographic evidence in the Garhwal Himalaya we know that there have been two metamorphic events in the upper levels of the HHCS: one producing the principal assemblage (M1) overprinted by a second event (M2). This is most clearly preserved in the form of cordierite overgrowths, a common feature in the Himalaya (Brunel and Kienast, 1986; Hodges et al., 1992; Inger and Harris, 1992; Hodges et al., 1993; Davidson et al., 1997; Neogi et al., 1998; Vannay and Grasemann, 1998) and may be the cause of the development of fibrolitic sillimanite in the upper levels of the HHCS. These two events may be part of a continuous process or represent two temporally distinct tectonic events but either way the PT estimates for the upper levels of the HHCS presented here may combine early assemblages - comprising garnet, staurolite and kyanite in which the kyanite and staurolite have been corroded (see Chapter 2) - with later sillimanite, biotite and muscovite.

However, trying to quantitatively constrain this is effect is difficult as the mineral assemblages are likely to represent neither the primary assemblage nor the later overprint. In rare cases, however, approximate constraints can be placed on the two different periods of mineral growth, as for G135. Assuming the two assemblages

represent part of a continuous process the pseudosection modelling indicates decompression of between 1.5 and 4.3 kbar accompanied by a temperature decrease of >20 and <110°C.

Thus the assemblages at the top of the HHCS potentially contain minerals from two different tectonic settings: (i) a poorly constrained M1 possibly reaching kyanite-zone and, (ii) a high-temperature decompression event resulting in the development of fibrolitic sillimanite and cordierite. It is most likely that the PT estimates for the upper-HHCS presented here correspond most closely to the later M2 overprint.

In summary while the author feels that the methodology employed here is the most reliable and precise method for constraining PT conditions, only relative constraints can be used with any real certainty. Furthermore many of the questions raised here - diachronous closure of barometers and thermometers, poorly constrained water activity and uncertain assemblage selection – require more detailed work beyond the scope of this thesis.

### 3.4.3 Discussion of models for thermal development of Garhwal

The isothermal profile obtained here is similar to others obtained in the Himalaya (Hodges and Silverberg, 1988; Hubbard, 1989; Mohan et al., 1989; Inger and Harris, 1992; Macfarlane, 1995; Neogi et al., 1998; Vannay and Grasemann, 1998; Vannay, 1999). These thermal field gradients cannot represent a normal steady-state geothermal gradient in a single crustal slice as this should produce decreasing P *and* T upsection, albeit with a slight alteration to the profile resulting from thermal re-equilibration during exhumation. Hence models for the development of the profile in the Garhwal HHCS will be discussed in relation to models proposed for the Himalaya as a whole.

Hodges et al. (1988) explain the near-isothermal profile in the HHCS across the Himalaya with a model which implicitly considers the HHCS to have acted as a coherent body and that the profile represents a geotherm - albeit not a "normal"

geotherm. They suggested that isothermal temperatures were maintained throughout the HHCS by thermal buffering as a consequence of *in-situ* anatexis, whereby the migration of melts advects heat from the lower sections of the crust to higher thus maintaining constant temperatures throughout the section of interest. In Garhwal and in other parts of the Himalaya with similar PT profiles, migmatites are restricted to the upper part of the HHCS and could not, therefore, buffer temperatures. Alternatively Hodges and Silverberg (1988) suggested, for the Garhwal Himalaya, that leucogranites were sourced from deeper unexposed levels and advected heat to the upper-HHCS. If this were the case we might expect the extent of sillimanite growth and its spatial distribution to be linked to the leucogranites. In Garhwal this does not happen as the most abundant fibrolite growth is found in the Dhuali valley where the smallest leucogranite intrusions occur. Furthermore, the small volume of the melts and their relatively low temperatures (<750°C) limit their ability to advect heat. Thermal buffering or advection of heat by leucogranites seems, therefore, to be an unlikely cause for isothermal profiles.

Alternatively, the HHCS may record a diachronous thermal history either as separate events or recording different stages of the thermal history at different levels. For example, the sillimanite-grade metamorphism and the high temperatures at the top of the slab could be caused by a separate high-temperature metamorphic event overprinting the earlier "normal" geothermal gradient. Hodges and Silverberg (1988) suggested such a model for Garhwal based on the same section as presented here. Using Gibbs thermobarometry to obtain PT paths from garnets, they suggested that the HHCS underwent burial and an increase in temperature which was recorded only in the upper-HHCS. Thrust movement on the Malari fault explained the pressure increase but could not account for the required temperature increase and they suggested that the additional heat could have come from the leucogranites sourced lower in the section, as mentioned above. Petrological observations in the Garhwal Himalaya do suggest a second

metamorphic event but that it occurred during decompression. Additionally, the P-T paths calculated by Hodges and Silverberg (1988) were based on the Gibbs modelling of inappropriate garnet samples which lack compositional zoning, probably due to high-temperature intra-crystalline diffusion.

Yet another explanation for the isothermal profile is the focussing of heat below low thermal conductivity layers such that local high heat production results in a perturbed steady-state geotherm (Jaupart and Provost, 1985). The boundary between crystalline rocks with a high thermal conductivity and sedimentary rocks with a lower thermal conductivity results in greater heat transport parallel to layering in the crystalline rocks and a thermal high at the top of the crystalline layers . The steady state (shown in Figure 3.16) corresponds to an undisturbed layering but if the boundary is the result of faulting then the transient geotherm needs to be considered. Whether this results in a thermal high will critically depend upon: (a) the orientation and sense of movement on the fault, principally whether it brings hot rocks or cold rocks onto the crystalline basement and; (b) the rate of movement, which is important for the rate of equilibration between footwall and hangingwall. At intermediate rates of movement a normal fault will result in cooling of the footwall rocks and prevent the development of a thermal blanketing effect. So this model requires that the fault be reverse.

This model is potentially attractive as thermal contrasts may be high across the STDS in the Dhuali valley with the crystalline HHCS below the fault and TSS above the fault although very few quantitative data exist on thermal conductivity contrasts. The resultant thermal conductivity contrast may well have contributed to elevated temperatures at the top of the slab relative to the normal geotherm. However, since the Malari fault is presently identified as a normal fault it is difficult to produce the thermal blanketing as described. Had the Malari fault been inactive or a thrust fault prior to extension, then the elevated temperatures could be developed. Thus the timing

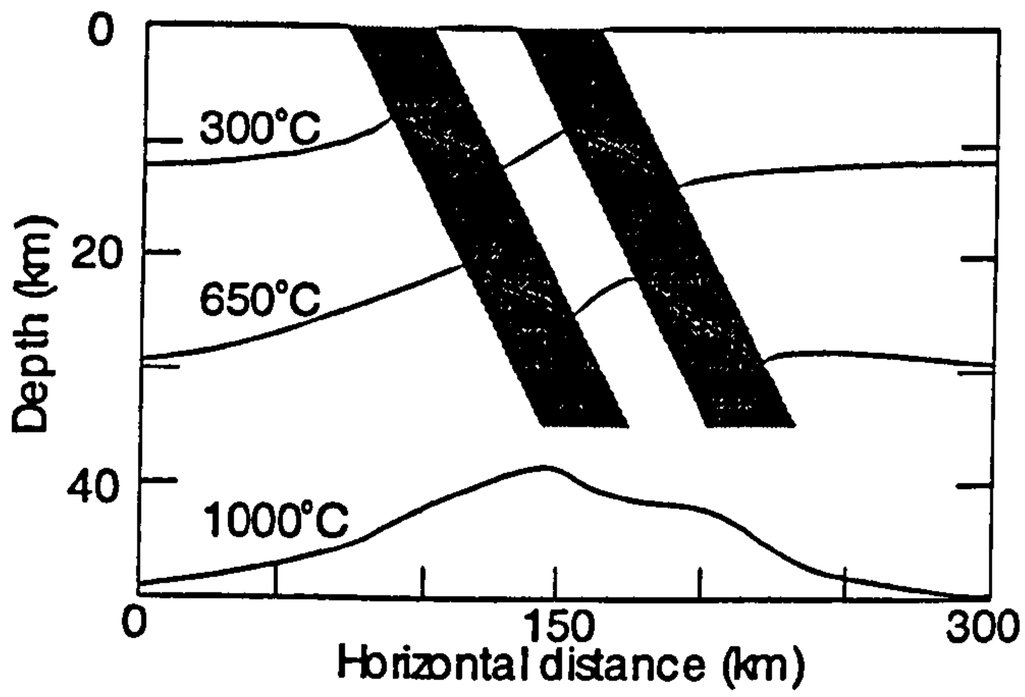


*Figure 3.16 Steady-state model for two layers of low thermal conductivity shown in brown. The lines correspond to three isotherms: 300°C, 650°C and 1000°C. The temperature increases dramatically towards the boundaries of the layers. From Jaupart and Provost (1985).*

relationship between movement on the Malari fault and the development of the mineral assemblages (i.e. metamorphism) is critical.

Deformation provides a final mechanism for developing isothermal temperature gradients. In these models the exposed section does not represent a contiguous sequence of crustal rocks. Rather, they represent spatially distinct rocks emplaced tectonically at their present relative positions. These models come in a variety of forms from discrete thrusts within the HHCS (e.g. Swapp and Hollister, 1991; Reddy et al., 1993), distributed shear through the entire HHCS (e.g. Jain and Manickavasagam, 1993; Grujic et al., 1996) to crustal scale folds (Searle and Rex, 1989) and vary from post-metamorphic to syn-metamorphic deformation. To assess such models requires detailed petrography and structural analysis. However, a few constraints can be proposed for Garhwal and the Himalaya as a whole.

The deformation within the HHCS across the whole orogen is predominantly ductile, limiting deformation to temperatures >~300°C. The relationship between deformation and the growth of the main metamorphic minerals, however, is more complicated. In Garhwal this relationship varies depending on the position in the HHCS or Harsil formation: at the base of the HHCS the main assemblage is pre-deformation whereas in the Harsil formation it is syn-deformation. However, throughout the HHCS the deformation is a top-to-the-south directed shear while at the top of the section there is an overprint of top-to-the-north movement. Furthermore, nowhere in Garhwal does the last metamorphic phase outlast deformation suggesting that post-peak metamorphic

deformation must have an important role in the present day exposure of the rocks. It is likely, therefore, that the HHCS and MCTZ of the Garhwal Himalaya have undergone extensive deformation both during and following metamorphism.

### 3.4.4 Inverted metamorphism in the MCTZ and basal-HHCS

Inverted metamorphism within the MCT has received much attention since the elegant hot-iron model of Le Fort (1975). In this model the inverted metamorphic profile across the MCTZ represents the frozen geotherm resulting from the thrust emplacement of a thick, hot, HHCS re-equilibrating with the underthrust LH. While such a model appears superficially attractive it clearly cannot satisfy the pressure gradient observed here (Figure 3.2). Several other problems also arise with this model. Firstly, not all PT profiles from the MCTZ support such a model. Secondly, even if they did, the preservation of an inverted transient geotherm is difficult given thermal relaxation and realistic exhumation rates (Molnar and England, 1990). Furthermore, recent 2-D modelling suggests that, with a simple thrust geometry, as envisaged by Le Fort (1975), and sensible boundary conditions and parameters, it is impossible to develop an inverted isotherm in the first place (Grasemann, 1993).

Some authors suggest that the inverted metamorphic field gradient was related to frictional heating along the MCT (England et al., 1992) and specifically related this to the formation of leucogranites. While this is also an attractive model it does not satisfy the field observations that the highest temperatures occur above the fault. Also the high shear stresses required on the fault (50-100 MPa) would be difficult to sustain at high temperatures due to the weakening of the rock, particularly when melting is induced.

Alternatively, as for the HHCS, the inversion of isograds could be the result of post-metamorphic deformation of a normal metamorphic sequence (e.g. Jain and Manickavasagam, 1993; Hubbard, 1996). This could occur either as distributed shear throughout the MCTZ or along discrete thrusts. This is supported by the variability in

pressure recorded by samples in the vicinity of the MCTZ. Such a model is also supported by the petrological evidence which shows that in many areas, including Garhwal, deformation outlasted metamorphism – e.g. rotated inclusion trails and assymetric augen. Furthermore, in Garhwal, deformation within the MCTZ is not limited to the ductile region as many brittle faults have displaced originally continuous sequences.

Combining deformation with thermal re-equilibration, Royden (1993) produced an analytical model, in which material in the footwall of a fault is accreted to a 30 km thick hangingwall during uplift and erosion. This showed that a steady-state geotherm would be produced with the highest temperatures preserved above the fault in a profile similar to that seen in Figure 3.2 and obtained by Hubbard (1989). Moreover, a locally inverted sequence would occur across and below the fault. One drawback to this model is that to obtain a steady state requires significant time spans for thrusting along the MCT, timespans which were not available during the orogeny. However, Royden (1993) suggests that transient geotherms of a similar form would be developed.

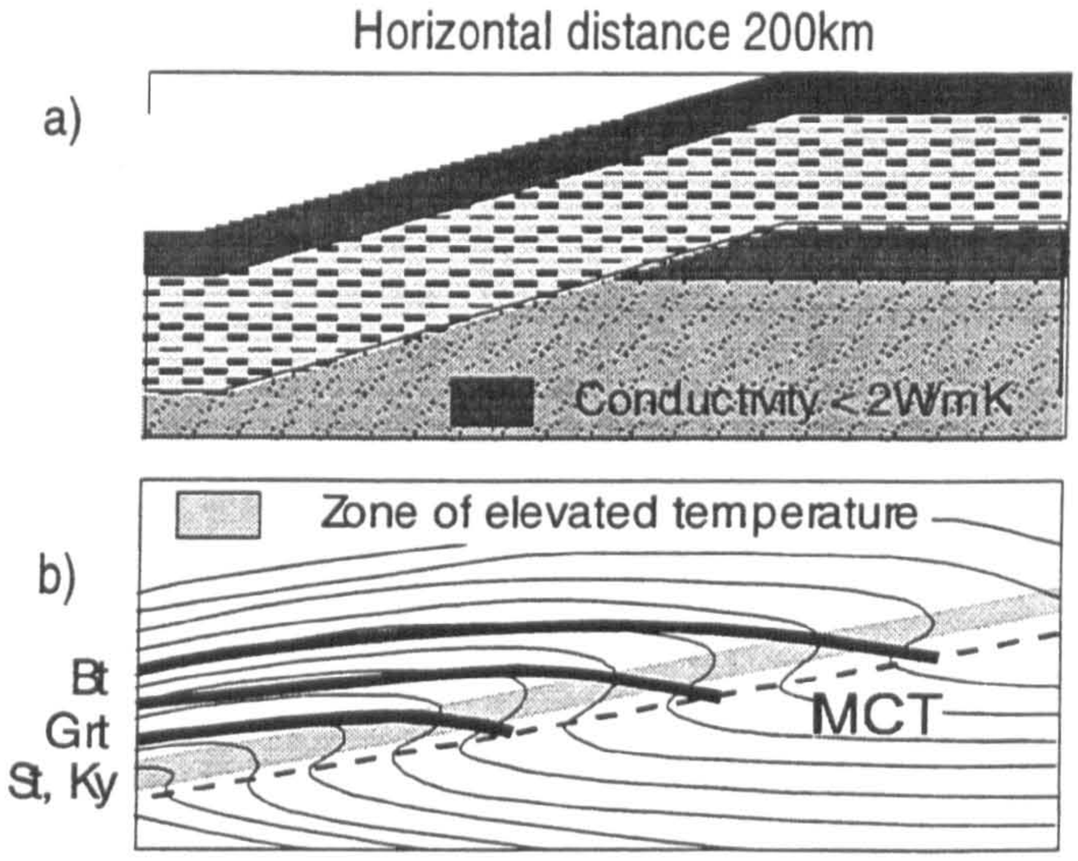


*Figure 3.17 (a) Geometry for model of Grasemann (1993). Dark layers represent low thermal conductivity layers as might be representative of the Tethys Himalaya and Lesser Himalaya, top and bottom respectively. The base of the crust lies at 35 km. This geometry results in an elevated thermal gradient in the initial starting conditions (b) Sketch of possible initial state of thrusting along the MCT. The isograds are cut off by the thrust. With increased deformation along the high-temperature zone the isograds would be folded over.*

In a numerical solution with a similar geometry but without accretion or erosion Grasemann (1993) also produced a similar profile to that observed in Figure

3.2. In this 2-D model the HHCS is assumed to be a solid slab thrust over the LH along a discrete fault (MCT). To obtain any significant temperature inversion the HHCS is required to have an elevated thermal profile prior to thrusting and the base of the HHCS must be insulated by low thermal conductivity rocks such as sediments (Figure 3.17). In cross-section the thermal high does not lie on the MCT but some distance above the fault (Figure 3.17). Given a more realistic model, with some internal deformation of the HHCS, it is likely that deformation would be concentrated along high-temperature layers increasing the velocity of material relative to surrounding lower temperature areas and accentuating the thermal high above the fault.

However, it is unlikely that movement on the MCT was not accompanied by some erosion or that syn-metamorphic deformation did not accrete material to the hangingwall. Perhaps a more realistic model would be a combination of Royden (1993) and Grasemann (1993). Qualitatively combining the two models is not difficult as the two models give very similar results: a thermal high in the hangingwall and geologically appropriate temperatures. Such a model could satisfactorily explain the inverted thermal profile in the MCTZ and the basal HHCS. Post-metamorphic deformation could account for the pressure profile as well as the 'noise' in the dataset. Unfortunately, as for the HHCS, assessing the extent of this deformation is beyond the scope of this thesis but it is clear that a combination of these models satisfies the field observations and PT results.

# Chapter 4 - Timing of prograde metamorphism

## *4.1 Introduction*

In Chapter 3 pseudosection modelling was used to elucidate the thermal evolution of samples in Garhwal and rim PT estimates were made to determine the "peak" PT conditions attained by these rocks. However, as outlined in Chapter 1 and Chapter 3 the critical factor is to link such information through time. Chronological information has recently been measured in the Zanskar area of NW India (Vance and Harris, 1999) using Sm-Nd garnet dating. The advantages of this approach are that it provides constraints on a mineral that is both robust against isotopic resetting (Ganguly et al., 1998b) *and* provides information on pressure, temperature and deformation as well as time. However, the approach also has several drawbacks. Firstly, the Nd contents of garnet are low (< 1 ppm) so that the isotopic analyses are technically difficult. Secondly, and more importantly, the interpretation of ages is made ambiguous by the possibility of incorporating small inclusions of REE-rich minerals such as monazite (Chapter 6 Zhou and Hensen, 1995). In this Chapter new Sm-Nd data for garnets from the Garhwal Himalaya are presented in order to extend the dataset already obtained for Zanskar (Vance and Harris, 1999). In addition, however, we attempt to *exploit* the presence of monazite inclusions in garnet to obtain precise time information more readily using *in situ* SIMS U-Th-Pb analysis (cf. Harrison et al., 1997b; Zhu et al., 1997; Foster, In Prep.) and to relate the latter to the additional petrological data contained in the garnet itself. These two chronometric approaches are combined with detailed analysis of P-T pseudosections (see Chapter 3 and Vance and Mahar, 1998) to obtain a uniquely constrained prograde thermal history for part of the Himalayan orogenic belt.

## 4.2 Geological setting

The samples studied here come from the HHCS in both the Bhagirathi and Alaknanda valleys (Figure 4.1). Details of the setting are given in Chapter 2 and it is only

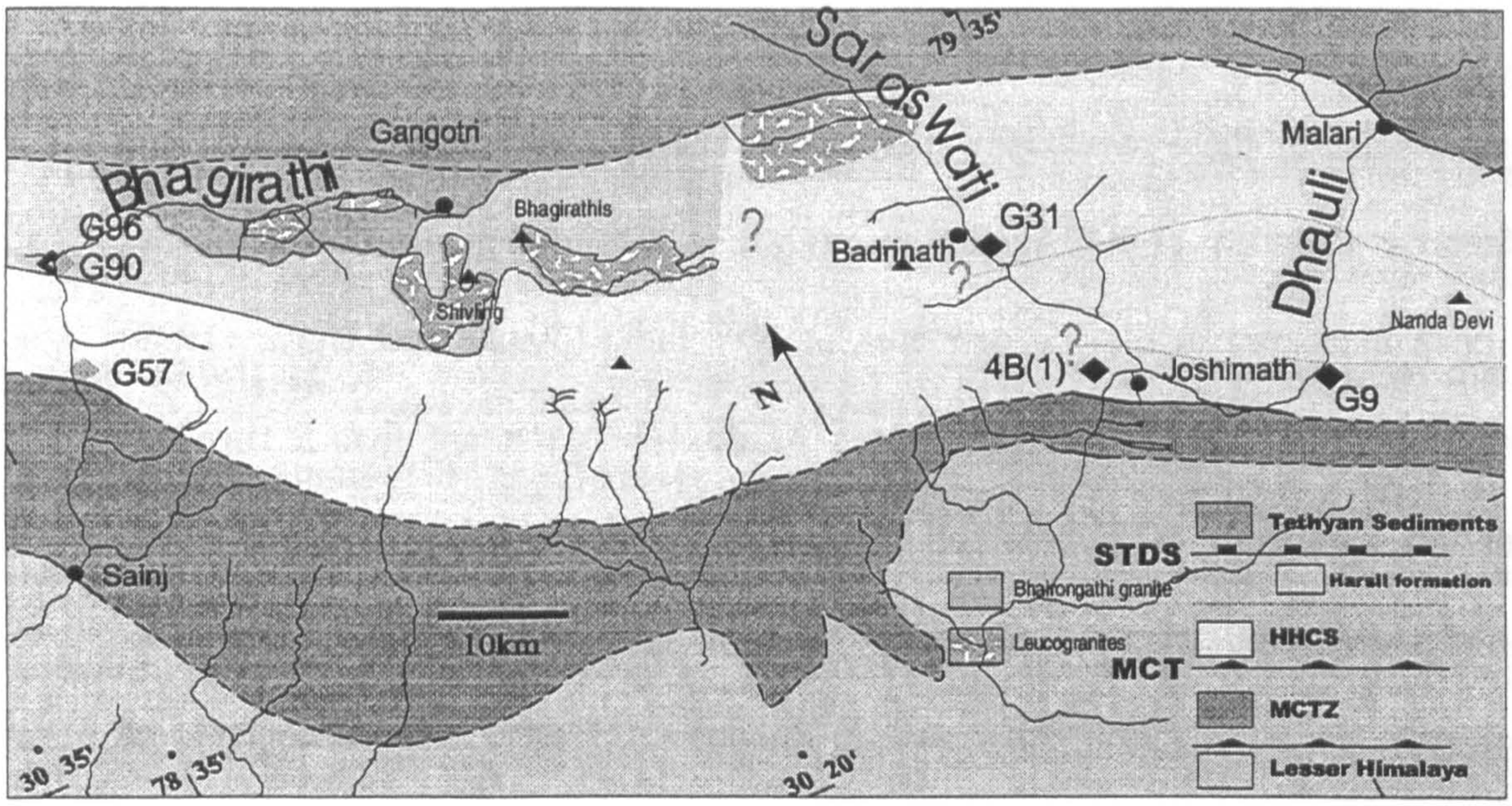


*Figure 4.1 Schematic geology of the Garhwal Himalaya (modified from Virdi (1986); Metcalfe, (1993); Scaillet et al., (1995)). Sm-Nd garnet data localities marked with filled black diamonds. U-Th-Pb monazite data localities marked with grey diamonds. The exposure along the western river valley, the Bhagirathi, is separated into the Harsil formation and the HHCS.*

summarised here. The HHCS can be separated into several litho-tectonic units which differ from one valley to the next. As previously mentioned in Chapter 2 the HHCS in the Bhagirathi valley comprises a kyanite-grade gneissic unit which is capped by the Harsil formation; a series of amphibolite-grade pelitic schists. In the Alaknanda and Dhauli valleys the HHCS can be conveniently separated into three units; the basal, mid and upper HHCS consisting predominantly of gneisses, quarzites and schists respectively (Figure 4.1). The correlation of these lithological units between valleys is difficult, given the inaccessible nature of the terrain between the two areas. However, it is tentatively suggested here that the Harsil formation, rather than belonging to the TSS, correlates with the mid- to upper-HHCS of the Alaknanda and Dhuali valleys. This is based on the similar sedimentary character and metamorphic grade of the lithologically

defined units.

### 4.2.1 Sample description and petrology

The six rocks studied here come from within the HHCS and the Harsil formation as shown on Figure 4.1. Three samples - G96, G31(1) and G90 - are from high structural levels within the upper-HHCS and Harsil formation while the other three - G9, 4B(1) and G57 - come from lower structural levels nearer the Main Central Thrust.

Sample G96 garnet comes from the boundary between a biotite-schist and a quartz vein within the Harsil formation, Bhagirathi valley. This geometry results in approximately half the garnet having a sieve texture, with predominantly quartz inclusions, and the other half being gem quality. Electron-microprobe traverses of garnet in sample G96 parallel and perpendicular to the lithological layering indicate very flat Fe, Mg and Ca and only very slight Mn zonation, indicating near-complete homogenisation of the major elements at elevated temperatures ($Alm_{48}$, $Py_{7}$, $Grs_{31}$ and $Sps_{14}$;See Chapter 6 for profiles) The optical purity of the sample resulted in the separation of rather large fragments of garnet for the Grt 1 Sm-Nd separate. Because this led to difficulties during digestion, the remaining garnet was crushed further before a duplicate aliquot was separated. For reasons detailed later, it is believed that the Grt 1 aliquot was biased towards the earlier grown garnet.

Sample G31(1) is a deformed decimetre sized leucogranite in the upper-HHCS of the Alaknanda valley. The garnets are typically <5 mm across and show smooth zoning in the major elements ($Alm_{66\text{-}71}$, $Py_{9\text{-}13}$, $Grs_{0\text{-}4}$ and $Sps_{13\text{-}24}$; Figure 4.2a). Inclusions of tourmaline quartz and small needles of rutile have been identified and the garnet exhibits optical oscillatory zoning. Sillimanite needles form aggregates which cross-cut garnet in the sample and the fabric in the surrounding rock. Comparison of the major-element composition, determined by electron microprobe, of an aliquot of the garnet used for Sm-Nd isotopic analysis and that of the garnet traverse, established that the

garnet used for isotopic analysis was predominately derived from within the rim of the garnet (Figure 4.2a).

A study of the leucogranite composition indicates that it formed during fluid-present melting of the crust as compared to the fluid-absent anatexis of the larger leucogranites along the length of the chain (Chapter 5 Harris et al., 1993).

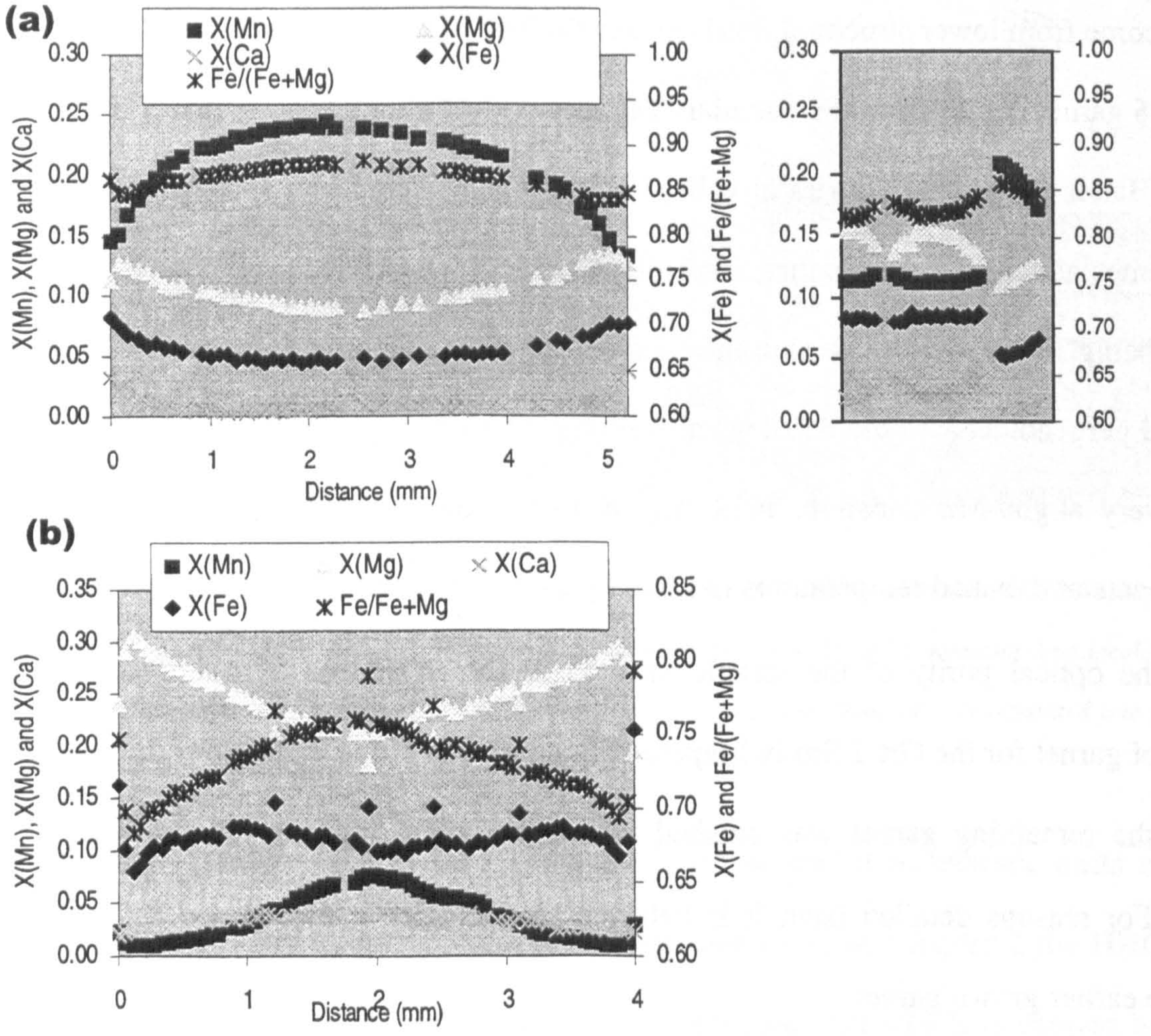


*Figure 4.2 Composition of selected garnets measured by electron-microprobe and recalculated as mole fractions Also shown is the Fe/Fe+Mg ratio.(a) G31(1) and (b) G90 from the upper-HHCS and Harsil formation respectively. Analyses of fragments taken from the aliquot used for isotopic dating are shown next to the major-element profile for G31(1).*

Sample G90 contains the low-variance assemblage garnet, staurolite, biotite, gedrite, plagioclase, quartz and kyanite with accessories of rutile, monazite and tourmaline and unoriented retrogressive chlorite. Garnet crystals are typically <5 mm, euhedral to subhedral, with inclusions of rutile, quartz, opaques and monazite. The garnet preserves

prograde zoning ($Alm_{0.66-0.69}$ $Py_{0.22-0.31}$ $Spss_{0.08-0.01}$ $Grs_{0.04-0.02}$) with a decreasing Fe/(Fe+Mg) ratio from core to rim (Figure 4.2b). A narrow retrogressive rim is developed with a large increase in Fe, decrease in Mg and slight increase in Mn. Staurolite forms euhedral to subhedral crystal <1 mm which show varying degrees of retrogression and lie unoriented in the matrix. Gedrite forms aggregates of small needles to larger laths, <1mm long, which lie in the fabric defined by biotite. Kyanite forms rare large crystals of up to 3mm and is generally corroded by biotite. Plagioclase is $An_{0.08-0.1}$.

Sample G9 is a muscovite schist from the basal-HHCS in the Alaknanda valley in the kyanite zone. The garnet in the sample has a bell-shaped Mn profile, an increasing Fe content from core to rim and a step in Ca and Mg near the rim ($Alm_{80-57}$, $Py_{10-20}$, $Grs_{19-6}$ and $Sps_{25-10}$; Figure 4.3a). A small Mn increase occurs at the rim suggesting garnet resorption during retrograde re-equilibration. Sm-Nd isotopic analyses were carried out on a second garnet from the same hand specimen. Comparison of the major-element composition of an aliquot of the garnet used for isotopic analysis and a garnet traverse, shows that the garnet used for isotopic analysis was dominated by the rim of the garnet (Figure 4.3a).

4B1 is a gneiss containing garnet, biotite, plagioclase, quartz and muscovite from the basal-HHCS just above the MCT in the Alaknanda valley. The garnet forms anhedral crystals, is extremely clean and shows a flattened major-element profile with small variations over some segments ($Alm_{65-52}$, $Prp_{9-2}$, $Grs_{18-12}$ and $Sps_{27-12}$). An aliquot of garnet was separated from the whole rock by heavy liquids and hand picking.

Sample G57 contains the higher variance assemblage garnet, biotite, plagioclase, muscovite and quartz with accessories of rutile, monazite and apatite with small amounts of retrogressive chlorite. Garnet forms euhedral to subhedral crystals up to 4 mm and preserves prograde zoning (Figure 4.3b) with a decreasing Fe/Fe+Mg ratio and smooth zoning in the major elements ($Alm_{0.67-0.69}$ $Py_{0.21-0.25}$ $Sps_{0.07-0.03}$ $Grs_{0.04-0.05}$).

Additionally a small retrograde rim occurs with an increase in Mn content and decrease in Fe/Fe+Mg. Biotite forms the main foliation and along with quartz defines an old ribbon texture containing recrystallised quartz. Muscovite forms large platy laths which generally lie in the foliation although some lie at a high angle to it. Plagioclase is $An_{0.13-0.16}$ and shows little zoning.

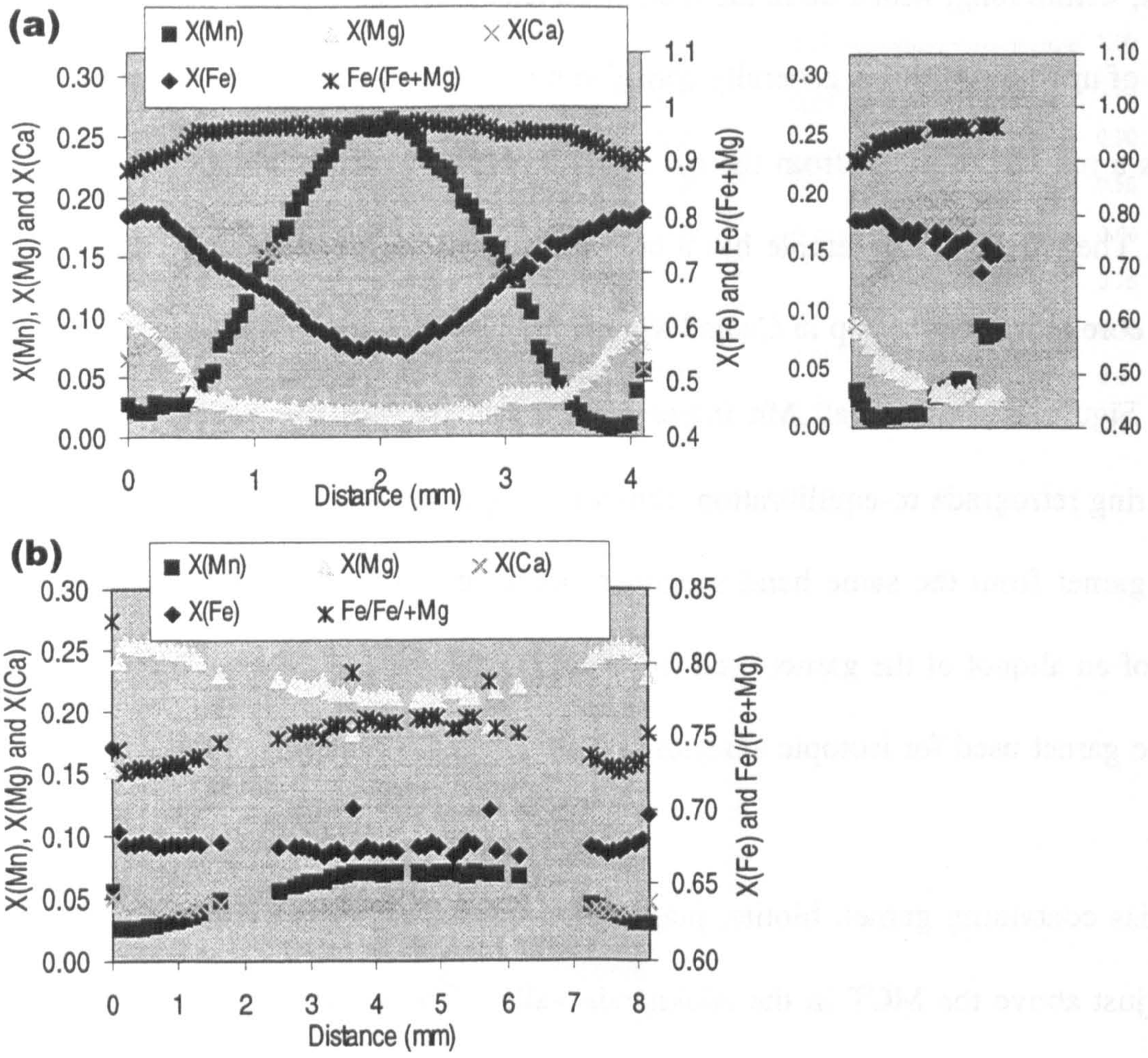


*Figure 4.3 Composition of garnet measured by electron-microprobe and recalculated as mole fractions. Also shown is the Fe/Fe+Mg ratio.(a) G9 and (b) G57. Analyses of fragments taken from the aliquot used for isotopic dating are shown next to the major-element profile for G9.*

## 4.3 Methodology

This chapter uses three separate methodologies in order to build up a complete picture of the early thermal history of the Garhwal Himalaya.

Pressure-temperature conditions for the thermal peak were obtained using the now well-

documented average PT procedure of Thermocalc (Powell and Holland, 1994; Holland and Powell, 1998). Details specific to each sample are given with the description of the results. The methodology used to extract pressure-temperature histories using the compositional zonation in garnet along with model pseudosections contoured for garnet composition, is described in detail in Chapter 3.

For Sm-Nd analysis, impure garnet separates were obtained by either crushing single crystals or by bulk separation techniques (see sample description for specific details). The samples were then purified by hand-picking under a binocular microscope to obtain an optically pure separate of 10-50 mg. Samples were washed and transferred into PFA screw-cap beakers and spiked with a mixed $^{149}Sm/^{150}Nd$ tracer. Chemical dissolution, separation and mass spectrometric techniques are similar to those described in Cohen et al. (1988). Isotopic ratios were measured in static mode on a MAT 262 thermal ionisation mass spectrometer at ETH Zurich. Blank levels were 5±3 pg for Nd and always negligible. Further details are given in Appendix C.

## 4.4 Results

### 4.4.1 Pressure-temperature constraints

While pressure-temperature estimates for near-peak conditions have been made for all of the samples, the prograde major-element zonation in G9 has been specifically exploited using a pseudosection to extract the pressure-temperature history during garnet growth (cf. Vance and Mahar, 1998). Mineral analyses and endmember activities for all PT estimates are summarised in Appendix E.

A PT pseudosection for G9 has already been described in Chapter 3 and only a brief summary of the important aspects will be given here. The predicted mineral assemblage changes are rather simple with chlorite being stable with garnet and plagioclase at low temperatures, biotite joining the assemblage at higher temperatures and chlorite leaving

the stable assemblage at temperatures around 580°C at moderate to high pressures. All three of the independent compositional contours for the garnet core overlap with each other at a pressure and temperature of about 6 kbar and 520°C respectively (see Chapter 3). Unusually, in this case the pseudosection also models the garnet compositions outside the core quite adequately (Figure 3.14a) so that the composition and the P-T path can be successfully tracked until about half of the distance to the rim - or at the point where Mn ≈ 7 mole percent – resulting in a rather flat PT path up to ~570°C and 8.5 kbar. The rim composition (avoiding the Mn-rich rim associated with resorption) and that of the matrix assemblage records a pressure and temperature for rim growth of about 620°C and 9.5 kbar.

Additionally the outer 200μm or so of the garnet displays an increase in Mn. The grid suggests that in the biotite-plagioclase-garnet field, at temperatures equivalent to rim growth in the garnet, this can only be produced by a pressure decrease and must be accompanied by garnet resorption (Figure 3.14a). The increase in Mn, then, must result from diffusion of Mn released from resorption of the rim back into the remaining garnet. As noted previously (Vance and Mahar, 1998) this feature records decompression subsequent to the end of garnet growth though a quantitative estimate of the amount of decompression is precluded by the problems with modelling the garnet rim composition mentioned above. While the details of pseudosections for different bulk compositions are quite different the general topologies are similar. It is noteworthy, therefore, that similar small increases in Mn are seen in the profiles for samples G90 and G57. These two samples also record sharp increases in Fe in this region which is also consistent (Figure 4.2b and Figure 4.3b) with decompression at high temperatures.

Garnet in sample G9, therefore, grew during an increase in temperature of about 80-100°C with only modest increase in pressure of between 2 and 5 kbar. In addition, the

evolving garnet compositions record a linear increase in temperature with pressure. This evolution, in this sample from lower structural depths within the HHCS, is very different from those followed by garnets in the Zanskar Himalaya from higher structural levels (Vance and Mahar, 1998). The latter show PT paths that might be considered typical of the early period of a tectonometamorphic cycle (cf. England and Thompson, 1984) with fast burial early on accompanied by only limited temperature increase, followed by isobaric heating. The PT path for sample G9, on the other hand, records heating with only a small amount of burial and, as such, might be considered to represent thermal re-equilibration after the main phase of burial has ceased. In addition, all three metasedimentary samples with garnets that show zonation in the major elements, record an indeterminate amount of decompression after garnet growth had ceased.

Major-element zoning in garnet from G57 is small but, nevertheless, indicates a normal prograde growth history. However, attempts at modelling the PT evolution of the sample using pseudosections as for G9 resulted in poor core PT estimates. This is likely to be a result of limited high-temperature diffusional homogenisation of the original zoning pattern as rim PT estimates (calculated as for G9) indicate a PT of 767 ± 36°C and 10.6 ± 1.5 kbar, sufficient for significant intracrystalline diffusion.

P-T estimates for sample G96, which is almost completely homogenised, indicate rim equilibration temperatures and pressures of 631 ± 38°C and 9.5 ± 1.2 kbar. Given the diffusion implied by homogenisation, the temperature is probably only a minimum estimate (Spear, 1991).

Intriguingly biotite in sample 4B(1), in which garnet also has only limited major-element zoning, records systematic variations in Fe/(Fe+Mg) ratios away from the zones containing garnet, implying incomplete equilibration on the thin-section scale. This may arise from a lack of a fluid-bearing phase in the rock and PT estimates using

Thermocalc show a strong variation with $a_{H20}$. The rim PT estimate as well as the $a_{H20}$ were obtained by searching in T- and P-$a_{H20}$ space for the best statistical fit among a number of dehydration equilibria calculated by Thermocalc (See Chapter 3). This approach resulted in a PT of 703 ± 39°C and 12 ± 1.3 kbar at an $a_{H20}$ of 0.6 for final equilibration of the garnet rim with the matrix assemblage (as compared to 772 ± 43°C and 12.9 ± 1.4 kbar at an $a_{H20}$ of 1). As for G96, however, given the diffusion implied by homogenisation, the temperature is probably only a minimum estimate and prograde information is impossible to extract from this garnet.

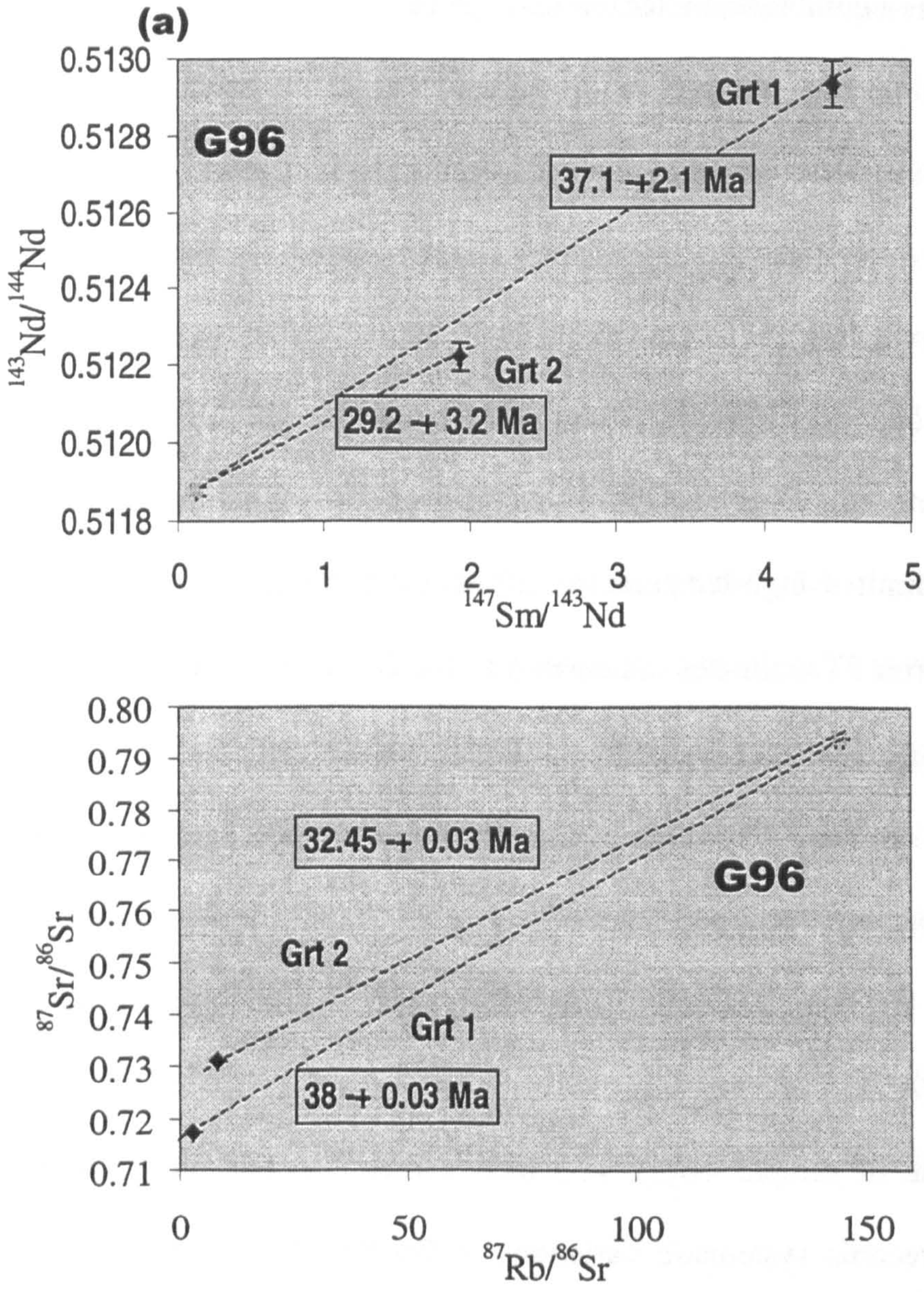


*Figure 4 next page for continuation and caption*

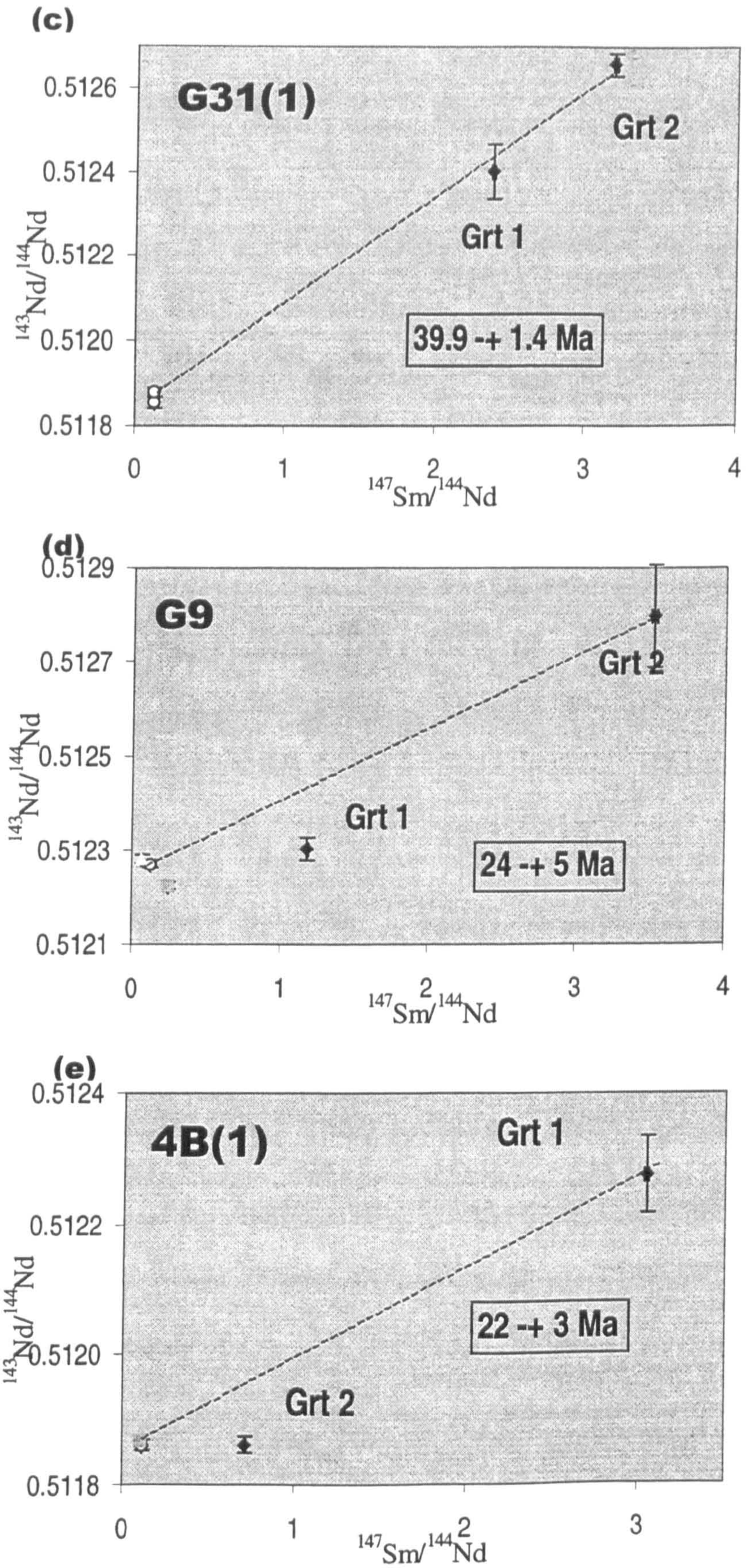


*Figure 4.4 Sm-Nd and Rb-Sr isochron diagrams for garnet samples discussed in the text. Data presented in Table 2 and Table 3. Garnet - red diamonds; whole rock - white circle; biotite - brown square; muscovite - yellow triangle (a) G96 Sm-Nd isochrons (b) G96 Rb-Sr isochrons (c) G31(1) (d) G9 (e) 4B(1).*

### 4.4.2 Sm-Nd isotopic results

The errors given in Tables 1-3 and in the ensuing discussion of all the isotopic data are 2 sigma. Age determination was made using a York regression (York, 1966).

*Table 4.1 Summary of Sm-Nd TIMS ID and isotope ratio analyses.*

| *G96* | *Nd (ppm)* | *Sm (ppm)* | *Sm/Nd* | $^{147}Sm/^{144}Nd$ [1] | $^{143}Nd/^{144}Nd$ [2] |
|---|---|---|---|---|---|
| Grt 1 | 0.066 | 0.489 | 7.403 | 4.4758 | 0.512936 (60) |
| Grt 2 | 0.158 | 0.504 | 3.193 | 1.9302 | 0.512225 (37) |
| Bt | 5.424 | 1.053 | 0.194 | 0.1173 | 0.511879 (12) |
| **G31(1)** | | | | | |
| Grt 1 | 0.237 | 1.252 | 5.285 | 3.1949 | 0.512657 (25) |
| Grt 2 | 0.055 | 0.219 | 3.945 | 2.3847 | 0.512401 (66) |
| WR | 1.5237 | 0.3390 | 0.223 | 0.1345 | 0.511855 (13) |
| WR 2 | 1.5980 | 0.3541 | 0.222 | 0.1339 | 0.511880 (10) |
| **G9** | | | | | |
| Grt 1 | 0.086 | 0.168 | 1.961 | 1.1853 | 0.512303 (24) |
| Grt 2 | 0.207 | 1.203 | 5.821 | 3.5195 | 0.512798 (108) |
| WR | 35.446 | 7.533 | 0.213 | 0.1285 | 0.512269 (8) |
| Bt | 7.63 | 3.09 | 0.405 | 0.2452 | 0.512224 (8) |
| Ms | 17.05 | 1.82 | 0.107 | 0.0645 | 0.512281 (8) |
| **4B1** | | | | | |
| Grt 1 | 0.1507 | 0.7607 | 5.048 | 3.0514 | 0.512277 (58) |
| Grt 2 | 0.6677 | 0.7934 | 1.188 | 0.7183 | 0.511861 (12) |
| WR | 24.888 | 4.9398 | 0.198 | 0.1203 | 0.511861 (8) |
| Bt | 6.9338 | 1.295 | 0.187 | 0.1129 | 0.511868 (8) |

*[1] All errors 0.5% except G31(1) Grt2 (1.5%) and CZG-23 Grt1 (1.2%). [2] Replicate measurements (n=40) of the La Jolla Nd Standard gave 0.511853±0.000008 (2σ) over the period that these analyses were performed.*

*Table 4.2 Summary of Rb-Sr TIMS ID and isotope ratio analyses.*

| *G96* | *Sr (ppm)* | *Rb (ppm)* | *Rb/Sr* | $^{87}Rb/^{86}Sr$ | $^{87}Sr/^{86}Sr$ [1] |
|---|---|---|---|---|---|
| Bt | 3.577 | 177.267 | 49.561 | 144.603 | 0.793873 (44) |
| Grt1 | 0.023 | 0.023 | 0.977 | 2.829 | 0.717375 (38) |
| Grt2 | 0.035 | 0.100 | 2.890 | 8.381 | 0.731099 (38) |

*[1] Replicate measurements of the NBS987 standard gave 0.710291±0.000028 (2σ) over the period that these analyses were performed.*

Two isotope dilution analyses of G96 were carried out on gem-quality separates for which the data are summarised in Table 4.1 and Table 4.2. The analyses yielded some

of the highest Sm/Nd ratios ever obtained from a pelitic garnet (3-7.4) and extremely low concentrations. The surprising result is that the two separates gave distinct Sm-Nd ages of 37.1 ± 2.1 Ma and 29.2 ± 3.2 Ma for Grt 1 and Grt 2 respectively (Figure 4.4a). However, equally surprisingly, the Rb-Sr ages on the same aliquots give similarly distinct ages (Figure 4.4b). The fact that the Sm-Nd and Rb-Sr ages on the two separates are concordant is a strong indication that these are robust growth ages. It was noted above that the initial hand-picked aliquot (Grt 1) consisted of a few large fragments (10-15 pieces) while the sample was crushed further before a second separate (Grt 2) was obtained. In view of the concordant ages I infer that the first separate may have been biased towards the early grown portions of the garnet. It is also noteworthy that these concordant age variations have been preserved despite the partial homogenisation of the major elements.

Two isotopic analyses of G31(1) were obtained on a hand-picked separate obtained from a single garnet (Grt 1, Grt 2, Table 4.1). A reproducible age, using the whole rock as the low Sm/Nd phase, of 39.9 ± 1.4 Ma was obtained (Figure 4.4c).

Two analyses were made on separates from a single garnet in sample G9 (Grt 1, Grt 2, Table 4.1). The two garnet separates do not fall on an isochron with the whole rock (Figure 4.4d) suggesting some disequilibrium between one of the garnet analyses and the reservoir from which they grew. This is likely to be the result of inclusions incorporated into the analysis of Grt 1. A study of the effect of such inclusions and comparison of concentrations obtained from *in-situ* analysis of garnets in sample G9 by LA-ICP-MS (Chapter 6) shows that Grt 2 represents very clean garnet with a limited potential contribution from inclusions. The incorporation of micro-inclusions may also explain the deviation of the mineral separates from the whole rock value. The age obtained from Grt 2 and the whole rock is 23.9 ± 4.8 Ma.

Two aliquots of garnet were analysed from sample 4B1 which, as for G9, do not form

an isochron with the whole-rock analysis (Figure 4.4e) Identical concentrations obtained between LA-ICP-MS and ID analyses (Chapter 6) indicate that Grt 2 represents very clean garnet with no inclusion contributions, suggesting that the age of 21.7 ± 2.9 Ma is robust.

### 4.4.3 U-Th-Pb monazite dating

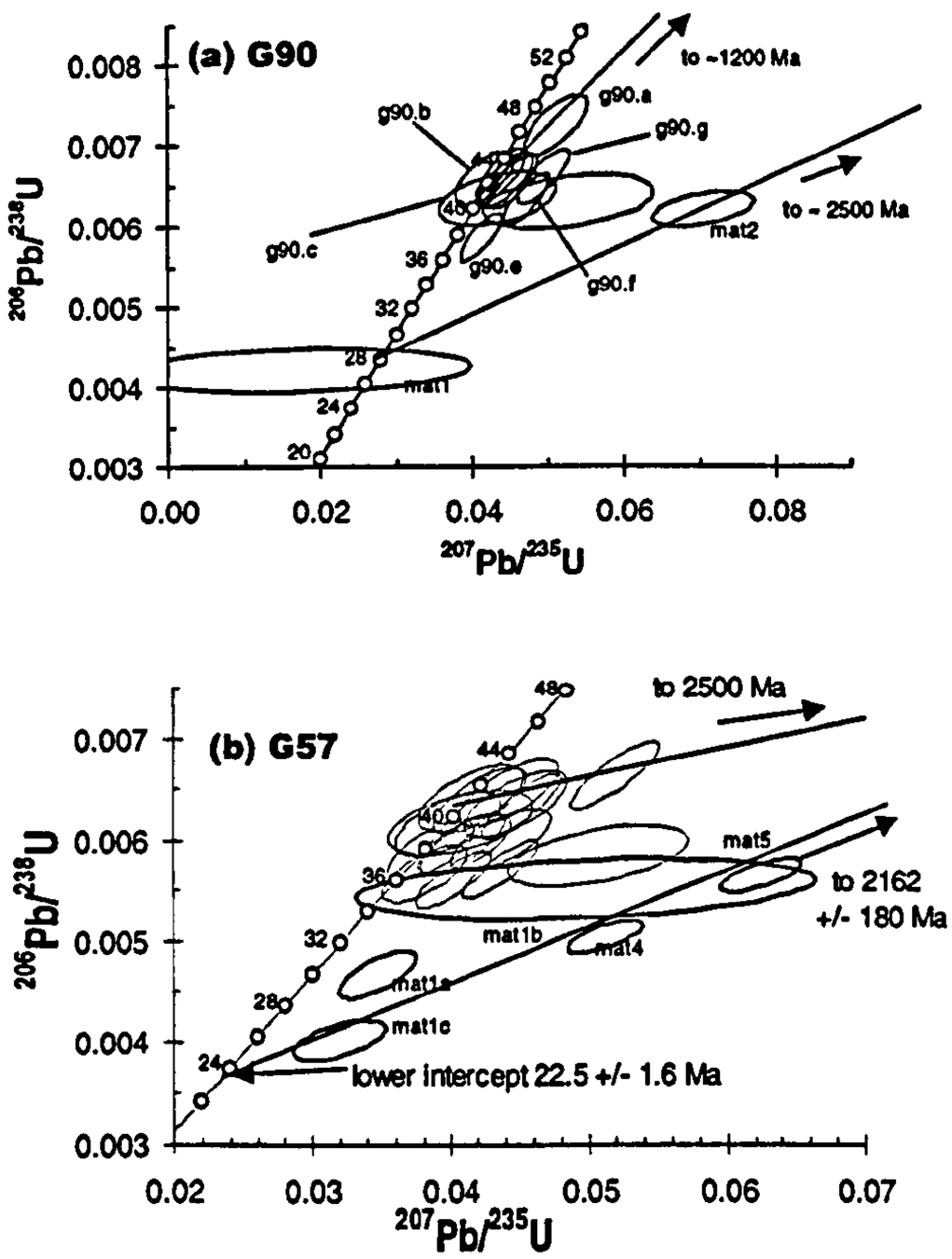


*Figure 4.5 U-Pb Concordia diagram for monazites in sample G90 (a) and G57 (b).*

Ten monazite micro-inclusions within a single garnet and two matrix monazites were analysed within sample G90 from the Harsil formation using the SHRIMP by Gavin Foster at the University of Perth. The U-Th-Pb results of this investigation are presented in Table 4.3 while the U-Pb results are illustrated in a standard concordia plot in Figure 4.5a. Monazite inclusions cluster around 40 Ma (Figure 4.5a) with only around 30% (90b, 90c, 90e) lying on concordia. The average U-Pb and Th-Pb ages of these three concordant points is 41.8 ± 2.5 Ma, and 40.7 ± 1.3 Ma respectively. All other monazite inclusions show very minor discordance due to small contributions of varying amounts of old inherited Pb. One of the two matrix analyses shows more discordance while the other is concordant but has a much younger age than the inclusions at 28 Ma.

*Table 4.3 Summary of shrimp data for sample G90 and G57*

| | | | | | Atomic ratios | | | | | | Apparent Ages (Ma) | | | | | |
|---|---|---|---|---|---|---|---|---|---|---|---|---|---|---|---|---|
| Sample | $f^{206}$ | U (ppm) | Th (ppm) | Th/U | $206^c/238$ | error | $207^c/235$ | error | $208^c/232$ | error | $206^c/238$ | error | $207^c/235$ | error | $208^c/232$ | error |
| G57 | | | | | | | | | | | | | | | | |
| 1.a | 0.3 | 4445 | 46510 | 10.5 | 0.005606 | 0.00012 | 0.040207 | 0.0011 | 0.001806 | 0.000049 | 36.0 | 0.7 | 40.0 | 1.1 | 36.5 | 1.0 |
| 1.b | 0.7 | 4403 | 53726 | 12.2 | 0.005963 | 0.00012 | 0.040888 | 0.0012 | 0.001972 | 0.000054 | 38.3 | 0.8 | 40.7 | 1.2 | 39.8 | 1.1 |
| 1.c | 0.9 | 5041 | 47527 | 9.4 | 0.005664 | 0.00012 | 0.038117 | 0.0013 | 0.001862 | 0.000051 | 36.4 | 0.7 | 38.0 | 1.3 | 37.6 | 1.0 |
| 1.d | 0.0 | 3779 | 56787 | 15.0 | 0.006626 | 0.00014 | 0.051902 | 0.0013 | 0.002085 | 0.000057 | 42.6 | 0.9 | 51.4 | 1.3 | 42.1 | 1.1 |
| 1.e | 1.1 | 3215 | 46943 | 14.6 | 0.006404 | 0.00013 | 0.041461 | 0.0016 | 0.002009 | 0.000055 | 41.2 | 0.8 | 41.2 | 1.5 | 40.6 | 1.1 |
| 1.f | 0.3 | 5300 | 56285 | 10.6 | 0.006325 | 0.00013 | 0.045158 | 0.0012 | 0.001973 | 0.000054 | 40.6 | 0.8 | 44.8 | 1.2 | 39.8 | 1.1 |
| 1.g | 1.2 | 7228 | 48466 | 6.7 | 0.005894 | 0.00012 | 0.038578 | 0.0013 | 0.001775 | 0.000049 | 37.9 | 0.8 | 38.4 | 1.3 | 35.8 | 1.0 |
| 1.h | 1.2 | 5258 | 56305 | 10.7 | 0.005949 | 0.00012 | 0.040985 | 0.0014 | 0.001981 | 0.000054 | 38.2 | 0.8 | 40.8 | 1.4 | 40.0 | 1.1 |
| 1.i | 1.2 | 3805 | 43474 | 11.4 | 0.006156 | 0.00013 | 0.039832 | 0.0016 | 0.001940 | 0.000053 | 39.6 | 0.8 | 39.7 | 1.6 | 39.2 | 1.1 |
| 2.a | 1.0 | 3947 | 55948 | 14.2 | 0.006455 | 0.00013 | 0.044190 | 0.0015 | 0.002045 | 0.000056 | 41.5 | 0.9 | 43.9 | 1.5 | 41.3 | 1.1 |
| 2.b | 0.9 | 4605 | 50847 | 11.0 | 0.006382 | 0.00013 | 0.042086 | 0.0014 | 0.001954 | 0.000053 | 41.0 | 0.8 | 41.9 | 1.4 | 39.5 | 1.1 |
| 2.c | 0.3 | 5029 | 58476 | 11.6 | 0.005703 | 0.00012 | 0.043579 | 0.0011 | 0.001830 | 0.00005 | 36.7 | 0.8 | 43.3 | 1.1 | 37.0 | 1.0 |
| 2.c1 | 3.2 | 3925 | 58243 | 14.8 | 0.005835 | 0.00012 | 0.050661 | 0.0027 | 0.001974 | 0.000054 | 37.5 | 0.8 | 50.2 | 2.6 | 39.9 | 1.1 |
| 2.d | 1.3 | 4924 | 52972 | 10.8 | 0.005995 | 0.00012 | 0.043632 | 0.0015 | 0.001992 | 0.000054 | 38.5 | 0.8 | 43.4 | 1.5 | 40.2 | 1.1 |
| 2.e | 2.2 | 3554 | 44957 | 12.6 | 0.006165 | 0.00013 | 0.040711 | 0.0021 | 0.001947 | 0.000053 | 39.6 | 0.8 | 40.5 | 2.1 | 39.3 | 1.1 |
| 2.f | 1.1 | 3996 | 49522 | 12.4 | 0.006349 | 0.00013 | 0.044738 | 0.0015 | 0.002024 | 0.000055 | 40.8 | 0.8 | 44.4 | 1.5 | 40.9 | 1.1 |
| mat1a | 1.2 | 6142 | 63921 | 10.4 | 0.004665 | 0.00010 | 0.034647 | 0.0011 | 0.001423 | 0.000039 | 30.0 | 0.6 | 34.6 | 1.1 | 28.7 | 0.8 |
| mat1b | 26.2 | 8174 | 59428 | 7.3 | 0.005510 | 0.00012 | 0.049779 | 0.0068 | 0.001690 | 0.000049 | 35.4 | 0.8 | 49.3 | 6.7 | 34.1 | 1.0 |
| mat1c | 2.3 | 5903 | 60644 | 10.3 | 0.004013 | 0.00008 | 0.031926 | 0.0014 | 0.001282 | 0.000035 | 25.8 | 0.5 | 31.9 | 1.4 | 25.9 | 0.7 |
| mat4 | 0.0 | 6789 | 87278 | 12.9 | 0.005034 | 0.00006 | 0.051137 | 0.0011 | 0.001461 | 0.000012 | 32.4 | 0.4 | 50.6 | 1.1 | 29.5 | 0.2 |
| mat5 | 0.0 | 7664 | 77946 | 10.2 | 0.005642 | 0.00007 | 0.062403 | 0.0012 | 0.001713 | 0.000015 | 36.3 | 0.4 | 61.5 | 1.2 | 34.6 | 0.3 |
| G90 | | | | | | | | | | | | | | | | |
| 1.a | 0.4 | 2715 | 31889 | 11.7 | 0.007254 | 0.00015 | 0.051125 | 0.0017 | 0.002198 | 0.000063 | 46.6 | 1.0 | 50.6 | 1.7 | 44.4 | 1.3 |
| 1.b | 0.5 | 5019 | 59386 | 11.8 | 0.006632 | 0.00014 | 0.043877 | 0.0013 | 0.002009 | 0.000055 | 42.6 | 0.9 | 43.6 | 1.3 | 40.6 | 1.1 |
| 1.b1 | 0.6 | 4539 | 54002 | 11.9 | 0.006587 | 0.00014 | 0.044552 | 0.0014 | 0.002012 | 0.000055 | 42.3 | 0.9 | 44.3 | 1.4 | 40.6 | 1.1 |
| 1.c | 0.9 | 4490 | 46157 | 10.3 | 0.006593 | 0.00014 | 0.041653 | 0.0016 | 0.002033 | 0.000056 | 42.4 | 0.9 | 41.4 | 1.5 | 41.0 | 1.1 |
| 1.c1 | 0.0 | 4159 | 51145 | 12.3 | 0.006338 | 0.00013 | 0.047156 | 0.0013 | 0.001957 | 0.000054 | 40.7 | 0.8 | 46.8 | 1.3 | 39.5 | 1.1 |
| 1.d | 6.0 | 3602 | 50180 | 13.9 | 0.006311 | 0.00014 | 0.052736 | 0.0046 | 0.001873 | 0.000052 | 40.6 | 0.9 | 52.2 | 4.5 | 37.8 | 1.1 |
| 1.f | 0.3 | 4553 | 54470 | 12.0 | 0.00662 | 0.00014 | 0.049492 | 0.0014 | 0.002011 | 0.000055 | 42.5 | 0.9 | 49.0 | 1.4 | 40.6 | 1.1 |
| 1.e | 3.7 | 5207 | 60706 | 11.7 | 0.006345 | 0.00013 | 0.04334 | 0.0032 | 0.002053 | 0.000056 | 40.8 | 0.9 | 43.1 | 3.1 | 41.5 | 1.1 |
| 1.g | 0.5 | 8067 | 68950 | 8.5 | 0.005876 | 0.00012 | 0.041174 | 0.0011 | 0.001799 | 0.000049 | 37.8 | 0.8 | 41.0 | 1.1 | 36.3 | 1.0 |
| 1.h | 0.4 | 4778 | 56640 | 11.9 | 0.006566 | 0.00014 | 0.045453 | 0.0013 | 0.001989 | 0.000054 | 42.2 | 0.9 | 45.1 | 1.3 | 40.2 | 1.1 |
| mat1 | 23.3 | 3551 | 37129 | 10.5 | 0.004217 | 0.00011 | 0.017298 | 0.0092 | 0.00191 | 0.000063 | 27.1 | 0.7 | 17.4 | 9.3 | 38.6 | 1.3 |
| mat2 | 1.6 | 2546 | 25345 | 10.0 | 0.006219 | 0.00009 | 0.070515 | 0.0027 | 0.001981 | 0.000027 | 40.0 | 0.6 | 69.2 | 2.7 | 40.0 | 0.5 |

$f^{206}$ = common $^{206}Pb$ expressed as a percentage of total $^{206}Pb$ measured

all errors are are expressed as 1 sigma

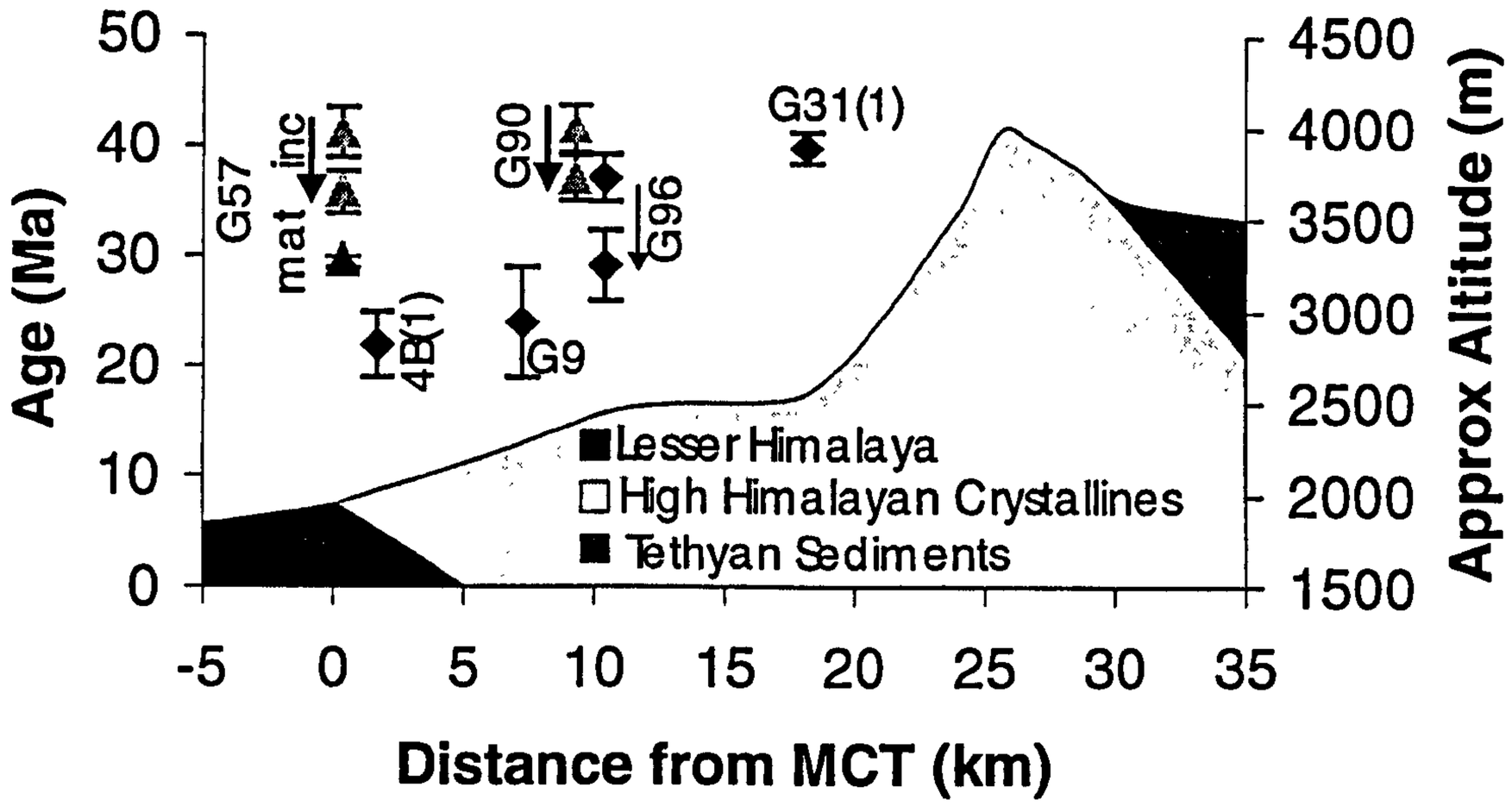


*Figure 4.6 Summary of age data for the Garhwal Himalaya plotted against distance from the MCT. A schematic cross-section of the tecton-stratigraphic units is taken from the Dhuali Valley. Samples from the Bhagirathi are plotted assuming that the Vaikrita thrust marks a consistent boundary between Lesser Himalaya/MCTZ and the HHCS. Th-Pb monazite inclusions in garnet = grey triangles, Th-Pb matrix monazite = green triangle, garnet data = red diamonds. Arrows show the range of ages for monazites included in garnet and the two analyses from G96.*

Three matrix monazites and fifteen monazite micro inclusions within two garnets were analysed within sample G57. The results are illustrated in a standard U-Pb concordia plot in Figure 4.5b, and presented along with Th-Pb data in Table 4.3. Monazite inclusions typically cluster around concordia at 40 Ma, with around 50% lying on concordia from 36.2 ± 1.5 Ma (G571c) to 41.1 ± 1.7 Ma (G571e). Th-Pb ages for these concordant points are 41.2 ± 1.2 Ma (G571g) to 35.8 ± 1.1 Ma (G572a) with the ages randomly distributed within the garnet. Matrix monazites are typically discordant due to mixing between 3 different components (40 Ma, ~2100 Ma, and <25Ma). While the discordance of the matrix monazites could be the result of Pb diffusion at high temperatures (~750°C), rare-earth-element chemistry (Foster, In Prep.) demonstrates that this three -way discordance arises because matrix monazites underwent a further growth phase some time after garnet had grown. The youngest Th-Pb age of 25.8 ± 0.7 Ma (Mat1c) indicates that this new growth must have occurred after ~25 Ma. Analysis Mat1a appears to represent a mixture of all three components. However, the other four

matrix monazites, define a chord that suggests that this new growth occurred at 22.5 ± 1.6 Ma (Figure 4.5b). This age is clearly in accordance with the Sm-Nd data from similar structural levels - G9 and 4B(1) - and with other 22 Ma ages recorded from MCT zone rocks from elsewhere in the Himalaya (e.g. Hubbard and Harrison, 1989).

Figure 4.6 combines the garnet Sm-Nd data with the Th-Pb ages for concordant monazites and a schematic cross-section of the Garhwal Himalaya. This clearly shows the younging to the south of the garnet ages and the overlap in ages of the monazites in G90 ang G57 with the growth of garnet in G96 and the crystallisation of garnet in G31(1).

## *4.5 Discussion*

### 4.5.1 Accuracy of age data and interpretation

There are several issues that relate to the accuracy and interpretation of the ages that must be addressed before proceeding to a tectonic interpretation. The samples for Sm-Nd analysis underwent an initial screening process using the SEM in order to avoid REE-rich inclusions such as monazite. The two techniques employed here of Sm-Nd garnet dating and U-Th-Pb dating of monazite inclusions are, therefore, mutually exclusive. Nevertheless, the great advantage of the current dataset is the availability of both these types of data on very similar samples. In this case, features such as the concordancy of the two data types allow greater confidence in the accuracy and significance of the ages.

Several studies have shown that accessory phases may contribute to, and indeed dominate, "garnet" isotopic data - a feature which is explored in more detail in Chapter 6, and a brief discussion is presented here. These inclusions, which are often so small (< 10-20μm) that their physical separation is impossible, have two effects on the apparent ages of garnets. Firstly, REE-rich inclusions with low Sm/Nd ratios, such as monazite

and allanite, lower the Sm/Nd ratio of the impure garnet separate (e.g. Vance and O'Nions, 1992). Secondly, inclusions of different ages to the garnets can so dominate the REE budget of the garnet separate that the age obtained is in error (Chapter 6). There are a number of criteria for identifying and resolving the role of inclusions in effecting the garnet age. Firstly, the measured Sm/Nd ratios of the garnet separates are in themselves an indication of the purity of the garnet separate, especially if they can be compared with *in-situ* measurements of Sm/Nd ratios in the actual garnet lattice (Chapter 6). Secondly, duplicate analyses of garnet fractions that are variably affected by REE-rich inclusions (reflected in variable Sm/Nd ratios) but that yield reproducible ages, suggest that the inclusions have isotopically equilibrated with the garnet and that the resultant age really dates garnet (Chapter 6). Finally, concordance, both between analyses for different isotopic systems (eg. Sm-Nd and Rb-Sr for G96) and between garnet Sm-Nd analyses and monazite inclusions, would suggest that the ages are robust.

In the case of G96 the rare concordance of the Rb-Sr and Sm-Nd isotopic systems indicates that inclusions are not responsible for the ages obtained. Indeed the gem quality of the sample resulted in some of the highest Sm/Nd ratios ever obtained for pelitic garnet. In the case of G31(1) the two analyses show a spread in $^{147}Sm/^{144}Nd$ and reproducible ages. The variation in $^{147}Sm/^{144}Nd$ may be the result of trace-element zoning or from inclusions. The concordance of the two analyses indicates that, even if the variation results from inclusions, they were in equilibrium with the whole rock-garnet system. The older age from G96 is 37 ± 2 Ma whereas the age of garnet in G31(1) is 39.9 ± 1.4 Ma. These are in impressive agreement with concordant monazite inclusions from sample G90, from similar structural levels, whose Th-Pb age is 40.7 ± 1.3 Ma. In addition, the younger Sm-Nd age of 29 ± 3 Ma from G96 is the same as the single concordant matrix monazite from G90 of 28 Ma..

In the case of G9 and 4B1 there is some disequilibrium between duplicate garnet

separates and the whole rock. However, a comparison of concentrations obtained for the high Sm/Nd ratio analyses (Grt 2 in G9 and Grt 1 in 4B1) with the *in-situ* analyses of REE concentrations obtained by LA-ICP-MS (Chapter 6) indicated that the bulk of Nd and Sm measured by ID in these analyses comes from the garnet lattice itself. The ages of these two separates are 24 ± 5 Ma and 22 ± 3 Ma for samples G9 and 4B1, respectively. These ages are distinctly younger than the monazite inclusion ages from sample G57 (41-36 Ma), from similar structural levels. However, the discordia defined by the four matrix monazites in this sample yields an age of 22.5 ± 1.6 Ma, identical to the garnet Sm-Nd ages.

In summary, the ages from all three isotopic systems employed here - U-Th-Pb, Sm-Nd and Rb-Sr - require conditions of high temperature mineral growth and resetting in the period 42-28 Ma in the upper levels of the HHCS and from 41-22 Ma at lower levels. The issue now is the interpretation of mineral ages.

Recent experimental measurements of the diffusion rate of Sm and Nd in garnet (Ganguly et al., 1998a) have shown that the diffusion rate of these elements is very similar to those of Fe and Mg (Ganguly et al., 1998b). In this case the Sm-Nd ages for samples G9 and G31(1), which both preserve strong major-element zoning, must represent garnet growth. In both these cases electron microprobe analyses show that the garnet used for dating comes from near the rim of the garnet (Figure 4.3a and b). However, in samples which have undergone substantial diffusional homogenisation of their prograde major-element zoning the interpretation is more difficult - 4B1 and G96.

The effect of diffusional homogenisation for any given element in garnet will depend upon the diffusion rates and the chemical potential gradients within and outside the garnet. If the garnet remains a closed system, i.e. no chemical potential gradients exist between garnet and its surrounding, only intra-crystalline diffusion occurs and the older core ages will mix only with the younger rim ages. If complete homogenisation occurs

in this way the age obtained will represent the average of the growth age. If, on the other hand, the garnet has exchanged with the surrounding rock by inter-crystalline diffusion the age obtained will relate to the closure temperature of the garnet Sm-Nd system.

The preservation of similar age variations across G96 for both the Rb-Sr and Sm-Nd system suggests that either these too are growth ages or that the diffusion rate of Sm, Nd, Rb and Sr are very similar in garnet. The available diffusion data do suggest that the diffusion rates of Sr and Nd in garnet are rather similar at 600-800°C (Coghlan, 1990; Ganguly et al., 1998a). Given, the observation that the major elements in G96 do not show any significant zonation, it is possible that the isotopic data from this sample date closure during cooling. However, the temperature recorded by the mineral compositions is 600-660°C. Calculation of the closure temperature for both Sm-Nd and Fe-Mg in garnet (Dodson, 1973) suggests that cooling rates need to be much slower than 1°C $Ma^{-1}$ for such a temperature to be recorded. While this is incompatible with the minimum *average* cooling rates for the upper-HHCS of ~25°C $Ma^{-1}$ between 28 and 16 it may suggest that G96 underwent a period of slow cooling after growth and before more rapid cooling at a later stage. Alternatively, it implies that there is a decoupling of the Sm-Nd and Fe-Mg systems whereby Fe and Mg exchange with the surrounding rock, resulting in closure at ~630°C, while Sm-Nd do not exchange preserving growth, or average growth, ages. However similar ages are obtained from monazites in sample G90 and garnet in sample G96 - samples which come from within 500m of each other. Concordant monazite inclusion ages from sample G90 and the core estimate of G96 yield the same age as do concordant matrix monazite in G90 and the younger garnet age for G96. It, therefore, seems likely that the garnet ages are growth ages only with only limited Sm-Nd exchange with the matrix. There is also the further matter of sample selection for although G96 Grt 1 was biased towards the core there will have been some

contribution from rim portions while Grt 2 is likely to represent an additional averaging of the growth age, due to the more even sample selection. Thus garnet in sample G96 grew *at least* 37 Ma ago and continued until *at least* 29 Ma.

In the case of 4B1 the temperature recorded by the major elements is over 700°C while the Sm-Nd age is 22 Ma. Again a similar calculation to that performed above for G96 suggests that this age must lie somewhere between average growth age and a cooling age through >700°C.

The closure temperature for the U-Th-Pb system in monazite is thought to be around 700-750°C (Parrish, 1990), temperatures higher than any recorded by most of the rocks studied here though lower structural levels may have reached or exceeded this level as late as 22 Ma. In addition, however, Zhu et al. (1997) have concluded that monazites within garnet may not isotopically re-equilibrate at temperatures below 800°C because of the high postulated closure temperature for the U-Pb system in garnet (Mezger et al., 1992; Burton et al., 1995). In addition, these inclusions will not be available for mineral reaction after growth of the garnet around them. Given that the temperature for the garnet isograd lies at 450-600°C, significantly below the closure temperature of U-Th-Pb in monazite, the ages of monazite inclusions in garnet must date monazite growth. This is further supported by both the random distribution of ages within the garnet and the much younger ages obtained for garnet at similar structural levels - G9 and 4B1.

The matrix monazites, however, are invariably discordant and point towards younger ages than the inclusions. Because these grains are not shielded by garnet, they will be available for new growth, recrystallisation and isotopic re-equilibration after garnet growth. To distinguish between these three possibilities chemical analyses of monazites were obtained on the electronmicroprobe (Foster, In Prep.). These indicate that matrix monazites show significant chemical differences from those included within garnet (higher La/Y and lower $ThO_2/UO_2$ ratios ). This is interpreted to indicate that the the

matrix monazites underwent a further growth period after the monazites included within garnet.

Both the garnet Sm-Nd ages and the monazite ages from high structural levels within the HHCS of Garhwal indicate metamorphic mineral growth from 41 Ma terminating (at high temperatures) at 28 Ma. This overlaps with ages already obtained from middle structural levels in Zanskar to the west (33-27 Ma: Vance and Harris, 1999) but extends to older values. For lower structural levels nearer the MCT minerals record ages between 41 and 22 Ma which, while they overlap with those from Zanskar, extend to much younger values.

### 4.5.2 Collisional heat sources in the Himalaya

Previous studies of the thermal structure of orogenic belts based solely on pressure-temperature data have always suffered from the uncertainty that the apparent thermal gradients were not obtained synchronously (e.g. Hodges et al., 1988; England et al., 1992). Indeed thermal modelling of metamorphic belts suggests that they were unlikely to have been (England and Thompson, 1984). In the present case, however, the chronological data on monazite inclusions and garnet, in combination with the pressure-temperature constraints, provide a unique snapshot of the thermal structure of an orogen in the early stages of collision and metamorphism.

Continental collision between India and Asia occurred along the Indus Tsangpo Suture Zone, ~100 km to the north of the HHCS, and is believed to have been initiated in the Zanskar region at ~55 Ma and further to the east (e.g. Garwhal) at 50 Ma (Rowley, 1996). While ages for high-temperature processes ~20-25 Ma, as found here for the lower levels of the HHCS, are rather difficult to reconcile simply with collision at 50-55 Ma (England et al., 1992), ages for mineral growth of around 40-30 Ma are completely consistent with a thermal response to collision at 50-55 Ma (England and Thompson, 1984).

However, the garnets in Zanskar record burial at 40-35 Ma rather than 50-55 Ma (Vance and Mahar, 1998; Vance and Harris, 1999) which must have been in response to thrusts and nappes south of the main suture zone and active well after 50-55 Ma. This may also be the case for Garhwal but no constraint is as yet available on the pressure evolution in the period 40-35 Ma. However, in the Harsil formation in Garhwal minimum rim P-T estimates of 630 °C and 9.5 ± 1.2 kbar, from G96, indicate that near the end of garnet growth, at or after 29 Ma, the Harsil formation was buried to at least 30 km (lithostatic gradient of 27 MPa $km^{-1}$). This burial must have been caused by a cover belonging to the Tethyan Sedimentary Sequence (TSS) which at present lies to the north. Significant thickening of the TSS must have occurred because the restored thickness of the TSS is ~10 km (Searle, 1987), and this must have resulted from movement on thrusts lying structurally above and to the north of the present exposure.

Additionally, garnet growth in the small leucogranitic body from which sample G31(1) was derived occurred at 40 Ma. This observation implies that temperatures within the upper levels of the HHCS in Garhwal were sufficient to produce small melts at 40 Ma. Chapter 5 demonstrates that temperatures of formation for these small melt bodies were ~630°C and that these samples formed by vapour-present melting of the HHCS.

However, structurally below the leucogranite sample G31(1) in sample G57, monazites were growing from 41 Ma to 36 Ma and were subsequently included in garnet. It is difficult to apply a PT constraint to the growth of monazite, but in this case due to the methodology the temperature of garnet growth in G57 constrains the upper limit for the temperature of monazite growth. Unfortunately, the garnet in sample G57 has a homogenised major-element profile so that precise modelling of the pressure-temperature evolution during garnet growth is not possible. However, preliminary modelling of the mineral assemblage suggests that garnet isograd lies at <550°C (Figure 4.7). Alternatively, constraining temperatures for monazite growth in pelitic rocks,

estimates suggest that monazite growth occurs at ~525°C (Smith and Barreiro, 1990). Thus, sample G57 can only have been at temperatures of 500-550°C in the period 41-36 Ma, when the monazites grew.

It appears, then, that rocks close to sample G31(1) were at temperatures of ~630°C while temperatures of 500-550°C existed in sample G57 which is *presently* ~22 km structurally *beneath* G31(1) – assuming no major lateral variations. Thus the temperatures recorded at 40 Ma across the presently exposed orogen suggest an inverted geothermal gradient. This has since been overprinted by later thermal equilibration to produce the near isothermal profile recorded by rocks in the Garhwal Himalaya HHCS and elsewhere (see Chapter 3).

One possible explanation for the profile is that the exposed rocks have been tectonically emplaced at their present structural levels. Thus the upper-levels of the HHCS could have attained temperatures of >630°C while the lower parts of the HHCS were at shallower levels and further to the south. Subsequent thrust emplacement would have juxtaposed nappes which were in distinctly different parts of the orogen at 40 Ma. Furthermore, since G31(1) lies within the HHCS, this would imply that the thrust must also lie *within* the presently exposed HHCS of Garhwal.

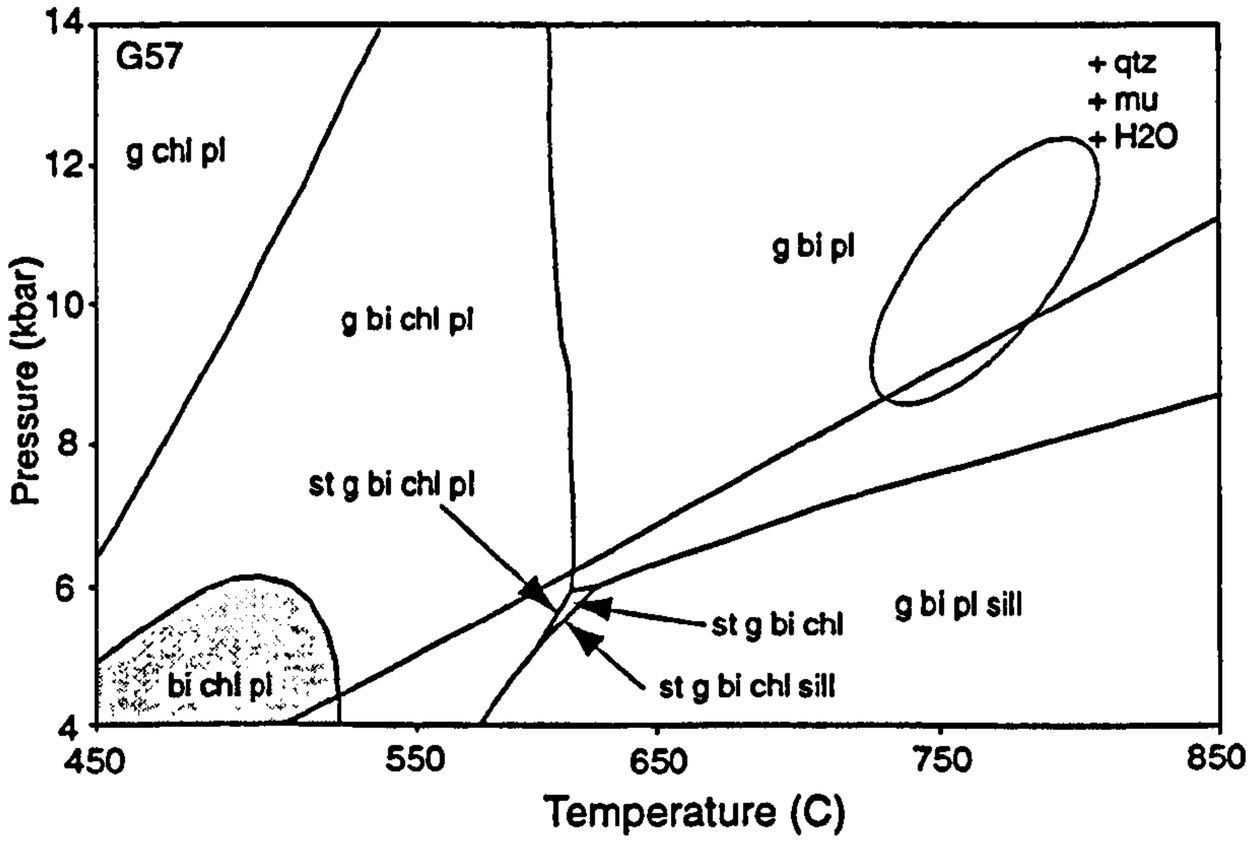


*Figure 4.7 Pseudosection for sample G57 showing the phase boundaries. Of particular interest here is the position of the garnet-in isograd at ~550°C. Garnet absent field is shaded grey. Rim PT estimate is shown by ellipse*

There are, however, alternative explanations. The thermal profile could result from

thrust emplacement close to 40 Ma and would represent a snapshot of a sawtooth geotherm produced as result of the rapid emplacement of hot crust over cooler crust (England and Thompson, 1984). One-dimensional thermal modelling suggests that following instantaneous overthrusting an inverted thermal structure can persist for periods of about 5 Ma (Molnar et al., 1983; England and Thompson, 1984). In this model G31(1) would lie in the hangingwall of the thrust, or very close to it, and G57 within the footwall. Interest has tended to focus on such sawtooth geotherms as a possible mechanism to explain inverted metamorphism in the footwall to the MCT. However, if sawtooth geotherms are attainable in the crust this model can only work if the shortening that led to the inverted geotherm occurred after 45 Ma and, given the size of the inversion, much closer to 40 Ma. This model, then, would predict the shortening that led to the inverted gradient to have occurred within the HHCS after initial collision at around 40 Ma - as appears to have occurred in Zanskar further west. However, 2-D numerical modelling using geologically feasible parameters shows that such temperature inversion is not produced (Grasemann, 1993).

One final possibility is that the small crustal melts, represented by G31(1), formed by anomalous heat sources in the crust, including; shear heating, advection of heat by intrusions or locally high concentrations of radiogenic heat-producing elements. There is no field evidence for the last two of these possibilities as mafic intrusions are very limited in volume and are probably related to the pre-Himalayan history of the HHCS and there is no lithological variation that could produce locally high-heat production. Shear heating, however, cannot be unequivocally ruled out because, although it is difficult to maintain high shear stresses in the presence of a melt, the localised nature of these melts and their small volume mean that only limited heating is required. Evidence for such shear heating is, unfortunately, likely to be overwritten due to later re-crystallisation during subsequent metamorphism and, although there are no clear

tectonic breaks in the HHCS in Garhwal, it is pervasively deformed by varying amounts of top-to-the-south shear. This model would also imply that thrusting occurred close to G31(1) at 40 Ma.

All three possible explanations for temperatures of >630°C in the upper-HHCS whilst temperatures <550°C existed in the basal-HHCS imply that thrusting occurred close to G31(1) - within the HHCS - and that it occurred at or after 40 Ma. This means that rocks structurally above G31(1) underwent burial and significant metamorphism prior to 40 Ma and, as a corollary, that PT constraints obtained from them cannot be used in any obvious way to constrain thermal models relating to later tectonic events such as the widespread anatexis at 24-17 Ma. Furthermore, models which assume that the isothermal to inverted temperature profile across the HHCS in Garhwal, and potentially elsewhere in the Himalaya, records a snapshot of the crust are inappropriate (e.g. Hodges et al., 1988). Indeed, the isothermal profiles probably result from the combination of thermal conditions in the crust attained at both different times and positions during the orogen, which, without chronological information combined with temperature constraints, would have been invisible.

### 4.5.3 Crustal melting and the pre-exhumation thermal structure

One of the outstanding problems in Himalayan geology is the process resulting in the formation of the large leucogranite intrusions presently exposed at the top of the HHCS and formed at 24-17 Ma. Early one-dimensional modelling suggested that insufficient heat would remain in the crust at ~23 Ma if instantaneous thickening occurred at 50 Ma (England et al., 1992) and many of the models for the formation of the leucogranites have therefore been linked to the necessity for additional heat sources. Furthermore, debate has concentrated on the causal relationship between movement on the principal structures – the MCT and STDS - and anatexis. For example, local heat sources may have been augmented by shear heating on the Main Central Thrust - active at ~ 22 Ma

(Hubbard and Harrison, 1989). Alternatively, melting may have occurred by decompression melting caused by rapid extensional movement on the STDS – a model which requires high temperatures prior to fault movement (e.g. >680°C at ~5 kbar) and rapid decompression (Harris and Massey, 1994).

There is a growing recognition that the migmatites often found at the top of the HHCS are not the source for the larger leucogranite melts (see Chapter 5 and Brouand et al., 1990; Inger and Harris, 1993; Barbey et al., 1996). Indeed, in Garhwal, the leucogranite laccoliths can be seen to be fed from the HHCS below the Harsil formation (Searle et al., 1993; Scaillet et al., 1995; Searle et al., Subm.). Furthermore, the evidence presented here suggests that at the time of anatexis (~23 Ma) only the basal-HHCS was still at temperatures approaching those required for anatexis. It seems likely, therefore, that the source for the High Himalayan Leucogranites is in the basal-HHCS of Garhwal for which the youngest ages and highest temperatures are obtained.

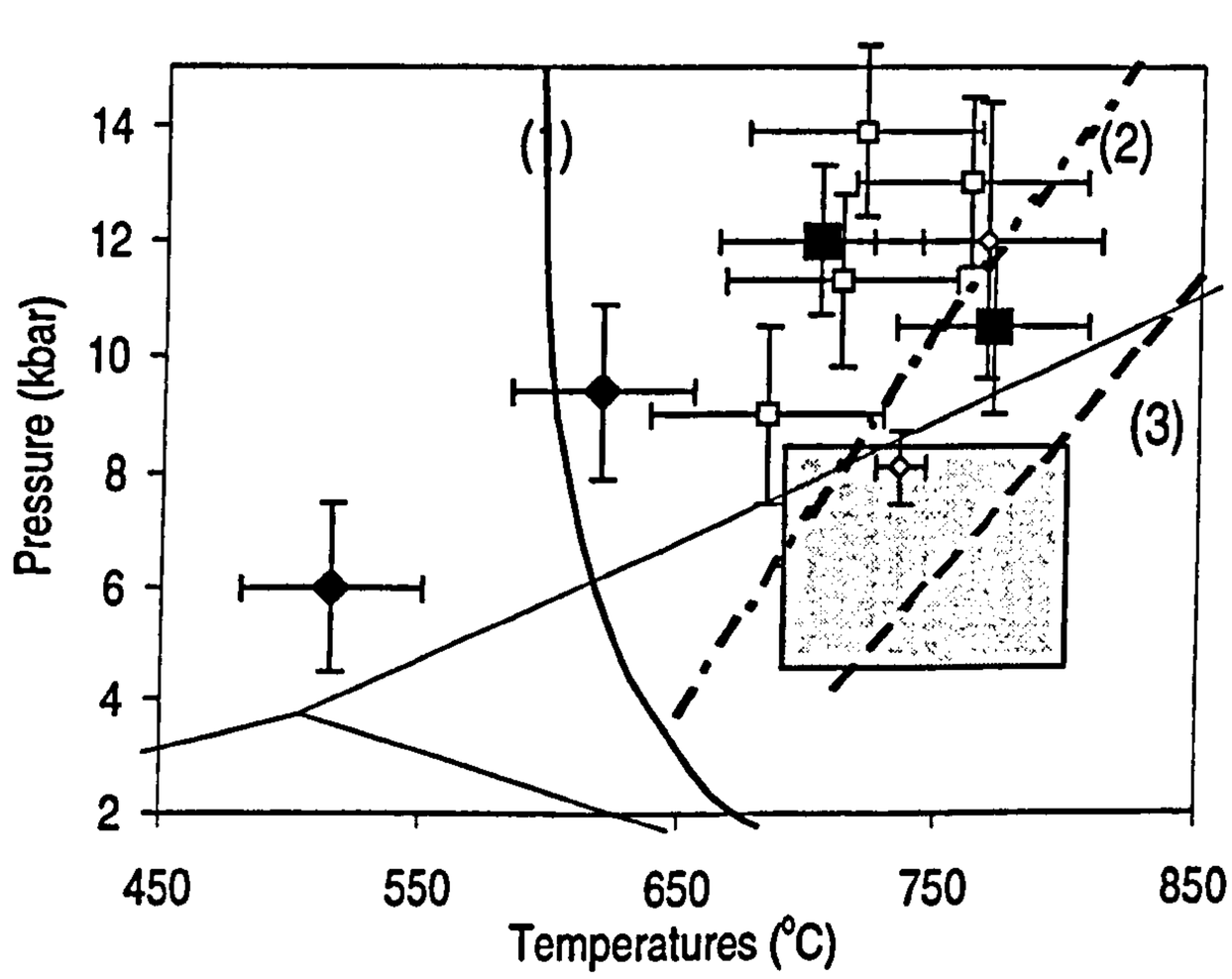


*Figure 4.8 PT estimates for rocks of the basal-HHCS with appropriate melting solidi. Solid line (1) represents the wet-melting solidus of Le Breton and Thompson (1988). Dashed line (2) represents muscovite-melting solidus of Petö (1976). Dashed line (3) represents the high-temperature dehydration-melting solidus for a kyanite-zone metapelite from the HHCS of Langtang, Nepal (Patino Douce and Harris, 1998). Sample G9 (filled diamonds) Sample G57 and 4B(1) (filled squares). Other data from the basal-HHCS of the Alaknanda valley (open squares see Chapter 3) and from Metcalfe (1993) (open diamonds). Grey box represents approximate melt production field for the HHL*

Unfortunately, because no constraints from the homogenised garnet in 4B1 or from the monazite in G57 are available on the thermobarometric *evolution,* these data tell us nothing about how these rocks achieved these temperatures - whether by local heating (eg. shear heating) at 22 Ma or simply by heating in response to burial. However, there are a number of observations that suggest that there is no requirement for additional shear heating on the MCT. Firstly, sample G9, ~10 km above the MCT, was still undergoing heating at 24 Ma, implying that the basal HHCS was still continuing to heat in response to burial at this time. Secondly, this observation is consistent with the data from Zanskar, further west along the orogen, where a complete PT path has been extracted from garnet and shows that garnets there were still recording heating in response to burial at about 27 Ma. This, in addition to the theoretical difficulty of maintaining significant shear stresses in the presence of a melt, suggest that shear heating is neither necessary nor viable.

The leucogranites in the Harsil formation are known to have been intruded in an extensional regime (Scaillet et al., 1995) suggesting that the STDS was active at the time of intrusion. It appears likely that in Garhwal, as for other parts of the orogen, the HHCS was exhumed during movement on the MCT and tectonic denudation by the STDS (Hodges et al., 1992). Vance et al., (1998a) showed that in Zanskar the thermal effect of tectonic denudation by movement on the STDS was delayed by some 3-5 Ma at distance from the normal fault, although the decompression effect was likely to be felt instantaneously. Thus rocks denuded by the STDS are likely to have undergone rapid decompression but the thermal response is likely to have been delayed. However, if movement on the MCT occurred synchronously with movement on the STDS this would tend to cool the basal-HHCS. These two competing effects cannot be constrained here but, numerical modelling suggests that the isotherms in the region of a thrust in a convergent orogen will be brought closer together - resulting in near-isothermal

decompression for rocks brought up along the thrust (Jamieson et al., 1998).

Whether the basal-HHCS could have been the source for the High Himalayan Leucogranites can be qualitatively explored by comparing temperatures recorded by the basal-HHCS with the principal melt-forming reactions. The temperatures attained in the basal part of the HHCS in Garhwal are plotted on Figure 4.8 (mineral data presented in Chapter 3 and Appendix E. Two PT estimates for the HHCS of the Bhagirathi from Metcalfe, 1993). In response to tectonic denudation by the STDS, rocks which were at similar temperatures to those presented in Figure 4.8 could easily pass through the muscovite-dehydration reaction and into the melt field by decompression as envisaged by Harris and Massey (1994).

## 4.6 Conclusions

From the data discussed above, it is clear that the thermal models which suggest that orogen wide thermal re-equilibration would have finished and cooling began prior to anatexis at 20-25 Ma – thus requiring additional heat sources for melting - are inappropriate. The basic assumption of these models is that crustal thickening occurs very quickly at 50 Ma and then stops. This is clearly not the case in the Himalaya. Early collision is thought to have occurred at ~55-50 Ma, with the formation of eclogites to the west and structurally to the north (de Sigoyer et al., 1999). In Zanskar and Garhwal the upper- to mid- HHCS responded to burial by 41 Ma - some 15 Ma after initial collision (Vance and Harris 1999). Additionally, the heating recorded by G9, at lower structural levels within the HHCS at around 24 Ma must imply burial shortly before this time. Finally, the locus of deformation was transferred to the MCT at 22 Ma (Hubbard and Harrison 1989) and later to the MBT ~6 Ma (MacFarlane, 1993). All these observations are consistent with the idea of a foreland-propagating thrust system in the Himalaya (Searle, 1987). The net effect of this process is to lengthen the time period during which the crust remains hot as more and more heat is moved into a relatively

narrow orogenic belt. Such a process may ultimately be responsible for the longevity of high temperatures in the Himalaya and crustal melting at 20-25 Ma.

Perhaps most importantly for the study of orogenesis elsewhere is that, in the Himalaya in the period from collision at ~55-50 Ma to the present, there has been a continual tectonic reorganisation of heat-producing material within the orogen on timescales of ~10-15 Ma. Thus techniques which cannot constrain thermobarometric variations on these timescales are unlikely to illuminate even the first-order tectonic controls in orogens. Indeed, without PTt constraints even in very young mountain belts tectonic features – such as the intra-HHCS thrusting presented here – may be overlooked.

# Chapter 5 - Vapour-present melting in the Himalaya: a common feature of orogenesis?

## *5.1 Introduction*

Granite production from crustal protoliths can occur either under vapour-present melting or during mica-dehydration reactions (e.g. Le Breton and Thompson, 1988). However, the high solubility of water in granite magmas means that the melt volumes formed by vapour-present melting will be limited by the availability of a large volumes of a vapour phase. Additionally, the positive dP/dT slope of the vapour-present melt reaction means that melts formed in this way will crystallise before rising significantly in the crust. For these reasons vapour-present melting is not considered important in the generation of large volumes of granites that have segregated from their source regions (Clemens and Vielzeuf, 1987).

However, the production of water during prograde metamorphism means that a free fluid phase may be available in the early stages of orogeny and it might be expected that they will result in limited partial melting of crustal rocks. In this chapter geochemical and chronometric data are reported from a small group of crustally-derived melts that indicate vapour-presenting melting in the Himalayan orogen did occur and that it significantly predated the well documented High Himalayan Leucogranites formed under fluid-absent conditions.

## *5.2 The Vaikrita Group of Garhwal Himalaya*

The geological setting of the rocks dealt with in this chapter are detailed in Chapter 2. However, a few relevant details are repeated here. The Vaikrita Group of the Garhwal Himalaya display many of the principal characteristics of the HHCS exposed elsewhere in the orogen (Hodges and Silverberg, 1988; Metcalfe, 1993). The Vaikrita Group is bounded to the south by the Vaikrita thrust which has been correlated with the MCT of

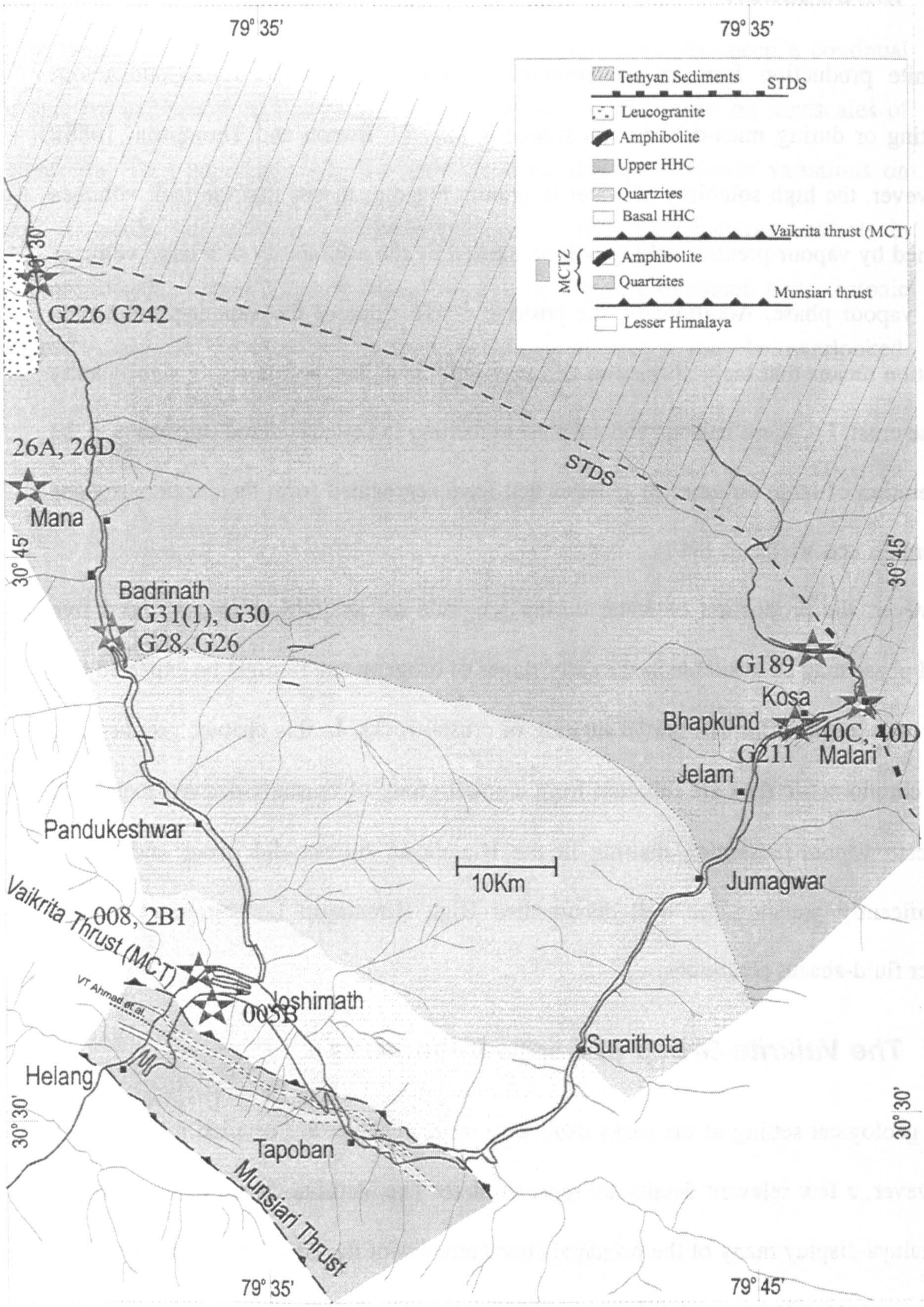


*Figure 5.1 Geological map showing the principal lithotectonic divisions in the Alaknanda valley (modified from Virdi, 1986). Sample localities shown with a diamond (Green, deformed granites; Red, undeformed granites; purple, HHCS metamorphic rocks). The Alaknanda valley is separated into the basal-, middle- and upper-HHCS the boundaries between which are in the shown in grey.*

Nepal (Valdiya, 1980; Ahmad et al., In press). Below the Vaikrita thrust lies Main Central Thrust Zone which is bounded by the Munsiari thrust to the south (Metcalfe, 1993). As for other sections of the HHCS, the Vaikrita Group is bound to the north by the STDS which varies from a brittle fault in the east to a more ductile fault system in the Bhagirathi valley in the west (Scaillet et al., 1995; Searle et al., Subm.).

The HHCS in the Alaknanda valley can conveniently be separated into three units: the basal-, mid- and upper-HHCS (Figure 5.1, after Virdi (1986)). The basal-HHCS consist of kyanite-grade gneisses which grade into the mid-HHCS, dominated by quartzites. The upper-HHCS comprises schists, calc-silicates, gneisses, quartzites and, towards the upper most sections, increasing volumes of leucogranite melts culminating in large intrusions in the Arwa valley. To the north of the Arwa valley the low-grade metasediments have been identified as the Tethyan Sedimentary Series (Heim and Gansser, 1939).

PTt histories for metapelitic assemblages of the Garhwal Himalaya have been explored using Sm-Nd garnet chronometry and *in-situ* U-Th-Pb monazite dating (Chapter 4). The results show that garnet growth was initiated by ~37 Ma and continued up to at least ~29 Ma during burial and heating, similar to PTt paths derived from garnets in Zanskar (Vance and Mahar, 1998; Vance and Harris, 1999). Furthermore, these studies indicate that at the time of anatexis (~22 Ma) the highest temperatures were attained in the basal-HHCS.

The leucogranite samples presented here form two groups that can be distinguished in the field. Decimetre-sized, deformed leucogranites intrude the metasedimentary sequence and samples are restricted to the base of the upper-HHCS in the Alaknanda valley (Figure 5.1). They are comprised of quartz, K-feldspar, plagioclase, tourmaline and garnet and are often folded with the axial planes parallel to the main foliation in the metasediments. Sillimanite needles form aggregates in veins which cross-cut both

garnet and tourmaline in the leucogranites and are aligned with the fabric in the surrounding rock. Sillimanite shows variable retrogression by unoriented muscovite. The second group of granites, principally from the Alaknanda (Figure 5.1), lie further up section and are generally undeformed and form metre-wide dykes either parallel to, or cross cutting the foliation in the metasediments. They are comprised of quartz, K-feldspar, plagioclase, muscovite, biotite, tourmaline and garnet in varying quantities and represent the well characterised early-Miocene melting event which produced the larger intrusions in the Garhwal region such as the Gangotri laccoliths and the other High Himalayan Leucogranites across the orogen (e.g. Scaillet et al., 1990; Harrison et al., 1999).

This chapter contrasts the chronology and geochemistry of these two granite types and specifically discusses the origin of the early leucogranites which have gone unnoticed in the voluminous literature on Himalayan granites.

## *5.3 Analytical Techniques*

Whole-rock major- and trace-element analyses were obtained on an ARL Fisons wavelength dispersive XRF spectrometer at the Open University. Major-elements were determined on glass discs prepared by fusing powdered sample with Spectroflux 105. Trace elements were determined from pressed powder pellets. One-sigma analytical precision for trace-element data (Rb, Sr, Y, Zr, Nb, Ba, Pb) is 2% relative for concentrations >100 ppm and better than 10% relative for concentrations <100 ppm.

Whole-rock REE, Th and U concentrations were measured by instrumental neutron activation analysis (INAA) of powdered samples at the Open University. One sigma analytical precision on INAA data is 5% relative for concentrations <0.5 ppm and better than 3% relative for concentrations >0.5 ppm.

For chronometric studies a single, whole, garnet crystal was separated from the sample, crushed and an optically pure aliquot obtained by hand picking in propanol under an

optical microscope. Chemical dissolution, separation and mass spectrometric techniques are similar to those described in Cohen et al. (1988) except for the departures detailed in Appendix C.

## 5.4 Geochemistry of Deformed leucogranites

The deformed leucogranites of the Vaikrita Group sampled here contrast strongly, not only in field characteristics, but also in their geochemistry with the undeformed leucogranites. The latter group may be correlated with the Early Miocene (24-17 Ma) High Himalayan leucogranites that are amongst the most intensely studied granites in the world (see review in Harrison et al., 1998). These intrusions occur across the Himalayan orogen, emplaced as sheets and sills into high-grade and weakly metamorphosed metasediments (Le Fort et al., 1987). The youngest, and most representative phase of these intrusions is a strongly peraluminous muscovite, tourmaline leucogranite with garnet phenocrysts sometimes present. The major-element abundances and modal mineralogy of Himalayan leucogranites indicate minimum-melt compositions formed at pressures of 500-1000 MPa (5-10 kbar) (Inger and Harris, 1993). Their isotope geochemistry (Sr, Nd and Pb) is strongly indicative of a metasedimentary source (Gariépy et al., 1985; Deniel et al., 1987), confirmed more recently by experimental melting studies of kyanite-grade metasedimentary rocks from the Langtang section of the High Himalaya (Patino Douce and Harris, 1998).

The deformed granites have remained poorly studied but, the $^{87}Sr/^{86}Sr$ and $\varepsilon_{Nd}$ for G31(1) of 0.764 and –15 respectively (calculated at 40 Ma) lie within the range of values for the HHCS (see Ahmad et al., In press), indicative of a crustal origin and consistent with a source in HHCS. Additionally the deformed leucogranites fall within the $^{87}Sr/^{86}Sr$ and $\varepsilon_{Nd}$ range of the more voluminous Miocene leucogranites ($\varepsilon_{Nd}$ –13 to –15, $^{87}Sr/^{86}Sr$ 0.777-0.747; Scaillet, (1990); Stern et al., (1989), and, thus, are

*Himalaya.*

| | Undeformed leucogranites | | | | | | | | | | Deformed leucogranites | | | | Pelites | | | | | | | |
|---|---|---|---|---|---|---|---|---|---|---|---|---|---|---|---|---|---|---|---|---|---|---|
| **Sample** | **G242** | **G226** | **G75** | **G189** | **G74** | **17-97** | **26A-97** | **26D-97** | **40C-97** | **40D-97** | **G26** | **G28** | **G30** | **G31(1)** | **005b** | **008** | **035A** | **035C** | **2B(1)** | **G100** | **G211** | **Gangotri** |
| **Majors elements** | | | | | | | | | | | | | | | | | | | | | | |
| SiO2 | 73.88 | 74.64 | 74.39 | 74.59 | 73.22 | 74.02 | 74.40 | 73.98 | 73.65 | 74.32 | 77.27 | 75.16 | 75.79 | 75.89 | 70.74 | 60.73 | 75.01 | 70.17 | 70.68 | 73.02 | 73.49 | 73.01 |
| TiO2 | 0.10 | 0.05 | 0.06 | 0.09 | 0.07 | 0.06 | 0.04 | 0.11 | 0.09 | 0.06 | 0.06 | 0.10 | 0.06 | 0.05 | 0.75 | 0.70 | 0.67 | 0.74 | 0.69 | 0.58 | 0.69 | 0.07 |
| Al2O3 | 14.85 | 14.78 | 15.25 | 14.91 | 15.11 | 15.26 | 14.98 | 14.93 | 15.03 | 14.73 | 13.41 | 14.20 | 14.99 | 13.89 | 12.60 | 16.65 | 11.57 | 14.78 | 13.52 | 12.63 | 12.83 | 15.24 |
| Fe2O3 | 1.08 | 0.60 | 0.65 | 0.62 | 0.72 | 0.71 | 0.61 | 0.46 | 0.79 | 0.70 | 0.88 | 0.62 | 1.04 | 1.05 | 5.14 | 7.23 | 4.40 | 6.06 | 3.63 | 2.37 | 5.93 | 1.13 |
| MnO | 0.04 | 0.01 | 0.03 | 0.02 | 0.02 | 0.01 | 0.01 | 0.01 | 0.02 | 0.03 | 0.07 | 0.03 | 0.10 | 0.13 | 0.08 | 0.09 | 0.06 | 0.06 | 0.02 | 0.02 | 0.12 | 0.02 |
| MgO | 0.15 | 0.09 | 0.07 | 0.12 | 0.10 | 0.10 | 0.16 | 0.14 | 0.13 | 0.09 | 0.19 | 0.21 | 0.19 | 0.11 | 2.59 | 3.36 | 1.16 | 1.03 | 3.76 | 4.22 | 1.10 | 0.12 |
| CaO | 0.68 | 0.64 | 0.50 | 0.52 | 0.52 | 0.67 | 0.82 | 0.77 | 0.70 | 0.53 | 1.95 | 1.21 | 0.80 | 0.59 | 2.01 | 2.75 | 0.84 | 0.50 | 0.50 | 0.34 | 0.47 | 0.58 |
| Na2O | 4.06 | 4.07 | 5.00 | 1.89 | 4.23 | 4.03 | 4.54 | 2.94 | 4.17 | 4.31 | 3.90 | 3.21 | 2.36 | 2.09 | 2.83 | 3.95 | 1.44 | 0.91 | 3.37 | 3.34 | 0.69 | 4.31 |
| K2O | 4.10 | 4.67 | 3.61 | 5.52 | 4.49 | 4.46 | 4.35 | 5.64 | 4.47 | 3.97 | 1.94 | 4.02 | 3.92 | 4.98 | 2.17 | 2.68 | 3.17 | 4.02 | 2.05 | 2.11 | 3.85 | 4.56 |
| P2O5 | 0.17 | 0.13 | 0.19 | 0.15 | 0.19 | 0.09 | 0.06 | 0.15 | 0.16 | 0.17 | 0.06 | 0.09 | 0.10 | 0.10 | 0.17 | 0.18 | 0.11 | 0.08 | 0.14 | 0.11 | 0.04 | 0.25 |
| LOI | 0.82 | 0.50 | 0.60 | 1.12 | 0.55 | 0.63 | 0.42 | 0.76 | 0.63 | 0.71 | 0.86 | 0.66 | 0.51 | 0.43 | 0.52 | 1.05 | 1.05 | 1.76 | 0.91 | 1.04 | 1.12 | 0.71 |
| **Total** | 99.93 | 100.19 | 100.35 | 99.55 | 99.22 | 100.05 | 100.38 | 99.89 | 99.84 | 99.62 | 100.59 | 99.50 | 99.87 | 99.31 | 99.59 | 99.37 | 99.49 | 100.11 | 99.26 | 99.77 | 100.32 | 99.65 |
| Rb | 312 | 295 | 440 | 202 | 477 | 382 | 171 | 247 | 393 | 467 | 56 | 106 | 106 | 132 | 108 | 137 | 150 | 231 | 86 | 88 | 164 | 416 |
| Sr | 79 | 36 | 23 | 96 | 33 | 51 | 47 | 74 | 67 | 48 | 119 | 175 | 122 | 154 | 139 | 159 | 69 | 65 | 63 | 67 | 92 | 44 |
| Y | 15 | 9 | 12 | 29 | 11 | 7 | 24 | 18 | 9 | 9 | 4 | 11 | 6 | 6 | 30 | 30 | 26 | 37 | 26 | 14 | 34 | 13 |
| Zr | 44 | 31 | 31 | 40 | 33 | 38 | 26 | 25 | 40 | 30 | 14 | 11 | 22 | 19 | 216 | 123 | 257 | 247 | 192 | 185 | 216 | 35 |
| Nb | 16 | 9 | 23 | 11 | 20 | 13 | 1 | 11 | 13 | 13 | 1 | 2 | 1 | 1 | 14 | 14 | 15 | 18 | 10 | 10 | 13 | 13 |
| Ba | 177 | 127 | 62 | 273 | 103 | 151 | 126 | 229 | 178 | 95 | 264 | 799 | 755 | 1322 | 332 | 1038 | 701 | 628 | 297 | 330 | 849 | 128 |
| La | 9.60 | 5.30 | 8.40 | | 8.80 | 7.70 | 10.40 | 7.90 | 10.00 | 6.00 | 5.80 | 4.20 | 3.70 | 3.50 | | | | | | | | |
| Ce | 21.70 | 11.80 | 16.00 | 27.30 | 15.60 | 15.60 | 20.70 | 15.30 | 20.20 | 11.40 | 10.60 | 7.40 | 7.10 | 6.10 | | | | | | | | |
| Nd | 10.80 | 5.60 | 8.90 | 13.30 | 9.00 | 7.30 | 10.20 | 6.40 | 10.00 | 5.60 | 4.60 | 3.20 | 3.10 | 2.90 | | | | | | | | |
| Sm | 2.34 | 1.33 | 1.27 | | 1.26 | 1.70 | 2.19 | 1.60 | 2.39 | 1.30 | 0.82 | 0.73 | 0.71 | 0.59 | | | | | | | | |
| Eu | 0.40 | 0.28 | 0.20 | 0.61 | 0.26 | 0.37 | 0.30 | 0.56 | 0.46 | 0.25 | 0.93 | 1.31 | 1.10 | 1.38 | | | | | | | | |
| Tb | 0.54 | 0.33 | 0.35 | 0.81 | 0.33 | 0.33 | 0.63 | 0.45 | 0.42 | 0.34 | 0.12 | 0.20 | 0.14 | 0.11 | | | | | | | | |
| Yb | 1.39 | 0.74 | 0.84 | 3.98 | 0.70 | 0.40 | 2.29 | 1.41 | 0.55 | 0.68 | 1.57 | 1.09 | 1.75 | 2.07 | | | | | | | | |
| Lu | 0.20 | 0.09 | 0.10 | | 0.11 | 0.07 | 0.33 | 0.20 | 0.08 | 0.10 | 0.28 | 0.16 | 0.29 | 0.36 | | | | | | | | |
| Th | 4.61 | 3.41 | 3.60 | 5.55 | 3.50 | 4.63 | 6.62 | 4.84 | 4.86 | 2.47 | 1.89 | 1.40 | 1.37 | 1.16 | | | | | | | | |
| U | 12.80 | 6.30 | 20.90 | | 22.20 | 7.80 | 17.80 | 4.40 | 8.80 | 9.70 | 0.80 | 1.00 | 1.50 | 1.40 | | | | | | | | |
| Ta | 3.93 | 1.28 | 2.02 | 1.74 | 2.78 | 7.76 | 0.02 | 0.75 | 3.99 | 3.18 | 0.10 | 0.32 | 0.23 | 0.26 | | | | | | | | |
| Hf | 1.89 | 1.34 | 1.44 | 1.50 | 1.40 | 1.76 | 1.06 | 1.09 | 1.55 | 1.27 | 0.76 | 0.50 | 1.06 | 1.12 | | | | | | | | |
| $^{87}Sr/^{86}Sr$ | | | | | | | | | | | | | | 0.765893 | | | | | | | | |
| 2 sigma | | | | | | | | | | | | | | 0.000028 | | | | | | | | |
| $^{87}Rb/^{86}Sr$ | | | | | | | | | | | | | | 2.4969 | | | | | | | | |
| Sample at 40 Ma | | | | | | | | | | | | | | 0.764474 | | | | | | | | |
| $^{143}Nd/^{144}Nd$ | | | | | | | | | | | | | | 0.511855 | | | | | | | | |
| 2 sigma | | | | | | | | | | | | | | 0.000013 | | | | | | | | |
| $^{147}Sm/^{144}Nd$ | | | | | | | | | | | | | | 0.1345 | | | | | | | | |
| eNd | | | | | | | | | | | | | | -15 | | | | | | | | |

indistinguishable from them isotopically.

The major-element compositions of the deformed granites (Table 5.1) are somewhat variable, ranging from granitic to trondhjemitic (G26). Interestingly trondhjemitic compositions have been obtained from melting micaceous protoliths, but only in the presence of a free-fluid phase (Patino Douce and Harris, 1998). Compared with the Miocene leucogranites the compositions of the deformed granites are generally more ferric (with higher concentrations of Fe, Mn, Mg) and have higher Ca/(Na+K) ratios, indicative of a larger melt fraction. The high silica abundances in sample G66 (>77%) is indicative of either fluid activity (pegmatites are commonly enriched in silica above the expected minimum-melt abundances) or of entrained quartz from the protolith.

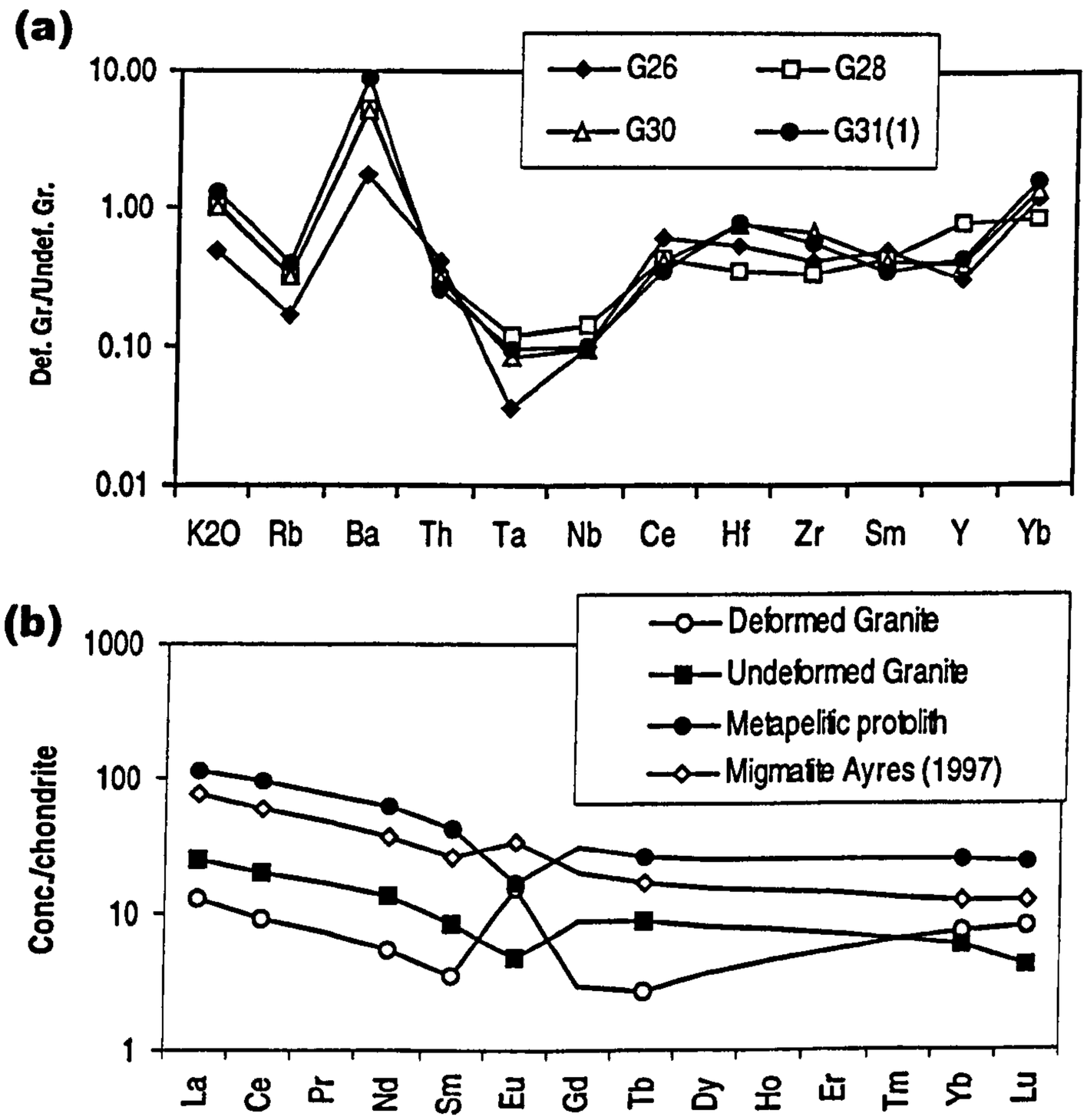


*Figure 5.2 (a) Spidergram for the trace-element composition of deformed leucogranites normalised against average composition for undeformed leucogranites taken from samples presented in Table 5.1. (b) Chondrite normalised REE plot for measured values of both deformed and undeformed leucogranites and metapelites. Migmatite from Zanskar (Ayres, 1997)*

Trace-element abundances also provide strong contrasts with the later leucogranites. Depletions in HFS elements like Zr, Y and LREE in the deformed leucogranites can be attributed to lower melt temperatures resulting in lower solubilities of accessory phases in the melt such as monazite, apatite and xenotime (Ayres and Harris, 1997). The deformed leucogranites are characterised by rather flat chondrite-normalised REE profiles except for the marked positive Eu anomaly (Figure 5.2b). In this respect they contrast strongly with the large negative Eu anomaly of the younger leucogranites. The lower Rb/Sr ratios of the deformed granites are indicative of higher melt fractions, assuming both granites are derived from similar sources. The increase in Ba concentrations in the deformed leucogranites relative to the young leucogranites indicates that the restite contained little, if any, potassic phases like alkali feldspar or biotite. Alternatively the very high Ba concentrations in one deformed leucogranite (G31) may indicate Ba mobility by fluids: a feature associated with crustal melting which has been documented by other Himalayan studies (Weinberg and Searle, 1999).

## *5.5 Discussion: Origin of the deformed leucogranites*

At the lowest temperatures at which melting is possible (<650 °C), fluid phase-present melting results in high melt fractions (25-40% depending on the modal composition of the protolith). With increasing temperatures, fluid-absent muscovite melting, followed by fluid-absent biotite melting become possible, each reaction imposing characteristic Rb, Sr, Ba concentrations on the melt (Harris et al., 1995). A preliminary estimate for the solidus temperature can be obtained from the solubility of zircon and of monazite in the melt, obtained from Zr and LREE concentrations using the calibrations of Harrison and Watson (1983), and Montel (1993) respectively. For the deformed leucogranites, temperatures of 630-640°C are obtained from both thermometers, about 100°C lower than those of typical Himalayan leucogranites (Ayres and Harris, 1997). Bearing in mind these are probably maximum temperature estimates due to the possibility of

inheritance, such low temperatures preclude dehydration melting of biotite as a possible origin.

In determining the petrogenesis of granitic rocks only the behaviour of those trace elements that are predominantly sited in major phases can be modelled from appropriate partition coefficients (Harris et al., 1995). Stoichiometric coefficients for balanced melt reactions under both fluid-present and fluid-absent conditions have been determined from: (i) microprobe analyses of muscovite, biotite, and feldspar compositions from a typical pelitic schist and; (ii) the major-element composition of an average deformed leucogranite (Table 5.2).

*Table 5.2 Modal compositions of granite, metapelites with modelled restite*

| | Undeformed granite | Deformed granite | Average pelite | Restite (fluid present) | Resitite (fluid absent) |
|---|---|---|---|---|---|
| Quartz | 33 | 43 | 49 | 69 | 56 |
| Alkali-Feldspar | 22 | 18 | 0 | 0 | 9 |
| Plagioclase | 33 | 25 | 10 | 1 | 9 |
| Muscovite | 6 | 12 | 20 | 0 | 0 |
| Biotite | 0 | 2 | 10 | 16 | 11 |
| Garnet | 1 | 0 | 5 | 8 | 6 |
| Tourmaline | 5 | 0 | 5 | 0 | 0 |
| Kyanite | 0 | 0 | 1 | 7 | 9 |
| $C_l/C_o$ (Rb) | | | | 0.9-1.2 | 1.2-2.0 |
| $C_l/C_o$ (Sr) | | | | 1.0-2.0 | 0.2-0.6 |

In the presence of a fluid phase, a schist that contained no alkali feldspar would generate melts via the reaction

$$Mu + 0.60Q + 0.47Pl + 0.13V = 1.95L + 0.15Sill \qquad (1)$$

assuming a pre-crystallisation $H_2O$ content of 10% in the melt (Holtz and Johannes, 1991). Coefficients are given in mass units. A melt fraction of ~0.39 will result (limited by the exhaustion of muscovite, which virtually coincides with that of plagioclase for a

typical pelite assemblage). However the precise proportions of muscovite and plagioclase that react under conditions of fluid flushing depend on temperature and pressure (Patino Douce and Harris, 1998). Moreover, although the Mg component of reactant muscovite is sufficient to generate the concentration of Mg in the melt such that no significant biotite contribution is required, it is probable that a small proportion of biotite would break down as is observed under some experimental conditions (Holtz and Johannes, 1991).

Under fluid phase-absent conditions the stoichiometric coefficients of the balanced equations depend on the melt fraction obtained. If modelled from the melt fractions obtained experimentally by Patino Douce and Harris, (1998) a melt fraction of 0.12 results from a modal abundance of 20% muscovite in the source and a pre-crystallisation $H_2O$ content of 6% in the melt (Holtz and Johannes, 1991). This results in the reaction

$$Mu + 0.23Q + 0.10Pl = 0.6L + 0.33Ksp + 0.38Sill. \qquad (2)$$

As for fluid phase-present melting, biotite is not essential to balance the Fe, Mg concentration in the Himalayan granite, although minor quantities of biotite have been identified as a product in experimental melting of Himalayan pelites (Patino Douce and Harris, 1998). Reactions 1 and 2 provide reactions that are generally consistent with both mass balance and experimental constraints.

These two reactions will have strongly contrasting effects on the Rb, Sr and Ba concentrations in the melt. Under equilibrium conditions it is possible to derive the modal composition of the restite by mass-balance calculations, and to apply the appropriate partition coefficients to predict the trace-element partitioning between melt and source. For this study the partition coefficients of Blundy and Wood (1991) and Nash and Crecraft (1985) have been used for melts of leucogranite composition and

have assumed melting occurred by continuous removal and collection of the melt (Harris et al., 1993).

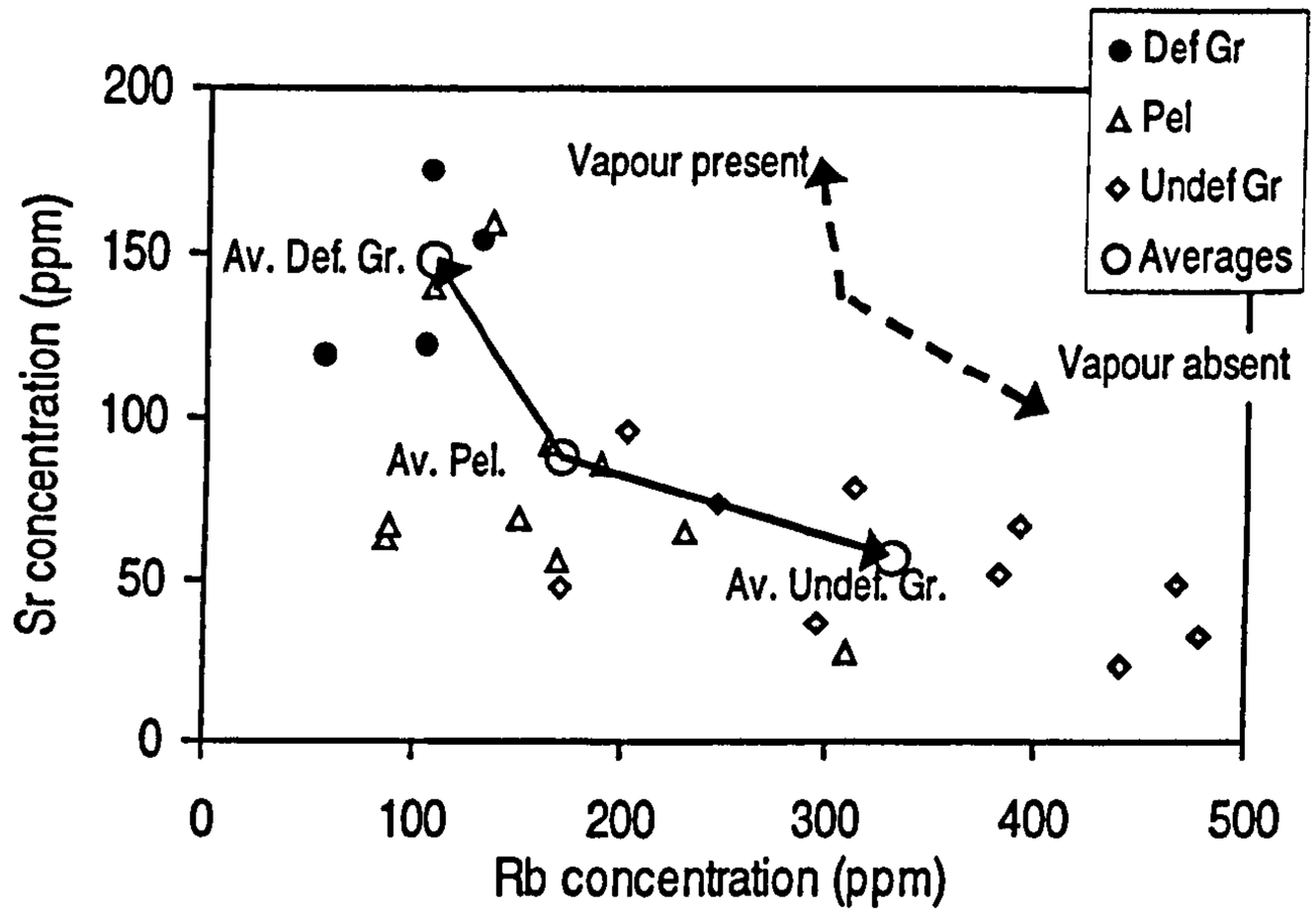


*Figure 5.3 Rb, Sr diagram showing the range of values corresponding to undeformed granites (grey diamonds), deformed granites (filled circles) and pelites from the HHCS (open diamonds). Vectors for the variation from average pelite (Av. Pel. - open circle) to average deformed granite (Av. Def. Gr.- open circle) and average undeformed granite (Av. Undef. Gr. .- open circle) are shown as black arrows. Modelled vectors corresponding to vapour-present and vapour-absent melting as discussed in the text are shown as dashed arrows.*

The calculated restite compositions and trace element distribution between melt and source ($C_l/C_o$) are given in Table 5.2. The variation in $C_l/C_o$ is due to the possible range of protolith compositions, principally the range of muscovite and plagioclase abundances in different pelites. Despite the range of Rb and Sr in the analysed pelites (Figure 5.3) it is clear that the deformed granites have slight depletion of Rb and strong enrichment in Sr relative to their source; $C_l/C_o=1$ and $C_l/C_o>1$ for Rb and Sr respectively are characteristic of fluid phase-present melting where high melt fractions depletes the restite in feldspar (see model vectors in Figure 5.3). In contrast fluid-absent melting results in $C_l/C_o>1$ for Rb and $C_l/C_o<<1$ for Sr due to the high modal proportions of feldspar in the restite. The trace-element data, therefore, suggest an origin of fluid phase-absent melting for the younger leucogranites as has been proposed for the large Himalayan leucogranite bodies in previous studies (Harris et al., 1995) and fluid phase-

present melting for the deformed leucogranites. Strong Ba depletion in the melt relative to source is predicted by both models, unless biotite is absent from the restite, but in that case strong Rb enrichment would also result in the melt. The highly variable Ba concentrations in both source and melt might suggest that Ba was particularly mobile during anatexis.

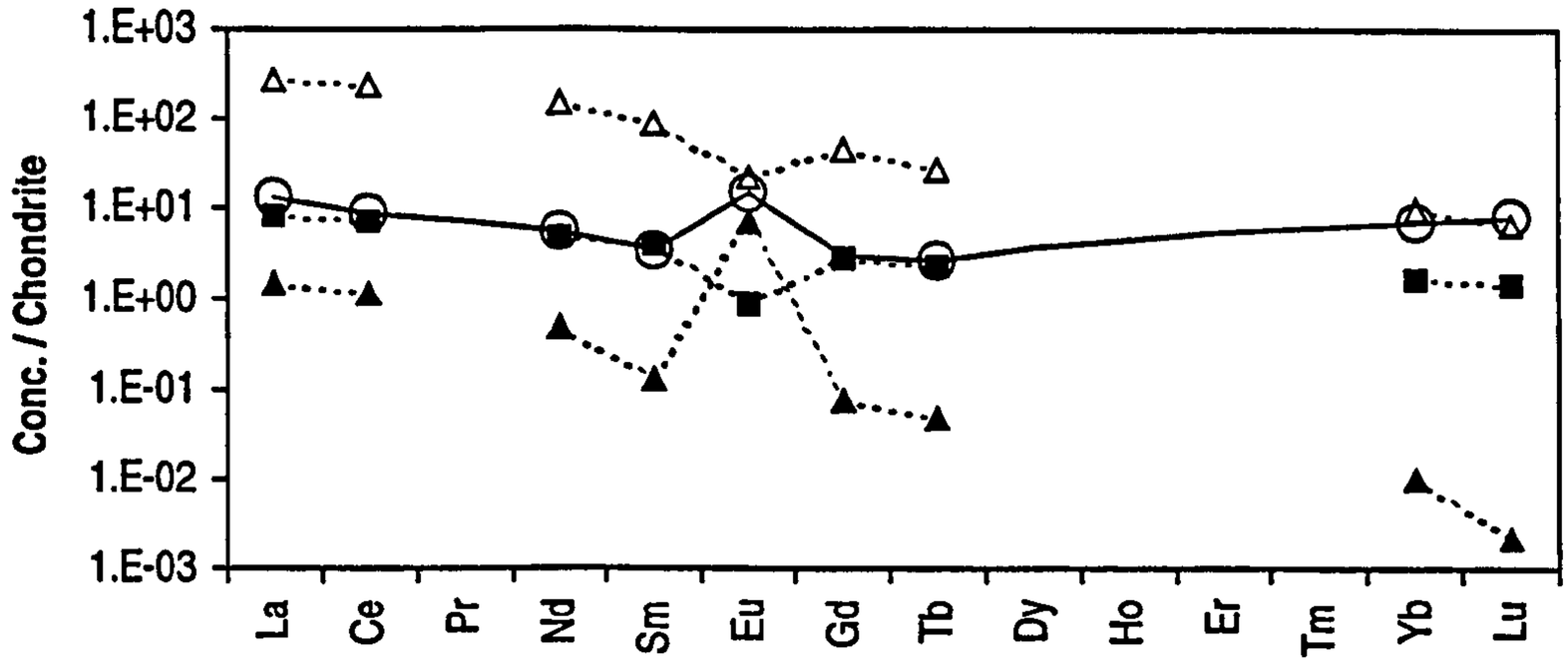


*Figure 5.4 Chondrite normalised REE plot for modelled REE element patterns compared to the measured deformed leucogranite composition (open circles). Modelled results are; open diamonds assuming equilibrium melting of major phases, solid squares from assuming dissolution of accessory phases, solid triangles from assuming disequilibrium melting of accessory phases.*

REE behaviour in granitic systems may be treated in two contrasting ways. If it is assumed that REE in the melt are determined by equilibrium partitioning between melt and restite (Hanson, 1978), as in the above treatment of Rb and Sr, large LREE abundances and a negative Eu anomaly are predicted (Figure 5.4); the high LREE/HREE ratio results entirely from assuming equilibrium of HREE between garnet and melt. As has been observed in previous studies such an approach is unlikely to be successful both because the REE are controlled primarily by accessory phase dissolution and also because temperatures are too low for equilibrium partitioning to be achieved, particularly for garnet-bearing assemblages (Harris et al., 1995).

An alternative approach is to model the dissolution of key accessory phases using the appropriate solubility equation for each phase (Ayres and Harris, 1997). By inferring the

zircon, monazite and apatite contributions from the abundances of Zr, Th and P respectively in the granite, and assuming accessory phase compositions for these phases given in Table 2 of Ayres and Harris (1997), the resulting REE profile may be compared with the observed REE profile of the granites (Figure 5.4). Although the LREE fit closely with the observed values (these are contributed almost entirely from monazite dissolution) there is poor correlation of the HREE, and the predicted negative Eu anomaly, which reflects the negative anomaly of the source rock, is at variance with the observed positive anomaly. Whilst the HREE can be ascribed to variable HREE/LREE in the accessory phases in the Garhwal protoliths, the positive Eu anomaly is more difficult to account for.

When a melt forms under disequilibrium conditions the trace element budget in the reactant phases is transferred directly to the melt. For the vapour phase-present reaction (equation 1) the contributing phases are muscovite and plagioclase. The resulting REE profile from disequilibrium melting (Figure 5.4) has a strong positive Eu anomaly derived from the reacting plagioclase. However for the remaining REE their concentrations are much lower than are observed in the granite.

The high Rb/Sr ratios for the undeformed granites of (~6) is consistent with fluid-phase absent melting from a source with ~20% muscovite and 10% plagioclase (Harris et al., 1993), as has been used to model the melting reaction (Table 2). However the decrease in Rb/Sr from metapelite to deformed granite (from an average of 2.0 to ~0.7) is not easily explained by equilibrium melting, but may result from disequilibrium melting where the Sr in the source is sited overwhelmingly in plagioclase which is consumed by the melt reaction; in contrast the Rb in the source is only partially sited in muscovite (the bulk lying in biotite, unaffected by the reaction). A Rb/Sr in the melt of ~0.6 is predicted by disequilibrium melting of muscovite, plagioclase and quartz (Harris et al., 1993). Some chemical disequilibrium under the low solidus temperatures suggested

here is highly probable; for T<650°C, Sr would be expected to take >1 Ma to equilibrate across a 1 mm plagioclase crystal according to the diffusion parameters of Giletti and Casserly (1994). Under conditions of fluid influx temperature oversteps may occur such that melt formation and extraction are both rapid processes, occurring within a few thousand years (Rubie and Brearley, 1990; Harris et al., In press). It is proposed that both accessory phase dissolution and disequilibrium melting of muscovite and plagioclase occurred concurrently resulting in the observed REE profile. Such a process will be favoured by (i) low melt temperatures leading to sluggish diffusion of Eu between melt and restite and (ii) conditions of fluid influx to source rocks above minimum melt temperatures (Rubie and Brearley, 1990).

## 5.6 Time constraints on deformed leucogranites

Garnet in sample G31(1) was separated in order to carry out a chronometric study of the deformed leucogranites. Garnets in G31(1) are typically ≤5 mm across and show smooth zoning in the major elements with high Mn concentrations ($Alm_{66-71}$, $Py_{9-13}$, $Grs_{0-4}$ and $Sps_{13-24}$; Figure 5.5). Inclusions of tourmaline, quartz and small oriented rutile needles - absent from the rim of the garnet - have been identified and the garnet exhibits optical oscillatory zoning. The high Mn concentration, optical oscillatory zoning and rutile exsolution confirm its igneous

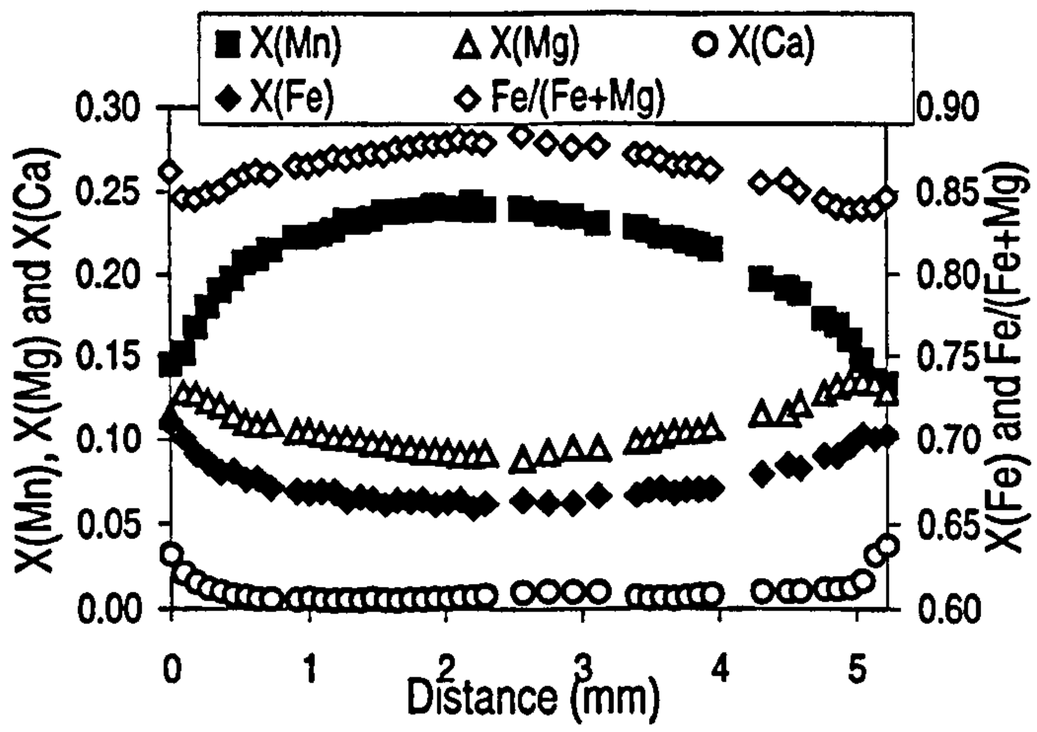


*Figure 5.5 Major-element composition of garnet in sample G31(1) measured by electron-microprobe recalculated as mole fractions. Also shown is the Fe/Fe+Mg ratio. Linear rim-rim traverse.*

origin.

A fraction of the aliquot used for the chronometric study was mounted for electron microprobe analysis and a comparison of the major-element composition to the garnet traverse established that the garnet used for isotopic analysis was predominantly from within the rim of the garnet (Figure 5.5).

Two isotopic analyses of garnet from G31(1) and two whole-rock analyses were obtained and are presented in Table 5.3. The two whole-rock analyses yield slightly different ages when taken with the two garnet analyses (39.9±1.4 Ma, MSWD=1.6 and 38.6±1.4 Ma, MSWD=2.1 for whole rock 1 and 2 respectively). Both ages are within error of each other and the isochron yielding the lowest MSWD is shown in Figure 5.6. The preservation of smooth zoning in the garnet supports the interpretation that this age is the growth age of the rim of the garnet and given the duplication and relatively high $^{147}Sm/^{144}Nd$ ratios, this inference is considered to be robust.

*Table 5.3 Summary of Sm-Nd TIMS ID and isotope ratio analyses.*

| G31(1) | *Nd (ppm)* | *Sm (ppm)* | *Sm/Nd* | $^{147}Sm/^{144}Nd$ [1] | $^{143}Nd/^{144}Nd$ [2] |
|---|---|---|---|---|---|
| Grt 1 | 0.237 | 1.252 | 5.285 | 3.1949 | 0.512657 (25) |
| Grt 2 | 0.055 | 0.219 | 3.945 | 2.3847 | 0.512401 (66) |
| WR 1 | 1.5237 | 0.3390 | 0.222 | 0.1345 | 0.511855 (13) |
| WR 2 | 1.5980 | 0.3541 | 0.222 | 0.1339 | 0.511880 (10) |

*[1] All errors 0.5% except G31(1) Grt2 (1.5%) and CZG-23 Grt1 (1.2%). [2] Replicate measurements (n=40) of the La Jolla Nd Standard gave 0.511853±0.000008 ($2\sigma_m$) over the period that these analyses were performed.*

## 5.7 Discussion

The geochemical data and modelling presented above indicate that the small deformed leucogranites found in the upper-HHCS of Garhwal formed during vapour-present melting of the crust. The positive Eu anomaly and REE thermometry suggests that the

melting occurred under disequilibrium conditions at temperatures of <650°C. This conclusion, taken together with chronometry on garnet from sample G31(1), indicate that temperatures above the vapour-present solidus were attained within the HHCS by ~40 Ma. Although these melts are apparently limited in extent their identification has important implications for the prograde evolution of the orogen.

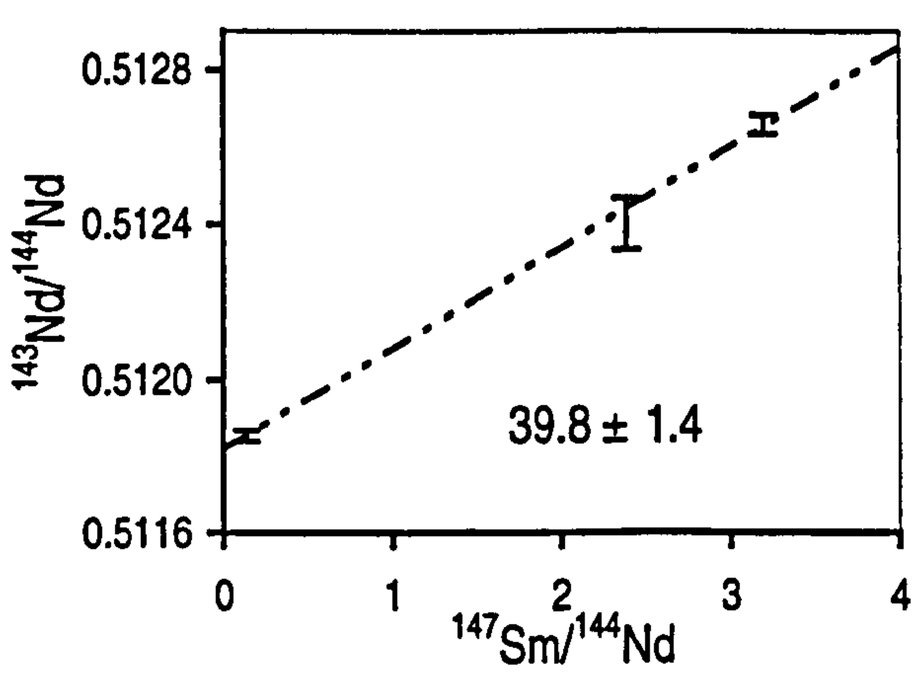


*Figure 5.6 Isochron for both garnet analyses and whole rock 1.*

The melts that formed the deformed leucogranites are likely to have been fluid saturated and, therefore, were generated along a solidus with negative slope (Figure 5.7) and thus would not have been able to ascend far before crystallising. Since, the Sr and Nd isotopes are consistent with extraction from within the HHCS, it is probable that the source region for these melts lies close to their emplacement position and, hence, within the upper-HHCS.

The most likely source for these early leucogranites is, therefore, the anatectic migmatites exposed in the upper levels of the HHCS. There are several lines of evidence that support this conclusion and that also imply a different source for the younger and more voluminous Miocene leucogranites. Firstly, in a study of the migmatites from the HHCS of Nepal, Barbey et al. (1996) and Brouand et al. (1990) identified low-Zr tonalitic leucosomes with positive Eu anomalies and low Rb/Sr ratios that are ascribed to either metamorphic differentiation or disequilibrium melting. These leucosomes have strong geochemical similarities with the deformed leucogranites in this study. Secondly monazite dating of migmatites from the Annapurna and Marsyandi sections yield ages of ~35 Ma (Godin et al., 1999) and a >34 Ma component (Coleman,

1998) respectively. This may be interpreted as the age of an early melting event resulting from vapour-present anatexis during the development of the orogenic wedge. The *in-situ* migmatites and small melts such as those in this study were subsequently intruded by the main Miocene anatectic event derived from deeper crustal levels. Thirdly Sr-isotopic evidence from the Langtang section of the HHCS of central Nepal indicates a strong contrast between the migmatites and underlying kyanite schists, with the Miocene leucogranites correlating not with the migmatites they intrude but with the deeper lithologies in the HHCS (Inger and Harris, 1993; Harris and Massey, 1994). Finally in the Gangotri valley, Garhwal, dykes feed the Miocene leucogranite laccoliths that intrude the Harsil formation from the HHCS below (Searle et al., 1993; Scaillet et al., 1995) suggesting that the source for these younger granites lies within the lower sections of the HHCS.

The proportion of $H_2O$ required in the protolith is about 11-17% for fluid-saturated melts to form at pressures of 5-10 kbars (Johannes and Holtz, 1990). During prograde metamorphism, fluids resulting from subsolidus dehydration reactions may migrate to low-strain zones allowing localised melting at structurally controlled sites. Fluid ingress could be facilitated by channalised advection along active shear zones (Butler et al., 1997) and could be sourced from heating of a cold underthrust slab during crustal thickening (Le Fort, 1975).

Once melting is initiated the magma is unlikely to remain fluid saturated during prograde conditions due to the high solubility of $H_2O$ in siliceous melts. The melt fraction will then be undersaturated in $H_2O$ , buffered by the available $H_2O$ in the system whilst $a_{H20}$ falls below unity. If temperatures increase above the muscovite dehydration reaction $a_{H20}$ is buffered at ~0.8 (Harris et al., 1995) and the modal proportion of mica in the protoliths will thereafter determine the melt fraction (Patino Douce and Johnston, 1991).

Crystallisation of the early-formed melt during prograde metamorphism will only be possible if the melt escapes from its source, rising to shallower crustal levels or if the protolith is exhumed. At present it is not clear whether this portion of the Himalaya was being exhumed but in Zanskar the HHCS were undergoing burial at ~40 Ma (Vance and Harris, 1999). For fluid-saturated melts that fail to escape from their source (e.g. migmatite leucosomes) crystallisation is only possible when the rock cools below the wet-melting solidus. In the Himalaya the important point to note here is that partially molten migmatites could persist over timescales >10 Ma (from 40-25 Ma). This has several far-reaching implications: (i) accessory phases within the leucosomes will retain some younger crystallisation ages as well as ages corresponding to the formation of the melts, this could account for some of the variability in monazite and zircon ages in the HHCS from ~35 Ma (Godin et al., 1999) to ~20 Ma (Noble and Searle, 1995; Coleman, 1998); (ii) the preservation of melts for periods >10 Ma at high temperatures will overprint many of the chemical signatures associated with their early formation masking their origin; (iii) the persistence of such melts will have a dramatic effect on the rheology of the crustal material during ongoing tectonics. Specifically they may reduce the shear stress in high-strain zones and initiate

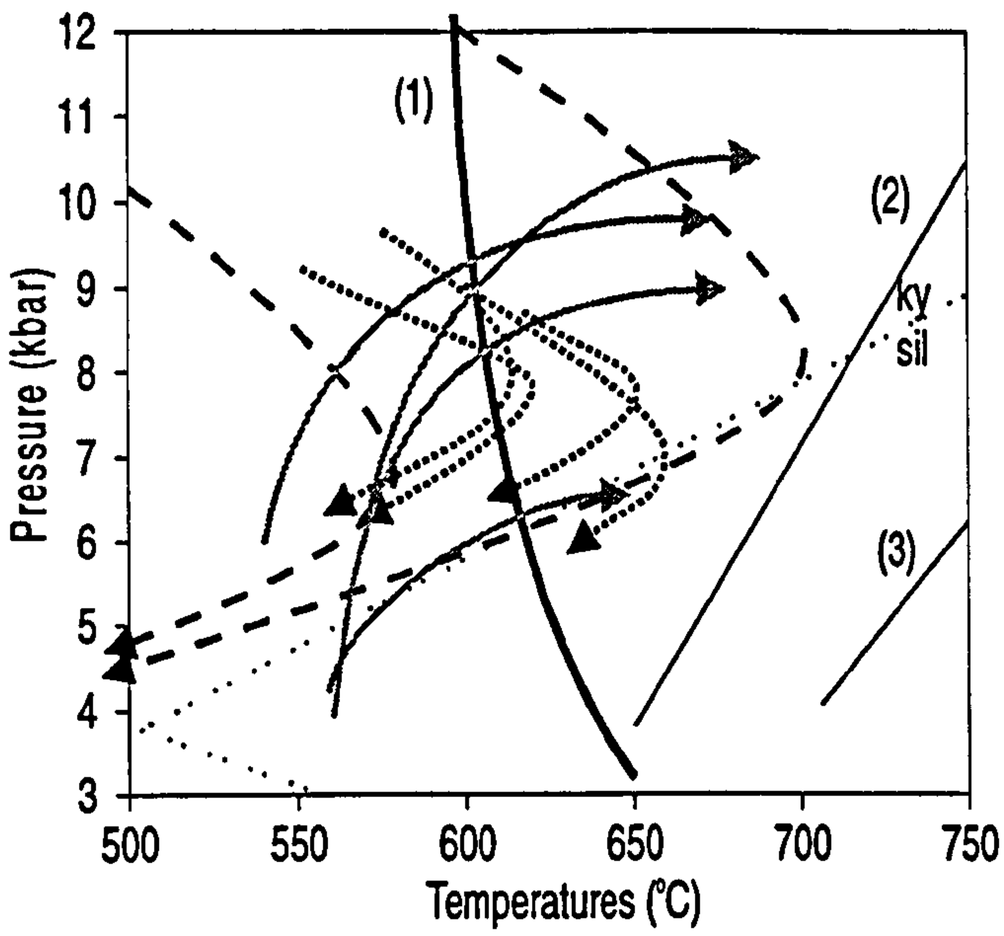


*Figure 5.7 PT paths followed from the Zanskar Himalaya (Vance and Harris, 1999), Wopmay orogen (St. Ongé, 1987) and Fleur de Lys Supergroup (Jamieson, 1990). Solid line (1) represents the wet-melting solidus of Le Breton and Thompson, (1988). Dashed blue line (2) represents muscovite-melting solidus of Petö (1976). Dashed line (3) represents the high-temperature dehydration-melting solidus for a kyanite-zone metapelite from the HHCS of Langtang, Nepal (Patino Douce and Harris, 1998).*

exhumation through wedge tectonics (Dahlen, 1984; Platt 1993)

These considerations are not restricted to the Himalaya and the identification of prograde fluid-saturated melts has broader implications for orogenic studies. The prograde PT paths of assemblages from a wide range of orogenic belts cross the vapour-present melting solidus (Figure 5.7), implying that anatexis would occur in rocks of pelitic or greywacke composition provided a free fluid phase were available.

Thus the apparent absence of prograde melting in many orogenic belts may result not only from the very restricted distribution of an aqueous fluid, but also from the fact that unless these melts escape from their protoliths they will persist as magma in the crustal pile and record young crystallisation ages similar to those of magmas formed by dehydration melting during, or shortly following, peak metamorphism. However, the data presented here indicates that melts formed along the prograde path by vapour-present melting will have a distinct geochemical signature that is likely to be shared with the migmatites of their source regions. Now that this has been recognised in the Himalaya it may prove easier to identify similar early melting events in other orogens.

# Chapter 6 - Comparison of laser ablation ICP-MS and isotope dilution REE analyses - implications for Sm-Nd garnet geochronology

## *6.1 Introduction*

Garnet is a participant in many thermobarometrically well-defined mineral equilibria and has, therefore, long been used by metamorphic petrologists to determine pressure and temperature conditions during metamorphism (e.g. Spear 1993 and references therein). More recently, because garnet fractionates parent/daughter ratios for several isotopic decay systems dating of garnets has proved possible for the age determination of metamorphic and igneous events (Christensen et al., 1989; Mezger et al., 1989; Vance and O'Nions, 1990; Burton and O'Nions, 1991; Thöni and Jagoutz, 1992; Vance and O'Nions, 1992; Getty et al., 1993; von Quadt and Gebauer, 1993; Hensen and Zhou, 1995; Thöni and Miller, 1996; Yamamoto and Nakamura, 1996; Duchene et al., 1997; Mork et al., 1997; Stowell and Goldberg, 1997; Vance and Harris, 1999). However, garnet contains very small absolute amounts of the trace elements involved (ppm-ppb levels) and it has generally been recognised that geochronology with garnet is particularly susceptible to contamination by small amounts of Nd-, Sr- and Pb-rich accessory minerals such as zircon, monazite and allanite (Vance and O'Nions, 1992; DeWolf et al., 1996; Vance et al., 1998b). The extent to which inclusions contribute to the U-Pb, Sm-Nd, Rb-Sr and Lu-Hf budget within an analysis thus has important implications for the interpretation of age data obtained from garnets.

Garnets commonly contain small inclusions of accessory minerals (down to a size of 5 microns or less: e.g. Figure 6.1), which often prove impossible to identify visually and hence to separate mechanically from garnet for conventional isotope ratio and isotope dilution (ID) analysis. Various methods have been developed to identify inclusions in, or eliminate them from, a garnet ID analysis. DeWolf et al. (1996) have used induced

fission-track mapping to demonstrate that U contents of some almandine-pyrope garnets are very low (<0.5ppb) and that small inclusions dominate the U-Pb budget of the studied garnets. Vance et al. (1998b), in a step-leaching study, reached the same conclusion for almandine-rich garnets from the Himalaya. On the other hand, DeWolf et al. (1996) showed that an andradite-grossular garnet had lattice U concentrations similar to those measured by ID analysis. In addition, other step-leaching studies (Frei et al., 1995; Frei et al., 1997; Schaller et al., 1997) have concluded that garnet lattices do contain significant amounts of radiogenic Pb, though no abundance data are available from these studies.

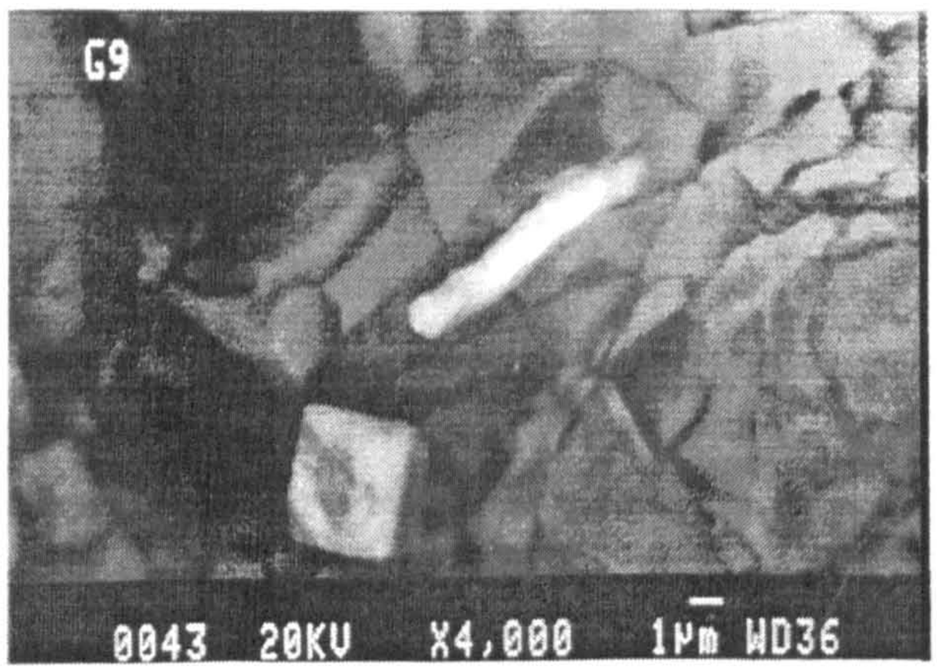


*Figure 6.1 SEM photo. Inclusions of monazite (elongate) and zircon (square) in sample G9 up to 8 microns in length.*

The step-leaching approach is likely to chemically fractionate different elements so that parent/daughter ratios are not extractable. For Pb this is not a problem because Pb has three radiogenic isotopes which are not expected to be fractionated during the chemical leaching process. Two of these, $^{207}Pb$ and $^{206}Pb$, define the age of a sample without the need for parent-daughter ratio determination (Frei et al., 1995; Frei et al., 1997; Schaller et al., 1997). Unfortunately for the Sm-Nd system precise REE abundances are essential so that a step leaching approach would be less useful. In general, concentrations of Sm and Nd are expected to be very low in garnet while the Sm/Nd ratio is expected to be high. In contrast, inclusions of phases such as monazite and allanite have very high REE concentrations but low Sm/Nd ratios. Therefore, one approach to determining the contribution of inclusions to garnet isotopic studies is to compare concentrations and Sm/Nd ratios obtained by conventional isotope-dilution and isotope-ratio analysis with

those obtained from *in-situ* analyses that demonstrably sample the garnet lattice. The techniques available include secondary ion mass spectrometry (SIMS) and laser ablation inductively-coupled mass spectrometry (LA-ICP-MS). Previous studies using the ion microprobe (Hickmott et al., 1987; Hickmott and Spear, 1992; Sisson and Bacon, 1992; Sevigny, 1993; Schwandt et al., 1996) and LA-ICP-MS (Fedorowich et al., 1995; Bea, 1996; Bea et al., 1997) have confirmed the low concentrations of Sm and Nd for pelitic garnets up to upper-amphibolite grade.

Previous *in-situ* studies of REE have been performed for petrogenetic purposes. In order to asses the effect of inclusions on chronological data an approach is required that combines conventional isotopic analysis with *in-situ* measurements of Sm and Nd concentrations. In chapter presents the results of the first such study for the Sm-Nd isotopic system. LA-ICP-MS has been used to obtain *in-situ* REE concentration profiles across three garnets from the High Himalayan Crystallines (HHC) of the Garhwal Himalaya and one garnet from the Bohemian Massif, along with data on separates of the Bohemian Massif garnets. Isotopic data for the Garhwal samples have been presented in Chapter 4. The combined datasets allow an assessment of the potential effect of Sm-Nd rich inclusions on conventional garnet Sm-Nd data.

## 6.2 Experimental techniques

### 6.2.1 Laser ablation ICP-MS

Experiments were carried out with an excimer laser system at ETH Zurich (193 nm, ArF, ETH Zürich Günther et al., 1997) linked to an ELAN 6000 ICP-MS (Perkin Elmer, Norwalk, USA). The output energy was set to 160 mJ allowing a pulse energy of 2.4 mJ for an 80 μm pit and a repetition rate of 10 Hz. The carrier gas flow flushing the ablation cell was 1.2 l/min helium mixed with 0.84 l/min argon behind the ablation cell (Günther and Heinrich, in prep.).

The principal advantage of LA-ICP-MS for this study is its high spatial resolution and consequent facility for avoiding small inclusions or, conversely, to analyse small fluid inclusions. Garnet samples were mounted as for normal electron microprobe analysis so that surface inclusions larger than 10μm across could be identified, using an optical microscope and video camera prior to analysis and hence avoided. The pit size was generally 20-60μm across so that garnet without inclusions could be analysed. Laser pits have a finite depth and hence inclusions may be encountered beneath the surface during ablation. This problem can be eliminated by monitoring the signal in time slices so that any extreme departures from the background concentrations in the garnet can be easily identified.

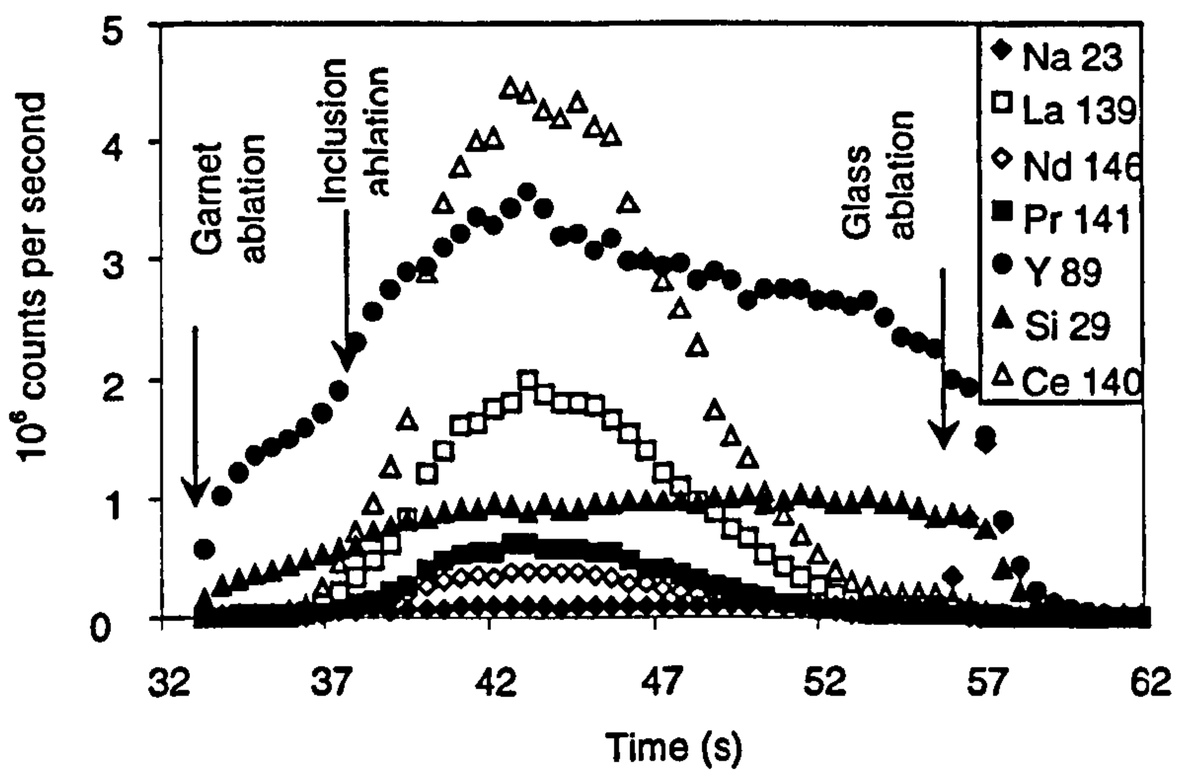


*Figure 6.2 Time resolved LA-ICP-MS analysis of garnet G9 on a spot where an inclusion was encountered during ablation. The Si signal, representing ablation of the garnet, is initially associated with low REE concentrations which rapidly increase upon ablation of an inclusion. Ablation of the glass mount is marked by an increase in the Na signal.*

The time evolution of the signal for a pit where an inclusion was encountered (Figure 6.2) indicates that after 37 seconds of analysis, the initial weak LREE signals increase dramatically. The rapid change and the relative proportions of the LREE suggests the ablation of a LREE-enriched inclusion such as allanite. Near the end of the ablation sequence, at 56 seconds, the Na signal increases marking the ablation of the glass mount used. This is a particularly extreme example but illustrates the response of the system to inclusions, indeed, the laser system has been designed to allow the analyses of small fluid inclusions of 5-10 μm and extremely small

ablation-related transient signals can be observed due to the small transport time between ablation and analysis (0.3 seconds).

The total measurement time for each analysis spot was 90 seconds, split into 30 seconds gas blank acquisition and 60 seconds data acquisition for the sample resulting in a penetration rate of ~ 0.5 $\mu ms^{-1}$. NIST 612 glass was used as an external calibration standard and $SiO_2$ was used for internal normalisation. The concentrations obtained were considered meaningful when they were twice the limit of dectection (LOD); example's of which are presented in Appendix G for an 80 µm and 10 µm pit analysing the REEs, U, Ti , V, Cr, Rb, Sr, Y, Zr and Ba as well as Si, Fe, Mg, Ca and Mn. The data reduction procedure of Longerich et al. (1996) was used. The results were screened for inclusion effects (e.g. Figure 6.2) to produce REE concentration analyses in profiles across the garnets.

### 6.2.2 Isotope dilution

Impure garnet separates were obtained by either crushing single crystals or by bulk separation techniques (see sample description below for specific details). The samples were then purified by hand-picking under a binocular microscope to obtain an optically pure separate of 10-50 mg. Samples were washed and transferred into PFA screw-cap beakers and spiked with a mixed $^{149}Sm/^{150}Sm$ tracer. Further details of the techniques are given in Cohen et al. (1988) and Appendix C.

## *6.3 Sample description*

Samples G96, G31 (1) and G9 are representative of the metamorphic core of the Himalayan orogen in the Garhwal region of India.

The bulk of the garnet in G96, only partly visible at the base of Figure 6.3a, has a sieve texture with inclusions of quartz, feldspar, biotite and zircons. An electron microprobe traverse of the gem quality portion of a single garnet shows that Fe, Mg and Ca have flat

PAGE

NUMBERING

AS ORIGINAL

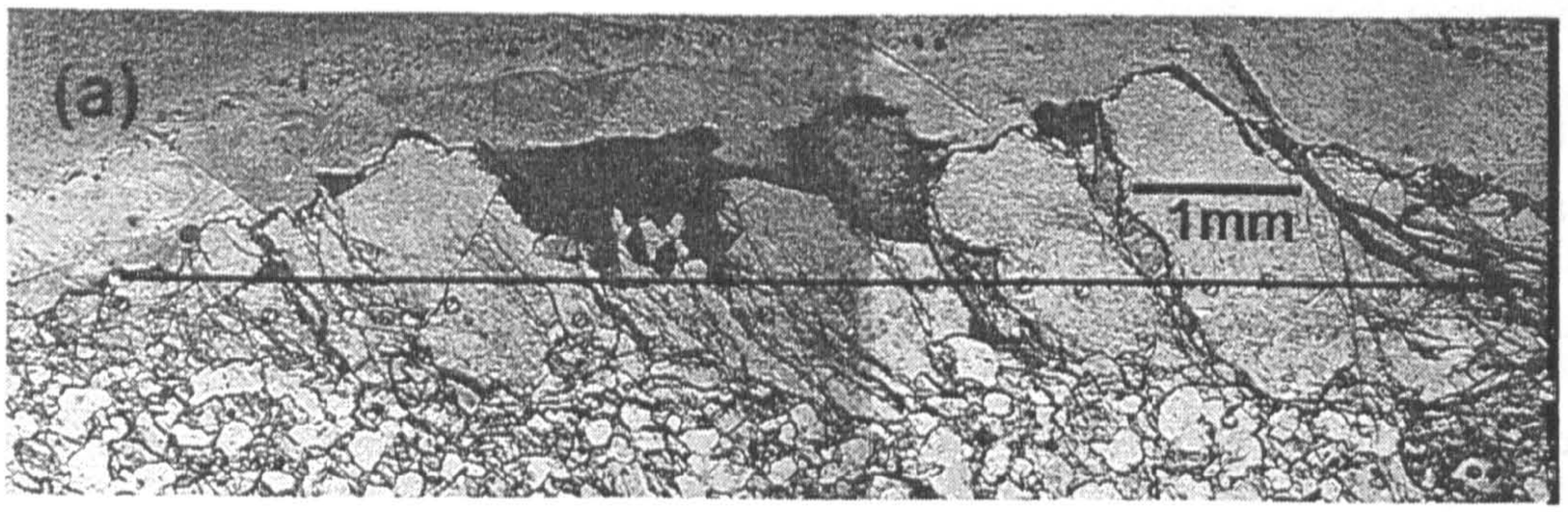


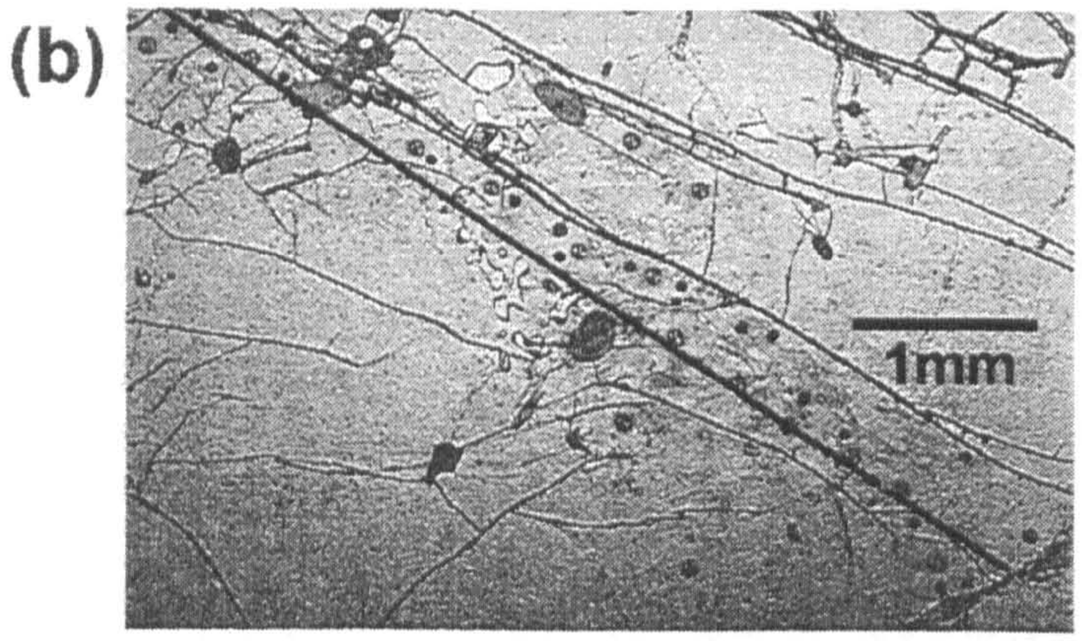


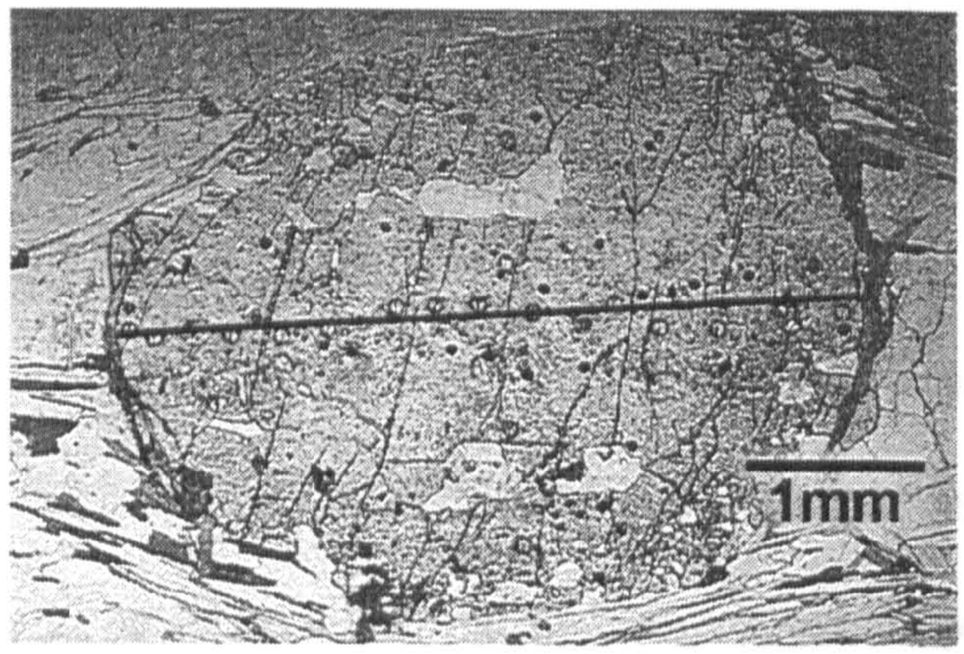


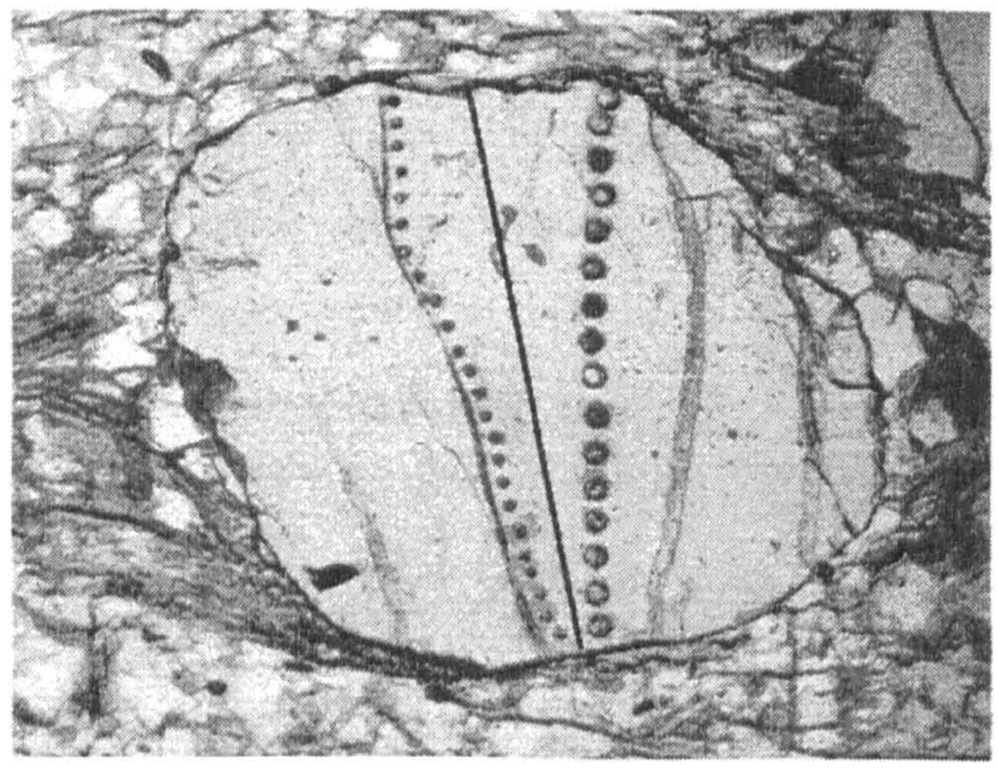


*Figure 6.3 Photomicrographs of garnets used in LA-ICP-MS analyses. Electron microprobe traverse along lines shown.*

*(a) G96. (b) G31(1) (c) G9 (d) CZG-23*

mm in length (Figure 6.3c). It has a typical bell-shaped Mn profile, an increasing Fe content from core to rim and a step in Ca and Mg near the rim ($Alm_{80-57}$, $Py_{10-20}$, $Grs_{19-6}$ and $Sps_{25-10}$: Figure 6.6a). Rim equilibration temperatures were calculated using Thermocalc at 616 ± 29 °C and 9.4 ± 1.3 kbar. Isotopic analyses were carried out on a second garnet from the same hand specimen. Comparison of the major-element composition of an aliquot of the garnet used for isotopic analysis and a garnet traverse, shows that the garnet used for isotopic analysis was dominated by the rim of the garnet.

*Table 6.1 Summary of Sm-Nd TIMS ID and isotope ratio analyses.*

| ***CZG23*** | ***Nd (ppm)*** | ***Sm (ppm)*** | ***Sm/Nd*** | $^{147}Sm/^{144}Nd$ [1] | $^{143}Nd/^{144}Nd$ [2] |
|---|---|---|---|---|---|
| Grt1 | 5.997 | 9.560 | 1.594 | 0.9640 | 0.514010 (42) |
| Grt2 | 7.399 | 13.388 | 1.809 | 1.0943 | 0.514252 (26) |
| Grt core | 6.159 | 9.309 | 1.512 | 0.9141 | 0.513864 (8) |
| Grt3 | 7.281 | 8.519 | 1.170 | 0.7075 | 0.513498 (14) |
| WR Bt-rich | 20.870 | 5.764 | 0.276 | 0.1669 | 0.512131 (26) |
| WR leuco. | 13.904 | 3.378 | 0.243 | 0.1469 | 0.512168 (20) |

*[1] All errors 0.5% except G31(1) Grt2 (1.5%) and CZG-23 Grt1 (1.2%). [2] Replicate measurements (n=40) of the La Jolla Nd Standard gave 0.511853±0.000008 ($2\sigma_m$) over the period that these analyses were performed.*

Sample CZG23 comes from a banded granulite gneiss in the Moldanubian Zone of the southern Bohemian Massif. The garnet is spherical, 1.1 mm in diameter (Figure 6.3d) and has a composition of $Alm_{62-49}$, $Py_{28-24}$, $Grs_{25-6}$ and $Sps_{2-1}$ (Figure 6.7a). It is present in both the feldspar- and biotite-rich portions of the rock. There is strong retrograde zoning in the outer 200μm of the grain. Thermodynamic modelling using pseudosections and the bulk composition of the rock (Vance and Mahar, 1998; Kosler and Vance, in prep.) suggest a peak P-T ca 1100 °C and 20 kbar followed by a rapid isothermal decompression down to <5 kbar. These extreme conditions are in agreement with other P-T estimates (Carswell and O'Brien, 1993) from this terrain. The decompression resulted in garnet resorption and, probably, formation of the retrograde

zoning in the rim. The small size of the garnets precluded single-grain Sm-Nd dating and a bulk mineral separate has been used instead. In addition, in order to resolve the prograde and retrograde history of the garnet, the grains were air-abraded and the cores analysed separately.

## 6.4 Results

### 6.4.1 G96

Two isotope dilution analyses of G96 were carried out on gem-quality separates for which the data have been presented in Chapter 4. The interpretation of these ages is also discussed in Chapter 4. However, it is worth repeating for the present field of interest that the low concentrations, high Sm/Nd ratios and the concordant Sm-Nd and Rb-Sr ages suggest that the analyses represent pure garnet unaffected by inclusions.

*Table 6.2 LA-ICP-MS analyses of G96 separate*

| *Nd (ppm)* | *Sm (ppm)* | *Sm/Nd* |
|---|---|---|
| 0.05 | 0.39 | 7.8 |
| 0.08 | 0.54 | 6.8 |
| 0.07 | 0.51 | 7.3 |
| 0.07 | 0.52 | 7.4 |
| 0.08 | 0.50 | 6.3 |
| 0.08 | 0.52 | 6.5 |

A LA-ICP-MS traverse was made over the gem quality section of an equivalent garnet to that used in the isotopic analyses (Figure 6.3a) as well as an aliquot of the separate used for isotopic analyses. The garnet separate results are summarised in Table 6.2. The concentrations obtained from the separate agree well with the ID analysis Grt 1 (Chapter 4) confirming both the concentrations and the high Sm/Nd ratio obtained. ID analysis Grt 2 has a Sm concentration that also agrees well with the separate but the Nd concentration is almost twice the highest concentration obtained by laser ablation with a consequent lower Sm/Nd ratio.

In the traverse concentrations of Nd and Sm are low (25-79 ppb Nd and 268-493 ppb Sm) and the Sm/Nd ratio varies from 5.1 to 14.9 (Figure 6.4c). The HREE show zoning with a maximum enrichment from core to rim of 2-4.8 for Yb. This enrichment is less

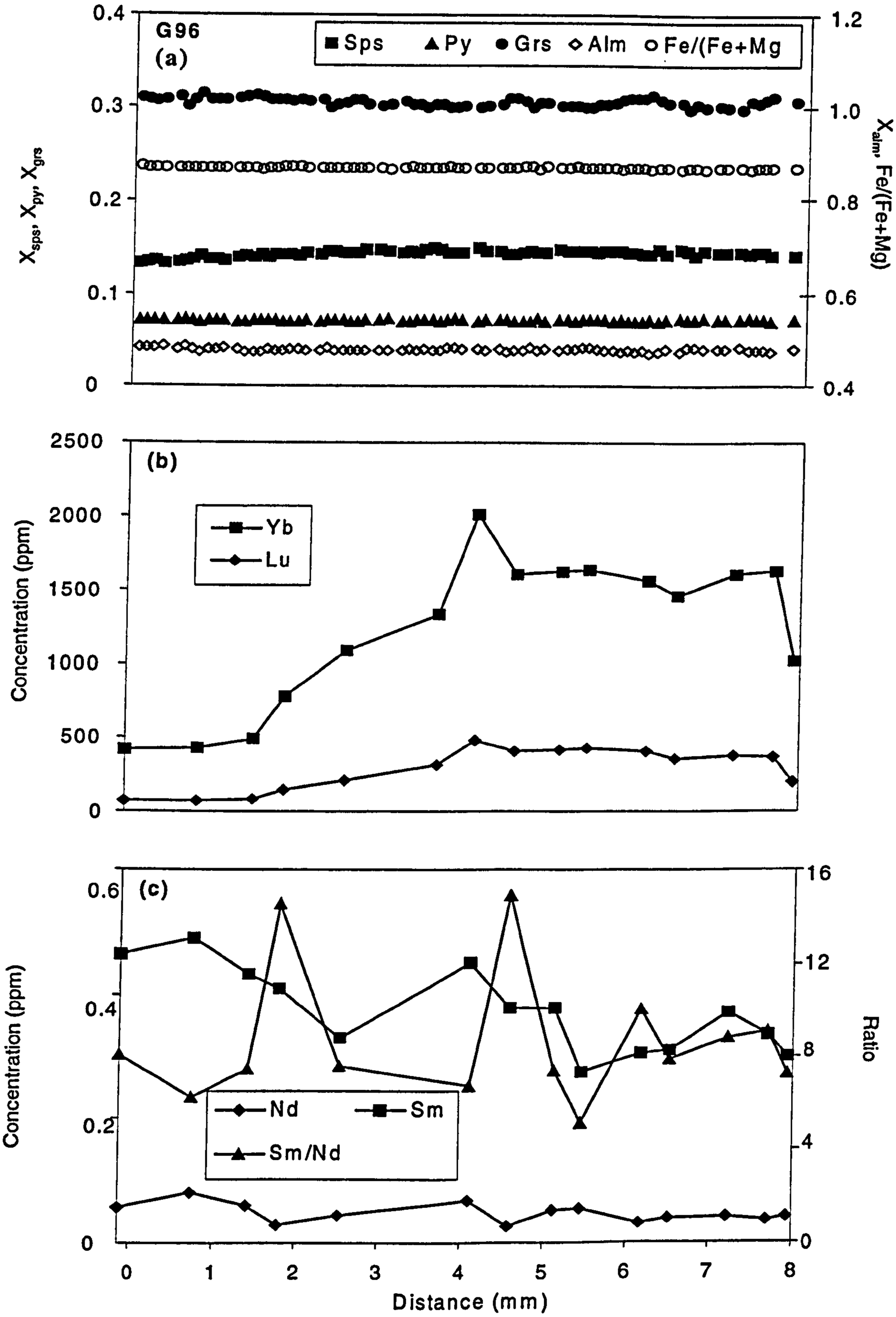


*Figure 6.4 Electron microprobe and LA-ICP-MS analyses for G96. All distances correspond to the traverse shown in Figure 6.3a (a) major-element profile (b) Yb and Lu zonation profile. (c) Sm, Nd and Sm/Nd zonation profile.*

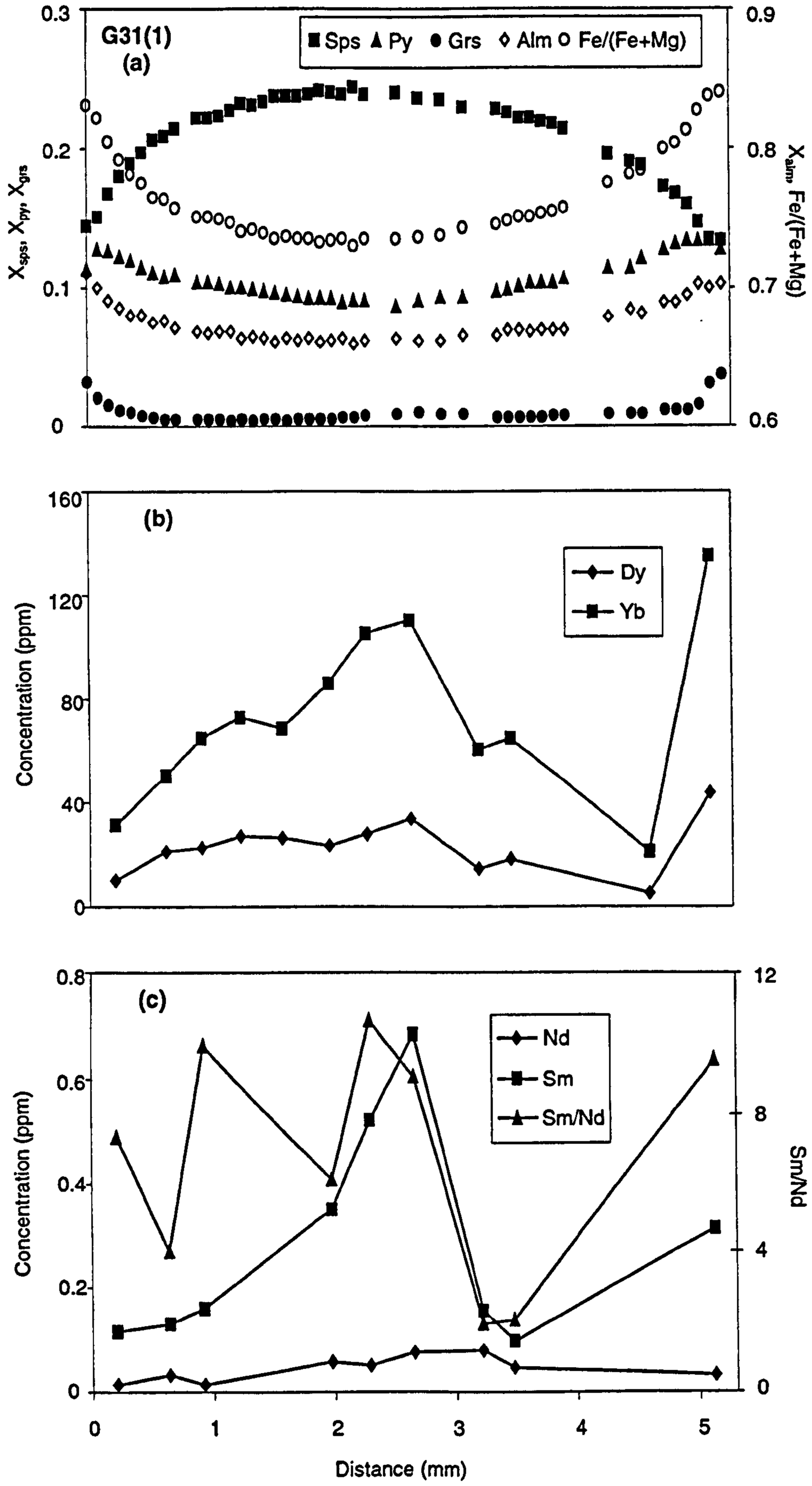


*Figure 6.5 Rim to rim electron microprobe and LA-ICP-MS analyses for G31(1). All distances correspond to the traverse shown in Figure 6.3b (a) major-element profile (b) Dy and Yb zonation profile. (c) Sm, Nd and Sm/Nd zonation profile.*

significant than that previously found for other amphibolite-facies pelitic garnets but similar to that obtained for a sillimanite zone garnet (6.8 times Yb enrichment Schwandt et al., 1996).

### 6.4.2 G31(1)

Two isotopic analyses of G31(1) were obtained on a hand-picked separate obtained from a single garnet (Grt 1, Grt 2, Chapter 4). Both gave low Sm and Nd concentrations (60-240ppb Nd, 0.2-1.3ppm Sm), high Sm/Nd ratios (4 - 5.3) and a reproducible age using the whole rock as the low Sm/Nd phase (39.9 ± 1.4 Ma).

The concentrations of Nd and Sm obtained by a LA-ICP-MS traverse of a single garnet (Figure 6.5c) are extremely low (from 16-79 ppb and 52-684 ppb respectively) and the Sm/Nd ratio varies from 1.97 to 10.66. The HREE, represented by Dy and Yb, show strong zonation from core to rim and the concentrations of all REE increase in the outer 200 μm-as can be seen on the right hand side of (Figure 6.5b,c). An earlier, less precise, traverse sampling closer to the rim on the left hand side of Figure 6.5 revealed a similar increase in REE concentrations demonstrating that the change at the rim is symmetrical. ID analysis Grt 2 has low concentrations of Nd and Sm and a high Sm/Nd ratio - all well within the range obtained by LA-ICP-MS. On the other hand Grt1 has Nd and Sm concentrations approximately 3 and 2 times the maximum obtained by *in-situ* analysis respectively. However, the Sm/Nd ratio obtained by ID is high (5.3) and within the range given by LA-ICP-MS.

### 6.4.3 G9

Two ID analyses were made on separates from a single garnet (Grt 1, Grt 2; Chapter 4). Grt1 has extremely low concentrations (90 ppb Nd and 170 ppb Sm )and a low Sm/Nd ratio (1.96) while Grt2 has higher concentrations (200 ppb Nd and 1.2 ppm Sm) and a higher Sm/Nd ratio (5.8). On the isochron diagram the two garnet separates do not fall

on an isochron with the whole rock (Chapter 4) suggesting some disequilibrium between one of the garnets and the reservoir from which they grew. Such disequilibrium The LA-ICP-MS absolute concentrations are extremely low for the LREE. The HREE show extremely strong zonation as demonstrated by Yb on Figure 6.6b. Sm and Nd concentrations vary from 525-1760 ppb and 52 to 156 ppb and Sm shows the reverse trend from the HREE with low concentrations in the core (Figure 6.6c).

ID analysis Grt2 falls within the Sm and Sm/Nd ratio range and within error of the Nd concentrations. On the other hand, the Nd and Sm concentrations for ID analysis Grt1 fall within the range obtained by LA-ICP-MS but with a lower Sm/Nd ratio.

### 6.4.4 CZG23

Two ID analyses were made on bulk mineral separates (Grt1 and Grt2) and one on air-abraded garnet cores (Grt core) from the biotite-rich layer of the granulite gneiss (Table 6.1). In addition, a bulk garnet separate from the feldspar-rich portion of the rock was also analysed (Grt 3). The unusually high Sm and Nd concentrations in all the analysed garnet samples might be taken as indicative of contamination of the garnet separates with Nd-rich inclusions. However, and crucially in this case, they also have relatively high Sm/Nd and $^{143}Nd/^{144}Nd$ ratios (Table 6.1). Grt1, Grt2 and Grt core all have Sm and Nd concentrations in the range 9.3 -13.4 and 6.0 - 7.4 ppm, respectively. All three garnet fractions fall on the same Sm-Nd isochron with the whole-rock, giving an age of 351 ± 6 Ma (Figure 6.8). This age overlaps with that calculated for a Grt3 - whole-rock pair from the felsic portion of the rock (362 ± 7 Ma) and with other garnet Sm-Nd ages from the same rock unit (J. Kosler and D. Vance, unpublished data).

The concentration ranges overlap with those obtained from the LA-ICP-MS profile across a garnet from the mafic portion of the rock (3-11.1ppm and 0.6-7.6ppm for Sm and Nd respectively). The traverse shows a strong and symmetrical zoning both for the LREE and HREE in the central part of the grain (Figure 6.7b,c).

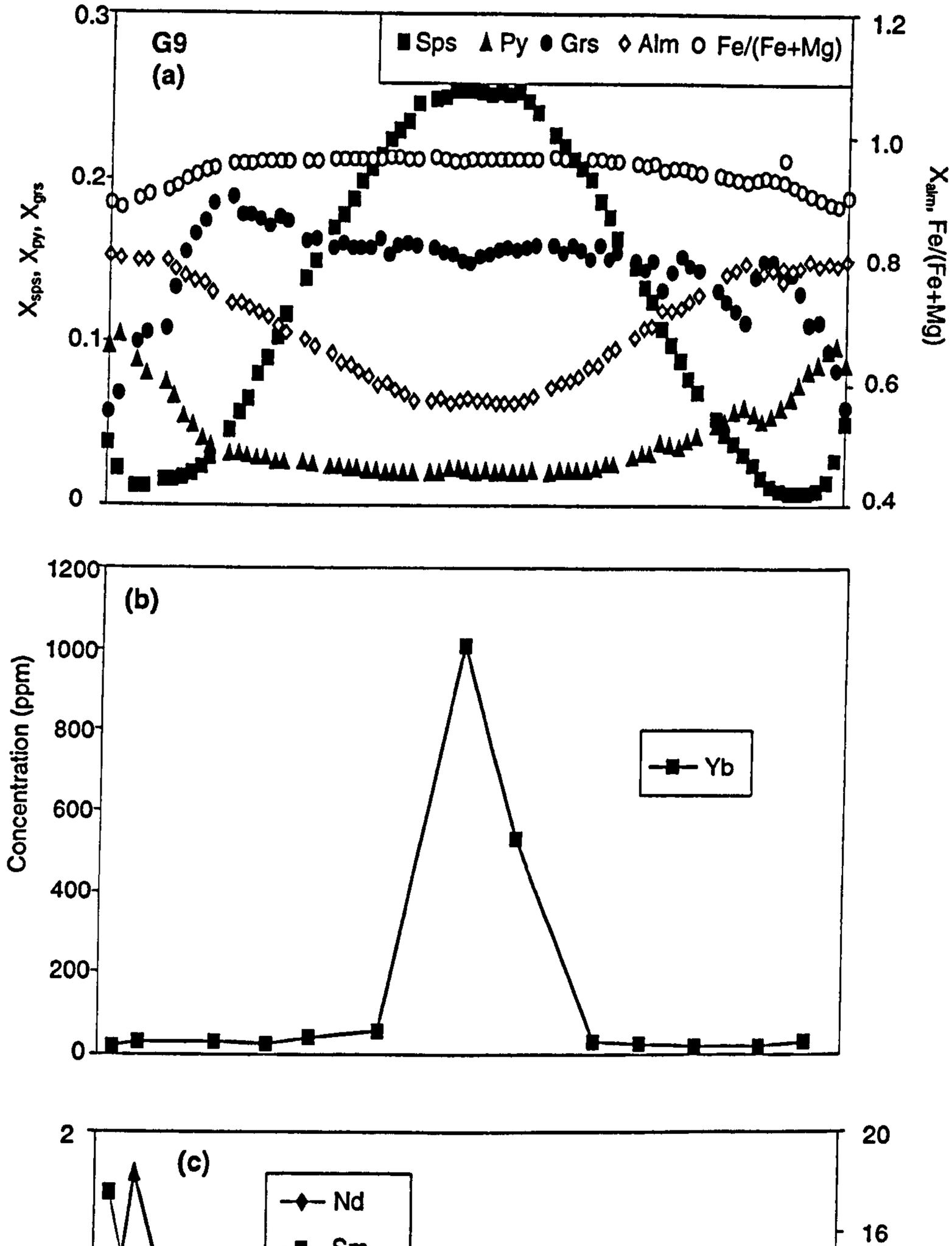


*Figure 6.6 Rim to rim electron microprobe and LA-ICP-MS analyses for G9. All distances correspond to the traverse shown in Figure 6.3c. (a) Major-element profile. (b) Yb zonation profile. (c) Sm, Nd and Sm/Nd zonation profile.*

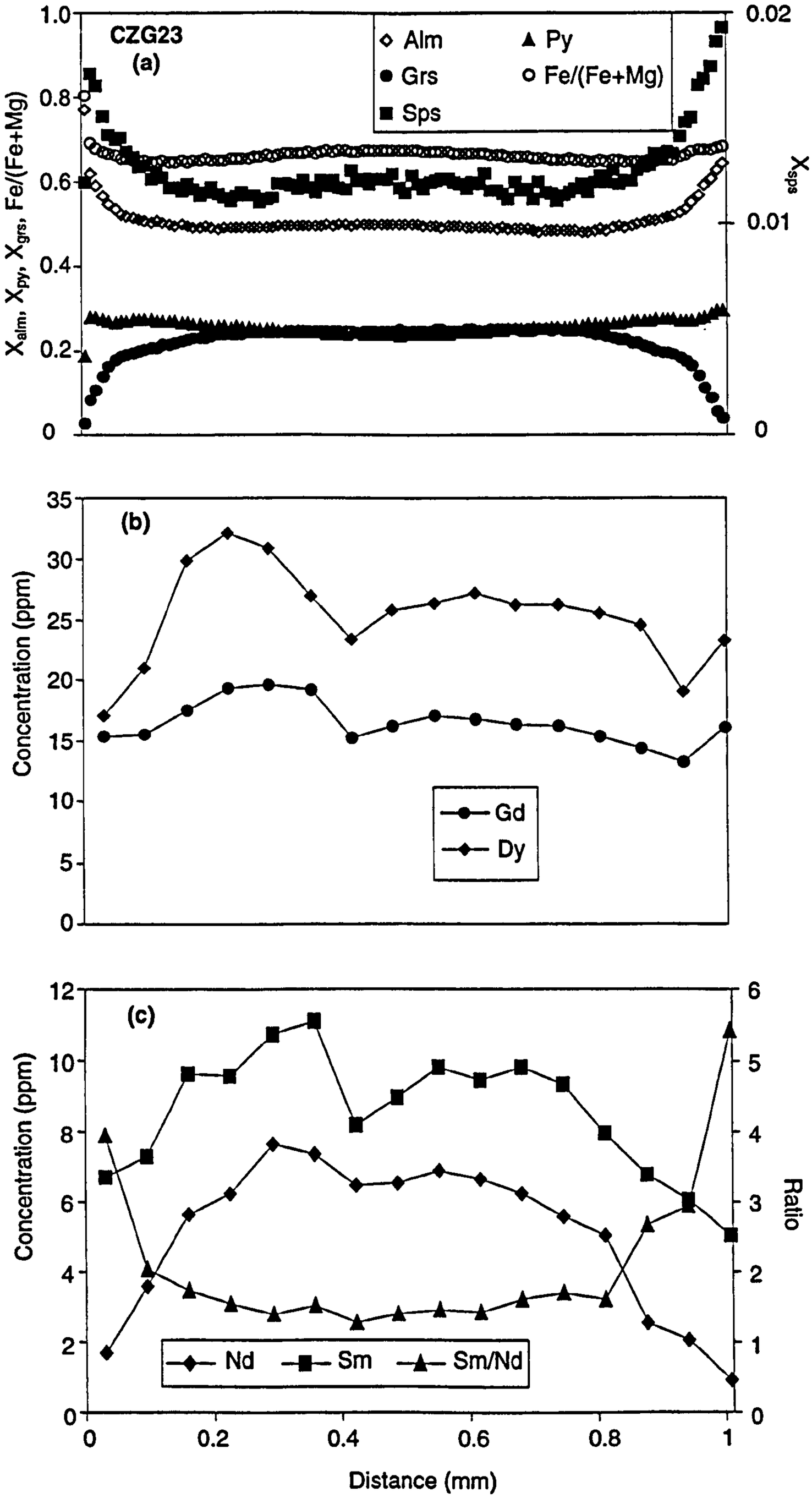


*Figure 6.7 Rim to rim electronmicroprobe and LA-ICP-MS analyses for CZG23. All distances correspond to the traverse shown in Figure 6.3d. (a) Major-element profile. (b) Gd and Yb zonation profile. (c) Sm, Nd and Sm/Nd zonation profile.*

could have a number of causes and will be dealt with in detail in the discussion.Despite strong zoning in absolute REE concentrations, the Sm/Nd ratio of ca. 1.5 is constant across the core. The change in the Sm/Nd ratio in the rim can be correlated with the major cation profiles which also show changes in concentrations towards the garnet rim on the same scale (Figure 6.7a,b). The most prominent feature of the major-element profile is the sharp increase in Mn near the rim. Since garnet itself is the only major metamorphic phase that incorporates significant amounts of Mn, this sharp increase is probably a result of garnet resorption during decompression and resultant diffusion of the Mn back into the garnet (c.f. Vance and Mahar, 1998). Given the preference of garnet for Sm over Nd, preferential uptake of Sm during this resorption is also the most likely explanation for the shift in the Sm/Nd ratio.

A comparison of the range of Sm and Nd concentrations obtained from two LA-ICP-MS profiles (3.0 - 11.1 and 0.6 - 7.6 ppm, respectively, from rim to core) and those obtained by ID analysis suggests that, as a result of hand-picking separation, the bulk garnet samples (Grt1, Grt2) were biased towards the core. Specifically, the measured ID concentrations are similar to those obtained by LA-ICP-MS for the core. In fact, the bulk Sm and Nd concentrations calculated from volume-weighting of the LA-ICP-MS traverse across the garnet grain are 3.4 and 7.3 ppm, respectively whereas the ID concentrations are 6-7.4ppm and 9.6-13.3 ppm for garnet from the biotite-rich part of the rock (Grt 1 and Grt 2; Appendix G). In general, however, the LA-ICP-MS *in-situ* analyses are clearly consistent with the conclusion that the high Sm and Nd concentrations obtained from the isotope dilution analysis of garnet from CZG23 are representative of garnet and are not affected by REE-rich inclusions.

## 6.5 Discussion

The data presented here further demonstrate the ability of *in-situ* analysis to reveal substantial sub-grain heterogeneity in the trace-element concentrations of minerals

(Hickmott et al. 1987, Hickmott and Spear 1992, Sevigny 1993, Schwandt et al. 1996, Bea 1996). LA-ICP-MS is particularly useful for measuring very low concentrations of the REE. In addition, and of specific importance for this study, LA-ICP-MS allows the unequivocal measurement of the lattice concentrations of trace elements so that the effect of inclusions in bulk separates can be assessed. The two datasets obtained in this study allow us to make a comparison between conventional isotopic data from bulk separates and real lattice concentrations and permit some general conclusions on the robustness of garnet ages and the potential effect of inclusions. Before discussing the data in detail, however, possible sources of bias and error in our approach are assessed first.

*Table 6.3 Summary of Sm-Nd TIMS ID and isotope ratio analyses for CZG-23*

| CZG23 | Nd | Sm | Sm/Nd | $^{147}Sm/^{144}Nd$ | $2\sigma$ | $^{143}Nd/^{144}Nd$[1] | $2\sigma$ |
|---|---|---|---|---|---|---|---|
| Grt1 | 5.997 | 9.56 | 1.594 | 0.9640 | 0.0056 | 0.514010 | 0.000021 |
| Grt2 | 7.399 | 13.388 | 1.809 | 1.0940 | 0.0010 | 0.514252 | 0.000013 |
| Grt3 | 7.281 | 8.519 | 1.17 | 0.7075 | 0.0004 | 0.513498 | 0.000007 |
| Grt core | 6.159 | 9.309 | 1.512 | 0.9141 | 0.0007 | 0.513864 | 0.000003 |
| WR Bt-rich | 20.87 | 5.764 | 0.276 | 0.1669 | 0.0001 | 0.512131 | 0.000013 |
| WR leucocr. | 13.904 | 3.378 | 0.243 | 0.1469 | 0.0007 | 0.512168 | 0.000010 |

[1] *Replicate measurements (n=40) of the La Jolla Nd Standard gave 0.511853±0.000008 (2σ) over the period that these analyses were performed. Data collected by Jan Kosler*

### 6.5.1 Potential sources of bias and error

Clearly, direct comparisons of the concentrations obtained in ID and LA-ICP-MS require that the same material be analysed in both cases. Unfortunately, conventional isotopic analysis is a destructive processes. One potential approach would be to perform the LA-ICP-MS analysis first on material that is then used for isotopic analysis. This is precluded, however, by the difficulty of retrieving clean garnet from the mount used for laser ablation due to the excessive cleaning required to remove contamination produced

by the mount material. Consequently laser ablation analyses on aliquots of the material picked for ID analysis (G96) or on separates grain within the same hand-specimen were performed. Implicit in our approach is the assumption that there are no large variations between garnets in any one hand specimen. Several steps have been taken in order to ensure that the two data sets are comparable. For example, in the case of G31 and G9 aliquots of the separate for bulk isotopic analysis have been micro probed as well as a profile across the grain used for LA-ICP-MS so that the region of garnet represented by the ID analysis can identified. In both cases, the major-element concentrations indicate that the picked aliquots are dominated by material from the rim of the garnet. In addition, for G96, LA-ICP-MS analyses both on an aliquot of the picked separate and in a profile across a separate grain have been performed. The aliquot has very similar Sm and Nd concentrations to the profile analysed which, in part, justifies our assumption that the variations between different garnets in one hand-specimen are small.

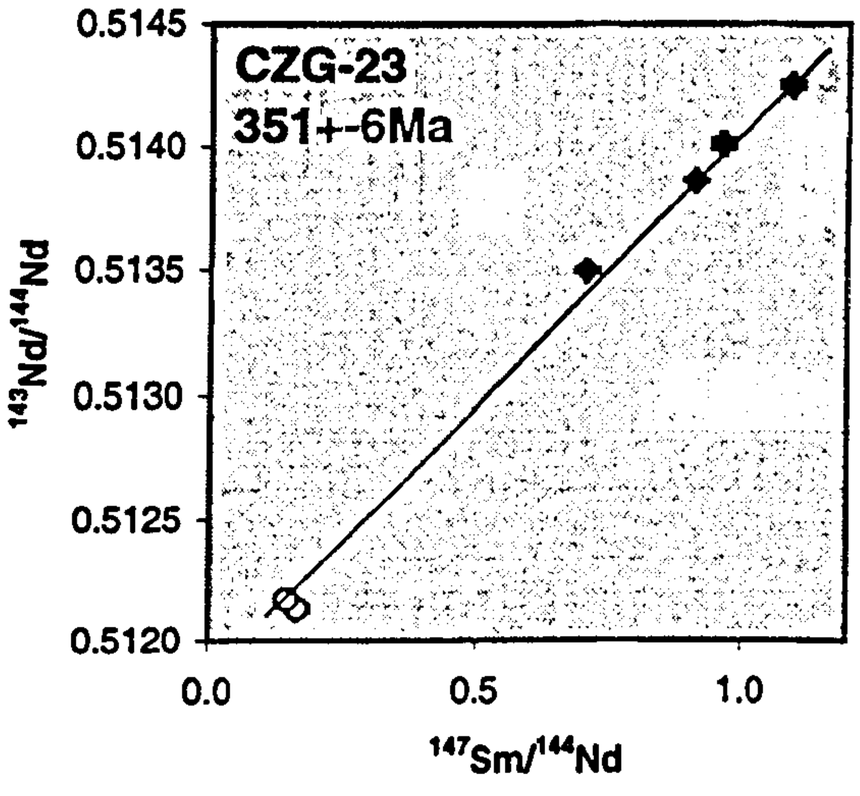


*Figure 6.8 Sm-Nd and Rb-Sr isochron diagram for CZG-23. Diamond = garnet and solid square = whole rock. See Table 6.1 for isotopic analyses.*

However, G96 is not zoned in either major elements or Sm and Nd. It is clear from this and other work (c.f. Hickmott et al., 1987; Hickmott and Spear, 1992; Sevigny, 1993; Bea, 1996; Schwandt et al., 1996) that garnets are often zoned in REE, in common with the major elements. It is also clear, however, that major-element profiles vary little between garnets of the same size in one rock (eg. Ayres and Vance, 1997). If this is also the case for REE then our approach of performing LA-ICP-MS analyses on similarly sized garnets as for isotopic analysis would give comparable results. On the

other hand, given the fact that Sm and Nd in pelitic rocks are located predominantly in accessory phases (Ayres and Harris, 1997), the local reservoir from which an individual garnet grows is likely to be much more heterogeneous in the absolute amounts of REE available than is the case for major elements.

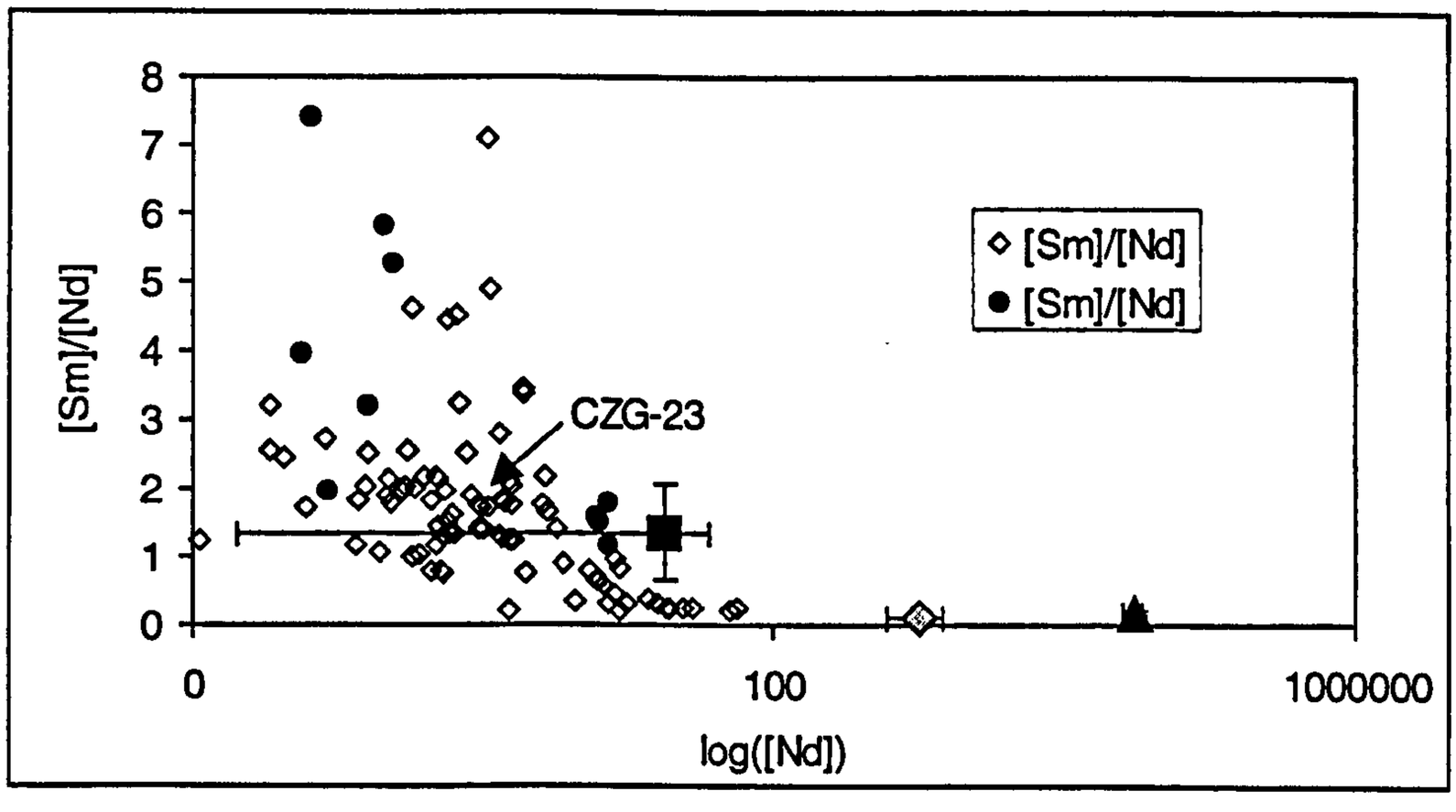


*Figure 6.9 Sm/Nd vs. Nd for garnets from conventional isotopic ID analyses in the literature. The solid square represents an average zircon, grey diamond allanite and solid triangle monazite (error bars are one std. deviation). Garnet data from Humphries and Cliff, (1982); Vance, (1986); Vance and O'Nions, (1990); Burton and O'Nions, (1991); Burton and O'Nions, (1992); Mezger et al., (1992); Thöni and Jagoutz, (1992); Vance and O'Nions, (1992); Getty et al., (1993); von Quadt, (1993); von Quadt and Gebauer, (1993); Hensen and Zhou, (1995); Brueckner et al., (1996); Vance and Harris, (1999). Zircon, monazite and allanite data from Gromet and Silver (1983); Maas et al., (1992); Montel, (1993); Bea, (1996); Ayres, (1997); Pan, (1997); Finger et al., (1998).*

### 6.5.2 Comparison of Nd and Sm concentrations: zoning and inclusion effects

The principal Nd-rich inclusions found in garnet are monazite and allanite. The potential effect of these phases on the Sm-Nd systematics of a bulk garnet separate would be to increase the measured concentrations but to reduce the Sm/Nd ratio. This effect has been observed previously (Vance and O'Nions, 1992) and is demonstrated by a compilation of published garnet data (Figure 6.9) which confirms the strong relationship between measured Nd concentrations and the Sm/Nd ratio for conventional analyses of garnet separates. Further, this relationship is completely consistent with

mixing between a pure garnet lattice component (represented by the ICP-MS analyses presented here) and monazite or allanite inclusions (open square and solid triangle at very high Nd concentrations). In detail, a few data including CZG-23 plot significantly off the trend with Sm/Nd ratios around 1.5-2 and high Nd concentrations. An increase in LREE concentration has been noted for high-pressure granulite rocks (Bea, 1996) which may, in part, explain the high Sm and Nd concentrations in sample CZG-23 which experienced pressures of ~20kbar.

In apparent contrast to the general trend, a correlation of decreasing Sm/Nd with increasing Nd between aliquots for G9, G31(1) and CZG23 is not apparent. For example, the aliquot of G31(1) with the higher Sm/Nd ratio also has the highest concentrations, while a similar observation is made for G9. The variations from one aliquot to another could still be the result of the incorporation of inclusions into the ID analyses. For example, incorporation of a xenotime inclusion could increase both the REE concentrations and the Sm/Nd ratio. However, xenotime has never been reported as an inclusion in garnet and has not been observed here despite a thorough search using the SEM. It seems more likely that, in these cases, the variations from one aliquot to another are a reflection of real variations in the lattice concentrations. The large variations across any single grain shown by the LA-ICP-MS suggest that slight sampling bias from one ID analysis to another may result in significant variations in Sm and Nd concentrations and Sm/Nd ratio. This makes interpretation of the isochrons and modelling of the inclusions in terms of concentrations more difficult. It should be noted, however, that the broad concentration ranges are consistent with those obtained by ID. Some specific samples are discussed below.

Separate Grt 2 from sample G31(1) falls within the concentration and Sm/Nd ratio range obtained by LA-ICP-MS (Table 6.1, Figure 6.5c) Grt 1, on the other hand, has Sm and Nd concentrations that are 2-3 times higher than any obtained by *in-situ* analysis.

The Sm/Nd ratio for this aliquot is within the range of values represented in the profile but is also higher than that for Grt 1. These observations are clearly inconsistent with the relationship depicted in Figure 6.9 and suggest two possible explanations. The first of these is that a xenotime inclusion(s) has been incorporated into the Grt 1 aliquot thus elevating both the Sm and Nd concentrations as well as the Sm/Nd ratio. As noted above, however, xenotime inclusions have not been observed here or in any other garnet. The second possibility is that there are variations in the Sm-Nd composition of garnet in this rock that are not sampled by the LA-ICP-MS analyses. It has already been proposed, based on major-element composition, that the samples for ID analyses are dominated by the rim of the garnet. Examination of Figure 6.5c demonstrates that in this part of the profile Nd, Sm concentrations and the Sm/Nd ratios vary by a factor of 2-3. Clearly, these observations, accompanied by slight variations in the average provenance within the garnet of the picked separates, could easily explain the observed relationships without recourse to a xenotime inclusion. In any case, the similarity in the ages of the two separates indicates that the age of any hypothetical xenotime inclusion is identical to that of the garnet.

Garnet from sample G9 displays similar systematics to that of G31(1). As with the latter, one of the G9 ID analyses (Grt 1) has a Nd concentration that is outside, but a Sm concentration and a Sm/Nd ratio that is within, the range measured by LA-ICP-MS. The other analysis, Grt 1, has concentrations that are consistent with, but an Sm/Nd ratio a factor of two below, the LA-ICP-MS analyses. These observations are, again, inconsistent with incorporation of a LREE-enriched inclusion. Xenotime is again discounted because of its apparent absence. In common with G31(1), the major-element composition of the garnet indicated that the ID aliquots for G9 are dominated by the rim of the garnet. Likewise, Figure 6.6c demonstrates that this is the region of the garnet with the greatest variation (by about a factor of 3) in the Nd, Sm concentrations and in

the Sm/Nd ratio. The preferred explanation for G31(1), that the relationships seen in the ID aliquots can be explained by incomplete sampling of the range of concentrations and ratios in garnet by LA-ICP-MS, may also apply here.

The significant difference between G9 and G31(1) is that, for the former, the two garnet analyses do not yield the same Sm-Nd age with respect to the whole rock. In G9 the analysis with the low Sm/Nd ratio (Grt 1) lies well below the line defined by Grt 2 and the whole rock. Old inclusions of LREE-enriched accessories such as allanite or

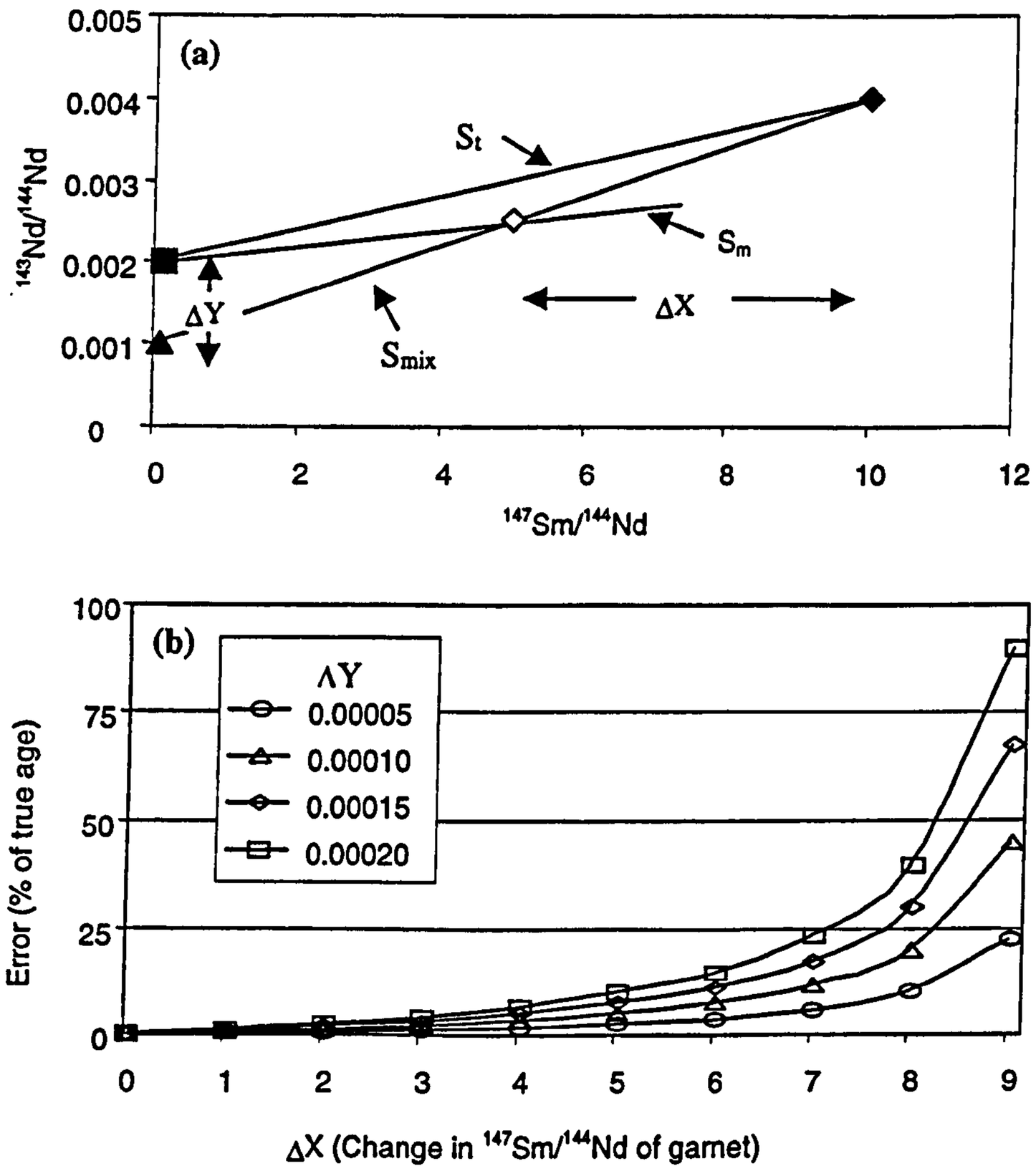


*Figure 6.10 Determination of age bias produced by the incorporation of old LREE-enriched inclusions into conventional garnet analyses. (a) Schematic isochron diagram showing the effect of inclusions on garnet dating. Solid diamond; pure garnet. Open diamond; measured garnet. Solid triangle; inclusion. Solid square; effective bulk composition. The slopes St and Sm are the slopes used for age determination of the true garnet and measured garnet respectively and Smix is the slope of the pure garnet-inclusion mixing line. (b) Age bias (%) resulting from the incorporation of an inclusion that is out of equilibrium with the effective bulk composition. Lines represent varying $^{143}Nd/^{144}Nd$ shifts between the inclusion and effective bulk composition (ΔY). Calculations are for a 30 Ma garnet with a $^{147}Sm/^{144}Nd$ of 10.*

monazite could explain this disequilibrium but for the fact that this separate also has lower Nd and Sm concentrations. Moreover, there is no known phase that could mix with a pure garnet, such as might be represented by Grt 2, to produce the Sm/Nd ratio of Grt 1. At present, the reason for this disequilibrium is unclear but I note that a biotite separate from this sample also shows significant isotopic disequilibrium. Such isotopic disequilibrium is likely to be caused by inhomegeonously distributed or variably equilibrated microinclusions. Step leaching experiments on mineral separates would distinguish between different isotopic reservoirs within the separates but were unfortunately out of the scope of this thesis.

### 6.5.3 The effect of inclusions on age determination

It appears from the above discussion that the conventional isotopic analyses presented here are largely free of the effect of inclusions. However, this may not be the case for many data in the literature (see Figure 6.9). Many of such analyses have Sm-Nd characteristics that are consistent with mixing between pure garnet, as typified by the *in-situ* analyses presented here and elsewhere, and LREE-enriched inclusions such as monazite or allanite. The inadvertent incorporation of these inclusions would have two major implications for chronometry with garnets. Firstly, in the case where included phases are the same age as the garnet, the only serious consequence is that the low Sm/Nd inclusion lowers the Sm/Nd ratio of the separate so that the age resolution is greatly reduced (eg. Bowtell et al., 1994) or, in extreme cases, completely eradicated (eg.Vance and O'Nions, 1992). A more serious consequence, however, results from the possibility that the inclusions are not the same age as the garnet – i.e. that they have been isotopically isolated from the whole rock for times longer than the age of the garnet and that there was significant isotopic disequilibrium between the inclusion and the rest of the rock at the time of garnet growth. The age obtained from such an impure garnet separate may not only be wrong but, if the downward shift in the Sm/Nd ratio is

not too great, it may be reasonably precise.

The effects of an inclusion on a garnet Sm/Nd age may be illustrated by a simple model (Figure 6.10a). The effective bulk composition (EBC) from which the garnet grows is marked by a solid square. This is effectively the whole rock minus any inclusions that are in isotopic disequilibrium with the whole rock. A hypothetical pure garnet separate is represented by a solid diamond and the composition of the accessory phase that is isolated from the whole rock by a solid triangle. A measured garnet separate, representing a mixture between pure garnet and inclusion, is plotted as the open diamond. The line with slope ($S_m$) determines the derived age from these analyses which differs from the slope ($S_t$) that defines the true age of the garnet. Also shown on the figure is the mixing line of slope $S_{mix}$ between the pure garnet and the inclusion. The shift in age between the true value ($t_t$) and that measured ($t_m$) will result from the difference in the slopes $S_m$ and $S_t$ as follows:

$$t_m - t_t = \frac{\ln(1+S_t)}{\lambda} - \frac{\ln(1+S_m)}{\lambda}$$

$$= \frac{1}{\lambda}\left[\ln\left(\frac{1+S_t}{1+S_m}\right)\right]$$

The slopes of the lines are determined by the values of the $^{147}Sm/^{144}Nd$ (X) and $^{143}Nd/^{144}Nd$ ratios (Y) of the effective bulk composition or whole rock ($X_{ebc}$,$Y_{ebc}$) pure garnet ($X_{pg}$,$Y_{pg}$), impure garnet ($X_{ig}$,$Y_{ig}$) and inclusion ($X_i$,$Y_i$). The equation that governs the shift in age from true to measured is simplified if it is assumed the EBC has an $^{147}Sm/^{144}Nd$ and a $^{143}Nd/^{144}Nd$ ratio of zero. This simply moves the reference frame of the isochron plot. The inclusion Sm/Nd ratio is taken to be the same as the whole rock - in fact, allanite and monazite typically have $^{147}Sm/^{144}Nd$ ratios lower than whole rocks but this has negligible effects on the modelling presented below. It is also convenient to define a parameter $\Delta X$ which is the shift in $^{147}Sm/^{144}Nd$ between pure and

impure garnet and a parameter ΔY, the shift in $^{143}Nd/^{144}Nd$ between the inclusion and the effective bulk composition. Then the shift between the true age and that obtained from the measured impure garnet, $t_m$-$t_t$ is given by:

$$tm - tt = \frac{1}{\lambda} \ln \left[ \frac{\left(1 + \frac{Y_{pg}}{X_{pg}}\right)}{\left(1 + \frac{(X_{pg} - \Delta X)\left(\frac{Y_{pg} + \Delta Y}{X_{pg}}\right) - \Delta Y}{(X_{pg} - \Delta X)}\right)} \right]$$

Typical numerical values of $X_{pg}$ can be obtained from the LA-ICP-MS data and can be as high as 10-12. For a pure garnet fraction about 30 Ma old with an $X_{pg}$ of 10, Y ($^{143}Nd/^{144}Nd$) relative to the EBC would be about 0.002000. Figure 6.10b shows the percentage bias on the age as a function of ΔX (shift in $^{147}Sm/^{144}Nd$ of garnet) and for a range of ΔY (difference in $^{143}Nd/^{144}Nd$ between EBC and inclusion) for this scenario. The shift in the age from true to measured is most strongly dependant on ΔX, since it increases exponentially as $X_{ig}$ tends towards $X_i$. ΔY (the shift between EBC and inclusions represented by the different lines) plays a less important role but, as would be expected, the error increases with ΔY for any given ΔX. Because the value of $X_i$ has been taken to be the same as the whole rock, any non-zero value of ΔY corresponds to an inclusion isolated from the whole rock for an infinite time. In reality, for values of $^{147}Sm/^{144}Nd$ of 0.07 in an allanite or a monazite and one of 0.12 in a whole rock (typical for pelitic rocks of interest), the range of ΔY considered here (0-0.0002) corresponds to inclusions isolated for 0-600 Ma before garnet growth. The situation when ΔY=0 corresponds to the inclusions being in equilibrium with the EBC at the time of garnet growth and will result in the concordance of all garnet analyses with no introduced error. The situation when ΔY = 0.0002 corresponds to a 600Ma old inclusion within a

30 Ma old garnet.

There are several general conclusions to be drawn from the above analysis. Firstly, and perhaps counter-intuitively, the apparent age of an impure garnet separate contaminated by very old LREE-enriched inclusions will itself be *younger* than the true age of the garnet. This is a simple consequence of the fact that the LREE-enriched reservoir will, given time, develop a Nd-isotope signature that is less radiogenic than the whole rock. Secondly, Figure 6.10b shows that for $^{147}Sm/^{144}Nd$ ratios of impure garnet separates that are more than 50% below that of the pure garnet, the apparent age will deviate significantly from the true value. On the other hand, for Sm/Nd ratios that are 50-100% of the true garnet value, the deviation of the apparent from the true age will be less than, or similar to, typical analytical uncertainties (0-10%). However the rather salutary fact is that, for the Nd-Sm concentrations in the Himalayan garnets studied here, only of the order of *a part per million* of the garnet separate need be monazite to effect a 50% reduction in the Sm/Nd ratio from that for the pure garnet.

In general, the above arguments suggest that the safest approach to dating garnets is to pick duplicate separates. In this case contamination by Nd-rich inclusions should be indicated by significantly variable Sm/Nd ratios. Where garnet-whole rock ages are analytically reproducible, then either the inclusions must have been isolated from the whole rock at the same time as the garnet or the measured Sm/Nd ratios are all close enough to the real garnet value to be result in a negligible shift in the age (Figure 6.10b). Either way, the duplicated date is a good measure of the age of the garnet. If, on the other hand, the ages are not reproducible then the most likely reason is that some of the analyses are so contaminated by inclusions that the measured age for low Sm/Nd garnet analyses is significantly younger than the true age. In this case, the age of the analysis with the highest Sm/Nd ratio is likely to be closest to the true value but not necessarily equal to it - in fact, it will be a minimum age. In this and other cases, LA-

ICP-MS concentration determinations such as those obtained here will be useful in determining exactly how robust such ages are.

The above modelling can also be applied to minerals such as zircon which fractionate Sm from Nd, by considering a negative $\Delta Y$; the equivalent of the solid triangle (inclusion) on Figure 6.10a lying above the effective bulk composition. As shown on Figure 6.10 zircon would also increase the Nd and Sm concentrations but would increase the measured age from the true age. However, the low concentrations of Sm and Nd in zircon would require the incorporation of prohibitively large amounts of this mineral in a "garnet" separate. In addition, the dissolution procedure used here and elsewhere for garnet, i.e. vials at low pressure rather than hydrothermally in a bomb, would not be expected to dissolve any zircon inclusions.

For samples discussed here it has been argued that the variations in Sm/Nd ratio recorded by the duplicate garnet separates is a result of real variation in the lattice concentrations. While no included phase is likely to cause the relationships observed the presence of such an inclusion cannot be discounted unequivocally and it is worth discussing the data in terms of the above analysis.

On the isochron diagram of G31(1) the two garnet analyses are concordant (Figure 6.8e) suggesting that any inclusions incorporated into the analyses were in equilibrium with the whole rock-garnet system or that both analyses are sufficiently close to the true garnet for there to be no significant shift from the true age. This applies equally to CZG23 for which the several garnet analyses are concordant. This conclusion is supported by the general similarity in the Sm and Nd concentrations and Sm/Nd ratios obtained by LA-ICP-MS and ID analyses.

G9 represents a distinctly less favourable case since the two garnet fractions are not concordant with the whole rock suggesting that the displacement of Grt1 and possibly Grt2 may be the result of the incorporation of inclusions that were not in equilibrium

with the whole rock-garnet system. In the case of G9, this suggestion is corroborated by the fact that the Sm/Nd ratios measured by LA-ICP-MS range from 5 to 18 while those for the ID analyses are 2 and 6. One can use the calculations outlined above, and used in Figure 6.10, in a semi-quantitative fashion to assess the robustness of the G9 ages as follows. First estimates of $\Delta Y$, $X_{pg}$ and $Y_{pg}$ are required. $\Delta Y$ can be determined assuming a worst case scenario of an inclusion completely isolated from the EBC for ~600Ma before being incorporated into the garnet ($\Delta Y$=0.0002). $X_{pg}$ and $Y_{pg}$ can be calculated using the range of Sm/Nd ratios obtained by LA-ICP-MS and assuming an age of 30 Ma; a situation similar to Figure 6.10b. Taking the Grt 1 analysis with a $^{147}Sm/^{144}Nd$ ratio of 1.19, these calculations suggest that the age given by this fraction relative to the whole rock could be too low by 68-86% - the range resulting from the range in $X_{pg}$ as derived from the LA-ICP-MS analyses. On the other hand for Grt 2, which has a $^{147}Sm/^{144}Nd$ ratio of 5.8, the age could be too low by 1-20%. In other words, the real age of the G9 garnet could be as high as 31 Ma as opposed to 24 Ma.

## 6.6 Conclusions

LREE-enriched micro-inclusions may contribute to some conventional Sm-Nd isotopic analyses obtained by isotope dilution on garnet separates. One method for determining the extent to which such inclusions affect individual garnet analyses is to verify the concentrations of Sm, Nd and the Sm/Nd ratio obtained by comparison with *in-situ* analyses of the garnet lattice. To measure the extremely low concentrations of Sm and Nd in the garnet lattice, high sensitivity LA-ICP-MS was used. These measurements demonstrate that conventional techniques can result in garnet analyses which are largely free from the effects of such inclusions and result in meaningful and reliable age information.

A simple model which explores the significance of these inclusions for garnet

chronometry demonstrates that the incorporation of tiny amounts of LREE-enriched minerals can dramatically alter the isotopic information obtained from garnets. Furthermore, if LREE-enriched inclusions incorporated into garnets have been isolated from the effective bulk composition during garnet growth they will result in a younger measured age than the true age. Such modelling is not limited to the Sm-Nd system and can clearly be adapted for other isotopic systems (Rb-Sr, U-Pb, Lu-Hf) which have been used with garnets and which are also likely to be affected by the incorporation of accessory phases enriched in the elements of interest. Nevertheless the extent to which these inclusions affect the garnet isotopic data can best be constrained by duplicating garnet analyses, (demonstrating that any inclusions if present were in isotopic equilibrium with the garnet-effective bulk composition) and/or by verifying that the elemental concentrations of measured garnets corresponds to the lattice concentrations measured *in-situ*.

Finally the accessory phases which may affect garnet chronometry (monazite, zircon, allanite) are themselves often used for high precision dating (e.g. Parrish, 1990). Age data from these accessory minerals is then related to pressure and temperature information from the major rock forming minerals such as garnet. However, given the reported incidence of isotopic disequilibrium between garnet and such accessory phases (this study Zhou and Hensen, 1995; Vance et al., 1998b) it cannot be assumed that the age of the accessory phase is related to age of crystallisation of the major phases.

# Chapter 7 - Trace-element zoning in garnet

## *7.1 Introduction*

There is currently a growing interest in the use of trace-element zoning in garnets as a record of petrogenetic processes (Hickmott et al., 1987; Hickmott and Shimizu, 1990; Hickmott and Spear, 1992; Brueckner et al., 1996; Schwandt et al., 1996; Spear and Kohn, 1996). Indeed the ubiquity of garnet in a wide range of bulk compositions and its use in well-calibrated geothermometers and barometers make its chemistry of special interest. In particular, because of the slow diffusion rates of the major-elements at amphibolite-facies conditions (see Ganguly et al., 1998a), the compositional signature of early metamorphism is preserved in garnet cores. Thus major-element zoning in garnets can provide constraints on changing pressure and temperature conditions from metamorphic terrains (Tracy et al., 1976; Spear and Selverstone, 1983; Vance and Mahar, 1998).

The Electron Microprobe (EMP) is regularly used to study the major-element zoning of garnets and has been used to measure a narrow range of trace-elements (Spear and Kohn, 1996), but for many other trace-elements of interest the detection limits are significantly greater than typical concentrations in garnet. With the development of the Secondary Ion Microprobe (SIMS) and Laser Ablation Inductively Coupled Plasma Mass Spectrometry (LA-ICP-MS) detection limits for many trace-elements have been reduced.

In this chapter the LA-ICP-MS data for the full trace-element dataset obtained during the Sm-Nd study outlined in Chapter 6 is used to examine the controls on trace-element partitioning into garnet. Firstly, however, the controls on rare earth (REE) and other trace element zoning in garnets are discussed. This is followed by a brief description of the analytical techniques of LA-ICP-MS. Then the data from three garnets measured by

LA-ICP-MS are presented with a discussion.

## 7.2 Controls on trace-element zonation

In both igneous and metamorphic rocks the controls on trace element zonation are likely to be numerous. While it is impossible to determine unique solutions to the zonation patterns observed, different processes will be characterised by particular styles of zonation. Below, the major controls on trace element zonation in both igneous and metamorphic rocks are discussed including: garnet crystal chemistry, mineral equilibria and non-equilibrium processes.

*Garnet crystal-chemical controls*

In a melt the partition of trace-elements into the crystal lattice of a growing mineral can be expressed as a partition coefficient ($Kd_{grt\text{-}melt}$). For elements which partition strongly into garnet, termed compatible, Kd is greater than 1. For elements which are incompatible in mineral structures, Kd is less than 1. Measured garnet partition coefficients for a silicate melt show that the heavy REE (HREE) are highly compatible in garnet and Kd decreases smoothly to the light REE (LREE) which are highly incompatible (Sisson and Bacon, 1992). An important feature of the incompatibility of the LREE in garnet is that, as a general rule, they will be incorporated into the growing garnet in proportion to their concentration in the surrounding rock or melt (McKay, 1989). Conversely, given the high Kd for some of the HREE, the growth of garnet may itself affect the concentrations of some REE in the rock or melt.

It has been demonstrated that the value of Kd for some trace-elements in silicate minerals can be successfully explained by the lattice strain model of Blundy and Wood (1994). This model describes trace-element partitioning of an element in terms the element's ionic radius, the size of the lattice site into which the trace-element partitions, the elastic modulus of the site and the theoretical ideal partition coefficient for that site.

As the major-element composition of the crystal changes the site size and elastic moduli will vary as a result of the differences in ionic radii and charge balance. Since major-element composition is itself a function of pressure, temperature and bulk rock major-element composition, so will the partitioning behaviour of trace-elements into garnet. In this way a correlation between major-element and trace-element composition would be expected. For example, in the garnet-silicate melt system, Westrenen et al. (Subm.) show, for pyrope-grossular (Py-Grs) garnets, that from $Py_{84}$ to $Py_9$ $Kd_{La}$ increases from 0.004 to 0.2 -showing that the incorporation of Ca into the garnet increases the partition of the LREE. In the case of metamorphic garnets the Ca content is also a function of pressure and it might be expected that LREE concentration may vary with the pressure at which garnet grew (e.g. Bea et al., 1997).

If the crystal chemistry of the garnet dominates the incorporation of trace elements this would result in a correlation between major and trace-element *zoning*; for example zonation in which the Ca content of garnet increases might be expected to show corresponding increases in LREE content. Such crystal-chemical controls will not be limited to igneous systems and will also affect trace element partition in metamorphic rocks: it has been suggested that high Mn and Ca contents may increase the compatibility of the HREE and LREE respectively (Schwandt et al., 1993; Schwandt et al., 1996). Unfortunately, the effect of the different major elements has not been extensively explored and little is known of the extent to which each major element changes the partition coefficients.

However, if crystal chemistry does play an important role the changing pressure and temperature during metamorphism and the near ubiquitous presence of major-element zonation in garnets at upper amphibolite grade (see review in Tracy, 1982) would be expected to contribute to trace-element zonation.

*Mineral equilibria*

In a crystallising melt there will be many other minerals which incorporate trace-elements to varying extents. The $Kd_{grt}$ will then also be a function of the other minerals present. The partition coefficient between the garnet and all the other components of the system (minerals and melt), $Kd_{bulk}$, will be the sum of the $Kd_{grt\text{-}mineral/melt}$ multiplied by their modal proportions. For example, the presence of negative Eu anomalies in garnets from granites (Harris et al., 1992; Sevigny, 1993) probably results from the growth of the garnet in the presence of crystallising feldspar, reducing the $Kd_{grt\text{-}mineral/melt}$ for Eu.

While changes to the modal proportions of rock-forming minerals and their compositions will affect the $Kd_{bulk}$, changes in accessory minerals will be of particular importance because in felsic rocks the bulk of REE reside in accessory phases (Bea, 1996) in which they form essential structural constituents. Such a process was suggested by Sevigny (1993) for a crystallising leucogranite in which monazite was the major control on LREE distributions in garnet phenocrysts.

If accessory phases such as monazite, apatite, zircon, ilmenite and allanite are the major control on REE and trace-element distribution in garnets correlations between specific elements, depending upon the accessory phase crystallising at the time, would be expected. For example the presence of monazite in equilibrium with garnet should lead to correlations between LREE, Th and P. Similarly, the presence of apatite (MREE and P), zircon (HREE, Zr, U and Hf), ilmenite (MREE, Ti, Nb), allanite (LREE, Th) might lead to other correlations.

Such reasoning can be extended to metamorphic rocks in which accessory phases also contain the bulk of trace and rare earth elements (Ayres et al., 1997). The important difference is that during metamorphism, under equilibrium conditions, the mineral composition and assemblage of the rock changes continually due to divariant net transfer reactions caused by varying mineral stability. The result would be that the

growing garnet would record significant concentration changes as different minerals become stable relative to others. Nevertheless, the same correlations between the elements should occur as above. Few authors have attempted to correlate trace-element zoning to accessory phases stability although Hickmott and Spear (1992) attempted to explain trace- and major-element zoning in a metamorphic rock in terms of changing major-mineral stability.

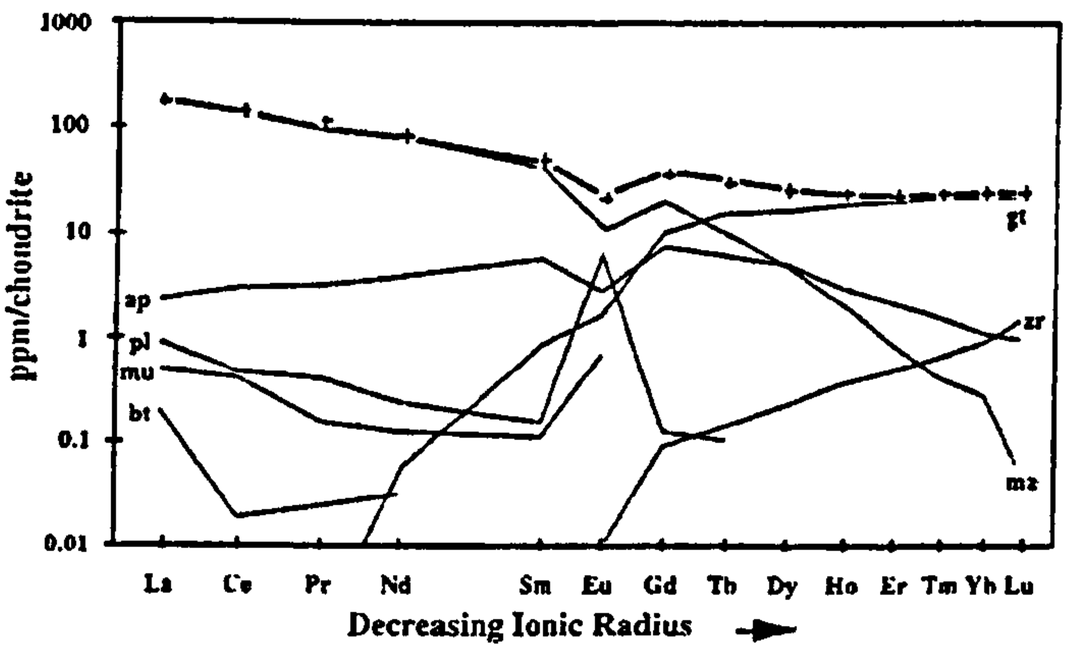


*Figure 7.1 Modelled chondrite-normalised REE distributions between phases in metapelite assemblage calculated by mass balance. From Ayres (1997).*

*Non-equilibrium processes*

In closed system metamorphic and igneous rocks equilibrium is rarely attained (as demonstrated by mineral zoning) and non-equilibrium processes play an important role during garnet growth. These can be placed between two endmembers: (i) limitations on elemental supply to the growing minerals due to intercrystalline diffusion controls (e.g. Albarede and Bottinga, 1972; Carlson, 1989) and; (ii) intracrystalline diffusion controls (resulting in more permanent changes in the effective bulk composition (EBC) or melt during growth).

*Intercrystalline diffusion controls*

In a situation where the garnet growth rate is such that elemental diffusion through the matrix or melt is not sufficient to maintain equilibrium, local concentration gradients develop in the rock, as illustrated in Figure 7.2. The strong partitioning into the garnet of the HREE (represented by red line in Figure 7.2a) results in a decrease in the HREE

concentration locally around the garnet and as growth continues the gradient becomes more pronounced (Figure 7.2b). As a result the HREE concentrations in the garnet decrease as the garnet grows (red zonation profile in Figure 7.2c). On the other hand, due to the incompatibility of the LREE in the garnet, the LREE concentration around garnet increases during growth (blue line in Figure 7.2a). Intercrystalline diffusion controls would result in a rapid decrease in HREE concentration with a concomitant, although less pronounced, increase in the LREE concentration. Furthermore, these effects may occur intermittently and repeatedly.

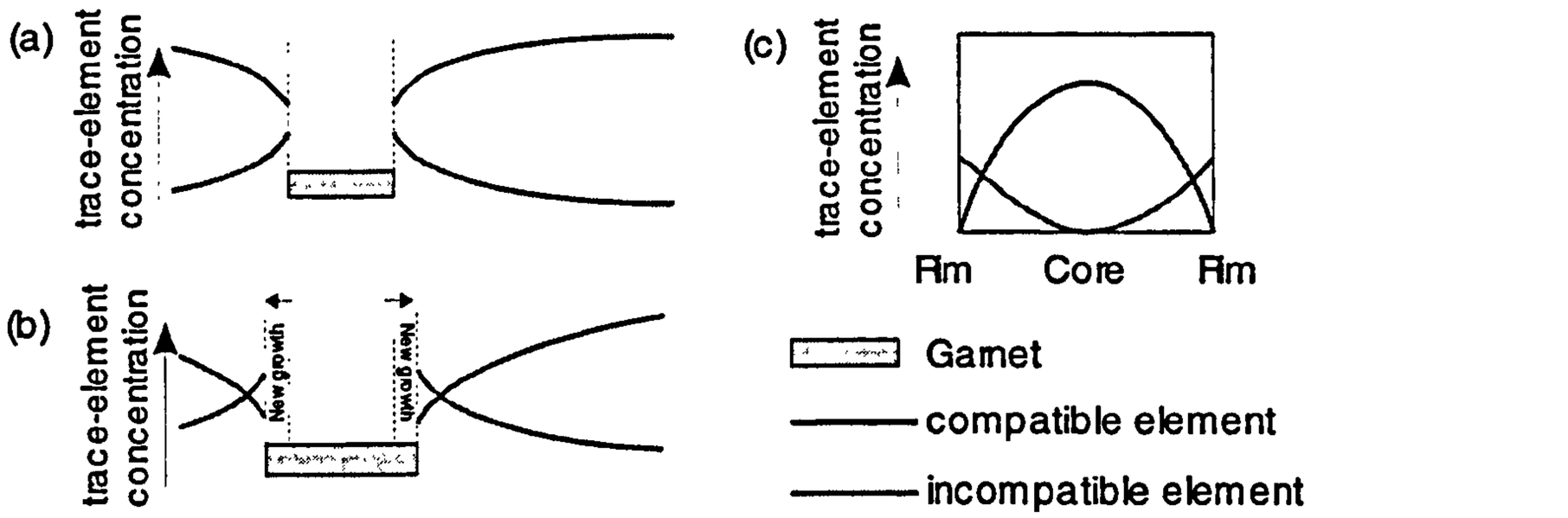


*Figure 7.2 Effect of slow intergranular diffusion on garnet growth. Schematic concentration gradients around a garnet. (a) Growth of the garnet depletes the area in compatible elements (red) and enriches it in incompatible elements (blue). (b) subsequent growth accentuates this effect. (c) possible schematic trace element zonation preserved in garnet. This effect may act on small time scales producing only limited or multiple periods of growth as shown in (c).*

This may apply equally to metamorphic and igneous systems although the controls on diffusion in a metamorphic matrix and a liquid melt will be different. In metamorphic rocks the intercrystalline diffusion will be a complicated function of, amongst other things, temperature, water content and fluid connectivity as measured by the dihedral angle – which themselves are functions of metamorphic reactions, rock type and other factors. Despite such complicated systematics, if this process dominates trace-element zoning in garnet, the *difference* in zoning from one trace-element profile to the next should be a function of the *relative* partition coefficients and element intercrystalline

diffusion rates.

*Intracrystalline diffusion controls*

If on the other hand intercrystalline diffusion is not the rate-limiting process no concentration gradients will develop around the growing garnet (Figure 7.3a). However, the growth of minerals with low intracrystalline diffusion rates will result in permanent changes to the EBC or melt (blue line Figure 7.3a). A well known example of this in metamorphic rocks is the depletion of the EBC in Mn due to garnet sequestering the Mn during growth. This process can be successfully modelled by Rayleigh fractionation (Hollister, 1966) and explains the common occurrence of bell-shaped Mn profiles in garnets at amphibolite facies. This process also occurs in igneous systems whereby the growth of minerals depletes the remaining melt in certain elements.

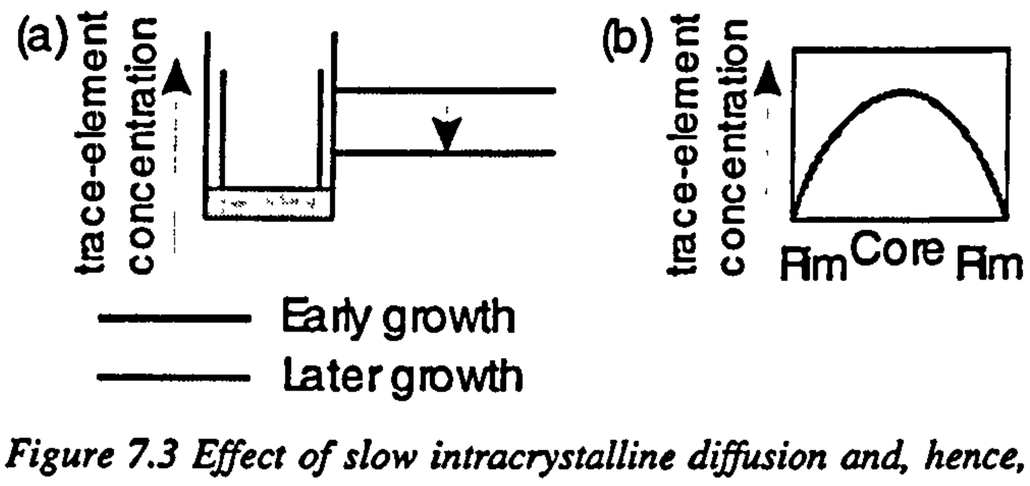


*Figure 7.3 Effect of slow intracrystalline diffusion and, hence, fractionation. No concentration gradients develop in the rock (flat lines in (a)). (a) growth of garnet or any other mineral depletes the EBC in elements from that shown in red to blue. (b) schematic profile produced in growing garnet as a result of fractionation. Unlike intercrystalline diffusion controls the area around the garnet is permanently reduced in the elements of interest and cannot reach higher concentrations during later growth. However, the two processes are not mutually exclusive.*

The extent to which the growth of a mineral affects the REE composition of the EBC will depend upon mass balance (concentration of the element times the proportion of the rock made up of that mineral) and the extent to which the mineral remains closed to the rest of the rock (a function of size and intracrystalline diffusion rates). As previously noted the bulk of REE reside in accessory phases in both felsic igneous and metamorphic systems and many of the accessory phases also have very low diffusion rates because the REE often form essential structural components to the minerals. Therefore, if this process dominates we would expect to see the same correlations between particular groups of elements as for changing mineral stability -

monazite (LREE, Th and P), apatite (MREE and P), zircon (HREE, Zr, U and Hf), ilmenite (MREE, Ti, Nb), allanite (LREE, Th). If these minerals are growing at the same time as garnet the net affect would always be to reduce concentrations in the growing garnet.

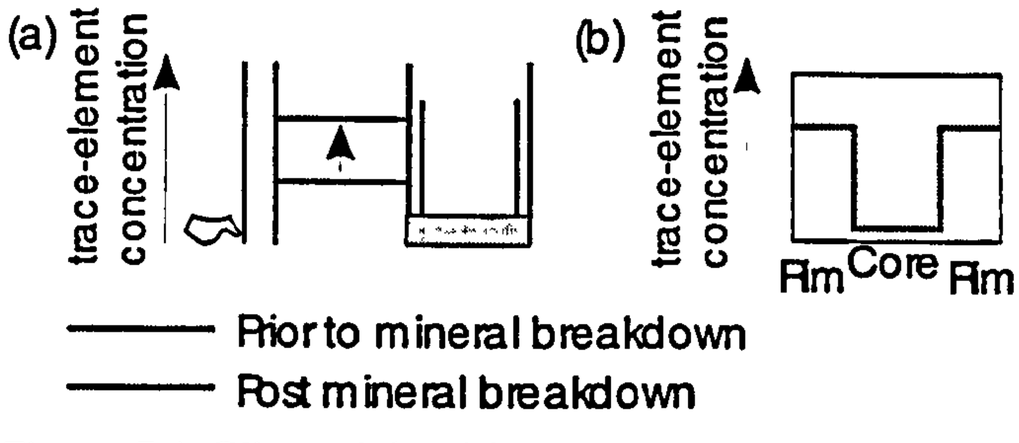


*Figure 7.4 Effect of breakdown of inherited minerals (a) breakdown of accessory phase results in an increase in the concentration of elements incorporated in it. (b) possible schematic profile produced by such an effect. A similar profile may be produced by the influx of elements in an open system.*

Alternatively if minerals that previously did not communicate with the system, because of slow intragranular diffusion, become open to the system the net effect would be to increase concentrations in the growing garnet (Figure 7.4). This may occur in metamorphic rocks due to the inheritance of metastable minerals (e.g. Parrish and Hodges, 1996). During the early stages of metamorphism their slow intracrystalline diffusion rates will result in no communication with the rest of the rock, however, during continued heating and burial they may break down suddenly enriching the EBC in the elements contained within them (Figure 7.4).

Given the compatibility of the HREE in garnet and the slow intracrystalline diffusion rates, we might expect the growth of the garnet to affect their concentrations in the EBC as is the case for Mn.

*Open-system behavior*

If the rock acts as an open-system and the trace-elements of interest are mobile then this could also contribute to trace-element zoning in garnet. Such zonation would be similar to the effect shown in Figure 7.4 except that the elements involved would be correlated with a particular fluid composition or to elements mobile during metamorphism.

*Intracrystalline diffusion*

Slow intracrystalline diffusion in garnet is a prerequisite for the preservation of zoning in any element and it is worth noting that all the non-equilibrium processes also require slow intracrystalline diffusion so that elements, once incorporated into the crystal lattice of garnet or other phases, are effectively removed from the EBC or melt. However, at high temperatures intracrystalline diffusion may result in changes to the original growth zoning, obscuring original information.

*Previous studies*

Non-equilibrium processes have been invoked previously to explain trace element zonation. For example, Hickmott et al. (1987) suggested zonation in garnets from Alpine assemblages exposed in the Tauern Window resulted from variations in the EBC (i) by open system behaviour or (ii) the breakdown of refractory minerals. Also Hickmott and Shimizu (1990) in a study of a garnet from a contact aureole in the Kwoiek Area, British Columbia suggested that Ti concentrations were buffered by accessory ilmenite which also contributed to changes in the EBC by its breakdown. In addition they suggested zoning in the HREE resulted from limited elemental supply to the garnet surface caused by rapid growth rates. A recent study by Schwandt et al. (1996) examined trace element zoning for garnets from the same lithology but varying metamorphic grade. They suggested that depletion of the EBC in REE by garnet or other minerals played a major role, resulting in high core concentrations and lower rim concentrations in garnet. This is qualitatively the same as the Rayleigh fractionation of Mn proposed by Hollister (1966). However this did not explain all the variations observed and they additionally suggested that elemental supply was limited by slow intergranular diffusion as well as crystal chemistry controls.

## 7.3 Aims of this study

Clearly the above processes are not mutually exclusive but the signatures of each process may be recognisable. The aims of this study are to examine the trace element zonation of garnets from the Garhwal Himalaya in order to understand the major controls. LA-ICP-MS was used as a quick, accurate and precise method for identifying the distribution of REE and trace-elements in three garnet samples from the Garhwal Himalaya which have also been used in chronometric studies. These included: (i) a garnet from a deformed leucogranitic melt (G31(1)); (ii) a zoned garnet from a medium-grade metamorphic rock (G9) and; (iii) a metamorphic garnet that has undergone high-temperature diffusional homogenisation (G96).

## 7.4 Experimental procedure

### 7.4.1 Laser ablation ICP-MS

Previous studies have shown the potential of LA-ICP-MS to obtain accurate and precise trace element analyses from garnet (Jenner et al., 1993; Fedorowich et al., 1995; Bea, 1996; Bea et al., 1997). Experiments for this study were carried out with an excimer laser system at ETH Zürich, (193 nm, ArF, Günther et al., 1997) linked to an ELAN 6000 ICP-MS (Perkin Elmer, Norwalk, USA). The output energy was set to 160 mJ allowing a pulse energy of 2.4 mJ for an 80 μm pit and a repetition rate of 10 Hz. The carrier gas flow flushing the ablation cell was 1.2 l/min helium mixed with 0.84 l/min argon behind the ablation cell (Günther and Heinrich, in prep.).

The principal advantage of LA-ICP-MS for this study is the spatial resolution available and the resultant ability to measure zonation on the scale of μm. The total measurement time for each analysis spot was 90 s, split into 30s gas blank acquisition and 60s data acquisition for the sample. Data collection runs were bracketed by analyses of NIST 612 glass as an external calibration standard and $SiO_2$ measured by electron microprobe was

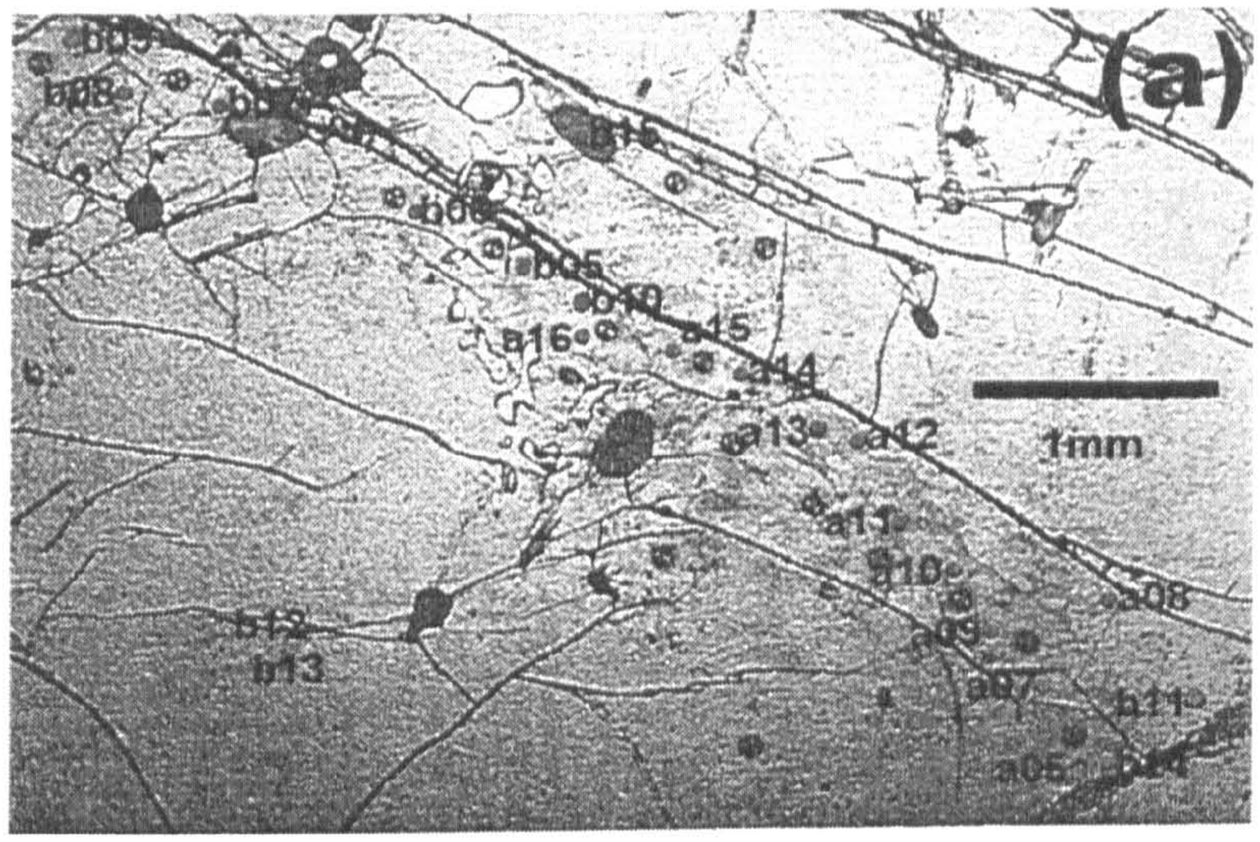


*Figure 7.5 Photomicrographs showing position of LA holes for (a) G31(1)a (b) G9a and (c) G96a. Major-element electron microprobe traverse approximately follows line of ablation hole. See Figure 6.3 for G31(1) and G9. Numbers refer to ablation analyses as summarised in Appendix G. In (b) green spots correspond to traverse of G9 perpendicular to that presented in Figure 7.8.*

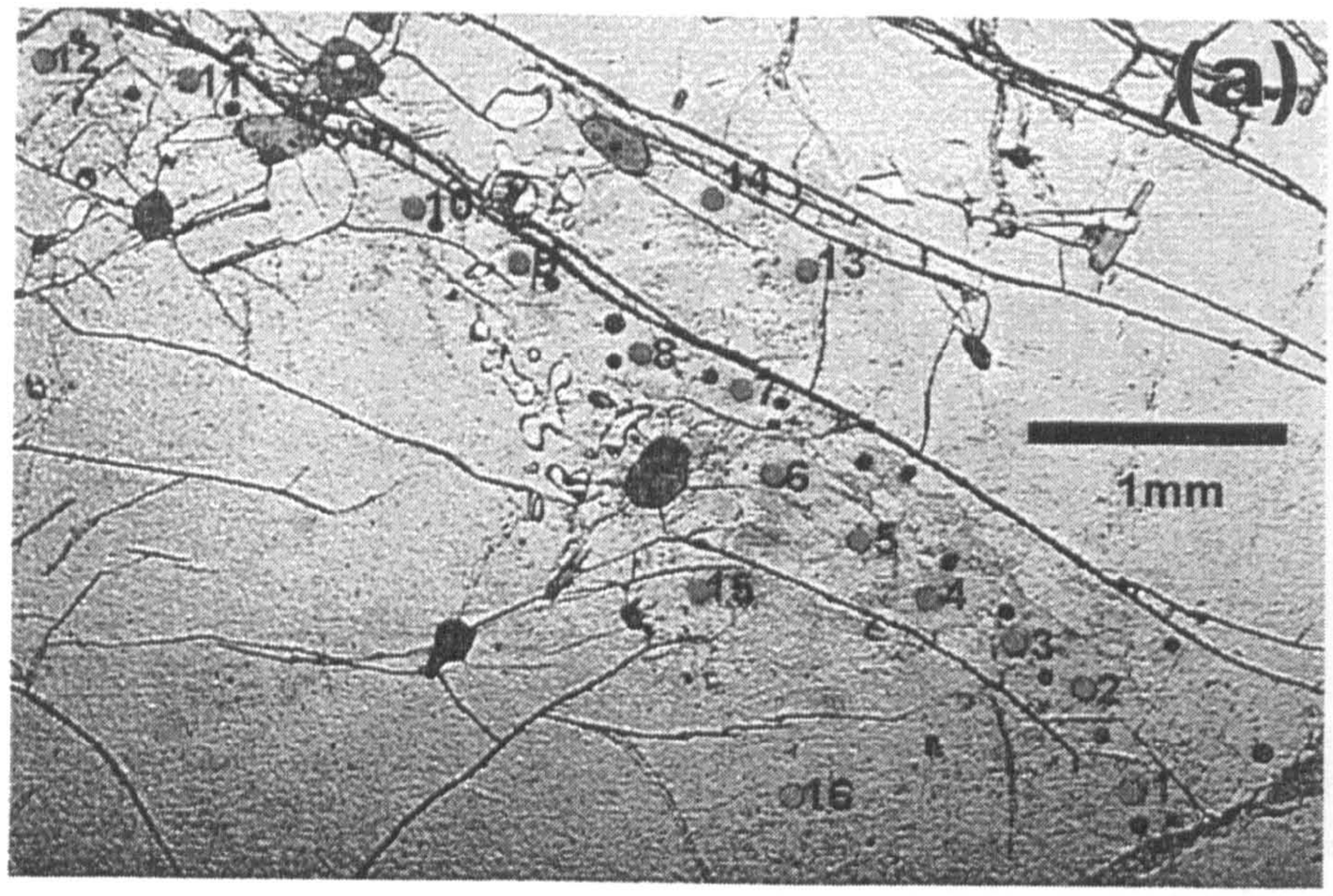



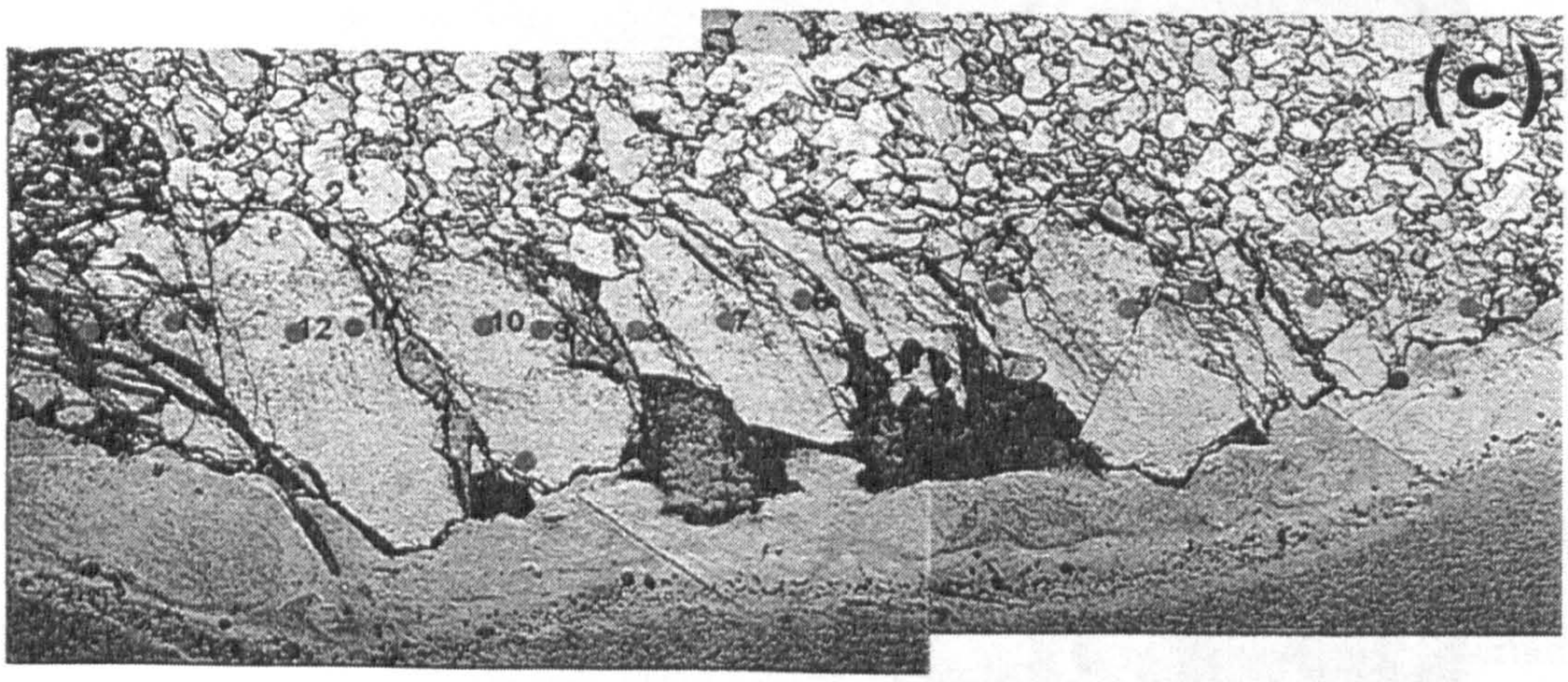


*Figure 7.6 Photomicrographs showing positions of LA holes for (a) G31(1)b (b) G9b and (c) G96b. For position of major-element electron microprobe traverse see Figure 6.3. Numbers refer to ablation analyses as summarised in Appendix G (see comments).*

used as internal standard. The data reduction procedure of Longerich et al. (1996) was used. The results were screened for inclusion effects to produce REE concentration analyses in profiles across the garnets.

All data presented here are above the limits of detection (LOD), calculated for each spot. Signal acquisition was optimised for $SiO_2$ and trace elements. Major-element data was collected in analogue mode but is not reliable and as such is not discussed further here.

## *7.5 Results*

Two sets of measurements were made. In the first, REE and other trace-elements were measured. Traverse pits are shown in Figure 7.5 along with the position of the electron microprobe traverse. For the second set of measurements the limits of detection were improved to allow a better analysis of the LREE: traverse pits are shown in Figure 7.6.

### 7.5.1 G31(1)

*Major-element profile (EMP)*

Sample G31(1) is from a small decimetre-sized leucogranite intruded at the base of the upper-High Himalayan Crystalline Series (HHCS) (see Chapter 2 and 5). The leucogranite has been deformed and shows late cross-cutting sillimanite growth. The garnet analysed by EMP and LA-ICP-MS was 5.2 mm in diameter (Figure 7.5a and Figure 7.6a) and shows smooth zoning in the major-elements ($Alm_{66-71}$, $Prp_{9-13}$, $Grs_{0-4}$ and $Sps_{13-24}$; Figure 7.7a). The increase in Ca at the edge of the garnet corresponds to a clear outer rim ~200 μm from the edge of the grain as shown on Figure 7.7c. The garnet contains inclusions of quartz, tourmaline, needles of rutile less than 5μm long and exhibits visible oscillatory zoning. The visible zoning correlates with the density of rutile needles within the garnet and may be a function of Ti concentration or trace-elements associated with them. The igneous origin of the garnet is confirmed by the

oscillatory zoning, negative Eu anomaly (see below) and high spessartine content typical of igneous garnets (e.g. Harris et al., 1992)

*LA-ICP-MS trace-element profiles*

Two traverses were carried out on this sample; G31(1)a and G31(1)b across the same garnet (Figure 7.5a and Figure 7.6a). Data for the major elements ($Al_2O_3$, MgO, $SiO_2$, CaO and FeO) and the REE and other trace elements ($TiO_2$, $Na_2O$, V, Cr, Rb, Sr, Y, Zr, Ba and U) were collected for G31(1)a. For G31(1)b only the REE, major elements ($Al_2O_3$, $SiO_2$ and CaO) and Y, U, $Na_2O$ were collected in order to improve the sensitivity for the REE. All the data is presented in Appendix G.

As expected Figure 7.7b shows that G31(1) has an HREE enrichment when compared to chondrite. Additionally Figure 7.7b and c show that there is a decreasing concentration from the core to just within the rim in the M-HREE. This general pattern is broken at the rim where there is a marked increase in the REE concentrations at the outer ablation pits (see Yb in Figure 7.7c). Additionally, the chondrite-normalised pattern for the outer rim is distinct from the chondrite-normalised pattern for the rest of the garnet: Dy-Yb display a concave pattern for all spots other than the outer-rim which has a convex pattern (Figure 7.7b). In more detail the profile across the garnet shows a slightly asymmetrical zonation pattern for REE without a close correlation between the MREE and HREE.

The other trace-elements vary in broadly the same way as the HREE with decreasing concentrations from core to rim (Figure 7.7d). However, they do not exactly parallel the REE elements and both Ti and Zr show a spiky variation across the garnet probably resulting from rutile needle concentration changes. Unfortunately the size of the visible zoning, which correlates with rutile needle concentration changes, is smaller than was sampled here and the variations cannot be directly correlated with the banding. U also shows large variations and a strong enrichment in the core and reaches absolute

concentrations of 8 ppm although the presence of the tiny rutile needles means that a contribution from them cannot be ruled out.

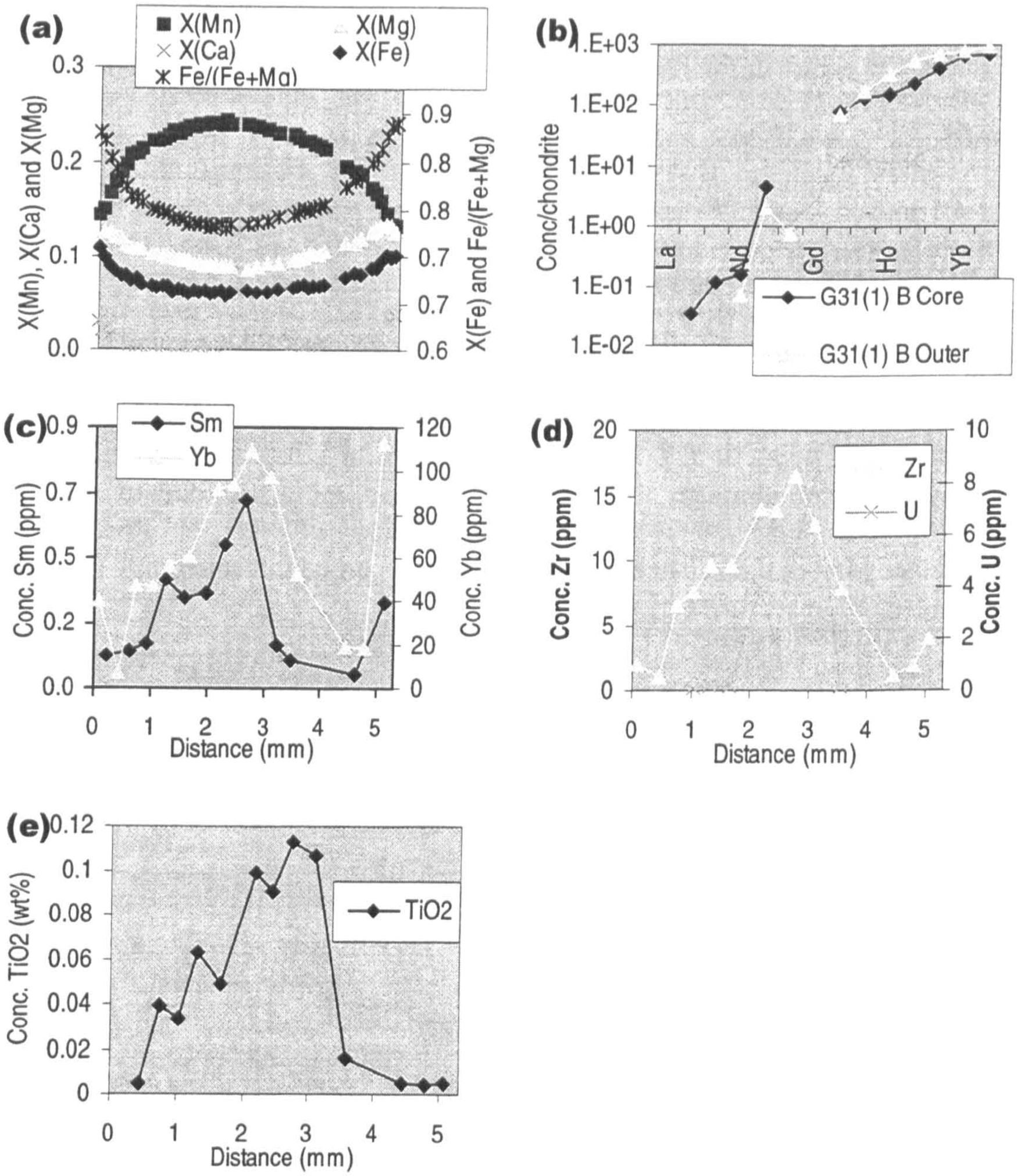


*Figure 7.7 Data for G31(1)a and b. All distances correspond to the traverse shown in Figure 7.5a and Figure 7.6a. (a) Major-element profile. The outer rim is marked by an increase in the Ca concentration and is inclusion free (b) Chondrite-normalised patterns for Core, Rim and Inner Rim analyses. Despite similar concentrations for the core and outer rim the patterns are significantly different. (c) Traverse data for Sm and Yb note the increase in REE concentrations as shown by Yb is symmetrical across the garnet and limited to the outer rim (d) Profile for Zr and U. (e) Profile for $TiO_2$*

### 7.5.2 G9

*Major-element profile (EMP)*

G9 is from a muscovite schist in the kyanite zone of the High Himalayan Crystalline. The garnet used for LA-ICP-MS and electron microprobe analysis from G9 is ellipsoidal and 4.1 mm in length (Figure 7.5b). Major-element zonation shows a bell-shaped Mn profile typical for this grade of garnet, an increasing Fe content from core to rim and a step in Ca and Mg near the rim ($Alm_{80-57}$, $Prp_{10-20}$, $Grs_{19-6}$ and $Sps_{25-10}$; Figure 7.8a). Rim equilibration pressure and temperatures were calculated using Thermocalc at 616±29°C and 9.5±1.3 kbar although this is likely to be a minimum due to the resorption of the outer parts of the garnet erasing previously recorded information.

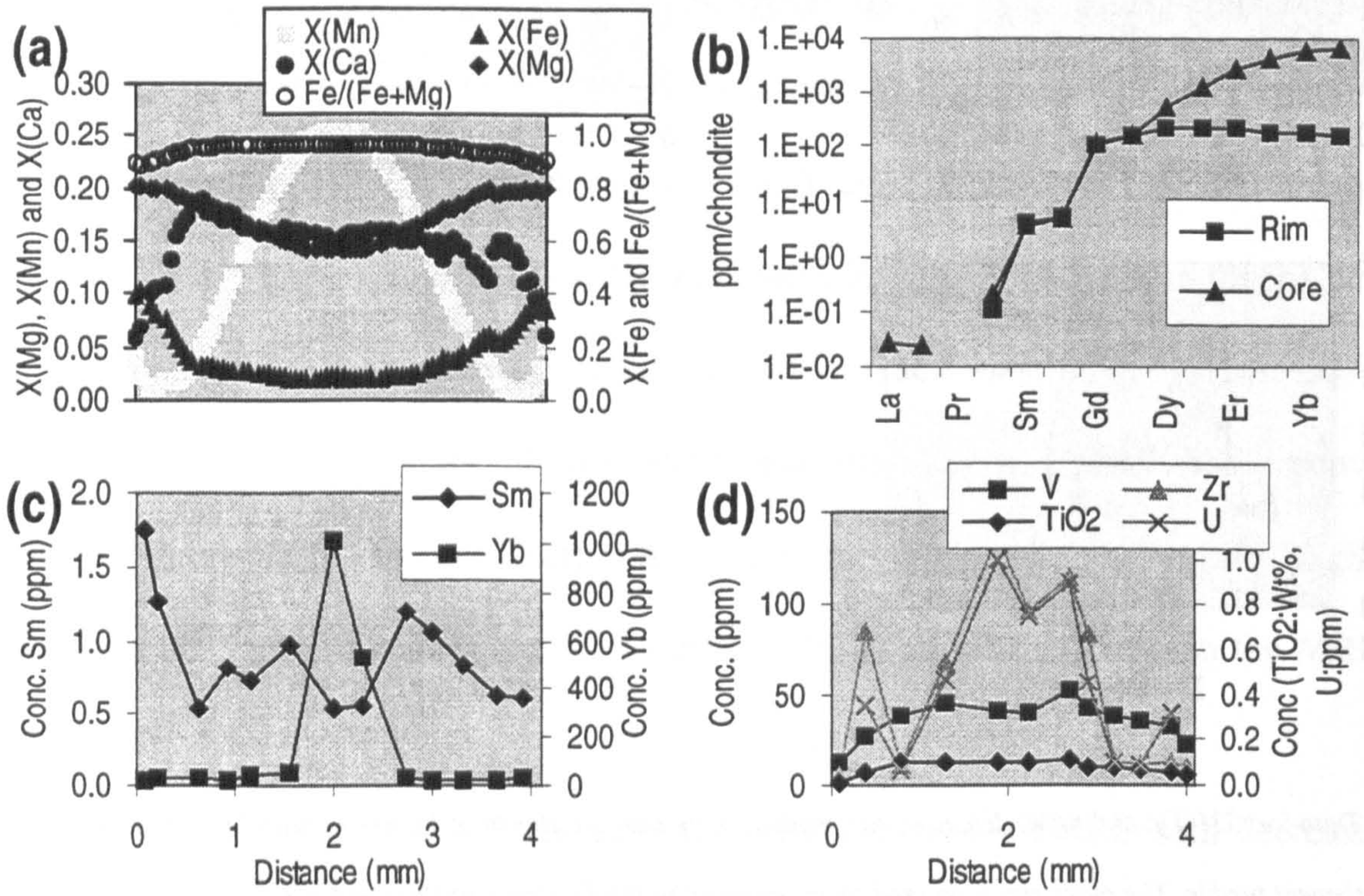


*Figure 7.8 G9. All distances correspond to the traverse shown in Figure 7.5b and Figure 7.6b. (a) Major-element profile. A smooth bell-shaped Mn profile with a slight increase in the rim, Ca is irregular and slightly asymmetrical but shows a strong decrease at the rim. (b) Chondrite-normalised REE plots. Note the smooth HREE enriched profile for the core and flattened HREE outside the core. (c) Selected REE showing the extreme zonation in the HREE from the core of the garnet outwards and the reverse zonation over the same length scale for the MREE (Sm) The profile outwards from this region displays more erratic behaviour (d) $TiO_2$, V, Zr and U profiles across the garnet.*

*LA-ICP-MS REE and trace-element profiles*

Two LA-ICP-MS traverses were carried out on a single garnet; G9a and G9b. Absolute concentrations of the REE and trace-elements were within error for G9a and G9b. Elements collected were the same as for G31(1)a and G31(1)b respectively and are summarised in Appendix G.

All REE analyses show HREE-enriched chondrite-normalised profiles relative to the M-LREE, however, the M-HREE patterns for different parts of the garnet are distinctly different (Figure 7.8b). This correlates with the concentration profiles in which very high HREE concentrations in the core of the garnet drop to much lower concentrations outside the two central analyses (e.g. Yb in Figure 7.8c). The large drop in concentration is shown by Lu-Dy, although to a decreasing extent. Tb and Gd have flat profiles across this section of the garnet but Nd, Sm and Eu show an inverse correlation with the HREE: a low concentration in the central two analyses increasing outwards from the core (e.g. Sm in Figure 7.8c). In summary the core is highly enriched in HREE and depleted in the LREE relative to the rest of the profile and the HREE decrease outside of the core is concomitant with an increase in the L-MREE. Outside of the central four analyses the patterns are more complicated with a pronounced asymmetry in the MREE as shown by Sm (Figure 7.8c).

Of the other trace-elements V and $TiO_2$ profiles show a broad pattern with a concentration decrease from the core outwards (Figure 7.8d). Zr and U have very similar profiles, distinctly different from all the other elements, with an initial increase in concentration outwards from the core and then a decrease towards the rim (Figure 7.8d).

### 7.5.3 G96

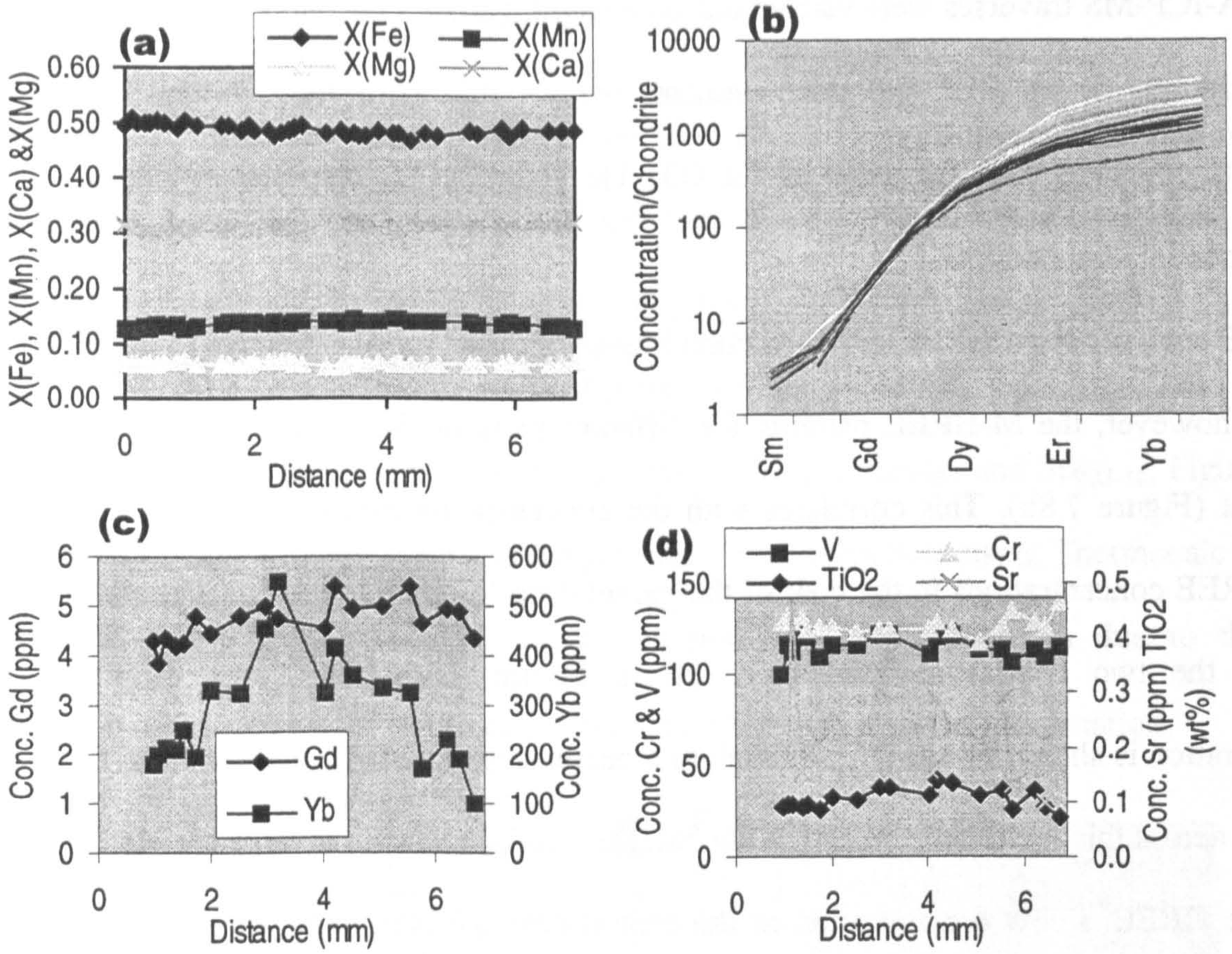


*Figure 7.9 G96a all distances correspond to the traverse shown in Figure 7.5c. (a) Major-element profile showing slight Mn zonation but flattened Mg, Fe and Ca. (b) Chondrite-normalised REE plots. (c) Gd and Yb zonation profile note the preservation of a more pronounced Yb profile than Gd (d) flat V, Cr and Sr concentration profiles with a slight zonation in $TiO_2$.*

*Major-element profile (EMP)*

Traverses were obtained on two garnets from the same upper-amphibolite grade pelitic schist in the HHC of the Garhwal Himalaya; G96a and G96b. Both garnets grew over a lithological boundary between a quartz vein and a biotite rich schist. Generally two-thirds of the garnet has a sieve texture with inclusions of quartz, feldspar, biotite and some small inclusions of zircon. The remaining third is near gem quality with only a few minute zircon inclusions. G96a was cut parallel to the schistosity through the poikioblastic section of the garnet and G96b was cut perpendicular to the foliation through the gem quality section which grew in the biotite schist. The electron

microprobe traverses for both garnets (Figure 7.9a and Figure 7.10a) show flat Fe, Mg and Ca profiles and slight Mn zonation indicating near complete homogenisation of the major-elements ($Alm_{48}$, $Prp_7$, $Grs_{31}$ and $Sps_{14}$) at elevated temperature. P-T estimates using Thermocalc (Holland and Powell 1985, Holland and Powell 1990) indicate rim equilibration temperatures and pressures of 652 ± 44 °C and 10.8 ± 1.2 kbar. Because significant homogenisation has occurred the temperature is probably only a minimum estimate.

*LA-ICP-MS REE and trace-element profiles*

REE and trace-elements for G96a and G96b were collected as for G31(1)a and b respectively and are summarised in Appendix G.

There is a HREE enrichment for all analysed points in both G96a and G96b (Figure 7.9b and Figure 7.10b) but, the absolute concentrations are greater in G96b and the zoning patterns are also different.

In G96a Gd-Lu show broadly symmetrical patterns with decreasing concentrations from core to rim and a more pronounced zonation for the heavier REE (Figure 7.9c). Ti (and Y, Zr) shows a similar gently decreasing concentration profiles to the REE elements (Figure 7.9d), whereas Cr and V show an almost flat profile with little variation across the garnet.

G96b also has an HREE-enriched chondrite-normalised pattern with stronger zoning in the HREE profile than for G96a. Figure 7.10c shows a large decrease around the central analyses of the traverse. However a broad pattern appears in which the HREE (Yb-Er) are concentrated in the core and decrease towards the rim and the M-LREE (Dy-Sm), with the exception of the central three analyses, show a broadly inverse pattern (Figure 7.10b). The variation between the two types of behaviour is smooth as shown by Ho which has a behaviour intermediate between the M-LREE and HREE (Figure 7.10d).

While both garnets in this sample show HREE enriched profiles the zonation patterns

are significantly different. This may be due to the position of the two traverses through the garnets and differences between garnets in the same sample locality; G96a is a traverse parallel to the lithological layering and G96b is a different garnet and cut perpendicular to the layering. This probably results in garnets with traverses through distinctly different portions and very different spatial controls on their zoning profiles.

The absolute concentration enrichment from core to rim for the HREE (e.g. Yb enrichment of 5.5 in G96a) is lower than other garnets presented here and lower than that found in other studies below the sillimanite zone (Hickmott et al., 1987; Schwandt et al., 1996) but similar to garnets from the sillimanite zone (Yb enrichment of 6.6 Schwandt et al., 1996). This may result from the partial homogenisation of initial HREE profile by intracrystalline diffusion at high temperature.

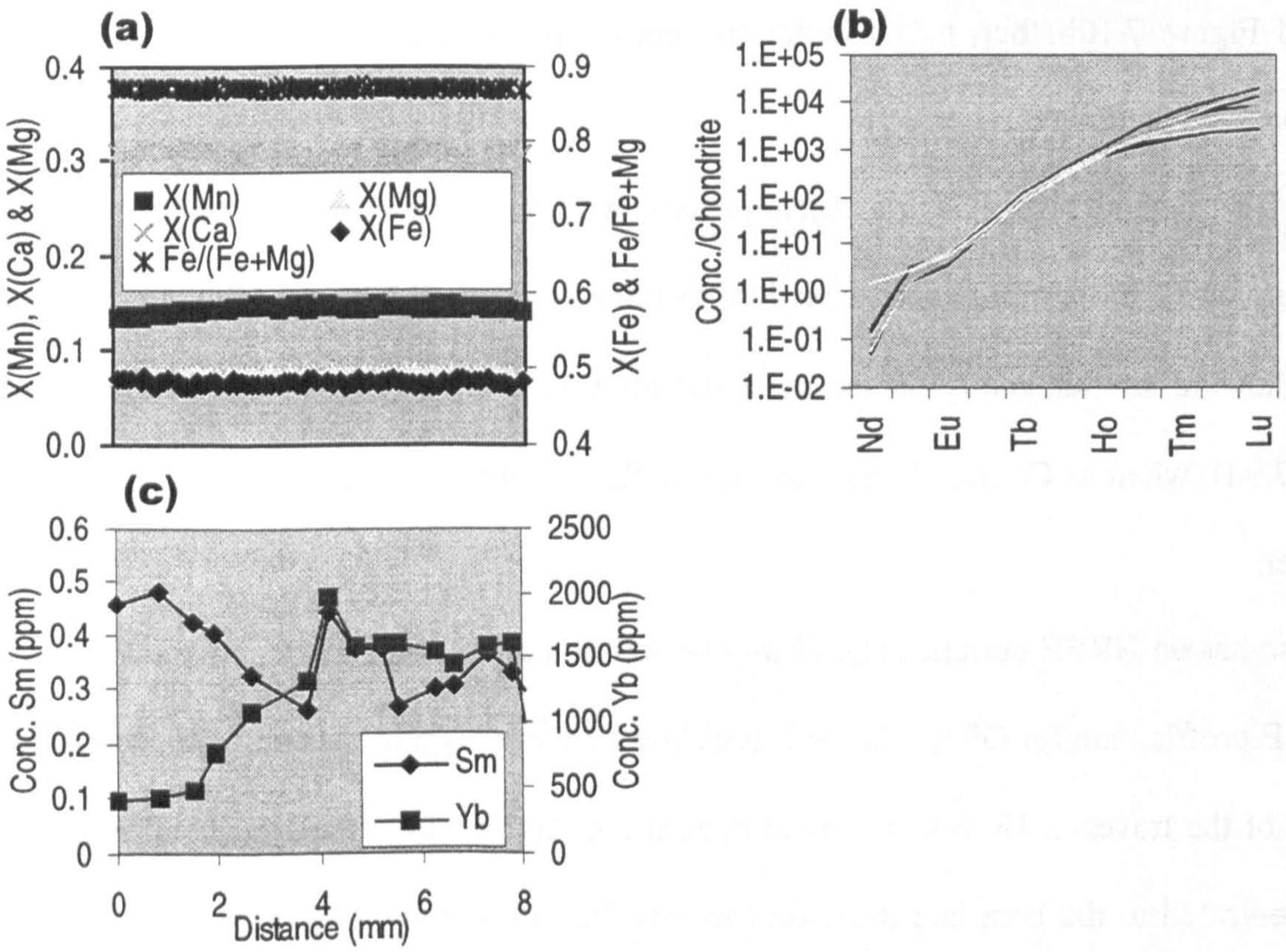


*Figure 7.10. G96b. All distances correspond to the traverse shown in Figure 7.6a. (a) Major-element profile showing slight Mn zonation but flattened Mg, Fe and Ca (b) Chondrite-normalised REE plots note the diverging HREE (Ho-Yb) concentrations (c) Sm and Yb profiles (d) Ho profile.*

## 7.6 Discussion

### 7.6.1 Major controls on zonation; fractionation and accessory phase growth

The major feature of the REE zonation patterns presented here is that of decreasing concentrations from core to rim for the M-HREE, which also applies to the LREE for G311). (Ayres (1997) showed that the bulk of the HREE in metamorphic rocks are contained in garnet, due to their high partition coefficients, the low diffusivity of REE in garnet and the large modal proportion of garnet (Figure 7.1). Thus it is likely that the growth of garnet will be the major control on the availability of HREE in the rock, and hence zonation patterns within the crystal. This has been proposed, and successfully modelled, for Mn in metamorphic rocks (Hollister, 1966) and results in the well-known bell-shaped Mn profiles typical of metamorphic garnets up to upper-amphibolite facies (Tracy, 1982). Modelling of the profile is a function of the partition coefficient of the element in question, the elemental concentration in the rock and the proportion of garnet grown. While the partition coefficient for Mn in garnet will vary with pressure and temperature this does not appear to have a noticeable effect and profiles can be successfully modelled using simple Rayleigh fractionation models, with $Kd_{grt:whole\ rock}$ of between 60-100 (Ayres and Vance, 1997). It may be reasonable to assume that the HREE will act in much the same way as Mn as they are also granatophile elements with high partition coefficients in garnet (Sisson and Bacon, 1992).

Garnet in sample G9 has a well developed "bell-shaped" Mn profile which can be successfully modelled by Rayleigh fractionation using the whole rock Mn concentration, a typical partition coefficient for Mn in pelitic rocks (Ayres and Vance, 1997) and a final garnet modal proportion consistent with that seen in thin section (Figure 7.11a). This can then be applied to the REE elements in sample G9 with Kd's calculated from the core concentration/bulk rock concentration for each REE and is

shown in Figure 7.11b. While the HREE profile is qualitatively similar to that shown by Yb in Figure 7.8c (i.e. a decreasing concentration) the extreme concentration decrease away from the core in the sample is not reproduced by such modelling. G31(1) and G96 also show a general decreasing HREE profile and while such a model accounts for the first order features of the HREE patterns in these three samples it cannot, on its own, account for the zonation of the HREE.

Figure 7.11 also shows the modelled profile for Sm which due to a Kd less than 1 results in an increase in concentration from core to rim: this effect would be more pronounced for the lighter REE elements due to lower partition coefficients. Such a modelled profile does not satisfy the observed Sm profile except perhaps in the central section of the garnet where Sm concentrations increase outwards from core to rim before becoming much more variable than can be accounted for by such a simplistic model. Clearly other processes are affecting the REE zonation profiles obtained for these samples and a clue to what these may be can be seen in G31(1).

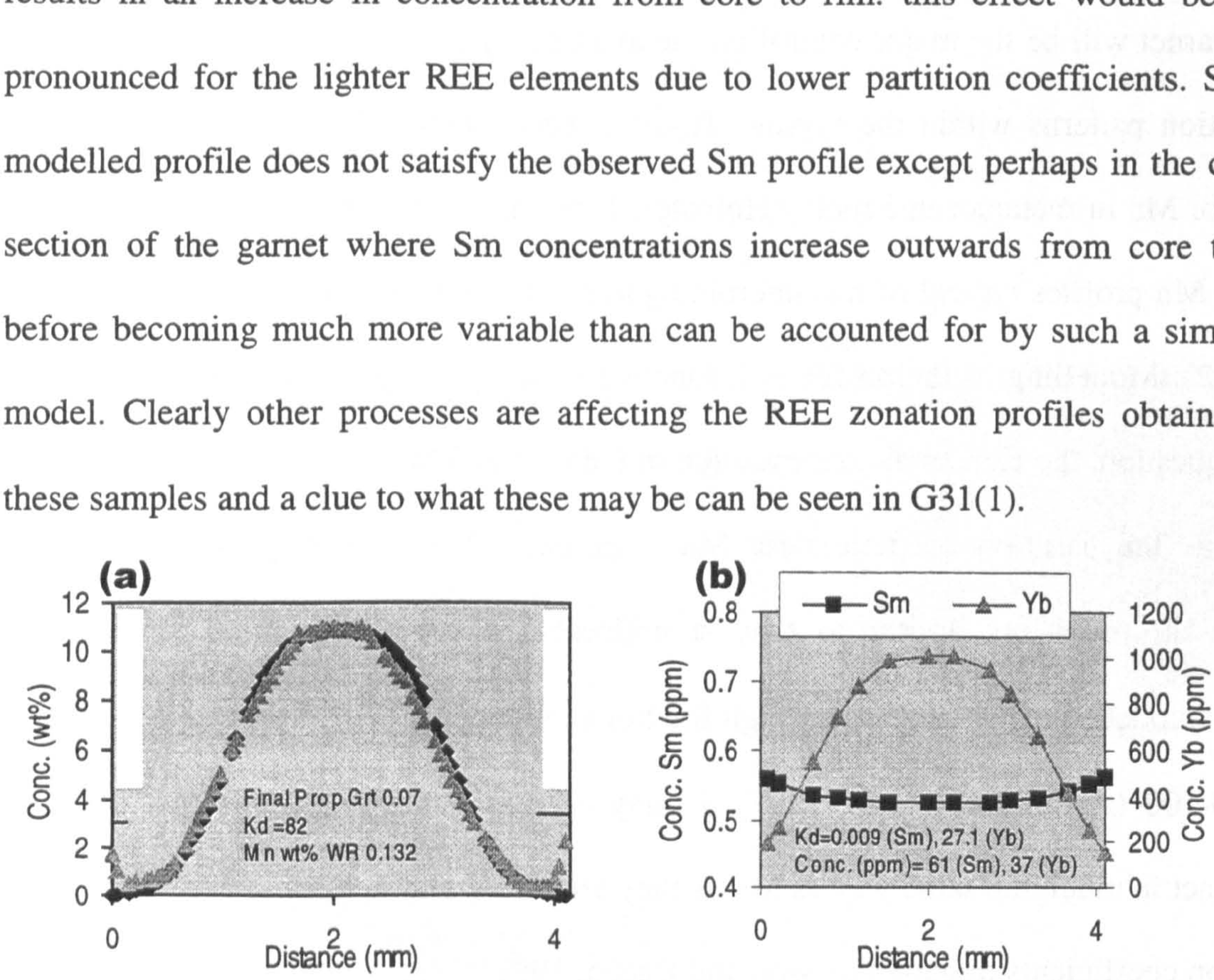


*Figure 7.11 G9 (a) modelled Rayleigh fractionation profile for Mn (black diamonds) compared to the true profile (green triangles). There is an extremely close fit for the bulk of the profile except at the rim due to back diffusion of Mn into the garnet. Modal proportion used to fit the curve correlates approximately with that seen in thin section. (b) modelled REE profiles. Kd obtained from core/bulk rock concentration ratio and the same modal proportion as for (a).*

In G31(1) all the REE elements measured show decreasing concentrations in a rimward direction with the exception of the final rim analyses (Figure 7.7c). Such an effect

cannot be produced for the L-MREE simply by fractionation of the system by garnet because garnet will not significantly deplete the EBC in these elements due to their extremely low concentrations in garnet. However, as shown by Ayres and Harris (1997) and Bea (1996), the bulk of the L-MREE in felsic and metamorphic rocks lie in the accessory phases and, specifically, apatite and monazite. If these minerals also have slow intracrystalline diffusion rates for the REE they will fractionate the L-MREE during growth, resulting in a decreasing concentration available for incorporation into the garnet. Garnet will act as a sensitive monitor to such fluctuations in L-MREE because incompatible elements will be incorporated into the lattice in direct proportion to their concentration in the EBC of the growing garnet (McKay, 1989). Thus qualitatively the decrease in the L-MREE can be attributed to the fractionation effect of the other minerals in the system.

*Figure 7.12 Photomicrograph of apatite crystals enclosed in feldspar in sample G31(1).*

Additionally, at any single moment in the growth of the garnet the effect of other phases growing within the EBC of the garnet will result in variations in the Kd for those REE, e.g. the growth of another accessory phase incorporating Sm into its lattice will result in a lower Kd for the garnet. To pinpoint which accessory phases produce such fractionation effects and changes in Kd the elements they contain need to be correlated with changes in the profiles seen in the garnet (see Intercrystalline diffusion controls). In the case of G31(1) a clue to this can seen in the chondrite-normalised patterns (Figure 7.7b). The patterns for all spots excluding the rim show a concave M-HREE pattern

between Tb and Yb, consistent with lower Kd's than would be normally expected from the generally smooth HREE-enriched patterns. The principle accessory phase to incorporate these elements is apatite (Figure 7.1). This may account for the change from concave to convex chondrite-normalised patterns at the rim of G31(1) (Figure 7.7b and c) because the termination of apatite crystallisation would result in an increase in the $Kd_{grt:melt}$. This hypothesis is further supported by the occurrence of apatite within feldspar crystals (Figure 7.12) suggesting that it was not forming during the final stages of crystallisation.

Returning to G9, the rapid changes in concentration seen from the core outwards also correlate with changes in the chondrite-normalised patterns (Figure 7.8b and c) and may be related to the effect of accessory phases. The changes in the chondrite-normalised patterns indicate the effect of accessory phases incorporating the REE from Tb-Lu. Changes in the partition coefficients between the garnet and its EBC are likely to be caused by other HREE enriched minerals such as zircon and apatite, thus the interpretation would be that during initial growth of the garnet it was the only stable phase incorporating HREE into its structure and hence had high partition coefficients resulting in high concentrations. However, shortly after garnet growth started the formation of a mineral such as zircon reduced the partition coefficients. The subsequent growth of both zircon and garnet resulted in the rapid fractionation of the HREE and the observed profile. This hypothesis is supported by the intriguing Zr zonation profile in garnet in which, from core to rim, the concentration is

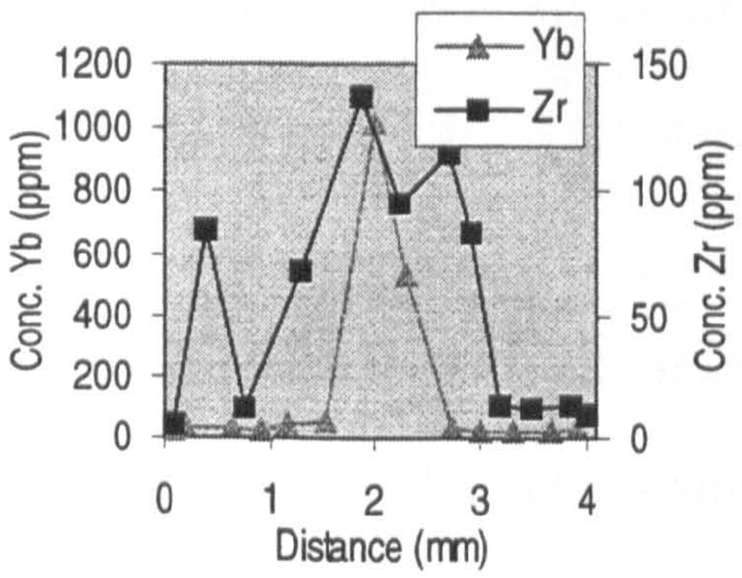


*Figure 7.13 Yb and Zr concentrations in G9 showing the increase in Zr concentration correlating with the high Yb concentrations followed by a decrease in Zr concentration and Yb.*

initially low, increases and then subsequently decreases correlating with the decrease in the HREE concentrations and changes in the REE chondrite-normalised pattern (Figure 7.13). This is qualitatively similar to igneous rocks whereby the concentration in Zr within the melt reaches a maximum prior to the initiation of Zr crystallisation and subsequent decrease in the concentration of Zr in the melt.

Clearly the first order features of the HREE, some of the LREE and some of the other trace-element zonation profiles in garnet can be accounted for by fractionation of the system by garnet and accessory phases with low intracrystalline diffusion rates. The phases responsible and their crystallisation history can potentially be constrained by their effect on the $Kd_{garnet:whole\ rock}$ as shown on chondrite-normalised patterns. However, more complicated features of the trace-element zonation in garnets (see G9 outside the central four analyses) which deviate from this simple model are more difficult to explain. Of the different additional controls some are discussed below.

### 7.6.2 Intercrystalline diffusion controls

An alternative process for producing decreasing concentrations of compatible elements is by limited elemental supply to the growing mineral either by slow intergranular diffusion or by interface kinetics (see Intercrystalline diffusion controls). Hickmott and Shimizu (1990) explored a simple model for intercrystalline diffusion control of element supply to a growing crystal. They showed that for any given rapid growth rate incompatible elements will increase in concentration in the crystal while compatible elements will decrease more rapidly than the incompatibles in much the same way as for fractionation (Figure 7.11). This is a possible alternative explanation for the variation in REE in the core of G9 (Figure 7.8c). Rapid growth associated with the core of the garnet would result, according to Hickmott and Shimizu (1990), in a rapid rimward decrease in the HREE component, as the HREE concentration around the garnet is depleted by strong partitioning into the garnet. On the other hand, the LREE

concentration in the growing garnet would increase as the concentration around the garnet increases due to the incompatibility of the LREE (Figure 7.2). This could qualitatively explain the rapid decrease in Yb with a concomitant, but slower, increase in Sm at the centre of G9 (Figure 7.8c). If this is the major control on the zoning of the REE it should also apply to other trace-elements as a function of their compatibility. Using the data of Sisson and Bacon (1992) Zr should be less compatible than V ($K_d$ Zr=0.4; V=7) and, therefore, if slow diffusion relative to growth rate is the major control Zr should increase in concentration and V should decrease more rapidly. Figure 7.14 shows that while there is an increase in Zr there is also a slight increase in V, followed by a subsequent decrease, more pronounced in Zr, rimwards. This simple analysis, however, depends on similar intercrystalline diffusion rates for the two elements, something which may vary with conditions.

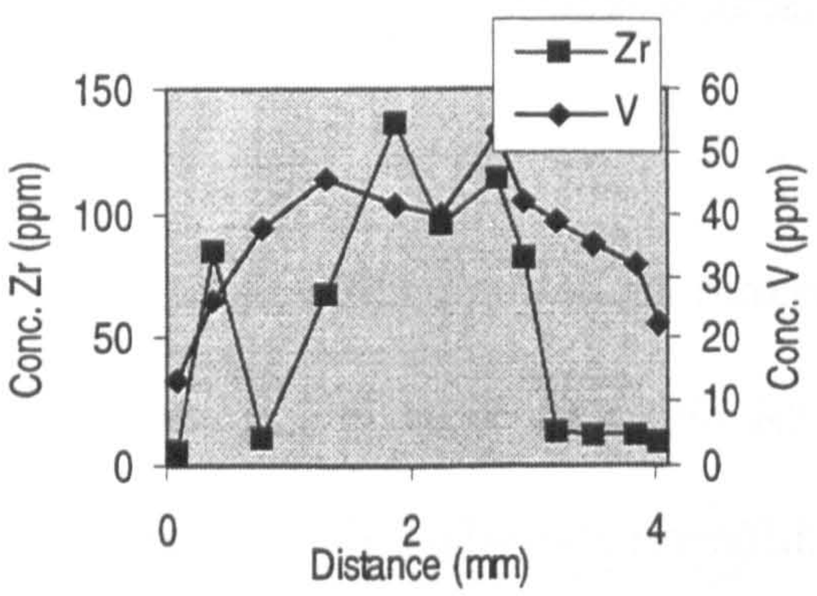


*Figure 7.14 G9 zonation in Zr and V.*

Without more accurate distribution coefficients for particular bulk compositions and knowledge of its mineral assemblage at the time of growth, it will remain difficult to quantitatively predict the behaviour of the REE and other trace elements. Nevertheless, if intercrystalline diffusion plays a dominant factor in the distribution of elements in metamorphic rocks it may account for some of the more puzzling features of the garnets studied here including the diverging patterns of LREE and HREE at the rims of G9 which show opposite patterns at either margin of the garnet. For example if the main source of REE and trace elements is in accessory phases and the intergranular diffusion is slow, the intergranular fluid around them will either be depleted or enriched in their associated elements. Thus the chemical gradients within the intergranular fluid will be spatially controlled by accessory phases during and

post growth.

### 7.6.3 Garnet crystal-chemistry

It has been suggested that the incorporation of Ca into the eightfold-coordinated site of garnet produces a more open structure that allows larger cations such as the LREE to enter into the garnet more easily (Schwandt et al., 1993). This has been confirmed by garnet/melt partition experiments carried out on pyrope-grossular garnets Westrenen et al. (Subm.) in which the partition coefficients for the LREE increase with increasing Ca content.

Unfortunately it is difficult to make comparisons between the garnets here given their different bulk compositions, histories and zonation patterns. However, major-element profiles can be compared to the REE profiles for individual garnets. For G31(1) a large increase in REE concentrations correlates with the Ca increase in the rim perhaps agreeing with this suggestion. However, the greatest increase in REE for G31(1) is for the elements Ho-Tm (Figure 7.7b and c) rather than the LREE. In the case of G9, which shows a large change in Ca content at the rim (Figure 7.8a), the REE do not show a consistent response and on one side of the garnet increase and on the other decrease. This suggests that Ca is not a major control on REE concentration although the usefulnees of the LREE data is limited by the extremely low concentrations of La, Ce, and Pr.

Schwandt et al. (1996) suggested that the Mn content in the garnet may enhance the compatibility of the HREE, based on the correlation between high HREE concentrations, high HREE/LREE ratios and high Mn concentrations garnet cores. The present data also show the same features with decreasing Mn and REE concentrations from garnet cores to rims. However the strong correlation observed between Mn and the HREE is in fact related to fractionation of the HREE by the garnet in a similar way as has been suggested for Mn (Hollister, 1966) and discussed above.

Although garnet crystal chemistry demonstrably plays a role in the incorporation of REE in some cases (Westrenen et al., Subm.) it is, at present, poorly understood. While it is possible that it contributes to zoning of REE and other trace-elements in the garnets studied here it demonstrably does not play the dominant role.

### 7.6.4 Post growth inter- and intragranular diffusion

All non-equilibrium processes and the preservation of trace element zoning require slow intragranular diffusion rates. The data presented here, however, allows some qualitative comments to be made. The almost homogenised garnet G96 shows slight Mn zoning (Figure 7.9a and Figure 7.10a) and also shows the preservation of HREE and LREE zoning. However, this zoning is significantly less extreme than for the other pelitic garnets: G9 and garnets below the sillimanite zone studied by Schwandt et al. (1996). Given the strong REE zonation of the garnets at lower metamorphic grades and the ubiquitous presence of major-element zoning of garnets up to sillimanite zone temperatures, it is likely that G96 was zoned, although it is impossible to know the form this took.

If this premise is true the reduction of the major-element zonation profile is probably due to high-temperature intragranular diffusion and is likely to have affected the REE as well. The preservation of a reduced HREE, LREE, Mn and trace-element profile as well as isotopic differences between different portion of the garnet (see Chapter 4) suggest that the diffusion of the REE is equal to or slower than the major-elements.

## *7.7 Conclusions*

The rim to rim traverses of all three garnets studied here show broadly decreasing concentrations of HREE and trace-elements from the core to rim caused primarily by fractionation of the EBC by garnet and/or other minerals.

In addition to fractionation of the EBC temporal changes in Kd appear to be preserved

in both G9 and G31(1) whereby changing accessory mineral stability has caused concentration changes. The effect this has on each of the REE is different and is easily visible in the chondrite-normalised patterns. The change in concave to convex pattern in G31(1) is attributed to the saturation of apatite in the melt and the change from sloping HREE to flat HREE in G9 is attributed to the combined effect of zircon growth and fractionation. Whilst this is not a unique interpretation in the case of G9 (initial rimwards decrease from the core may also be produced by slow intergranular diffusion relative to garnet growth rates) it is likely to be the dominant factor. Such features suggest that garnet can act as a monitor for metamorphic reactions involving minerals with high REE or trace-elements concentrations such as monazite, zircon, allanite. Indeed, a recent study of zircons from eclogites in the Bohemian massif showed that ~490 Ma zircons had HREE-enriched chondrite-normalised patterns and that ~340 Ma zircons had flat HREE chondrite normalised patterns. The HREE-encriched pattern was interpreted as magmatic in origin and the flat pattern as a result of growth in the presence of garnet, allowing these authors to correlate precise age information with petrogenetic processes (von Quadt and Gunther, 1999).

However, some of the more complicated and detailed features seen in the garnets studied here are still difficult to explain in these simple terms. There are many other processes which result in changes to the chemical system such as the breakdown of pre-existing minerals, fluid influx, fluid availability, oxidation state and other interrelated processes. Nevertheless, garnet can clearly act as a monitor of the chemical system during its growth and can, potentially, yield information about such processes.

One of the future potential aspects of the work presented here is the integration of thermobarometric and accessory phase stability information obtained from garnet zonation with the precise age information obtained from accessory phases. This could, potentially, provide tight constraints on the petrogenetic history of the rocks as well as

give insights into the microscopic processes occurring during mineral growth. However, further work is required to (i) obtain trace-element concentrations which can be unequivocally linked to individual accessory phase behaviour (such as Th and P) and (ii) improve the sensitivity of LA-ICP-MS to allow more precise analyses of the LREE which often occur in extremely low abundance in garnet.

# Chapter 8 - Conclusions

Simple numerical modelling of overthrust terrains has always assumed that thrust emplacement can be considered to be instantaneous (e.g. England and Thompson, 1984). This assumption largely arose from the observation that thrusting occurs at plate tectonic rates or a few 10's of cm per year, while the rate of heat transport in the crust is much slower. The thermal time constant of a block of crust that is 35 km thick and has a thermal diffusivity of $K$=1x10$^{-6}$ m$^2$/s is ~40 Ma: given by t=x$^2$/$K$. However, the considerable complexity in real orogens is unlikely to be modelled by such simple approaches for the following reasons. Firstly, Grasemann (1993) has shown that the simplification of instantaneous thrusting is not consistent with geologically feasible deformation rates. Secondly, the long history of thrusting seen in the Himalaya, albeit at different locations at different times, produces much more complicated thermal histories than simple one-dimensional models. Finally, the interactions between tectonic structures and heat is likely to be complicated in the continental crust because of the strong temperature control on crustal rheology (Ranalli, 1995) and the importance of the redistribution of heat producing elements during orogenesis (e. g. Jamieson et al., 1998).

In this thesis attempts have been made, combining garnet and accessory phase chronometry, thermobarometry, petrology and structural geology, to constrain the distribution of heat in the crust and relate that to the evolution of the Himalaya. Additionally, the systematics of the garnet isotopic and trace-element system have been studied to further understand the limitations to, and further uses of, garnet. The study of REE and other trace-elements in garnet also hint at the microscopic processes that control elemental distribution in metamorphic and igneous rocks, potentially opening new stores of information on the rock history.

In this chapter the PTt history of the HHCS will be placed in the context of the evolving

orogenic wedge from continental collision to the present day and a simple model proposed for the development of the exposed sequence, including the production of the well-studied Miocene crustal melts.

## 8.1 Pre-collision reconstruction

The development of northern India prior to continental collision is recorded in the sediments that presently lie to the north of the Himalaya. Sedimentary history began in the late Proterozoic, and recorded a late Pan-African orogenic event around the Cambrian-Ordovician boundary, probably related to the assembly of the Gondwana supercontinent (Gaetani and Garzanti, 1991). A record of this event is also preserved in the metamorphic history of the upper-HHCS in Garhwal with the preservation of Cambrian garnets (see additional text Argles et al., Subm.) and may be responsible for the granites intruded into the Harsil formation (Bhairongathi granite Stern et al., 1989). In addition Rb-Sr errorchrons for the metasediments of the HHCS in Garhwal suggest that much of the crystalline material currently exposed in the HHCS was deposited and partially metamorphosed in the early-Paleozoic (Ahmad et al., In press). This hypothesis is supported by the preservation of metamorphic assemblages in Ordovician granites in the Spiti region (Chawla et al., 1999) and suggests that the HHCS are part of the Indian shield on which the TSS were deposited.

The Lesser Himalaya, over which the HHCS are now emplaced, have distinct isotopic characteristics indicating a much older origin than the HHCS and suggesting that the HHCS does not represent the basement to the Lesser Himalaya (Parrish and Hodges, 1996; Ahmad et al., In press). However, the exact relationship between them – (either an unconformity (Parrish and Hodges, 1996) or a thrust relationship of distinctly different terrains (Ahmad et al., In press)) - is still unclear. The pre-Himalayan metamorphic history of the HHCS and the relationship between the Lesser Himalaya and the HHCS still remain poorly constrained. Answers to such questions may perhaps

be found in the Nanga Parbat syntaxis which appears to have many of the features of the HHCS but samples deeper crustal levels (Whittington, 1997).

Subsequent to the Pan-African event, a long period of epicontinental deposition in shallow seas lasted until the Early Permian, when a neo-Tethyan rift began to open between paleo-India and microcontinents to the north (Gaetani and Garzanti, 1991). The subsequent history can be subdivided into two megasequences. The first began with breakup in the Late Permian and lasted until the end of the Jurassic. The second started in the Early Cretaceous with the final detachment of India from Gondwana and the opening of the Indian Ocean, and ended with the onset of India-Eurasia collision in the Early Eocene (Gaetani and Garzanti, 1991). This long history built up a thick sequence (~6km) of sedimentary rocks on the northern passive margin of the Indian shield (Searle, 1987), extending to the north some 200-300 km (Steck et al., 1998) and now forming the TSS.

During northward subduction of the Tethys ocean floor beneath the Asian continent calc-alkaline batholiths formed to the north of the present Indus-Tsangpo suture (Debon et al., 1986).

The timing of the continental collision is still unclear partly due to confusion in the literature about the implications of the various geological features associated with collision (see Chapter 1). Nevertheless, suturing of India with Asia and the onset of intra-continental tectonics (i.e. deformation of continental material) appears to have occurred at ~49 Ma (Rowley, 1998) and is recorded in changes in the northward plate motion of India at that time (Patriat and Achache, 1984). The onset of such deformation appears to have occurred diachronously across the range with collision earlier in the northwest of the range due, in part, to the collision of microcontinental fragments with the Indian margin (Rowley, 1996).

With the continued northward motion of India a series of nappes developed in the TSS,

best studied in the Northwest Himalaya between Zanskar and the Sutlej valley (Steck et al., 1998). Perhaps the earliest metamorphic consequence of the collision is preserved in the Tso Morari nappe in which eclogites formed at ~55 Ma (de Sigoyer et al., 1999), in response to deep burial of portions of the northern Indian continental crust.

Subsequently deformation propagated southwards, possibly forming the migmatites in the upper-HHCS. Small melt segregations from this melting event at 40 Ma are only rarely preserved (or understudied) in the upper-HHCS (see Chapter 5). The initiation of melting so early in the development of the orogen may be due to the heating of some rocks above the wet-melting solidus at significantly lower temperatures than the Miocene melting event which formed the HHL by dehydration melting of the lower-HHCS (Harris et al., 1993). Alternatively, the production of the small melts at 40 Ma, and possibly some of the migmatites, was due to thrust emplacement and infiltration of fluids from the overthrust rocks in a manner similar to that envisaged by Le Fort et al. (1987) for the generation of the Miocene leucogranites. However, contrary to Le Fort et al. (1987) such thrusting would be located within the exposed HHCS of Garhwal rather than on the MCT.

Deformation and nappe development propagated southwards with thrust movements at ~40 Ma. Evidence for such thrust displacements is found in the response of rocks in the Harsil formation and HHCS of both Zanskar and Garhwal which show growth of garnet during burial and heating (see Chapter 4 and Vance and Mahar, 1998; Vance and Harris, 1999). That the unmetamorphosed equivalents of the HHCS are preserved within the Outer (i.e. southern) Lesser Himalaya by out-of-sequence thrusting is an intriguing possibility raised by the similar geochemical characteristics of the outer Lesser Himalaya and the HHCS/TSS (Ahmad et al., In press).

The thrusts and nappes responsible for this burial are still not well constrained but, simple calculations of the thermal response of the crust to burial suggest that it lies

around the level of the STDS, presently a normal fault (see Chapter 4 and Vance and Harris, 1999). In the Bhagirathi valley, Garhwal, this lies above the presently exposed Harsil formation and does not, therefore, coincide with the Jhala Normal Fault of Searle et al. (Subm.) and Metcalfe (1993).

The tectonic evolution of the HHCS at 40-25 Ma is still poorly understood but, the probably existence of intra-HHCS thrusting (Chapter 4) suggests that reorganisation of the HHCS may have occurred in this period. In the Harsil formation the youngest ages recorded suggest that metamorphism continued up to at least 29 Ma (Chapter 4). The youngest ages from Zanskar suggest that parts of the HHCS reached peak metamorphic conditions shortly after 27 Ma (Vance and Harris, 1999). It may be that intra-HHCS thrusting terminated metamorphism (via exhumation) in the upper-HHCS around ~27 Ma via exhumation - a possibility hinted at by the partial resetting of monazite in the Harsil formation at 27 Ma (Chapter 4). This would account for the observation that the age of peak metamorphism in the mid-levels of the HHCS predating anatexis by ~4-6 Ma, and for the prograde heating of the basal-HHCS as recently as ~24 Ma (Sample G9; Chapter 4).

Anatexis of the basal-HHCS, either following postulated intra-HHCS thrust emplacement at ~27 Ma or thrusting at ~40 Ma, could have coincided temporally with the movement on the MCT and STDS. Movement on these two faults led to much of the HHCS passing through ~350°C at 22-16 Ma (Metcalfe, 1993; Oliver et al., 1995; Searle et al., Subm.). The metamorphic history of the HHCS ends with this period but, the MCT was reactivated at ~8 Ma (Catlos et al., 1999) in Garhwal.

In summary there appears to be a continual evolution of thrusting from north to south in the orogen in accordance with the rules of forward thrust propagation characterised by the development of a number of nappes producing an orogenic wedge (Steck et al., 1998). The continued reorganisation of the orogenic wedge accounts for the observation

that temperatures were increasing within the basal-HHCS close to the time of movement on the MCT and suggests that heat sources other than thermal re-equilibration are not *necessarily* required for anatexis of the crust. Indeed it is only some 25 Ma after the onset of continental collision that rocks of appropriate composition attain temperatures sufficient for vapour-absent melting - the only type of melt reaction capable of producing significant melt volumes in the crust (Clemens and Vielzeuf, 1987; Thompson and Connoly, 1995).

## 8.2 A model for the structure, anatexis and exhumation of the HHCS

The data presented here emphasise the importance of very simple aspects of the thermotectonic evolution of the crust – namely the position of deformation in the crust (which rocks are buried or uplifted and when) and the response of the crust to burial via thermal equilibration and internal heat production (explored in the simplest thermal models). The similarity of the results obtained here with those of Zanskar suggest that they may be generally applicable to a larger portion of the Himalaya.

It seems reasonably clear that, in Garhwal at least, rocks in the basal HHCS were continuing to heat in response to overthrusting at times as late as 24 Ma. It is also clear that the rocks in this part of the orogen were sufficiently hot to melt at this time (Figure 4.8). In this case, the possibility arises that the Miocene melting in the Himalaya is not causally related to the MCT but that it preceded it (c.f. Nelson et al., 1996)and occurred as a result of heting in response to burial by thrusts above the MCT.

While, traditionally the MCT and STDS have often been thought of as causes of anatexis in the belt, it is possible that the causal relationship be the reverse provided that melting has occurred simply as a response to thickening of the crust. What effect would melting in the crust have on the tectonic and thermal evolution of the HHCS? This idea

will be explored further below in the light of the new data presented here on the thermal history of Garhwal.

Possible causal relationships between thrust and normal faulting, anatectic melting and exhumation in the Himalaya were explored by England and Molnar (1993a). Two of the proposed possible causes for normal faulting - a reduction in the horizontal normal stress applied at the boundaries and an increase in the surface height of the belt – do not correspond to any recorded changes at the time of leucogranite formation and movement on the MCT and STDS. However, the other two are of particular interest; (i) a reduction in the shear traction at the base of the belt and; (ii) a reduction in the strength of the material within the belt. Either of these two would result from anatexis of the HHCS and could contribute to the initiation of thrust faulting and normal faulting respectively. Indeed, a situation in which both thrust and normal faulting initiated as a response to melting within the crust would result in a positive feedback between the various processes: decreases in the strength of the crustal material produced by anatexis would increase thrust and normal fault movements and as a consequence increase melt production by a decompression process similar to that envisaged by Harris and Massey (1994).

Such a model, in which exhumation of the HHCS occurs by synchronous movement on the STDS and MCT, is similar to the extrusion models for the HHCS (Burchfiel and Royden, 1985; Kundig, 1989; Hodges et al., 1993; Jain and Manickavasagam, 1993; Grujic et al., 1996). In this respect the model presented below it is a combination of: (i) the development of a sequence of thrust nappes resulting in temperatures capable of melting the lower crust with; (ii) the extrusion model for exhumation of the HHCS.

A simple, schematic model for such a process is presented in Figure 8.1 in which it is assumed *a priori* that following development of a thick orogenic wedge from 50 Ma to ~23 Ma as outlined above, high temperatures and anatexis at deeper levels result in

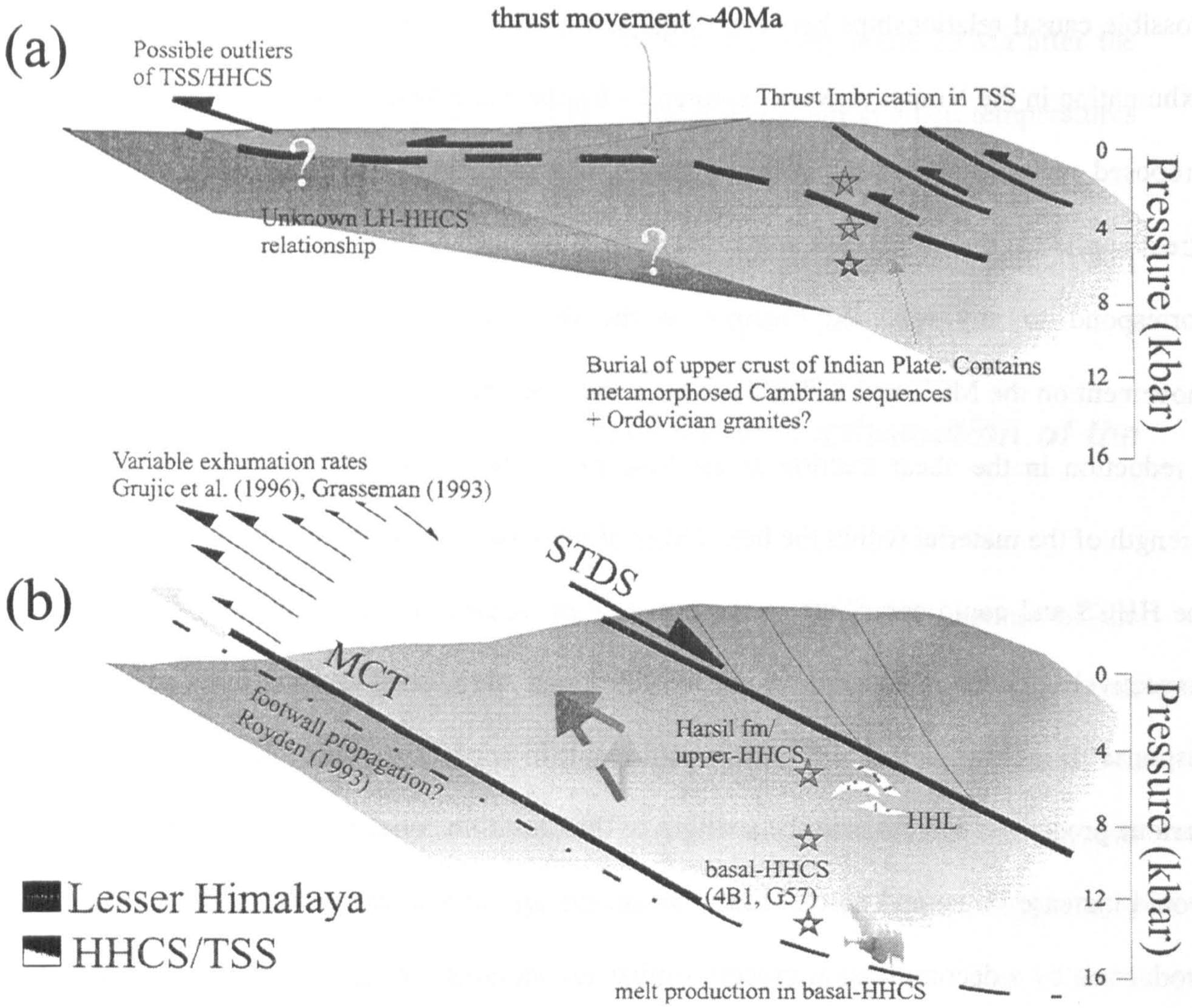


*Figure 8.1 Schematic model for metamorphism and anatexis of the HHCS. (a) Burial and metamorphism from 40 Ma to~25 Ma. Thrust imbrication of the TSS results in burial of different crustal levels represented by stars. From top to bottom: (i) parts of the TSS; (ii) metamorphosed Cambrian sequences of the upper- and mid-HHCS and (iii) mid- to lower-crustal rocks of the basal-HHCS. Continued thickening leads to (b) The crustal wedge attains temperatures sufficient for anatexis of the basal-HHCS and initiates thrusting in the basal-HHCS and collapse of the orogen along the STDS resulting in extrusion of the wedge in a manner similar to Grujic et al. (1996). The HHL are intruded into the upper levels of the HHCS previously metamorphosed and melted during the early stages of orogenesis. All samples undergo rapid tectonic denudation accompanied with erosional denudation resulting in variable exhumation as shown by the length of the arrows.STDS has normal fault displacement and there is a possible footwall propagation of the MCT as envisaged by Royden (1993).*

weakening of the crust, concentrating deformation in the lower crust. Extrusion, and exhumation, of the crustal material occurs with the hot semi-molten crust emplaced over cooler rocks in the hangingwall and as a result accreted to the footwall - the passage of the hot material over the base is enhanced by ensuring that footwall cooling of the high-temperature hangingwall is not significant. Additionally, reduction in the constitutive strength of the crust results in extensional movement on the normal faults above the HHCS, enhancing melt production by passing rocks into the melt field as envisaged by Harris and Massey (1994). Displacements along the STDS occur on the over-steepened thrusts which bound the HHCS to the north and may be lubricated by the emplacement of leucogranitic melts into the previously metamorphosed and still high temperature upper-HHCS.

The thermal effect from normal fault displacements would be felt first in the upper-HHCS and delayed in the basal-HHCS with the upper-HHCS entering into sillimanite and cordierite field, but not attaining sufficient temperatures for large-scale melting (for petrological observations see Chapter 3). This would also result in the overprinting of top-to-the-south shear fabrics, developed during the burial of the upper-HHCS, by top-to-the-north fabrics developed by the STDS.

The rapid exhumation would result in near-isothermal decompression of the basal-HHCS, which would bring the isotherms closer toghether (Whittington, 1995). This leads to the extremely rapid cooling through the Ar closure temperatures of biotite and muscovite as seen by Vance et al. (1998a) in Zanskar. Whether the basal-HHCS could produce the melt volumes at the appropriate times depends on the exhumation rates for the basal-HHCS and the timing of movement on the STDS. The rate of exhumation is controlled by movement on the MCT and STDS and will be a function of tectonic denudation, as a result of STDS normal movement, and enhanced erosional denudation, as a response to thrust movement on the MCT. Thus, in this model, movement of the

STDS and MCT are genetically linked to melting of the crust rather than the other way round.

## 8.3 Discussion

### 8.3.1 Comparison to other models

The critical feature in this model is the variable exhumation velocities across the HHCS driven by rheological variations related to temperature. Jamieson et al. (1998) used such temperature dependent rheology in a numerical thermo-mechanical model of orogenesis. In Jamieson et al. (1998) the model geometry is based on fixed lithospheric movements - a down going plate against a stationary mantle wedge - and displacements for rocks initially above 35 km are modelled assuming a temperature dependent rheology, isostatic compensation and altitude dependent erosion. The fixed lithospheric displacements result in two shears in the upper 35 km, one in the direction of plate motion and the other opposite to that (Figure 8.2a). Where this model deviates from the geometry seen in the Himalaya is that the principal shear leading to exhumation of the crustal rocks makes an acute angle with the plane of the suducting lithosphere (i.e. dips to the south) whereas in the Himalaya the principal shear makes an obtuse angle to the plane of the subducting lithosphere (i.e. dips to the north; Figure 8.2a). However, what is of interest here is not the geometries but the thermal response of crustal rocks to burial and exhumation and, specifically, the effect of a temperature-dependent rheology on orogenesis.

Expressly stated in the modelling is the interest in the redistribution of heat producing material during orogenesis and it is the various initial distributions of heat production that are explored. Two models, CE and CF, have initial conditions that closely correspond to those expected in the Himalaya (Figure 8.2a). In the first model, CE, high heat producing material is brought into the orogen along the down going plate. In

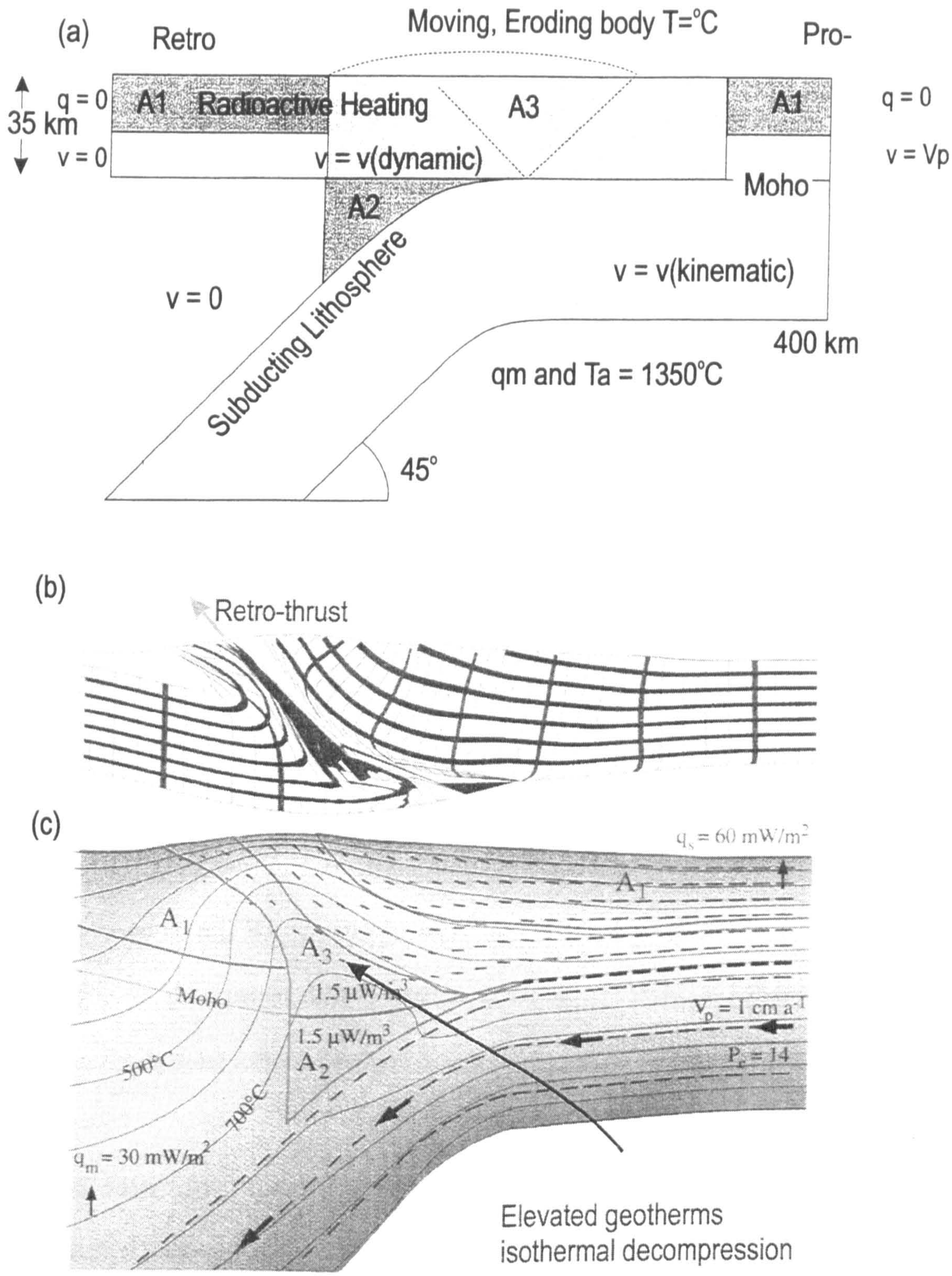


*Figure 8.2 (a) Model geometry for thermo-mechanical model of Jamieson et al. (1998). Heat production in different units A1, A2 and A3 was varied between models. Model CE modelled high heat production (1.5 µW/m$^3$) for unit A3 and model CF modelled high heat production in both A2 and A3; (b) results of model CF after 28 Ma showing the crustal deformation field. Grid lines and stripes were originally horizontal and vertical. Deformation is concentrated along the retro shear; (c) thermal structure of the orogen at 28 Ma. Note in particular the raised isotherms in the vicinity of the crustal shear.*

model CF crustal material is brought in as for model CE but, additionally, a block of high heat producing material lies in the lithospheric wedge simulating subducted sediments during the early stages of subduction. The first-order feature of both these models is the competition between cooling by the down-going plate and heating by high heat producing material, either in the crust or lithospheric wedge.

There are three features of these numerical models of particular relevance to the model proposed here. Firstly the deformation is highly concentrated along crustal shear zones due to the feedback between temperature and rheology – shears raise the geotherms resulting in weaker rocks and more concentrated deformation. Secondly, rocks above the shear zones undergo almost isothermal decompression over a period of several million years. Again this is a result of the dragging up of the isotherms and means that the thermal history of these rocks terminates in rapid near surface cooling as seen by Vance et al. (1998a). The more extreme effect melt would have on rock strength, as proposed here, would result in considerably enhanced exhumation rates along the shear zones and, potentially, catastrophic exhumation as envisaged by Hollister and Crawford (1986). Finally, rocks exhumed from the deepest levels in model CF (Jamieson et al., 1998) attain temperatures of 743°C at pressures consistent with metamorphism in the kyanite field. This is very similar to the conditions recorded in rocks from the basal-HHCS of Garhwal (Chapter 2 and 3).

On a smaller scale, exhumation along the MCT is closely approximated by the 2-D numerical model proposed by Grasemann (1993) in which an already hot crust is thrust over a ramp with a thermal conductivity contrast reducing heat loss to the footwall (See Chapter 3). The highest temperatures occur above the fault (see Chapter 3) and, as suggested by Grasemann (1993), such high temperatures, even in the absence of a melt, would considerably facilitate syn-metamorphic shearing in the HHCS. The need for a thermal conductivity contrast is potentially obviated as the accretion of the hot material

to the basal thrust would reduce cooling of the zones above.

### 8.3.2 Comparison to observations

The model proposed here can successfully account for many of the chronometric, petrologic and thermobarometric observations made both in Garhwal and across the orogen. Firstly the model requires that the development of the MCT and STDS occurs after the formation of the first melts. For the MCT present chronometric data suggests that this is exactly the situation seen in the Himalaya today. Studies show that the MCT was active at 22-20 Ma (Hubbard and Harrison, 1989; Metcalfe, 1993; Parrish, 1993; Coleman, 1998). Formation of the large leucogranite in Garhwal occurred earlier ~23 Ma (Searle et al., Subm.), as did melt formation at Manaslu (Harrison et al., 1999) and Makalu (Schärer, 1984) in Nepal.

The agreement between STDS movement and first leucogranite melt production, however, is less clear. The present data place, for example, STDS movement in Zanskar as early as 26 Ma (Inger, 1998) and crustal melts have been dated at 17-25 Ma (Searle, 1995). In the central Himalaya the constraints on the relative timing of melt production and STDS movement are inextricably linked as crosscutting or deformed leucogranites are used to time movement of the STDS (Edwards and Harrison, 1997; Searle et al., 1997b; Hodges et al., 1998; Harrison et al., 1999) and thus do not constrain earliest movement.

A specific test of the model is that the PTt evolution for the source regions should discriminate between different heat sources - such as shear heating from thermal relaxation. Given that the basal-HHCS of Garhwal are the likely source regions for the High Himalayan Leucogranites it is there that the best constraints on anatectic melting models are likely to lie. Unfortunately, neither of the two dated samples near the MCT presented in Chapter 4 clearly constrains the PTt path. From the prograde zoning in garnet, consistent with burial and heating, G57 indicates simple thermal relaxation for

the basal-HHCS but the growth period of the garnet is only constrained to between 36 Ma and 22 Ma. Garnet in 4B(1), on the other hand, is constrained to have grown at ~22 Ma but has unfortunately lost all prograde information due to high-temperature homogenisation.

Additionally the model predicts that some of the products of the melt produced during exhumation lie as some distance above the MCT and in the differentially deformed basal extruding wedge. In Nepal the MCT lies at the sillimanite isograd and there is evidence for leucogranite production at ~22 Ma within the MCT zone (Coleman, 1998). However, in Garhwal footwall rocks of the MCT only reach staurolite grade and there is no evidence for the formation of melts in the MCTZ or above. This may to some extent be the result of later reactivation of the MCT cutting across the original sequence in the orogen or, alternatively, the two sections are sampling different structural levels - Nepal being the deeper of the two. It is, therefore, in Nepal that there is the greatest likely hood of determining the relative age and chemistry of deformed leucogranites formed during the earliest stages of anatexis in the Miocene.

This model, as for the any model incorporating decompression, has the advantage of explaining the common observation of decompression textures in the upper levels of the HHCS (Brunel and Kienast, 1986; Hodges et al., 1992; Inger and Harris, 1992; Hodges et al., 1993; Davidson et al., 1997; Neogi et al., 1998; Vannay and Grasemann, 1998) - also be found in Garhwal in the form of cordierite rims on staurolite and kyanite assemblages within the Harsil formation. The structural reorganisation of the orogen maintained high temperatures throughout the crustal wedge until the synchrounous movement on the STDS and MCT. In this manner units near the top of the wedge passed into the low-P high-T field as shown by cordierite. Additionally petrological observations in Garhwal indicate that the basal-HHCS underwent its first phase of metamorphism in the kyanite field and that post-metamorphic deformation resulted in

deformation of primary kyanite and the development of secondary sillimanite or kyanite (Hodges and Silverberg, 1988). Indeed in Garhwal the extremely high temperatures and, most importantly, the age constraints at ~22 Ma obtained from samples near the MCT are consistent with such a model.

The model can qualitatively account for the PT data in the HHCS and some of the structural features associated with exhumation. As argued in Chapter 4 the isothermal temperature profile across the HHCS presented in Chapter 3 is partly the result of thrust imbrication within the HHCS, juxtaposing metamorphic rocks which attained peak conditions diachronously and at different places in the orogen. However, the basal-HHCS may be considered as a single unit. In Garhwal the thermal profile for the basal-HHCS has the highest temperatures *above* the MCT (Figure 3.2 and, Grasemann (1993)), as would be expected in this model and a feature also seen in other parts of the orogen (Hubbard, 1989).

## *8.4 Using garnet chronometry*

U-Pb, Sm-Nd and Rb-Sr garnet chronometry is hampered by the incorporation of U, Sm and Rb rich inclusions which will often mask the signal from the garnet lattice itself. If such minerals were in equilibrium with the garnet and surroundings during growth they will not affect the age data, although they may make it difficult to obtain. However, when such minerals are out of equilibrium with the garnet they may significantly alter the chronometric information obtained.

Given a knowledge of the relative concentrations of elements of interest in both inclusions and garnet the effect the inclusions have on chronometric information can be explored by simple modelling (Chapter 6). A complementary study to this is to separate the contributions from accessories and from the garnet itself by utilising the variable dissolution characteristics of the inclusions and garnet (Vance et al., 1998b). While both these approaches demonstrate that the Sm-Nd systematics of garnet are highly

susceptible to even tiny inclusions, the effect that they have will generally be to destroy all chronometric information. Whether the inclusions have affected chronometric information can be qualitatively constrained by comparing concentrations in the garnet lattice, inclusions and dissolved garnet. However, the best approach is by reproducing the chronometric results with a sufficient spread in parent/daughter ratios thus demonstrating that any inclusions, if present, were in isotopic equilibrium with the garnet during growth.

## *8.5 Potential for use of trace-element zoning*

The slow diffusion of elements in the garnet lattice permit its use as a chronometer and for the extraction of PT information from major-element zoning. These features also mean that trace-element zoning will be preserved, giving information on the chemistry of the surrounding rock during growth. Thus garnet may potentially record chemical changes in metamorphic rocks: e.g. fluid influxes, mineral stability changes or fractionation of the EBC. The work presented here suggest that in igneous and metamorphic garnets, up to upper-amphibolite facies conditions, fractionation of the effective bulk composition by minerals with low-intracrystalline diffusion rates is the primary control on trace-element zonation. The changes in REE concentrations across the garnet can be qualitatively linked to changes in the fractionating minerals due to their different chemical signatures.

While there are many additional potential causes for trace-element zonation, the relative significance of each them is, as yet, poorly understood. However, studies here demonstrate that LA-ICP-MS can be a powerful technique for the measurement of concentrations at the part-per-billion level in garnet. This technique may lead to new sources of information on chemical processes in metamorphosing and crystallising rocks.

# References


Ague, J. J., 1991. Evidence for major mass transfer and volume strain during regional metamorphism of pelites. Geology, 19: 855-858.

Ahmad, T. et al., In press. Isotopic constraints on Himalayan thrust systems; evidence from the Garhwal Himalaya. .

Albarede, F. and Bottinga, Y., 1972. Kinetic disequilibrium in trace element partitioning between phenocrysts and host lava. Geochimica and Cosmochimica Acta, 36: 141-156.

Argles, T. W., Prince, C. I., Foster, G. L. and Vance, D., Subm. New garnets for old: cautionary tales from young mountain belts. .

Auden, J. B., 1937. The structure of the Himalaya in Garhwal. Rec. Geol. Surv. India, 71: 407-433.

Ayres, M. W., 1997. Trace-element behaviour during high-grade metamorphism and anatexis of the Himalayas, Open University, Milton Keynes, 354 pp.

Ayres, M. and Harris, N., 1997. REE fractionation and Nd-isotope disequilibrium during crustal anatexis: Constraints from Himalayan leucogranites. Chemical Geology, 139(1-4): 249-269.

Ayres, M. and Vance, D., 1997. A comparative study of diffusion profiles in Himalayan and Dalradian garnets: Constraints on diffusion data and the relative duration of the metamorphic events. Contributions to Mineralogy and Petrology, 128(1): 66-80.

Ayres, M., Harris, N. and Vance, D., 1997. Possible constraints on anatectic melt residence times from accessory mineral dissolution rates: an example from Himalayan leucogranites. Mineralogical Magazine, 61: 29-36.

Bahuguna, V. K. and Saklani, P. S., 1988. Tectonics of the Main Central Thrust in Garhwal Himalaya, U. P. J. Geol. Soc. India, 31: 197-209.

Barbey, P., Brouand, M., LeFort, P. and Pecher, A., 1996. Granite-migmatite genetic link: The example of the Manaslu granite and Tibetan Slab migmatites in central Nepal. Lithos, 38(1-2): 63-79.

Bea, F., 1996. Residence of Ree, Y, Th and U in Granites and Crustal Protoliths - Implications For the Chemistry of Crustal Melts. Journal of Petrology, 37(3): 521-552.

Bea, F., Montero, P., Garuti, G. and Zacharini, F., 1997. Pressure-dependence of rare earth element distribution in amphibolite- and granulite-grade garnets. A LA-ICP-MS study. Geostandards Newsletter-the Journal of Geostandards and Geoanalysis, 21(2): 253-270.

Beck, R. A. et al., 1995. Stratigraphic evidence for an early collision between northwest India and Asia. Nature, 373: 55-58.

Berman, R. G., 1988. Internally consistent thermodynamic data for minerals in the system $Na_2O$-$K_2O$-CaO-MgO-FeO-$Fe_2O_3$-$Al_2O_3$-$SiO_2$-$H_2O$-$CO_2$. Journal of Petrology, 29: 445-452.

Besse, J. et al., 1984. Palaeomagnetic estimates of crustal shortening in the Himalayan thrusts and Zangbo suture. Nature, 311: 621-626.

Bilham, R. et al., 1997. GPS measurements of present-day convergence across the Nepal Himalaya. Nature, 386(6620): 61-64.

Blundy, J. D. and Wood, B. J., 1991. Crystal-chemical controls on the partitioning of Sr and Ba between plagioclase feldspar, silicate melts, and hydrothermal solutions. Geochemica et Cosmochimica Acta, 55: 193-209.

Blundy, J. D. and Wood, B. J., 1994. Prediction of crystal-melt partition coefficients from elastic moduli. Nature, 372: 452-454.

## References


Bowtell, S. A., Cliff, R. A. and Barnicoat, A. C., 1994. Sm-Nd isotopic evidence on the age of eclogitization in the Zermatt-Saas ophiolite. Journal of Metamorphic Geology, 12: 187-196.

Brouand, M., Banzet, G. and Barbey, P., 1990. Zircon behaviour during crustal anatexis - Evidence from the Tibetan Slab migmatites (Nepal). Journal of Volcanology and Geothermal Research, 44(1-2): 143-161.

Brueckner, H. K., Blusztajn, J. and Bakunczubarow, N., 1996. Trace-Element and Sm-Nd Age Zoning in Garnets From Peridotites of the Caledonian and Variscan Mountains and Tectonic Implications. Journal of Metamorphic Geology, 14(1): 61-73.

Brunel and Kienast, 1986. Étude pétro-structurale des chevauchements ductile himalayens sur la transversale de L'Everest-Makalu (Népal oriental). Canadian Journal of Earth Sciences, 23: 1117-1137.

Burchfiel, B. C. and Royden, L. H., 1985. North-south extension within the convergent Himalayan region. Geology, 13: 679-682.

Burchfiel, B. C. et al., 1992. The south Tibet detachment system, Himalayan orogen: Extension contemporaneous with and parallel to shortening in a collisional mountain belt. The geological society of America, Special paper 269.

Burg, J. P. and Chen, G. M., 1984. Tectonics and structural zonation of southern Tibetan China. Nature, 311(219-233).

Burg, J. P. et al., 1984. Deformation of leucogranites of the crystalline Main Central Thrust Sheet in southern Tibet (China). Journal of Structural Geology, 6: 535-542.

Burton, K. W. and O'Nions, R. K., 1991. High-resolution garnet chronometry and the rates of metamorphic processes. Earth and Planetary Science Letters, 107: 649-671.

Burton, K. W. and O'Nions, R. K., 1992. The timing of mineral growth across a regional metamorphic sequence. Nature, 357: 235-238.

Burton, K. W., Kohn, M. J., Cohen, A. S. and O'Nions, R. K., 1995. The relative diffusion of Pb, Nd, Sr and O in garnet. Earth and planetary Science Letters, 133: 199-211.

Butler, R. W. H., Harris, N. B. W. and Whittington, A. G., 1997. Interactions between deformation, magmatism and hydrothermal activity during active crustal thickening: A field example from Nanga Parbat, Pakistan Himalayas. Mineralogical Magazine, 61(1): 37-52.

Carlson, W. D., 1989. The significance of intergranular diffusion to the mechanisms and kinetics of porphyroblast crystallisation. Contributions to Mineralogy and Petrology, 103: 1-24.

Carswell, D. A. and O'Brien, P. J., 1993. Thermobarometry and tectonic significance of high pressure granulites: examples from the Moldanubian zone of the Bohemian Massif in Lower Austria. Journal of Petrology, 34: 427-459.

Catlos, E. J. et al., 1997. Further evidence for Late Miocene reactivation of the Main Central Thrust (Nepal Himalaya) and the significance of the MCT-I. EOS, 78.

Catlos, E. J., Harrison, T. M., Searle, M. P. and Hubbard, M. S., 1999. Evidence for Late Miocene reactivation of the Main Central Thrust: From Garhwal to the Nepali Himalaya. Terra Nostra, 2(14th Himalaya-Karakoram-Tibet workshop, Kloster Ettal, Germany): 20-22.

Chawla, H. S., Marquer, D., Kramers, J. D. and Villa, M. I., 1999. When was the "inverted metamorphism" in the HHC formed? Structural and petrological analyses of the Kinnar Kailas granite, Sutlej Valley, India. Journal of Conference abstracts, 4(1): 52.

Christensen, J. N., Rosenfeld, J. L. and DePaolo, D., 1989. Rates of tectonometamorphic processes from rubidium and strontium isotopes in garnet. Science, 244: 1465-1469.

Clemens, J. D. and Vielzeuf, D., 1987. Constraints on melting and magma production in the crust. Earth and Planetary Science Letters, 86: 287-306.

Coghlan, R. A. N., 1990. Studies in diffusional transport: Grain boundary transport of oxygen in feldspars, diffusion of oxygen, strontium and the REEs in garnet and thermal histories of granitic intrusions in South-Central Maine using oxygen isotopes. Ph.D. Thesis, Brown University, Providence, Rhode Island.

Cohen, A. S., O'Nions, R. K., Siegentheler, R. and Griffin, W. L., 1988. Chronology of the pressure-temperature history recorded by a granulite terrain. Contributions to Mineralogy and Petrology, 98: 303-311.

Coleman, M. E., 1996. Orogen-parallel and orogen-perpendicular extension in the central Nepalese Himalayas. GSA Bulletin, 108(12): 1594-1607.

Coleman, M. E., 1998. U-Pb constraints on Oligocene-Miocene deformation and anatexis within the Central Himalaya, Marsyandi Valley, Nepal. American Journal of Science, 298: 553-571.

Coward, M. P. and Butler, R. W. H., 1985. Thrust tectonics and the deep structure of the Pakistan Himalaya. Geology, 13: 417-420.

Dahlen, F. A. 1990. Noncohesive critical Coulomb wedges: An exact solution. Journal of Geophysical Researches., 44, 33-50.

Davidson, C., Grujic, D. E., Hollister, L. S. and Schmid, S. M., 1997. Metamorphic reactions related to decompression and synkinematic intrusion of leucogranite, High Himalayan Crystallines, Bhutan. Journal of Metamorphic Geology, 15(5): 593-612.

de Sigoyer, J. et al., 1999. Timing of HP-LT Tso-Morari evolution: from continental subduction to collision in NW Himalaya. Terra Nostra, 2(14th Himalaya-Karakoram-Tibet workshop, Kloster Ettal, Germany): 141-142.

Debon, F., Le Fort, P., Sheppard, S. M. F. and Sonet, J., 1986. The four plutonic belts of the Transhimalaya-Himalaya: a chemical, mineralogical, isotopic, and chronological synthesis alaong a Tibet-Nepal section. Journal of Petrology, 27(1): 219-250.

Deniel, C. et al., 1987. Isotopic study of the Manaslu granite (Himalaya, Nepal): inferences on the age and source of Himalayan leucogranites. Contributions to Mineralogy and Petrology, 96: 78-92.

DeWolf, C. P. et al., 1996. The role of inclusions in U-Pb and Sm-Nd garnet chronology: Stepwise dissolution experiments and trace uranium mapping by fission track analysis. Geochimica et Cosmochimica Acta, 60: 121-134.

Dezes, P. J. et al., 1999. Synorogenic extension: Quantitative constraints on the age and displacement of the Zanskar shear zone (northwest Himalaya). Geological Society of America Bulletin, 111(3): 364-374.

Dodson, M. H., 1973. Closure temperature in cooling geochronological and petrological systems. Contributions to Mineralogy and Petrology, 40: 259-274.

Droop, G. T. R. and Harte, B., 1995. The effect of Mn on the phase relations of medium-grade pelites: constraints from natural assemblages on petrogenetic grid topology. Journal of Petrology, 36(6): 1549-1578.

Duchene, S. et al., 1997. The Lu-Hf dating of garnets and the ages of the Alpine high-pressure metamorphism. Nature, 387(6633): 586-589.

Dymoke, P. and Sandiford, M., 1992. Phase relationships in Buchan facies series pelitic assemblages: calculations with application to andalusite-staurolite parageneses in the Mount Lofty Ranges, South Australia. Contributions to Mineralogy and Petrology, 110: 121-132.

Edwards, M. A. and Harrison, T. M., 1997. When did the roof collapse? Late Miocene north-south extension in the high Himalaya revealed by Th-Pb monazite dating of the Khula Kangri granite. Geology, 25(6): 543-546.

Edwards, M. A. et al., 1996. Multi-stage development of the southern Tibet detachment system near Khula Kangri. New data from Gonto La. Tectonophysics, 260: 1-19.

England, P. C. and Thompson, A. B., 1984. Pressure-Temperature-Time paths of regional metamorphism I. Heat transfer during the evolution of regions of thickened crust. Journal of Petrology, 25: 894-928.

England, P. C. and Houseman, G. A., 1988. The mechanics of the Tibetan Plateau. Philosophical Transactions of the Royal Society of London A, 326: 301-320.

England, P. and Molnar, P., 1993a. Cause and effect among thrust and normal faulting, anatectic melting and exhumation in the Himalaya. In: P.G. Treloar and M.P. Searle (Editors), Himalayan Tectonics. Geological Society of London Special Publication. Geol. Soc. London, London, pp. 401-411.

England, P. and Molnar, P., 1993b. The interpretation of inverted metamorphic isograds using simple physical models. Tectonics, 12(1): 145-157.

England, P., LeFort, P., Molnar, P. and Pêcher, A., 1992. Heat sources for Tertiary metamorphism and anatexis in the Annapurna-Manaslu region of Central Nepal. Journal of Geophysics Research, 97B: 2107-2128.

Fedorowich, J. S., Jain, J. C. and Kerrich, R., 1995. Trace-Element Analysis of Garnet By Laser-Ablation Microprobe Icp-Ms. Canadian Mineralogist, 33(Pt2): 469-480.

Ferry, J. M. and Spear, F. S., 1978. Experimental calibration of the partitioning of Fe and Mg between biotite and garnet. Contributions to Mineralogy and Petrology, 66: 113-117.

Finger, F., Broska, I., Roberts, M. P. and Schermaier, A., 1998. Replacement of primary monazite by apatite-allanite-epidote coronas in an amphibolite facies granite gneiss from the eastern Alps. American Mineralogist, 83(3-4): 248-258.

Florence, F. P. and Spear, F. S., 1993. Influences of reaction history and chemical diffusion on P-T calculations for staurolite schists from the Littleton Formation, northwest New Hampshire. American Mineralogist, 78: 345-359.

Foster, G., Kinny, P., Prince. C., Vance, D. and Harris, N., Subm. The significance of monazite U-Th-Pb age data in metamorphic assemblages: a combined study of monazite and garnet chronometry. EPSL

France-Lanord, C., Derry, L. and Michard, A., 1993. Evolution of the Himalya since Miocene time: isotopic and sedimentological evidence from the Bengal Fan. In: P.J. Treloar and M.P. Searle (Editors), Himalayan Tectonics. Geological Society of London Special Publication 74. Geological Society of London, London, pp. 605-622.

Frei, R., Binno, G. G. and Prospert, C., 1995. Dating a Variscan P-T loop with staurolite. Geology, 23: 1095-1098.

Frei, R. et al., 1997. Single mineral dating by the Pb-Pb step-leaching method: assessing the mechanisms. Geochimica et Cosmochimica acta, 61: 393-414.

Gaetani, M. and Garzanti, E., 1991. Multicyclic History of the Northern India Continental-Margin (Northwestern Himalaya). Aapg Bulletin-American Association of Petroleum Geologists, 75(9): 1427-1446.

Ganguly, J., Cheng, W. and Chakraborty, S., 1998a. Cation diffusion in aluminosilicate garnets: experimental determination in pyrope-almandine diffusion couples. Contributions to Mineralogy and Petrology, 131(171-180).

Ganguly, J., Tirone, M. and Hervig, R. L., 1998b. Diffusion kinetics of samarium and neodymium in garnet, and a method for determining cooling rates of rocks. Science, 281: 805-807.

Gansser, A., 1964. Geology of the Himalayas. Interscience publishers, London, 289 pp.

Gapais, D., Pêcher, A., Gilbert, E. and Ballevre, M., 1992. Synconvergence spreading of the Higher Himalaya crystalline in Ladakh. Tectonics, 11: 1045-1056.

Gariépy, C., Allègre, C. J. and Ronghau, X., 1985. The Pb-isotope geochemistry of

granitoids from the Himalaya-Tibet collision zone: implications for crustal evolution. Earth and Planetary Science Letters, 74: 220-234.

Getty, S. R. et al., 1993. Sm-Nd dating of multiple garnet growth events in an arc-continent collision zone, northwestern US Cordillera. Contributions to Mineralogy and Petrology, 115: 45-57.

Giletti, B. J. and Casserly, J. E. D., 1994. Strontium diffusion kinetics in plagioclase feldspars. Geochimica et Cosmochimica Acta, 58: 3785-3793.

Godin, L., Brown, R. L., Hanmer, S. and Parrish, R., 1999. Back folds in the core of the Himalayan orogen: an alternative interpretation. Geology, 27(2): 151-154.

Grambling, J. A., 1981. A regional gradient in the composition of metamorphic fluids in pelitic schists, Pecos Baldy, New Mexico. Contributions to Mineralogy and Petrology, 94: 149-164.

Grasemann, B., 1993. Numerical modelling of the thermal history of the NW Himalayas, Kulu Valley, India. In: P.J. Treloar and M.P. Searle (Editors), Himalayan Tectonics. Geological Society of London Special Publication. Geol. Soc. London, London, pp. 475-484.

Gromet, L. P. and Silver, L. T., 1983. Rare earth element distribution among minerals in a granodiorite and their petrogenetic implications. Geochimca Cosmochimica Acta, 47: 925-939.

Grujic, D. et al., 1996. Ductile Extrusion of the Higher Himalayan Crystalline in Bhutan - Evidence From Quartz Microfabrics. Tectonophysics, 260(1-3): 21-43.

Guillot, S. et al., 1995. Contact metamorphism and depth of emplacement of the Manaslu granite (central Nepal). Implications for Himalayan orogenesis. Tectonophysics, 241: 99-119.

Günther, D. and Heinrich, C. A., in prep. Enhanced Sensitivity Laser Ablation-ICP-MS using Helium as Aerosol Carrier. .

Günther, D., Frischknecht, R., Heinrich, C. A. and Kahlert, H.-J., 1997. Capabilities of an Argon Fluoride 193 nm Excimer Laser for Laser Ablation Inductively Coupled Plasma Mass Spectrometry Microanalysis of Geological Materials. , 12: 939-944.

Hanson, G. N., 1978. The application of trace elements to the petrogenesis of igneous rocks of granitic composition. Earth and planetary science letters, 38: 26-43.

Harris, N. B. W. and Inger, S., 1992. Trace element modelling of pelite-derived granites. Contributions to mineralogy and petrology, 110: 46-56.

Harris, N. and Massey, J., 1994. Decompression and anatexis of Himalayan metapelites. Tectonics, 13: 1537-1546.

Harris, N. B. W., Gravestock, P. and Inger, S., 1992. Ion-Microprobe Determinations of Trace-Element Concentrations in Garnets From Anatectic Assemblages. Chemical Geology, 100(1-2): 41-49.

Harris, N., Inger, S. and Massey, J., 1993. The role of fluids in the formation of High Himalayan leucogranites. In: P.J. Treloar and M.P. Searle (Editors), Himalayan Tectonics. Geol. Soc. London Spec. Publ., London, pp. 391-400.

Harris, N., Ayres, M. and Massey, J., 1995. Geochemistry of Granitic Melts Produced During the Incongruent Melting of Muscovite - Implications For the Extraction of Himalayan Leucogranite Magmas. Journal of Geophysical Research-Solid Earth, 100(B8): 15767-15777.

Harris, N., Vance, D. and Ayres, M., In press. From sediment to granite: timescales of anatexis in the upper crust. Chemical Geology.

Harrison, T. M. and Watson, E. B., 1983. Kinetics of zircon dissolution and zirconium diffusion in granitic melts of variable water content. Contributions to Mineralogy and Petrology, 84: 66-72.

Harrison, T. M., Lovera, O. M. and Grove, M., 1997a. New insights into the origin of two contrasting Himalayan granite belts. Geology, 25(10): 899-902.

Harrison, T. M. et al., 1997b. A Late Miocene-Pliocene origin for the Central Himalayan inverted metamorphism. Earth and Planetary Science Letters, 146(1-2): E1-E7.

Harrison, T. M., Grove, M., Lovera, O. M. and Catlos, E. J., 1998. A model for the origin of Himalayan anatexis and inverted metamorphism. Journal of Geophysical Research-Solid Earth, 103(B11): 27017-27032.

Harrison, T. M. et al., 1999. Origin and episodic emplacement of the Manaslu intrusive complex, central Himalaya. Journal of Petrology, 40(1): 3-19.

Hauck, M. L. et al., 1998. Crustal structure of the Himalayan orogen at *90* east longitude from Project INDEPTH deep reflection profiles. Tectonics, 17(4): 481-500.

Heim, A. and Gansser, A., 1939. Central Himalayas: geological observations of the Swiss Expedition 1936. Memoires de la Societe Helvetica des Sciences Naturelles, 73: 1-245.

Hensen, B. J. and Zhou, B., 1995. Retention of isotopic memory in garnets partially broken down during an overprinting granulite-facies metamorphism: implications for the Sm-Nd closure temperature. Geology, 23: 225-228.

Herren, E., 1987. Zanskar shear zone: northeast-southwest extension within the Higher Himalaya (Ladakh, India). Geology, 15: 409-413.

Hickmott, D. M. and Shimizu, N., 1990. Trace-element zoning in garnet from the Kwoiek area, British Columbia: disequilibrium partitioning during garnet growth? Contributions to Mineralogy and Petrology, 104: 619-630.

Hickmott, D. and Spear, F. S., 1992. Major- and Tace-element zoning in garnets from calcareous pelites in the NW Shelburne falls quadrangle, Massachusetts: Garnet growth histories in retrograded rocks. Journal of Petrology, 33(5): 965-1005.

Hickmott, D. D., Shimizu, N., Spear, F. S. and Selverstone, J., 1987. Trace element zoning in a metamorphic garnet. Geology, 15: 573-576.

Hirn, A. et al., 1995. Seismic anisotropy as an indicator of mantle flow beneath the Himalayas and Tibet. Nature, 375.

Hodges, K. V. and Crowley, P. D., 1985. Error estimation and empirical geothermobarometry for pelitic systems. American Mineralogist, 70: 702-709.

Hodges, K. V. and Silverberg, D. S., 1988. Thermal Evolution of the Greater-Himalaya, Garhwal, India. Tectonics, 7(3): 583-600.

Hodges, K. V., Le Fort, P. and Pêcher, A., 1988. Possible thermal buffering by crustal anatexis in collisional orogens: thermobarometric evidence from the Nepalese Himalaya. Geology, 16: 707-710.

Hodges, K. V. et al., 1992. Simultaneous Miocene extension and shortening in the Himalayan orogen. Science, 258: 1466-1470.

Hodges, K. V. et al., 1993. The metamorphic signature of contemporaneous extension and shortening in the central Himalayan orogen: data from the Nyalam transect, southern Tibet. Journal of Metamorphic Geology, 11: 721-737.

Hodges, K. et al., 1998. Evidence for rapid displacement on Himalayan normal fault and the importance of tectonic denudation in the evolution of mountain ranges. Geology, 26(6): 483-486.

Holland, T. J. B. and Powell, R., 1985. An internally consistent thermodynamic dataset with uncertainties and correlations: 2. Data and results. Journal of Metamorphic Geology, 3: 343-370.

Holland, T. J. B. and Powell, R., 1990. An enlarged and updated internally consistent thermodynamic dataset with uncertainties and correlations: the system $K_2O$-$Na_2O$-CaO-MgO-MnO-FeO-$Fe_2O_3$-$Al_2O_3$-$TiO_2$-C-$H_2$-$O_2$. Journal of metamorphic geology, 8: 89-124.

Holland, T. and Powell, R., 1998. An internally-consistent thermodynamic data set for

phases of petrological interest. Journal of Metamorphic Geology, 16: 309-343.
Hollister, L., 1966. Garnet zoning: An interpretation based on the Rayleigh fractionation model. Science, 154: 1647-1651.
Hollister, L. S. and Crawford, M. L., 1986. Melt-enhanced deformation: A major tectonic process. Geology, 14: 558-561.
Holtz, F. and Johannes, W., 1991. Genesis of peraluminous granites I. Experimental investigation of melt compositions at 3 and 5kb and various H2O activities. Journal of Petrology, 32(5): 935-958.
Hubbard, M. S., 1989. Thermobarometric constraints on the thermal history of the Main Central Thrust Zone and Tibetan Slab, eastern Nepal Himalaya. Journal of Metamorphic Geology, 7: 19-30.
Hubbard, M., 1996. Ductile shear as a cause of inverted metamorphism: Example from the Nepal Himalaya. Journal of Geology, 104: 493-499.
Hubbard, M. S. and Harrison, T. M., 1989. $^{40}Ar/^{39}Ar$ age constraints on deformation and metamorphism in the main central thrust zone and Tibetan slab, eastern Nepal Himalaya. Tectonics, 8(4): 854-880.
Humphries, F. J. and Cliff, R. A., 1982. Sm-Nd dating and cooling history of Scourian granulites, Scotland. Nature, 295: 515-517.
Inger, S., 1998. Timing of an extensional detachment during convergent orogeny: new Rb-Sr geochronological data from the Zanskar shear zone, northwestern Himalaya. Geology, 26(3): 223-226.
Inger, S. and Harris, N. B. W., 1992. Tectonothermal evolution of the High Himalayan Crystalline Sequence, Langtang Valley, northern Nepal. Journal of Metamorphic Geology.
Inger, S. and Harris, N., 1993. Geochemical constraints on leucogranite magmatism in the Langtang Valley, Nepal Himalaya. Journal of Petrology, 34(2): 345-368.
Jain, A. K. and Anand, A., 1988. Deformational and strain patterns of an intracontinental collision ductile shear zone-an example from the Higher Gahwal Himalaya. Journal of Structural Geology, 10(7): 717-734.
Jain, A. K. and Manickavasagam, R. M., 1993. Inverted metamorphism in the intracontinental ductile shear zone during Himalayan collision tectonics. Geology, 21: 407-410.
Jain, A. K., Singh, S., Manicavasgam, R. M. and Chander, R., 1995. Excursion guide to the Himalayan collision zone, Bhagirathi valley, Garhwal Himalaya, Department of Earth Sciences, University of Roorkee, India.
Jamieson, R. A., 1990. Metamorphism of an Early Palaeozoic continental margin, western Baie Verte Peninsula, Newfoundland. Journal of Metamorphic Geology, 8: 269-288.
Jamieson, R. A., Beaumont, C., Fullsack, P. and Lee, B., 1998. Barrovian regional metamorphism: where's the heat. In: P.J. Treloar and P.J. O'Brien (Editors), What drives metamorphism and metamorphic reactions? Geological Society of London, Special Publications. Geological Society, London, pp. 23-51.
Jaupart, C. and Provost, A., 1985. Heat focussing, granite genesis and inverted metamorphic gradients in continental collision zones. Earth and Planetary Science Letters, 73: 385-397.
Jenner, G. A. et al., 1993. Determination of Partition-Coefficients For Trace-Elements in High- Pressure Temperature Experimental Run Products By Laser-Ablation Microprobe Inductively-Coupled Plasma-Mass Spectrometry (Lam-Icp-Ms). Geochimica Et Cosmochimica Acta, 57(23-24): 5099-5103.
Johannes, W. and Holtz, F., 1990. Formation and composition of H2O-undersaturated granitic melts. In: J.R. Ashworth and M. Brown (Editors), High-temperature metamorphism and crustal anatexis. Unwin Hyman, London, pp. 87-101.

## References


Johnson, M. R. W. and Oliver, G. J. H., 1990. Precollision and postcollision thermal events in the Himalaya. Geology, 18: 753-756.

Klootwijk, C. T. et al., 1992. An Early India-Asia Contact - Paleomagnetic Constraints From Ninetyeast Ridge, Odp Leg 121. Geology, 20(5): 395-398.

Kosler, J. and Vance, D., in prep. Constraints on Sm-Nd diffusion rates from laser ablation ICP-MS analyses and conventional dating of prograde garnets. .

Kundig, R., 1989. Domal structures and high-grade metamorphism in the Higher Himalayan Crystalline, Zanskar Region, north-west Himalaya, India. Journal of Metamorphic Geology, 7: 43-55.

Lasaga, A. C., 1983. Geospeedometry: an extension of geothermometry. In: S.K. Sazena (Editor), Advances in physical geochemistry Volume 3, Kinetics and equilibrium in mineral reactions. Springer-Verlag, New York, pp. 81-114.

Le Breton, N. and Thompson, A. B., 1988. Fluid-absent (dehydration) melting of biotite in metapelites in the early stages of crustal anatexis. Contributions to mineralogy and petrology, 99: 226-237.

Le Fort, P., 1975. Himalayas: the collided range. Present knowledge of the continental arc. American Journal of Science, 275A: 1-44.

Le Fort, P. et al., 1987. Crustal generation of the Himalayan leucogranites. Tectonphysics, 134: 39-57.

Lin, J. and Watts, D. R., 1988. Paleomagnetic constraints on Himalayan-Tibetan tectonic evolution. Philosophical Transactions of the Royal Society, London, A326: 177-188.

Longerich, H. P., Jackson, S. E. and Günther, D., 1996. Laser Ablation Inductively Coupled Plasma Mass Spectrometric Transient Signal Data Acqusition and Analyte Concentration Calculation. , 11: 899-904.

Maas, R. et al., 1992. The Earth's oldest known crust: a geochronological and geochemical study of 3900-4200 Ma old detrital zircons from Mt. Narriter and Jack Hills, Western Australia. Geochimica et Cosmochimica Acta, 56: 1281-1300.

MacFarlane, A. M., 1993. Chronology of tectonic events in the crystalline core of the Himalaya, Langtang National Park, central Nepal. Tectonics, 12: 1004-1025.

Macfarlane, A. M., 1995. An Evaluation of the Inverted Metamorphic Gradient At Langtang National-Park, Central Nepal Himalaya. Journal of Metamorphic Geology, 13(5): 595-612.

Mahar, E. M. et al., 1997. The effect of Mn on mineral stability in metapelites. Journal of Metamorphic Geology, 15: 223-238.

Massey, J. A., 1994. Fluid circulation and fault controlled magmatism in the Central Himalayas, Open University, Milton Keynes, lots pp.

McKay, G. A., 1989. Partitioning of rare earth elements between major silicate minerals and basaltic melts, Mineralogical Society of America Reviews in Mineralogy, pp. 45-78.

Meigs, A. J., Burbank, D. W. and Beck, R. A., 1995. Middle-Late Miocene (Greater-Than-10 Ma) Formation of the Main Boundary Thrust in the Western Himalaya. Geology, 23(5): 423-426.

Metcalfe, R. P., 1990. A thermotectonic evolution for the Main Central Thrust and Higher Himalaya, Western Garhwal, India, University of Leicester.

Metcalfe, R. P., 1993. Pressure, temperature and time constraints on metamorphism across the Main Central Thrust zone and High Himalayan Slab in the Garwhal Himalaya. In: P.J. Treloar and M.P. Searle (Editors), Himalayan Tectonics. Geological Society of London Special Publication. Geological Society of London, London, pp. 485-500.

Mezger, K., Essene, E. J. and Halliday, A. N., 1992. Closure temperatures of the Sm-Nd system in metamorphic garnets. Earth and Planetary Science Letters, 113: 397-409.

Mezger, K., Hanson, G. N. and Bohlen, S. R., 1989. U-Pb systematics of garnet: dating of the growth of garnet in the Late Archean Pikwitonei granulite domain at Cauchon and Natawahunea Lakes, Manitoba, Canada. Contributions to Mineralogy and Petrology, 101: 136-148.

Mohan, A., Windley, B. F. and Searle, M. P., 1989. Geothermobarometry and development of inverted metamorphism in the Darjeeling-Sikkim region of the eastern Himalaya. Journal of metamorphic geology, 7: 95-110.

Molnar, P. and Tapponnier, P., 1975. Cenozoic tectonics of Asia: effects of a continental collision. Science, 189: 429-426.

Molnar, P. and England, P., 1990. Temperatures, heat flux and frictional stress near major thrust faults. Journal of Geophysical Research, 24: 635-661.

Molnar, P., Chen, W. and Padovani, E., 1983. Calculated temperatures in overthrust terrains and possible combinations of heat sources responsible for the Tertiary granites in the greater Himalaya. Journal of Geophysical Research, 88(B8): 6415-6429.

Montel, J.-M., 1993. A model for monazite/melt equilibrium and application to the generation of graniic magmas. Chemical geology, 110: 127-146.

Mork, M. B. E., Sundvoll, B. and Stabel, A., 1997. Sm-Nd dating of gabbro- and garnet-bearing contact metamorphic/anatectic rocks from Krutfjellet, Nordland, and some geochemical aspects of the intrusives. Norsk Geologisk Tidsskrift, 77(1): 39-50.

Nash, W. P. and Crecraft, H. R., 1985. Partition coefficients for trace elements in silicic magmas. Geochemica et Cosmochimica Acta, 49: 2309-2322.

Nelson, K. D. et al., 1996. Partially molten middle crust beneath southern Tibet: Synthesis of project INDEPTH results. Science, 274(5293): 1684-1688.

Neogi, S., Dasgupta, S. and Fukuoka, M., 1998. High P-T polymetamorphism, dehydration melting, and generation of migmatites and granites in the Higher Himalayan Crystalline Complex, Sikkim, India. Journal of Petrology, 39(1): 61-99.

Newton, R. C. and Haselton, H. T., 1981. Thermodynamics of the garnet-plagioclase-$Al_2SiO_5$-quartz geobarometer. In: R.C. Newton, A. Navrotsky and B.J. Wood (Editors), Thermodynamics of Minerals and Melts. Springer-Verlag, Ney York, pp. 131-147.

Noble, S. R. and Searle, M. P., 1995. Age of crustal melting and leucogranite formation from U-Pb zircon and monazite dating in the western Himalaya, Zanskar, India. Geology, 23(12): 1135-1138.

Oliver, G. J. H., Johnson, M. R. W. and Fallick, A. E., 1995. Age of metamorphism in the Lesser Himalaya and the Main Central Thrust zone, Gahrwal India: results of illite crystallinity, $^{40}Ar$-$^{39}Ar$ and K-Ar studies. Geological Magazine, 132: 139-149.

Pan, Y. M., 1997. Zircon- and monazite-forming metamorphic reactions at Manitouwadge, Ontario. Canadian Mineralogist, 35(Pt1): 105-118.

Parrish, R. R., 1990. U-Pb Dating of Monazite and Its Application to Geological Problems. Canadian Journal of Earth Sciences, 27(11): 1431-1450.

Parrish, R. R., 1993. Miocene (22±1) Ma metamorphism and two stage thrusting in the greater Himalayan sequence, Annapurna Sanctuary, Nepal. Geological Society of America, Abstracts with Programs, 25: A174.

Parrish, R. R. and Hodges, K. V., 1996. Isotopic constraints on the age and provenance of the Lesser and Greater Himalayan sequences, Nepalese Himalaya. Geological Society of America Bulletin, 108(7): 904-911.

Parsons, B. and McKenzie, D. P., 1978. Mantle convection and the thermal structure of the plates. Journal of Geophysics Researches, 82: 803-27.

Patel, R. C. et al., 1993. Extensional tectonics in the Himalayan orogen, Zanskar, NW

India. In: M.P. Treloar and M.P. Searle (Editors), Himalayan Tectonics. Geological Society of London Special Publications. Geological Society of London, London, pp. 445-469.

Pati, U. C. and Rao, P. N., 1983. Geotectonics of the Main Central Thrust of U. P. Himalaya. In: P.S. Saklani (Editor), Himalayan Shears. English bookstores, N. Delhi, pp. 59-68.

Patino Douce, A. E. and Johnston, A. D., 1991. Phase equilibria and melt productivity in the pelitic system: implications for the origin of peraluminous granitoids and aluminous granulites. Contributions to Mineralogy and Petrology, 107: 202-218.

Patino Douce, A. E. and Harris, N., 1998. Experimental constraints on Himalayan Anatexis. Journal of Petrology, 39(4): 689-710.

Patriat, P. and Achache, J., 1984. India-Eurasia collision chronology has implications for crustal shortening and driving mechanisms of plates. Nature, 311: 615-621.

Patzelt, A., Li, H. M., Wang, J. D. and Appel, E., 1996. Palaeomagnetism of Cretaceous to Tertiary sediments from southern Tibet: Evidence for the extent of the northern margin of India prior to the collision with Eurasia. Tectonophysics, 259(4): 259-284.

Pecher, A., 1989. The metamorphism of the Central Himalaya. Journal of Metamorphic Geology, 7: 31-41.

Pecher, A., 1991. The contact between the higher Himalaya crystallines and the Tibetan sedimentary series: Miocene large-scale dextral shearing. Tectonics, 10(3): 587-598.

Pecher, A. and Scaillet, B., 1989. La structure du Haut-Himalaya au Garhwal. Ecol. Geol. Helv, 82: 665-668.

Petö, P., 1976. An experimental investigation of melting reactions involving muscovite and paragonite in the silica-undersaturated portion of the system $K_2O$-$Na_2O$-$Al_2O_3$-$SiO_2$-$H_2O$. Progr. Exper. Petrol., 3: 41-45.

Platt, J. P., 1993. Exhumation of high-pressure rocks: A review of concepts and processes. Terra Nova, 5, 119-133.

Pognante, U. and Lombardo, B., 1989. Metamorphic evolution of the High Himalayan crystallines in SE Zanskar, India. Journal of Metamorphic Geology, 7: 9-17.

Pognante, U. et al., 1990. The crystalline units of the High Himalayas in the Lahul-Zanskar region (northwest India): metamorphic-tectonic history and geochronology of the collided and imbricated Indian plate. Geological magazine, 127(2): 101-116.

Powell, M., 1986. Continental underplating model for the rise of the Tibetan plateau. Earth and Planetary Science Letters, 81: 79-74.

Powell, R. and Holland, T., 1994. Optimal geothermometry and geobarometry. American Mineralogist, 79: 120-133.

Powell, R., Holland, T. and Worley, B., 1998. Calculating phase diagrams involving solid solutions via non-linear equations, with examples using THERMOCALC. Journal of Metamorphic Geology, 16(4): 577-588.

Ranalli, G., 1995. Rheology of the Earth. Chapman and Hall, London, 413 pp.

Ratschbacher, L. W., Frisch, G., Liu, G. and Chen, C., 1994. Distributed deformation in southern and western Tibet during and after India-Asia collision. Journal of Geophysical Research, 99: 19,917-19,945.

Reddy, S. M., Searle, M. P. and Massey, J. A., 1993. Structural evolution of the High Himalayan gneiss sequence of the Langtang Valley, Nepal. In: P.J. Treloar and M.P. Searle (Editors), Himalayan Tectonics. Geol. Soc. London Spec. Pub., pp. 375-390.

Rowley, D. B., 1996. Age of initiation of collision between India and Asia: A review of stratigraphic data. Earth and Planetary Science Letters, 145: 1-13.

Rowley, D. B., 1998. Minimum age of initiation of collision between India and Asia

North of Everest based on the subsidence history of Zhepure mountain section. Journal of Geology, 106: 229-235.

Royden, L. H., 1993. The steady-state thermal structure of eroding orogenic belts and accretionary prisms. Journal of Geophysical Research, 98B: 4487-4507.

Rubie, D. C. and Brearley, A. J., 1990. A model for rates of disequilibrium during metamorphism. In: J.R. Ashworth and M. Brown (Editors), High-Temperature metamorphism and crustal anatexis, Mineralogical Society Series Volume 2. Unwin Hyman Ltd., London, pp. 57-86.

Saklani, P. S. and Bahuguna, V. K., 1983. Main central thrust zone and associated imbricate structures in Chhatera area, Garhwal Himalaya. In: P.S. Saklani (Editor), Himalayan Shears. English bookstores, N. Delhi, pp. 1-9.

Scaillet, B., Francelanord, C. and Lefort, P., 1990. Badrinath-Gangotri Plutons (Garhwal, India) - Petrological and Geochemical Evidence For Fractionation Processes in a High Himalayan Leukogranite. Journal of Volcanology and Geothermal Research, 44(1-2): 163-188.

Scaillet, B., Pecher, A., Rochette, P. and Champenois, M., 1995. The Gangotri Granite (Garhwal Himalaya) - Laccolithic Emplacement in an Extending Collisional Belt. Journal of Geophysical Research-Solid Earth, 100(B1): 585-607.

Schaller, M. et al., 1997. Pb stepwise leaching (PbSL) dating of garnet-addressing the inclusion problem. Schweizerische Mineralogische Und Petrographische Mitteilungen, 77(1): 113-121.

Schärer, U., 1984. The effect of initial $^{230}Th$ disequilibrium on young U-Pb ages: the Makalu case, Himalaya. Earth and Planetary Science Letters, 67: 191-204.

Schärer, U., Xu, R. H. and Allegre, C. J., 1986. U-(Th)-Pb systematics and ages of Himalayan leucogranites, South Tibet. Earth and Planetary Science letters, 77: 35-48.

Schelling, D., 1992. The tectonostratigraphy and structure of the eastern Nepal Himalaya. Tectonics, 11: 925-943.

Schwandt, C. S., Papike, J. J., Shearer, C. S. and Brearley, A. J., 1993. A SIMS investigation of REE chemistry of garnet in garnetite associated with the Broken Hill Pb-Sn-Ag orebodies, Australia. Canadian Mineralogist, 31: 371-379.

Schwandt, C. S., Papike, J. J. and Shearer, C. K., 1996. Trace element zoning in pelitic garnet of the Black Hills, South Dakota. American Mineralogist, 81: 1195-1207.

Searle, M. P., 1986. Structural evolution and sequence of thrusting in the High Himalaya, Tibetan-Tethys and Indus suture zones of Zanskar and Ladakh, Western Himalaya. Journal of Structural Geology, 8(8): 923-936.

Searle, M. P., 1987. The closing of Tethys and the tectonics of the Himalaya. Geological Society of America Bulletin, 98: 678-701.

Searle, M. P., 1995. The timing of metamorphism, magmatism and cooling in the Zanskar, Garwal, and Nepal Himalaya. Journal of Nepal Geological Society, 11: 103-120.

Searle, M. P., 1999. Extensional and compressional faults in the Everest-Lhotse massif, Khumbu Himalaya, Nepal. Journal of the Geological Society, London, 156: 227-240.

Searle, M. P. and Rex, A. J., 1989. Thermal model for the Zanskar Himalaya. Journal of Metamorphic Geology, 7: 127-134.

Searle, M. P., Metcalfe, R. P., Rex, A. J. and Norry, M. J., 1993. Field relations, petrogenesis and emplacement of the Bhagirathi leucogranite, Garhwal Himalaya. In: P.J. Treloar and M.P. Searle (Editors), Himalayan Tectonics. Geological Society Special Publication. Geological Society of London, London, pp. 429-444.

Searle, M., Corfield, R. I., Stephenson, B. and McCarron, J., 1997a. Structure of the North Indian continental margin in the Ladakh-Zanskar Himalayas : implications

for the timing of obduction of the Spontang ophiolite, India-Asia collision and deformation events in the Himalaya. Geological Magazine, 134(3): 297-316.

Searle, M. P. et al., 1997b. Shisha Pangma leucogranite, south Tibetan Himalaya: Field relations, geochemistry, age, origin, and emplacement. Journal of Geology, 105(3): 295-317.

Searle, M. P., Noble, S. R., Hurford, A. J. and Rex, A. J., Subm. Age of crustal melting, emplacement and exhumation history of the Shivling leucogranite, Garhwal Himalaya. Geological Magazine.

Seitz, J. F., Tewari, A. P. and Obradovich, J., 1976. A note on the absolute age of the tourmaline-granite, Arwa valley, Garhwal Himalaya.

Sevigny, J., 1993. Monazite controlled Sm/Nd fractionation in leucogranites: an ion microprobe study of garnet phenocrysts. Geochimica et Cosmochimica Acta, 57: 4095-4102.

Shah, S. K. and Sinha, A. K., 1974. Stratigraphy and tectonics of the "Tethyan " zone in a part of western Kumaun Himalaya. Himalayan Geology, 4: 1-27.

Sisson, T. W. and Bacon, C. R., 1992. Garnet High-Silica Rhyolite Trace-Element Partition-Coefficients Measured By Ion Microprobe. Geochimica Et Cosmochimica Acta, 56(5): 2133-2136.

Smith, H. A. and Barreiro, B., 1990. Monazite U-Pb dating of staurolite-grade metamorphism in pelitic schists. Contributions to Mineralogy and Petrology, 105: 602-615.

Sorkhabi, R. B. and Stump, E., 1993. Rise of the Himalaya: A geochronologic approach. GSA Today, 3(4).

Sorkhabi, R. B., Stump, E., Foland, K. A. and Jain, A. K., 1996. Fission-Track and Ar-40/Ar-39 Evidence For Episodic Denudation of the Gangotri Granites in the Garhwal Higher Himalaya, India. Tectonophysics, 260(1-3): 187-199.

Spear, F. S., 1991. On the Interpretation of Peak Metamorphic Temperatures in Light of Garnet Diffusion During Cooling. Journal of Metamorphic Geology, 9(4): 379-388.

Spear, F. S. and Selverstone, J., 1983. Quantitative P-T paths from zoned minerals: theory and tectonic implications. Contributions to Mineralogy and Petrology, 83: 348-357.

Spear, F. S. and Kohn, M. J., 1996. Trace element zoning in garnet as a monitor of crustal melting. Geology, 24(12): 1099-1102.

Spear, F. S. and Parrish, R. R., 1996. Petrology and Cooling Rates of the Valhalla Complex, British- Columbia, Canada. Journal of Petrology, 37(4): 733-765.

Spear, F. S., Kohn, M. J. and Paetzold, S., 1995. Petrology of the regional sillimanite zone, west-central New Hampshire, U.S.A., with implications for the development of inverted isograds. American Mineralogist, 80: 361-376.

Srivastava, P. and Mitra, G., 1994. Thrust geometries and deep structure of the outer and lesser Himalaya, Kumaon and Garhwal (India): Implications for evolution of the Himalayan fold-and-thrust belt. Tectonics, 13(1): 89-109.

Srivastava, P. and Mitra, G., 1995. Deformation Mechanisms and Inverted Thermal Profile in the North- Almora-Thrust Mylonite Zone, Kumaon-Lesser-Himalaya, India. Journal of Structural Geology, 18(1): 27-39.

St. Ongé, M., 1987. Zoned poikiloblastic garnets: P-T paths and syn-metamorphic uplift through 30km of structural depth, Wopmay orogen, Canada. Journal of Petrology, 28: 1-21.

Stäubli, A., 1989. Polyphase metamorphism and the development of the Main Central Thrust. Journal of Metamorphic Geology, 7: 73-93.

Steck, A. et al., 1998. Geological transect across the Tso Morari and Spiti areas: The nappe structures of the Tethys Himalaya. Eclogae Geologicae Helvetiae, 91(1): 103-122.

Stern, C. R. et al., 1989. The Bhagirathi leucogranite of the High Himalaya (Garhwal, India); Age, petrogenesis, and tectonic implications. Geological Society of America, Special Paper 232: 33-45.

Stowell, H. H. and Goldberg, S. A., 1997. Sm-Nd garnet dating of polyphase metamorphism: Northern Coast Mountains, south-eastern Alaska, USA. Journal of Metamorphic Geology, 15(4): 439-450.

Swapp, S. M. and Hollister, L. S., 1991. Inverted metamorphism within the Tibetan Slab of Bhutan: Evidence for a tectonically transported heat-source. Canadian Mineralogist, 29: 1019-1041.

Symmes, G. H. and Ferry, J. M., 1991. Evidence from mineral assemblages for infiltration of pelitic schists by aqueous fluids during metamorphism. Contributions to Mineralogy and Petrology, 108: 419-438.

Tapponier and Molnar, 1976. Slip-line field theory and large-scale continental tectonics. Nature, 264: 32-39.

Thompson, A. B. and Connoly, J. A. D., 1995. Melting of the continental crust: Some thermal and petrological constraints on anatexis in continental collision zones and other tectonic settings. Journal of Geophysical Research, 100(B8): 15565-15579.

Thöni, M. and Jagoutz, E., 1992. Some new aspects of dating eclogites in orogenic belts: Sm-Nd, Rb-Sr and Pb-Pb isotopic results from the Austroalpine Saualpe and Koralpe type locality (Carinthia/Styria, southeastern Austria). Geochimica et Cosmochimica Acta, 56: 347-368.

Thöni, M. and Miller, C., 1996. Garnet Sm-Nd data from the Saualpe and the Koralpe (Eastern Alps, Austria): chronological and P-T constraints on the thermal and tectonic history. Journal of Metamorphic Geology, 14: 453-466.

Tracy, R. J., 1982. Compositional zoning and inclusions in metamorphic minerals. In: J.M. Ferry (Editor), Characterisation of metamorphism through mineral equilibria. Mineralogical Society of America, Reviews in mineralogy, Washington, pp. 355-397.

Tracy, R. J., Robinson, P. and Thompson, A. B., 1976. Garnet composition and zoning in the determination of temperature and pressure of metamorphism, central Massachusetts. American Mineralogist, 61: 762-775.

Tuisku, P., Ruostesuo, P. and Hakkinen, A.-M., 1987. The metamorphic behaviour and petrogenetic significance of zinc in amphibolite facies, staurolite-bearing mica schists, Puolankajarvi Formation, Central Finland. Geochimica et Cosmochimica Acta, 51: 1639-1650.

Turcotte, D. and Schubert, G., 1982. Geodynamics. Wiley, New York.

Valdiya, K. S., 1980. The two intracrustal boundary thrusts of the Himalaya. Tectonophysics, 66: 323-348.

Valdiya, K. S., 1988. Tectonics and evolution of the central sector of the Himalaya. Phil. Trans. R. Soc. London, A 326: 151-175.

Vance, D., 1986. Isotopic investigations of the thermal and chemical structure of the lithosphere, Cambridge, Cambridge.

Vance, D., 1995. Rate and time controls on metamorphic processes. Geological Journal, 30: 241-259.

Vance, D. and O'Nions, R. K., 1990. Isotopic chronometry of zoned garnets: growth kinetics and metamorphic histories. Earth and Planetary Science Letters, 97: 227-240.

Vance, D. and O'Nions, R. K., 1992. Prograde and retrograde thermal histories from the central Swiss Alps. Earth and Planetary Science Letters, 114: 113-129.

Vance, D. and Holland, T., 1993. A detailed isotopic and petrological study of a single garnet from the Gassetts Schist, Vermont. Contributions to Mineralogy and Petrology, 114: 101-118.

## References


Vance, D. and Mahar, E., 1998. Pressure-temperature paths form P-T pseudosections and zoned garnets: potential , pitfalls and examples from the Zanskar Himalaya, NW India. Contributions to Mineralogy and Petrology, 132: 225-245.

Vance, D. and Harris, N., 1999. The timing of prograde metamorphism in the Zanskar Himalaya. Geology, 27: 395-398.

Vance, D., Ayres, M., Kelley, S. and Harris, N. B. W., 1998a. The thermal response of a metamorphic belt to extension: constraints from laser Ar data on metamorphic micas. Earth and Planetary Science Letters, 162: 153-164.

Vance, D., Meier, M. and Oberli, F., 1998b. The influence of high U-Th inclusions on the U-Th-Pb systematics of almandine-pyrope garnet: Results of a combined bulk dissolution, stepwise-leaching and SEM study. Geochimica et Cosmochimica Acta, 62(21/22): 3527-3540.

Vannay, J.-C., Graseman, B. and Zachary, D. S., 1999. Himalayan inverted metamorphism constrained by oxygen isotope thermometry. Terra Nostra, 2(14th Himalaya-Karakoram-Tibet workshop, Kloster Ettal, Germany). 161-162.

Vannay, J.-C. and Hodges, K. V., 1996. Tectonometamorphic evolution of the Himalayan metamorphic core between the Annapurna and Dhaulagiri, central Nepal. Journal of Metamorphic Geology, 14: 635-656.

Vannay, J. C. and Grasemann, B., 1998. Inverted metamorphism in the High Himalaya of Himachal Pradesh (NW India): phase equilibria versus thermobarometry. Schweizerische Mineralogische Und Petrographische Mitteilungen, 78(1): 107-132.

Vidal, P. et al., 1984. Geochemical comparison between Himalayan and Hercynian leucogranites. Physics of the Earth and Planetary Interiors, 35: 179-190.

Vidal, P., Cocherie, A. and Le Fort, P., 1982. Geochemical investigations of the origin of the Manaslu leucogranite (Himalaya, Nepal). Geochimica et Cosmochimica Acta, 46: 2279-2292.

Virdi, N. S., 1986. Lithostratigraphy and structure of the central crystallines in the Alaknanda and Dhauliganga valleys of Garhwal. U. P. In: P.S. Saklani (Editor), Himalayan Thrust and Associated Rocks. Current trends in geology, Dehra Dun, pp. 155-166.

von Quadt, A., 1993. The Saxonian Granulite Massif - New Aspects From Geochronological Studies. Geologische Rundschau, 82(3): 516-530.

von Quadt, A. and Gebauer, D., 1993. Sm-Nd and U-Pb Dating of Eclogites and Granulites From the Oberpfalz, Ne Bavaria, Germany. Chemical Geology, 109(1-4): 317-339.

von Quadt, A. and Gunther, D., 1999. Evolution of Cambrian eclogitic rocks at the northern margin of th Bohemian massif: a conventional and LA-ICP-MS U-Pb Zircon and Sm-Nd study. Journal of Conference abstracts, 4(1): 86.

Waters, D. J., 1999. Web pages on mineral analyses and thermobarometry. .

Weinberg, R. F. and Searle, M. P., 1999. Volatile-assisted intrusion and autometasomatism of leucogranites in the Khumbu Himalaya, Nepal. The Journal of Geology, 107: 27-48.

Westrenen, W. v., Blundy, J. and Wood, B., Subm. Cystal-chemical controls on trace element partitioning between garnet and anhydrous silicate melt. American Mineralogist.

Whittington, A. G., 1995. Exhumation overrated at Nanga Parbat, northern Pakistan. Tectonophysics, 206: 215-226.

Whittington, A. G., 1997. The thermal, metamorphic and mamatic evolution of a rapidly exhuming terrane: the Nanga Parbat Massif, northern Pakistan, Open University, Milton Keynes, 433 pp.

Worley, B. and Powell, R., 1999. High-precision relative thermobarometry: theory and a worked example. .

Yamamoto, H. and Nakamura, E., 1996. The teconic implications of Sm-Nd isotope ages of garnet granulites of the Kohistan complex, Northern Pakistan. Preprint.

York, D., 1966. Least squares fitting of a straight line. Canadian Journal of Physics, 44: 1079-1086

Zhao, W., Nelson, K. D. and Team, P. I., 1993. Deep seismic reflection evidence for continental underthrusting beneath southern Tibet. Nature, 366: 557-559.

Zhou, B. and Hensen, B. J., 1995. Inherited Sm-Nd isotope components preserved in monazite inclusions within garnet in leucogneiss from East Antarctica and implications for closure temperature studies. Chemical Geology, 121: 317-326.

Zhu, X. K., O'Nions, R. K., Belshaw, N. S. and Gibb, A. J., 1997. Lewisian crustal history from in situ SIMS mineral chronometry and related metamorphic textures. Chemical Geology, 136: 205-218.

# Appendix A - Sample Localities

Loc. Refers to sample localities on maps in this Appendix. Alak. = alaknanda, Bhag. = Bhagirathi, IS = *In-situ*, F = not *in-situ*, Orient. = orientation of thin section (right-hand rule unless otherwise stated), ts= thin section, ps = probe section, m = majors element XRF analyses, t = trace elements XRF analyses.

Samples are held at the OU. See Figure A.1 and Figure A.2 for sample localities.

Whole-rock geochemical data is summarised in Appendix D

Selected mineral data is in Appendix E or in text. A full dataset is available from the author.

## Sample localities

| No. | Loc | River | Unit | Description | So | Orient | Minerals | Sections | Geochem | INAA |
|---|---|---|---|---|---|---|---|---|---|---|
| **4A.1** | 5A | Alak. | MCT | schist | IS | | grt, bt, ms, qtz, pl, chl, | ts, ps | | |
| **4A.2** | 5A | Alak. | MCT | schist | IS | | grt, bt, ms, qtz, | ts | m, t | |
| **4A.3** | 5A | Alak. | MCT | schist | IS | | grt, bt, ms, qtz, st, | ts, ps | m, t | |
| **4A.4** | | Alak. | MCT | gneiss | F | | grt, bt, ms, qtz, | ts, ps | | |
| **6A** | 6A | Alak. | HHC | migmatite | IS | | grt, bt, ms, qtz, pl, | ts | | |
| **3A** | 3A | Alak. | MCT | | IS | 022/85E | bt, ms, qtz, | ts | | |
| **1B.2** | 1B | Alak. | HHC | migmatite | ? | | grt, bt, ms, qtz, kfs, pl, | ts | | |
| **2B.1** | 2B | Alak. | HHC | gneiss | IS | 060/74S | grt, bt, ms, qtz, kfs, pl, ky, | ts | m, t | |
| **2B.2** | 2B | Alak. | HHC | gneiss | IS | | grt, bt, qtz, kfs, pl, ky, | ts | | |
| **4B.1** | 4B | Alak. | HHC | gneiss | IS | | grt, bt, ms, qtz, pl, st, ru, clz? | ts, ps | m, t | INAA |
| **1** | 4B | Alak. | HHC | | F | | grt, bt, ms, qtz, kfs, pl, chl, | ts, ps | | |
| **3** | 4C | Dhauli | HHC | schist | IS | | grt, | ts | | |
| **4** | 4C | Dhauli | HHC | calc silicate | IS | | grt, qtz, cc, cpx, hbl | ts | | |
| **5** | 5C | Dhauli | HHC | quartzite | IS | 186/40W | bt, ms, qtz, pl, | ts | | |
| **6** | 5C | Dhauli | HHC | | IS | | bt, ms, qtz, pl, | ts | | |
| **7** | 5C | Dhauli | HHC | schist | IS | | grt, bt, ms, qtz, pl, chl, tur, | ts | | |
| **8** | 6C | Dhauli | HHC | schist | IS | 308/29 | grt, bt, ms, qtz, pl, | ts | | |
| **9** | 6C | Dhauli | HHC | schist | IS | | grt, bt, ms, qtz, pl, | ts | m, t | INAA |
| **11** | 7C | Dhauli | HHC | schist | IS | | grt, bt, ms, qtz, pl, ky, chl, tur, ru, | ts | m, t | |
| **12** | 7C | Dhauli | HHC | schist | IS | | grt, ky, | ts | | |
| **13** | 7C | Dhauli | HHC | schist | IS | | grt, bt, ms, qtz, pl, ky, | ts | | |
| **14** | 1D | Alak. | HHC | | IS | | grt, ms, qtz, ru, ep? | ts | | |
| **15** | 1D | Alak. | HHC | | IS | | grt, bt, ms, qtz, chl, ru, ep? | ts | | |
| **16** | 3D | Alak. | HHC | | IS | 042/64 | grt, bt, ms, qtz, pl, chl, ep, amph | ts, ps | | |
| **18** | 3D | Alak. | HHC | migmatite | IS | | grt, bt, ms, qtz, kfs, pl, sil, chl, | ts | | |
| **19** | 4D | Alak. | HHC | gt pegmatite | IS | | grt, qtz, tur, | ps | | |
| **20** | 4Da | Alak. | HHC | leucogranite | F | | | ts | | |
| **21** | 5D | Alak. | HHC | leucogranite | IS | | | ts | | |
| **22** | 5D | Alak. | HHC | leucogranite | IS | | | ts | | |
| **23** | 5D | Alak. | HHC | leucogranite | IS | | bt, ms, qtz, kfs, pl, | ts | | |
| **24** | 2E | Alak. | HHC | gneiss | IS | | grt, bt, ms, qtz, pl, sil, st, oa | ts | | |

## Sample localities

| No. | Loc | River | Unit | Description | So | Orient | Minerals | Sections | Geochem | INAA |
|---|---|---|---|---|---|---|---|---|---|---|
| 25 | 3E | Alak. | HHC | leucogranite | IS | | grt, tur, | ts | | |
| 26 | 4E | Alak. | HHC | Strained Leucogranit | IS | | grt, bt, ms, qtz, kfs, pl, | ts | m, t | INAA |
| 27 | 4E | Alak. | HHC | gneiss | IS | | grt, bt, ms, qtz, kfs, pl, sil, | ts | | |
| 28 | 4E | Alak. | HHC | Strained Leucogranit | IS | | grt, bt, ms, qtz, pl, sil, chl, | ts | m, t | INAA |
| 29 | 4E | Alak. | HHC | migmatite | IS | 006/82 | grt, bt, ms, qtz, kfs, pl, sil, ky, | ts | | |
| 30 | 4E | Alak. | HHC | Strained Leucogranit | IS | | grt, bt, ms, qtz, kfs, pl, sil, | ts | m, t | INAA |
| 31(1) | 4E | Alak. | HHC | Strained Leucogranit | IS | | grt, bt, ms, qtz, kfs, pl, sil, tur, | ps | m, t | INAA |
| 31(2) | 1F | Alak. | HHC | gneiss | IS | | grt, bt, ms, qtz, pl, | ts | | |
| 32 | 2F | Dhauli | HHC | gneiss | IS | | grt, bt, ms, qtz, pl, ky, | ts | | |
| 33 | 4F | Dhauli | HHC | | IS | | grt, bt, ms, qtz, pl, ru, | ts | | |
| 34 | 4F | Dhauli | HHC | gneiss | IS | | grt, bt, ms, qtz, pl, st, | ts | | |
| 35 | 8F | Dhauli | MCT | schist | IS | | grt, bt, ms, qtz, chl, graphite | ts | | |
| 36 | 9F | Dhauli | MCT | schist | IS | | grt, bt, ms, qtz, pl, chl, tur, | ts | | |
| 37 | 10F | Dhauli | MCT | gneiss | IS | | grt, bt, ms, qtz, pl, | ts | | |
| 38 | Nig1 | Alak. | HHC | schist | IS | | grt, bt, ms, qtz, pl, chl, | ts | | |
| 39 | Nig2 | Alak. | HHC | gneiss | IS | | | ts | | |
| 40 | Nig3 | Alak. | HHC | | IS | | grt, bt, ms, qtz, pl, ky, chl, tur, ru, | ts | | |
| 41 | 2G | | HHC | | IS | 304/84 | grt, bt, ms, qtz, pl, | ts | | |
| 42 | 2G | | HHC | Strained Leucogranit | IS | 228/48 | grt, ms, qtz, kfs, pl, | ts | m, t | INAA |
| 43 | 1H | Alak. | LH | calc silicate | IS | 058/69 | ms, qtz, cc | ts | | |
| 44 | 3I | Bhag. | MCT | bi granite | IS | | bt, ms, qtz, kfs, pl, | ts | | |
| 45 | 5I | Bhag. | MCT | schist | IS | | grt, bt, ms, qtz, chl, tur, ep, | ts | | |
| 46 | 3I | Bhag. | MCT | amphibolite | IS | | qtz, pl, cpx, hbl | ts | | |
| 47 | 3I | Bhag. | MCT | gneiss strained | IS | | bt, ms, qtz, kfs, pl, tur, | ps | m, t | INAA |
| 48 | 3I | Bhag. | MCT | amphibolite | IS | | bt, qtz, pl, ep, amph | ts | | |
| 49 | 2J | Bhag. | MCT | schist | IS | 356/82 | grt, bt, ms, qtz, chl, | ts, ps | m, t | |
| 50 | 2J | Bhag. | MCT | schist | IS | | grt, bt, | ts | | |
| 51 (1) | 4J | Bhag. | HHC | migmatite | F | | grt, bt, ms, qtz, kfs, pl, ep, ap | ts | | |
| 51 (2) | 4J | Bhag. | HHC | migmatite | F | | bt, ms, qtz, pl, ep, | ts | m, t | |
| 51 (3) | 4J | Bhag. | HHC | migmatite | F | | bt, ms, qtz, pl, ep, | ts | | |
| 51 (4) | 4J | Bhag. | HHC | migmatite | F | | bt, ms, qtz, kfs, tur, cc | ts | | |

## Appendix A

### Sample localities

| No. | Loc | River | Unit | Description | So | Orient | Minerals | Sections | Geochem | INAA |
|---|---|---|---|---|---|---|---|---|---|---|
| 51 (5) | 4J | Bhag. | HHC | migmatite | F | | bt, qtz, pl, ep, clz | ts | m, t | |
| 52 | 6I | Bhag. | MCT | calc silicate | IS | | bt, qtz, cc | ts, ps | | |
| 53 | 6I | Bhag. | MCT | amphibolite | IS | 332/78 | bt, qtz, hbl | ts | | |
| 54 | 1I | Bhag. | LH? | gneiss | IS | | bt, ms, qtz, kfs, ep, | ts | | |
| 55 | 5J | Bhag. | HHC | schist | IS | 355/78 | grt, bt, ms, qtz, pl, ky, tur, zir | ts | | |
| 56 | 6J | Bhag. | HHC | schist | IS | | grt, bt, qtz, pl, ky, mnz | ts | | |
| 57 | 7I | Bhag. | HHC | gneiss | IS | | grt, bt, ms, qtz, pl, | ts, ps | | |
| 58 | 1I | Bhag. | LH? | amphibolite | IS | | bt, qtz, pl, hbl | ts | | |
| 59 | 2I | Bhag. | MCT | amphibolite | IS | | bt, qtz, pl, ep, hbl | ts | | |
| 60 | 2I | Bhag. | MCT | gneiss | IS | | bt, qtz, kfs, pl, ep, hbl | ts | | |
| 61 | 1K | Bhag. | HHC | psammite | IS | | grt, bt, qtz, pl, ep, hbl, sphene | ts | | |
| 62 | 2K | Bhag. | HHC | schist | IS | | bt, ms, qtz, kfs, pl, sil, ky, st, tur, | ts | m, t | |
| 63 | 2K | Bhag. | HHC | vein material | IS | | bt, ms, qtz, kfs, pl, ky, | ts | | |
| 64 | 2K | Bhag. | HHC | schist | IS | | bt, ms, qtz, tur, | ts | | |
| 65 | 2K | Bhag. | HHC | schist | IS | | grt, bt, ms, qtz, pl, ky, ep, | ts, ps | m, t | |
| 66 | 4K | Bhag. | HHC | amphibolite | IS | | grt, bt, qtz, kfs, pl, ep, sphene, hbl | ts | | |
| 67 | 4K | Bhag. | HHC | schist | IS | | grt, bt, ms, qtz, pl, | ts | | |
| 68 | 4K | Bhag. | HHC | big mu | IS | | ms, | ts | | |
| 69 | 4K | Bhag. | HHC | schist | IS | | ms, tur, | ts | | |
| 70 | 1L | Bhag. | HHC | schist | IS | | grt, bt, ms, qtz, pl, | ts | | |
| 71 | 1L | Bhag. | HHC | schist | IS | | bt, ms, qtz, pl, tur, | ts | | |
| 72 | 2L | Bhag. | HHC | schist | IS | | grt, bt, ms, qtz, pl, chl, tur, | ts | | |
| 73 | 2L | Bhag. | HHC | schist | IS | | grt, bt, ms, qtz, chl, | ts | | |
| 74 | 4L | Bhag. | HHC | leucogranite | IS | | ms, qtz, kfs, pl, tur, | ts | m, t | INAA |
| 75 | 5L | Bhag. | HHC | leucogranite | IS | | grt, | ts | m, t | INAA |
| 77 | 7L | Bhag. | HHC | bi granite | IS | | bt, ms, qtz, kfs, pl, ep, sphene | ts | m, t | INAA |
| 78 | 8L | Bhag. | HHC | reaction rim | IS | 052/62 | | ts | | |
| 79 | 9L | Bhag. | HHC | schist | IS | | grt, bt, ms, qtz, pl, st, | ts, ps | | |
| 80 | 8L | Bhag. | HHC | quartzite | IS | | grt, bt, qtz, pl, chl, ap | ts | | |
| 81 | 8L | Bhag. | HHC | quartzite | IS | | bt, ms, qtz, tur, ep, | ts | | |
| 82 | 8L | Bhag. | HHC | schist | IS | | grt, bt, ms, qtz, tur, | ts | | |

| No. | Loc | River | Unit | Description | So | Orient | Minerals | Sections | Geochem | INA A |
|---|---|---|---|---|---|---|---|---|---|---|
| 83 | 8L | Bhag. | HHC | schist | IS | | grt, bt, ms, qtz, | ts | | |
| 85 | 10L | Bhag. | HHC | schist | IS | | bt, ms, qtz, | ts | | |
| 86 | 10L | Bhag. | HHC | schist | IS | | | ts | | |
| 87 | 1M | Bhag. | HHC | schist | IS | 254/68 | bt, ms, qtz, pl, ky, | ts | m, t | |
| 88 | nr 1M | Bhag. | HHC | | IS | | bt, ms, qtz, pl, sil, chl, oa | ts | | |
| 89 | nr 1M | Bhag. | HHC | schist | IS | 290/56N | | ts | | |
| 90 | nr 1M | Bhag. | HHC | schist | IS | | grt, bt, qtz, sil, ky, st, oa | ts, ps | | |
| 91 | 3M | Bhag. | HHC | calc silicate | IS | | grt, bt, ms, qtz, pl, chl, ep, hbl | ts | | |
| 92 | 5M | Bhag. | HHC | schist | IS | | grt, bt, ms, qtz, pl, ap | ts | | |
| 93 | 4M | Bhag. | HHC | schist | IS | | bt, ms, qtz, pl, | ts | | |
| 94 | 7M | Bhag. | HHC | schist | IS | | bt, ms, qtz, kfs, pl, tur, | ts | | |
| 95 | 7M | Bhag. | HHC | schist | IS | | bt, ms, qtz, | ts | | |
| 96 | 8M | Bhag. | HHC | quartzite | NIS | | grt, bt, ms, | ts | | |
| 97 | 9M | Bhag. | HHC | schist | IS | | grt, bt, ms, qtz, pl, ky, tur, | ts, ps | | |
| 99 | 12M | Bhag. | HHC | quartzite | IS | | | ts | | |
| 100 | 9M | Bhag. | HHC | schist | IS | | grt, bt, ms, qtz, pl, ky, tur, ep, | ts, ps | m, t | |
| 101 | 6M | Bhag. | HHC | schist | IS | | bt, ms, qtz, pl, tur, | ts | | |
| 102 | 1N | Bhag. | HHC | pelite | F | | grt, bt, qtz, | ts | | |
| 103 | 1N | Bhag. | HHC | | IS | 096/80 | bt, ms, qtz, ap | ts | | |
| 104 | 1N | Bhag. | HHC | gneiss and leuco | F | | bt, ms, qtz, pl, sil, tur, oa? | ts, ps | | |
| 105 | 1N | Bhag. | HHC | schist | F | | grt, bt, ms, qtz, pl, | ts | | |
| 107 | 3P | Bhag. | HHC | leucogranite | IS | | bt, ms, qtz, kfs, pl, tur, hbl, ap | ts | | |
| 108 | 3P | Bhag. | HHC | slate | F | | bt, qtz, pl, | ts | | |
| 109 | 3P | Bhag. | HHC | leucogranite | IS | | bt, ms, qtz, kfs, pl, tur, | ts | | |
| 111 | 5P | Bhag. | HHC | schist | IS | 338/64 | bt, ms, qtz, pl, ky, | ts | | |
| 112 | 5P | Bhag. | HHC | tourmaline | IS | | bt, ms, qtz, kfs, pl, tur, | ts | | |
| 113 | 5P | Bhag. | HHC | schist | IS | | bt, ms, qtz, pl, ky, tur, | ts | | |
| 114 | 6P | Bhag. | HHC | schist | IS | 324/00 | bt, ms, qtz, pl, ky, st, | ts | | |
| 116 | 3Q | Bhag. | HHC | schist | IS | 330/44 | grt, bt, ms, qtz, pl, sil, chl, ep, | ts | | |
| 117 | 6Q | Bhag. | HHC | leucogranite | IS | | grt, ms, qtz, kfs, pl, | ts | | |
| 118 | 8Q | Bhag. | HHC | gneiss | IS | 312/54 | bt, qtz, kfs, pl, tur, ep, | ts | | |

## Appendix A

### Sample localities

| No. | Loc | River | Unit | Description | So | Orient | Minerals | Sections | Geochem | INAA |
|---|---|---|---|---|---|---|---|---|---|---|
| 119 | 8Q | Bhag. | HHC | pegmatite | F | | grt, | ts | | |
| 122 | 1R | Bhag. | HHC | schist | IS | 350/80 | bt, ms, qtz, pl, | ts | | |
| 123 | 1R | Bhag. | HHC | | IS | 028/42 | grt, bt, qtz, pl, | ts | | |
| 124 | 1R | Bhag. | HHC | | F | | bt, qtz, ky, st, | ts | | |
| 125 | 2S | Bhag. | HHC | bi granite | IS | | grt, bt, ms, qtz, kfs, pl, | ts | m, t | INAA |
| 126 | 2S | Bhag. | HHC | slate | IS | 268/64 | | ts | | |
| 127 | 2S | Bhag. | HHC | schist | IS | 342/18 | bt, ms, qtz, chl, tur, | ts | | |
| 128 | 2S | Bhag. | HHC | bi granite | IS | | grt, | ts | | |
| 132 | 4T | Bhag. | HHC | schist | IS | 201/77W | grt, bt, ms, qtz, chl, | ts | | |
| 133 | 4T | Bhag. | HHC | schist | IS | 288/54W | grt, bt, ms, qtz, | ts | | |
| 134 | 5T | Bhag. | HHC | slate | F | | bt, ms, qtz, | ts | | |
| 135 | 5T | Bhag. | HHC | schist | IS | | bt, qtz, ky, crd, st, | ps | m, t | |
| 136 | 3O | Bhag. | HHC | schist | IS | | grt, qtz, pl, ep, hbl | ts | | |
| 137 | 5T | Bhag. | HHC | schist | IS | | bt, qtz, pl, st, chl, | ts | | |
| 138 | 6U | Bhag. | HHC | leucogranite | IS | | qtz, kfs, pl, tur, | ts | | |
| 139 | | Bhag. | HHC | gneiss | IS | | grt, bt, qtz, pl, | ts | | |
| 140 | | Bhag. | HHC | | IS | | bt, qtz, pl, oa | ts | | |
| 141 | 1V | Bhag. | HHC | schist | IS | | bt, ms, qtz, tur, | ts | | |
| 142 | 1V | Bhag. | HHC | schist | IS | 059/58 | | ts | | |
| 143 | 1V | Bhag. | HHC | schist | IS | | bt, ms, qtz, pl, ky, tur, ap | ts | | |
| 144 | 1V | Bhag. | HHC | schist | IS | | grt, bt, ms, qtz, | ts | | |
| 146 | 1W | Bhag. | TS | slate | F | | bt, ms, qtz, kfs, | ts | | |
| 147 | 1W | Bhag. | TS | slate | F | | bt, ms, | ts | | |
| 148 | 1W | Bhag. | HHC | cataclasite | IS | | bt, ms, qtz, | ts | | |
| 149 | 2W | Bhag. | HHC | sc | IS | | bt, qtz, ky, | ts | | |
| 150 | 5W | Bhag. | HHC | quartzite | F | | grt, bt, qtz, | ts | | |
| 151 | 8W | Bhag. | HHC | quartzite | IS | | bt, ms, qtz, pl, cc | ts | | |
| 152 | 8W | Bhag. | HHC | quartzite | IS | | bt, ms, qtz, pl, chl, | ts | | |
| 153 | 2X | Bhag. | HHC | tourmaline schist | IS | | bt, ms, qtz, pl, tur, | ts | | |
| 154 | 4X | Bhag. | HHC | tourmaline leucogran | IS | | bt, qtz, pl, tur, | ts | | |
| 155 | 1Y | Bhag. | HHC | calc silicate | F | | bt, qtz, cc | ts | | |

## Sample localities

| No. | Loc | River | Unit | Description | So | Orient | Minerals | Sections | Geochem | INA A |
|---|---|---|---|---|---|---|---|---|---|---|
| 156 | 3Y | Bhag. | HHC | amphibolite | F | | grt, bt, ms, qtz, pl, ep, | ts | | |
| 157 | 4Y | Bhag. | HHC | gneiss | IS | | bt, ms, qtz, kfs, pl, ep, | ts | | |
| 159 | 6Y | Bhag. | HHC | calc silicate | F | | grt, bt, qtz, pl, ep, hbl, ap | ts | | |
| 160 | 6Y | Bhag. | HHC | gneiss | F | | grt, | ps | m, t | |
| 161 | | Bhag. | | | | | | ts | | |
| 162 | | Bhag. | | | | | | ts | | |
| 164 | 4Z | Bhag. | MCT | schist | IS | | grt, bt, ms, qtz, pl, chl, tur, hbl | ts | | |
| 165 | 8Z | Bhag. | MCT | gneiss | IS | 341/74 | bt, ms, qtz, | ts, ps | | |
| 166 | 5Z | Bhag. | MCT | schist | IS | | grt, bt, ms, qtz, chl, | ts, ps | m, t | |
| 167 | 9Z | Bhag. | MCT | mafic | IS | | | ts | | |
| 168 | 10Z | Bhag. | MCT | gneiss | IS | | bt, ms, qtz, kfs, pl, tur, | ts | | |
| 169 | | | | psammite | IS | | ms, qtz, pl, | ts | | |
| 169 (2) | 13Y | Bhag. | MCT | amphibolite | IS | | bt, ms, qtz, kfs, pl, ep, amph, zir | ts | | |
| 170 | 13Y | Bhag. | MCT | psammite | IS | | ms, qtz, kfs, pl, cc, pyrite | ts | | |
| 170 (2) | 3AB | Dhauli | TS | quartzite | IS | 234/72 | | ts | | |
| 171 | 7AB | Dhauli | TS | shale | IS | | ms, qtz, | ts | | |
| 172 | 10AB | Dhauli | TS | unknown | IS | | ms, qtz, pl, pyrite | ts | | |
| 173 | 13AB | Dhauli | TS | dirty limestone | IS | 250/24 | ms, | ts | | |
| 174 | 14AB | Dhauli | HHC | granite | IS | 122/39SW | ms, qtz, kfs, pl, | ts | | |
| 175 | 15AB | Dhauli | HHC | ? | IS | | | ts | | |
| 176 | 17AB | Dhauli | HHC | leucogranite | IS | 068/82 | ms, qtz, kfs, pl, | ts | | |
| 177 | 17AB | Dhauli | HHC | leucogranite | IS | | ms, qtz, kfs, pl, | ts | | |
| 178 | 1AC | Dhauli | HHC | leucocratic mat | IS | | grt, bt, ms, qtz, | ts | | |
| 179 | 1AC | Dhauli | HHC | gneiss | IS | 206/64 | grt, bt, ms, qtz, pl, sil, chl, | ts | | |
| 180 | 1AC | Dhauli | HHC | gneiss | IS | | grt, bt, ms, qtz, pl, sil, | ts, ps | | |
| 181 | 2AC | Dhauli | HHC | gneiss | IS | | grt, bt, ms, qtz, pl, | ts, ps | | |
| 182 | 2AC | Dhauli | HHC | gneiss | IS | | grt, bt, ms, qtz, pl, sil, chl, | ts | | |
| 183 | 2AC | Dhauli | HHC | gneiss | IS | | grt, bt, ms, qtz, pl, sil, chl, | ts | | |
| 184 | 4AC | Dhauli | HHC | gneiss | IS | | grt, bt, ms, qtz, kfs, sil, | ts | | |
| 185 | 4AC | Dhauli | HHC | gneiss | IS | | bt, ms, qtz, kfs, sil, | ts | | |
| 186 | 5AC | Dhauli | HHC | granite gneiss | IS | | grt, bt, qtz, kfs, pl, | ts | | |

| No. | Loc | River | Unit | Description | So | Orient | Minerals | Sections | Geochem | INA A |
|---|---|---|---|---|---|---|---|---|---|---|
| 187 | 5AC | Dhauli | HHC | schist | IS | 058/85 | grt, bt, ms, qtz, kfs, sil, | ts | | |
| 188 | 6AC | Dhauli | HHC | gneiss | IS | | bt, ms, qtz, kfs, pl, | ts | | |
| I88(B) | 1AD | Dhauli | HHC | gneiss | IS | 200/61 | bt, ms, qtz, kfs, pl, sil, | ts | | |
| 189 | 1AD | Dhauli | HHC | leucogranite | F | | grt, ms, qtz, kfs, pl, | ts | m, t | INAA |
| 190 | 1AD | Dhauli | HHC | mafic | F | | grt, bt, qtz, pl, ep, hbl | ts | | |
| 191 | 2AD | Dhauli | TS | fault gouge? | IS | | | ts | | |
| 192 | 3AD | Dhauli | TS | quartzite | IS | | | ts | | |
| 193 | 4AD | Dhauli | TS | limestone | IS | | cc | ts | | |
| 194 | 5AD | Dhauli | HHC | gneiss | IS | | grt, bt, ms, qtz, pl, sil, ep, | ts | | |
| 195 | 2AD | Dhauli | HHC | gneiss | IS | 220/62 | | ts | | |
| 196 | 2AD | Dhauli | TS | limestone | IS | | cc | ts | | |
| 197 | nr. 2AI | Dhauli | HHC | gt gneiss | IS | 043/71 | grt, | ts | | |
| 198 | 6AD | Dhauli | HHC | ? | IS | 355/56 | ms, qtz, kfs, pl, cc | ts | | |
| 199 | 7AD | Dhauli | TS | limestone | IS | | ms, qtz, | ts | | |
| 200 | 1AE | Dhauli | HHC | gneiss | IS | | grt, bt, ms, qtz, kfs, pl, | ts | | |
| 201 | 1AE | Dhauli | HHC | calc silicate | IS | | grt, ms, qtz, pl, chl, ep, sphene | ts, ps | | |
| 202 | | Dhauli. | | | | | grt, bt, ms, qtz, kfs, pl, | ts | | |
| 203 | 8AE | Dhauli | HHC | gneiss | IS | | grt, bt, ms, qtz, pl, | ts | | |
| 204 | 8AE | Dhauli | HHC | amphibolite | IS | | grt, qtz, chl, cpx, cc, amph, sphen | ts | | |
| 205 | 8AE | Dhauli | HHC | gneiss | IS | 330/12 | grt, bt, ms, qtz, | ts | m, t | |
| 205 (B) | 1AF | Dhauli | HHC | leucocratic | IS | | sil, | ts | | |
| 206 | 1AF | Dhauli | HHC | gneiss | F | | grt, bt, ms, qtz, pl, sil, chl, | ts, ps | | |
| 207 | 3AF | Dhauli | HHC | gneiss | IS | | grt, bt, ms, qtz, pl, chl, | ts | | |
| 208 | 3AF | Dhauli | HHC | gneiss | IS | 074/89 | grt, bt, ms, qtz, pl, chl, | ts | | |
| 209 | 6AF | Dhauli | HHC | gneiss | IS | | grt, bt, ms, qtz, pl, sil, chl, | ts | m, t | |
| 210 | 7AF | Dhauli | HHC | gneiss | IS | | bt, ms, qtz, kfs, pl, sil, chl, | ts | | |
| 211 | 9AF | Dhauli | HHC | gneiss | IS | 232/68 | grt, bt, ms, qtz, kfs, pl, sil, | ts | m, t | |
| 212 | 9AF | Dhauli | HHC | calc silicate | IS | | grt, qtz, pl, chl, sphene, cpx | ts | | |
| 218 | 1AG | Dhauli | TS | quartzite | IS | | ms, qtz, opaques | ts | | |
| 219 | 3AG | Dhauli | TS | mudstone | IS | | ms, qtz, | ts | | |
| 220 | Ar | Arwa | HHC | bi granite | F | | grt, bt, ms, qtz, kfs, pl, sil, | ts | | |

| No. | Loc | River | Unit | Description | So | Orient | Minerals | Sections | Geochem | INA A |
|---|---|---|---|---|---|---|---|---|---|---|
| 221 | Ar | Arwa | HHC | schist | F | | ms, tur, | ts | | |
| 222 | Ar | Arwa | HHC | leucogranite | F | | bt, qtz, kfs, pl, tur, | ts | | |
| 223 | Ar | Arwa | HHC | gneiss | F | | bt, ms, qtz, kfs, pl, tur, | ts | | |
| 224 | Ar | Arwa | HHC | layered leucogranite | F | | | ts | | |
| 225 | Ar | Arwa | HHC | schist | F | | bt, qtz, crd, | ts | | |
| 226 | Ar | Arwa | HHC | leucogranite | F | | ms, qtz, kfs, pl, tur, | ts | m, t | INAA |
| 227 | Ar | Arwa | HHC | bi granite | F | | | ts | | |
| 228 | Ar | Arwa | TS | ? | F | | bt, ms, qtz, | ts | | |
| 229 | Ar | Arwa | HHC | schist | F | | bt, ms, ky, crd, corundum | ts | | |
| 230 | 3AI | Saras. | HHC | gneiss | IS | | grt, ms, qtz, kfs, pl, sil, | ts | | |
| 231 | 3AI | Saras. | HHC | gneiss | IS | | grt, bt, ms, qtz, kfs, pl, sil, ep, mn | ts | | |
| 232 | 1AJ | Saras. | HHC | amphibolite | IS | | qtz, cpx, hbl | ts | | |
| 233 | 1AJ | Saras. | HHC | calc silicate | IS | | bt, ms, qtz, kfs, pl, sil, chl, | ts | | |
| 234 | 4AJ | Saras. | HHC | gneiss | IS | | bt, qtz, pl, | ts | | |
| 235 | 5AJ | Saras. | HHC | quartzite | IS | | bt, ms, qtz, pl, sil, | ts | | |
| 236 | | Alak. | HHC | gneiss | IS | 083/80 | grt, bt, ms, qtz, pl, ky, | ts | | |
| 237 | | Alak. | HHC | gneiss | IS | | grt, | ts | | |
| 238 | 2AK | Dhauli | MCT | gneiss | IS | | grt, bt, ms, qtz, st, | ts | | |
| 239 | 4AK | Dhauli | HHC | schist | IS | | grt, | ts | | |
| 240 | 4AK | Dhauli | HHC | ? | IS | 276/30 | bt, qtz, ged | ts | | |
| 241 | 5AK | Dhauli | HHC | quartzite | IS | 308/40 | grt, bt, ms, qtz, | ts | | |
| 242 | | | | leucogranite | | | bt, ms, qtz, kfs, pl, tur, | ts | m, t | INAA |
| 243 | | | | | | | ms, qtz, kfs, pl, tur, | ts | | |

## Second Field Season October 1997

| | | | | | | | | | | |
|---|---|---|---|---|---|---|---|---|---|---|
| 1 97 | 1A | Bhag. | HHC | leucogranite dyke | IS | | grt, ms, qtz, kfs, pl, | ts | | |
| 2 97 | 4A | Bhag. | HHC | schist | IS | | bt, ms, qtz, st, | ts | | |
| 3 97 | C | Bhag. | HHC | leucogranite | F | | ms, qtz, kfs, pl, tur, | ts | | |
| 4 97 | C | Bhag. | HHC | bi granite | F | | grt, bt, ms, qtz, kfs, pl, | ts | | |
| 5 97 | C | Bhag. | HHC | bi granite | F | | ms, qtz, kfs, pl, chl, | ts | | |
| 6A 97 | C | Bhag. | TS | sediment | F | | ms, qtz, kfs, pl, chl, | ts | | |

## Appendix A

### Sample localities

| No. | Loc | River | Unit | Description | So | Orient | Minerals | Sections | Geochem | INAA |
|---|---|---|---|---|---|---|---|---|---|---|
| **6B 97** | C | Bhag. | TS | sediment | F | | qtz, chl, | ts | | |
| **6C 97** | C | Bhag. | TS | sediment | F | | ms, qtz, | ts | | |
| **7A 97** | C | Bhag. | TS | sediment | F | | ms, qtz, pl, | ts | | |
| **7B 97** | C | Bhag. | TS | sediment | F | | grt, bt, ms, qtz, kfs, pl, | ts | | |
| **7C 97** | C | Bhag. | TS | sediment | F | | ms, qtz, | ts | | |
| **8 97** | 1D | Bhag. | HHC | bi granite | F | | grt, bt, ms, qtz, kfs, pl, chl, | ts | | |
| **9 97** | 4A/D | Bhag. | HHC | schist | IS | | grt, ky, | ts | | |
| **10 97** | 4A/D | Bhag. | HHC | schist | IS | | bt, ms, qtz, sil, crd, st, ru, mnz, zi | ts, ps | | |
| **11 97** | | | | | | | | ts | | |
| **12 97** | | | | | | | | ts | | |
| **13 97** | 1E | Bhag. | HHC | psammite | IS | | grt, bt, qtz, chl, | ts | | |
| **14 97** | 2E | Bhag. | HHC | schist | IS | | grt, st, | ts | | |
| **15 97** | 3E | Bhag. | HHC | schist | IS | | grt, bt, ms, qtz, st, | ts | | |
| **16 97** | | Bhag. | HHC | schist | IS | | grt, bt, | ts | | |
| **17 97** | | Bhag. | HHC | leucogranite | IS | | bt, qtz, kfs, pl, tur, | ts | m, t | INAA |
| **18 97** | | Bhag. | HHC | migmatite | F | | bt, ms, qtz, kfs, pl, | ts | | |
| **19 97** | | | | | | | | ts | | |
| **20 97** | | Mand. | HHC | schist | F | | grt, bt, ms, qtz, pl, sil, ky, st, tur, | ts | | |
| **21 97** | | Mand. | HHC | gneiss | F | | grt, | ps | | |
| **22 97** | | Mand. | HHC | gneiss | IS | | grt, | ps | | |
| **23 97** | | Alak. | LH | quartzite | IS | ? | | ts | | |
| **24 97** | | Alak. | HHC | schist | IS | 066/44 | grt, bt, qtz, pl, amph | ts, ps | | |
| **25A 97** | J2 | Alak. | HHC | leucogranite | F | | ms, qtz, kfs, pl, | ts | | |
| **25B 97** | J2 | Alak. | HHC | leucogranite | F | | ms, qtz, kfs, pl, tur, mnz | ts | | |
| **25C 97** | J2 | Alak. | HHC | leucogranite | F | | ms, qtz, kfs, pl, mnz | ts | | |
| **26A 97** | K1 | Alak. | HHC | leucogranite | F | | bt, ms, qtz, kfs, pl, | ts | m, t | INAA |
| **26B 97** | K1 | Alak. | HHC | leucogranite | F | | bt, ms, qtz, kfs, pl, | ts | m, t | INAA |
| **26C 97** | K1 | Alak. | HHC | leucogranite | F | | bt, ms, qtz, kfs, pl, | ts | m, t | INAA |
| **26D 97** | K1 | Alak. | HHC | leucogranite | F | | bt, ms, qtz, kfs, pl, | ts | m, t | INAA |
| **27 97** | L1 | Dhauli | HHC | gneiss | IS | | grt, bt, ms, qtz, kfs, sil, | ts, ps | | |
| **28 97** | L1 | Dhauli | HHC | gneiss | IS | 20/342 | bt, ms, qtz, pl, | ts | | |

## Sample localities

| No. | Loc | River | Unit | Description | So | Orient | Minerals | Sections | Geochem | INAA |
|---|---|---|---|---|---|---|---|---|---|---|
| 29 97 | | Dhauli | TS | shale | IS | 341/26 | ms, qtz, chl, graphite | ts | | |
| 30A 97 | | Dhauli | HHC | leucogranite | IS | | qtz, pl, tur, | ts | m, t | INAA |
| 30B 97 | | Dhauli | HHC | leucogranite | IS | | qtz, kfs, pl, tur, | ts | | |
| 31 97 | N1 | Dhauli | HHC | schist | IS | | grt, | ts | | |
| 32 97 | N1 | Dhauli | HHC | pegmatite | F | | | ts | | |
| 33 97 | N1 | Dhauli | HHC | gneiss | F | | grt, bt, ms, qtz, pl, chl, cc | ts | | |
| 34 97 | N1 | Dhauli | HHC | migmatite | F | | bt, ms, qtz, pl, | ts | | |
| 35 97 | N1 | Dhauli | HHC | migmatite | F | | grt, bt, ms, qtz, kfs, pl, sil, | ts | | |
| 36 97 | N1 | Dhauli | HHC | schist | F | | bt, ms, qtz, sil, ep, | ts | | |
| 37 97 | N3 | Dhauli | HHC | gneiss | IS | | bt, ms, qtz, kfs, sil, chl, | ts | | |
| 38 97 | N3 | Dhauli | HHC | gneiss | IS | 331/58 | grt, bt, ms, qtz, kfs, pl, sil, | ts | | |
| 39 97 | N3 | Dhauli | HHC | gneiss | IS | 240/89 | bt, ms, qtz, kfs, pl, sil, | ts | | |
| 40A 97 | O1 | Dhauli | HHC | amphibolitic schist | IS | | | ts | | |
| 40B 97 | O1 | Dhauli | HHC | gneiss | IS | | bt, qtz, kfs, pl, ep, | ts | | |
| 40C 97 | O1 | Dhauli | HHC | leucogranite | IS | | | ts | m, t | INAA |
| 40D 97 | O1 | Dhauli | HHC | leucogranite | IS | | ms, qtz, kfs, pl, | ts | m, t | INAA |
| 41 97 | P1 | Dhauli | MCT | schist | IS | 308/60 | grt, | ts | | |
| 42 97 | P2 | Dhauli | MCT | schist | IS | | bt, ms, qtz, ep, | ts | | |
| 43 97 | P3 | Dhauli | MCT | gneiss | IS | 106/54 | bt, ms, qtz, kfs, pl, | ts, ps | | |
| 44 97 | | Dhauli | MCT | quartzite | IS | | bt, ms, qtz, kfs, pl, ep, | ts | | |
| 45 97 | Q1 | Dhauli | MCT | schist | IS | | bt, ms, qtz, pl, | ts | | |
| 46 97 | Q1 | Dhauli | MCT | schist | IS | | grt, bt, ms, qtz, chl, tur, ep, | ts, ps | | |
| 47 97 | Q1 | Dhauli | MCT | amphibolite | IS | | bt, qtz, hbl | ts | | |
| 48 97 | Q2 | Dhauli | MCT | calc silicate | IS | | grt, bt, ms, qtz, cc, cl-pyx, dol | ts | | |
| 49 97 | Q2 | Dhauli | MCT | calc sil. + leuc | IS | | | ps | | |
| 50 97 | Q3 | Dhauli | MCT | leucogranite | IS | | | ts | | |
| 51 97 | Q1 | Dhauli | MCT | schist | IS | | grt, bt, ms, qtz, pl, tur, | ts | | |
| 52 97 | Q1 | Dhauli | MCT | schist | IS | | grt, bt, ms, qtz, pl, tur, | ts | | |
| 53 97 | Q4 | Dhauli | HHC | fsp bi shear fabric | IS | 301/36 | | ts | | |
| 54 97 | | Alak. | HHC | calc silicate | IS | | grt, bt, ms, qtz, kfs, cc, sphene | ts | | |
| 54B 97 | | | | | | | grt, bt, ms, qtz, | ts | | |

## Appendix A

### Sample localities

| No. | Loc | River | Unit | Description | So | Orient | Minerals | Sections | Geochem | INA A |
|---|---|---|---|---|---|---|---|---|---|---|
| 55 97 | N4 | Dhauli | HHC | amphibolite | IS | 066/64 | | ps | | |
| 56 97 | R3 | Dhauli | HHC | mylonite | IS | 316/26 | grt, ms, qtz, kfs, pl, | ts | | |
| 57/97 | | | | | | | grt, qtz, pl, hbl | ts, ps | | |
| V1/97 | 1F | Bhag. | MCT | Schists/calc-silicates | IS | | | | | |
| V2/97 | | Bhag. | MCT | Schists/calc-silicates | IS | | | | | |
| V3/97 | | Bhag. | MCT | Schists/calc-silicates | IS | | | | | |
| V4/97 | | Bhag. | MCT | Schists/calc-silicates | IS | | | | | |
| **Samples collected by Judy Baker** | | | | | | | | | | |
| 2LP | | Saras. | HHC | | | | | ps | | |
| 2eb4a | | | | | | | grt, bt, ms, pl, | ps | | |
| 2ee | | | | | | | grt, bt, ms, pl, | ps | | |
| 2eja | | | | | | | grt, bt, ms, pl, | ps | | |
| 2en2 | | | | | | | grt, bt, ms, | ps | | |
| 2en3 | | | | | | | grt, bt, ms, pl, chl, | ps | | |
| 2esb | | | | | | | grt, bt, ms, pl, chl, | ps | | |
| 2se | | | | | | | grt, ms, pl, | ps | | |
| 2sn | | | | | | | grt, bt, ms, pl, | ps | | |
| 2sq | | | | | | | grt, bt, ms, pl, | ps | | |
| 2gn | | | | | | | kfs, | ps | | |
| 2gxa | | | | | | | grt, bt, ms, kfs, pl, | ps | | |
| 2hdib | | | | | | | grt, bt, ms, kfs, pl, | ps | | |
| 2hh | | | | | | | grt, bt, ms, kfs, pl, | ps | | |
| 2jb | | | | | | | grt, bt, ms, pl, | ps | | |
| 2jh | | | | | | | grt, bt, ms, | ps | | |
| 2jm | | | | | | | grt, bt, ms, kfs, pl, | ps | | |
| 2km | | | | | | | grt, bt, ms, pl, | ps | | |
| 2lw | | | | | | | grt, bt, ms, pl, | ps | | |
| 2ly | | | | | | | grt, bt, ms, kfs, pl, | ps | | |
| 2nj | | | | | | | grt, bt, ms, pl, st, amph | ps | | |
| 2no | | Bhag. | | | | | grt, bt, ms, pl, | ps | | |

| No. | Loc | River | Unit | Description | So | Orient | Minerals | Sections | Geochem | INA A |
|---|---|---|---|---|---|---|---|---|---|---|
| aea | | Bhag. | | | | | grt, bt, ms, pl, | ps | | |
| ahb | | | | | | | grt, | ps | | |
| 004a | | | | | | | grt, bt, ms, pl, | ps | | |
| 004b | | | | | | | grt, bt, ms, kfs, | ps | | |
| 005a | | | | | | | grt, bt, ms, kfs, | ps | | |
| 005b | | | | | | | grt, bt, kfs, | ps | m, t | |
| 005c | | | | | | | | ps | m, t | |
| 006a | | | | | | | grt, bt, ms, pl, | ps | | |
| 006b1 | | | | | | | grt, bt, ms, pl, | ps | | |
| 007 | | | | | | | grt, bt, pl, chl, | ps | | |
| 008a | | | | | | | grt, bt, | ps | m, t | |
| 014a | | | | | | | grt, bt, ms, pl, ky, | ps | m, t | |
| 014b | | | | | | | | ps | m, t | |
| 016c1 | | | | | | | grt, bt, ms, pl, ky, | ps | | |
| 017a | | | | | | | grt, bt, ms, pl, | ps | | |
| 021 | | | | | | | bt, pl, crd, st, amph, sphr | ps | | |
| 023 | | | | | | | grt, bt, ms, pl, | ps | | |
| 024 | | | | | | | | ps | | |
| 026 | | | | | | | | ps | | |
| 035c | | | | | | | | ps | m, t | |
| 035b | | | | | | | | ps | m, t | |
| 035a | | | | | | | | ps | m, t | |

## Samples collected for Fisson Track analysis

| | | | | |
|---|---|---|---|---|
| KIT2 | 9AB | Dhauli | TS | calcareous | IS |
| KIT3 | 16AB | Dhauli | HHC | granitoid | IS |
| KIT4 | 1AC | Dhauli | HHC | leucocratic vein | IS |
| KIT5 | 6AD | Dhauli | HHC | granitoid | IS |
| KIT6 | 8AD | Dhauli | TS | arkose | IS |
| KIT7 | 1AF | Dhauli | HHC | leucocratic | IS? |
| KIT8 | 10AF | Dhauli | HHC | leucogranite | IS |

## Appendix A

### Sample localities

| No. | Loc | River | Unit | Description | So | Orient | Minerals | Sections | Geochem | INA A |
|---|---|---|---|---|---|---|---|---|---|---|
| **KIT9** | 2AG | Dhauli | TS | sanstone | IS | | | | | |
| **KIT10** | 4AG | Dhauli | TS | limestone | IS | | | | | |
| **KIT11** | 5AG | Dhauli | HHC | leucogranite | IS | | | | | |

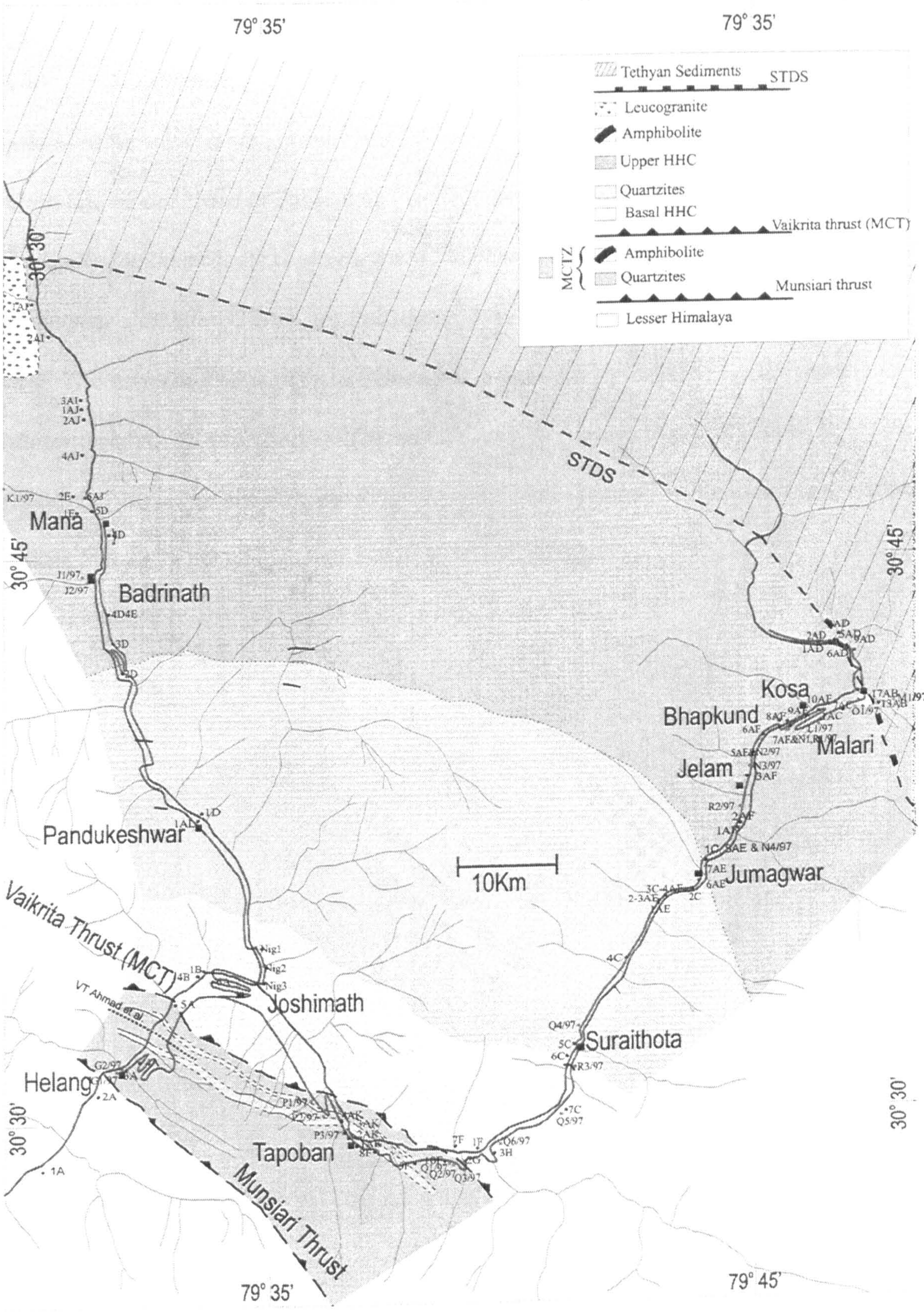


*Figure A.1 Sample localities for the Alaknanda valley.*

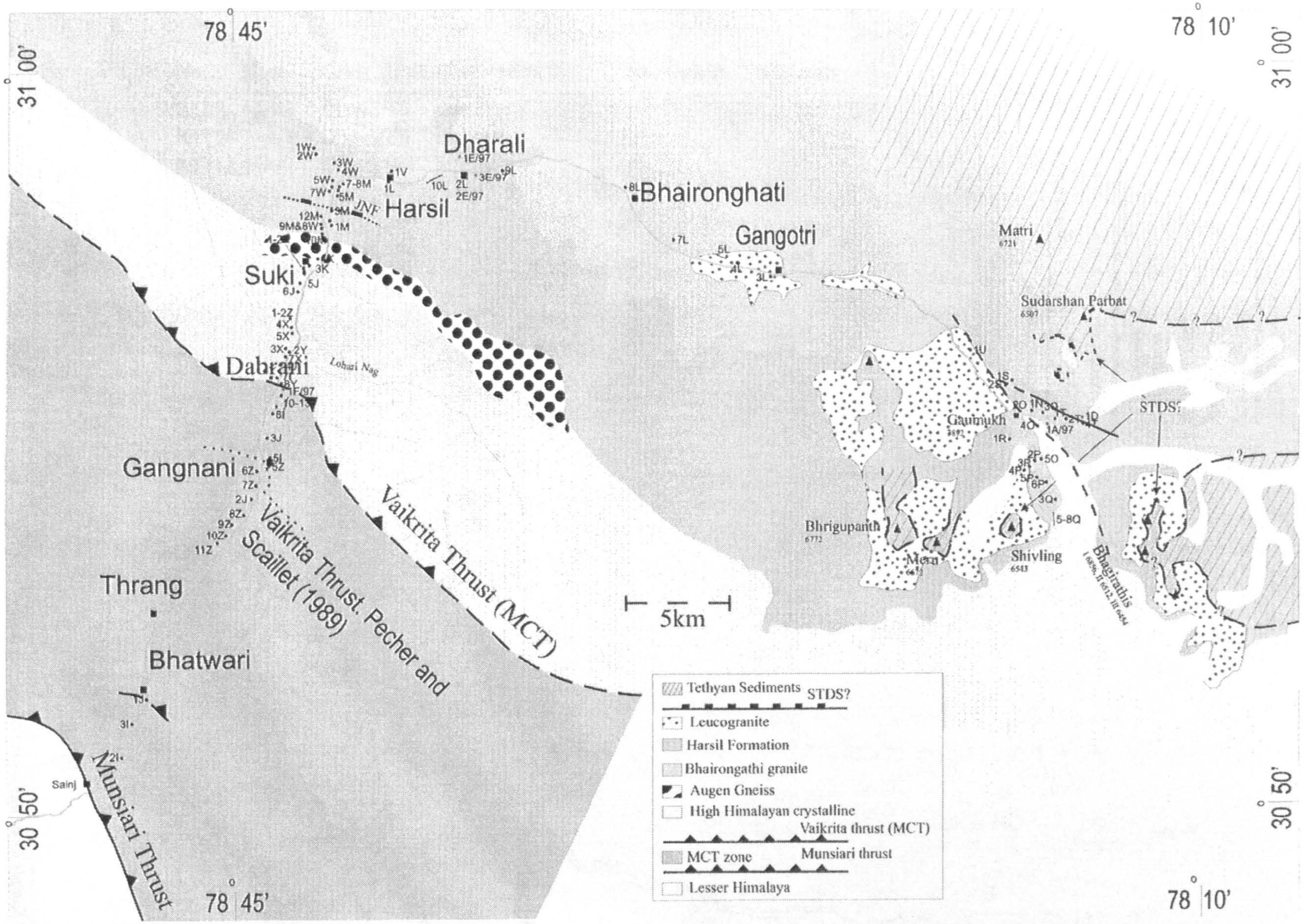


*Figure A.2 Sample Localities for the Bhagirathi valley*

# Appendix B - Thermobarometric techniques

## *B.1 Thermocalc annotated example output*

*Below is an example of Thermocalc output used in Chapter 3. Text in italics is the authors otherwise it is output from Thermocalc and Ax98. Mineral endmember abbreviations are listed in* Table B.1.

*The firstly for thermocalc to determine a temperature and pressure it requires mineral endmember activities. These are calculated from microprobe data using the program Ax98. The mineral endmember activities are calculated by Ax98 using the same solid solution models as are used in Thermocalc and are summarised in* Table B.2. *The endmember activities are then input into Thermocalc in a data file, an example of which is given below:*

```
%th d4a3 600, 7    "%"  indicates text for information only
py      0.002
gr      0.0021
alm     0.44
mst     0.0016
fst     0.41
mu      0.68
pa      0.98
cel     0.019
phl     0.069
ann     0.037
east    0.051
san     0.81
ab      0.93
q                  no activity indicates that it is unity i.e. no solid solution
H2O
*
```

*If errors on the endmember activities are not given Thermocalc assigns an error to the activities. Using the supplied endmembers Thermocalc calculates a complete set of independent reactions which could be formed an example of which is given below;*

Independent set of reactions

1) phl + east + 6q = py + 2cel

2) 2mst + 25phl + 4san + 68q = 18py + 29cel
3) 5py + 2mst + 23cel = 23east + 76q + 4H2O
4) 21py + 6mst + 41ann + 12san = 41alm + 19cel + 34east
5) 6fst + 75phl + 12san + 204q = 46py + 8alm + 87cel
6) 2mst + 17phl + 4ab + 44q = 14py + 4pa + 17cel

*Using the mineral end-member activites thermocalc calculates thermodynamic data and errors for each of the reactions as shown below;*

| | P(T) | sd(P) | A | sd(a) | b | C | ln_K | Sd(ln_K) |
|---|---|---|---|---|---|---|---|---|
| 1 | 7.9 | 2.88 | 65.13 | 3.91 | 0.02782 | -3.658 | -8.492 | 1.348 |
| 2 | 6.3 | 3.48 | 958.89 | 28.18 | 0.42384 | -45.228 | -146.24 | 21.334 |
| 3 | 6.5 | 3.92 | 1108.09 | 23.91 | 0.0483 | -35.544 | -128.65 | 18.929 |
| 4 | 12.5 | 10.37 | -1538.86 | 125.67 | 1.28816 | -23.087 | 96.687 | 28.064 |
| 5 | 7.1 | 3.26 | 2960.76 | 84.1 | 1.25381 | -137.94 | -428.85 | 60.825 |
| 6 | 6.1 | 3.61 | 661.34 | 17.84 | 0.22936 | -29.283 | -95.844 | 14.353 |

*The thermodynamic data defines position of the reaction in PT space for each equation and the error. The intersection of these lines in PT space yields the average PT (avPT) result. The error on the intersection is calculated by a chi test weighting for the more precise reactions. This yields an average PT, errors and a measure of the correlation between the lines and the significance of the intersection as shown below.*

T = 721°C, sd = 47

P = 12.1 kbar, sd = 3.1, cor = 0.851, sigfit = 1.43

*If the significance of the fit is greater than that specified by Thermocalc then the PT result is not meaningful. In this case more detailed information is available on the contribution of each mineral endmember to the calculated average PT. This often highlights suspect data. As detailed by Thermocalc (some punctuation added by the author):*

avP, avT, sd's, cor, fit are result of doubling the uncertainty on ln(a). ln(a) is suspect if any are very different from lsq values. e* are ln(a) residuals normalised to ln(a) uncertainties: large absolute values, say >2.5, point to suspect info. "hat" are the diagonal elements of the hat matrix: large values, say >0.46, point to influential data.

For 95% confidence, fit (= sd(fit)) < 1.54 however a larger value may be OK - look at the diagnostics!

| | avP | sd | avT | sd | cor | fit |
|---|---|---|---|---|---|---|
| lsq | 12.1 | 3.1 | 721 | 47 | 0.851 | 1.43 |

| | P | sd(P) | T | sd(T) | cor | fit | e* | Hat |
|---|---|---|---|---|---|---|---|---|
| py | 13.08 | 2.67 | 738 | 41 | 0.863 | 1.2 | -1.6 | 0.12 |
| alm | 10.96 | 3.02 | 706 | 45 | 0.871 | 1.29 | 0.83 | 0.09 |
| mst | 11.36 | 3.09 | 706 | 49 | 0.872 | 1.35 | 0.86 | 0.2 |
| fst | 11.76 | 3.12 | 718 | 46 | 0.854 | 1.4 | -0.38 | 0.04 |
| pa | 11.69 | 3.2 | 726 | 47 | 0.68 | 1.4 | 0.38 | 0.6 |
| cel | 13.44 | 3 | 734 | 43 | 0.86 | 1.27 | -1.32 | 0.25 |
| phl | 12.72 | 3.17 | 732 | 50 | 0.871 | 1.39 | 0.55 | 0.13 |
| ann | 11.33 | 2.89 | 706 | 45 | 0.865 | 1.29 | -1.19 | 0.13 |
| east | 12.15 | 3.17 | 721 | 48 | 0.861 | 1.43 | 0 | 0.05 |
| san | 11.85 | 3.06 | 715 | 48 | 0.858 | 1.4 | 0.38 | 0.04 |
| ab | 12.01 | 3.1 | 723 | 47 | 0.796 | 1.42 | -0.19 | 0.15 |
| q | 12.15 | 3.06 | 721 | 47 | 0.851 | 1.43 | 0 | 0 |
| H2O | 12.15 | 3.06 | 721 | 47 | 0.851 | 1.43 | 0 | 0 |

*Of the mineral endmembers used in this calculation muscovite has already been removed as it had an e* of –3.06 - well above the value given above and its inclusion resulted in a very poor fit for the avPT. The present data satisfy the fit specified for this sample (1.54) and are therefore acceptable. The removal of mineral endmembers should normally be justified for geological reasons although many endmembers have very poorly constrained activity models.*

*Table B.1 Formulae of end-members used here from the Holland and Powell (1998) dataset.*

| *Ortho & Ring Silicates* | | |
|---|---|---|
| Pyrope | Py | $Mg_3 Al_2 Si_3 O_{12}$ |
| Almandine | Alm | $Fe_3 Al_2 Si_3 O_{12}$ |
| Spessartine | spss | $Mn_3 Al_2 Si_3 O_{12}$ |
| Grossular | gr | $Ca_3 Al_2 Si_3 O_{12}$ |
| Andradite | andr | $Ca_3 Fe_2 Si_3 O_{12}$ |
| Andalusite | and | $Al_2 SiO_5$ |
| Kyanite | ky | $Al_2 SiO_5$ |
| Sillimanite | sill | $Al_2 SiO_5$ |
| Mg-staurolite | mst | $Mg_4 Al_{18} Si_{7.5} O_{48} H_4$ |
| Fe-staurolite | fst | $Fe_4 Al_{18} Si_{7.5} O_{48} H_4$ |

| | | |
|---|---|---|
| Mn-staurolite | mnst | $Mn_4 Al_{18} Si_{7.5} O_{48} H_4$ |
| Cordierite | crd | $Mg_2 Al_4 Si_5 O_{18}$ |
| Fe-cordierite | fcrd | $Fe_2 Al_4 Si_5 O_{18}$ |
| Mn-cordierite | mncrd | $Mn_2 Al_4 Si_5 O_{18}$ |
| ***Chain Silicates*** | | |
| Tremolite | tr | $Ca_2 Mg_5 Si_8 O_{24} H_2$ |
| Ferroactinolite | fact | $Ca_2 Fe_5 Si_8 O_{24} H_2$ |
| Tschermakite | ts | $Ca_2 Mg_3 Al_4 Si_6 O_{24} H_2$ |
| Gedrite | ged | $Mg_5 Al_4 Si_6 O_{24} H_2$ |
| ***Sheet Silicates*** | | |
| muscovite | mu | $KAl_3 Si_3 O_{12} H_2$ |
| celadonite | cel | $KmgAlSi_4 O_{12} H_2$ |
| Fe-celadonite | fcel | $KfeAlSi_4 O_{12} H_2$ |
| paragonite | pa | $NaAl_3 Si_3 O_{12} H_2$ |
| margarite | ma | $CaAl_4 Si_2 O_{12} H_2$ |
| phlogopite | phl | $KMg_3 AlSi_3 O_{12} H_2$ |
| annite | ann | $KFe_3 AlSi_3 O_{12} H_2$ |
| Mn-biotite | mnbi | $KMn_3 AlSi_3 O_{12} H_2$ |
| eastonite | east | $KMg_2 Al_3 Si_2 O_{12} H_2$ |
| Na-phlogopite | naph | $NaMg_3 AlSi_3 O_{12} H_2$ |
| clinochlore | clin | $Mg_5 Al_2 Si_3 O_{18} H_8$ |
| amesite | ames | $Mg_4 Al_4 Si_2 O_{18} H_8$ |
| Al-free chlorite | afchl | $Mg_6 Si_4 O_{18} H_8$ |
| daphnite | daph | $Fe_5 Al_2 Si_3 O_{18} H_8$ |
| Mn-chlorite | mnchl | $Mn_5 Al_2 Si_3 O_{18} H_8$ |
| **Framework Silicates** | | |
| albite | ab | $NaAlSi_3 O_8$ |
| high albite | abh | $NaAlSi_3 O_8$ |
| Microcline | mic | $KAlSi_3 O_8$ |
| Sanidine | san | $KAlSi_3 O_8$ |
| Anorthite | an | $CaAl_2 Si_2 O_8$ |
| Quartz | q | $SiO_2$ |
| **Oxides & Hydroxides** | | |
| Rutile | ru | $TiO_2$ |
| Hematite | Hem | $Fe_2 O_3$ |
| Ilmenite | Ilm | $FeTiO_3$ |
| **Elements & Gases** | | |
| Water fluid | H2O | $H_2O$ |
| Carbon dioxide | CO2 | $CO_2$ |

*Table B.2 Summary of activity models used in Ax98 for minerals of interest. Abbreviations are summarised in Table B.1. "Max Ratio" is maximum allowed ferric/ferrous iron.*

| Name and abbreviation | | Mixing model and ferric iron |
|---|---|---|
| Garnet | G | 2-site mixing. Ferric from Cation Sum = 8 for 12 oxygens. py.alm=2.5, gr.py=41.4 - 0.0188T, py.andr=73, alm.andr=60, spss.andr=60 (kJ) |
| Feldspar | Pl | Holland and Powell (1992) model 1. All ferric. |
| | Ksp | Waldbaum & Thompson (1969). All ferric |
| Staurolite | St | 4-site ideal Fe-Mg mixing. All ferrous |

| | | |
|---|---|---|
| Muscovite | Mu | Holland and Powell (1998) nonideal mu-cel-fcel-pa interactions. Ferric from Tet + Oct cation sum = 6.05 for 11 oxygens. Max Ratio = 0.7 |
| Ilmenite-hematite | Ilhem | 2-site ideal mixing. 3 oxygens, 2 cations. |
| Cordierite | Cd | 2 site mixing. 18 oxygens, 11 cations. WfeMg=1.5, WMnMg=1.5 (kJ) |
| Chlorite | Chl | Ordered Al(M4) model. (Holland et al., 1998). Ferric from: Cation Sum<=10 for 14 oxygens. Max Ratio = 0.2. Wcl-da = 2.5,Wcl-am = 18, Wam-da = 20.5 (kJ) |

## *B.2 Notes on producing pseudosections from Thermocalc*

While the principles of using thermocalc are outlined elsewhere (Powell et al., 1998) for a more gentle basic introduction see Roger Powell's website at http://rubens.its.unimelb.edu.au/~rpowell. For mineral and dataset information see Tim Holland's web page at http://www.esc.cam.ac.uk/astaff/holland Also try http://www.earth.ox.ac.uk/~davewa/ for some extra hints. Don't forget to get the latest dataset (HP98 at time of going to press). Below however, are a few ***additional hints*** gleaned from using thermocalc....

When starting out predict what minerals you will have. You can do this from the bulk composition calculations of Al', X(Fe) and X(Mn) or from looking at a series of AFM diagrams such as in Frank Spear's monograph (Spear, 1993). This part seems a bit dodgy to me as you don't really know what minerals *might* have been there but nevertheless....

Once you have decided which minerals are likely to appear search for the lowest possible variance assemblage. You may not find this.

Then work up variance till you find some fields.

Once you have found some fields (e.g. three overlapping trivariant fields) adjust your starting mineral composition guesses and search for the lower variance assemblages in the areas where the higher variance assemblages overlap. The lower variance assemblages may be extremely small and therefore always use the smallest possible pressure and temperature step size i.e. smallest likely area of PT and maximum number

of steps.

Once you have found the lowest variance assemblage determine the boundaries of the field using the "setmodeiso" and "zeromodeiso" facilities (see Holland and Powell websites for details of scripting). Finding boundaries can be greatly speeded up if you find the invariant points first i.e. where *two* minerals go to zero. Once you have found the invariant points you will probably need to recalculate the univariant boundaries as the errors on the points may be larger than the size of the fields (see diagrams in Chapter 3).

From there work in a circular pattern from the lowest variance field calculating which minerals go to zero and hence the field boundaries. As an example, around a divariant field of grt, st, bt, als, chl, mu, plag, q, and H2O there are often [chl], [st] and [als] fields ([ ] indicates absent). Each of these ***must*** therefore have a boundary against the other field at which the absent mineral goes to zero from the other field. So start by finding, for example, the als=0 boundary to the [chl] field.

It is important to bear in mind that there may be other minerals which become stable away from the starting divariant field and therefore producing other divariant fields. These other minerals can be constrained by using petrogenetic grids. An example of this is cordierite as it can only appear below a certain pressure.

The next step is to contour the PT space for compositional contours of minerals of interest specifically garnet which preserves most of its growth zoning. When calculating these "isopleths" make sure that you reduce the initial guesses for the minerals because Thermocalc cannot calculate isopleths if the total cations in the mineral (desired + starting guesses) is greater than one.

Also Thermocalc seems very picky about finding isopleths and it may be necessary to change the starting guesses for all the minerals so that they agree with the calculated compositions in the PT area in which you are working.

**Good luck!**

# Appendix C - Analytical Techniques

## *C.1 Whole rock elemental analyses*

### C.1.1 Sample preparation

Weathered surfaces were removed and whole-rock samples were split into <3cm fragments. The fragments were then crushed using a hardened steel jaw crusher. Powders were obtained using an agate tema mill for 10-20 minutes. Rock powders were dried for a minimum of 24 hrs prior to use in any analytical procedure.

### C.1.2 Elemental geochemistry

Major- and trace-element analyses of whole-rock powders were obtained by wavelength dispersive XRF spectrometry at the Open University. Whole-rock major-element analysis were obtained from glass discs, which were prepared as follows. Dried whole-rock powder was mixed in a 5:1 ratio with lithium metaborate/tetraborate flux (Spectroflux 100B). The mixture was fused for 20 minutes at 900 °C in a Pt - 5% Au crucible, during which time it was stirred at 5 minute intervals in order to avoid entrapment of gas bubbles. The fused mixture was poured into a preheated, 3.6 cm diameter mould, and formed using a sprung press, thus producing a 1.5 mm thick glass disc. Loss on ignition values were calculated by percentage weight loss after igniting the sample powder at 100 °C for 30 minutes.

Trace-elements were analysed from pressed powder pellets, which were prepared by thoroughly mixing 9-10 g of rock powder with 7 ml of PVP-methyl cellulose binder. Thorough and quick mixing was ensured by gently kneading the mixture in a 2" square resealable sample bag (technique developed by J. Watson, the Open University). The mixture was pressed into a 3.8 cm stainless-steel mould using a hydraulic press at 10 Pa pressure. Pellets were dried overnight at 80-100 °C prior to analysis.

During analysis (carried out by J. Watson), X-rays were generated using a 3 kW Rh anode end-window X-ray tube, with AX06, PET, Ge111, LiF200 and LiF220 diffracting crystals. Elemental intensities were corrected for background and known peak interferences, and instrumental drift was accounted for using a drift monitor. 1-sigma analytical precision is 2% relative for concentrations >100 ppm and better than 10 relative for concentrations >10 ppm.

0.3g of dry powder was weighed into a polythene capsule, the lid of which was then air-tight sealed using a soldering iron. Nine samples and two standards (AC-2 microgranite, Whin Sill internal standard) were loaded into a polythene cylinder, with an accurately weighed iron foil between each capsule in order to monitor neutron flux variations along the length of the cylinder. Samples were irradiated at the Imperial College Reactor Centre in a thermal neutron flux of $5*10^{12} ncm^2/s$ for 24-30 hours. Samples were left for a week prior to analysis in order to allow short-lived isotopes to decay. Analysis were performed at the Open University by N. Rogers. Details of counting conditions, peak fitting, calibration and corrections are described by Potts et al. (1985). 1-sigma analytical precision is 5% relative for concentration <0.5 ppm and better than 3% for concentrations >0.5 ppm.

## *C.2 Isotopic analyses*

### C.2.1 Sample preparation

Impure garnet was separated from hand-specimen by a variety of techniques. Bulk-separates were obtained by crushing the sample to ~200 μm and removing garnet with heavy liquids. Alternatively, single crystals were removed from the whole-rock and crushed to obtain a separate from either individual crystals or a mixture of crystals. Large garnets were cut in half using a slow-saw and one half mounted for electron-microprobe analysis and the other half separated into core and rim portions.

Once a garnet separate was obtained, pieces without visible inclusions were separated under propanol (to reduce surface reflections) using a binocular microscope. The samples were then cleaned in ultrasonic baths of methanol, acetone and $H_2O$ prior to dissolution.

Between 100-200 g of whole-rock were crushed of which a ~100 mg representative portion was dissolved for analysis.

### C.2.2 Chemical separation and mass spectrometry

Chemical and mass-spectrometric techniques were very similar those of Cohen et al. (1988) and only the differences from that approach are detailed here. The principal difference is that samples were spiked at dissolution and the isotope composition and isotope dilution measurements were made on the total sample. This was achieved using high purity $^{150}Nd/^{149}Sm$ and $^{84}Sr/^{85}Rb$ spikes. Samples were spiked so as to minimise spike correction to the isotope ratio measurement while maintaining ~0.5% precision on the Sm/Nd and Rb/Sr ratios. For the particular Sm-Nd spike used, the spike correction was always less than the internal precision on the mass spectrometric analysis if the measured $^{150}Nd/^{144}Nd$ was less than about 0.4. This was routinely achieved. Garnet samples were digested on a hot-plate for ~3 days in closed PFA screw-cap beakers. Whole-rocks were digested at 180°C for 3 days in bombs. Total procedural blanks for Nd were 5-15pg and always negligible.

Mass spectrometric runs were carried out statically on a MAT 262 mass spectrometer at ETH Zürich. For Nd samples were loaded on double Re filaments and masses 150-143 measured. A correction for $^{144}Sm$ on $^{144}Nd$ was made using mass $^{147}Sm$ but was always negligible. Isotope ratios are normalised to $^{146}Nd/^{144}Nd = 0.7219$. Repeated analyses of the La Jolla Nd standard ($n > 30$) gave $0.511853 \pm 0.000007$ ($2\sigma_m$). For Sm analyses the sample was loaded on single Re or Ta filaments. Masses 146-149 were measured in

static mode. 147-149 were used for isotope dilution measurements and fractionation correction. A correction for $^{148}Nd$ correction was made using $^{146}Nd$ and was always small.

Sr techniques are as for Cohen et al. (1988) except that the Sr fraction from the cation column was further purified on small (50 µl) Sr spec columns, eluting with $HNO_3$ and $H_2O$. Total procedural blanks for the garnet analyses, carried out at ETH Zürich, were 20-40 pg. Samples were loaded on single filaments according to the method of Birck and Allegre (1986) which allowed around 1 ng of Sr to be measured to an internal precision of less than 100 ppm. Mass spectrometry was carried out statically on a MAT 262 mass spectrometer and ratios normalised to $^{86}Sr/^{88}Sr = 0.1194$. Repeat measurements of the NBS 987Sr standard gave 0.710317±0.000031. $^{87}Rb$ correction to the $^{87}Sr$ measurements is not trivial with spike Rb present in the Sr analysis as the $^{87}Rb/^{85}Rb$ ratio in the separated sample may not be natural. In fact, given the loss of the spike Rb from the Sr fraction during chromatographic separation and the subsequent addition of blank, the measured $^{85}Rb/^{87}Rb$ ratio in the Sr fraction should lie somewhere between the spike and normal value. For these analyses $^{87}Rb$ correction was therefore done by plotting the measured 87/86 ratio against the measured 85/86 ratio. The slope of the resulting line gives the $^{87}Rb/^{85}Rb$ ratio of the Rb in the Sr fraction while the intercept gives the sample $^{87}Sr/^{86}Sr$ ratio.

# Appendix D - Whole rock chemistry

**XRF Majors**

| Sample | 005b | 005c | 008 | 014A | 014B | 035A | 035B | 035C | 2B(1) |
|---|---|---|---|---|---|---|---|---|---|
| SiO2 | 70.74 | 74.33 | 60.73 | 72.31 | 76.1 | 75.01 | 75.47 | 70.17 | 70.68 |
| TiO2 | 0.745 | 0.663 | 0.7 | 0.757 | 0.668 | 0.67 | 0.161 | 0.743 | 0.685 |
| Al2O3 | 12.6 | 9.97 | 16.65 | 12.37 | 10.65 | 11.57 | 13.91 | 14.78 | 13.52 |
| Fe2O3 | 5.14 | 4.66 | 7.23 | 4.75 | 4.25 | 4.4 | 1.41 | 6.06 | 3.63 |
| MnO | 0.078 | 0.164 | 0.089 | 0.053 | 0.078 | 0.063 | 0.013 | 0.059 | 0.022 |
| MgO | 2.59 | 2.3 | 3.36 | 3.48 | 1.9 | 1.16 | 0.29 | 1.03 | 3.76 |
| CaO | 2.01 | 4.27 | 2.75 | 0.77 | 1.15 | 0.84 | 0.7 | 0.5 | 0.5 |
| Na2O | 2.83 | 1.86 | 3.95 | 2.18 | 2.11 | 1.44 | 3.28 | 0.91 | 3.37 |
| K2O | 2.17 | 0.59 | 2.68 | 1.87 | 1.97 | 3.17 | 3.93 | 4.02 | 2.05 |
| P2O5 | 0.171 | 0.092 | 0.183 | 0.169 | 0.135 | 0.114 | 0.295 | 0.076 | 0.135 |
| LOI | 0.52 | 0.72 | 1.05 | 0.95 | 0.79 | 1.05 | 1.05 | 1.76 | 0.91 |
| Total | 99.594 | 99.619 | 99.372 | 99.659 | 99.801 | 99.487 | 100.509 | 100.108 | 99.262 |
| | | | | | | | | | |
| Rb | 107.7 | 24.9 | 137.2 | 75.2 | 92.5 | 149.5 | 318.6 | 230.5 | 86.3 |
| Sr | 138.5 | 92.3 | 159.1 | 55.3 | 98 | 69 | 39.1 | 65.4 | 62.8 |
| Y | 29.9 | 34 | 30.1 | 32.5 | 26.4 | 25.9 | 9.5 | 37.1 | 25.8 |
| Zr | 216 | 209 | 123 | 217 | 239 | 257 | 60 | 247 | 192 |
| Nb | 13.9 | 11.6 | 14.2 | 11.6 | 9.2 | 15.4 | 19.6 | 18.4 | 9.8 |
| Ba | 332 | 86 | 1038 | 396 | 467 | 701 | 87 | 628 | 297 |
| Pb | 40 | 14 | 21 | 8 | 17 | 11 | 31 | 15 | 6 |
| Th | 13 | 14 | 16 | 12 | 12 | 17 | 8 | 18 | 12 |
| U | 4 | 3 | 6 | 3 | 3 | 3 | 8 | 4 | 3 |
| Sc | 9 | 9 | 19 | 11 | 8 | 8 | 2 | 10 | 10 |
| V | 83 | 66 | 180 | 91 | 73 | 65 | 5 | 92 | 92 |
| Cr | 87 | 69 | 125 | 95 | 69 | 55 | 9 | 71 | 73 |
| Co | 17 | 15 | 22 | 14 | 11 | 13 | 4 | 16 | 13 |
| Ni | 36 | 31 | 42 | 37 | 30 | 23 | 0 | 26 | 41 |
| Cu | 22 | 4 | 37 | 11 | 8 | 9 | 11 | 5 | 1 |
| Zn | 78 | 61 | 116 | 42 | 54 | 60 | 64 | 87 | 44 |
| Ga | 14 | 12 | 22 | 15 | 13 | 16 | 20 | 23 | 18 |
| Mo | 0 | 0 | 0 | 0 | 0 | 0 | 0 | 0 | 0 |
| As | 3 | 7 | 2 | 3 | 10 | 0 | 1 | 2 | 2 |
| S | 37 | 53 | 776 | 149 | 77 | 59 | 62 | 58 | 27 |
| | | | | | | | | | |
| La | | | | | | | | | |
| Ce | | | | | | | | | |
| Nd | | | | | | | | | |
| Sm | | | | | | | | | |
| Eu | | | | | | | | | |
| Tb | | | | | | | | | |
| Yb | | | | | | | | | |
| Lu | | | | | | | | | |
| Th | | | | | | | | | |
| U | | | | | | | | | |
| Ta | | | | | | | | | |
| Hf | | | | | | | | | |
| Cs | | | | | | | | | |
| Zn | | | | | | | | | |
| W | | | | | | | | | |

**XRF Majors**

| Sample | 4A(2) | 4A(3) | 4B(1) | G100 | G11 | G125 | G135 | G160 | G166 |
|---|---|---|---|---|---|---|---|---|---|
| SiO2 | 69.72 | 64.63 | 77.39 | 73.02 | 71.55 | 77.59 | 61.6 | 56.24 | 51.22 |
| TiO2 | 0.686 | 0.791 | 0.66 | 0.577 | 0.78 | 0.055 | 1.032 | 0.864 | 0.896 |
| Al2O3 | 13.36 | 18.33 | 9.82 | 12.63 | 12.07 | 12.23 | 19.33 | 19.94 | 21.89 |
| Fe2O3 | 5.38 | 6.78 | 4 | 2.37 | 4.99 | 1.57 | 6.63 | 8.17 | 13.31 |
| MnO | 0.092 | 0.083 | 0.071 | 0.016 | 0.054 | 0.059 | 0.087 | 0.156 | 0.18 |
| MgO | 2.69 | 1.39 | 1.79 | 4.22 | 3.62 | 0.05 | 5.83 | 3.22 | 3.05 |
| CaO | 1.67 | 0.58 | 1.75 | 0.34 | 0.84 | 0.43 | 0.17 | 1.94 | 0.69 |
| Na2O | 1.97 | 0.83 | 2.28 | 3.34 | 2.43 | 3.36 | 1.38 | 1.84 | 0.69 |
| K2O | 2.97 | 3.91 | 1.44 | 2.11 | 1.95 | 3.7 | 1.19 | 5.26 | 5.66 |
| P2O5 | 0.149 | 0.112 | 0.142 | 0.111 | 0.174 | 0.037 | 0.099 | 0.2 | 0.09 |
| LOI | 0.81 | 2.56 | 0.4 | 1.04 | 1.13 | 0.55 | 2.49 | 1.7 | 2.42 |
| Total | 99.497 | 99.996 | 99.743 | 99.774 | 99.588 | 99.631 | 99.838 | 99.53 | 100.096 |
| | | | | | | | | | |
| Rb | 127.8 | 189.9 | 76.2 | 88.3 | 80.3 | 474.9 | 54 | 275.1 | 265 |
| Sr | 102.7 | 53 | 97.4 | 66.5 | 60.3 | 6.7 | 30.2 | 138 | 45.4 |
| Y | 27 | 33.3 | 24.9 | 13.5 | 31.3 | 54.4 | 45 | 55.7 | 21.5 |
| Zr | 189 | 215 | 244 | 185 | 240 | 48 | 225 | 135 | 145 |
| Nb | 10.9 | 15.1 | 9.2 | 10 | 12.5 | 18.7 | 17.3 | 21 | 9.5 |
| Ba | 669 | 674 | 463 | 330 | 381 | 19 | 276 | 1528 | 863 |
| Pb | 15 | 13 | 18 | 15 | 8 | 22 | 3 | 29 | 6 |
| Th | 14 | 20 | 14 | 12 | 13 | 13 | 21 | 37 | 18 |
| U | 5 | 4 | 3 | 3 | 4 | 31 | 8 | 2 | 2 |
| Sc | 13 | 13 | 6 | 6 | 13 | 3 | 24 | 18 | 22 |
| V | 95 | 131 | 66 | 42 | 90 | 4 | 171 | 191 | 163 |
| Cr | 90 | 97 | 67 | 50 | 98 | 7 | 152 | 132 | 145 |
| Co | 17 | 13 | 9 | 4 | 15 | 2 | 21 | 24 | 29 |
| Ni | 40 | 21 | 25 | 28 | 43 | 2 | 52 | 45 | 52 |
| Cu | 19 | 97 | 16 | 2 | 14 | 14 | 11 | 89 | 5 |
| Zn | 70 | 92 | 48 | 27 | 45 | 35 | 64 | 116 | 69 |
| Ga | 17 | 24 | 11 | 13 | 13 | 20 | 32 | 26 | 31 |
| Mo | 0 | 1 | 0 | 0 | 0 | 2 | 1 | 0 | 0 |
| As | 0 | 23 | 0 | 7 | 1 | 3 | 8 | 0 | 0 |
| S | 30 | 384 | 29 | 205 | 171 | 24 | 587 | 61 | 53 |
| | | | | | | | | | |
| La | | | 33.4 | | | | | | |
| Ce | | | 67.5 | | | 15 | | | |
| Nd | | | 30.6 | | | 30.7 | | | |
| Sm | | | 5.98 | | | 19 | | | |
| Eu | | | 1.15 | | | 4.11 | | | |
| Tb | | | 0.85 | | | 0.06 | | | |
| Yb | | | 2.71 | | | 1.34 | | | |
| Lu | | | 0.39 | | | 7.71 | | | |
| Th | | | 14.7 | | | 1.19 | | | |
| U | | | 3 | | | 11.967 | | | |
| Ta | | | 1.06 | | | 32 | | | |
| Hf | | | 7.61 | | | 4.84 | | | |
| Cs | | | 3.91 | | | 2.98 | | | |
| Zn | | | 52 | | | 455 | | | |
| W | | | | | | 0.0049 | | | |

**XRF Majors**

| Sample | G189 | G205 | G209 | G211 | G226 | Dup | G242 | G26 | G28 |
|---|---|---|---|---|---|---|---|---|---|
| SiO2 | 74.59 | 44.64 | 82.81 | 73.49 | 74.64 | | 73.88 | 77.27 | 75.16 |
| TiO2 | 0.09 | 1.36 | 0.277 | 0.688 | 0.049 | | 0.101 | 0.056 | 0.096 |
| Al2O3 | 14.91 | 27.52 | 7.88 | 12.83 | 14.78 | | 14.85 | 13.41 | 14.2 |
| Fe2O3 | 0.62 | 10.93 | 3.42 | 5.93 | 0.6 | | 1.08 | 0.88 | 0.62 |
| MnO | 0.019 | 0.214 | 0.027 | 0.119 | 0.014 | | 0.038 | 0.069 | 0.025 |
| MgO | 0.12 | 2.67 | 0.47 | 1.1 | 0.09 | | 0.15 | 0.19 | 0.21 |
| CaO | 0.52 | 0.29 | 0.5 | 0.47 | 0.64 | | 0.68 | 1.95 | 1.21 |
| Na2O | 1.89 | 0.55 | 1.65 | 0.69 | 4.07 | | 4.06 | 3.9 | 3.21 |
| K2O | 5.52 | 8.56 | 2.27 | 3.85 | 4.67 | | 4.1 | 1.94 | 4.02 |
| P2O5 | 0.149 | 0.197 | 0.034 | 0.035 | 0.134 | | 0.171 | 0.061 | 0.093 |
| LOI | 1.12 | 3.14 | 0.47 | 1.12 | 0.5 | | 0.82 | 0.86 | 0.66 |
| Total | 99.548 | 100.071 | 99.808 | 100.32 | 100.187 | | 99.93 | 100.586 | 99.504 |
| | | | | | | | | | |
| Rb | 201.8 | 353.8 | 73.4 | 164 | 295.1 | | 311.7 | 56.3 | 106 |
| Sr | 95.8 | 89.3 | 84.8 | 91.7 | 36.3 | | 79 | 119 | 174.6 |
| Y | 29.2 | 64.6 | 15 | 34.1 | 9.2 | | 15 | 4.3 | 11.1 |
| Zr | 40 | 335 | 101 | 216 | 31 | | 44 | 14 | 11 |
| Nb | 11.3 | 26.5 | 5.9 | 13.1 | 8.5 | | 15.6 | 1.3 | 1.8 |
| Ba | 273 | 1335 | 532 | 849 | 127 | | 177 | 264 | 799 |
| Pb | 46 | 46 | 22 | 19 | 40 | | 56 | 38 | 59 |
| Th | 6 | 33 | 6 | 14 | 3 | | 5 | 0 | 1 |
| U | 4 | 7 | 1 | 1 | 7 | | 9 | 1 | 3 |
| Sc | 4 | 32 | 4 | 12 | 1 | | 2 | 5 | 2 |
| V | 0 | 178 | 28 | 83 | 3 | | 5 | 5 | 7 |
| Cr | 5 | 168 | 25 | 60 | 7 | | 8 | 6 | 6 |
| Co | 1 | 28 | 7 | 21 | 2 | | 1 | 1 | 2 |
| Ni | 3 | 52 | 4 | 27 | 1 | | 2 | 3 | 3 |
| Cu | 5 | 32 | 4 | 86 | 3 | | 2 | 20 | 5 |
| Zn | 12 | 119 | 32 | 68 | 29 | | 51 | 8 | 10 |
| Ga | 18 | 34 | 9 | 17 | 22 | | 21 | 14 | 12 |
| Mo | 0 | 0 | 0 | 0 | 0 | | 0 | 0 | 0 |
| As | 8 | 0 | 0 | 0 | 3 | | 3 | 2 | 1 |
| S | 20 | 37 | 48 | 669 | 24 | | 27 | 20 | 31 |
| | | | | | | | | | |
| La | | | | | | 5.3 | 9.6 | 5.8 | 4.2 |
| Ce | | | | | 5.7 | 11.8 | 21.7 | 10.6 | 7.4 |
| Nd | 27.3 | | | | 11.1 | 5.6 | 10.8 | 4.6 | 3.2 |
| Sm | 13.3 | | | | 5.5 | 1.33 | 2.34 | 0.82 | 0.73 |
| Eu | | | | | 1.28 | 0.276 | 0.4 | 0.93 | 1.31 |
| Tb | 0.61 | | | | 0.276 | 0.33 | 0.54 | 0.12 | 0.2 |
| Yb | 0.81 | | | | 0.325 | 0.74 | 1.39 | 1.57 | 1.09 |
| Lu | 3.98 | | | | 0.74 | 0.09 | 0.2 | 0.28 | 0.16 |
| Th | | | | | 0.09 | 3.41 | 4.61 | 1.89 | 1.4 |
| U | 5.55 | | | | 3.16 | 6.3 | 12.8 | 0.8 | 1 |
| Ta | | | | | 6.3 | 1.28 | 3.93 | 0.1 | 0.32 |
| Hf | 1.74 | | | | 1.36 | 1.34 | 1.89 | 0.76 | 0.5 |
| Cs | 1.5 | | | | 1.42 | 8.6 | 18.1 | 4.38 | 2.94 |
| Zn | 200 | | | | 285 | 30 | 48 | | |
| W | 0.0375 | | | | 0.00889 | | | | |

**XRF Majors**

| Sample | G30 | G31(1) | Dup | G49 | G51(2)L | G51(2)M | G51(5) | G62 | G65 |
|---|---|---|---|---|---|---|---|---|---|
| SiO2 | 75.79 | 75.89 | | 56.71 | 75.4 | 75.49 | 75.37 | 70.83 | 64.44 |
| TiO2 | 0.062 | 0.049 | | 0.775 | 0.018 | 0.643 | 0.551 | 0.703 | 0.769 |
| Al2O3 | 14.99 | 13.89 | | 21.19 | 14.61 | 11.47 | 10.35 | 13.4 | 17.15 |
| Fe2O3 | 1.04 | 1.05 | | 10.67 | 0.27 | 4.38 | 4.07 | 4.81 | 6.35 |
| MnO | 0.1 | 0.131 | | 0.103 | 0.038 | 0.065 | 0.103 | 0.043 | 0.08 |
| MgO | 0.19 | 0.11 | | 1.87 | 0.05 | 2.29 | 1.93 | 2.22 | 2.54 |
| CaO | 0.8 | 0.59 | | 0.69 | 4.1 | 2.4 | 4.92 | 0.9 | 0.92 |
| Na2O | 2.36 | 2.09 | | 1 | 3.92 | 2 | 1.09 | 3.37 | 2.58 |
| K2O | 3.92 | 4.98 | | 4.22 | 0.58 | 2.33 | 1.51 | 2.17 | 3.27 |
| P2O5 | 0.104 | 0.095 | | 0.094 | 0.016 | 0.159 | 0.146 | 0.094 | 0.167 |
| LOI | 0.51 | 0.43 | | 2.75 | 0.82 | 0.5 | 0.84 | 1.11 | 1.62 |
| Total | 99.866 | 99.305 | | 100.072 | 99.822 | 101.727 | 100.88 | 99.65 | 99.886 |
| | | | | | | | | | |
| Rb | 105.6 | 131.6 | | 190.6 | 10.8 | 139.1 | 84.3 | 114.4 | 149.9 |
| Sr | 121.9 | 153.5 | | 81.7 | 200.1 | 109.8 | 130.1 | 107.1 | 76 |
| Y | 5.6 | 6 | | 34 | 7.5 | 25.6 | 31.6 | 27.7 | 32.4 |
| Zr | 22 | 19 | | 139 | 49 | 236 | 211 | 227 | 194 |
| Nb | 1.2 | 1.3 | | 13.9 | 0.5 | 11.7 | 9.5 | 15.8 | 17.6 |
| Ba | 755 | 1322 | | 565 | 139 | 537 | 398 | 506 | 763 |
| Pb | 55 | 62 | | 5 | 41 | 19 | 20 | 488 | 134 |
| Th | 0 | 1 | | 21 | 0 | 18 | 19 | 18 | 19 |
| U | 1 | 1 | | 3 | 3 | 3 | 3 | 5 | 5 |
| Sc | 5 | 3 | | 28 | 2 | 7 | 6 | 14 | 17 |
| V | 4 | 7 | | 137 | 3 | 76 | 56 | 84 | 109 |
| Cr | 4 | 7 | | 134 | 3 | 67 | 59 | 86 | 112 |
| Co | 1 | 1 | | 22 | 1 | 11 | 10 | 9 | 19 |
| Ni | 3 | 2 | | 46 | 1 | 27 | 24 | 15 | 32 |
| Cu | 5 | 4 | | 4 | 2 | 42 | 3 | 13 | 34 |
| Zn | 8 | 3 | | 37 | 3 | 60 | 53 | 221 | 179 |
| Ga | 14 | 11 | | 27 | 12 | 13 | 11 | 19 | 22 |
| Mo | 0 | 0 | | 0 | 0 | 0 | 0 | 1 | 0 |
| As | 3 | 6 | | 2 | 1 | 0 | 2 | 6 | 1 |
| S | 21 | 27 | | 51 | 18 | 38 | 32 | 561 | 1373 |

| | | | |
|---|---|---|---|
| La | 3.7 | | 3.5 |
| Ce | 7.1 | 2.8 | 6.1 |
| Nd | 3.1 | 4.8 | 2.9 |
| Sm | 0.71 | 2 | 0.59 |
| Eu | 1.1 | 0.37 | 1.38 |
| Tb | 0.14 | 1.37 | 0.11 |
| Yb | 1.75 | 0.15 | 2.07 |
| Lu | 0.29 | 2.08 | 0.36 |
| Th | 1.37 | 0.34 | 1.16 |
| U | 1.5 | 0.85 | 1.4 |
| Ta | 0.23 | 0.9 | 0.26 |
| Hf | 1.06 | 0.22 | 1.12 |
| Cs | 3.11 | 1.04 | 2.81 |
| Zn | | 125 | |
| W | | | |

**XRF Majors**

| Sample | G74 | G75 | G77 | G87 | G9 | Dup | 17/97 | 26A/97 |
|---|---|---|---|---|---|---|---|---|
| SiO2 | 73.22 | 74.39 | 72.54 | 50.19 | 68.8 | | 74.02 | 74.4 |
| TiO2 | 0.069 | 0.06 | 0.488 | 1.12 | 0.585 | | 0.063 | 0.038 |
| Al2O3 | 15.11 | 15.25 | 13.34 | 27.95 | 17.21 | | 15.26 | 14.98 |
| Fe2O3 | 0.72 | 0.65 | 3.33 | 7.02 | 5.04 | | 0.71 | 0.61 |
| MnO | 0.021 | 0.031 | 0.049 | 0.05 | 0.132 | | 0.012 | 0.007 |
| MgO | 0.1 | 0.07 | 0.79 | 3.66 | 0.87 | | 0.1 | 0.16 |
| CaO | 0.52 | 0.5 | 2.13 | 0.96 | 0.6 | | 0.67 | 0.82 |
| Na2O | 4.23 | 5 | 2.76 | 1.21 | 1.9 | | 4.03 | 4.54 |
| K2O | 4.49 | 3.61 | 4.02 | 4.68 | 3.62 | | 4.46 | 4.35 |
| P2O5 | 0.188 | 0.185 | 0.104 | 0.56 | 0.087 | | 0.092 | 0.055 |
| LOI | 0.55 | 0.6 | 0.5 | 2.52 | 1.47 | | 0.63 | 0.42 |
| Total | 99.218 | 100.346 | 100.051 | 99.92 | 100.314 | | 100.047 | 100.38 |
| | | | | | | | | |
| Rb | 477.4 | 440.1 | 174.5 | 255.5 | 160.6 | | 382.3 | 170.9 |
| Sr | 32.8 | 23.1 | 101.8 | 73.4 | 64.6 | | 51.4 | 47 |
| Y | 10.5 | 11.5 | 49.1 | 66.5 | 51.4 | | 7.4 | 24.4 |
| Zr | 33 | 31 | 198 | 322 | 280 | | 38 | 26 |
| Nb | 19.6 | 22.8 | 12.1 | 20.6 | 17.9 | | 12.7 | 0.5 |
| Ba | 103 | 62 | 555 | 862 | 747 | | 151 | 126 |
| Pb | 47 | 38 | 18 | 23 | 14 | | 67 | 108 |
| Th | 4 | 4 | 25 | 30 | 14 | | 6 | 6 |
| U | 14 | 16 | 8 | 6 | 4 | | 7 | 12 |
| Sc | 1 | 0 | 8 | 24 | 9 | | 1 | 0 |
| V | 1 | 3 | 44 | 166 | 57 | | 4 | 3 |
| Cr | 4 | 7 | 16 | 130 | 38 | | 7 | 3 |
| Co | 2 | 1 | 7 | 10 | 10 | | 2 | 1 |
| Ni | 1 | 1 | 7 | 13 | 17 | | 2 | 2 |
| Cu | 3 | 3 | 4 | 8 | 9 | | 1 | 2 |
| Zn | 62 | 55 | 38 | 107 | 80 | | 46 | 16 |
| Ga | 25 | 26 | 18 | 31 | 26 | | 21 | 15 |
| Mo | 0 | 0 | 0 | 1 | 0 | | 0 | 0 |
| As | 7 | 1 | 3 | 0 | 0 | | 0 | 0 |
| S | 22 | 18 | 44 | 575 | 70 | | 19 | 20 |
| | | | | | | | | |
| La | 8.8 | | | | 40.3 | 39.2 | 7.7 | 10.4 |
| Ce | 15.6 | 8.4 | | | 86.6 | 87 | 15.6 | 20.7 |
| Nd | 9 | 16 | 105 | | 43.3 | 41.6 | 7.3 | 10.2 |
| Sm | 1.26 | 8.9 | 44.8 | | 9.3 | 9.2 | 1.7 | 2.19 |
| Eu | 0.26 | 1.27 | | | 1.33 | 1.35 | 0.37 | 0.3 |
| Tb | 0.33 | 0.2 | 1.1 | | 1.48 | 1.49 | 0.33 | 0.63 |
| Yb | 0.7 | 0.35 | 1.43 | | 6.2 | 6.46 | 0.4 | 2.29 |
| Lu | 0.11 | 0.84 | 4.61 | | 0.92 | 0.97 | 0.07 | 0.33 |
| Th | 3.5 | 0.1 | | | 17 | 16.8 | 4.63 | 6.62 |
| U | 22.2 | 3.597 | 22.6 | | 3.4 | 3.8 | 7.8 | 17.8 |
| Ta | 2.78 | 20.9 | | | 1.49 | 1.51 | 7.76 | 0.02 |
| Hf | 1.4 | 2.02 | 1.13 | | 8.59 | 8.49 | 1.76 | 1.06 |
| Cs | 31 | 1.44 | 5.94 | | 8.31 | 8.24 | 45.7 | 3.79 |
| Zn | 58 | 435 | 175 | | 79 | 79 | 45 | 18 |
| W | | 0.00652 | 0.01205 | | | | | |

| 26B/97 | XRF Majors Sample | 26C/97 | 26D/97 | 30A/97 | 40C/97 | 40D/97 | G42 | G47 |
|---|---|---|---|---|---|---|---|---|
| 67.26 | SiO2 | 71.7 | 73.98 | 75.73 | 73.65 | 74.32 | 74.91 | 74.9 |
| 0.229 | TiO2 | 0.119 | 0.106 | 0.02 | 0.09 | 0.062 | 0.092 | 0.035 |
| 17.28 | Al2O3 | 16.08 | 14.93 | 14.08 | 15.03 | 14.73 | 14.03 | 14.18 |
| 1.98 | Fe2O3 | 0.63 | 0.46 | 0.66 | 0.79 | 0.7 | 1.01 | 0.61 |
| 0.025 | MnO | 0.011 | 0.007 | 0.02 | 0.021 | 0.027 | 0.035 | 0.007 |
| 0.45 | MgO | 0.17 | 0.14 | 0.08 | 0.13 | 0.09 | 0.13 | 0.12 |
| 0.88 | CaO | 0.93 | 0.77 | 0.44 | 0.7 | 0.53 | 0.61 | 0.55 |
| 3.94 | Na2O | 3.46 | 2.94 | 7.29 | 4.17 | 4.31 | 3.22 | 3.78 |
| 7.01 | K2O | 6.08 | 5.64 | 0.21 | 4.47 | 3.97 | 4.92 | 4.75 |
| 0.103 | P2O5 | 0.169 | 0.153 | 0.145 | 0.158 | 0.174 | 0.212 | 0.172 |
| 0.61 | LOI | 0.71 | 0.76 | 0.42 | 0.63 | 0.71 | 0.82 | 0.66 |
| 99.767 | Total | 100.059 | 99.886 | 99.095 | 99.839 | 99.623 | 99.989 | 99.764 |
| | | | | | | | | |
| 350.8 | Rb | 260.9 | 246.7 | 17.2 | 392.6 | 466.5 | 311.5 | 200.4 |
| 79.5 | Sr | 92.5 | 73.5 | 10.1 | 66.9 | 48.1 | 18.3 | 79.1 |
| 46.5 | Y | 21.8 | 17.5 | 14.3 | 8.6 | 9 | 8.7 | 7.5 |
| 30 | Zr | 26 | 25 | 61 | 40 | 30 | 29 | 23 |
| 13.2 | Nb | 8.5 | 10.9 | 25.3 | 12.7 | 12.7 | 11.8 | 10.6 |
| 347 | Ba | 388 | 229 | 4 | 178 | 95 | 36 | 222 |
| 64 | Pb | 60 | 47 | 257 | 45 | 39 | 28 | 31 |
| 31 | Th | 3 | 6 | 12 | 4 | 2 | 2 | 4 |
| 11 | U | 2 | 4 | 9 | 7 | 7 | 9 | 5 |
| 4 | Sc | 4 | 5 | 0 | 1 | 1 | 1 | 1 |
| 3 | V | 2 | 3 | 3 | 5 | 1 | 3 | 3 |
| 4 | Cr | 3 | 4 | 4 | 8 | 3 | 5 | 5 |
| 3 | Co | 2 | 2 | 1 | 1 | 2 | 1 | 2 |
| 3 | Ni | 2 | 2 | 1 | 2 | 1 | 2 | 2 |
| 3 | Cu | 1 | 2 | 1 | 4 | 1 | 1 | 10 |
| 55 | Zn | 18 | 13 | 48 | 54 | 42 | 29 | 31 |
| 19 | Ga | 20 | 21 | 26 | 24 | 22 | 19 | 20 |
| 0 | Mo | 0 | 0 | 0 | 0 | 0 | 0 | 0 |
| 4 | As | 1 | 2 | 0 | 6 | 2 | 0 | 1 |
| 22 | S | 17 | 16 | 157 | 17 | 15 | 74 | 24 |
| | | | | | | | | |
| 15.5 | La | 10.1 | 7.9 | 6.5 | 10 | 6 | | |
| 30.3 | Ce | 19.9 | 15.3 | 14.1 | 20.2 | 11.4 | 9.5 | 4.8 |
| 14 | Nd | 8.7 | 6.4 | 8 | 10 | 5.6 | 16.4 | 9 |
| 3.07 | Sm | 2.26 | 1.6 | 2.17 | 2.39 | 1.3 | 9.4 | 4.1 |
| 0.67 | Eu | 0.73 | 0.56 | 0.08 | 0.46 | 0.25 | 1.15 | 1.2 |
| 1.06 | Tb | 0.6 | 0.45 | 0.52 | 0.42 | 0.34 | 0.16 | 0.15 |
| 3.98 | Yb | 1.66 | 1.41 | 1.56 | 0.55 | 0.68 | 0.35 | 0.31 |
| 0.58 | Lu | 0.25 | 0.2 | 0.29 | 0.08 | 0.1 | 1.22 | 0.57 |
| 8.37 | Th | 4.7 | 4.84 | 9.61 | 4.86 | 2.47 | 0.17 | 0.08 |
| 15.9 | U | 4.8 | 4.4 | 9 | 8.8 | 9.7 | 3.23 | 4 |
| 1.29 | Ta | 0.8 | 0.75 | 32.2 | 3.99 | 3.18 | 23.5 | 4.6 |
| 0.988 | Hf | 1 | 1.09 | 3.475 | 1.55 | 1.27 | 1.3 | 3.62 |
| 19.4 | Cs | 14.8 | 7 | 5.15 | 95.5 | 212 | 1.68 | 1.098 |
| 53 | Zn | 21 | 19 | 53 | 54 | 41 | 300 | 200 |
| | W | | | 0.0069 | | 0.0079 | | |

# Appendix E - Summary of mineral chemistry

| Sample | 2no | 2no | 2no | 2no | 2nj | 2nj | 2nj | 2nj | 2km | 2km | 2km |
|---|---|---|---|---|---|---|---|---|---|---|---|
| mineral | grt | bt | mu | fsp | st | bt | fsp | grt | smu | bt | fsp |
| SiO2 | 37.33 | 35.12 | 44.35 | 60.76 | 26.95 | 37.09 | 65.68 | 38.62 | 45.82 | 35.48 | 63.24 |
| TiO2 | 0 | 3.01 | 1.26 | 0 | 0.87 | 1.56 | 0.08 | 0 | 1.32 | 3.31 | 0.01 |
| Al2O3 | 20.9 | 17.74 | 34.44 | 23.55 | 52.37 | 17.2 | 21.05 | 21.38 | 32.14 | 18.04 | 22.26 |
| Cr2O3 | 0 | 0.07 | 0.07 | 0.05 | 0.11 | 0 | 0.02 | 0.01 | 0.06 | 0.12 | 0 |
| Fe2O3 | 1.09 | 0 | 0 | 0.04 | 0 | 2.32 | 0 | 1.3 | 0 | 0 | 0.08 |
| FeO | 32.62 | 18.49 | 1.11 | 0 | 13.06 | 11.83 | 0 | 31.08 | 1.71 | 18.05 | 0 |
| MnO | 2.28 | 0.07 | 0 | 0 | 0.07 | 0.05 | 0 | 0.95 | 0 | 0.03 | 0.06 |
| MgrtO | 4.13 | 9.93 | 0.5 | 0 | 2.49 | 15.87 | 0 | 6.75 | 1.39 | 10.23 | 0 |
| CaO | 1.82 | 0 | 0 | 5.32 | 0.01 | 0 | 2.02 | 1.28 | 0 | 0 | 3.67 |
| Na2O | 0 | 0.25 | 1.19 | 8.51 | 0.5 | 0.55 | 10.84 | 0.1 | 0.73 | 0.16 | 9.35 |
| K2O | 0 | 9.4 | 9.1 | 0.05 | 0 | 8.08 | 0 | 0 | 9.95 | 9.37 | 0.12 |
| totals | 100.17 | 94.1 | 92.04 | 98.29 | 96.43 | 94.57 | 99.7 | 101.45 | 93.13 | 94.79 | 98.79 |
| cations | | | | | | | | | | | |
| Si | 2.983 | 2.705 | 3.045 | 2.742 | 7.599 | 2.741 | 2.896 | 2.993 | 3.129 | 2.701 | 2.825 |
| Ti | 0 | 0.175 | 0.065 | 0 | 0.185 | 0.087 | 0.003 | 0 | 0.068 | 0.189 | 0 |
| Al | 1.969 | 1.611 | 2.787 | 1.253 | 17.41 | 1.499 | 1.094 | 1.953 | 2.588 | 1.619 | 1.172 |
| Cr | 0 | 0.004 | 0.004 | 0.002 | 0.024 | 0 | 0.001 | 0 | 0.003 | 0.007 | 0 |
| Fe3+ | 0.066 | 0 | 0 | 0.001 | 0 | 0.129 | 0 | 0.076 | 0 | 0 | 0.003 |
| Fe2+ | 2.18 | 1.192 | 0.064 | 0 | 3.079 | 0.731 | 0 | 2.014 | 0.098 | 1.149 | 0 |
| Mn | 0.154 | 0.005 | 0 | 0 | 0.018 | 0.003 | 0 | 0.062 | 0 | 0.002 | 0.002 |
| Mgrt | 0.492 | 1.14 | 0.052 | 0 | 1.046 | 1.748 | 0 | 0.78 | 0.141 | 1.16 | 0 |
| Ca | 0.156 | 0 | 0 | 0.257 | 0.003 | 0 | 0.096 | 0.106 | 0 | 0 | 0.176 |
| Na | 0 | 0.038 | 0.158 | 0.744 | 0.271 | 0.079 | 0.928 | 0.015 | 0.096 | 0.024 | 0.809 |
| K | 0 | 0.925 | 0.798 | 0.003 | 0 | 0.763 | 0 | 0 | 0.868 | 0.911 | 0.007 |
| Total Cations | 8 | 7.794 | 6.973 | 5.003 | 29.635 | 7.779 | 5.018 | 8 | 6.99 | 7.764 | 4.995 |

| Sample | 2hdib | 2hdib | 2hdib | 2hdib | 2hdib | 2grtxa | 2grtxa | 2grtxa | 2grtxa | 2grtu | 2grtu |
|---|---|---|---|---|---|---|---|---|---|---|---|
| mineral | grt | mu | ksp | pl | bt | grt | bt | mu | fsp | grt | bt |
| SiO2 | 36.36 | 45.11 | 63.57 | 63.67 | 32.96 | 36.75 | 33.82 | 45.51 | 62.22 | 36.26 | 33.66 |
| TiO2 | 0 | 0.62 | 0.26 | 0 | 2.67 | 0 | 2.74 | 0.56 | 0.01 | 0 | 3.2 |
| Al2O3 | 20.24 | 35.76 | 18.29 | 21.52 | 18.73 | 20.13 | 18.37 | 35.91 | 21.93 | 20.26 | 17.84 |
| Cr2O3 | 0.02 | 0 | 0 | 0.05 | 0 | 0 | 0.01 | 0.01 | 0.01 | 0.05 | 0.01 |
| Fe2O3 | 1.05 | 0 | 0.01 | 0.11 | 0 | 1.29 | 0 | 0 | 0.04 | 1.73 | 0 |
| FeO | 37.51 | 1.21 | 0 | 0 | 26.07 | 36.96 | 25.61 | 1.25 | 0 | 33.76 | 25.46 |
| MnO | 0.47 | 0 | 0.04 | 0 | 0.05 | 1.34 | 0.19 | 0 | 0 | 5.03 | 0.2 |
| MgrtO | 1.67 | 0.36 | 0 | 0 | 4.21 | 1.93 | 4.51 | 0.47 | 0.02 | 1.69 | 5 |
| CaO | 1.97 | 0.02 | 0 | 2.87 | 0 | 1.46 | 0 | 0 | 3.37 | 1.13 | 0 |
| Na2O | 0 | 0.58 | 1.33 | 9.86 | 0.29 | 0.06 | 0.11 | 0.52 | 8.95 | 0.01 | 0.11 |
| K2O | 0 | 10.39 | 15.3 | 0.27 | 9.68 | 0.01 | 9.47 | 10.28 | 0.19 | 0 | 9.58 |
| totals | 99.29 | 94.06 | 98.81 | 98.34 | 94.67 | 99.92 | 94.83 | 94.51 | 96.75 | 99.93 | 95.08 |
| cations | | | | | | | | | | | |
| Si | 2.987 | 3.042 | 2.975 | 2.856 | 2.634 | 2.998 | 2.682 | 3.049 | 2.832 | 2.968 | 2.667 |
| Ti | 0 | 0.031 | 0.009 | 0 | 0.161 | 0 | 0.163 | 0.028 | 0 | 0 | 0.19 |
| Al | 1.96 | 2.842 | 1.009 | 1.138 | 1.765 | 1.936 | 1.718 | 2.837 | 1.177 | 1.955 | 1.667 |
| Cr | 0.002 | 0 | 0 | 0.002 | 0 | 0 | 0.001 | 0 | 0 | 0.004 | 0.001 |
| Fe3+ | 0.065 | 0 | 0 | 0.004 | 0 | 0.079 | 0 | 0 | 0.001 | 0.106 | 0 |
| Fe2+ | 2.577 | 0.068 | 0 | 0 | 1.742 | 2.522 | 1.699 | 0.07 | 0 | 2.311 | 1.687 |
| Mn | 0.033 | 0 | 0.001 | 0 | 0.003 | 0.093 | 0.013 | 0 | 0 | 0.349 | 0.013 |
| Mgrt | 0.204 | 0.036 | 0 | 0 | 0.501 | 0.234 | 0.533 | 0.047 | 0.002 | 0.207 | 0.591 |
| Ca | 0.173 | 0.001 | 0 | 0.138 | 0 | 0.127 | 0 | 0 | 0.165 | 0.099 | 0 |
| Na | 0 | 0.076 | 0.12 | 0.857 | 0.046 | 0.01 | 0.017 | 0.068 | 0.79 | 0.001 | 0.017 |
| K | 0 | 0.895 | 0.914 | 0.015 | 0.988 | 0.001 | 0.959 | 0.88 | 0.011 | 0 | 0.97 |
| Total Cations | 8 | 6.991 | 5.029 | 5.009 | 7.839 | 8 | 7.783 | 6.978 | 4.979 | 8 | 7.803 |

| Sample | 2km | 2jm | 2jm | 2jm | 2jm | 2jh | 2jh | 2jh | 2esb | 2esb | 2esb | 2esb |
|---|---|---|---|---|---|---|---|---|---|---|---|---|
| mineral | grt | grt | mu | bt | fsp | grt | mu | bt | grt | chl | mu | bt |
| SiO2 | 37.5 | 36.53 | 47.55 | 33.29 | 63.26 | 36.46 | 44.82 | 33.94 | 36.52 | 23.78 | 35.26 | 38.09 |
| TiO2 | 0.03 | 0 | 0.84 | 2.89 | 0 | 0.11 | 0.75 | 3.13 | 0.01 | 0.12 | 1.89 | 1.73 |
| Al2O3 | 21.01 | 20.35 | 30.76 | 17.06 | 22.68 | 19.95 | 35.12 | 17.43 | 20.66 | 21.55 | 17.3 | 18.49 |
| Cr2O3 | 0 | 0.08 | 0.03 | 0 | 0.01 | 0 | 0.03 | 0.01 | 0 | 0.01 | 0.02 | 0.03 |
| Fe2O3 | 1.48 | 0.9 | 0 | 0 | 0.01 | 1.5 | 0 | 0 | 2.29 | 0.4 | 12.3 | 0 |
| FeO | 30.31 | 34.55 | 2.77 | 26.69 | 0 | 37.16 | 1.35 | 25.45 | 32.03 | 27.76 | 11.07 | 18.96 |
| MnO | 1.36 | 3.65 | 0.01 | 0.45 | 0 | 1.21 | 0 | 0.14 | 3.18 | 0.08 | 0 | 0 |
| MgrtO | 4.62 | 1.32 | 1.26 | 4.68 | 0 | 1.68 | 0.43 | 5.21 | 1.7 | 12.49 | 8.54 | 7 |
| CaO | 3.85 | 2.4 | 0 | 0.13 | 4.17 | 1.72 | 0.03 | 0 | 3.74 | 0 | 0 | 0.49 |
| Na2O | 0 | 0 | 0.29 | 0.19 | 8.9 | 0.02 | 0.67 | 0.1 | 0.11 | 0.05 | 0.16 | 1.7 |
| K2O | 0 | 0 | 9.86 | 8.84 | 0.2 | 0.01 | 9.82 | 9.37 | 0.03 | 0.04 | 9.3 | 8.2 |
| totals | 100.2 | 99.78 | 93.39 | 94.22 | 99.23 | 99.81 | 93.04 | 94.79 | 100.3 | 86.28 | 95.85 | 94.7 |
| cations | | | | | | | | | | | | |
| Si | 2.972 | 2.988 | 3.237 | 2.678 | 2.813 | 2.986 | 3.05 | 2.692 | 2.955 | 2.595 | 2.658 | 2.885 |
| Ti | 0.002 | 0 | 0.043 | 0.175 | 0 | 0.007 | 0.039 | 0.187 | 0.001 | 0.01 | 0.107 | 0.099 |
| Al | 1.963 | 1.963 | 2.469 | 1.618 | 1.189 | 1.926 | 2.818 | 1.63 | 1.971 | 2.773 | 1.537 | 1.651 |
| Cr | 0 | 0.005 | 0.002 | 0 | 0 | 0 | 0.002 | 0.001 | 0 | 0.001 | 0.001 | 0.002 |
| Fe3+ | 0.088 | 0.056 | 0 | 0 | 0 | 0.092 | 0 | 0 | 0.139 | 0.033 | 0.698 | 0 |
| Fe2+ | 2.009 | 2.364 | 0.158 | 1.796 | 0 | 2.545 | 0.077 | 1.688 | 2.167 | 2.534 | 0.698 | 1.201 |
| Mn | 0.092 | 0.253 | 0 | 0.03 | 0 | 0.084 | 0 | 0.009 | 0.218 | 0.007 | 0 | 0 |
| Mgrt | 0.546 | 0.161 | 0.128 | 0.561 | 0 | 0.205 | 0.043 | 0.616 | 0.205 | 2.031 | 0.959 | 0.79 |
| Ca | 0.327 | 0.211 | 0 | 0.012 | 0.199 | 0.151 | 0.002 | 0 | 0.324 | 0 | 0 | 0.04 |
| Na | 0 | 0 | 0.039 | 0.029 | 0.767 | 0.003 | 0.089 | 0.016 | 0.017 | 0.011 | 0.023 | 0.25 |
| K | 0 | 0 | 0.858 | 0.909 | 0.011 | 0.001 | 0.854 | 0.949 | 0.003 | 0.006 | 0.895 | 0.793 |
| Total Cations | 8 | 8 | 6.933 | 7.807 | 4.981 | 8 | 6.973 | 7.788 | 8 | 10 | 7.576 | 7.711 |

| Sample | 2grtu | 2grtu | 2fq | 2fq | 2fq | 2fq | 2fn | 2fn | 2fn | 2fn | 2fc | 2fc |
|---|---|---|---|---|---|---|---|---|---|---|---|---|
| mineral | fsp | mu | grt | mu | bt | fsp | mu | grt | bt | fsp | mu | bt |
| SiO2 | 63.66 | 44.74 | 36.75 | 45.34 | 34.2 | 65.03 | 45.32 | 37.14 | 35.02 | 65.6 | 46.48 | 36.13 |
| TiO2 | 0.04 | 1.15 | 0.09 | 1.2 | 2.15 | 0.04 | 1.01 | 0.04 | 2.46 | 0 | 0.89 | 2.04 |
| Al2O3 | 22.21 | 34.58 | 20.22 | 32.95 | 16.96 | 21.11 | 34.36 | 20.5 | 17.62 | 20.77 | 32.24 | 17.79 |
| Cr2O3 | 0.03 | 0 | 0 | 0 | 0.03 | 0 | 0 | 0 | 0.05 | 0.03 | 0.01 | 0.03 |
| Fe2O3 | 0.02 | 0 | 2.19 | 0 | 0 | 0.01 | 0 | 1.02 | 0 | 0 | 0 | 0 |
| FeO | 0 | 1.41 | 33.89 | 2.08 | 24.97 | 0 | 1.38 | 36.56 | 21.06 | 0 | 1.74 | 17.23 |
| MnO | 0 | 0.03 | 1.98 | 0.06 | 0.16 | 0 | 0 | 0.29 | 0.06 | 0 | 0.03 | 0.17 |
| MgrtO | 0.05 | 0.42 | 0.91 | 0.8 | 5.95 | 0 | 0.6 | 2.45 | 8.46 | 0 | 1.61 | 10.96 |
| CaO | 3.36 | 0 | 4.61 | 0 | 0 | 2.38 | 0 | 2.33 | 0 | 1.8 | 0 | 0 |
| Na2O | 9.29 | 0.52 | 0.13 | 0.48 | 0.15 | 10.22 | 0.85 | 0.03 | 0.13 | 9.9 | 0.37 | 0.18 |
| K2O | 0.27 | 10.34 | 0 | 10.01 | 9.51 | 0.1 | 8.83 | 0.04 | 9.3 | 0.07 | 10.11 | 9.48 |
| totals | 98.94 | 93.2 | 100.8 | 92.94 | 94.07 | 98.89 | 92.35 | 100.4 | 94.16 | 98.17 | 93.49 | 94.02 |
| cations | | | | | | | | | | | | |
| Si | 2.836 | 3.051 | 2.974 | 3.106 | 2.731 | 2.89 | 3.088 | 2.996 | 2.727 | 2.923 | 3.156 | 2.761 |
| Ti | 0.001 | 0.059 | 0.005 | 0.062 | 0.129 | 0.001 | 0.052 | 0.003 | 0.144 | 0 | 0.045 | 0.117 |
| Al | 1.167 | 2.78 | 1.929 | 2.661 | 1.597 | 1.106 | 2.76 | 1.949 | 1.617 | 1.091 | 2.58 | 1.603 |
| Cr | 0.001 | 0 | 0 | 0 | 0.002 | 0 | 0 | 0 | 0.003 | 0.001 | 0.001 | 0.002 |
| Fe3+ | 0.001 | 0 | 0.134 | 0 | 0 | 0 | 0 | 0.062 | 0 | 0 | 0 | 0 |
| Fe2+ | 0 | 0.08 | 2.293 | 0.119 | 1.668 | 0 | 0.078 | 2.466 | 1.371 | 0 | 0.099 | 1.101 |
| Mn | 0 | 0.001 | 0.136 | 0.003 | 0.011 | 0 | 0 | 0.02 | 0.004 | 0 | 0.002 | 0.011 |
| Mgrt | 0.003 | 0.042 | 0.11 | 0.082 | 0.708 | 0 | 0.061 | 0.295 | 0.981 | 0 | 0.163 | 1.248 |
| Ca | 0.161 | 0 | 0.4 | 0 | 0 | 0.113 | 0 | 0.201 | 0 | 0.086 | 0 | 0 |
| Na | 0.802 | 0.069 | 0.02 | 0.063 | 0.024 | 0.881 | 0.112 | 0.004 | 0.02 | 0.855 | 0.049 | 0.027 |
| K | 0.016 | 0.9 | 0 | 0.876 | 0.97 | 0.006 | 0.768 | 0.004 | 0.925 | 0.004 | 0.876 | 0.926 |
| Total Cations | 4.987 | 6.984 | 8 | 6.972 | 7.838 | 4.998 | 6.92 | 8 | 7.792 | 4.961 | 6.971 | 7.795 |

| Sample | 2en2 | 2en2 | 2en2 | 2en2 | 26 | 26 | 26 | 26 | 023a | 023a | 023a |
|---|---|---|---|---|---|---|---|---|---|---|---|
| mineral | bt | grt | mu | st | grt | mu | bt | fsp | bt | grt | mu |
| SiO2 | 36.52 | 37.22 | 45.13 | 26.94 | 36.81 | 45.68 | 35.55 | 61.02 | 36.16 | 37.78 | 45.75 |
| TiO2 | 1.34 | 0.07 | 0.49 | 0.38 | 0.01 | 0.88 | 1.81 | 0.02 | 1.67 | 0.03 | 0.48 |
| Al2O3 | 18.71 | 20.94 | 34.74 | 52.55 | 20.7 | 32.85 | 17.16 | 24.08 | 17.93 | 20.96 | 36.34 |
| Cr2O3 | 0.01 | 0.04 | 0.01 | 0.06 | 0.05 | 0.05 | 0.04 | 0 | 0.09 | 0.02 | 0 |
| Fe2O3 | 0 | 1.11 | 0 | 0 | 1.98 | 0 | 0 | 0.01 | 0 | 1.33 | 0 |
| FeO | 16.86 | 36.08 | 0.99 | 12.2 | 30.06 | 2.14 | 18.14 | 0 | 15.87 | 30.86 | 0.57 |
| MnO | 0 | 0.07 | 0 | 0.02 | 2.07 | 0 | 0.07 | 0 | 0.06 | 1.11 | 0.04 |
| MgrtO | 11.26 | 3.39 | 0.66 | 1.64 | 2.34 | 1.21 | 10.54 | 0 | 11.58 | 5.91 | 0.54 |
| CaO | 0 | 1.71 | 0 | 0 | 5.55 | 0 | 0 | 5.79 | 0 | 1.74 | 0 |
| Na2O | 0.54 | 0.04 | 1.38 | 0.91 | 0.09 | 1.06 | 0.23 | 8.47 | 0.28 | 0.08 | 1.32 |
| K2O | 8.72 | 0 | 8.93 | 0 | 0.06 | 9.81 | 9.77 | 0.06 | 9.22 | 0.04 | 8.85 |
| totals | 93.97 | 100.67 | 92.34 | 94.7 | 99.71 | 93.69 | 93.34 | 99.45 | 92.86 | 99.84 | 93.89 |
| cations | | | | | | | | | | | |
| Si | 2.768 | 2.977 | 3.078 | 7.697 | 2.965 | 3.107 | 2.761 | 2.726 | 2.774 | 2.989 | 3.055 |
| Ti | 0.076 | 0.004 | 0.025 | 0.082 | 0 | 0.045 | 0.106 | 0.001 | 0.096 | 0.001 | 0.024 |
| Al | 1.672 | 1.974 | 2.793 | 17.7 | 1.966 | 2.634 | 1.571 | 1.268 | 1.622 | 1.955 | 2.861 |
| Cr | 0.001 | 0.003 | 0.001 | 0.014 | 0.003 | 0.003 | 0.002 | 0 | 0.005 | 0.001 | 0 |
| Fe3+ | 0 | 0.067 | 0 | 0 | 0.12 | 0 | 0 | 0 | 0 | 0.079 | 0 |
| Fe2+ | 1.069 | 2.413 | 0.056 | 2.915 | 2.025 | 0.122 | 1.178 | 0 | 1.018 | 2.042 | 0.032 |
| Mn | 0 | 0.005 | 0 | 0.005 | 0.141 | 0 | 0.005 | 0 | 0.004 | 0.074 | 0.002 |
| Mgrt | 1.272 | 0.404 | 0.067 | 0.698 | 0.281 | 0.122 | 1.22 | 0 | 1.324 | 0.696 | 0.053 |
| Ca | 0 | 0.147 | 0 | 0 | 0.479 | 0 | 0 | 0.277 | 0 | 0.147 | 0 |
| Na | 0.079 | 0.006 | 0.182 | 0.505 | 0.014 | 0.14 | 0.035 | 0.734 | 0.041 | 0.012 | 0.171 |
| K | 0.844 | 0 | 0.778 | 0 | 0.006 | 0.852 | 0.969 | 0.003 | 0.904 | 0.004 | 0.755 |
| Total Cations | 7.781 | 8 | 6.98 | 29.62 | 8 | 7.025 | 7.849 | 5.008 | 7.788 | 8 | 6.953 |

| Sample | 2fc | 2fc | 2en3 | 2en3 | 2en3 | 2en3 | 2en3 | 2eja | 2eja | 2eja | 2eja |
|---|---|---|---|---|---|---|---|---|---|---|---|
| mineral | fsp | grt | grt | mu | bt | fsp | chl | grt | fsp | mu | bt |
| SiO2 | 60.98 | 37.52 | 37.11 | 45.94 | 36.41 | 59 | 24.2 | 37.26 | 63.67 | 45.92 | 35.26 |
| TiO2 | 0 | 0 | 0.12 | 0.47 | 1.43 | 0 | 0.11 | 0 | 0.01 | 1.25 | 3.28 |
| Al2O3 | 23.01 | 21.33 | 20.69 | 34.29 | 17.95 | 25.22 | 22.23 | 20.89 | 22.55 | 33.48 | 17.53 |
| Cr2O3 | 0.09 | 0.06 | 0.07 | 0 | 0.07 | 0.09 | 0 | 0 | 0.02 | 0.05 | 0 |
| Fe2O3 | 0 | 1.19 | 1.45 | 0 | 0 | 0.02 | 0.84 | 1.43 | 0.07 | 0 | 0 |
| FeO | 0 | 27.08 | 30.36 | 0.96 | 18.67 | 0 | 22.76 | 30.37 | 0 | 1.66 | 19.16 |
| MnO | 0.03 | 1.38 | 0.12 | 0.07 | 0 | 0.02 | 0.1 | 2.02 | 0 | 0.01 | 0.12 |
| MgrtO | 0 | 3.71 | 1.88 | 0.92 | 10.54 | 0 | 15.71 | 3.28 | 0 | 1 | 9.32 |
| CaO | 5.13 | 7.56 | 8.31 | 0 | 0.01 | 7.28 | 0 | 4.7 | 3.85 | 0 | 0 |
| Na2O | 8.37 | 0.02 | 0 | 0.98 | 0.27 | 7.45 | 0.13 | 0.04 | 9.62 | 0.63 | 0.25 |
| K2O | 0.17 | 0 | 0 | 10.1 | 8.73 | 0.08 | 0.01 | 0.04 | 0.17 | 9.91 | 9.54 |
| totals | 97.78 | 99.85 | 100.1 | 93.74 | 94.09 | 99.16 | 86.07 | 100 | 99.98 | 93.91 | 94.46 |
| cations | | | | | | | | | | | |
| Si | 2.764 | 2.969 | 2.97 | 3.103 | 2.782 | 2.654 | 2.577 | 2.977 | 2.815 | 3.103 | 2.717 |
| Ti | 0 | 0 | 0.007 | 0.024 | 0.082 | 0 | 0.009 | 0 | 0 | 0.063 | 0.19 |
| Al | 1.229 | 1.99 | 1.952 | 2.73 | 1.617 | 1.338 | 2.791 | 1.968 | 1.176 | 2.667 | 1.592 |
| Cr | 0.003 | 0.004 | 0.004 | 0 | 0.004 | 0.003 | 0 | 0 | 0.001 | 0.003 | 0 |
| Fe3+ | 0 | 0.071 | 0.088 | 0 | 0 | 0.001 | 0.067 | 0.086 | 0.002 | 0 | 0 |
| Fe2+ | 0 | 1.792 | 2.032 | 0.054 | 1.193 | 0 | 2.027 | 2.03 | 0 | 0.094 | 1.234 |
| Mn | 0.001 | 0.093 | 0.008 | 0.004 | 0 | 0.001 | 0.009 | 0.137 | 0 | 0 | 0.008 |
| Mgrt | 0 | 0.438 | 0.224 | 0.093 | 1.2 | 0 | 2.493 | 0.39 | 0 | 0.101 | 1.07 |
| Ca | 0.249 | 0.641 | 0.713 | 0 | 0.001 | 0.351 | 0 | 0.402 | 0.183 | 0 | 0 |
| Na | 0.736 | 0.003 | 0 | 0.128 | 0.04 | 0.65 | 0.027 | 0.005 | 0.825 | 0.083 | 0.037 |
| K | 0.01 | 0 | 0 | 0.871 | 0.852 | 0.004 | 0.001 | 0.004 | 0.01 | 0.855 | 0.939 |
| Total Cations | 4.993 | 8 | 8 | 7.008 | 7.771 | 5.002 | 10 | 8 | 5.012 | 6.968 | 7.786 |

| Sample | 023a | 016c1 | 016c1 | 016c1 | 016c1 | 014a | 014a | 014a | 006b1 | 006b1 | 006b1 | 006b1 |
|---|---|---|---|---|---|---|---|---|---|---|---|---|
| mineral | fsp | grt | bt | fsp | mu | grt | bt | fsp | grt | bt | fsp | mu |
| SiO2 | 63.12 | 37.18 | 35.09 | 64.24 | 44.27 | 38.17 | 37.58 | 65.63 | 36.64 | 35.6 | 63.56 | 45.99 |
| TiO2 | 0 | 0.04 | 3.33 | 0 | 1.27 | 0 | 1.54 | 0 | 0.07 | 2.35 | 0 | 1.38 |
| Al2O3 | 22.22 | 20.75 | 18.68 | 22.64 | 34.79 | 21.12 | 18.71 | 21.31 | 20.39 | 17.89 | 22.24 | 33.15 |
| Cr2O3 | 0 | 0.09 | 0.08 | 0.03 | 0.14 | 0 | 0.02 | 0.06 | 0 | 0.15 | 0.03 | 0.07 |
| Fe2O3 | 0.03 | 1.28 | 0 | 0.12 | 0 | 1.03 | 0 | 0 | 1.13 | 0 | 0 | 0 |
| FeO | 0 | 31.44 | 18.3 | 0 | 1.18 | 30.04 | 14.87 | 0 | 32.56 | 17.76 | 0 | 1.25 |
| MnO | 0.01 | 1.86 | 0.22 | 0 | 0.02 | 0.82 | 0.06 | 0 | 1.81 | 0.02 | 0.01 | 0.07 |
| MgrtO | 0 | 4.85 | 8.91 | 0 | 0.57 | 7.27 | 13.01 | 0 | 3.68 | 10.72 | 0 | 1.1 |
| CaO | 3.74 | 1.91 | 0 | 3.88 | 0 | 1.32 | 0 | 2.26 | 2.24 | 0 | 3.63 | 0 |
| Na2O | 9.78 | 0.02 | 0.19 | 8.89 | 0.69 | 0.02 | 0.28 | 9.92 | 0 | 0.19 | 9.54 | 0.95 |
| K2O | 0.09 | 0 | 9.57 | 0.09 | 9.72 | 0.01 | 8.94 | 0.04 | 0.02 | 9.16 | 0 | 9.5 |
| totals | 99.01 | 99.41 | 94.37 | 99.9 | 92.67 | 99.79 | 95.02 | 99.21 | 98.54 | 93.87 | 99.02 | 93.46 |
| cations | | | | | | | | | | | | |
| Si | 2.819 | 2.978 | 2.692 | 2.831 | 3.027 | 2.995 | 2.785 | 2.9 | 2.984 | 2.73 | 2.831 | 3.113 |
| Ti | 0 | 0.003 | 0.192 | 0 | 0.065 | 0 | 0.086 | 0 | 0.004 | 0.136 | 0 | 0.07 |
| Al | 1.17 | 1.959 | 1.689 | 1.176 | 2.805 | 1.954 | 1.634 | 1.11 | 1.957 | 1.617 | 1.168 | 2.646 |
| Cr | 0 | 0.006 | 0.005 | 0.001 | 0.008 | 0 | 0.001 | 0.002 | 0 | 0.009 | 0.001 | 0.004 |
| Fe3+ | 0.001 | 0.077 | 0 | 0.004 | 0 | 0.061 | 0 | 0 | 0.069 | 0 | 0 | 0 |
| Fe2+ | 0 | 2.106 | 1.174 | 0 | 0.068 | 1.972 | 0.922 | 0 | 2.217 | 1.139 | 0 | 0.071 |
| Mn | 0.001 | 0.126 | 0.014 | 0 | 0.001 | 0.054 | 0.004 | 0 | 0.125 | 0.001 | 0 | 0.004 |
| Mgrt | 0 | 0.579 | 1.018 | 0 | 0.058 | 0.85 | 1.437 | 0 | 0.446 | 1.226 | 0 | 0.111 |
| Ca | 0.179 | 0.164 | 0 | 0.183 | 0 | 0.111 | 0 | 0.107 | 0.195 | 0 | 0.173 | 0 |
| Na | 0.847 | 0.003 | 0.028 | 0.76 | 0.092 | 0.003 | 0.04 | 0.85 | 0 | 0.029 | 0.825 | 0.124 |
| K | 0.005 | 0 | 0.938 | 0.005 | 0.848 | 0.001 | 0.846 | 0.002 | 0.002 | 0.897 | 0 | 0.821 |
| Total Cations | 5.022 | 8 | 7.751 | 4.961 | 6.972 | 8 | 7.754 | 4.971 | 8 | 7.784 | 4.997 | 6.965 |

| Sample | 2ee | 2ee | 2ee | 2ee | 2eb4a | 2eb4a | 2eb4a | 2eb4a | 017a | 017a | 017a | 017a |
|---|---|---|---|---|---|---|---|---|---|---|---|---|
| mineral | grt | fsp | bt | mu | grt | cmu | cbt | fsp | grt | bt | mu | fsp |
| SiO2 | 37.21 | 63.14 | 35.82 | 45.16 | 37.2 | 45.07 | 35.35 | 64.69 | 36.62 | 34.61 | 44.63 | 63.46 |
| TiO2 | 0.06 | 0 | 1.34 | 0.5 | 0.04 | 0.78 | 2.38 | 0 | 0 | 3.09 | 1 | 0 |
| Al2O3 | 20.57 | 22.45 | 17.66 | 35.93 | 20.92 | 34.89 | 17.91 | 21.45 | 20.56 | 18.52 | 34.97 | 22.6 |
| Cr2O3 | 0.03 | 0.05 | 0 | 0.03 | 0 | 0 | 0 | 0 | 0.02 | 0 | 0 | 0.01 |
| Fe2O3 | 2.2 | 0.02 | 0.14 | 0 | 0.86 | 0 | 0 | 0.14 | 1.38 | 0 | 0 | 0 |
| FeO | 33.61 | 0 | 19.53 | 0.87 | 34.7 | 0.94 | 18.6 | 0 | 29.99 | 19.98 | 1.24 | 0 |
| MnO | 0.08 | 0 | 0.03 | 0.01 | 1.23 | 0.03 | 0 | 0 | 6.98 | 0.24 | 0 | 0.04 |
| MgrtO | 2.15 | 0 | 9.95 | 0.35 | 3.53 | 0.7 | 9.55 | 0 | 3.02 | 8.07 | 0.53 | 0 |
| CaO | 4.7 | 3.95 | 0 | 0 | 1.6 | 0 | 0 | 2.67 | 1 | 0 | 0 | 3.94 |
| Na2O | 0.19 | 9.37 | 0.25 | 1.57 | 0.05 | 1.08 | 0.47 | 10.29 | 0 | 0.29 | 0.6 | 9.4 |
| K2O | 0.04 | 0.05 | 8.33 | 7.89 | 0 | 9 | 8.09 | 0.05 | 0.02 | 9.62 | 9.88 | 0.17 |
| totals | 100.8 | 99.03 | 93.05 | 92.32 | 100.1 | 92.5 | 92.36 | 99.3 | 99.6 | 94.43 | 92.85 | 99.63 |
| cations | | | | | | | | | | | | |
| Si | 2.976 | 2.815 | 2.779 | 3.057 | 2.986 | 3.067 | 2.751 | 2.87 | 2.974 | 2.681 | 3.043 | 2.814 |
| Ti | 0.004 | 0 | 0.078 | 0.025 | 0.002 | 0.04 | 0.139 | 0 | 0 | 0.18 | 0.051 | 0 |
| Al | 1.94 | 1.18 | 1.615 | 2.868 | 1.98 | 2.799 | 1.643 | 1.122 | 1.969 | 1.692 | 2.811 | 1.182 |
| Cr | 0.002 | 0.002 | 0 | 0.002 | 0 | 0 | 0 | 0 | 0.001 | 0 | 0 | 0 |
| Fe3+ | 0.132 | 0.001 | 0.008 | 0 | 0.052 | 0 | 0 | 0.005 | 0.085 | 0 | 0 | 0 |
| Fe2+ | 2.248 | 0 | 1.267 | 0.049 | 2.329 | 0.054 | 1.211 | 0 | 2.037 | 1.295 | 0.071 | 0 |
| Mn | 0.005 | 0 | 0.002 | 0.001 | 0.084 | 0.002 | 0 | 0 | 0.48 | 0.016 | 0 | 0.002 |
| Mgrt | 0.256 | 0 | 1.15 | 0.035 | 0.422 | 0.071 | 1.108 | 0 | 0.365 | 0.931 | 0.054 | 0 |
| Ca | 0.403 | 0.189 | 0 | 0 | 0.138 | 0 | 0 | 0.127 | 0.087 | 0 | 0 | 0.187 |
| Na | 0.029 | 0.81 | 0.038 | 0.207 | 0.008 | 0.142 | 0.071 | 0.885 | 0 | 0.044 | 0.079 | 0.809 |
| K | 0.004 | 0.003 | 0.825 | 0.682 | 0 | 0.782 | 0.804 | 0.003 | 0.002 | 0.952 | 0.86 | 0.01 |
| Total Cations | 8 | 5 | 7.763 | 6.927 | 8 | 6.956 | 7.726 | 5.011 | 8 | 7.791 | 6.969 | 5.004 |

| Sample | 006a | 006a | 006a | 006a | 005b | 005b | 005b | 005a | 005a | 005a | 005a |
|---|---|---|---|---|---|---|---|---|---|---|---|
| mineral | grt | bt | mu | fsp | bt | fsp | grtt | grt | bt | mu | fsp |
| SiO2 | 37.74 | 35.06 | 46.05 | 61.53 | 36.65 | 60.75 | 38.37 | 38.08 | 35.28 | 46.01 | 63.07 |
| TiO2 | 0 | 2.59 | 1.5 | 0 | 2.18 | 0.01 | 0 | 0.07 | 2.56 | 1.48 | 0.07 |
| Al2O3 | 21.01 | 17.03 | 32.56 | 23.24 | 17.61 | 24.08 | 21.32 | 21.11 | 17.06 | 31.77 | 22.75 |
| Cr2O3 | 0 | 0.08 | 0.07 | 0.02 | 0.06 | 0.02 | 0 | 0.02 | 0.03 | 0 | 0 |
| Fe2O3 | 0.9 | 0 | 0 | 0.08 | 0 | 0 | 0.96 | 0.66 | 0 | 0 | 0.02 |
| FeO | 29.44 | 18.31 | 2 | 0 | 15.89 | 0 | 23.1 | 28.34 | 18.63 | 2.05 | 0 |
| MnO | 1.32 | 0.12 | 0 | 0.02 | 0.14 | 0.01 | 1.63 | 1.38 | 0.09 | 0 | 0 |
| MgrtO | 3.75 | 10.5 | 1.17 | 0 | 12.42 | 0 | 4.07 | 3.61 | 10.12 | 1.48 | 0 |
| CaO | 5.99 | 0 | 0 | 5.01 | 0 | 5.9 | 10.74 | 7.12 | 0 | 0 | 4.25 |
| Na2O | 0 | 0.22 | 0.69 | 9.06 | 0.23 | 8.55 | 0 | 0.06 | 0.13 | 0.49 | 9.25 |
| K2O | 0 | 9.52 | 9.94 | 0.11 | 9.61 | K2O | 0.04 | 0.01 | 9.6 | 9.86 | 0.17 |
| totals | 100.2 | 93.42 | 93.99 | 99.09 | 94.8 | 99.41 | 100.2 | 100.5 | 93.5 | 93.14 | 99.58 |
| cations | | | | | | | | | | | |
| Si | 2.991 | 2.724 | 3.118 | 2.757 | 2.76 | 2.718 | 2.993 | 3 | 2.741 | 3.142 | 2.801 |
| Ti | 0 | 0.151 | 0.076 | 0 | 0.123 | 0 | 0 | 0.004 | 0.15 | 0.076 | 0.002 |
| Al | 1.963 | 1.56 | 2.599 | 1.228 | 1.564 | 1.27 | 1.961 | 1.961 | 1.562 | 2.557 | 1.191 |
| Cr | 0 | 0.005 | 0.004 | 0.001 | 0.004 | 0.001 | 0 | 0.001 | 0.002 | 0 | 0 |
| Fe3+ | 0.054 | 0 | 0 | 0.003 | 0 | | 0.056 | 0.039 | 0 | 0 | 0.001 |
| Fe2+ | 1.951 | 1.19 | 0.113 | 0 | 1.001 | 0 | 1.507 | 1.868 | 1.211 | 0.117 | 0 |
| Mn | 0.088 | 0.008 | 0 | 0.001 | 0.009 | 0 | 0.108 | 0.092 | 0.006 | 0 | 0 |
| Mgrt | 0.443 | 1.216 | 0.118 | 0 | 1.394 | 0 | 0.473 | 0.424 | 1.171 | 0.151 | 0 |
| Ca | 0.509 | 0 | 0 | 0.241 | 0 | 0.283 | 0.898 | 0.601 | 0 | 0 | 0.202 |
| Na | 0 | 0.033 | 0.09 | 0.787 | 0.034 | 0.742 | 0 | 0.009 | 0.019 | 0.064 | 0.797 |
| K | 0 | 0.945 | 0.86 | 0.006 | 0.925 | 0.09 | 0.004 | 0.001 | 0.952 | 0.86 | 0.01 |
| Total Cations | 8 | 7.832 | 6.979 | 5.024 | 7.812 | 5.019 | 8 | 8 | 7.813 | 6.966 | 5.004 |

| Sample | 004a | 004a | 004a | 004a | G90 | G90 | G90 | G90 | G57 | G57 | G57 |
|---|---|---|---|---|---|---|---|---|---|---|---|
| mineral | grt | mu | bt | fsp | grt | fsp | bt | chl | mu | bt | fsp |
| SiO2 | 37.15 | 45.68 | 36.85 | 62.11 | 38.16 | 66.79 | 38.22 | 27.05 | 48.27 | 36.29 | 63.95 |
| TiO2 | 0.02 | 0.55 | 1.78 | 0 | 0.01 | 0 | 1.65 | 0.15 | 1.08 | 2.25 | 0 |
| Al2O3 | 20.43 | 35.74 | 18.32 | 22.63 | 21.77 | 21.11 | 18.06 | 22.56 | 33.77 | 18.29 | 21.75 |
| Cr2O3 | 0.05 | 0.08 | 0.09 | 0 | 0 | 0 | 0 | 0 | 0 | 0 | 0 |
| Fe2O3 | 0.95 | 0 | 0 | 0.01 | 2.31 | 0 | 2.23 | 0 | 0.81 | 0 | 0 |
| FeO | 33.92 | 1.15 | 18.74 | 0 | 30.02 | 0 | 11.36 | 15.72 | 0.68 | 17.04 | 0 |
| MnO | 1.09 | 0 | 0.04 | 0.05 | 0.51 | 0 | 0.02 | 0.02 | 0.01 | 0.06 | 0 |
| MgrtO | 2.83 | 0.68 | 10.79 | 0 | 7.81 | 0 | 15.55 | 22.29 | 1.21 | 11.54 | 0 |
| CaO | 3.42 | 0 | 0 | 4.23 | 0.92 | 1.87 | 0 | 0.01 | 0 | 0 | 3.09 |
| Na2O | 0 | 1.69 | 0.16 | 8.89 | 0 | 10.28 | 0.58 | 0 | 0.76 | 0.23 | 9.87 |
| K2O | 0 | 8.22 | 9.1 | 0.03 | 0 | 0.04 | 7.59 | 0 | 8.07 | 8.78 | 0.08 |
| totals | 99.87 | 93.81 | 95.89 | 97.94 | 101.51 | 100.09 | 95.26 | 87.8 | 94.67 | 94.49 | 98.74 |
| cations | | | | | | | | | | | |
| Si | 2.997 | 3.057 | 2.764 | 2.8 | 2.943 | 2.921 | 2.776 | 2.693 | 3.178 | 2.741 | 2.853 |
| Ti | 0.001 | 0.028 | 0.101 | 0 | 0.001 | 0 | 0.09 | 0.011 | 0.053 | 0.128 | 0 |
| Al | 1.943 | 2.82 | 1.62 | 1.203 | 1.979 | 1.089 | 1.546 | 2.648 | 2.621 | 1.629 | 1.144 |
| Cr | 0.003 | 0.004 | 0.005 | 0 | 0 | 0 | 0 | 0 | 0 | 0 | 0 |
| Fe3+ | 0.058 | 0 | 0 | 0 | 0.134 | 0 | 0.122 | 0 | 0.04 | 0 | 0 |
| Fe2+ | 2.288 | 0.064 | 1.176 | 0 | 1.936 | 0 | 0.69 | 1.309 | 0.037 | 1.076 | 0 |
| Mn | 0.074 | 0 | 0.003 | 0.002 | 0.033 | 0 | 0.001 | 0.002 | 0.001 | 0.004 | 0 |
| Mgrt | 0.34 | 0.068 | 1.206 | 0 | 0.898 | 0 | 1.683 | 3.307 | 0.119 | 1.299 | 0 |
| Ca | 0.296 | 0 | 0 | 0.204 | 0.076 | 0.088 | 0 | 0.001 | 0 | 0 | 0.148 |
| Na | 0 | 0.22 | 0.024 | 0.777 | 0 | 0.872 | 0.082 | 0 | 0.097 | 0.034 | 0.854 |
| K | 0 | 0.702 | 0.872 | 0.001 | 0 | 0.002 | 0.704 | 0 | 0.679 | 0.847 | 0.005 |
| Total Cations | 8 | 6.964 | 7.77 | 4.988 | 8 | 4.972 | 7.693 | 9.972 | 6.825 | 7.757 | 5.004 |

| Sample | 004b | 004b | 004b | 004b | 2ly | 2ly | 2ly | 2ly | 2ly | 2lw | 2lw |
|---|---|---|---|---|---|---|---|---|---|---|---|
| mineral | grt | bt | mu | fsp | grt | bt | mu | pl | ksp | grt | bt |
| SiO2 | 37.77 | 36.49 | 45.87 | 62.53 | 36.63 | 34.41 | 45.36 | 62.67 | 63.59 | 37.41 | 35.11 |
| TiO2 | 0.02 | 2.28 | 0.58 | 0.03 | 0.05 | 3.27 | 0.89 | 0 | 0.22 | 0 | 2.89 |
| Al2O3 | 21.21 | 17.78 | 33.14 | 23.22 | 20.53 | 18.39 | 34.95 | 22.54 | 18.48 | 20.57 | 19.31 |
| Cr2O3 | 0.05 | 0.05 | 0.02 | 0.02 | 0.08 | 0 | 0.01 | 0.05 | 0.04 | 0.04 | 0 |
| Fe2O3 | 0.79 | 0 | 0 | 0.04 | 2.26 | 0 | 0 | 0 | 0 | 0.7 | 0 |
| FeO | 29.58 | 17.28 | 1.45 | 0 | 31.08 | 22.26 | 1.33 | 0 | 0 | 32.04 | 19.02 |
| MnO | 1.82 | 0.17 | 0.01 | 0 | 6.18 | 0.18 | 0.03 | 0 | 0 | 3.27 | 0.22 |
| MgrtO | 3.44 | 10.61 | 1.22 | 0 | 2.12 | 6.25 | 0.49 | 0 | 0 | 3.86 | 8.46 |
| CaO | 5.96 | 0 | 0 | 4.72 | 1.59 | 0 | 0 | 4.14 | 0 | 1.93 | 0 |
| Na2O | 0 | 0.05 | 0.68 | 8.93 | 0.13 | 0.04 | 0.42 | 9.48 | 1.18 | 0 | 0.23 |
| K2O | 0 | 9.2 | 9.69 | 0.08 | 0.03 | 9.67 | 10.45 | 0.1 | 15.16 | 0 | 9.88 |
| totals | 100.7 | 93.9 | 92.67 | 99.57 | 100.7 | 94.46 | 93.94 | 98.98 | 98.68 | 99.82 | 95.14 |
| cations | | | | | | | | | | | |
| Si | 2.985 | 2.783 | 3.132 | 2.779 | 2.96 | 2.693 | 3.064 | 2.802 | 2.974 | 3.004 | 2.683 |
| Ti | 0.001 | 0.131 | 0.03 | 0.001 | 0.003 | 0.192 | 0.045 | 0 | 0.008 | 0 | 0.166 |
| Al | 1.976 | 1.599 | 2.667 | 1.216 | 1.956 | 1.697 | 2.784 | 1.188 | 1.019 | 1.947 | 1.74 |
| Cr | 0.003 | 0.003 | 0.001 | 0.001 | 0.005 | 0 | 0.001 | 0.002 | 0.002 | 0.003 | 0 |
| Fe3+ | 0.047 | 0 | 0 | 0.001 | 0.137 | 0 | 0 | 0 | 0 | 0.042 | 0 |
| Fe2+ | 1.955 | 1.102 | 0.083 | 0 | 2.1 | 1.457 | 0.075 | 0 | 0 | 2.152 | 1.215 |
| Mn | 0.122 | 0.011 | 0.001 | 0 | 0.423 | 0.012 | 0.002 | 0 | 0 | 0.222 | 0.015 |
| Mgrt | 0.405 | 1.206 | 0.124 | 0 | 0.255 | 0.729 | 0.049 | 0 | 0 | 0.462 | 0.963 |
| Ca | 0.505 | 0 | 0 | 0.225 | 0.138 | 0 | 0 | 0.198 | 0 | 0.167 | 0 |
| Na | 0 | 0.007 | 0.09 | 0.769 | 0.02 | 0.005 | 0.055 | 0.822 | 0.107 | 0.001 | 0.034 |
| K | 0 | 0.896 | 0.845 | 0.004 | 0.003 | 0.966 | 0.901 | 0.006 | 0.906 | 0 | 0.964 |
| Total Cations | 8 | 7.737 | 6.972 | 4.997 | 8 | 7.752 | 6.976 | 5.017 | 5.015 | 8 | 7.78 |

| Sample | G57 | G96 | G96 | G96 | G96 | 2jb | 2jb | 2jb | 2jb | 2hh | 2hh |
|---|---|---|---|---|---|---|---|---|---|---|---|
| mineral | grt | fsp | bt | mu | grt | grt | bt | mu | fsp | grt | bt |
| SiO2 | 38.11 | 60.58 | 36.06 | 46.47 | 37.58 | 36.29 | 33.77 | 44.79 | 64.23 | 36.74 | 34.3 |
| TiO2 | 0.01 | 0 | 3.11 | 0.49 | 0.01 | 0 | 1.43 | 0.36 | 0.01 | 0 | 2.84 |
| Al2O3 | 21.39 | 25.71 | 16.83 | 32.13 | 20.48 | 20.15 | 18.35 | 33.56 | 21.75 | 20.44 | 18.35 |
| Cr2O3 | 0 | 0 | 0 | 0 | 0 | 0.1 | 0 | 0 | 0 | 0.01 | 0.01 |
| Fe2O3 | 1.32 | 0.06 | 0 | 0 | 1.15 | 1.31 | 0 | 0 | 0.03 | 1.8 | 0 |
| FeO | 30.84 | 0 | 21.31 | 2.55 | 22.32 | 32.81 | 24.3 | 1.78 | 0 | 32.13 | 22.08 |
| MnO | 1.13 | 0 | 0.17 | 0 | 5.57 | 4.76 | 0.39 | 0.09 | 0.02 | 5.96 | 0.15 |
| MgrtO | 6.53 | 0 | 8.79 | 1.46 | 1.58 | 2.09 | 5.91 | 0.67 | 0 | 2.48 | 6.42 |
| CaO | 1.53 | 6.92 | 0.04 | 0.02 | 11.06 | 1.59 | 0 | 0 | 3.01 | 0.68 | 0.01 |
| Na2O | 0 | 7.64 | 0.05 | 0.28 | 0 | 0 | 0.1 | 0.51 | 9.88 | 0.1 | 0.25 |
| K2O | 0 | 0.12 | 9.72 | 10.8 | 0 | 0 | 9.87 | 10.58 | 0.2 | 0 | 9.97 |
| totals | 100.9 | 101 | 96.1 | 94.2 | 99.76 | 99.11 | 94.14 | 92.35 | 99.12 | 100.3 | 94.41 |
| cations | | | | | | | | | | | |
| Si | 2.976 | 2.669 | 2.756 | 3.156 | 3.001 | 2.981 | 2.692 | 3.093 | 2.856 | 2.977 | 2.693 |
| Ti | 0.001 | 0 | 0.179 | 0.025 | 0.001 | 0 | 0.086 | 0.019 | 0 | 0 | 0.168 |
| Al | 1.969 | 1.335 | 1.517 | 2.572 | 1.928 | 1.951 | 1.725 | 2.732 | 1.14 | 1.953 | 1.698 |
| Cr | 0 | 0 | 0 | 0 | 0 | 0.006 | 0 | 0 | 0 | 0 | 0.001 |
| Fe3+ | 0.077 | 0.002 | 0 | 0 | 0.069 | 0.081 | 0 | 0 | 0.001 | 0.11 | 0 |
| Fe2+ | 2.014 | 0 | 1.362 | 0.145 | 1.491 | 2.253 | 1.62 | 0.103 | 0 | 2.177 | 1.45 |
| Mn | 0.075 | 0 | 0.011 | 0 | 0.376 | 0.331 | 0.027 | 0.005 | 0.001 | 0.409 | 0.01 |
| Mgrt | 0.76 | 0 | 1.001 | 0.147 | 0.188 | 0.256 | 0.702 | 0.069 | 0 | 0.3 | 0.751 |
| Ca | 0.128 | 0.327 | 0.004 | 0.001 | 0.947 | 0.14 | 0 | 0 | 0.143 | 0.059 | 0 |
| Na | 0 | 0.653 | 0.008 | 0.037 | 0 | 0 | 0.016 | 0.068 | 0.852 | 0.016 | 0.039 |
| K | 0 | 0.007 | 0.949 | 0.936 | 0 | 0 | 1.005 | 0.933 | 0.011 | 0 | 1 |
| Total Cations | 8 | 4.992 | 7.786 | 7.02 | 8 | 8 | 7.871 | 7.023 | 5.005 | 8 | 7.809 |

| Sample | 2lw | 2lw |
|---|---|---|
| mineral | fsp | mu |
| SiO2 | 61.66 | 45.03 |
| TiO2 | 0.03 | 1.07 |
| Al2O3 | 23.93 | 34.51 |
| Cr2O3 | 0.05 | 0.07 |
| Fe2O3 | 0.04 | 0 |
| FeO | 0 | 1.14 |
| MnO | 0 | 0 |
| MgrtO | 0.04 | 0.64 |
| CaO | 5.4 | 0 |
| Na2O | 8.6 | 0.32 |
| K2O | 0.23 | 10.36 |
| totals | 100 | 93.13 |
| cations | | |
| Si | 2.738 | 3.065 |
| Ti | 0.001 | 0.055 |
| Al | 1.253 | 2.769 |
| Cr | 0.002 | 0.004 |
| Fe3+ | 0.001 | 0 |
| Fe2+ | 0 | 0.065 |
| Mn | 0 | 0 |
| Mgrt | 0.003 | 0.065 |
| Ca | 0.257 | 0 |
| Na | 0.741 | 0.042 |
| K | 0.013 | 0.9 |
| Total Cations | 5.01 | 6.965 |

| Sample | 2hh | 2hh |
|---|---|---|
| mineral | ksp | fsp |
| SiO2 | 63.67 | 65.19 |
| TiO2 | 0.24 | 0 |
| Al2O3 | 18.34 | 21.61 |
| Cr2O3 | 0.04 | 0.03 |
| Fe2O3 | 0.01 | 0 |
| FeO | 0 | 0 |
| MnO | 0 | 0.01 |
| MgrtO | 0 | 0 |
| CaO | 0 | 2.32 |
| Na2O | 1.08 | 9.76 |
| K2O | 15.27 | 0.27 |
| totals | 98.69 | 99.21 |
| cations | | |
| Si | 2.979 | 2.885 |
| Ti | 0.009 | 0 |
| Al | 1.012 | 1.127 |
| Cr | 0.002 | 0.001 |
| Fe3+ | 0.001 | 0 |
| Fe2+ | 0 | 0 |
| Mn | 0 | 0.001 |
| Mgrt | 0 | 0 |
| Ca | 0 | 0.11 |
| Na | 0.098 | 0.838 |
| K | 0.912 | 0.015 |
| Total Cations | 5.011 | 4.977 |

## Mineral data

### Sm-Nd

| Sample | G9 Grt 1 | G9 Grt 2 | G9 Wm | G9 Bt | G31(1) Grt 1 | G31(1) Grt 2 | G33 Grt 1 | G96 Grt 1 | G96 Grt 2 | G96 Bt | 4A(2) Grt 1 | 4B(1) Grt 1 | 4B(1) Grt 2 |
|---|---|---|---|---|---|---|---|---|---|---|---|---|---|
| [Nd] | 0.086 | 0.207 | 17.050 | 7.629 | 0.237 | 0.056 | 6.798 | 0.066 | 0.158 | 5.424 | 12.263 | 0.151 | 0.668 |
| [Sm] | 0.168 | 1.203 | 1.820 | 3.094 | 1.252 | 0.219 | 1.919 | 0.489 | 0.504 | 1.053 | 2.765 | 0.761 | 0.793 |
| [Sm]/[Nd] | | | | | | | | | | 0.194 | | | |
| $^{147}Sm/^{144}Nd$ | 1.1853 | 3.5195 | 0.0645 | 0.2452 | 3.1949 | 2.3847 | 0.1706 | 4.4758 | 1.9302 | 0.1173 | 0.1363 | 3.0514 | 0.7183 |
| 2 sigma | 0.0011 | 0.0098 | 0.0001 | 0.0001 | 0.0068 | 0.0017 | 0.0003 | 1 per mil | 0.0070 | 0.0004 | 0.0028 | 0.0225 | 0.0014 |
| $^{143}Nd/^{144}Nd$ | 0.512303 | 0.51280 | 0.512281 | 0.512224 | 0.512657 | 0.512401 | 0.511698 | 0.512936 | 0.512225 | 0.511879 | 0.511855 | 0.512277 | 0.511861 |
| 2 sigma | 0.000024 | 0.00011 | 0.000008 | 0.000008 | 0.000025 | 0.000066 | 0.000005 | 0.000060 | 0.000038 | 0.000012 | 0.000015 | 0.000058 | 0.000012 |

| Sample | 4B(1) Bi | G156 Grt 1 | G31 (II) Grt 1 | G50 Grt 1 | G160 Grt Rim | G160 Grt Core | 2LP Grt 1 | 2LP Grt 2 | G207 Grt 1 | G49 Grt 1 | G166 Grt 1 |
|---|---|---|---|---|---|---|---|---|---|---|---|
| [Nd] | 6.934 | 1.737 | 11.180 | 27.073 | 3.052 | 4.989 | 2.650 | 4.150 | 16.012 | 29.470 | 11.914 |
| [Sm] | 1.295 | 0.544 | | 6.001 | 1.540 | 1.140 | 1.710 | 2.198 | 6.274 | 6.450 | 3.345 |
| [Sm]/[Nd] | | | | | | | | | | | |
| $^{147}Sm/^{144}Nd$ | 0.1129 | 0.1892 | | 0.1340 | 0.3051 | 0.1380 | 0.3900 | 0.3202 | 0.3704 | 0.1323 | 0.1697 |
| 2 sigma | 0.0001 | 0.0008 | | 0.0016 | 0.0028 | 0.0011 | 0.0076 | 0.0001 | 0.0640 | 0.0019 | 0.0016 |
| $^{143}Nd/^{144}Nd$ | 0.511870 | 0.511808 | 0.511922 | 0.511341 | 0.511712 | 0.511624 | 0.512750 | 0.51254 | 0.511997 | 0.511334 | 0.511474 |
| 2 sigma | 0.000008 | 0.000008 | 0.000009 | 0.000009 | 0.000008 | 0.000012 | 0.000018 | 0.00015 | 0.000008 | 0.000008 | 0.000008 |

### Rb-Sr

| Sample | G9 Grt 1 | G31(1) Grt 1 | G31(1) Grt 2 | G33 Grt 1 | G96 Grt 1 | G96 Grt 2 | G96 Bt | 4A(2) Grt 1 | 4B(1) Grt 2 | G31 (II) Grt 1 |
|---|---|---|---|---|---|---|---|---|---|---|
| [Sr] | 0.013 | 0.023 | 0.018 | 0.013 | 3.577 | 0.350 | 3.577 | 0.401 | 0.357 | 0.317 |
| [Rb] | 0.182 | 0.012 | | 0.004 | 0.023 | 0.100 | 177.300 | 0.032 | 0.077 | |
| [Rb]/[Sr] | 14.304 | 0.536 | 0.000 | 0.328 | 0.006 | 0.286 | 49.567 | 0.080 | 0.216 | |
| $^{87}Rb/^{86}Sr$ | 41.6510 | 1.5590 | | 0.9538 | 2.8290 | 8.3810 | 144.6030 | 0.2323 | 0.6269 | |
| 2 sigma | 1 per mil | 1 per mil | | 1 per mil | 1 per mil | 1 per mil | 1 per mil | 0.0020 | 0.0031 | 1 per mil |
| $^{87}Sr/^{86}Sr$ | 0.77632 | 0.75238 | 0.75676 | 0.74025 | 0.717375 | 0.731099 | 0.793873 | 0.745880 | 0.743364 | 0.739438 |
| 2 sigma | 0.00011 | 0.00021 | 0.00074 | 0.00054 | 0.000038 | 0.000038 | 0.000044 | 0.000028 | 0.000028 | 0.000028 |

## Whole-rock data

**Sm-Nd**

| Sample | G9 | G9 dup 2 | G31 | G31 rpt | G31 rpt 2 | 4B(1) | G33 | G160 | 2LP |
|---|---|---|---|---|---|---|---|---|---|
| [Nd] | 35.446 | 53.987 | 1.524 | 1.598 | 1.266 | 24.888 | 26.530 | 54.382 | 49.435 |
| [Sm] | 7.533 | 10.552 | 0.339 | 0.354 | 0.313 | 4.938 | 5.283 | 10.481 | 10.084 |
| [Sm]/[Nd] | 0.213 | 0.195 | 0.222 | 0.222 | 0.247 | 0.198 | 0.199 | 0.193 | 0.204 |
| $^{147}Sm/^{144}Nd$ | 0.1285 | 0.1182 | 0.1345 | 0.1339 | 0.1496 | 0.1203 | 0.1204 | 0.1165 | 0.1233 |
| 2 sigma | 1 per mil | 0.0005 | 1 per mil | 1 per mil | 0.0001 | 1 per mil | 0.0002 | 0.0010 | 1 per mil |
| $^{143}Nd/^{144}Nd$ | 0.512269 | 0.512282 | 0.511855 | 0.511880 | 0.511879 | 0.511861 | 0.511661 | 0.511687 | 0.511817 |
| 2 sigma | 0.000008 | 0.000008 | 0.000013 | 0.000010 | 0.000008 | 0.000008 | 0.000017 | 0.000017 | 0.000026 |

**Rb-Sr**

| Sample | G9 | G31 | G31 rpt | 4B(1) |
|---|---|---|---|---|
| [Sr] | 83.335 | 360.510 | 157.300 | 98.681 |
| [Rb] | 151.769 | 128.550 | 134.990 | 104.209 |
| [Rb]/[Sr] | 1.821 | 0.357 | 0.858 | 1.056 |
| $^{87}Rb/^{86}Sr$ | 5.3018 | 1.2159 | 2.4969 | 3.0676 |
| 2 sigma | 0.0014 | 1 per mil | 1 per mil | 1 per mil |
| $^{87}Sr/^{86}Sr$ | 0.771132 | 0.728902 | 0.765893 | 0.748800 |
| 2 sigma | 0.000014 | 0.000008 | 0.000008 | 0.000009 |

## Appendix G - LA-ICP-MS summary

| | G31(1)a | | | | | | | | | | | | | | | | |
|---|---|---|---|---|---|---|---|---|---|---|---|---|---|---|---|---|---|
| **Analysis** | ju24a05 | ju24a07 | ju24a09 | ju24a10 | ju24a11 | ju24a12 | ju24a14 | ju24a15 | ju24a16 | ju24b05 | ju24b06 | ju24b07 | ju24b08 | ju24b09 | ju24b10 | ju24b11 | ju24b12 |
| **Distance (mm)** | 0.08 | 0.45 | 0.75 | 1.04 | 1.31 | 1.66 | 2.17 | 2.42 | 2.74 | 3.09 | 3.57 | 4.45 | 4.79 | 5.07 | | | |
| **La** | n.d. | n.d. | n.d. | n.d. | n.d. | n.d. | 0.03 | n.d. | n.d. | n.d. | n.d. | n.d. | n.d. | n.d. | 0.03 | n.d. | n.d. |
| **Ce** | n.d. | n.d. | 0.03 | n.d. | n.d. | n.d. | 0.08 | 0.05 | 0.11 | 0.14 | n.d. | n.d. | n.d. | n.d. | 0.10 | 0.03 | 0.27 |
| **Pr** | n.d. | n.d. | n.d. | n.d. | n.d. | 0.05 | n.d. | n.d. | n.d. | 0.21 | n.d. | n.d. | n.d. | n.d. | 0.05 | 0.03 | n.d. |
| **Nd** | n.d. | n.d. | n.d. | n.d. | n.d. | n.d. | 0.21 | n.d. | 0.35 | 0.41 | n.d. | n.d. | n.d. | n.d. | 0.12 | n.d. | n.d. |
| **Sm** | n.d. | n.d. | 0.24 | n.d. | 0.24 | 0.28 | 0.61 | 0.57 | 0.75 | 0.54 | n.d. | n.d. | n.d. | n.d. | 0.65 | 0.13 | n.d. |
| **Eu** | n.d. | 0.07 | n.d. | n.d. | n.d. | n.d. | n.d. | n.d. | n.d. | n.d. | n.d. | n.d. | n.d. | n.d. | 0.05 | 0.03 | n.d. |
| **Gd** | 1.84 | 0.58 | 1.90 | 2.19 | 2.45 | 2.00 | 3.40 | 3.38 | 4.01 | 2.60 | 1.00 | 0.45 | 0.39 | 2.48 | 3.68 | 1.34 | n.d. |
| **Tb** | 1.19 | 0.45 | 1.53 | 1.79 | 1.84 | 1.71 | 2.37 | 2.54 | 2.89 | 2.02 | 1.06 | 0.39 | 0.29 | 2.04 | 2.87 | 0.98 | 1.15 |
| **Dy** | 20.78 | 3.51 | 19.30 | 20.61 | 21.01 | 20.84 | 30.22 | 28.50 | 34.02 | 25.31 | 13.68 | 6.13 | 3.12 | 37.60 | 33.67 | 14.59 | 13.68 |
| **Ho** | 7.13 | 0.64 | 4.42 | 4.85 | 4.86 | 5.02 | 7.57 | 6.78 | 8.87 | 7.00 | 3.99 | 1.41 | 0.90 | 16.38 | 8.42 | 4.08 | 3.11 |
| **Er** | 31.15 | 2.09 | 18.33 | 18.33 | 20.81 | 21.21 | 32.06 | 31.13 | 38.45 | 32.01 | 18.09 | 5.79 | 4.93 | 80.40 | 37.37 | 16.42 | 13.84 |
| **Tm** | 5.68 | 0.61 | 4.62 | 4.71 | 5.31 | 5.71 | 8.70 | 8.55 | 10.24 | 8.85 | 4.84 | 1.65 | 1.51 | 15.05 | 9.61 | 3.25 | 3.37 |
| **Yb** | 40.12 | 6.79 | 47.51 | 47.13 | 56.20 | 60.44 | 91.42 | 93.94 | 109.06 | 97.28 | 52.65 | 18.89 | 18.28 | 112.88 | 105.24 | 26.94 | 40.83 |
| **Lu** | 6.50 | 1.17 | 7.26 | 6.98 | 8.93 | 9.78 | 15.50 | 15.72 | 18.08 | 16.72 | 8.65 | 2.96 | 3.56 | 21.78 | 17.39 | 3.65 | 5.95 |
| **Na2O** | 0.01 | 0.07 | 0.08 | 0.05 | 0.06 | 0.06 | 0.08 | 0.06 | 0.07 | 0.07 | 0.05 | 0.02 | 0.03 | 0.03 | 0.11 | 0.08 | 0.04 |
| **SiO2** | 37.00 | 37.00 | 37.00 | 37.00 | 37.00 | 37.00 | 37.00 | 37.00 | 37.00 | 37.00 | 37.00 | 37.00 | 37.00 | 37.00 | 37.00 | 37.00 | 37.00 |
| **TiO2** | n.d. | 0.00 | 0.04 | 0.03 | 0.06 | 0.05 | 0.10 | 0.09 | 0.11 | 0.11 | 0.02 | 0.00 | 0.00 | 0.00 | 0.11 | 0.01 | 0.09 |
| **V** | 5.32 | n.d. | n.d. | n.d. | n.d. | n.d. | n.d. | n.d. | n.d. | n.d. | n.d. | n.d. | n.d. | 13.18 | n.d. | 2.75 | n.d. |
| **Cr** | n.d. | 18.97 | 19.15 | 20.44 | 20.30 | 20.67 | 22.80 | 20.92 | 22.49 | 23.46 | 15.68 | 27.37 | 18.41 | 21.09 | 17.28 | 16.87 | n.d. |
| **Rb** | n.d. | n.d. | n.d. | n.d. | n.d. | n.d. | n.d. | n.d. | n.d. | n.d. | n.d. | n.d. | n.d. | n.d. | 0.24 | 0.16 | n.d. |
| **Sr** | n.d. | n.d. | n.d. | 0.80 | n.d. | n.d. | n.d. | n.d. | 0.23 | n.d. | n.d. | n.d. | n.d. | n.d. | 0.10 | 0.26 | n.d. |
| **Y** | 205 | 25 | 136 | 144 | 150 | 150 | 221 | 210 | 248 | 189 | 109 | 47 | 30 | 390 | 246 | 126 | 101 |
| **Zr** | 2.02 | 1.10 | 6.62 | 7.59 | 9.62 | 9.66 | 13.98 | 13.86 | 16.60 | 12.79 | 7.90 | 1.22 | 1.83 | 4.02 | 14.56 | 1.82 | 4.98 |
| **Ba** | n.d. | n.d. | 0.29 | n.d. | n.d. | n.d. | n.d. | n.d. | n.d. | n.d. | n.d. | n.d. | n.d. | n.d. | 0.23 | 0.35 | n.d. |
| **U** | n.d. | n.d. | 0.30 | 0.09 | 0.17 | 0.19 | 3.94 | 1.89 | 5.34 | 8.24 | 0.19 | n.d. | n.d. | n.d. | 4.04 | 0.05 | n.d. |
| **Comments** | T1 | T2 | T3 | T4 | T5 | T6 | T7 | T8 | T9 | T10 | T11 | T12 | T13 | T14 | near cen rim | | ru |

**G31(1)a cont.**

| Analysis | ju24b13 | ju24b14 | ju24b15 | ju24a06 | ju24a08 | ju24a13 |
|---|---|---|---|---|---|---|
| Distance (mm) | | | | | | |
| La | n.d. | n.d. | n.d. | n.d. | n.d. | n.d. |
| Ce | n.d. | n.d. | 0.23 | n.d. | n.d. | n.d. |
| Pr | n.d. | n.d. | n.d. | n.d. | n.d. | n.d. |
| Nd | n.d. | n.d. | n.d. | n.d. | n.d. | n.d. |
| Sm | n.d. | n.d. | n.d. | n.d. | n.d. | 0.32 |
| Eu | n.d. | n.d. | n.d. | n.d. | n.d. | n.d. |
| Gd | n.d. | n.d. | n.d. | 1.48 | 0.98 | 2.21 |
| Tb | 0.83 | 0.68 | n.d. | 1.35 | 1.02 | 1.90 |
| Dy | 11.39 | 9.82 | n.d. | 19.19 | 14.36 | 22.95 |
| Ho | 3.60 | 2.61 | n.d. | 5.54 | 3.66 | 5.64 |
| Er | 13.86 | 10.93 | n.d. | 19.48 | 14.25 | 24.40 |
| Tm | 3.68 | 2.89 | n.d. | 3.39 | 3.55 | 6.21 |
| Yb | 41.07 | 22.88 | 0.78 | 22.89 | 33.92 | 64.99 |
| Lu | 5.86 | 3.53 | n.d. | 2.84 | 5.18 | 10.33 |
| Na2O | 0.04 | 0.02 | 2.07 | 0.02 | 0.06 | 0.16 |
| SiO2 | 37.00 | 37.00 | 37.00 | 37.00 | 37.00 | 37.00 |
| TiO2 | 0.05 | 0.01 | 0.39 | 0.00 | 0.04 | 0.09 |
| V | n.d. | n.d. | 5.76 | 3.17 | n.d. | n.d. |
| Cr | n.d. | n.d. | n.d. | 20.48 | 16.11 | 18.03 |
| Rb | n.d. | n.d. | n.d. | n.d. | n.d. | n.d. |
| Sr | n.d. | n.d. | n.d. | n.d. | n.d. | 0.12 |
| Y | 99 | 86 | 1 | 160 | 109 | 166 |
| Zr | 4.58 | 1.21 | <0.57 | 2.79 | 6.25 | 9.03 |
| Ba | n.d. | n.d. | n.d. | n.d. | n.d. | 0.41 |
| U | n.d. | n.d. | n.d. | n.d. | n.d. | 0.43 |
| Comments | ru | rim | tour | T1.1 | T2 ru | T6b |

| | G31(1)b | | | | | | | | | | | | | | | |
|---|---|---|---|---|---|---|---|---|---|---|---|---|---|---|---|---|
| **Analysis** | al08f03 | al08f04 | al08f05 | al08f06 | al08f07 | al08f08 | al08f09 | al08f10 | al08f11 | al08f12 | al08f13 | al08f14 | al08f15 | al08f16 | al08f17 | al08f18 |
| **Distance (mm)** | 0.21 | 0.63 | 0.93 | 1.25 | 1.59 | 1.98 | 2.28 | 2.66 | 3.22 | 3.48 | 4.62 | 5.13 | | | | |
| **La** | n.d. | n.d. | n.d. | n.d. | n.d. | n.d. | n.d. | n.d. | n.d. | 0.01 | n.d. | n.d. | n.d. | 0.02 | 0.01 | 0.01 |
| **Ce** | n.d. | 0.02 | n.d. | n.d. | 0.01 | n.d. | n.d. | 0.02 | 0.03 | 0.03 | n.d. | n.d. | n.d. | 0.18 | 0.04 | 0.02 |
| **Pr** | n.d. | 0.00 | n.d. | n.d. | n.d. | n.d. | 0.00 | 0.01 | 0.01 | 0.02 | n.d. | n.d. | 0.00 | 0.06 | 0.01 | 0.01 |
| **Nd** | 0.02 | 0.03 | 0.02 | n.d. | n.d. | 0.06 | 0.05 | 0.08 | 0.08 | 0.05 | n.d. | 0.03 | 0.09 | 0.45 | 0.08 | 0.06 |
| **Sm** | 0.12 | 0.13 | 0.16 | 0.40 | 0.33 | 0.35 | 0.52 | 0.69 | 0.16 | 0.10 | 0.05 | 0.31 | 0.56 | 0.92 | 0.23 | 0.30 |
| **Eu** | n.d. | n.d. | 0.01 | n.d. | n.d. | n.d. | n.d. | n.d. | 0.01 | 0.01 | 0.01 | 0.04 | 0.00 | 0.02 | 0.01 | 0.01 |
| **Gd** | n.d. | n.d. | n.d. | n.d. | n.d. | n.d. | n.d. | n.d. | n.d. | n.d. | n.d. | n.d. | n.d. | n.d. | n.d. | n.d. |
| **Tb** | 0.76 | 1.67 | 1.77 | 2.25 | 2.22 | 1.93 | 2.20 | 2.83 | 1.13 | 1.27 | 0.42 | 2.58 | 2.31 | 4.06 | 1.30 | 1.88 |
| **Dy** | 10.21 | 20.88 | 22.45 | 26.78 | 26.17 | 23.48 | 27.54 | 33.53 | 14.65 | 17.97 | 4.87 | 43.99 | 28.02 | 47.51 | 16.76 | 23.28 |
| **Ho** | 2.75 | 5.03 | 5.48 | 6.17 | 6.04 | 5.86 | 7.14 | 8.47 | 4.10 | 4.81 | 1.13 | 18.63 | 7.24 | 11.30 | 4.47 | 5.53 |
| **Er** | 12.77 | 19.64 | 22.82 | 25.52 | 24.95 | 27.29 | 32.80 | 37.42 | 19.03 | 21.56 | 5.38 | 92.19 | 33.09 | 47.99 | 20.29 | 23.68 |
| **Tm** | 3.19 | 5.04 | 6.06 | 6.76 | 6.46 | 7.52 | 9.25 | 10.19 | 5.33 | 5.85 | 1.71 | 17.87 | 9.65 | 12.41 | 5.74 | 6.42 |
| **Yb** | 31.15 | 50.52 | 64.65 | 72.84 | 68.64 | 85.75 | 105.51 | 110.66 | 60.83 | 64.73 | 21.34 | 135.38 | 107.87 | 133.93 | 64.21 | 69.05 |
| **Lu** | 4.80 | 7.62 | 9.74 | 10.95 | 10.52 | 13.77 | 17.10 | 17.71 | 9.78 | 9.85 | 3.82 | 24.66 | 17.63 | 20.89 | 10.20 | 11.22 |
| **Na2O** | 0.01 | 0.04 | 0.04 | 0.04 | 0.04 | 0.04 | 0.04 | 0.04 | 0.04 | 0.04 | 0.02 | 0.01 | 0.04 | 0.04 | 0.04 | 0.04 |
| **SiO2** | 37.10 | 37.10 | 37.10 | 37.10 | 37.10 | 37.10 | 37.10 | 37.10 | 37.10 | 37.10 | 37.10 | 37.10 | 37.10 | 37.10 | 37.10 | 37.10 |
| **TiO2** | | | | | | | | | | | | | | | | |
| **V** | | | | | | | | | | | | | | | | |
| **Cr** | | | | | | | | | | | | | | | | |
| **Rb** | | | | | | | | | | | | | | | | |
| **Sr** | | | | | | | | | | | | | | | | |
| **Y** | 87 | 153 | 165 | 186 | 183 | 171 | 202 | 239 | 101 | 140 | 39 | 432 | 210 | 327 | 128 | 168 |
| **Zr** | | | | | | | | | | | | | | | | |
| **Ba** | | | | | | | | | | | | | | | | |
| **U** | 0.01 | 0.17 | 0.05 | 0.16 | 0.22 | 0.22 | 0.48 | 2.65 | 0.92 | 0.58 | 0.01 | 0.00 | 0.77 | 13.78 | 1.13 | 0.81 |
| **Comments** | 1 | 2 | 3 | 4 | 5 | 6 | 7 | 8 | 9 | 10 | 11 | 12 | 13 | 14 | 15 | 16 |

| | G9a | | | | | | | | | | | |
|---|---|---|---|---|---|---|---|---|---|---|---|---|
| Analysis | ju23c05 | ju23c06 | ju23c07 | ju23c08 | ju23c09 | ju23c10 | ju23c11 | ju23c12 | ju23c13 | ju23c14 | ju23c15 | ju23c16 |
| Distance (mm) | 4.02 | 3.84 | 3.48 | 3.19 | 2.91 | 2.70 | 2.23 | 1.87 | 1.30 | 0.78 | 0.39 | 0.08 |
| La | n.d. | n.d. | n.d. | n.d. | 0.56 | n.d. | 1.98 | n.d. | n.d. | n.d. | n.d. | n.d. |
| Ce | 1.51 | 0.09 | n.d. | n.d. | 1.24 | n.d. | 4.02 | n.d. | n.d. | n.d. | n.d. | n.d. |
| Pr | n.d. | n.d. | n.d. | n.d. | 0.15 | n.d. | 0.43 | n.d. | n.d. | n.d. | n.d. | n.d. |
| Nd | n.d. | 0.16 | n.d. | n.d. | 0.57 | n.d. | 1.93 | n.d. | n.d. | n.d. | n.d. | 0.18 |
| Sm | n.d. | 0.79 | 0.51 | 0.97 | 0.61 | 0.76 | 1.24 | 0.64 | 0.68 | n.d. | 0.77 | 1.37 |
| Eu | 0.22 | 0.49 | 0.34 | 0.55 | 0.48 | 0.52 | 0.34 | 0.26 | 0.47 | 0.29 | 0.58 | 0.81 |
| Gd | 9.26 | 13.03 | 7.03 | 8.66 | 10.80 | 9.05 | 8.13 | 7.07 | 11.40 | 7.43 | 12.42 | 18.65 |
| Tb | 4.49 | 5.95 | 3.72 | 3.62 | 5.75 | 3.97 | 5.79 | 5.67 | 6.58 | 3.14 | 5.42 | 5.86 |
| Dy | 45.44 | 43.24 | 31.01 | 33.08 | 66.44 | 41.13 | 105.74 | 102.70 | 79.38 | 30.00 | 40.28 | 39.99 |
| Ho | 10.49 | 7.29 | 6.55 | 7.08 | 16.37 | 10.74 | 50.34 | 47.73 | 21.70 | 6.65 | 7.45 | 7.66 |
| Er | 32.91 | 18.69 | 18.84 | 19.75 | 48.39 | 36.57 | 275.67 | 256.30 | 70.31 | 18.49 | 19.28 | 21.08 |
| Tm | 4.49 | 2.26 | 2.83 | 2.96 | 7.07 | 6.11 | 61.42 | 57.72 | 10.88 | 2.84 | 2.64 | 2.80 |
| Yb | 28.77 | 11.70 | 17.44 | 18.94 | 41.86 | 41.78 | 510.19 | 488.27 | 73.43 | 16.57 | 15.44 | 15.68 |
| Lu | 4.20 | 1.84 | 3.09 | 3.23 | 6.80 | 6.39 | 85.63 | 83.59 | 11.73 | 2.68 | 2.60 | 2.08 |
| Na2O | 0.01 | 0.06 | 0.08 | 0.03 | 0.03 | 0.02 | 0.04 | 0.05 | 0.04 | 0.03 | 0.01 | 0.03 |
| SiO2 | 36.80 | 36.80 | 36.80 | 36.80 | 36.80 | 36.80 | 36.80 | 36.80 | 36.80 | 36.80 | 36.80 | 36.80 |
| TiO2 | 0.04 | 0.05 | 0.07 | 0.08 | 0.08 | 0.11 | 0.10 | 0.11 | 0.10 | 0.10 | 0.05 | 0.01 |
| V | 22.55 | 31.86 | 34.96 | 38.54 | 41.85 | 53.01 | 39.95 | 41.52 | 45.54 | 37.88 | 26.18 | 13.11 |
| Cr | 50.96 | 51.19 | 44.11 | 40.77 | 46.60 | 47.47 | 54.72 | 44.39 | 40.41 | 37.06 | 44.03 | 35.46 |
| Rb | n.d. | 0.35 | n.d. | n.d. | n.d. | n.d. | n.d. | 0.45 | n.d. | n.d. | n.d. | n.d. |
| Sr | n.d. | n.d. | n.d. | n.d. | n.d. | n.d. | 0.44 | 0.26 | 0.80 | n.d. | n.d. | n.d. |
| Y | 284 | 202 | 190 | 208 | 525 | 391 | 1918 | 1649 | 666 | 205 | 204 | 214 |
| Zr | 9.65 | 12.51 | 11.72 | 13.21 | 82.93 | 114.74 | 95.55 | 137.09 | 67.96 | 11.28 | 85.40 | 5.16 |
| Ba | n.d. | 0.51 | n.d. | n.d. | n.d. | n.d. | n.d. | n.d. | n.d. | n.d. | n.d. | n.d. |
| U | n.d. | 0.32 | 0.09 | 0.10 | 0.45 | 0.90 | 0.75 | 0.99 | 0.46 | 0.07 | 0.35 | n.d. |
| Comments | T1 | T2 | T3 | T4 | T9 T5 | T6 | T7 | T8 | T9 | T10 | T11 | T12 |

| | G9b | | | | | | | | | | | | | |
|---|---|---|---|---|---|---|---|---|---|---|---|---|---|---|
| **Analysis** | al03b03 | al03b04 | al03b05 | al03b06 | al03b07 | al03b08 | al03b09 | al03b10 | al03b11 | al03b12 | al03b13 | al03b14 | al03b15 | al03b16 |
| **Distance (mm)** | 3.91 | 3.66 | 3.31 | 2.99 | 2.73 | 2.29 | 1.99 | 1.75 | 1.54 | 1.16 | 0.92 | 0.64 | 0.22 | 0.08 |
| **La** | n.d. | 0.01 | n.d. | n.d. | n.d. | n.d. | 0.01 | 403.42 | 0.03 | 0.02 | n.d. | n.d. | n.d. | 0.03 |
| **Ce** | 0.00 | 0.04 | 0.00 | 0.01 | 0.01 | 0.01 | 0.01 | 880.14 | 0.51 | 0.03 | 0.01 | 0.01 | 0.02 | 0.07 |
| **Pr** | n.d. | n.d. | n.d. | n.d. | 0.01 | 0.00 | n.d. | 93.47 | 0.01 | n.d. | n.d. | 0.00 | 0.00 | 0.01 |
| **Nd** | 0.05 | 0.13 | 0.08 | 0.12 | 0.13 | 0.06 | 0.10 | 368.51 | 0.11 | 0.09 | 0.10 | 0.08 | 0.07 | 0.16 |
| **Sm** | 0.60 | 0.62 | 0.83 | 1.05 | 1.20 | 0.54 | 0.52 | 82.53 | 0.97 | 0.72 | 0.81 | 0.53 | 1.28 | 1.76 |
| **Eu** | 0.30 | 0.21 | 0.47 | 0.71 | 0.72 | 0.41 | 0.30 | 11.49 | 0.63 | 0.42 | 0.45 | 0.29 | 0.83 | 1.01 |
| **Gd** | 10.38 | 7.65 | 8.57 | 12.36 | 10.98 | 8.94 | 7.44 | 85.66 | 10.52 | 11.03 | 10.49 | 7.61 | 20.46 | 21.05 |
| **Tb** | 5.83 | 4.21 | 3.87 | 5.83 | 4.64 | 6.55 | 6.28 | 17.11 | 5.24 | 6.27 | 5.38 | 4.23 | 9.71 | 6.74 |
| **Dy** | 55.01 | 36.73 | 33.98 | 50.92 | 41.53 | 118.05 | 128.94 | 139.81 | 53.90 | 61.21 | 47.83 | 40.33 | 75.82 | 45.08 |
| **Ho** | 12.22 | 7.35 | 7.24 | 10.49 | 9.81 | 51.66 | 67.92 | 35.80 | 13.99 | 14.20 | 10.56 | 9.23 | 15.26 | 8.87 |
| **Er** | 35.18 | 20.92 | 21.79 | 29.09 | 30.21 | 280.86 | 433.32 | 132.88 | 48.58 | 43.27 | 31.16 | 29.37 | 43.51 | 24.91 |
| **Tm** | 4.78 | 3.01 | 3.09 | 3.93 | 4.59 | 62.86 | 110.75 | 22.86 | 8.01 | 6.20 | 4.21 | 4.48 | 5.77 | 3.38 |
| **Yb** | 29.26 | 19.99 | 20.20 | 24.20 | 31.65 | 533.45 | 1010.65 | 166.26 | 56.38 | 40.90 | 26.05 | 32.10 | 33.11 | 20.65 |
| **Lu** | 4.27 | 3.37 | 3.19 | 3.53 | 4.74 | 85.06 | 169.80 | 25.34 | 8.63 | 6.21 | 3.90 | 5.44 | 4.81 | 2.96 |
| **Na2O** | 0.01 | 0.01 | 0.01 | 0.02 | 0.01 | 0.04 | 0.05 | 0.03 | 0.02 | 0.01 | 0.01 | 0.01 | 0.01 | 0.01 |
| **SiO2** | 37.20 | 37.20 | 37.20 | 37.20 | 37.20 | 37.20 | 37.20 | 37.20 | 37.20 | 37.20 | 37.20 | 37.20 | 37.20 | 37.20 |
| **TiO2** | | | | | | | | | | | | | | |
| **V** | | | | | | | | | | | | | | |
| **Cr** | | | | | | | | | | | | | | |
| **Rb** | | | | | | | | | | | | | | |
| **Sr** | | | | | | | | | | | | | | |
| **Y** | 311 | 205 | 217 | 348 | 322 | 1895 | 2427 | 1278 | 473 | 437 | 323 | 256 | 385 | 231 |
| **Zr** | | | | | | | | | | | | | | |
| **Ba** | | | | | | | | | | | | | | |
| **U** | 0.16 | 0.21 | 0.18 | 0.10 | 0.61 | 0.70 | 0.49 | 23.44 | 0.21 | 1.17 | 0.12 | 0.13 | 0.33 | 0.51 |
| **Comments** | 1 | 2 | 3 | 4 | 5 | 6 | 7 | 8 | 9 | 10 | 11 | 12 | 13 | 14 |

| | G96a | | | | | | | | | | | | | | | | |
|---|---|---|---|---|---|---|---|---|---|---|---|---|---|---|---|---|---|
| **Analysis** | ju23a05 | ju23a09 | ju23a10 | ju23a11 | ju23a12 | ju23a13 | ju23a14 | ju23a15 | ju23a16 | ju23b05 | ju23b06 | ju23b07 | ju23b08 | ju23b09 | ju23b10 | ju23b11 | ju23b12 |
| **Distance (mm)** | 0.99 | 1.08 | 1.21 | 1.39 | 1.52 | 1.75 | 2.02 | 2.55 | 3.00 | 3.23 | 4.03 | 4.21 | 4.53 | 5.06 | 5.56 | 5.78 | 6.23 |
| **La** | | 0.11 | 0.04 | | | | | | 0.69 | | | | | | | | |
| **Ce** | | 0.43 | 0.12 | 0.07 | 0.10 | 0.06 | | | 2.50 | 0.07 | 0.03 | | 0.03 | 0.25 | | | 0.02 |
| **Pr** | | 0.03 | | | | | | | 0.14 | | | | | | | | 0.04 |
| **Nd** | | 0.14 | 0.17 | | | | | | 0.72 | | | | | | | | |
| **Sm** | | 0.42 | 0.38 | 0.31 | 0.43 | 0.30 | 0.46 | 0.43 | 0.43 | 0.37 | | 0.53 | 0.37 | 0.32 | 0.44 | 0.46 | 0.46 |
| **Eu** | 0.20 | 0.25 | 0.27 | 0.27 | 0.26 | 0.25 | 0.32 | 0.29 | 0.29 | 0.46 | 0.26 | 0.30 | 0.27 | 0.29 | 0.29 | 0.31 | 0.27 |
| **Gd** | 4.28 | 3.83 | 4.37 | 4.22 | 4.24 | 4.79 | 4.46 | 4.79 | 4.99 | 4.76 | 4.57 | 5.38 | 4.94 | 5.02 | 5.41 | 4.65 | 4.97 |
| **Tb** | 3.16 | 2.95 | 3.31 | 3.35 | 3.19 | 3.24 | 3.90 | 3.85 | 4.06 | 4.18 | 3.60 | 4.25 | 4.12 | 3.88 | 4.13 | 3.28 | 3.79 |
| **Dy** | 59.76 | 55.30 | 59.64 | 61.55 | 60.80 | 57.11 | 75.76 | 75.66 | 84.89 | 85.80 | 68.71 | 86.11 | 80.99 | 74.34 | 79.88 | 57.68 | 68.10 |
| **Ho** | 24.41 | 23.28 | 25.25 | 26.36 | 27.81 | 23.76 | 34.69 | 35.55 | 41.90 | 45.58 | 33.82 | 42.78 | 38.62 | 35.91 | 36.65 | 23.58 | 28.85 |
| **Er** | 114.22 | 115.11 | 123.50 | 126.85 | 139.28 | 115.67 | 183.74 | 186.94 | 243.23 | 270.49 | 184.34 | 233.97 | 200.53 | 186.94 | 183.93 | 109.35 | 137.58 |
| **Tm** | 23.35 | 23.01 | 25.18 | 25.85 | 29.23 | 23.44 | 38.34 | 39.47 | 53.90 | 61.74 | 39.63 | 49.48 | 42.60 | 39.27 | 38.43 | 21.01 | 27.69 |
| **Yb** | 181.70 | 198.84 | 212.53 | 210.60 | 249.94 | 194.60 | 331.96 | 325.02 | 457.15 | 550.09 | 325.29 | 417.29 | 360.77 | 337.39 | 324.36 | 168.92 | 228.08 |
| **Lu** | 32.95 | 34.30 | 37.26 | 37.25 | 44.25 | 34.06 | 60.23 | 57.26 | 80.66 | 97.75 | 56.19 | 73.14 | 63.17 | 59.55 | 58.12 | 28.78 | 40.94 |
| **Na2O** | 0.02 | 0.08 | 0.12 | 0.12 | 0.14 | 0.04 | 0.09 | 0.03 | 0.08 | 0.09 | 0.03 | 0.06 | 0.08 | 0.06 | 0.04 | 0.04 | 0.05 |
| **SiO2** | 37.60 | 37.60 | 37.60 | 37.60 | 37.60 | 37.60 | 37.60 | 37.60 | 37.60 | 37.60 | 37.60 | 37.60 | 37.60 | 37.60 | 37.60 | 37.60 | 37.60 |
| **TiO2** | 0.09 | 0.09 | 0.09 | 0.09 | 0.10 | 0.08 | 0.11 | 0.11 | 0.13 | 0.13 | 0.11 | 0.14 | 0.13 | 0.11 | 0.12 | 0.08 | 0.12 |
| **V** | 100.47 | 115.67 | 111.77 | 121.60 | 119.72 | 109.38 | 115.85 | 115.63 | 121.65 | 121.65 | 110.84 | 120.47 | 121.60 | 113.35 | 113.58 | 106.90 | 114.15 |
| **Cr** | 128.37 | 131.23 | 128.70 | 131.65 | 124.60 | 126.22 | 125.10 | 123.37 | 123.76 | 124.63 | 124.27 | 128.88 | 124.39 | 117.48 | 125.80 | 135.40 | 128.73 |
| **Rb** | | 0.26 | 0.26 | 0.28 | 0.43 | | 0.36 | 0.39 | 0.44 | 0.43 | 0.30 | 0.83 | 0.33 | 0.30 | | | 0.25 |
| **Sr** | | 0.17 | 0.47 | 0.15 | 0.19 | 0.21 | 0.26 | 0.21 | 0.30 | 0.37 | 0.16 | 0.29 | 0.24 | 0.21 | 0.29 | 0.13 | 0.16 |
| **Y** | 726 | 698 | 767 | 791 | 818 | 720 | 1054 | 1100 | 1306 | 1429 | 1020 | 1306 | 1134 | 1037 | 1046 | 706 | 848 |
| **Zr** | 1.89 | 1.87 | 2.19 | 1.72 | 2.09 | 1.55 | 2.42 | 2.38 | 2.47 | 2.53 | 1.40 | 1.98 | 2.38 | 2.15 | 2.38 | 1.15 | 2.36 |
| **Ba** | | | | | | | | | | | | | | | | | |
| **U** | | 0.06 | | | | 0.35 | 0.02 | | 0.17 | 0.03 | | | 0.04 | | 0.40 | | |
| **Comments** | T01 | T2 | T03 | T04 | T05 | T06 | T07 | T08 | T09 | T10 | T11 | T12 | T13 | T14 | T15 | T16 | T17 |

| G96a cont. | | | | | |
|---|---|---|---|---|---|
| Analysis | ju23b13 | ju23b14 | ju23a06 | ju23a07 | ju23a08 |
| Distance (mm) | 6.45 | 6.72 | | | |
| La | | | | 23.63 | |
| Ce | | | | 49.25 | |
| Pr | | | | 5.81 | |
| Nd | | | | 21.27 | |
| Sm | 0.39 | 0.44 | | 4.73 | |
| Eu | 0.30 | 0.28 | 0.26 | 1.07 | 0.22 |
| Gd | 4.90 | 4.34 | 4.67 | 7.91 | 4.16 |
| Tb | 3.74 | 2.90 | 3.55 | 4.02 | 3.17 |
| Dy | 64.56 | 46.67 | 68.53 | 66.75 | 57.82 |
| Ho | 26.38 | 16.89 | 29.39 | 27.11 | 24.16 |
| Er | 118.09 | 70.57 | 143.40 | 125.52 | 116.91 |
| Tm | 23.50 | 12.81 | 28.84 | 24.72 | 22.46 |
| Yb | 187.98 | 100.18 | 243.53 | 205.41 | 187.98 |
| Lu | 33.97 | 17.19 | 43.26 | 36.54 | 33.83 |
| Na2O | 0.03 | 0.05 | 0.03 | 0.07 | 0.03 |
| SiO2 | 37.60 | 37.60 | 37.60 | 37.60 | 37.60 |
| TiO2 | 0.09 | 0.07 | 0.11 | 0.13 | 0.11 |
| V | 109.05 | 114.61 | 110.79 | 126.69 | 103.05 |
| Cr | 125.77 | 139.19 | 127.63 | 142.67 | 121.39 |
| Rb | | | | 0.34 | |
| Sr | 0.10 | | | 1.04 | |
| Y | 757 | 508 | 877 | 799 | 698 |
| Zr | 2.09 | 1.38 | 2.55 | 1.84 | 1.77 |
| Ba | | | | | |
| U | | 0.04 | | 2.43 | |
| Comments | T18 | T19 | T02Q | T03Q | T3BQ |

| G96b | | | | | | | | | | | | | | | | |
|---|---|---|---|---|---|---|---|---|---|---|---|---|---|---|---|---|
| Analysis | al03a03 | al03a04 | al03a05 | al03a06 | al03a07 | al03a08 | al03a09 | al03a10 | al03a11 | al03a12 | al03a13 | al03a14 | al03a15 | al03a16 | al03a17 | al03a18 |
| Distance (mm) | 0.00 | 0.86 | 1.54 | 1.91 | 2.65 | 3.77 | 4.20 | 4.69 | 5.23 | 5.56 | 6.28 | 6.63 | 7.32 | 7.79 | 8.03 | |
| La | n.d. | n.d. | n.d. | n.d. | n.d. | n.d. | n.d. | n.d. | n.d. | 0.00 | n.d. | n.d. | n.d. | 0.00 | n.d. | 0.77 |
| Ce | n.d. | n.d. | n.d. | 0.00 | n.d. | n.d. | n.d. | n.d. | n.d. | n.d. | 0.00 | n.d. | 0.00 | n.d. | 0.00 | 2.24 |
| Pr | n.d. | n.d. | n.d. | n.d. | n.d. | n.d. | 0.00 | n.d. | n.d. | n.d. | n.d. | n.d. | 0.00 | n.d. | n.d. | 0.21 |
| Nd | 0.06 | 0.08 | 0.06 | 0.03 | 0.04 | n.d. | 0.07 | 0.03 | 0.05 | 0.05 | 0.03 | 0.04 | 0.04 | 0.04 | 0.04 | 0.69 |
| Sm | 0.46 | 0.48 | 0.43 | 0.41 | 0.33 | 0.26 | 0.45 | 0.37 | 0.37 | 0.27 | 0.30 | 0.31 | 0.37 | 0.33 | 0.30 | 0.43 |
| Eu | 0.29 | 0.33 | 0.37 | 0.31 | 0.29 | 0.22 | 0.31 | 0.29 | 0.25 | 0.27 | 0.25 | 0.26 | 0.30 | 0.28 | 0.26 | 0.31 |
| Gd | 5.72 | 5.63 | 5.74 | 5.19 | 5.09 | 3.93 | 5.23 | 4.15 | 4.28 | 3.83 | 3.97 | 4.27 | 4.75 | 4.33 | 4.56 | 4.72 |
| Tb | 4.58 | 4.66 | 4.94 | 4.71 | 4.73 | 3.45 | 4.41 | 3.58 | 3.43 | 3.35 | 3.18 | 3.32 | 3.71 | 3.86 | 4.07 | 4.11 |
| Dy | 90.58 | 92.34 | 98.42 | 103.92 | 102.96 | 80.43 | 97.57 | 78.28 | 75.59 | 72.52 | 71.82 | 72.99 | 82.16 | 87.17 | 91.45 | 89.83 |
| Ho | 42.25 | 42.41 | 47.63 | 55.73 | 60.60 | 50.26 | 62.21 | 48.48 | 47.24 | 46.21 | 44.52 | 45.54 | 50.32 | 54.55 | 53.41 | 49.94 |
| Er | 216.82 | 224.20 | 262.46 | 352.66 | 413.67 | 386.17 | 491.68 | 390.61 | 377.09 | 376.02 | 356.88 | 356.66 | 389.88 | 423.19 | 366.87 | 317.17 |
| Tm | 47.25 | 49.18 | 56.43 | 86.14 | 108.36 | 117.45 | 159.46 | 127.03 | 125.97 | 125.14 | 121.26 | 117.02 | 128.04 | 134.22 | 100.13 | 80.37 |
| Yb | 410.71 | 419.41 | 481.65 | 766.83 | 1071.61 | 1313.46 | 1979.00 | 1583.10 | 1604.94 | 1611.54 | 1543.72 | 1440.99 | 1583.72 | 1604.83 | 1001.19 | 757.23 |
| Lu | 71.79 | 74.17 | 81.60 | 140.06 | 202.56 | 303.97 | 472.27 | 396.37 | 407.46 | 414.66 | 394.92 | 349.83 | 370.72 | 358.75 | 189.49 | 134.16 |
| Na2O | 0.04 | 0.03 | 0.04 | 0.05 | 0.05 | 0.05 | 0.06 | 0.05 | 0.05 | 0.05 | 0.05 | 0.06 | 0.05 | 0.06 | 0.05 | 0.05 |
| SiO2 | 37.80 | 37.80 | 37.80 | 37.80 | 37.80 | 37.80 | 37.80 | 37.80 | 37.80 | 37.80 | 37.80 | 37.80 | 37.80 | 37.80 | 37.80 | 37.80 |
| TiO2 | | | | | | | | | | | | | | | | |
| V | | | | | | | | | | | | | | | | |
| Cr | | | | | | | | | | | | | | | | |
| Rb | | | | | | | | | | | | | | | | |
| Sr | | | | | | | | | | | | | | | | |
| Y | 1248 | 1281 | 1476 | 1665 | 1795 | 1381 | 1885 | 1503 | 1437 | 1431 | 1371 | 1357 | 1564 | 1628 | 1542 | 1491 |
| Zr | | | | | | | | | | | | | | | | |
| Ba | | | | | | | | | | | | | | | | |
| U | 0.00 | 0.01 | 0.01 | 0.00 | 0.00 | 0.00 | 0.00 | 0.00 | 0.00 | 0.00 | 0.00 | 0.00 | 0.00 | 0.00 | 0.00 | 0.19 |
| Comments | 1 | 2 | 3 | 4 | 5 | 6 | 7 | 8 | 9 | 10 | 11 | 12 | 13 | 14 | 15 | |

| | 4B(1)a | | | | | | | | | | | |
|---|---|---|---|---|---|---|---|---|---|---|---|---|
| **Analysis** | ju25a05 | ju25a06 | ju25a07 | ju25a08 | ju25a09 | ju25a10 | ju25a11 | ju25a12 | ju25a13 | ju25a14 | ju25a15 | ju25a16 |
| **Distance (mm)** | | | | | | | | | | | | |
| **La** | 1.92 | 0.09 | n.d. | 0.07 | 0.14 | 0.02 | n.d. | 0.02 | n.d. | 0.03 | 0.02 | 0.02 |
| **Ce** | 0.69 | 0.97 | 0.07 | 0.02 | 0.02 | 0.12 | 0.04 | 0.12 | n.d. | 0.02 | 0.02 | 0.02 |
| **Pr** | 0.01 | 0.00 | 0.01 | 0.03 | 0.02 | 0.02 | 0.02 | 0.03 | 0.04 | 0.00 | 0.00 | 0.00 |
| **Nd** | 0.14 | 0.22 | 0.18 | 0.22 | 0.14 | 0.17 | 0.25 | 0.15 | 0.09 | 0.09 | 0.18 | 0.13 |
| **Sm** | 0.66 | 0.43 | 1.29 | 1.58 | 0.53 | 0.60 | 1.34 | 0.84 | 0.57 | 0.73 | 0.69 | 0.75 |
| **Eu** | 0.35 | 0.27 | 0.57 | 0.91 | 0.30 | 0.58 | 0.52 | 0.44 | 0.42 | 0.50 | 0.47 | 0.45 |
| **Gd** | 4.88 | 4.14 | 7.31 | 9.73 | 2.73 | 6.27 | 7.67 | 6.14 | 7.38 | 8.25 | 6.69 | 8.99 |
| **Tb** | 3.22 | 2.80 | 2.94 | 3.72 | 1.22 | 4.02 | 3.69 | 5.73 | 4.46 | 5.17 | 3.86 | 5.82 |
| **Dy** | 52.60 | 52.60 | 29.49 | 33.40 | 20.26 | 63.33 | 41.95 | 40.79 | 56.58 | 75.54 | 59.74 | 86.18 |
| **Ho** | 17.92 | 22.63 | 7.67 | 6.54 | 10.14 | 20.31 | 13.93 | 14.59 | 12.72 | 20.94 | 17.18 | 25.19 |
| **Er** | 57.14 | 92.53 | 30.75 | 19.56 | 61.33 | 61.09 | 76.11 | 60.22 | 26.34 | 53.47 | 43.42 | 65.28 |
| **Tm** | 7.18 | 14.98 | 6.55 | 3.50 | 13.93 | 7.35 | 18.85 | 9.92 | 2.13 | 5.22 | 4.32 | 6.31 |
| **Yb** | 38.61 | 82.18 | 62.21 | 29.27 | 113.33 | 36.19 | 169.69 | 64.29 | 7.41 | 21.53 | 19.18 | 26.97 |
| **Lu** | 4.51 | 11.10 | 12.62 | 5.53 | 18.28 | 4.12 | 32.51 | 9.05 | 0.79 | 2.55 | 2.48 | 3.27 |
| **Na2O** | 0.02 | 0.03 | 0.01 | 0.01 | 0.01 | 0.01 | 0.01 | 0.01 | 0.01 | 0.02 | 0.02 | 0.04 |
| **SiO2** | 37.00 | 37.00 | 37.00 | 37.00 | 37.00 | 37.00 | 37.00 | 37.00 | 37.00 | 37.00 | 37.00 | 37.00 |
| **TiO2** | 0.03 | 0.09 | 0.05 | 0.14 | 0.06 | 0.03 | 0.05 | 0.03 | 0.02 | 0.04 | 0.03 | 0.06 |
| **V** | 62.41 | 60.81 | 69.17 | 109.98 | 58.15 | 64.06 | 79.31 | 60.48 | 42.09 | 55.19 | 56.95 | 57.83 |
| **Cr** | 64.56 | 41.68 | 43.13 | 127.02 | 31.36 | 34.36 | 38.07 | 38.79 | 27.86 | 51.14 | 92.60 | 34.10 |
| **Rb** | n.d. | 0.62 | n.d. | n.d. | 0.21 | 2.73 | 0.13 | n.d. | n.d. | n.d. | 0.10 | 0.13 |
| **Sr** | 0.09 | 0.08 | 0.08 | 0.04 | 0.14 | 0.40 | 0.13 | 0.05 | n.d. | n.d. | 0.10 | n.d. |
| **Y** | 508 | 620 | 244 | 216 | 298 | 571 | 390 | 408 | 344 | 519 | 433 | 618 |
| **Zr** | 2.01 | 4.01 | 1.18 | 2.10 | 1.24 | 2.79 | 1.33 | 1.50 | 2.70 | 2.85 | 2.20 | 3.60 |
| **Ba** | n.d. | 0.35 | n.d. | n.d. | 2.57 | n.d. | n.d. | n.d. | n.d. | n.d. | n.d. | n.d. |
| **U** | 0.28 | 0.01 | 0.01 | 0.04 | 0.08 | 0.02 | 0.02 | 0.04 | n.d. | 0.02 | 0.04 | 0.08 |
| **Comments** | | | | | | | | | | | | |

| | CZG-23 | | | | | | | | | | | | | | |
|---|---|---|---|---|---|---|---|---|---|---|---|---|---|---|---|
| **Distance (mm)** | 0.03 | 0.10 | 0.16 | 0.23 | 0.29 | 0.36 | 0.42 | 0.49 | 0.55 | 0.62 | 0.68 | 0.75 | 0.81 | 0.88 | 0.94 |
| **La** | n.d. | n.d. | n.d. | n.d. | n.d. | n.d. | n.d. | n.d. | n.d. | n.d. | n.d. | n.d. | n.d. | n.d. | n.d. |
| **Ce** | 0.04 | 0.21 | 0.21 | 0.20 | 0.23 | 0.19 | 0.24 | 0.18 | 0.37 | 0.23 | 0.17 | 0.12 | 0.39 | 0.09 | 0.07 |
| **Pr** | 0.06 | 0.18 | 0.27 | 0.25 | 0.35 | 0.34 | 0.21 | 0.29 | 0.28 | 0.27 | 0.20 | 0.21 | 0.28 | 0.15 | 0.08 |
| **Nd** | 1.70 | 3.58 | 5.59 | 6.19 | 7.67 | 7.33 | 6.47 | 6.52 | 6.87 | 6.63 | 6.20 | 5.53 | 4.98 | 2.55 | 2.07 |
| **Sm** | 6.69 | 7.27 | 9.66 | 9.60 | 10.72 | 11.12 | 8.20 | 9.01 | 9.84 | 9.47 | 9.85 | 9.32 | 7.94 | 6.76 | 6.06 |
| **Eu** | 0.78 | 1.86 | 2.27 | 2.56 | 2.76 | 2.82 | 2.57 | 2.65 | 2.76 | 2.66 | 2.64 | 2.50 | 2.28 | 1.85 | 1.46 |
| **Gd** | 15.43 | 15.49 | 17.52 | 19.36 | 19.67 | 19.26 | 15.25 | 16.28 | 17.12 | 16.76 | 16.41 | 16.30 | 15.44 | 14.46 | 13.30 |
| **Tb** | 2.93 | 3.62 | 4.21 | 4.56 | 4.56 | 4.36 | 3.52 | 3.68 | 4.07 | 3.96 | 3.88 | 3.78 | 3.76 | 3.31 | 2.82 |
| **Dy** | 17.03 | 21.01 | 29.88 | 32.22 | 30.89 | 27.00 | 23.45 | 25.85 | 26.39 | 27.23 | 26.21 | 26.32 | 25.54 | 24.52 | 19.01 |
| **Ho** | 2.72 | 4.55 | 6.45 | 6.69 | 5.76 | 5.38 | 4.65 | 4.69 | 4.99 | 5.12 | 5.10 | 5.23 | 5.07 | 5.09 | 3.39 |
| **Er** | 6.31 | 12.38 | 20.21 | 19.05 | 16.31 | 15.21 | 12.87 | 13.05 | 13.36 | 14.88 | 14.36 | 14.65 | 15.05 | 14.94 | 9.50 |
| **Tm** | 0.85 | 1.79 | 2.80 | 2.79 | 2.17 | 2.09 | 1.79 | 1.82 | 1.67 | 1.77 | 1.99 | 2.06 | 2.06 | 2.17 | 1.22 |
| **Yb** | 6.02 | 10.80 | 19.67 | 16.42 | 14.07 | 12.75 | 10.66 | 9.91 | 10.94 | 10.89 | 11.81 | 12.57 | 14.05 | 13.65 | 7.43 |
| **Lu** | 0.54 | 1.76 | 2.89 | 2.52 | 1.90 | 1.80 | 1.54 | 1.43 | 1.50 | 1.57 | 1.68 | 1.92 | 2.27 | 2.24 | 0.96 |

| Limit of Detection | | | |
|---|---|---|---|
| Pit size (μm) | | 80 | 10 |
| Laser frequency (Hz) | | 20 | 10 |
| La | ppm | 0.010 | 0.237 |
| Ce | ppm | 0.007 | 0.127 |
| Pr | ppm | 0.010 | 0.217 |
| Nd | ppm | 0.041 | 1.074 |
| Sm | ppm | 0.065 | 1.263 |
| Eu | ppm | 0.013 | 0.285 |
| Gd | ppm | 0.074 | 1.371 |
| Tb | ppm | 0.011 | 0.139 |
| Dy | ppm | 0.036 | 0.599 |
| Ho | ppm | 0.007 | 0.144 |
| Er | ppm | 0.020 | 0.556 |
| Tm | ppm | 0.016 | 0.272 |
| Yb | ppm | 0.037 | 0.717 |
| Lu | ppm | 0.007 | 0.194 |

| Limit of Detection | | | |
|---|---|---|---|
| Pit size (μm) | | 80 | 10 |
| Laser frequency (Hz) | | 20 | 10 |
| U | ppm | 0.005 | 0.196 |
| Ti | wt% | 0.000 | 0.005 |
| V | ppm | 0.121 | 2.359 |
| Cr | ppm | 2.899 | 59.515 |
| Rb | ppm | 0.076 | 1.700 |
| Sr | ppm | 0.025 | 0.556 |
| Y | ppm | 0.015 | 0.323 |
| Zr | ppm | 0.030 | 0.623 |
| Ba | ppm | 0.099 | 1.947 |

# Appendix H - OU Rb-Sr summary

In order to better constrain the post peak deformation and exhumation path in the Alaknanda and Dhuali valleys a number of Rb-Sr mineral analyses were undertaken at the Open University. Given problems with previous studies regarding the incomplete attainment of Rb-Sr isotopic equilibrium between different phases (eg. Inger 1998), the initial analytical philosophy was to try to obtain mineral separates which were, as far as it was possible to judge, close to isotopic equilibrium. In the case of sample 43/97 (MCTZ augen gneiss), therefore, the approach was to obtain very small separates of feldspars and micas that were adjacent to each other and in textural equilibrium. In addition, the extent of equilbirium between micas wrapping feldspar augen and different portions of the augen was assessed by Rb-Sr analysis of different fractions of the augen from core to rim. For all other samples a bulk separate of muscovite was obtained and a bulk separate of feldspar (4B1, HW40A, HW61B) or the whole rock (23.97, G9) used as the low Rb/Sr phase. The problem with the first approach, however, was that the analytical blank was often large in comparison to the sample size and the resultant errors on the isotopic analyses are also large. In the case of the second approach the data, though intriguing in some respects, are complex. At this stage it is difficult to judge whether this complexity is due to: (i) further undientified analytical problems; (ii) disequilibrium between whole rock/feldspar and bulk separates of mica or; (iii) a real feature of the cooling and deformation history of the terrain. For these reasons, the data have not been written up fully but the results are given here with some short discussion. Sample preparation varied for each sample and is described with the sample details below. Chemical and mass spectrometric techniques were as for garnet samples (see Appendix C). The results are summarised in Table H.1. Sr blanks were 123 ± 104 pg (n = 4) and had an average $^{87}Sr/^{86}Sr$ of 0.7155 ± 57. The blank constituted 0-4 percent of

the analysed sample and blank corrections were applied to all mineral separates. NBS 987 standards gave $^{87}Sr/^{86}Sr$ of 0.710317 ± 31 (2σ, n=16) in the period of analysis. The 2 sigma errors in Table H.1 are full propagated errors including the uncertainty on the individual mass spectrometric analysis, standard analyses and the blank correction. These uncertainties are mostly dominated by the uncertainty on the blank correction to the Sr isotope composition. The uncertainty on the Rb/Sr ratio was assumed to be 1% (2 sigma) for all samples.

*Samples*

**43/97**: MCTZ augen gneiss. K-feldspar augen wrapped by, and breaking down to, muscovite was cut into segments A-E, representing a rim to rim profile, from which an optically pure separate was obtained by hand picking under propanol with a binocular microscope. Muscovite was removed from the edges of the augen and purified as for the feldspar separates. wm A.2 is from adjacent to feldspar A.2 while the spatial relationship of Wm.1 to the augen is not known.

**23/97**: Lesser Himalayan calc-silicate. A bulk separate of muscovite was obtained from the whole rock by crushing with an agate pestle and mortar under propanaol. Final hand picking of micas was carried out under a binocular microscope. A whole-rock sample was used as the low Rb/Sr phase and obtained as for XRF analyses (see Appendix C).

**G9, 4B1, HW40A and HW61B**: HHCS gneiss and schists. Bulk separates of micas and feldspars were obtained from whole-rock crushates and purified under a binocular microscope. G9 and 4B1 have been previously described (see Chapter 4). HW40A and HW61B are both leucogranites from the Dhuali valley. HW40A is highly deformed with the development of ribbon textures, kinked muscovites and sericitised feldspars. HW61B is undeformed with large platy muscovites and sericitised feldspars.

*Discussion*

The ages calculated from the blank-corrected isotope data are sumarised in Table H.2. The Rb-Sr ages for micas scatter from 450 to 4.5 Ma and have some rather enigmatic features. However, there is a preponderance of ages around 10 Ma which may have some significance. The data are discussed briefly below:

The data for sample 43.97, from the augen gneiss in the MCTZ, are the most detailed and all the ages are around 9-10 Ma, regardless of the mineral pair used to do the calculation. In other words, the age recorded by the feldspar fractions and the two mica separates are the same. Moreover, the age of the rim of the feldspar augen relative to the mica separates is identical to that of the core. Such a coincidence of ages suggests that the last re-equilibration between these phases occurred at this time. *A priori*, mobility of Rb and Sr at around 10 Ma could be due to either temperature-activated volume diffusion or to deformation. In the former case, these data would imply continued high temperature conditions at or above the closure temperature for the Rb-Sr system in white mica (~550°C - eg. Inger 1998) in the MCTZ until 9-10 Ma. This possibility is in agreement with the observation that garnet in MCTZ rocks in Nepal apparently grew as late as 6 Ma (Catlos, 1999 #2123). On the other hand, rocks in the MCTZ are highly deformed and it is possible that deformation and mass transfer on small scales until 6-10 Ma led to the continued recrystallisation and isotopic re-equlibration of both the Rb-Sr system in feldspar and the Th-Pb system in monazite.

The data for the other samples are much more equivocal and scattered. Sample 23.97, from the Lesser Himalaya, was chosen because it exhibited the same deformational style as rocks from the MCTZ. However, the preserved age is clearly pre-Himalayan and suggests that the Rb-Sr system in this rock has not re-equilibrated since 450 Ma. Two of the other samples also yield ages close to 10 Ma - biotite in G9 and muscovite in HW61B. However, muscovite in G9 is much older than either biotite or garnet from this

rock at 37 Ma. Moreover, sample HW40A muscovite also yields a surprisingly old age of 48 Ma. The reason for these discepancies is unclear. In the case of G9 muscovite, the Rb/Sr of the white mica is not as high as for other white micas analysed here and, as a result, is much more prone to problems with correction of the initial Sr isotope composition. For G9 this correction was done with a whole rock, an approach that is open to problems with alteration by fluids. Note that the change in the whole rock isotope composition required for the white mica to yield a 10 Ma age does not shift the age of the biotite significantly due to the very high Rb/Sr ratio of the latter. White mica in HW40A, on the other hand, does have a high Rb/Sr yet still yields an old age.

Taken as a whole, the dataset in Table H.2 point tantalisingly to very young Rb-Sr ages (5-10 Ma) for the whole of the HHCS, but this conclusion cannot be verified without much further work. If these young ages do turn out to be robust for the whole of the HHCS, Ar-Ar ages for the upper HHCS of 16-20 Ma, suggesting cooling beneath 300-400°C at these times, then resetting of the Rb-Sr system in white mica would appear to be much more dependent on deformation than thermally-activated diffusion. In this context, apart from the muscovite age in G9 which may have problems with correction for initial Sr, the older ages for HW40A and 23.97 may simply be a reflection of the timing of the last ductile deformation leading to recrystallisation in these rocks.

*Table H.1 Summary of Rb-Sr Tims ID and isotope ratio analyses. ($^{87}Sr/^{86}Sr$)bc refers to blank corrected values.*

| Sample | Phase | [Sr] | [Rb] | $^{87}Rb/^{86}Sr$ | $^{87}Sr/^{86}Sr$ | 2 sigma | ($^{87}Sr/^{86}Sr$)bc | 2 sigma |
|---|---|---|---|---|---|---|---|---|
| 23.97 | WR | 103.6 | 3.693 | 0.103 | 0.712438 | 0.000031 | 0.712438 | 0.000031 |
| | Wm | 17.84 | 231.9 | 38.52 | 0.9586 | 0.0010 | 0.9601 | 0.0021 |
| 43.97 | Wm A.2 | 19.48 | 511.9 | 76.65 | 0.788979 | 0.000085 | 0.7907 | 0.0021 |
| | Fsp A.2 | 440.2 | 352.1 | 2.331 | 0.78011 | 0.00017 | 0.78040 | 0.00049 |
| | Fsp B.2 | 480.4 | 469.6 | 2.848 | 0.780978 | 0.000036 | 0.78105 | 0.00010 |
| | fsp C.2 | 514.9 | 368.1 | 2.083 | 0.781263 | 0.000036 | 0.78136 | 0.00013 |
| | fsp D.2 | 345.2 | 332.9 | 2.810 | 0.781147 | 0.000031 | 0.781220 | 0.000094 |
| | fsp E.2 | 482.0 | 999.8 | 6.046 | 0.781921 | 0.000031 | 0.781951 | 0.000048 |
| | Wm .1 | 28.17 | 690.0 | 71.44 | 0.78898 | 0.00022 | 0.7900 | 0.0013 |
| | Fsp D.1 | 457.3 | 144.7 | 0.922 | 0.781 | 0.011 | 0.781 | 0.011 |
| | Fsp E.1 | 609.7 | 294.1 | 1.406 | 0.780630 | 0.000031 | 0.78096 | 0.00041 |
| 4B1 | bi | 6.738 | 489.9 | 211.5 | 0.761645 | 0.000050 | 0.76186 | 0.00027 |
| | fsp | 474.8 | 7.425 | 0.0454 | 0.74843 | 0.00057 | 0.748442 | 0.000060 |
| G9 | WR | 83.34 | 151.77 | 5.302 | 0.771132 | 0.000028 | 0.771158♣ | 0.000028 |
| | wm | 47.12 | 338.1 | 20.90 | 0.779222 | 0.000031 | 0.779268 | 0.000064 |
| | bi | 1.633 | 568.5 | 1026 | 0.89387 | 0.00013 | 0.9014 | 0.0094 |
| HW40A | wm | 9.791 | 282.2 | 85.08 | 0.913048 | 0.000069 | 0.9143 | 0.0015 |
| | fsp | 15.28 | 61.60 | 11.84 | 0.860057 | 0.000040 | 0.8647 | 0.0058 |
| HW61B | wm | 16.39 | 319.8 | 56.70 | 0.74933 | 0.000175 | 0.74945 | 0.00023 |
| | fsp | 479.3 | 12.23 | 0.0741 | 0.741110 | 0.000031 | 0.741119 | 0.000033 |

♣ *Corrected to OU value standard*

*Table H.2 Summary of ages obtained from Rb-Sr analyses in Table H.1*

| Sample | Pair | Age (Ma) |
|---|---|---|
| 43.97♣ | wm.1 - fsp A.2 | 9.8 ± 1.4 |
| | wm.1 - fsp B.2 | 9.2 ± 1.4 |
| | wm.1 - fsp C.2 | 8.8 ± 1.4 |
| | wm.1 - fsp D.2 | 9.0 ± 1.4 |
| | wm.1 - fsp E.1 | 9.1 ± 1.4 |
| | wm.1 - fsp E.2 | 8.7 ± 1.4 |
| 23.97 | wm-WR | 453 ± 6 |
| 4B (1) | bt-fsp | 4.5 ± 0.1 |
| G9 | bt-WR | 9.0 ± 0.7 |
| | wm-WR | 36.6 ± 0.6 |
| HW61B | wm-fsp | 10.4 ± 0.3 |
| HW40A | wm-fsp | 48 ± 6 |

♣*Wm A.2 gives identical age*